

On the evolutionary pathways of stars and extrasolar planets

Thesis by
Trevor Justin David

In Partial Fulfillment of the Requirements for the
degree of
Doctor of Philosophy

The logo for the California Institute of Technology (Caltech), featuring the word "Caltech" in a bold, orange, sans-serif font.

CALIFORNIA INSTITUTE OF TECHNOLOGY
Pasadena, California

2017
Defended August 14, 2017

© 2017

Trevor Justin David
ORCID: 0000-0001-6534-6246

All rights reserved

In memory of Anita Naomi Cole and Alexander Cochran Davis
“Nan and Sandy”

ACKNOWLEDGEMENTS

It has been a privilege to work with my thesis advisor, Lynne Hillenbrand. The significance of any of the work that follows is owed entirely to her ability to identify relevant and timely problems to study. I am grateful for the latitude she has granted me in our various projects to pursue the aspects of the research that interested me most, as well as for her patience and sense of humor which have enabled us to work smoothly together. Her skepticism, pragmatism, and sociological wisdom have kept me on the right track and I look forward to working together in the future.

I am also grateful to the YSOVAR group, specifically Ann Marie Cody, Luisa Rebull, and John Stauffer, for welcoming me to their meetings and taking the time to share their expertise on various topics in stellar astrophysics. Their enthusiasm for all things pertaining to young stars has been an inspiration along this journey through the exquisite *K2* datasets. A number of other *K2* collaborators across the globe have provided me with helpful and thoughtful input, including Keivan Stassun, Ed Gillen, Suzanne Aigrain, and Andrew Collier Cameron.

Much of the science presented here was enabled through the gracious support of the California Planet Search collaboration, specifically Andrew Howard, Howard Isaacson, David Ciardi, B.J. Fulton, Evan Sinukoff, Ian Crossfield, and Josh Schlieder. Erik Petigura in particular has proven both a great friend and mentor, and I am indebted to him for the hours he has spent helping me to improve my capabilities as a scientist and deepening my understanding of how best to approach research problems in astronomy.

Many other postdocs, staff scientists, and faculty have provided mentorship or friendship in one form or another over the years, and it has been a pleasure working alongside this talented group of individuals. These include Sasha Hinkley, Björn Benneke, John Carpenter, Jessie Christiansen, Justin Crepp, Jean-Michel Désert, Jim Fuller, Shri Kulkarni, Wal Sargent, Nick Scoville, Avi Shporer, Ji Wang, and my thesis committee members Konstantin Batygin, Heather Knutson, Dimitri Mawet, and Chuck Steidel.

I have been most fortunate to be a graduate student during a time that the *K2* mission has been returning observations of unprecedented precision for hundreds of thousands of stars. My science relies on the public nature of these data, and I would be remiss not to thank P.I. Steve Howell, the *Kepler/K2* team, the engineers

at NASA and Ball Aerospace, and the U.S. taxpayers for their parts in giving the *Kepler* telescope a second life. Material support for my research has been provided by the NSF through the Graduate Research Fellowship Program.

There are plenty of logistics involved in acquiring new data, traveling to conferences to present results, and carrying out day-to-day research activities. Thankfully, I've been spared these burdens by the friendly and efficient administrators of Cahill, as well as the astronomers, telescope operators, engineers, and supporting staff at Keck and Palomar Observatories. I am also grateful to France Córdova for personally endowing research funds that enabled me to travel and present my work as a Neugebauer Fellow.

My interest in astrophysics likely would have remained just that if not for the many talented educators I've been fortunate to learn from over the years. In order of appearance: Joe Vaughan, Fred Chromey, Debbie Elmegreen, Allyson Sheffield, Jamie Lombardi, Jim Challey, Brian Daly, Richard Ellis.

Thanks are owed to my officemates for tolerating me over the years: Ryan Trainor, Swarnima Manohar, Matt Schenker, Marin Anderson, and, in particular, the first year group of Ben "Charlotte" Montet, Mislav "Samantha" Baloković, and Yi "Miranda" Cao. I would also like to thank the other members of my incoming class, for whom I have graciously waited to see off before finishing up myself: Antonija Oklopčić, Allison Strom, and Abhilash Mishra. We made it through graduate school with plenty of guidance from our forebears, particularly Gwen Rudie and Drew Newman.

Caltech is a place of characters, but a few denizens of Cahill stand out in particular. Sirio Belli for disagreeing with me on everything, every time. Matt Schenker for introducing me to the world of third strikes, fuel dumps, and manufactured spend. Mike Bottom for enlivening discussions about circlons, space mirrors, and other alternative astrophysical theories.

My friends from outside the realm of astronomy, especially those I've known since well before I started down this path, have kept me sane and grounded. These include Ross Fredella, Chino and Joyce Kim, Skylar Hughes, Ian Miller, Jason Tragani, and Matt Fox. I would also like to thank my teammates from the Outlaws of the Pasadena Bronze B ice hockey league for a spirited inaugural season, despite our 3-14-3 record.

I am incredibly fortunate to have the enduring support of my family. My mother, Kristin Davis, and father, Sami David, for their encouragement and for inspiring

this passion. It began, as best as I can remember, when my mother woke me in the middle of the night to watch a meteor shower from our backyard. To my brother, Zach, my sister, Ariana, her family David, Scarlett, and William, and to Diana, E.J., and Zachary: I am lucky to call you family and always look forward to the time we spend together. I am particularly thankful for my niece and nephew, who never fail to cheer me up. I would especially like to thank the nurses and doctors of White Plains Hospital for seeing my mother through a life-saving surgery and its complicated aftermath, particularly Drs. Waheeda Mithani, Kaare Weber, John Train, and Angie.

I've learned the most from and owe the most to Anhie Nguyen, who illuminated my path from the Mid Hudson Valley to the San Gabriel Valley. The work that follows would not have been possible without her support. My world is immeasurably larger because of her, and for that I am forever grateful.

Verses to the Vassar Dome

*A low-built tower and olden,
Dingy but dear to the sight
And they that dwell therein are wont
To watch the stars at night.*

–Antonia C. Maury

ABSTRACT

In this thesis, I present several studies aimed at determining the evolutionary states of stars and the planets that orbit them. Multiple approaches are undertaken to determine the physical parameters of stars over a wide range of masses, and in the process I evaluate current theoretical models which are commonly used to indirectly determine the properties of stars and planets.

Chapter II concerns the ages of nearby stars more massive than the Sun. These stars, because they are bright and young (<1 Gyr) on the average, constitute attractive targets for surveys aiming to directly capture light from planets in wide orbits. The precise masses of directly imaged companions are important for constraining star and planet formation theories, but rely critically on the host star ages. I show that sky-projected rotational velocity is a vital parameter in age-determination for intermediate-mass stars. Rapid rotation induces large pole-to-equator gradients in the photospheric temperature and surface gravity, such that a star seen pole-on appears hotter and higher gravity (and thus younger) than a star with identical properties seen edge-on. I use intermediate-band photometry centered on the hydrogen Balmer series and projected rotational velocities to determine atmospheric parameters and ages for approximately 3500 nearby stars with masses in the range of $1\text{--}10 M_{\odot}$. I validate the method using four open clusters, in the process finding ages for α Persei and the Hyades that are younger at ~ 70 Myr and older at ~ 830 Myr, respectively, than canonical values.

In Chapters III through V, I present orbital solutions and fundamental parameters for eclipsing binaries (EBs), newly discovered from the *K2* mission, in the Pleiades open cluster (125 Myr) and the Upper Scorpius OB association (5–10 Myr). EBs, particularly those in coeval stellar populations, are valuable benchmarks for evaluating evolutionary models. Such benchmarks are particularly rare at low masses and young ages, and my work has increased the sample by 80% at $M < 1 M_{\odot}$ and $\tau \lesssim 150$ Myr. By jointly fitting eclipse observations and radial velocity measurements, one can directly determine the masses and radii of stars in an EB with percent-level precision. I use newly determined masses and radii to demonstrate a systematic temperature offset of approximately 200 K between empirical relations and model predictions. This result is in agreement with literature on the temperature suppression observed in low-mass stars, believed to be related to magnetic activity and inhibited convection. I show that stellar ages determined from the mass-radius

diagram appear systematically older than those determined for the same stars in a Hertzsprung-Russell (H-R) diagram. A precise distance determination for the Pleiades EB HCG 76 is in agreement with the literature consensus and formally excludes the now discredited trigonometric measurement from *Hipparcos*. The orbital periods, eccentricities, and stellar spin periods determined from *K2* photometry are compared with theoretical expectations from tidal dissipation. In Chapter VI, I present preliminary results on more recently discovered EBs in Upper Scorpius, and updated interpretations of previously published systems. I use the combined data to pave the way for an empirical pre-main-sequence mass-radius relation over a broad range of masses and determine an age of Upper Scorpius which is intermediate to the canonical age (3–5 Myr, as derived from low-mass pre-main-sequence stars) and a more recent estimate (9–13 Myr, as derived from intermediate-mass stars) from H-R diagram analyses.

In Chapter VII, I present observations of the low-mass pre-main-sequence star RIK-210. This star shows a variable eclipse-like signature, which persisted through 78 days of *K2* photometry but was apparently absent in archival photometry. Follow-up observations demonstrate that RIK-210 is a single star with no massive companion orbiting at the period of the eclipse-like signature. The flux diminutions are in phase with the stellar rotation, behavior seen in some young stars that are periodically obscured by an accretion disk, but RIK-210 lacks such a protoplanetary disk. I consider various explanations for the observations and favor a model in which charged dust is trapped in a rigidly-rotating magnetosphere. The source of such dust could be from one or more close-in planets or residual planet-forming material drifting in towards the star.

In Chapter VIII I present the discovery and characterization of K2-33 b, a Neptune-sized planet closely orbiting a low-mass star in Upper Scorpius and one of the youngest exoplanets currently known. K2-33 b provides evidence that planets with substantial gaseous envelopes can be found close to their stars shortly after dispersal of the primordial protoplanetary disk. Given the planet's age (5–10 Myr), *in situ* formation or migration through the protoplanetary disk are the only plausible formation scenarios. K2-33 b is unusually large in size when compared to planets with similar orbital periods around low-mass field stars. I interpret this as tentative evidence that the planet is still contracting, experiencing photoevaporative atmospheric mass-loss, or both. In Chapter IX I present preliminary results from a study aimed at determining the prevalence of close-in planets at the epoch of primordial disk

dispersal. Using *K2* photometry for hundreds of pre-main-sequence stars in Upper Scorpius I search for transiting planets, assess survey completeness, and determine the occurrence rates or upper limits to such rates for large planets in close orbits around low-mass stars. With the singular detection of K2-33 b, I determine a rate of close-in Neptune- to Jupiter-sized planets higher than that for low-mass field stars but in closer agreement with the rate for sub-Neptune planets. Given the extreme youth of K2-33 b, I tentatively interpret these results as an indication that the planet is a progenitor of the abundant class of close-in sub-Neptunes.

Considered collectively, my results highlight the importance of benchmark systems. Nearly all branches of astrophysics are reliant in some regard on stellar evolutionary models, but the magnitude and sense of any particular systematic offset contained in these models is often poorly understood. Eclipsing binaries and planets located in stellar clusters provide firm anchors to theoretical models aiming to predict the evolution of such objects. The need for benchmarks and model calibration is particularly acute at young ages, when stars and planets are rapidly evolving and where theoretical evolutionary models are highly uncertain. While statistical studies of large populations can yield far-reaching results that move fields forward, it is the detailed characterization of individual systems that often reveal salient clues about the inaccuracies of assumptions underlying larger scale studies. Benchmark systems, whether they are clusters, eclipsing binaries, or well-characterized planets, offer the best path forward in refining our understanding of the evolution of stars and planets.

PUBLISHED CONTENT AND CONTRIBUTIONS

David, T. J., Petigura, E. A., Hillenbrand, L. A., et al., 2017, “A Transient Transit Signature Associated with the Young Star RIK-210,” *The Astrophysical Journal*, 835, 168, DOI: 10.3847/1538-4357/835/2/168,

T.J.D. discovered the periodic signal, organized collaborators, prepared the photometric data, performed key analysis steps, and led the manuscript writing.

David, T. J., Conroy, K. E., Hillenbrand, L. A., et al., 2016a, “New Pleiades Eclipsing Binaries and a Hyades Transiting System Identified by K2,” *The Astronomical Journal*, 151, 112, DOI: 10.3847/0004-6256/151/5/112,

T.J.D. participated in spectroscopic observations, performed the photometric and radial velocity fitting, and led the analysis and manuscript writing.

David, T. J., Hillenbrand, L. A., Cody, A. M., Carpenter, J. M., & Howard, A. W., 2016b, “K2 Discovery of Young Eclipsing Binaries in Upper Scorpius: Direct Mass and Radius Determinations for the Lowest Mass Stars and Initial Characterization of an Eclipsing Brown Dwarf Binary,” *The Astrophysical Journal*, 816, 21, DOI: 10.3847/0004-637X/816/1/21,

T.J.D. discovered the eclipsing binaries, participated in spectroscopic observations, performed the photometric and radial velocity fitting, and led the analysis and manuscript writing.

David, T. J., Hillenbrand, L. A., Petigura, E. A., et al., 2016c, “A Neptune-sized transiting planet closely orbiting a 5-10-million-year-old star,” *Nature*, 534, 658, DOI: 10.1038/nature18293,

T.J.D. discovered the planet, organized collaborators, prepared the photometric data, performed key analysis steps, and led the manuscript writing.

David, T. J., & Hillenbrand, L. A., 2015, “The Ages of Early-type Stars: Strömgren Photometric Methods Calibrated, Validated, Tested, and Applied to Hosts and Prospective Hosts of Directly Imaged Exoplanets,” *The Astrophysical Journal*, 804, 146, DOI: 10.1088/0004-637X/804/2/146,

T.J.D. assembled the stellar sample, developed the methodology, performed all analyses, and led the writing of the manuscript.

David, T. J., Stauffer, J., Hillenbrand, L. A., et al., 2015, “HII 2407: An Eclipsing Binary Revealed By K2 Observations of the Pleiades,” *The Astrophysical Journal*, 814, 62, DOI: 10.1088/0004-637X/814/1/62,

T.J.D. performed the photometric and radial velocity fitting, and led the analysis and manuscript writing.

TABLE OF CONTENTS

Acknowledgements	iv
Abstract	viii
Published Content and Contributions	xi
Table of Contents	xii
List of Illustrations	xviii
List of Tables	xlviii
Chapter I: Introduction	1
1.1 Stellar evolutionary models and the need for calibrators	1
1.1.1 Eclipsing binaries	2
1.1.2 Evaluating pre-main-sequence models of low-mass stars	6
1.1.3 Convection, magnetic fields, and starspots	7
1.1.4 Apparent age spreads, accretion histories, and coevality within binaries	9
1.1.5 Multiplicity effects	10
1.1.6 Tidal dissipation in binary stars	11
1.1.7 Young star variability studies in the age of <i>Kepler/K2</i>	13
1.2 Towards measuring planetary evolution and migration timescales	17
1.2.1 Inflated planetary radii at young ages?	22
1.2.2 The masses of directly imaged companions	23
1.2.3 The future of exoplanet science at young ages	26
Chapter II: The ages of early-type stars: Strömgren photometric methods calibrated, validated, tested, and applied to hosts and prospective hosts of directly imaged exoplanets	27
Abstract	28
2.1 Introduction	29
2.1.1 The Era of Direct Imaging of Exoplanets	29
2.1.2 The Age Challenge	31
2.1.3 Our Approach	33
2.2 The Strömgren Photometric System	34
2.2.1 Description of the Photometric System	34
2.2.2 Extinction Correction	36
2.2.3 Utility of the Photometric System	37
2.3 Determination of Atmospheric Parameters T_{eff} , $\log g$	37
2.3.1 Procedure	37
2.3.2 Sample and Numerical Methods	40
2.3.3 Rotational Velocity Correction	40
2.4 Calibration and Validation Using the HM98 Catalog	43
2.4.1 Effective Temperature	43
2.4.2 Surface Gravity	52

2.4.2.1	Comparison with Double-Lined Eclipsing Binaries	52
2.4.2.2	Comparison with Spectroscopic Measurements . . .	59
2.4.3	Summary of Atmospheric Parameter Uncertainties	60
2.5	Age Estimation from Isochrones	67
2.5.1	Selection of Evolutionary Models	67
2.5.2	Bayesian Age Estimation	69
2.5.2.1	Bayes Formalism	70
2.5.2.2	Age and Mass Prior Probability Distribution Func- tions	71
2.5.2.3	Numerical Methods	72
2.5.2.4	Age and Mass Uncertainties	72
2.6	The Methodology Tested on Open Clusters	73
2.6.1	Process	75
2.6.2	Results	76
2.6.2.1	Ages from Bayesian Inference	76
2.6.2.2	Ages from Isochrone Fitting	80
2.7	The Methodology Applied to Nearby Field Stars	80
2.7.1	Empirical Mass-Age Relation	87
2.7.2	Empirical Spectral-Type-Age/Mass Relations	87
2.8	Discussion	87
2.8.1	Methods Previously Employed in Age Determination for Early Type Stars	90
2.8.2	Stars Below the Main Sequence	91
2.8.3	Stars of Special Interest	92
2.8.3.1	Sun	92
2.8.3.2	HR 8799	93
2.8.3.3	β Pic	94
2.8.3.4	κ And	94
2.8.3.5	ζ Delphini	95
2.8.3.6	49 Ceti	95
2.9	Conclusions	96
Appendices	98
2.A	Metallicity Effects	98
2.B	Confidence Intervals	99
2.C	Open Cluster Tables	100
2.D	Alternative Treatment of Open Clusters	106
Chapter III: HII 2407: An eclipsing binary revealed by K2 observations of the Pleiades	109
Abstract	110
3.1	Introduction	111
3.2	K2 Observations and Analysis	111
3.3	HII 2407	113
3.4	Orbital Parameter Fitting	118
3.5	Discussion	123
3.6	Summary	126

Acknowledgments	127
Chapter IV: New Pleiades eclipsing binaries and a Hyades transiting system identified by K2	128
Abstract	129
4.1 Introduction	130
4.2 Data	132
4.2.1 K2 Photometry and Detrending	134
4.2.2 Photometric Colors	134
4.2.3 Spectroscopy	135
4.3 Analysis	136
4.3.1 Estimation of Primary Star Properties	137
4.3.2 Light Curve Modeling	137
4.4 Results	138
4.4.1 HCG 76	138
4.4.2 MHO 9 (BPL 116)	147
4.4.3 HD 23642	150
4.4.4 HII 2407	158
4.4.5 AK II 465	158
4.4.6 vA 50 (HAN 87)	160
4.5 Test of Model Isochrones at Pleiades Age	163
4.6 Summary and Conclusions	166
Acknowledgments	169
Appendices	170
4.A Model results for Pleiades non-member EB AK II 465	170
Chapter V: K2 discovery of young eclipsing binaries in Upper Scorpius: Direct mass and radius determinations for the lowest mass stars and initial characterization of an eclipsing brown dwarf binary	172
Abstract	173
5.1 Introduction	174
5.2 K2 Observations and Analysis	175
5.2.1 Light Curve Extraction	176
5.2.2 Detrending Procedure	177
5.3 Spectroscopic Observations and Analysis	179
5.4 Orbital Parameter Fitting	184
5.5 Overview of System and Primary/Secondary Parameter Estimation	186
5.6 Results and Discussion of Individual Eclipsing Binaries	187
5.6.1 EPIC 203710387	188
5.6.2 EPIC 203868608	194
5.6.3 EPIC 203476597	202
5.7 General Discussion	206
5.7.1 Comparing EPIC 203710387 and UScoCTIO 5	208
5.7.2 On the Age of Upper Scorpius	211
5.7.3 Coevality Within and Between Systems	213
5.7.4 Chromospheric Activity Effects	214
5.7.5 Triple Systems in Upper Sco	215

5.8 Conclusion	216
Acknowledgments	219
Appendices	232
5.A Revised Parameters for UScoCTIO 5	232
Chapter VI: A pre-main-sequence mass-radius relation and the age of Upper Scorpius from eclipsing binaries	236
6.1 Introduction	236
6.2 Observations	237
6.3 Discussion of individual systems	241
6.3.1 EPIC 204760247 / HD 142883 / HR 5934	241
6.3.2 EPIC 204506777 / HD 144548	246
6.3.3 EPIC 203476597	246
6.3.4 EPIC 204432860 / RIK-60 / USco 48	246
6.3.5 EPIC 205207894 / RIK-72	252
6.3.6 EPIC 202963882	254
6.3.7 EPIC 205030103 / UScoCTIO 5	254
6.3.8 EPIC 203868608	255
6.3.9 EPIC 203710387	257
6.4 Pre-main-sequence evolution of intermediate-mass stars	259
6.5 The age of Upper Scorpius from eclipsing binaries	260
Chapter VII: A transient transit signature associated with the young star RIK-210264	
Abstract	265
7.1 Introduction	266
7.2 RIK-210	266
7.2.1 Stellar properties	267
7.2.2 Activity and Possible Disk	267
7.3 <i>K2</i> Light Curve and Analysis	269
7.3.1 Stellar variability fit	273
7.3.2 Periodicity	273
7.3.3 Ephemeris	274
7.3.4 Durations	274
7.3.5 Size of occulting material	275
7.3.6 Dip morphology	276
7.3.7 Bursts, Flares, and Starspots	276
7.3.8 Light curve parameterization	278
7.3.9 Short duration, shallow flux dips	285
7.4 Archival and follow up photometric monitoring	286
7.5 Spectroscopic Observations	289
7.5.1 Secondary line search	289
7.5.2 Projected rotational velocity	291
7.5.3 Radial velocities	291
7.5.4 Line profile variations	294
7.6 High-resolution Imaging	295
7.7 Discussion	297
7.7.1 Rotational modulation of high-latitude spots?	299

7.7.2	Eclipses of an accretion hotspot?	300
7.7.3	Eclipses of prominences?	301
7.7.4	Transits of magnetospheric clouds?	301
7.7.5	Obscuration by a circumstellar disk?	302
7.7.6	A co-rotating dust component?	304
7.7.7	Boil-off of a protoplanet atmosphere?	308
7.7.8	Tidal disruption of a planet?	308
7.7.9	Transits of an enshrouded protoplanet?	309
7.7.10	Significance of the corotation radius	312
7.7.11	Uniqueness of RIK-210	313
7.8	Conclusions	314
	Acknowledgments	316
	Chapter VIII: A Neptune-sized transiting planet closely orbiting a 5-10- million-year-old star	317
	Abstract	318
8.1	Methods	323
8.1.1	Stellar Membership and Properties.	323
8.1.2	Stellar Rotation and Independent Assessment of the Stellar Radius.	327
8.1.3	K2 Time Series Photometry Treatment.	327
8.1.4	Transit Model Fitting Analysis.	328
8.1.5	High Spectral Resolution Observations and Radial Velocities.	329
8.1.6	Limits on Companions from the Spectroscopic Data.	329
8.1.7	High-resolution Imaging.	330
8.1.8	Non-redundant Aperture Masking.	330
8.1.9	Limits on Companions from the Imaging Data.	331
8.1.10	Galactic Structure Model and Intracluster Contamination.	332
8.1.11	False Positive Probability Analysis.	333
8.1.12	Implications of Hierarchical Triple Scenarios.	333
8.1.13	Cluster Age.	334
8.1.14	K2-33 b in the Context of Other Claimed Young Planets.	335
	Chapter IX: The occurrence of close-in planets at the epoch of primordial disk dispersal	340
	Abstract	341
9.1	Introduction	342
9.2	Sample Selection	343
9.2.1	Proper motion analysis	345
9.2.2	Color-magnitude cuts	348
9.2.3	Disk-hosting stars	349
9.2.4	Stellar multiplicity	349
9.2.5	Crowded fields	351
9.2.6	Final selection scheme	352
9.2.7	Stellar characterization	352
9.3	Survey design	355
9.3.1	Aperture photometry and instrumental systematics corrections	355

9.3.2	Transit search pipeline	358
9.3.3	Manual vetting	359
9.3.4	Transit injection and recovery tests	359
9.3.5	Survey completeness	360
9.4	Determination of planet occurrence rates	366
9.4.1	Expected planet yields	369
9.5	Discussion	370
	Acknowledgments	372
	Bibliography	373

LIST OF ILLUSTRATIONS

<i>Number</i>	<i>Page</i>
1.1 Reproduction of Figure 2 from Wyatt (2008). The disk frequency, i.e. fraction of stars hosting protoplanetary disks, within stellar associations of different ages. The time available for forming planets with substantial gaseous envelopes is set by the protoplanetary disk dispersal timescale. Ages of young associations are typically derived from H-R diagram analyses using evolution models that are largely uncalibrated and contain systematic offsets.	2
1.2 Isochrones in the mass-radius plane. Solid and dashed curves are predictions from the solar metallicity MIST isochrones (Choi et al., 2016; Dotter, 2016) and BHAC15 (Baraffe et al., 2015) models, respectively. Stars with masses $M \lesssim 1.5 M_{\odot}$ contract monotonically towards the main sequence. The onset of nuclear reactions stalls contraction for higher mass stars and temporarily causes an increase in radius prior to settling on the MS, leading to the prominent “bump” in the mass-radius diagram. High-mass stars quickly evolve away from the MS, increasing in radius again after several Myr. This post-MS evolution at high masses is clearly demonstrated by the 50 and 100 Myr isochrones but for clarity the 1 Gyr isochrone is limited to stars less massive than $1.5 M_{\odot}$. Overplotted are double-lined EBs in young stellar associations (large shaded points) and in the field (white points). The field EB parameters are taken from the DEBCat compilation maintained by John Southworth.	5
1.3 Reproduction of Figure 10 from Mann et al. (2017). Sizes of transiting planets around low-mass stars as a function of host star mass (left) and incident flux (right). Only planets transiting host stars less massive than $0.65 M_{\odot}$ and with orbital periods <30 d are included. Young planets discovered from <i>K2</i> data are indicated by stars while field planets are shown as points. ©AAS. Reproduced with permission.	23

- 1.4 Reproduction of Figure 6 from Bowler (2016). Orange, green, and blue curves show theoretical predictions for the temporal evolution of luminosity of low-mass stars ($>80 M_{\text{Jup}}$), brown dwarfs ($14\text{--}80 M_{\text{Jup}}$), and planetary-mass companions ($<14 M_{\text{Jup}}$) respectively. Points represent directly imaged companions in either the planetary (blue) or brown dwarf (green) mass regimes. Large errors in the ages of host stars translate into large uncertainties in model-derived companion masses. The prevalence of directly imaged companions (i.e. extreme mass ratio companions at large orbital separations) has implications for star and planet formation theories. ©The Astronomical Society of the Pacific. Reproduced with permission. 24
- 2.1 *Top panels:* Evolution of $\log T_{\text{eff}}$ and $\log g$ with age for intermediate-mass stars, as predicted by PARSEC evolutionary models (Bressan et al., 2012). *Bottom panels:* Same evolutionary trends for $B - V$ (close to $b - y$) and M_V mag, as might be used to discern ages from color-magnitude diagram evolution (e.g. Nielsen et al., 2013). While the color and temperature trends reflect one another, the absolute magnitude trends are not as strong as the surface gravity trends when the stars are evolving from the main sequence after a few hundred Myr. The PARSEC models predict the precision in $\log g$ needed to distinguish a $1.5M_{\odot}$ star and a $2.0M_{\odot}$ star evolves from 0.0397 dex at ~ 30 Myr to 0.0242 dex at 100 Myr to 0.0378 dex at ~ 300 Myr. The precision in $\log g$ needed to distinguish a $1.5M_{\odot}$ star and a $3.0M_{\odot}$ evolves from 0.0085 dex at ~ 30 Myr to 0.0694 dex at 100 Myr to 0.5159 dex at ~ 300 Myr. The precision in $\log g$ needed to distinguish a $2.0M_{\odot}$ star and a $3.0M_{\odot}$ evolves from 0.0312 dex at ~ 30 Myr to 0.0936 dex at 100 Myr to 0.4781 dex at 300 Myr. 32
- 2.2 The $u, v, b, y, H\beta_{\text{wide}}$ and $H\beta_{\text{narrow}}$ passbands. Overplotted on an arbitrary scale is the synthetic spectrum of an A0V star generated by Munari et al. (2005) from an ATLAS9 model atmosphere. The $uvby$ filter profiles are those of Bessell (2011), while the $H\beta$ filter profiles are those originally described in Crawford (1966) and the throughput curves are taken from Castelli & Kurucz (2006). 34

- 2.3 *Top:* Three relevant $uvby\beta$ spaces for atmospheric parameter determination of our sample of BAF stars with $uvby\beta$ photometry in the HM98 catalog, and located within 100 pc of the Sun. Two stars were excluded from these figures for favorable scaling: Castor, which is an outlier in all three planes ($\beta < 2.4$, $a_0 > 1$, $b - y > 0.6$), and HD 17300, a poorly studied F3V star with $b - y > 0.6$. *Bottom:* The same plots as above, with the model color grids of Castelli & Kurucz (2006) and Castelli & Kurucz (2004) overlaid in the relevant regions of parameter space. The lines of constant T_{eff} (largely vertical) and of constant $\log g$ (largely horizontal) are annotated with their corresponding values. Some outliers have been pruned, and irrelevant groups of stars eliminated, for clarity in this second plot. 38
- 2.4 Vectors showing the magnitude and direction of the rotational velocity corrections at 100 (black), 200, and 300 (light grey) km s^{-1} for a grid of points in $\log(T_{\text{eff}})$ - $\log g$ space, with PARSEC isochrones overlaid for reference. While typical A-type stars rotate at about 150 km s^{-1} , high-contrast imaging targets are sometimes selected for slow rotation and hence favorable inclinations, typically $v \sin i < 50 \text{ km s}^{-1}$ or within the darkest black vectors. For rapid rotators, a 100% increase in the inferred age due to rotational effects is not uncommon. 41
- 2.5 *Top:* Comparison of the temperatures derived from the ATLAS9 $uvby\beta$ color grids (T_{uvby}) and the fundamental effective temperatures (T_{fund}) taken from B13 and N93. *Bottom:* Ratio of $uvby\beta$ temperature to fundamental temperature, as a function of T_{uvby} . For the majority of stars, the $uvby\beta$ grids can predict T_{eff} to within $\sim 5\%$ without any additional correction factors. 45

- 2.6 Ratio of the $uvby\beta$ temperature to fundamental temperature as a function of $v \sin i$, for the late (left), intermediate (middle), and early (right), group stars. The solid horizontal colored lines indicate the mean ratios in each case. The arrows represent both the magnitude and direction of change to the ratio T_{uvby}/T_{fund} after applying the FB98 rotation corrections. The dashed horizontal colored lines indicate the mean ratios after application of the rotation correction. The rotation correction appears to improve temperature estimates for early group stars, but worsen estimates for the late and intermediate groups. Notably, however, the vast majority of T_{eff} standards are slowly rotating ($v \sin i < 150 \text{ km s}^{-1}$). Note one rapidly rotating intermediate group star extends beyond the scale of the figure, with a rotation corrected T_{uvby}/T_{fund} ratio of ≈ 1.26 46
- 2.7 Ratio of the $uvby\beta$ temperature to fundamental temperature as a function of $[\text{Fe}/\text{H}]$. There is no indication that the grids systematically overestimate or underestimate T_{eff} for different values of $[\text{Fe}/\text{H}]$ 47
- 2.8 Comparison of the $uvby\beta$ derived $\log g$ values with fundamental values for the primary components of the double lined eclipsing binaries compiled in Torres et al. (2010). Red, teal, and black points represent late, intermediate, and early group stars, respectively. In each case the solid colored line represents the mean of the residuals, $\Delta \log g$ (in the sense of fundamental- $uvby\beta$). As can be seen, the mean offsets for the late and early groups is negligible. For the intermediate group, however, while only five stars were used for calibration, the $uvby\beta$ $\log g$ values are about 0.13 dex lower than the fundamental values on average. 53

- 2.9 Surface gravity residuals, $\Delta \log g$ (in the sense of fundamental- $uvby\beta$), as a function of $uvby\beta$ -determined $\log(T_{\text{eff}})$ (left) and $\log g$ (right). Solid points represent eclipsing binary primaries from Torres et al. (2010) and open circles are stars with spectroscopic $\log g$ determinations in N93. Of the 39 eclipsing binaries, only six have residuals greater than 0.2 dex in magnitude. This implies that the $uvby\beta$ grids determine $\log g$ to within 0.2 dex of fundamental values $\sim 85\%$ of the time. Surface gravity residuals are largest for the cooler stars. Photometric surface gravity measurements are in better agreement with spectroscopic determinations than the eclipsing binary sample. There is no indication for a global systematic offset in $uvby\beta$ -determined $\log g$ values as a function of either T_{eff} or $\log g$ 54
- 2.10 Surface gravity residuals, $\Delta \log g$ (in the sense of fundamental- $uvby\beta$), of eclipsing binary primaries as a function of $v \sin i$. Arrows indicate the locations of points after application of the Figueras & Blasi (1998) $v \sin i$ correction, where in this case late group stars received the same correction as the intermediate group. 55
- 2.11 Surface gravity residuals, $\Delta \log g$ (in the sense of fundamental- $uvby\beta$), as a function of $[\text{Fe}/\text{H}]$. The metallicity values have been taken primarily from Ammons et al. (2006), with additional values coming from Anderson & Francis (2012). While metallicities seem to exist for very few of the surface gravity calibrators used here, there does not appear to be a systematic trend in the residuals with $[\text{Fe}/\text{H}]$. There is a larger amount of scatter for the more metal-rich late-type stars, however the scatter is confined to a relatively small range in $[\text{Fe}/\text{H}]$ and it is not clear that this effect is due to metallicity effects. 55
- 2.12 Distributions of the true variations in T_{eff} (left) and $\log g$ (right) caused by our assumption of solar metallicity. The “true” T_{eff} and $\log g$ values are determined for the $\sim 68\%$ of our field star sample with $[\text{Fe}/\text{H}]$ measurements in XHIP and from linear interpolation between the set of atmospheric parameters determined in eight ATLAS9 grids (Castelli & Kurucz, 2006; Castelli & Kurucz, 2004) that vary from -2.5 to 0.5 dex in $[\text{M}/\text{H}]$ 64

- 2.13 The effect of interstellar reddening on atmospheric parameters derived from $uvby\beta$ photometry. The isochrones and mass tracks plotted are those of Bressan et al. (2012). The tail of each vector represents a given point in a specific photometric plane ($(b - y) - c_1$ for the late group stars in red, $a_0 - r^*$ for the intermediate group stars in teal, and $c_1 - \beta$ for the early group stars in black) and its corresponding value in $[T_{\text{eff}}, \log g]$. The tip of the vector points to the new value of $[T_{\text{eff}}, \log g]$ after each point in photometric space has been “dereddened” assuming arbitrary values of A_V . The shifts in $uvby\beta$ space have been computed according to the extinction measurements of Schlegel et al. (1998) and Crawford & Mandwewala (1976), assuming $A_V \simeq 4.237E(b - y)$. The magnitudes of A_V chosen for this figure represent the extremes of values expected for our sample of nearby stars and are meant to illustrate the directionality of the effects of reddening as propagated through the $uvby\beta$ planes. Finally, note for the early group (black vectors), the A_V values are an order of magnitude larger and much higher than expected for our sample. Again, this is to illustrate the directionality of the reddening effect, which is particularly small for the early group which rely on c_1 , the Balmer discontinuity index, for temperature, and β , a color between two narrow-band filters with nearly the same central wavelength, for $\log g$ 65
- 2.14 Comparison of PARSEC isochrones (solid lines), Ekström isochrones in the rotating case (dashed lines), and Ekström isochrones in the non-rotating case (dotted lines). The solid black lines are evolutionary tracks for stars of intermediate-mass, from the PARSEC models. All evolutionary tracks plotted are for solar metallicity. 67
- 2.15 Histograms of the visual extinction, A_V , in magnitudes for individual members of the four open clusters considered here. The extinction values are calculated using the relation $A_V = 4.237E(b - y)$, with the $(b - y)$ color excesses computed as described in § 2.2.2. 73

2.16 PARSEC isochrones and mass tracks (Bressan et al., 2012) in $\log T_{\text{eff}}$ - $\log g$ space and the isochrones of Ekström et al. (2012) (including rotation, plotted as dashed lines) with our $uvby\beta$ photometric determinations of the atmospheric parameters. For early and intermediate group stars, the black filled circles represent the $v \sin i$ corrected atmospheric parameters (using the FB98 formulae), while the open circles represent the uncorrected parameters. Note that the late-group stars do not receive a $v \sin i$ correction but are still plotted as filled circles. In both cases the point sizes are $\propto v \sin i$. The typical uncertainties in our $\log T_{\text{eff}}$ and $\log g$ determinations are represented by the error bars at the bottom of the figure. These uncertainties correspond to 1.6% or ≈ 0.007 dex in $\log T_{\text{eff}}$ and 0.091 dex (intermediate), and 0.145 dex (late) in $\log g$, corresponding to the RMS errors as determined in the effective temperature and surface gravity calibrations. *Top left:* IC 2602 members; the currently accepted age of IC 2602 is $\tau = 46^{+6}_{-5}$ Myr (Dobbie et al., 2010). *Top right:* Members of the α Persei cluster, which has a currently accepted age of $\tau = 90 \pm 10$ Myr (Stauffer et al., 1999). *Bottom left:* Pleiades members where the currently accepted age of the Pleiades is $\tau = 125 \pm 8$ Myr Stauffer et al., 1998. Of the ~ 20 Pleiads that sit below the zero age main sequence, 5 are known pulsators of the δ Scu or γ Dor variety. Additionally, there is an excess of slow rotators sitting below the ZAMS. Possible reasons for this observed behavior include systematics of the atmospheric models (several authors have noted problems with the treatment of convection in ATLAS9 models at this mass range), failure of the evolutionary models to predict the true width of the main sequence (though this effect is unlikely to be as large as the scatter seen here), and overaggressive dereddening procedures. *Bottom right:* Hyades cluster members where the currently accepted age of the Hyades is $\tau = 625 \pm 50$ Myr Perryman et al. (1998). Note the far left outlier, HD 27962, is a known blue straggler (Abt, 1985; Eggen, 1995) and was excluded by Perryman et al. (1998) in their isochrone-fitting analysis. The outlier far below the ZAMS, HD 27268, is a spectroscopic binary (Debernardi et al., 2000). 74

- 2.17 *Left panels:* 1D marginalized, normalized posterior PDFs in age, calculated from Bressan et al. (2012) evolutionary models, for individual open cluster members. Black, teal, and red histograms represent early, intermediate, and late group stars, respectively. *Middle panels:* Sums of the individual PDFs depicted on the left. This figure shows the total probability associated with the 200 age bins between $\log(\text{age/yr})=6.5$ to 10. The grey shaded regions indicate the currently accepted ages of IC 2602 (46_{-5}^{+6} Myr), α Per (90 ± 10 Myr), the Pleiades (125 ± 8 Myr), and the Hyades (625 ± 50 Myr). *Right panels:* Products of the individual PDFs depicted in the left panels. The grey shaded regions again depict the accepted literature age ranges of each cluster. 78
- 2.18 Best fitting isochrones found through χ^2 -minimization for four open clusters, with atmospheric parameters determined through $uvby\beta$ photometry. Left panels are the fully rotating Ekström et al. (2012) evolutionary models while right panels are the Bressan et al. (2012) models. For the Pleiades, the best fitting isochrone age (126 Myr) from the E12 models is within the currently accepted range of 125 ± 8 Myr. The B12 models give a best-fit age of 115 Myr, representing a fractional error of $\sim 8\%$ (or 1.25σ) relative to the accepted age. In the case of the Hyades (lower panels), the low and far left outliers are a spectroscopic binary and a blue straggler, respectively. Excluding these stars yields no change in the best-fitting isochrone for the E12 models and only moderately increases the best-fitting B12 model to 530 Myr. 81

- 2.19 Characterization of our sample of 3499 nearby field stars. *Upper panels:* histograms of the spectral types (left) and distances (right) of stars in our sample, taken from Anderson & Francis (2012). *Middle panels:* histograms of the V-band extinction in magnitudes (left), as derived by the IDL program described in § 2.2.2, and the [Fe/H] values in dex from Anderson & Francis (2012). *Lower panels:* histogram of the projected rotational velocities in our sample (left), with data taken from Glebocki & Gnacinski (2005), and $v \sin i$ as a function of spectral type (right) with grey x's indicating individual stars and black squares representing the mean $v \sin i$ in each spectral type bin. The error bars represent the standard deviation in $v \sin i$ values for each bin. The red triangles indicate the empirical $T_{\text{eff}}-v \sin i$ relation of Gray (2005) using the spectral-type- T_{eff} relation of Habets & Heintze (1981). 82
- 2.20 Histograms of the uncertainties (in mag) for different $uvby\beta$ indices for the sample of ~ 3500 field stars discussed in § 2.7. The solid lines in each plot indicate the position of the mean uncertainty in that parameter. Uncertainties in a_0 and r^* are calculated according to Eqns. (13) & (14). 83
- 2.21 H-R diagram for our sample of B0-F5 field stars within 100 pc. Thirteen stars with $\log g < 2.9$ are excluded in this figure. Several stars of interest are plotted in gold. As before, red, teal, and black scatter points correspond to late, intermediate, and early group stars, respectively. Values for the Sun are also plotted for reference. Of note, ~ 770 of the stars plotted are subgiants according to their XHIP luminosity classes, while only ~ 250 stars have $\log g < 3.8$, suggesting some spectral types are in error. 83

- 2.22 Normalized composite age PDFs for our sample of field B0-F5 stars within 100 pc. The normalized composite PDFs are created by summing the normalized, 1D marginalized age PDFs of individual stars in a given spectral type grouping. The black curve represents the composite pdf for all spectral types, while the colored curves represent the composite PDFs for the spectral type groups B0-B9, A0-A4, A5-A9, F0-F5 (see legend). Circles represent the expectation values of the composite PDFs, while squares represent the medians. The solid and dashed lines represent the 68% and 95% confidence intervals, respectively, of the composite PDFs. The statistical measures for these composite PDFs are also presented in Table 2.6. 88
- 2.23 Empirical spectral-type-age relation (left) and spectral-type-mass relation (right) for solar neighborhood B0-F5 stars. Grey x's represent individual stars, while the black scatter points represent the mean value in a given spectral type bin and the error bars represent the scatter in a that bin. 88
- 2.24 Comparison of ages for BAF field stars derived through 2D linear interpolation and Bayesian inference. Grey points represent those stars with $\Delta \log \text{age}/\text{yr} > 1$ (in the sense of Bayesian minus interpolated), which coincide with the same stars that reside below the MS. 92
- 2.25 2D joint posterior PDFs in age and mass for an early-type star with typical atmospheric parameter uncertainties (*left*) and the Sun (*right*), for which T_{eff} and $\log g$ are known to high precision. The dark, medium, and light blue shaded regions indicate the 68%, 95%, and 99% confidence contours. Above, 1D marginalized and normalized posterior PDF in age, with the shaded regions representing the same corresponding confidence intervals. Right, the same as above for mass. 93
- 2.26 Comparison of ATLAS9 color grids for different metallicities. 99

- 2.27 The effect of metallicity on $uvby\beta$ determinations of temperature, as predicted by model grids of Castelli & Kurucz (2006) and Castelli & Kurucz (2004). In the left-most figure, for given values of T_{eff} , or $(b - y)$, the ratio of the temperature given by the grid of metallicity $[M/H]=-0.5$ to the solar metallicity grid is depicted in the top panel. The bottom panel shows the ratio of the temperature given by a grid of metallicity $[M/H]=+0.5$ to the temperature given by the solar metallicity grid. In the temperature range of interest ($\approx 6500\text{K}$ - 8500K , or spectral types F5-A4), a shift of 0.5 dex in $[M/H]$ can produce variations up to $\sim 1\%$ in T_{eff} , with the smallest discrepancies occurring at approximately the F0-A9 boundary. The middle figure is analogous to the left figure, for the $a_0 - r^*$ grids which are used for stars between $\approx 8500\text{K}$ - 11000K (A3-B9). In this regime, shifts of 0.5 dex in metallicity can produce variations up to $\sim 2\%$ in temperature. Finally, for the hottest stars ($T_{\text{eff}} > 11000\text{ K}$, spectral types B9 and earlier), a 0.5 dex shift in metallicity can produce variations up to $\sim 6\%$ in effective temperature. 99
- 2.28 The effect of metallicity on $uvby\beta$ determinations of surface gravity, as predicted by model grids of Castelli & Kurucz (2006) and Castelli & Kurucz (2004). In the left-most figure, for given values of $\log g$, or c_1 , the ratio of the temperature given by the grid of metallicity $[M/H]=-0.5$ to the solar metallicity grid is depicted in the top panel. The bottom panel shows the ratio of the temperature given by a grid of metallicity $[M/H]=+0.5$ to the temperature given by the solar metallicity grid. In the temperature range of interest ($\approx 6500\text{K}$ - 8500K , or spectral types F5-A4), a shift of 0.5 dex in $[M/H]$ can produce variations up to ~ 0.1 dex in $\log g$. The middle figure is analogous to the left figure, for the $a_0 - r^*$ grids which are used for stars between $\approx 8500\text{K}$ - 11000K (A3-B9). In this regime, the gravity indicator r^* is particularly insensitive to metallicity, with shifts of 0.5 dex in metallicity producing variations of only ~ 0.05 dex or less in $\log g$. Finally, for the hottest stars ($T_{\text{eff}} > 11000\text{ K}$, spectral types B9 and earlier), a 0.5 dex shift in metallicity can produce variations up to ~ 0.1 dex in $\log g$ 100

- 2.29 *Left panels:* 1D marginalized, normalized posterior PDFs in age, calculated from Bressan et al. (2012) evolutionary models, for individual open cluster members. Black, teal, and red histograms represent early, intermediate, and late group stars, respectively. *Middle panels:* Sums of the individual PDFs depicted on the left. This figure shows the total probability associated with the 200 age bins between $\log(\text{age}/\text{yr})=6.5$ to 10. The grey shaded regions indicate the currently accepted ages of IC 2602 (46_{-5}^{+6} Myr), α Per (90 ± 10 Myr), the Pleiades (125 ± 8 Myr), and the Hyades (625 ± 50 Myr). *Right panels:* Products of the individual PDFs depicted in the left panels. The grey shaded regions again depict the accepted literature age ranges of each cluster. 107
- 3.1 Top panel: Systematics corrected *K2* SAP light curve with our GP stellar variability fit in orange. Observations circled in red were excluded from the variability fit. Bottom panel: Corrected light curve obtained from dividing out the variability fit and excluding outliers. 113
- 3.2 Systematics-corrected *K2* light curve phase-folded on the orbital period (top) and on the rotational period (bottom). Points are colored according to the time of observation. Rotational modulation of starspots is clearly demonstrated. The variable amplitude of the spot signature suggests a changing spot fraction. Though the eclipses are clearly not in phase with the rotational period, we discuss in § 7.7 the likelihood that the system is tidally synchronized with the difference in spot and orbital periods due to a latitudinal gradient in the rotation rate. 117
- 3.3 Best-fit JKTEBOP model to the *K2* photometry (top panels) and the Mermilliod et al. (1992) radial velocities (bottom panel). For each panel the residuals of the best fit model are plotted below. Measurement uncertainties in the top left and bottom panels are smaller than the points themselves. The increased scatter seen in primary eclipse is potentially due to spot activity and/or artifacts from the *Kepler* data reduction pipeline. The horizontal dashed line in the bottom panel indicates the best-fit systemic radial velocity. 120

- 3.4 Isochrones in the mass-radius plane with the components of HII 2407 and benchmark EBs from Torres et al. (2010) overplotted. From left to right, the evolutionary models depicted are from Siess et al. (2000), Baraffe et al. (2015), and Bressan et al. (2012). All models plotted are for solar metallicity ($Z=0.02$). Unlike the Torres et al. (2010) sample, the masses and radii of the HII 2407 components are model-dependent. 125
- 4.1 *K2* Campaign 4 pointing (grey) with observed Pleiades and Hyades members overlaid. Eclipsing or transiting systems discussed in this paper are indicated by pink points. 131
- 4.2 V vs $V - K_s$ photometric color magnitude diagram for the observed known members of the Pleiades (left) and Hyades (right) clusters. The red highlighted points are the EBs reported in this paper. 135
- 4.3 Top panel: The systematics corrected *K2* light curve for HCG 76 with our variability fit indicated by the orange curve. Outlier points excluded from this fit are marked by the red circles. Bottom panel: The rectified light curve, from dividing out the variability fit above, upon which we performed our fitting procedure. In both panels the gray shaded region highlights a portion of the light curve that is poorly modeled by the variability fit, leading to the introduction of systematics in the rectified light curve. 139
- 4.4 Lomb-Scargle periodogram of the variable light curve for HCG 76 (left) and the *K2* light curve for the object phase folded on the two strong rotational periods detected in the periodogram (middle and right panels). Outliers (both flares and eclipses) have been removed from the light curves in these figures for the purposes of illustrating the sinusoidal rotation signals. 139
- 4.5 Best-fit JKT_{EBOP} model to the *K2* photometry (top) and Keck/HIRES RVs (bottom) for HCG 76. 142

- 4.6 The positions of HCG 76 components relative to BHAC15 isochrones in the mass-radius plane (left), $T_{\text{eff}} - \log g$ plane (middle), and $T_{\text{eff}} - \log L/L_{\odot}$ plane (right). Square points represent best-fit values and errorbars indicate $1-\sigma$ uncertainties. We assumed 100 K uncertainties in the temperatures and propagated these through in determining the luminosity uncertainties. The two components are consistent within error of being coeval in the mass-radius plane at ~ 100 Myr, though they appear younger in the $T_{\text{eff}} - \log g$ plane. The luminosities calculated from the Stefan-Boltzmann law, the measured radii, and photometric temperatures, are significantly larger than the model predictions. 143
- 4.7 BHAC15 isochrones in the mass-temperature, radius-temperature, mass-luminosity, and radius-luminosity planes (clockwise from upper left panel) compared to the derived parameters for the HCG 76 components. In each panel, the dashed line indicates the 120 Myr isochrone shifted by 200 K towards cooler effective temperatures (or the luminosities resulting from such a shift). 144
- 4.8 Detrended normalized light curve for MHO 9 (BPL 116). The full unphased light curve is shown on the left with the phased light curve zoomed in on the primary eclipse shown on the right. 148
- 4.9 Lomb-Scargle periodogram for the systematics corrected light curve of MHO 9 (left), phased at the inferred rotation period (right). Eclipses are excluded in the scaling of this figure for clarity. 148
- 4.10 JKTEBOP fit to the *K2* light curve and RVs for MHO 9. The RV point near phase of 0.3 (corresponding to the UT 2016-01-24 observation) was not included in this analysis but is entirely consistent with our best fit. 149
- 4.11 Top panels: *K2* PDC SAP light curve for HD 23642 phase folded on the orbital period of ≈ 2.46 days, with the best-fit JKTEBOP model plotted in orange. Bottom panel: Literature radial velocities from Munari et al. (2004) and Groenewegen et al. (2007) with the best-fit JKTEBOP models indicated by the red and blue curves. In each panel the best-fit residuals are plotted below. 153
- 4.12 The complete *K2* light curve for HD 23642, phase folded on the best period and showing the best-fit JKTEBOP model in orange. The best fit residuals are plotted below. 154

- 4.13 PARSEC v1.2S 120 Myr isochrones (Bressan et al., 2012; Chen et al., 2015) in the mass-radius plane, of different metallicities. Several direct determinations of the masses and radii of the double-lined EB HD 23642 from the literature are indicated, along with our new determinations from the highly precise *K2* light curve and literature RVs. 155
- 4.14 Lomb-Scargle periodogram (left) and *K2* PDC light curve phase folded on the favored rotation period of vA 50 (right). The other significant peak in the periodogram is at the half-period alias. 161
- 4.15 Measured RVs of vA 50 (HAN 87, EPIC 210490365) folded on the two possible periods of ~ 3.48 and ~ 6.97 days, respectively. RVs from Mann et al. (2016b) are plotted with green circles while our reported RVs are plotted with blue squares. The dashed horizontal lines represent the median velocity of all RVs and is therefore assumed as the systemic velocity. The red curve represents a circular orbit with an amplitude of 0.3 km/s. This is not a fit, but rather a representative of the approximate maximum amplitude allowed by an RV curve to still be consistent with observations. This limit is used in Figure 4.16 to constrain the maximum mass of the companion for each of these periods and ultimately rule out a stellar companion. The blue curve on the left panel represents the maximum amplitude of the estimated mass of the planetary companion. 164
- 4.16 Expected RV semi-amplitude as a function of the mass of the companion, assuming $M_1 = 0.261M_\odot$ and $i = 90^\circ$, for both possible periods (3.48 days shown as a solid blue line, 6.97 days shown as a dashed red line). Dotted vertical lines represent the masses of Neptune and Jupiter, respectively. The dot-dashed horizontal line depicts the approximate maximum amplitude that would be consistent with the measured RVs shown in Figure 4.15. This clearly rules out a stellar-companion, which also implies that the true period is in fact 3.48 d. 165
- 4.17 Phase folded *K2* light curve of vA 50 with the best-fitting JKTEBOP transit model shown in orange. The fit residuals are shown in the bottom panel. 165

- 4.18 Mass-radius diagram for all currently known eclipsing binaries in the Pleiades star cluster. With the exception of HII 2407 which is single-lined, each system is double-lined with dynamically determined masses. The solid and dashed curves show PARSEC v1.2S and BHAC15 isochrones for solar metallicity ($Z=0.02$). 166
- 4.19 Top panels: *K2* PDC SAP light curve for AK II 465 phase folded on the orbital period, with the best-fit JKTEBOP model plotted in orange. Bottom panel: Radial velocities with the best-fit JKTEBOP models indicated by the red and blue curves. In each panel the best-fit residuals are plotted below. The structure in the residuals to the fit of the primary eclipse is likely due to inadequate modeling of limb darkening. 170
- 5.1 *Left column:* *K2* postage stamps showing the regions around the three EB systems. Orientation is such that north is up and east is left. The *K2* plate scale is $\sim 4''$ /pixel. The magenta circles indicate the photometric apertures used for light curve extraction. The points represent the nominal locations of the sources from the target pixel file header information and may not be centered on the star due to small errors in the WCS (World Coordinate System). For EPIC 203476597, the second, smaller aperture around the neighboring star to the west was used to compute the time-averaged flux which was ultimately subtracted from the raw EB light curve. *Right column:* DSS2 "infrared" views of the corresponding regions presented on the left. The potential for contamination in the *K2* photometry due to either unresolved or spatially resolved nearby sources is discussed in the text individually for each EB system. 176
- 5.2 For each of the three eclipsing binary systems, raw *K2* (top panels) and corrected (bottom panels) light curves. All fluxes are median normalized. The orange line indicates the cubic B-spline fits to the raw photometry used to produce the corrected fluxes. A noticeable change in the data quality between the first and second halves of Campaign 2 is seen in these sources (most prominently EPIC 203710387) as well as many others. 180

- 5.3 Sections of the HIRES spectra showing a photospheric region (lower left), the Li I 6707.8 Å and Ca I 6717 Å lines (upper left) and the H α line profiles (right). All three stars show H α activity and have Li I absorption. The spectra of EPIC 203710387 and EPIC 203868608 are clearly double-lined, as seen most prominently in the two components of H α emission (each of which is double-peaked) and in the doubled Li I absorption, but also in the TiO bandhead regions. The red line indicates a second spectrum of EPIC 203476597, which differs from the black (first) that it overlays in its H α profile and in the Li I line, where a small absorption blueward of line center moves to become enhanced absorption redward of line center. The full time series of spectra is shown for EPIC 203476597 in the H α panel; we interpret the profile variations as due to orbital motion of a faint young H α emitting secondary, which is indeed revealed in the absorption lines from differences and ratios of the spectra. 182
- 5.4 Phased *K2* light curves (black points) with best-fitting JKTEBOP models (red curves). Residuals are plotted below the model fits. Observational errors are determined by the RMS scatter in the out-of-eclipse portions of the light curves. From top to bottom, the periods of these three EBs are approximately 2.8 d, 4.5 d, and 1.4 d. 185
- 5.5 Available USNO *BV*, 2MASS *JHK*, UKIDSS *ZYJHK*, and WISE *W1, W2, W3, W4* photometry or 1σ upper limits (downward pointing triangles) compared to NextGen2 model atmospheres. For both EPIC 203710387 and EPIC 203868608, a model atmosphere with $T_{\text{eff}} = 3000$ K and $\log g = 4.0$ fits the photometry well. Adopting $A_V = 0.9$ mag (red line) produces a better fit to the photometry than an unreddened photosphere (black line). Although the stars have the same spectral type, and EPIC 203710387 is a clear double-line system with approximately equal size/temperature and therefore presumably luminosity components, EPIC 203868608 is the brighter source. For EPIC 203476597 a 5200 K model is adopted, requiring $A_V = 3.0$ mag (red line) to match the SED. The A_V values illustrated here are refined in the text based on a match to $J - H$ colors. 188

- 5.6 For each EB studied here, the radial velocity curve (upper panel) and best-fit residuals (lower panel). The measurements are phase-folded on the best-fit period from simultaneous fitting of RVs and the *K2* light curve with *JKTEBOP*. The red and blue points and curves are the observations and best-fit model, for the primary and secondary components, respectively. Each point indicates the weighted mean radial velocity derived from measurements over several spectral orders within a single spectrum. Each measurement receives a weight equal to the inverse of the variance. The error bars represent the corresponding standard deviation between the multiple measurements, which in the top panel are smaller than the points themselves. In the case of EPIC 203868608, which is a triple system, two measurements at essentially the mean systemic velocity of Upper Sco (~ 4 km s⁻¹) are indicated by the black crosses. These measurements are likely compromised due to the low expected velocity separation that is comparable to the spectrograph resolution, and were consequently excluded from the RV fits in order to obtain a good fit. 191
- 5.7 Distributions of selected free and derived parameters and their pairs from the MC fitting procedure in the circular orbit fit for EPIC 203710387. The 0.5-, 1.0-, 1.5-, and 2.0- σ contours are drawn. The dashed lines in the 1D parameter distributions represent the median and 68% confidence intervals of the distribution. This plot was created using the `triangle` PYTHON code (Foreman-Mackey et al. 2014, DOI:10.5281/zenodo.11020). 195

- 5.8 Isochrones in the mass-radius (top) and temperature-luminosity (bottom) planes with the three EBs discussed here and two other low-mass systems in Upper Sco: both components of UScoCTIO 5 (Kraus et al., 2015) and the primary of the triple system ScoPMS 20 (Mace et al., 2012). The BHAC15, PARSEC v1.2s (Bressan et al., 2012; Chen et al., 2014), Siess et al. (2000), and Pisa (Tognelli et al., 2011) pre-MS evolutionary models at solar metallicity ($Z=0.02$) are considered for comparison. The two components of EPIC 203710387 are overlapping in the mass-radius plane. UScoCTIO 5 and EPIC 203710387 have fundamentally determined masses and radii; errors are smaller than the points themselves. The eclipsing components of EPIC 203868608 also have fundamentally determined masses and radii, though large uncertainties remain for this system, particularly in the luminosities, for the reasons discussed in § 5.6.2. The tertiary of this system does not have fundamentally determined parameters and hence is represented by the filled black triangle. All other systems have parameters that depend on models and/or empirical relations. In the lower panel, the equal-temperature, equal-luminosity components of UScoCTIO 5 are offset for clarity. No single isochrone can reproduce the fundamentally determined masses and radii of both the EPIC 203710387 and the UScoCTIO 5 systems. 196
- 5.9 *Above*: A Lomb-Scargle periodogram analysis of the EPIC 203476597 raw light curve for 10,000 periods between 1 and 4 days, using the `lombscargle` routine in the `scipy.signal` PYTHON package. The peak at 3.21 days is the rotational period of the primary, while the peaks at 1.4 and 1.6 days represent the orbital period and half the rotational period, respectively. *Below*: The raw K2 light curve phase folded on the rotational period. 207

- 5.10 BHAC15 isochrones showing an enhanced view of the mass-radius plane (left), as well as the $T_{\text{eff}}\text{-log}(L/L_{\odot})$ (middle), and $T_{\text{eff}}\text{-log } g$ (right) planes. In each case the 3, 5, 8, 10, and 15 Myr isochrones are plotted, from darkest to lightest. The red points indicate the positions of both components of EPIC 203710387, while the black scatter points represent the components of UScoCTIO 5. The dark red shaded squares indicate the parameters of EPIC 203710387 from the eccentric orbit solution, while the light red open squares show the circular solution values. The components of UScoCTIO5 are assumed to have equal temperatures and luminosities, but are offset for clarity here. For both systems, the uncertainties in mass, radius, and $\log g$ are smaller than the points themselves. 207
- 5.11 BHAC15 isochrones in the mass-radius plane. Overplotted are compilations of double-lined EBs with fundamentally determined masses and radii, either in the pre-MS phase of evolution (Stassun et al., 2014) or MS/post-MS phases of evolution (Torres et al., 2010). At a fixed mass, the radius evolves vertically downward in this diagram. We include recently characterized, double-lined eclipsing members of Upper Sco. For UScoCTIO 5, first characterized by Kraus et al. (2015), we overplot our revised parameters. We additionally input small offsets to our derived parameters for EPIC 203710387 and EPIC 203868608 for visual clarity. We do not include the tertiary for this latter system since a fundamental determination of the mass and radius for that component was not possible. We stress that unquantifiable uncertainties remain for EPIC 203868608, but we include the EB components here for illustrative purposes. The pink points correspond to the triply eclipsing system HD 144548 (Alonso et al., 2015). 216
- 5.12 Best-fit JKT_{EBOP} models to our detrended *K2* light curve for UScoCTIO 5 (top panels) and the radial velocities published by K15 (bottom panel). The three red points in secondary eclipse (upper right), were excluded from the fitting procedure. These points, as well as others, were also excluded in the K15 analysis. 234

6.1	Color-magnitude diagram for Upper Sco, with EBs discovered in <i>K2</i> data highlighted by the colored points. The black points are members suggested in Luhman & Mamajek (2012). We have not applied any corrections to the photometry based on our knowledge of the mass or flux ratios of the binaries and higher order multiples studied here.	237
6.2	Speckle imaging results for four of the EBs discussed here. The data for EPIC 203476597 originate from the NESSI instrument on the WIYN telescope. For the rest, the speckle data were acquired with the DSSI instrument at Gemini South Observatory. EPIC 202963882 has a companion at 1.23", and its contrast at 692 nm and 880 nm are represented as the red and blue points respectively. We determined from Keck/HIRES spectroscopy that this companion is the EB.	238
6.3	Joint fits to the <i>K2</i> photometry and radial velocity time series of HR 5934. The two most discrepant secondary radial velocities, with large errors, originate from Andersen & Nordstrom (1983).	243
6.4	<i>K2</i> photometry of USco 48 phase-folded on the rotational modulation period, which is commensurate with the binary orbital period. The shallow, grazing eclipses are highlighted by dotted lines.	248
6.5	Joint fit of <i>K2</i> photometry and HIRES RVs for USco 48. In this fit the radius ratio was fixed at unity.	249
6.6	Fit to the radial velocities of RIK-72. The 17.1 d orbit is much shorter than the period of the EB, which is longer than the <i>K2</i> campaign of 78.8 d. The period is also longer than the 10.5 rotation period inferred from the light curve modulation.	253
6.7	Joint fits to the <i>K2</i> photometry and radial velocity time series of UScoCTIO 5.	256
6.8	Joint fits to the radial velocity time series of the spectroscopic binary component of EPIC 203868608. The curves show fits using parameters from 100 randomly selected links in the Monte Carlo chain.	258
6.9	Parameter covariances for the joint radial velocity fit of the spectroscopic binary component of EPIC 203868608.	259

6.10	Mass-radius diagram. Colored curves are theoretical predictions from the MIST models (Dotter, 2016; Choi et al., 2016) in the non-rotating case (solid) and rotating case (dotted). Eclipsing binaries in the Upper Scorpius OB association are represented by the black points. The black crosses show previously published solutions for EPIC 203710387 (David et al., 2016b) and UScoCTIO5 (Kraus et al., 2015).	261
6.11	Chi-squared statistic as a function of age for non-rotating MIST model fits to the eclipsing binary radii in Upper Scorpius. The χ^2_{\min} age of Upper Scorpius according to this model set is 7.4 Myr	262
6.12	Probability density functions in age for individual stars in eclipsing binaries in Upper Scorpius. Ages are derived from interpolation within MIST models.	263
7.1	Spectral energy distribution of RIK-210 along with a NextGen stellar atmosphere model (Hauschildt et al., 1999b) normalized to the J-band point. Including a small amount of reddening (black) improves the fit over the unreddened model (green).	269
7.2	K2 light curve of RIK-210 in 20-day segments (black points). The red curve indicates the iterative spline fit (variability fit A) used to remove the starspot modulation pattern. Blue arrows indicate the approximate positions of shallow dimming events. Below the light curve we plot the residuals of the variability fit, normalized to unity but shifted to a continuum value of 0.8 in this figure. A broad flux dip occurs near $\text{BJD} - 2454833 = 2087.8$, indicated by the arrow and bar in the second panel, however the variability fit shown here passes through it and so it is not apparent in the residuals.	270

7.3 *K2* light curve of RIK-210. In each panel, the point color indicates the relative time of observation (with red corresponding to earlier times). Upper left: photometry folded on the rotational/orbital period of 5.67 d. Bottom left: same as above, showing an enhanced view of the dimming events. Middle: Same as the upper left, but with vertical offsets applied after each rotation of the star. Right: Same as middle, showing an enhanced view of the dimming events. There is clear evolution in the depth, duration, and overall morphology of the dimming events, a strong indication against a transit by or eclipse of a single solid body of any size. Some flares appear to occur at approximately the same rotational phase, shortly after the transit events. 271

7.4 Individual dimming events within the *K2* light curve of RIK-210, after removing the starspot modulation. On the abscissa, the data are plotted in terms of time from the predicted minimum as determined from a linear ephemeris. The maximum depth, total duration, and time of minimum light are summarized in the lower right corner of each panel. 272

7.5 Top: Phase folded and binned *K2* light curve of RIK-210 after removing the starspot rotation signal via an iterative spline fit. Bottom: variance in the phased and binned light curve. Variability fit B was used to make this plot. 276

7.6 Waterfall diagram of RIK-210. Colors represent the *K2* light curve intensity, with blue corresponding to higher flux and red to lower flux. The primary dimming events that are the focus of this work are clearly seen as the dark red stripe, which changes in intensity, duration, and timing. At top left, a series of light blue stripes between phases of 0.2 and 0.3 are observed to apparently drift in phase over the first four cycles. These are some of the shallow flux dips discussed in § 7.3.9. Linear interpolation was performed over data gaps where spacecraft thruster firings were excluded. 277

7.7 Correlation between the dimming timing variations and egress slopes. *Ad hoc* uncertainties of 0.25 hr in timing variation and fractional uncertainties of 10% in slope are assumed. 282

- 7.8 Composite of two independent JKTEBOP model fits to the two minima in the first dimming event of RIK-210 in the *K2* photometry. At least some of the individual transits observed by *K2* are reasonably well fit by one to three spherical occulting bodies with large size relative to the star. The fit to the deeper dip alone is referred to later as the “minimum obscuration fit.” Variability fit B was used to make this figure. 283
- 7.9 JKTEBOP model (red) overplotted on the flattened *K2* light curve of RIK-210 (black points). The model above was fit to the deepest component of the first dimming event in the *K2* campaign, then refit to the entire light curve allowing only the period and time of mid-transit to vary. Few observations lie above this fit, perhaps suggestive of an underlying, spherical occulting body surrounded by a stream of dust or swarm of planetesimals. Variability fit B was used to make this figure, though the conclusions drawn are independent of the fit used. 283
- 7.10 Evolution of the primary dips in the *K2* light curve of RIK-210. In both panels, the top row shows data from the first dip, proceeding consecutively downwards to the bottom row, which shows the last observed dip. *Left:* the “minimum obscuration fit,” obtained by fitting a model to the deepest component of the first dimming event, with respect to subsequent individual transits. *Right:* evolution of the residuals to the fits depicted on the left. 284
- 7.11 Example of shallow dimming events seen late in the *K2* campaign. Here we show two events (indicated by different colored points) separated by 5.888 days with consistent depth, duration, and morphology. 286
- 7.12 Flattened and median filtered *K2* light curve of RIK-210. The data are phase-wrapped on the dip period of 5.6685 days. A grouping of shallow dips preceding the main dip is prominent for the first four rotation periods of the campaign, then largely disappears. Variability fit B was used to make this figure. 287

- 7.13 Left: Phase-binned and averaged light curves of RIK-210 at three epochs from WASP, *Kepler/K2*, and LCOGT (in both V and i' filters). Each light curve is phase-folded on the $K2$ dip ephemeris. A broad depression in the WASP data between phases 0.3 and 0.5 is suggestive that the dip may have been present in previous years, but drifting in phase, becoming narrower, or both. However, inspection of the WASP data by year suggests this feature in the combined light curve may be due primarily to a combination of a questionable dip in 2006 and evolution of the spot pattern, most notable in the 2008 data. Right: WASP data ordered by year, phase-binned and averaged by weighting data points inversely to their photometric uncertainties. Data are offset vertically from the 2006 median value. Errorbars correspond to the standard deviation in a given phase bin. Only WASP data with photometric errors <0.4 mag were used. There are typically 2500–8000 measurements per year. Although there appear to be dimming events in prior years (e.g. at phases of 0.2 and 0.4 in 2006, phase 0.65 in 2008, or phase 0.45 in 2009), further inspection of the data indicate that many of the narrow structures above result from only one or two nights of observations. 290
- 7.14 Median-subtracted radial velocities for RIK-210 phased on the period of the $K2$ light curve. The dotted line indicates the approximate location of the deep dimming events present in $K2$ photometry, but absent in ground-based follow-up acquired closer to the time of spectroscopic observations. For illustrative purposes we show redundant phases with lighter shaded points. 293
- 7.15 Variations of the $H\alpha$ profile (colored curves) as a function of rotational phase, from the Keck-I/HIRES spectra. The black line represents the phase-averaged $K2$ light curve. We emphasize that follow-up photometry, acquired around the same time as the spectra, did not show the $\sim 20\%$ dimming at phase = 0.5 observed by $K2$ 295
- 7.16 Constraints on the brightness (top panel) or mass (lower panel) of putative companions to RIK-210 from optical speckle imaging (blue and red regions), NIRC2 adaptive optics imaging (grey dashed line in top panel, grey region in bottom panel), a HIRES secondary spectral line search, and the RV time series. 297

- 7.17 Minimum orbital period for grains of varying compositions to exist in the solid phase, as a function of the central star's effective temperature. Dust sublimation temperatures are taken from Kobayashi et al. (2011), and the stellar parameters needed to calculate the corresponding orbital periods are obtained from the PARSEC v1.2s pre-main sequence models (Bressan et al., 2012; Chen et al., 2014). For each grain composition, the upper and lower boundaries of the shaded regions are set by the 5 and 10 Myr isochrones, respectively. The position of RIK-210 is shown by the black point. Dust grains with compositions ranging from carbon to obsidian could exist in the solid phase at the corotation radius, while iron grains may sublimate. . . . 307
- 7.18 Pericenter separation for a range of eccentricities assuming a semi-major axis of 0.05 AU (black line). The colored lines reflect the limiting Roche radius for bodies of varying densities. Eccentricities greater than 0.4 would be required to bring a body interior to its Roche limit for any of the densities plotted here. 309
- 7.19 Expected depths and durations for equatorial transits of RIK-210 by an optically thick Hill sphere for planets of various masses. Fiducial masses are plotted as black points and annotated with text. However, the planet mass and fraction of the Hill sphere that is optically thick is completely degenerate in this plane. Thus, we show the effect of how these fiducial planet masses move along this curve when only 90% of the Hill sphere is optically thick (open circles). The grey shaded region indicates the range of depths and durations observed in the *K2* light curve. 311
- 8.1 Light curve of K2-33. **a-d**, *K2* photometry in twenty-day segments. K2-33 varies in brightness by $\sim 3\%$ every 6.3 days owing to the rotation of its spotted surface. The planet K2-33 b transits its star every 5.4 days (red ticks). Another potential transit (blue tick in d), distinct from the K2-33 b transits, is possibly caused by a second planet with orbital period > 77.5 days. **e**, Stellar variability was removed prior to fitting transits. The data gap is due to excluded observations where the variability fit inadequately captured a systematic artifact in the light curve. **f**, *K2* photometry folded on the planet's orbital period with a transit model fit (red curve). BJD, barycentric Julian date. . . . 325

- 8.2 Constraints on astrophysical false positive scenarios. To confirm the planetary nature of K2-33 b, we considered and eliminated nearly all false positive scenarios involving eclipsing stellar binaries. **a**, The domain of sky-projected separation and contrast of a putative unassociated eclipsing stellar binary, aligned with K2-33 by chance. The blue hatched region shows eclipsing stellar binaries eliminated using multi-epoch adaptive optics imaging, which leverages stellar proper motion to provide sensitivity at all separations within $5''$. Green and purple regions represent constraints from optical spectra and seeing-limited imaging, respectively. Finally, eclipsing stellar binaries in the grey region cannot account for the observed transit depth and are eliminated. **b**, Limits on eclipsing stellar binaries associated with (that is, gravitationally bound to) K2-33. Constraints from imaging and spectroscopy are shown as a function of physical separation. The lack of detectable stellar acceleration provides an additional diagonal constraint at top left. Δmag , difference in magnitude. 326
- 8.3 Extended Data Figure 1. *K2* light curve for K2-33 phased on the stellar rotation period of 6.3 d. Semi-sinusoidal brightness variations due to rotational modulation of starspots. Point color indicates relative time of observation, with grey corresponding to earlier in the campaign and dark blue corresponding to later times. Brightness is lowest when the most heavily spotted hemisphere of the stellar surface is along the line of sight. The shape and evolution of the variability pattern depends on the number, geometry, distribution, and lifetime of spots, along with any latitudinal gradient in the rotational speed (differential rotation). The transits of K2-33 b are visible by eye in this figure and are too narrow in rotational phase to be attributed to any feature on or near the stellar surface. 336

- 8.4 Extended Data Figure 2. Model-dependent age of K2-33. **a**, Solid lines show mean stellar density as a function of effective temperature for pre-main-sequence stars having different ages, according to theoretical models (Baraffe et al., 2015). Grey points represent plausible combinations of density and temperature for K2-33 as determined by light-curve fits and stellar spectroscopy. **b**, Distribution of implied stellar age based on temperature, density, and pre-main sequence models. The implied age of 2–7 Myr is consistent with our adopted age of 5–10 Myr, derived independently. Dark and light grey shaded regions indicate 68% and 95% confidence intervals, respectively. 337
- 8.5 Extended Data Figure 3. Apparent radial velocity variations of K2-33. Line-of-sight velocities and 1σ uncertainties (standard deviations) with respect to Solar System barycenter from Keck/HIRES are indicated. Radial velocities (RVs) are mean-subtracted, and the abscissa shows the orbital phase of K2-33 b measured from *K2* photometry (mid-transit occurs at zero orbital phase). We rule out RV variations larger than 300 m s^{-1} at 68.3% confidence, corresponding to a $1.2 M_{\text{Jupiter}}$ planet mass. Curves show the expected radial velocity variations for planets having circular orbits and different masses M_{P} . Radial velocities due to a 1.0 Jupiter mass planet (blue) are consistent with our observations, while a 4.0 Jupiter-mass planet is ruled out at high confidence. 338
- 8.6 Extended Data Figure 4. Images of K2-33. **a**, *K2* target pixel file (TPF). **b**, Sloan Digital Sky Survey (SDSS) optical image. **c**, Keck/NIRC2 *K*-band image. Extents of the *K2* target pixel file, *K2* photometric aperture, and NIRC2 image are shown respectively with black, green, and purple boundaries. In each image, north is up and east is left. Three other sources identified by SDSS reside within the *K2* photometric aperture, one of which is a galaxy. All are 7.3–10.1 magnitudes fainter than K2-33 in the SDSS *r*-filter and below the detection limit of the NIRC2 images, and are thus too faint to produce the observed transits. 338

8.7	Extended Data Figure 5. Sensitivity to non-comoving sources in the vicinity of K2-33. The blue X marks the star’s position in 2011. Between 2011 and 2016, the star moved by $0.''1228 \pm 0.''0085$ (red X) owing to proper motion. Contours show <i>K</i> -band sensitivity to non-comoving stars from adaptive optics imaging from both epochs. The 2011 data set included non-redundant aperture masking, and provided tighter constraints. The combined sensitivity to non-comoving objects is the maximum contrast achieved for either data set. Owing to stellar proper motion, we achieved <i>K</i> -band contrasts of >3.3 mag throughout $\Delta R.A.-\Delta Dec$ plane, even at the 2011 and 2016 positions of K2-33.	339
9.1	Spatial distributions of all stars observed during Campaign 2 of the <i>K2</i> mission (grey points) and the subset of young stars considered in this study (black points). The concentration of black points near the middle of the detector mosaic is due to the densely populated ρ Oph cloud. The two blank squares in the mosaic are due to non-operational CCD modules.	343
9.2	Number density of stars in proper motion space observed during Campaign 2 of the <i>K2</i> mission. Blue points and contours indicate the region occupied by candidate members of the Upper Sco OB association, as determined with the machine-learning algorithm described in Riedel et al., <i>in prep.</i>	345
9.3	Hess diagrams for stars observed during Campaign 2 of the <i>K2</i> mission. Overplotted in purple is the sample of young stars considered here, and the Luhman & Mamajek (2012) sample is depicted with black stars. Empirical fits to the cluster sequence in each CMD are shown in blue-green, shifted blueward to encompass 95% of a known young star reference sample. The yellow-green dashed curves show 10 Myr isochrones at 140 pc, illustrating why current models are inadequate for CMD cuts.	350

9.4	<i>Gaia</i> G magnitude as a function of spectral type for Upper Sco members across a wide mass range (top) and for M-type stars only (bottom). Spectral types have been source from Preibisch et al. (2002), Slesnick et al. (2008), Luhman & Mamajek (2012), and Rizzuto et al. (2015). A 5th order polynomial fit is shown by the pink line. The standard error in the distance modulus from a normal distribution of distances with center 140 pc and width 20 pc is shown by the errorbar.	353
9.5	Histogram of the visual extinction in magnitudes as reported by three large surveys of GKM type members of Upper Sco.	356
9.6	$(G - K_s)$ vs. G color-magnitude diagram for our sample, showing our empirical fit to the cluster sequence (pink) and the PARSECv1.2S 10 Myr isochrone (purple). We use the empirical fit to approximate the intrinsic $(G - K_s)$ colors of our stars, some of which have disks and all of which are variably reddened. The approximate intrinsic $(G - K_s)$ color is then used to determine radius, mass, and temperature for our stars based on the PARSECv1.2S models.	356
9.7	Histogram of stellar rotation periods, determined from <i>K2</i> photometry (Rebull et al., <i>in prep.</i>), for our sample. The median rotation period of the entire sample is 2.1 d, and 3.3 d for the M-type stars (here defined as $11 \leq G \leq 15$ mag).	357
9.8	Histogram of the signal-to-noise ratios (SNR) of recovered transit injections (top) and the cumulative distribution function (CDF) for SNR.	361
9.9	Survey completeness in period-planet radius domain for stars brighter and fainter $G = 14$ mag (top left and top right, respectively), as well as slowly rotating (bottom left) and rapidly rotating (bottom right) stars brighter than $G = 15$ mag.	363
9.10	Survey completeness in the period-fractional radius domain (left) and the period-planet radius domain (right) for the M-type stars in our sample.	365

LIST OF TABLES

<i>Number</i>	<i>Page</i>
1.1 Eclipsing binary systems in sub-Gyr populations, ordered by age then ascending primary mass.	15
1.2 Known and proposed exoplanets in sub-Gyr populations detected via the transit or radial velocity method.	18
1.3 Transiting planet searches in coeval stellar populations.	20
2.1 Stars with fundamental determinations of T_{eff} through Interferometry	49
2.2 Primary Components of Double-lined Eclipsing Binaries with fundamental determinations of $\log g$	57
2.3 Stars with semi-fundamental determinations of $\log g$ through Balmer-line fitting	60
2.4 Open Cluster Ages.	79
2.5 Ages, Masses, and Atmospheric Parameters of Nearby B0-F5 Field Stars	86
2.6 Statistics of Composite Age PDFs.	87
2.7 Empirical Spectral-Type Relations for Main Sequence B0-F5 Stars.	89
2.8 IC 2602 members dereddened $uvby\beta$ photometry and atmospheric parameters.	101
2.9 α Persei members dereddened $uvby\beta$ photometry and atmospheric parameters.	102
2.10 Pleiades members dereddened $uvby\beta$ photometry and atmospheric parameters.	103
2.11 Hyades members dereddened $uvby\beta$ photometry and atmospheric parameters.	104
2.12 Open Cluster Ages: Analysis in Linear Age.	108
3.1 Best-fit Orbital Parameters	121
4.1 Newly identified eclipsing binaries	133
4.2 Previously known eclipsing binaries	133
4.3 Photometric magnitudes in V and K_s bands for reported EBs	133
4.4 Keck-I/HIRES Radial Velocities and Flux Ratios	136
4.5 System Parameters of HCG 76	145
4.6 System Parameters of MHO 9 (BPL 116)	151
4.7 System Parameters of HD 23642	156
4.8 Parameters derived for HD 23642 from the literature	157

4.9	Literature proper motion measurements for AK II 465	159
4.10	Keck/HIRES equivalent widths for AK II 465	159
4.11	Fit to the K2 transits of vA 50b	163
4.12	System Parameters of AK II 465	171
5.1	Keck-I/HIRES Radial Velocities and Flux Ratios	183
5.2	Keck-I/HIRES Equivalent Widths	184
5.3	System Parameters of EPIC 203710387	221
5.4	System Parameters of EPIC 203868608	226
5.5	System Parameters of EPIC 203476597	229
5.6	System Parameters of UScoCTIO 5	235
6.1	Keck-I/HIRES radial velocities	239
6.2	Literature radial velocities of HR 5934	242
6.3	System Parameters of HR 5934	244
6.4	System Parameters of USco 48	250
6.5	Parameters of the EPIC 203868608 spectroscopic binary	257
7.1	System properties of RIK-210	268
7.2	Parameters of the transient transit signature	281
7.3	Keck-I/HIRES radial velocities of RIK-210	296
7.4	Proposed explanations for the transient transits of RIK-210	298
8.1	System properties of K2-33	324
8.2	Keck/HIRES radial velocities for K2-33	335
9.1	Upper Sco membership studies	345
9.2	Parameter distributions of injected transit signals	360
9.3	Planet occurrence for young low-mass stars	368

Chapter 1

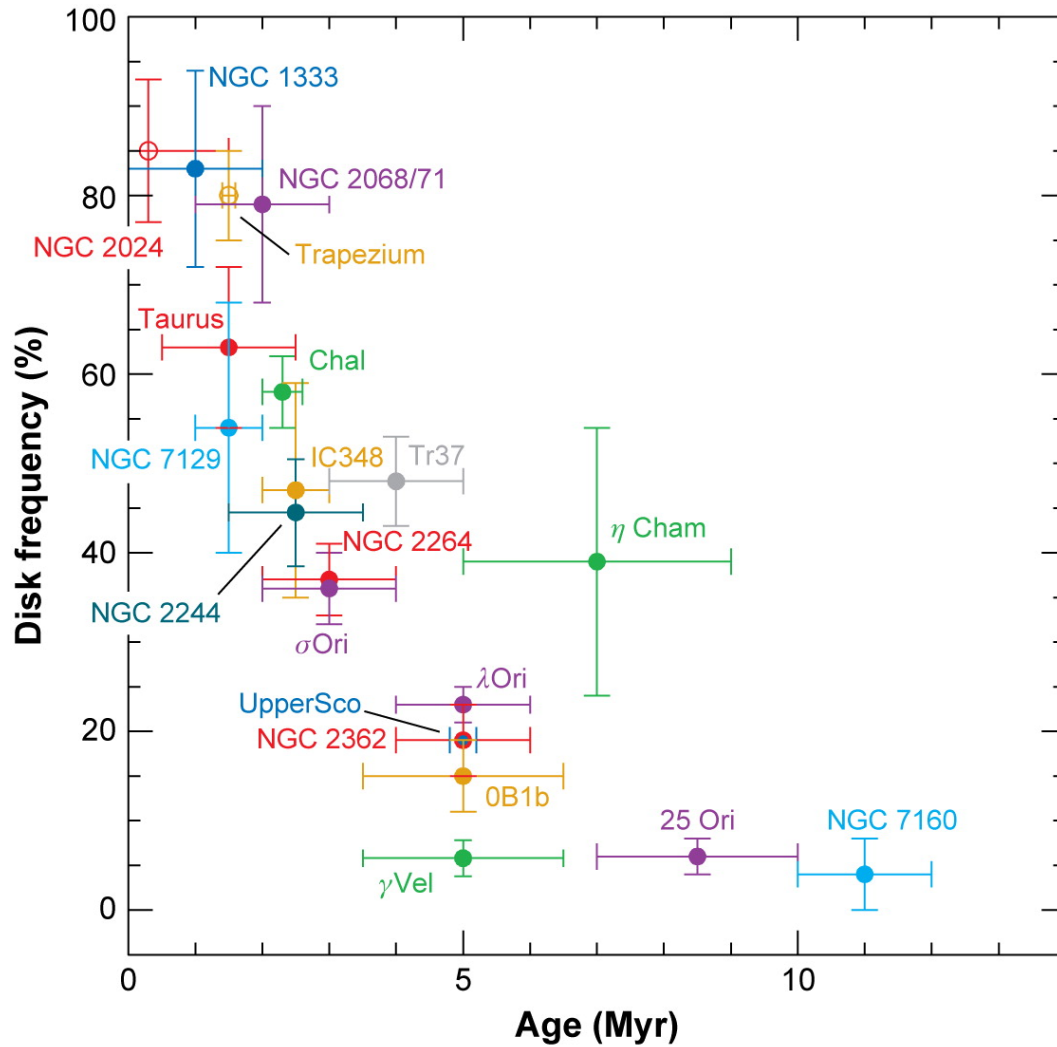
INTRODUCTION

1.1 Stellar evolutionary models and the need for calibrators

Much of contemporary astrophysics is reliant upon theoretical models that predict how the observable properties of stars evolve in time. The evolution of a star is governed by competing physical mechanisms which act over a broad range of length scales and timescales, bringing together the physics of the very small (e.g. quantum mechanical interactions between electromagnetic radiation and matter) and the very large (e.g. heat transfer in rotating, magnetized fluids). It is perhaps not surprising, then, that despite meaningful advances in the capabilities of computers to simulate stellar structure and evolution, discrepancies persist between the observed properties of stars and theoretical predictions.

For example, the inability of current evolutionary models to match the observed colors and luminosities of stars less massive than the Sun translates directly into uncertainties in the initial mass function, perhaps the most fundamental relation in stellar astrophysics and our most salient clue towards understanding how stars form (Bastian et al., 2010). Other foundational relationships in stellar astrophysics such as age-activity-rotation relations (Barnes et al., 2005; Mamajek & Hillenbrand, 2008; Meibom et al., 2015) are calibrated to clusters and other coeval stellar populations, the ages of which depend on evolutionary models. Likewise, the timescale for protoplanetary disk dispersal and thus giant planet formation is tied to the age scale of young clusters and star-forming regions (Figure 1.1), which are age-dated using pre-main sequence evolution models (Haisch et al., 2001; Hillenbrand, 2005; Mamajek, 2009). Stellar models also underpin much of our knowledge of extrasolar planets, the properties of which are measured only relative to the properties of host stars. Uncertainties in stellar models can thus introduce systematic biases in the masses, radii, and occurrence rates of extrasolar planets (e.g. Mann et al., 2012; Gaidos & Mann, 2013), all of which are important for understanding planet formation.

It is imperative, then, to establish confidence in stellar evolution models where possible and to expose their inadequacies when apparent. Evaluating stellar models is achieved through comparison with benchmarks: stars or star systems with precisely-




 Wyatt MC. 2008.
 Annu. Rev. Astron. Astrophys. 46:339–83

Figure 1.1: Reproduction of Figure 2 from Wyatt (2008). The disk frequency, i.e. fraction of stars hosting protoplanetary disks, within stellar associations of different ages. The time available for forming planets with substantial gaseous envelopes is set by the protoplanetary disk dispersal timescale. Ages of young associations are typically derived from H-R diagram analyses using evolution models that are largely uncalibrated and contain systematic offsets.

determined parameters based on well-understood physics and few, if any, theoretical assumptions.

1.1.1 Eclipsing binaries

The absolute dimensions and masses of stars can be directly measured from eclipsing, spectroscopic binaries. Apart from several dozen nearby stars, the surfaces of

which may be resolved using optical interferometry, eclipsing binaries (EBs) are the only stars for which sizes can be measured directly. In cases where the spectral lines of each star in a binary can be resolved (double-lined spectroscopic binaries), the radial velocities of each component can be measured and one can uniquely solve for the masses and the radii with precision typically less than a few percent (see Andersen, 1991; Torres et al., 2010, for reviews). The method is distance-independent, and in fact double-lined EBs allow for precise distance determinations; EBs have been used to measure the distances to benchmark open clusters (e.g. Southworth et al., 2005; David et al., 2016a; Gillen et al., 2017) and even other galaxies (Vilardell et al., 2010; Pietrzyński et al., 2013), as well as to calibrate more prolific distance measurement methods such as trigonometric parallax (Stassun & Torres, 2016a; Stassun & Torres, 2016b).

Of particular interest are EBs with (1) low component masses, (2) in the pre-main sequence (PMS) stage of evolution, or (3) belonging to coeval stellar populations. Low-mass EBs are valuable because it is at low masses where stellar evolution models are most uncertain and thus stand to benefit most from observational benchmarks (Torres, 2013). Recent interest in low-mass stars has also been driven by searches for exoplanets, which target these stars for the relatively large Doppler and transit signals induced by their planets. As the masses and sizes of exoplanets are measured only in a relative sense, absolute planet masses and sizes depend critically on empirical relationships (such as temperature–mass or temperature–radius conversions) which are established through benchmark systems. Although low-mass stars are the most populous in the galaxy, they have lower geometric probabilities of eclipsing relative to higher mass stars (at a given separation) owing to their smaller sizes. More importantly, low-mass stars are intrinsically faint and thus difficult to study. Consequently, well-characterized low-mass EBs are currently rare.

Also rare are EBs in the PMS phase, as this is a short-lived evolutionary stage in a star’s life and there are few nearby PMS stellar populations. Although the basic components of PMS evolution theory have existed for decades (e.g. Hayashi, 1961; Henyey et al., 1965; Iben, 1965), there have been few direct tests of these model predictions. The fundamental properties assigned to young stars depend almost entirely on these models, while even their basic parameters such as PMS lifetimes are not known directly. Our understanding of the formation and evolution of planets is tied directly to the stellar properties during this important evolutionary phase. Inaccurate assumptions about the temperature and luminosity of a young star of a

given mass translate into uncertainties in the locations of ice lines, for example. Stassun et al. (2014) provides a review of PMS EBs and a careful assessment of how their parameters compare with predictions from stellar evolution models. Since that work, several new PMS EBs have been added, which are summarized in Table 1.1 and shown in Figure 1.2. Broadly speaking, the discrepancies between PMS models and EBs are significant, highlighting the importance of identifying and precisely characterizing a large sample of benchmark objects from which systematic offsets can be mapped.

Finally, EBs in clusters or other stellar associations are valuable as they provide independent estimates of the distances and ages of the association, which are typically age-dated in the Hertzsprung-Russell (H-R) diagram. If the age, metallicity, and distance of an association are already well-established, then a double-lined EB in said association represents a rare benchmark system with known masses, radii, temperatures, luminosities, age, and metallicity.

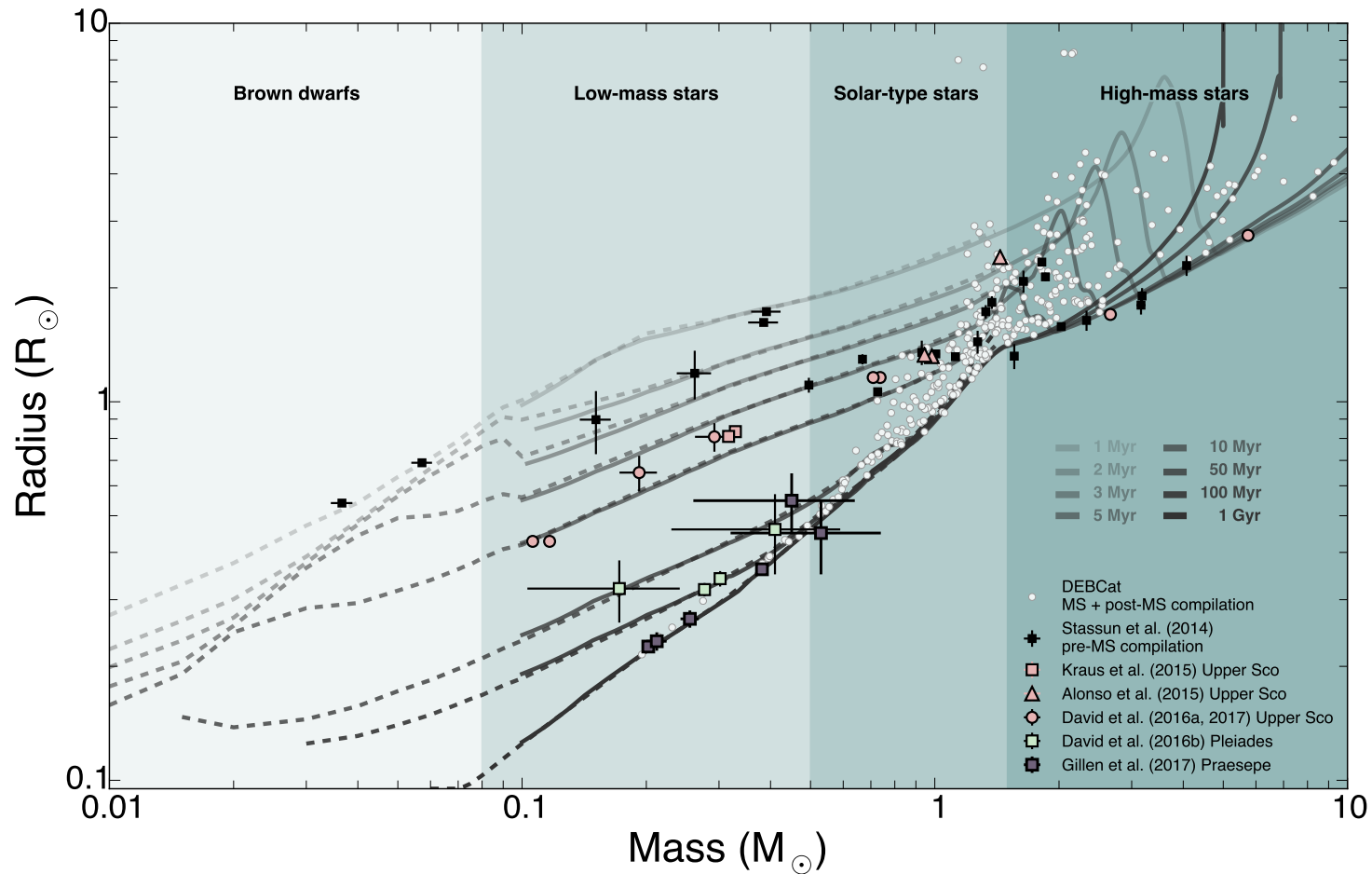


Figure 1.2: Isochrones in the mass-radius plane. Solid and dashed curves are predictions from the solar metallicity MIST isochrones (Choi et al., 2016; Dotter, 2016) and BHAC15 (Baraffe et al., 2015) models, respectively. Stars with masses $M \lesssim 1.5 M_{\odot}$ contract monotonically towards the main sequence. The onset of nuclear reactions stalls contraction for higher mass stars and temporarily causes an increase in radius prior to settling on the MS, leading to the prominent “bump” in the mass-radius diagram. High-mass stars quickly evolve away from the MS, increasing in radius again after several Myr. This post-MS evolution at high masses is clearly demonstrated by the 50 and 100 Myr isochrones but for clarity the 1 Gyr isochrone is limited to stars less massive than $1.5 M_{\odot}$. Overplotted are double-lined EBs in young stellar associations (large shaded points) and in the field (white points). The field EB parameters are taken from the DEBCat compilation maintained by John Southworth.

1.1.2 Evaluating pre-main-sequence models of low-mass stars

For the better part of two decades, EBs have been used to show that stellar models do not adequately reproduce the properties of low-mass stars. Specifically, low-mass EBs have effective temperatures that are systematically lower (an effect referred to as temperature suppression) and radii that are 5–15% larger than model predictions. This latter phenomenon is known as radius inflation and is observed in both field stars (Torres & Ribas, 2002; Ribas, 2003; López-Morales & Ribas, 2005; Ribas, 2006; Torres, 2013) and open clusters (Jackson & Jeffries, 2014).

Metallicity effects and missing opacity sources, both of which are known to be relevant in the inferred properties of low-mass stars, are not thought to be capable of producing the large observed radius discrepancies (Morales et al., 2010). Interestingly, Stassun et al. (2014) found that observed lithium abundances within benchmark PMS EBs are generally in good agreement with model predictions. That observation is one line of evidence seeming to suggest that, despite the observed discrepancies in surface properties, the internal structure of PMS stars predicted by models is accurate enough to reproduce lithium abundances in a general sense. Rather, the leading candidate thought to be responsible for the observed discrepancies is now thought to be magnetic fields, as discussed below.

Several authors have now systematically compared the predictions of PMS models to the dynamical mass measurements of the relatively few known benchmark objects (EBs, astrometric or spectroscopic binaries, and stars with measurable circumstellar disk rotation curves). There is broad consensus that modern PMS models produce accurate (<10% uncertainty) mass predictions for stars with masses $>1M_{\odot}$ (Hillenbrand & White, 2004; Mathieu et al., 2007; Stassun et al., 2014). Models are not so successful at lower stellar masses, however. Earlier studies (using mostly astrometric binaries and masses from circumstellar disk rotation curves) found that PMS models tend to underestimate the masses of low-mass stars (Hillenbrand & White, 2004; Mathieu et al., 2007). By contrast, a comparison of PMS EBs with a newer generation of theoretical models found that models *overestimate* masses by 50–100% for low-mass ($<1M_{\odot}$) stars (Stassun et al., 2014). The degree of overestimation is also observed to systematically increase towards lower masses. Furthermore, depending on the particular choice of model, the inferred mass and age can vary by factors of 2–3. The different predictions are likely due to different prescriptions for surface boundary conditions.

The discrepancies between models and observations of the temperatures of low-

mass PMS stars can not be considered in isolation but are related to the mass discrepancies. During the PMS stage, low-mass stars evolve essentially vertically in the H-R diagram as they contract at constant temperature along the fully convective Hayashi track. Thus, to first order, the mass of a low-mass PMS star is given by its temperature and its age by its luminosity (though distance effects, differential extinction, rotation, and peculiar accretion histories may make the latter relationship murkier, as discussed below). Recent evidence from low-mass EBs in coeval stellar populations indicates that most of the model discrepancies can be alleviated by a simple temperature offset of ~ 200 K, where models predict temperatures hotter than observed (Kraus et al., 2015; David et al., 2016b; David et al., 2016a). It remains an open question whether such an offset is due to missing physics (e.g. less efficient convection, magnetic fields, missing opacities), due to an offset in empirical spectral-type-temperature scales for young stars (from, e.g., the onset of molecular bands), or some combination of both.

1.1.3 Convection, magnetic fields, and starspots

While it has been established that most current theoretical models of low-mass stars systematically underestimate radii and overestimate photospheric temperatures (or equivalently underpredict masses), the exact physics missing from the models is still debated. Correlations between the degrees of radius inflation or temperature suppression with chromospheric H α and coronal X-ray emission levels (Torres et al., 2006; López-Morales, 2007; Morales et al., 2008; Stassun et al., 2012) seemingly suggests magnetic activity as the culprit. Observations (through e.g. Zeeman Doppler imaging) have shown significantly higher magnetic energy densities in low-mass stars relative to solar-type stars (Donati & Landstreet, 2009; Reiners, 2012), so it is perhaps not surprising that magnetism may play a critical role in the evolution of low-mass stars.

Magnetic fields inhibit the efficiency of convective energy transport (Chabrier et al., 2007) thereby reducing the temperature at the stellar surface and slowing contraction during the pre-MS stage. Starspots, a manifestation of magnetic fields at the stellar surface, cause a related effect in which the efficiency with which radiation can escape the star is reduced and thus the radius increases to compensate (e.g. Torres et al., 2006). The additional pressure support provided by strong magnetic fields may also be a factor in producing the observed temperature and radius anomalies (Mullan & MacDonald, 2001).

Several authors have now included prescriptions for magnetic fields or starspots in evolutionary models and investigated the resulting effects (D’Antona et al., 2000; Mullan & MacDonald, 2001; Feiden & Chaboyer, 2012a; Feiden & Chaboyer, 2012b; Feiden & Chaboyer, 2013; Feiden & Chaboyer, 2014). Generally, the claim is that magnetic models are better able to reproduce EB parameters and provide an explanation for the phenomena of radius inflation and temperature suppression. As an example, in the Upper Scorpius OB association, there appears to be an effect where more massive EBs appear younger than low-mass EBs (David et al., *in prep.*, and see Chapter VI) when using at least some model sets. This trend is opposite to the mass-dependent trend in H-R diagram ages. Incorporating magnetic fields into pre-MS evolution models can help to resolve the apparent age discrepancies between different EBs within Upper Sco if one invokes field strengths of a few hundred to a few thousand Gauss (Feiden, 2016a; MacDonald & Mullan, 2017). An open question about such magnetic models is whether the field strengths required to match observations are plausible.

Somers & Pinsonneault (2015) investigated the effects of including starspots in pre-MS evolution models of stars in the mass range of $0.1\text{--}1.2 M_{\odot}$. Those authors found that models of spotted stars lead to radii that are inflated by up to 10% at a given mass and age during pre-MS evolution. At the zero-age MS, the effect was similarly large for partially convective stars but less pronounced (<5%) for fully convective stars. Additionally, a spotted star of a given mass and age exhibits a lower temperature and lower luminosity relative to an unspotted star. The magnitude of the temperature suppression was found to be 7% on average, equating to a zero-point shift in Hayashi tracks and in good agreement with the ~ 200 K excesses found for model-derived temperatures of low-mass pre-MS EBs (e.g. Kraus et al., 2015; David et al., 2016a). Somers & Pinsonneault (2015) found that as a result of this temperature suppression, model-derived masses and ages may both be underestimated by up to factors of 2 and 2–10 (at a nominal age of 3 Myr), respectively.

Another factor to be considered is that eclipsing binary light curve models which do not account for the presence of starspots can lead to overestimated radii of a few percent by changing the eclipse morphologies relative to the ideal case of a homogeneous photosphere¹. The effect is particularly pronounced when the spots are located at high latitudes and substantial spot covering fractions (of tens of percent)

¹Specifically, as explained by Morales et al. (2010), stars with polar spots lack the circular symmetry of stars without spots and thus possess elongated isophotes. Eclipses are widened as a result and the sum of the stellar radii is overestimated.

are assumed (Morales et al., 2010). Lending weight to this concern is the fact that polar spots on low-mass stars are both theoretically predicted (e.g. Schuessler & Solanki, 1992; Granzer et al., 2000; Yadav et al., 2015) and observed (e.g. Hatzes, 1995; Washuettl & Strassmeier, 2001; Jeffers et al., 2007; Strassmeier, 2009). Additionally, spot covering fractions for active, low-mass stars (and particularly pre-MS stars) have been measured to be as high as $\sim 80\%$ (e.g. Petrov et al., 1994; O’Neal et al., 1998; O’Neal et al., 2001; O’Neal et al., 2004; Gully-Santiago et al., 2017).

A consistent picture is thus emerging in which magnetic fields and their byproducts (e.g. starspots) must clearly be accounted for, in one way or another, in the theoretical models of low-mass stars. Observers must also take care in modeling eclipsing binaries with clear signatures of starspots, to be certain that the stellar radii are not being systematically overestimated.

1.1.4 Apparent age spreads, accretion histories, and coevality within binaries

A known issue with age-dating young stellar associations in the H-R diagram is that members of a given population exhibit large spreads (sometimes >1 dex) in luminosity even across a narrow range in mass or spectral type (see e.g. Hillenbrand, 1997; Da Rio et al., 2010; Herczeg & Hillenbrand, 2015). Additionally, several authors have shown that age estimates of young stars in the H-R diagram are mass-dependent, such that the more massive members of a given association may appear up to ~ 2 – 5 times older than the low mass members (Hillenbrand et al., 2008; Mayne & Naylor, 2008; Naylor, 2009; Bell et al., 2013). The effect is particularly striking when comparing the ages of main sequence turnoff stars (often used as a high fidelity age indicator for older clusters) in a given association with those of the low-mass stars still contracting down the fully-convective Hayashi track.

Some have interpreted the observed luminosity spreads as intrinsic age spreads (e.g. Reggiani et al., 2011) of a few Myr, representing extended star formation episodes as one might expect from e.g. triggered star formation (Elmegreen & Lada, 1977). Others, however, have suggested the luminosity spreads may be a result of the peculiar accretion histories of individual stars (Hartmann et al., 1997; Baraffe et al., 2009; Baraffe & Chabrier, 2010). Other factors that can affect a star’s position in the H-R diagram, and which are particularly salient for pre-MS stars, are differing amplitudes of photometric variability, variable extinction in a star-forming region, and spatially unresolved multiples (Soderblom et al., 2014; Hartmann, 2001). However, Burningham et al. (2005) have shown that photometric variability alone

cannot account observed luminosity spreads, nor can variable extinction (Da Rio et al., 2010).

One parameter that is clearly important is spin. Stars of a given mass are observed to have a wide range of rotation periods, typically 1–10 d on the pre-MS (e.g. Rebull, 2001). The position of a pre-MS star in an H-R diagram is claimed to be correlated with its rotation rate, such that more rapid rotators appear younger (Littlefair et al., 2011). The overall effect of rotation on the evolution of young stars and on their apparent ages is complicated; rotation rate is linked both with magnetic energy densities in low-mass stars (Donati & Landstreet, 2009) and with accretion history (Littlefair et al., 2011, and references therein). In low-mass stars, magnetic fields themselves are thought to result from the combination of convection and rotation. Strong fields may be generated in rapid rotators, and these fields act to slow contraction along the pre-MS. Conservation of angular momentum requires stars to spin up as they contract, but once on the main sequence stars will lose angular momentum via magnetized winds and spin down.

Thus, another reason why pre-MS calibrators are so valuable is for their ability to test the degrees to which binaries and, more broadly, clusters are coeval. The results have implications for the limiting precisions with which we can know stellar parameters and for distinguishing between various theories of star formation (e.g. Shu et al., 1987; Elmegreen, 2000). Results to date indicate that within a given pre-MS population, binaries appear much more coeval than randomly selected pairs of stars within the same association (Kraus & Hillenbrand, 2009a). Stassun et al. (2014) quantified the discrepancy with respect to pre-MS EBs in particular, finding individual components of an EB appear coeval to within 20%, but apparent age spreads up to 50% are found between different EBs within the same association. This observation may reflect mass-dependent systematic offsets in evolutionary models, genuine age spreads within a presumed coeval population, or apparent age spreads due to e.g. distinct accretion histories. Further investigation is required to measure the magnitudes of these effects.

1.1.5 Multiplicity effects

Multiplicity is a generic outcome of star formation. Approximately half of all stars have one or more stellar companions, meaning the majority of stars in the galaxy reside in binaries or higher order multiples (see Duchêne & Kraus, 2013, for a review). For any given star, its multiplicity is often unknown and so accounting

for stellar multiples when e.g. age dating clusters or determining planet occurrence rates can be a particularly vexing problem. For the luminosity spreads discussed above, at least, attempts are typically made to clean samples of binaries and so multiplicity does not seem to be able to account for the observed discrepancies.

At least some of the issues noted above with pre-MS evolution models, however, have been linked to the high number of triples within the known sample of pre-MS EBs. Stassun et al. (2014) found that models could predict the masses of pre-MS EBs to 10% accuracy down to masses of $0.5 M_{\odot}$, if systems with known tertiaries were excluded from their analysis. For EBs in triple systems, however, the mass predictions were only accurate to about 50% or worse. Those authors speculated the more dramatic discrepancies might be due to the injection of heat into the EB through dynamical interactions with the tertiary component. About half of the EBs contained in that study have known tertiaries, and of those systems all of the eclipsing components have orbital periods $\lesssim 5$ d. This is in line with results from solar-type spectroscopic binaries in the field; Tokovinin et al. (2006) found as many as 96% of close spectroscopic binaries ($P_{\text{orb}} < 3$ d) have tertiary companions. Thus, there is a premium on identifying pre-MS EBs with long orbital periods (having a lower statistical probability of hosting a tertiary, as well as being less susceptible to tidal effects).

1.1.6 Tidal dissipation in binary stars

Binaries, and especially eclipsing systems, can also be used to test and improve the theory of tides. The theoretical endpoint of binary star evolution is a circular orbit in which each star is spinning synchronously with the orbit, with the spin axes aligned to the orbital angular momentum vector² (Ogilvie, 2014). The damping of primordial eccentricity and the spin-orbit synchronization are both consequences of tidal dissipation. Despite the prevalence of binary stars, a system in the tidal equilibrium described above has never been observationally verified with a high degree of certainty. Eclipsing systems are particularly valuable for tidal evolution studies: the relative timing of primary and secondary eclipses provide tight constraints on eccentricity and the longitude of periastron, and more importantly the degree of spin-orbit alignment can be directly measured through the Rossiter-McLaughlin effect (which is not possible for spectroscopic or astrometric binaries).

One of the few lines of direct observational evidence for tidal dissipation in binary

²In reality, the tidal equilibrium described may be impeded by other effects such as magnetic braking, stellar evolution, and gravitational radiation.

stars is the joint eccentricity–period distribution. The effects of tidal dissipation are imprinted in this distribution: lower eccentricities are observed at shorter orbital periods. Of prime interest are the timescales for tidal circularization and spin-orbit synchronization. Theoretically, these timescales depend on the internal structures of the stars in question, and calculating them represents a complicated problem at the intersection of celestial mechanics and fluid dynamics. Observationally, the circularization and synchronization timescales can be measured by studying binaries in stellar populations of varying ages. The most valuable benchmarks for such studies are double-lined EBs in clusters or associations.

The most robust measure of the tidal circularization timescale comes from a functional fit to the eccentricity-period distribution of binaries within clusters of different ages (Meibom & Mathieu, 2005; Meibom et al., 2006). The underlying idea is that binaries with some threshold eccentricity have a minimum period at a given age. That period, the “tidal circularization period,” increases with the age of a stellar population. Below the circularization period, all binaries are expected to be circularized, while above the period, binaries have a range of eccentricities. The method relies on building up a sizable sample of binaries with well-determined eccentricities (a task more difficult for longer period binaries). A large sample size is particularly important for guarding against binaries at intermediate or long periods which may have primordially low eccentricities. In principle, the circularization period may even be used to estimate the age of a stellar population (Mathieu & Mazeh, 1988).

Broadly speaking, observations of binaries in clusters have revealed discrepancies between expectations from theories of tidal evolution. Some theories posit that tidal circularization of close binaries should occur primarily during the PMS phase when stars and their convective envelopes are larger (Zahn & Bouchet, 1989). However, Meibom & Mathieu (2005) showed tidal dissipation proceeds to circularize orbits well after the PMS stage. While this observation is in agreement with other theoretical treatments of tides (Zahn, 1989; Claret & Cunha, 1997; Witte & Savonije, 2002), binaries are generally found to circularize much more quickly than theory predicts. The discrepancy is possibly related to theoretical prescriptions for convection, as tidal dissipation is expected to be more efficient in stars with convective envelopes (Zahn, 1975), which is also shown observationally (Van Eylen et al., 2016). With regards to synchronization timescales, recent observations of EBs in the Praesepe cluster have revealed systems that are circularized but not synchronized and in some cases rotating subsynchronously with the orbit (Gillen et al., 2017). The degree

of disagreement between the rotation periods (inferred photometrically) and orbital periods is larger than can be explained by differential rotation, which is expected to be negligible for these low-mass stars. While subsynchronous rotation has been observed previously in young clusters (Meibom et al., 2006), this result is surprising given that synchronization is expected to proceed more rapidly than circularization for close binaries (Zahn, 1977; Hut, 1981) and to be completed for close binaries at the age of Praesepe.

1.1.7 Young star variability studies in the age of *Kepler/K2*

After concluding its prime mission and following the failure of two reaction wheels, the *Kepler* space telescope was reoriented to continuously observe fields along the ecliptic for ~ 80 d at a time. The new mission, named *K2* (Howell et al., 2014), has delivered photometry for a much wider diversity of astrophysical sources with only a modest reduction in photometric precision (relative to the prime mission). The *K2* photometric campaigns in the vicinity of young stellar regions are particularly unprecedented in terms of the cadence, duration, and photometric precision achieved, as well as the wide area and number of stars surveyed. Prior to *K2*, there was only one other data set with remotely similar characteristics: 30 days of simultaneous *Spitzer* and *CoRoT* observations of the ~ 1 -5 Myr cluster NGC 2264 (Cody et al., 2014).

As an example of the unique contributions of the *K2* mission to the field of young stars and exoplanets, we highlight in bold the EBs and transiting planets discovered in *K2* photometry in Tables 1.1 & 1.2. The mission is responsible for nearly doubling the number of objects in both classes. The Stassun et al. (2014) review of PMS models was based on a sample of 13 PMS EBs. Since that work, 12 new PMS EBs have been discovered in *K2* time series photometry of Upper Sco, the Pleiades, and Praesepe (Alonso et al., 2015; Kraus et al., 2015; Lodieu et al., 2015a; David et al., 2015; David et al., 2016b; David et al., 2016a; Gillen et al., 2017). An additional four EBs in Upper Sco are currently being characterized (David et al., *in prep.*, see also Chapter VI). Of the 16 new PMS EBs mentioned, all but four are double-lined in optical spectra and thus excellent benchmark candidates.

In addition to the mission's EB and transiting planet contributions, *K2* has returned data of unprecedented detail and value to more general studies of young star variability. Young stars are some of the earliest recognized variable sources in the sky (e.g. Enebo, 1907; Zinner, 1913; Joy, 1945), inspiring a great number of research articles

(Kulkarni, 2016). Included among the *K2* contributions to young star variability studies are large samples of stars accreting from protoplanetary disks (Cody et al., 2017), being obscured by said disks (Ansdell et al., 2016), precise rotation periods for hundreds of stars (Rebull et al., 2016a; Rebull et al., 2016b; Stauffer et al., 2016; Rebull et al., 2017), and even new classes of optical variability associated with young, rapidly-rotating low-mass stars (Stauffer et al., 2017). Many of the explanations for the wide range of stellar variability seen have essentially not changed for decades, but we are now in a regime where the quality of the observations is far from a limiting factor in advancing our understanding.

In Chapters III through VI, I present the discovery and characterization of EBs in the Pleiades open cluster and the Upper Scorpius OB association. These results increase the sample of known PMS EBs by 80% at $M < 1 M_{\odot}$ and $\tau \lesssim 150$ Myr. I use these EBs to test PMS evolution models, finding systematic offsets in the ages of stars inferred from the mass-radius diagram as compared to the H-R diagram. I show that a self-consistent age for Upper Scorpius can be obtained from the mass-radius diagram using EBs in the mass range $0.3\text{--}5 M_{\odot}$, and pave the way for an empirical PMS mass-radius relation. In Chapter VII, I present a detailed study of the young star RIK-210, which exhibits a variable eclipse-like signature at the stellar rotation period in *K2* photometry. The star is single and seemingly distinct from the previously known “dipper” class of young stars, in that it does not exhibit a warm dust excess. I consider various models to explain the peculiar photometric behavior, ultimately favoring a scenario in which dust trapped in the magnetosphere is co-rotating with the star. The case of RIK-210 illustrates how searches for transiting planets around young stars are prone to a new class of false positives that are still not well understood.

Table 1.1: Eclipsing binary systems in sub-Gyr populations, ordered by age then ascending primary mass.

Name	M_{pri} (M_{\odot})	M_{sec} (M_{\odot})	R_{pri} (R_{\odot})	R_{sec} (R_{\odot})	Cluster ^a	Age (Myr)	Year	Refs.
2MJ0535-05	0.0572 ± 0.0033	0.0366 ± 0.0022	0.690 ± 0.011	0.540 ± 0.009	ONC	1–2	2006	1,2
JW 380	0.262 ± 0.025	0.151 ± 0.013	1.189 ± 0.175	0.897 ± 0.170	ONC	1–2	2007	3
Par 1802	0.391 ± 0.032	0.385 ± 0.032	1.73 ± 0.015	1.62 ± 0.015	ONC	1–2	2008	4,5
TY CrA	3.16 ± 0.08	1.64 ± 0.04	1.80 ± 0.10	2.08 ± 0.14	NGC 6726/7	3	1998	6
CoRoT 223992193	0.668 ± 0.012	0.4953 ± 0.0073	1.295 ± 0.040	1.107 ± 0.044	NGC 2264	3–6	2014	7
RS Cha	1.854 ± 0.016	1.817 ± 0.018	2.138 ± 0.055	2.339 ± 0.055	η Cha	4–7		8
EPIC 203868608 B ^b	Upper Sco	5–10	2016	9
EPIC 203710387	0.1183 ± 0.0028	0.1076 ± 0.0031	0.417 ± 0.010	0.450 ± 0.012	Upper Sco	5–10	2015	9,10
EPIC 202963882 B ^{c,d}	0.29 ± 0.03	0.19 ± 0.02	0.81 ± 0.08	0.65 ± 0.07	Upper Sco	5–10	2017	11
UScoCTIO 5	0.3336 ± 0.0022	0.3200 ± 0.0022	0.862 ± 0.012	0.852 ± 0.013	Upper Sco	5–10	2015	9,12
RIK-72 ^{c,d,e}	0.37 ± 0.04	...	0.87 ± 0.09	...	Upper Sco	5–10	2017	11
USco 48 ^d	0.737 ± 0.020	0.709 ± 0.021	1.159 ± 0.020	1.159 ± 0.020	Upper Sco	5–10	2017	11
EPIC 203476597 ^e	1.41 ± 0.17	...	1.72 ± 0.17	...	Upper Sco	5–10	2016	9
HD144548	0.984 ± 0.007	0.944 ± 0.017	1.319 ± 0.010	1.330 ± 0.010	Upper Sco	5–10	2015	13
	1.44 ± 0.04 ^f		2.41 ± 0.03 ^f					
HR 5934	5.74 ± 0.20	2.66 ± 0.070	2.751 ± 0.029	1.701 ± 0.018	Upper Sco	5–10	2017	11
V1174 Ori	1.006 ± 0.013	0.7271 ± 0.0096	1.338 ± 0.011	1.063 ± 0.011	Ori OB 1c	5–10	2004	14
NP Per	1.3207 ± 0.0087	1.0456 ± 0.0046	1.372 ± 0.013	1.229 ± 0.013	Per OB 2	6–15	2016	15
RXJ 0529.4+0041A	1.27 ± 0.01	0.93 ± 0.01	1.44 ± 0.10	1.35 ± 0.10	Ori OB 1a	7–13	2000	16,17,18
ASAS J0528+03	1.375 ± 0.028	1.329 ± 0.020	1.83 ± 0.07	1.73 ± 0.07	Ori OB 1a	7–13	2008	19
V453 Cyg	14.36 ± 0.20	11.11 ± 0.13	8.551 ± 0.055	5.489 ± 0.063	NGC 6871	10	2004	20
V618 Per	2.332 ± 0.031	1.558 ± 0.025	1.64 ± 0.10	1.32 ± 0.10	h Persei	13	2004	21
V615 Per	4.075 ± 0.055	3.179 ± 0.051	2.29 ± 0.14	1.903 ± 0.094	h Persei	13	2004	21
MML 53	0.994 ± 0.030	0.857 ± 0.026	2.201 ± 0.071 ^f		UCL	15	2010	22,23
HCG 76	0.2768 ± 0.0072	0.3020 ± 0.0073	0.319 ± 0.036	0.34 ± 0.11	Pleiades	125	2016	24
MHO 9	0.41 ± 0.18	0.172 ± 0.069	0.46 ± 0.11	0.321 ± 0.060	Pleiades	125	2016	24

Table 1.1 Continued: Young eclipsing binaries

Name	M_{pri} (M_{\odot})	M_{sec} (M_{\odot})	R_{pri} (R_{\odot})	R_{sec} (R_{\odot})	Cluster ^a	Age (Myr)	Year	Refs.
HII 2407 ^e	0.81 ± 0.08	0.18 ± 0.02	0.77 ± 0.13	0.21 ± 0.04	Pleiades	125	2015	25
HD 23642	2.203 ± 0.013	1.5488 ± 0.0093	1.727 ± 0.027	1.503 ± 0.045	Pleiades	125	2003	24, 26–29
2MJ0446+19	0.47 ± 0.05	0.19 ± 0.02	0.56 ± 0.02	0.21 ± 0.01	NGC 1647	150	2006	30
V818 Tau	1.06 ± 0.01	0.90 ± 0.02	0.76 ± 0.01	0.77 ± 0.01	Hyades	600–800	2002	31
AD 2615	0.212 ± 0.012	0.255 ± 0.013	0.233 ± 0.013	0.267 ± 0.014	Praesepe	600–800	2017	32
AD 3116 ^e	0.276 ± 0.020	0.0517 ± 0.0039	0.29 ± 0.08	0.11 ± 0.03	Praesepe	600–800	2017	32
AD 3814	0.3813 ± 0.0074	0.2022 ± 0.0045	0.3610 ± 0.0033	0.2256 ± 0.0063	Praesepe	600–800	2017	32, 33
AD 1508	0.45 ± 0.19	0.53 ± 0.21	0.548 ± 0.099	0.45 ± 0.10	Praesepe	600–800	2017	32

REFERENCES. — 1. Stassun et al. (2006); 2. Stassun et al. (2007); 3. Irwin et al. (2007); 4. Cargile et al. (2008); 5. Stassun et al. (2008); 6. Casey et al. (1998); 7. Gillen et al. (2014); 8. Torres et al. (2010); 9. David et al. (2016b); 10. Lodieu et al. (2015a); 11. David et al., *in prep.*; 12. Kraus et al. (2015); 13. Alonso et al. (2015); 14. Stassun et al. (2004); 15. Lacy et al. (2016); 16. Covino et al. (2000); 17. Covino et al. (2001); 18. Covino et al. (2004); 19. Stempels et al. (2008); 20. Southworth et al. (2004a); 21. Southworth et al. (2004b); 22. Hebb et al. (2010); 23. Hebb et al. (2011); 24. David et al. (2016a); 25. David et al. (2015); 26. Torres (2003); 27. Munari et al. (2004); 28. Southworth et al. (2005); 29. Groenewegen et al. (2007); 30. Hebb et al. (2006); 31. Torres & Ribas (2002); 32. Gillen et al. (2017); 33. Kraus et al. (2017).

NOTES. — Systems in bold were discovered from *K2* photometry.

^a ONC = Orion Nebula Cluster; UCL = Upper Centaurus Lupus; Upper Sco = Upper Scorpius.

^b Quadruple system. Requires AO-resolved spectroscopy to determine masses and radii.

^c Known tertiary companion.

^d Preliminary solution for masses and radii.

^e Single-lined. Masses and radii are model-dependent.

^f Tertiary component that is also eclipsing.

^g Radius sum (individual radii have not been determined).

1.2 Towards measuring planetary evolution and migration timescales

Much of exoplanetary science is focused on constraining planet formation theory on the basis of exoplanet demographics. The approach relies on compiling a large enough sample of “typical” exoplanets so that the peaks and valleys in the distribution of planets (in e.g. the mass-separation or radius-separation plane) become apparent. This line of reasoning has proven fruitful, despite the observational biases unique to different exoplanet detection methods. An orthogonal approach towards constraining planet formation and migration theories is by studying how the properties and prevalence of planets of various types evolve with time. Such an approach requires the precise characterization of exoplanets within young stellar populations, and a careful assessment of the sensitivity of exoplanet surveys that target young stars.

An obvious disadvantage to this approach is that precious few exoplanets have been discovered around young stars. This is simply because young stars are both scarce and unfavorable for transit and radial velocity surveys due to large amplitude variability, often on timescales similar to those of the signals induced by planets. Direct imaging is one technique which is actually better suited for young stars because planets are more luminous at younger ages, but after years of dedicated searches it has become apparent that the mass and separation range probed by current instruments is scarcely populated, i.e. giant planets on wide orbits are rare (e.g. Metchev & Hillenbrand, 2009; Bowler, 2016).

All of the currently known and proposed close-in exoplanets in sub-Gyr stellar populations are compiled in Table 1.2. Giant planets on wide orbits detected via direct imaging have been excluded from this compilation, as they were recently summarized in Table 1 of Bowler (2016). A notable recent addition to that list, however, is a directly imaged candidate around the proposed (and controversial) hot Jupiter host CVSO 30 in the Orion OB1a association, which is difficult to confirm via common proper motion due to the host star’s small proper motion (Schmidt et al., 2016).

Table 1.2: Known and proposed exoplanets in sub-Gyr populations detected via the transit or radial velocity method.

Parent Population	Age (Myr)	Planet	Host SpT	Period (d)	R_P (R_\oplus)	M_P^a (M_{Jup})	Method	Status	Year	Ref.
Taurus	≈ 2	V830 Tau b	M0	4.93 ± 0.05	...	0.63 ± 0.11	RV	confirmed	2016	1
Taurus	≈ 2	CI Tau b	K4IV	8.989 ± 0.020	...	8.08 ± 1.53	RV	candidate	2016	2
Orion OB1a	$\approx 2-3$	CVSO 30 b	M3	0.448413 ± 0.000040	21.4 ± 2.4	$<4.8 \pm 1.2$	transit	candidate	2012	3–10
Upper Sco	$\approx 5-10$	K2-33 b	$M3 \pm 0.5$	5.42513 ± 0.00029	5.8 ± 0.6	<3.6	transit	confirmed	2016	11,12
Taurus	≈ 17	TAP 26 b	K7	10.79 ± 0.14	...	1.66 ± 0.31	RV	confirmed	2017	13
AB Dor	35–80	BD+20 1790 b	K5Ve	$7.78287^{+0.00077}_{-0.00076}$...	6.37 ± 1.35	RV	confirmed	2010	14,15
Ursa Major	414 ± 23	HD 147513 b	G5V	528.4 ± 6.3	...	1.21	RV	confirmed	2004	16
Hyades	$\approx 650-800$	ϵ Tau b	K0III	594.9 ± 5.3	...	7.6 ± 0.2	RV	confirmed	2007	17
Hyades	$\approx 650-800$	HD 285507 b	K4.5V	6.0881 ± 0.0019	...	0.917 ± 0.033	RV	confirmed	2014	18
Hyades	$\approx 650-800$	K2-25 b	$M4.5 \pm 0.3$	3.484552 ± 0.000037	$3.43^{+0.95}_{-0.31}$	<3	transit	confirmed	2016	19,20
NGC 2423	≈ 750	NGC 2423 No. 3 b	A0	714	...	10.6	RV	confirmed	2007	21
Praesepe	≈ 800	Pr0201 b	F7.5	4.4264 ± 0.0070	...	0.540 ± 0.039	RV	confirmed	2012	22
Praesepe	≈ 800	Pr0211 b	G9.3	2.1451 ± 0.0012	...	1.844 ± 0.064	RV	confirmed	2012	22
Praesepe	≈ 800	Pr0211 c	G9.3	>3500	...	7.9 ± 0.2	RV	confirmed	2016	23
Praesepe	≈ 800	K2-95 b	M3	10.13509 ± 0.00050	3.7 ± 0.2	...	transit	confirmed	2016	24–27
Praesepe	≈ 800	K2-100 b	F8	1.673916 ± 0.000013	3.5 ± 0.2	...	transit	confirmed	2016	25,26
Praesepe	≈ 800	K2-101 b	K3	14.67729 ± 0.00083	2.0 ± 0.1	...	transit	confirmed	2017	26
Praesepe	≈ 800	K2-102 b	K4	9.9156 ± 0.0012	1.3 ± 0.1	...	transit	confirmed	2017	26
Praesepe	≈ 800	K2-103 b	K9	21.1696 ± 0.0017	2.2 ± 0.2	...	transit	confirmed	2017	26
Praesepe	≈ 800	K2-104 b	M1	1.97419 ± 0.00011	1.9 ± 0.2	...	transit	confirmed	2016	25,26
Praesepe	≈ 800	EPIC 211901114	M3	1.648932 ± 0.000071	9.6 ± 5.3	...	transit	candidate	2017	26

REFERENCES. — 1. Donati et al. (2016); 2. Johns-Krull et al. (2016a); 3. van Eyken et al. (2012); 4. Barnes et al. (2013); 5. Yu et al. (2015); 6. Ciardi et al. (2015); 7. Rätz et al. (2016); 8. Howarth (2016); 9. Johns-Krull et al. (2016b) 10. Onitsuka et al. (2017); 11. David et al. (2016c); 12. Mann et al. (2016a); 13. Yu et al. (2017); 14. Hernán-Obispo et al. (2010); 15. Hernán-Obispo et al. (2015); 16. Mayor et al. (2004); 17. Sato et al. (2007); 18. Quinn et al. (2014); 19. Mann et al. (2016b); 20. David et al. (2016a); 21. Lovis & Mayor (2007); 22. Quinn et al. (2012); 23. Malavolta et al. (2016); 24. Obermeier et al. (2016); 25. Libralato et al. (2016); 26. Mann et al. (2017); 27. Pepper et al. (2017);

^a The reported planet mass is the minimum mass, $M_P \sin i$.

Note: Systems discovered from K2 photometry are highlighted in bold.

Several authors have previously studied the roles of stellar age and environment on the measured occurrence rates of exoplanets, through both the transit and radial velocity (RV) detection methods. Gilliland et al. (2000) carried out the first dedicated search for transiting planets within a cluster, using *Hubble Space Telescope* photometry of tens of thousands of stars in the globular cluster 47 Tucanae. With no detections (compared to an expected ~ 17), those authors suggested the occurrence of close-in giant planets in that cluster may be fundamentally lower than the rate measured for field stars. Wel Drake et al. (2005) targeted the same cluster from the ground, and confirmed that there were no transiting hot Jupiters among nearly 22,000 targets, compared to an expected yield of seven planets based on solar neighborhood occurrence rates. Those authors attributed the dearth of hot Jupiters in 47 Tuc to that cluster's low metallicity ($[Fe/H]=-0.76$). However, the null results in 47 Tuc were reassessed by Masuda & Winn (2017) who showed that the discrepancy in hot Jupiter occurrence rates between that cluster and the field is less statistically significant after accounting for stellar mass-dependent effects and the low observed rate of transiting giant planets from *Kepler*. Similar null results have been found from ground-based photometry of tens of thousands of stars in the ω Centauri globular cluster (Wel Drake et al., 2008) and *HST* photometry of several thousand stars in the globular cluster NGC 6397 (Nascimbeni et al., 2012). The former study was only sensitive to planets larger than $\sim 1.5 R_{Jup}$ and the latter investigation could only place an upper limit on the rate of Jupiter-sized planets that is consistent with field statistics.

There have also been many transiting planet searches in open clusters of varying ages, all of them utilizing ground-based facilities with the exception of the recent surveys enabled by the *K2* mission. We summarize the results of transiting planet searches within coeval stellar populations in Table 1.3. With the exception of the *K2* studies, none of these candidates have been confirmed, some have turned out to be non-members, and most are unconvincing. It is likely that all of the ground-based surveys lacked the combination of detection efficiency and sample size needed in order to detect even a single transiting planet. van Saders & Gaudi (2011) performed a meta-analysis of an ensemble of open cluster transit surveys, concluding that the non-detections from these surveys were in fact consistent with expectations from the field occurrence rates of hot Jupiters.

Table 1.3: Transiting planet searches in coeval stellar populations.

Population	Type	Age (Myr)	Distance (pc)	[Fe/H] (dex)	Stars	Nights	Hours	Candidates (Confirmed)	Reference
NGC 2362	OC	5^{+1}_{-2}	1480	...	475	18	100	6 (0)	Miller et al. (2008)
Upper Scorpius	OBa	5–10	145 ± 2	≈ 0.0	~ 1000	78.8	1890	1 (1)	David et al. (2016c) and Mann et al. (2016a)
NGC 7086	OC	100	1500	...	1000	12	60	0	Rosvick & Robb (2006)
Pleiades (M45)	OC	125 ± 8	134 ± 3	$+0.02 \pm 0.03$	1014	70.9	1701	0	Gaidos et al. (2017)
NGC 2301	OC	140 ± 80	872	$+0.05 \pm 0.01$	4000	12	70	0	Howell et al. (2005)
NGC 2099 (M37)	OC	360 ± 190	1500 ± 100	$+0.05 \pm 0.04$	1450	24	~ 67	0	Hartman et al. (2009)
NGC 6633	OC	520 ± 250	415 ± 7	-0.08 ± 0.12	2000	186	131	0	Hidas et al. (2005)
Hyades (Melotte 25)	OC	720 ± 130	47 ± 1	$+0.13 \pm 0.05$	80	70.9	1701	1 (1)	Mann et al. (2016b) and David et al. (2016a)
NGC 2632 (Praesepe)	OC	730 ± 190	183 ± 8	$+0.16 \pm 0.08$	142	34	130	2 (0)	Pepper et al. (2008)
NGC 2632 (Praesepe)	OC	730 ± 190	183 ± 8	$+0.16 \pm 0.08$	~ 900	71.9	1727	7 (6)	Mann et al. (2017) and Libralato et al. (2016)
NGC 6940	OC	950 ± 460	770	+0.15	50000 [†]	18	22	2	Hood et al. (2005)
NGC 6811	OC	1000 ± 170	1107 ± 90	-0.19	377	310	7440	2 (2)	Meibom et al. (2013)
NGC 1245	OC	1070 ± 230	2800 ± 200	$+0.02 \pm 0.03$	870	19	78	6 (0)	Burke et al. (2006)
NGC 2660	OC	1310 ± 260	2826	$+0.04 \pm 0.03$	3000	19	150	0	von Braun et al. (2004) and von Braun et al. (2005)
NGC 6208	OC	1430 ± 400	1100	-0.01	5000	22	61	0	Lee et al. (2004)
NGC 7789	OC	1530 ± 200	2337	$+0.05 \pm 0.07$	2400	30	73	3 (0)	Bramich et al. (2005) and Bramich & Horne (2006)
NGC 2158	OC	1670 ± 450	3600 ± 400	-0.32 ± 0.08	5159	59	260	1 (0)	Mochejska et al. (2006)
NGC 6819	OC	2110 ± 440	2754 ± 305	$+0.09 \pm 0.01$	276	19	133	8 (0)	Street et al. (2003)
NGC 6253	OC	3500	1510	$+0.39 \pm 0.07$	383	24	72	3 (0)	Montalto et al. (2009) and Montalto et al. (2011)
NGC 188	OC	6270 ± 2300	1710 ± 80	$+0.11 \pm 0.04$	1450	45	87	0	Mochejska et al. (2008)
NGC 6791	OC	7000 ± 2460	4200	$+0.42 \pm 0.05$	3580	7	56	10 (0)	Bruntt et al. (2003)
NGC 6791	OC	7000 ± 2460	4200	$+0.42 \pm 0.05$	650	84	>300	0	Mochejska et al. (2005)
NGC 6791	OC	7000 ± 2460	4200	$+0.42 \pm 0.05$	3311	28	170	0	Montalto et al. (2007)
NGC 5139 (ω Cen)	GC	11520	4840 ± 340	-1.35	31000	25	225	0	Weldrake et al. (2008)
NGC 6397	GC	12670	2670	-1.76	2215	8.4	50	0	Nascimbeni et al. (2012)
NGC 104 (47 Tuc)	GC	13060	4700	-0.78	34000	8.3	199	0	Gilliland et al. (2000)
NGC 104 (47 Tuc)	GC	13060	4700	-0.78	21920	33	330	0	Weldrake et al. (2005)

Table adapted from Janes & Kim (2009). Ages and metallicities for open clusters originate from Netopil et al. (2016), when available, and from Marín-Franch et al. (2009) for globular clusters. Otherwise, ages and metallicities are taken from the planet search article referenced in line. Open cluster distances originate from Gaia Collaboration et al. (2017) when available, the planet search reference or the WEBDA open cluster database otherwise.

[†] This number represents the total number of stars surveyed, most of which are not cluster members. An estimate of the number of cluster members was not provided.

OC: open cluster; OBa: OB association; GC: globular cluster

From *Kepler* observations of the Gyr-old solar-metallicity open cluster NGC6811, Meibom et al. (2013) determined the occurrence rate of transiting planets smaller than Neptune to be equivalent for open clusters and field stars. Studies of the solar-age cluster M67 have concluded that giant planet occurrence, as measured by RVs, in the open cluster is in agreement with field statistics but that hot Jupiters seem to be more common in that cluster than in the field (Brucalassi et al., 2016; Brucalassi et al., 2017). Now, in the era of *K2*, it is possible to study the differential occurrence of planets across a wide range of stellar ages and environs. The mission has observed, and continues to observe, populations as young as only a few Myr (when protoplanetary disks are still present for a majority of stars) and as old as ~ 12 Gyr. After mapping the population of planets close to normal, solar-type stars, a natural progression is to compare these results against populations of varying evolutionary states, masses, and environments.

Different exoplanet detection methods measure different planetary properties and each method is subject to observational biases that limit its utility to specific regions of planet parameter space. The direct imaging method, for example, is currently sensitive only to giant planets on wide orbits and is biased towards planetary systems that are face-on. In principle, the masses of directly imaged planets could be measured through astrometry of the host star or radial velocities (given a favorable inclination), but this requires a long time baseline, high instrumental precision, and to date has not been feasible. Thus, the mass of a directly imaged exoplanet is inferred through its radiative properties (namely, its flux contrast with the host star) and theoretical models which predict planet luminosities as a function of age. Importantly, there are no known exoplanetary systems which allow us to assess the accuracy of such models. Nevertheless, direct imaging remains one of our best methods for studying planets on wide orbits.

The radial velocity method measures the minimum mass, $M_P \sin i$, of an exoplanet from the amplitude of a star's reflex motion as it orbits the center of mass of the star-planet system. The method is biased towards massive planets on close orbits, but current instruments are capable of measuring Jupiter analogs and even close-in Earth-mass planets for stars that are not too magnetically active. Because a star's inclination is often difficult to constrain, radial velocities are only useful for measuring planet masses in a statistical sense. Nevertheless, the method is critical for constructing the mass-radius relation of exoplanets and is less sensitive to inclination than the transit method (unlike the transit method, a nearly edge-on

orientation is not required to detect a planet orbiting far from its star).

For a transiting planet, the ratio of the planet radius to the host star radius is measured directly from the light curve and, given that the inclination is also constrained by the light curve, a precise mass can be measured from RVs. Thus, empirically constructing the mass-radius relation for exoplanets requires transiting planets. Much like EBs in clusters, transiting planets in clusters are our most valuable benchmarks for studying the evolution of planet properties. Differences in the mass-radius relations between young and old exoplanets would be a clear indication that evolutionary processes (e.g. gravitational contraction, atmospheric photoevaporation) govern exoplanet properties.

1.2.1 Inflated planetary radii at young ages?

Over the past three years, the *K2* mission (Howell et al., 2014) has had a profound impact on the burgeoning field of young exoplanetary science, contributing all of the secure transiting planets around known young stars. The sample includes a single planet in the Upper Scorpius OB association ($\approx 5\text{--}10$ Myr, David et al., 2016c; Mann et al., 2016a), a planet in the Hyades ($\approx 650\text{--}800$ Myr, Mann et al., 2016b; David et al., 2016a), and six planets and one candidate in Praesepe (≈ 800 Myr, Obermeier et al., 2016; Libralato et al., 2016; Mann et al., 2017; Pepper et al., 2017). To date, no transiting planets have been discovered in the Pleiades (≈ 125 Myr), despite the fact that the *K2* mission observed several hundred members (Gaidos et al., 2017).

Most of the young transiting exoplanets discovered with *K2* orbit low-mass stars, and an intriguing trend emerging from this population of planets is that they appear larger than typical close-in planets around field-age low-mass stars. That is, the occurrence rate of Neptune-sized close-in planets is seemingly higher for young low-mass stars than the rate measured for field age low-mass stars (Mann et al., 2017; Obermeier et al., 2016). Assuming these young planets are progenitors of the ubiquitous class of close-in “super-Earths” or “mini-Neptunes,” it is tempting to attribute the anomalously large radii to unfinished contraction or ongoing atmospheric mass loss. Indeed, there appears to be a distinct gap in the radius distribution of small planets discovered with *Kepler* (Fulton et al., 2017), a feature that some authors have attributed to photoevaporation and termed the “evaporation valley” (Owen & Wu, 2013; Owen & Wu, 2017). If photoevaporation is indeed important in the early evolution of the atmospheres of close-in, low-mass exoplanets, one might expect to observe enhanced mass-loss rates (through e.g. extended exospheres inferred

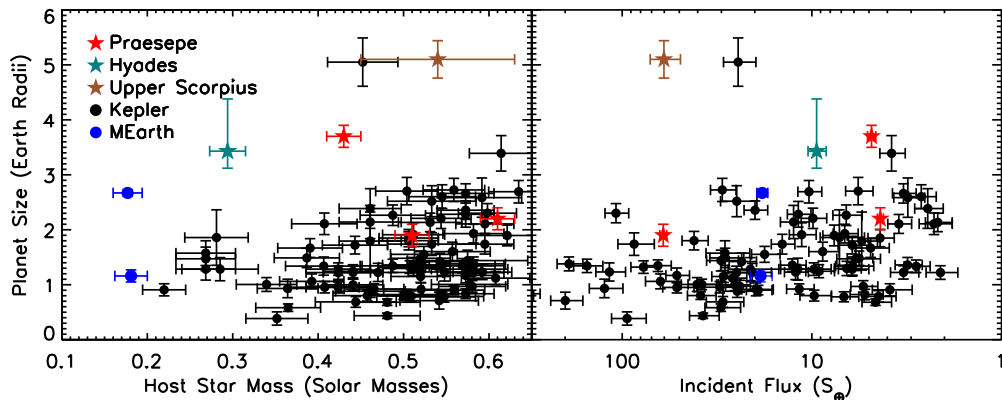


Figure 1.3: Reproduction of Figure 10 from Mann et al. (2017). Sizes of transiting planets around low-mass stars as a function of host star mass (left) and incident flux (right). Only planets transiting host stars less massive than $0.65 M_{\odot}$ and with orbital periods <30 d are included. Young planets discovered from *K2* data are indicated by stars while field planets are shown as points. ©AAS. Reproduced with permission.

from Ly- α absorption during transits) for such planets around young stars which are strong UV and X-ray emitters. This is a testable prediction that current and planned observations with the *Hubble Space Telescope* will address.

In Chapters IV and VIII I report the discovery and characterization of Neptune-sized transiting planets around low-mass stars in the Hyades and Upper Scorpius, respectively. Both planets, K2-25 b (Hyades) and K2-33 b (Upper Scorpius), exhibit the anomalously large radii discussed above and are considered intriguing targets for atmospheric characterization. The planet in Upper Scorpius, in particular, provides evidence that planets with significant gaseous envelopes can be found on short-period orbits shortly after the dispersal of the primordial planetary disk. In Chapter IX I present preliminary measurements of the occurrence rate of large planets orbiting low-mass stars at the age of Upper Scorpius. Initial results suggest the occurrence of close-in Neptune-sized planets at ~ 10 Myr is consistent with the rates measured for field stars.

1.2.2 The masses of directly imaged companions

While transit searches are most sensitive to close-in planets, direct imaging is sensitive only to planets at large separations from their host stars. In this sense, the methods are complementary and both are crucial to our understanding of how planets form. In principle, with sufficiently precise instruments, the contraction timescales of cold Jovian-mass exoplanets can be traced by observing planetary luminosities in stellar populations of different ages. In this way, one can discriminate

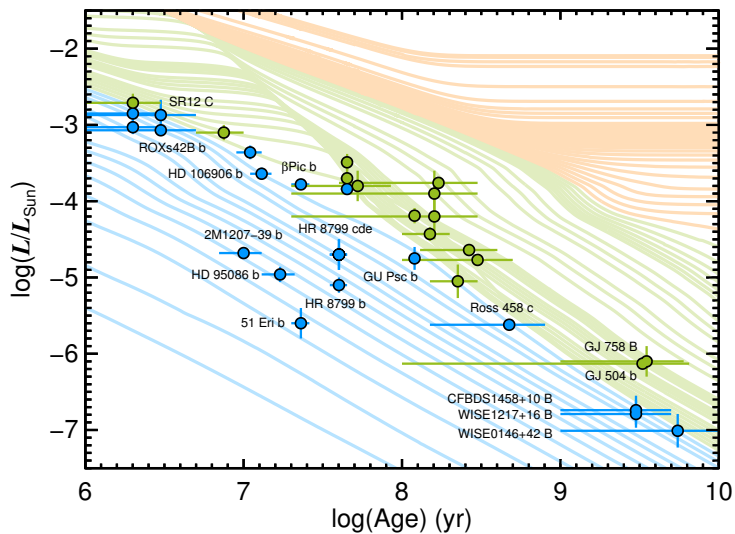


Figure 1.4: Reproduction of Figure 6 from Bowler (2016). Orange, green, and blue curves show theoretical predictions for the temporal evolution of luminosity of low-mass stars ($>80 M_{\text{Jup}}$), brown dwarfs ($14\text{--}80 M_{\text{Jup}}$), and planetary-mass companions ($<14 M_{\text{Jup}}$) respectively. Points represent directly imaged companions in either the planetary (blue) or brown dwarf (green) mass regimes. Large errors in the ages of host stars translate into large uncertainties in model-derived companion masses. The prevalence of directly imaged companions (i.e. extreme mass ratio companions at large orbital separations) has implications for star and planet formation theories. ©The Astronomical Society of the Pacific. Reproduced with permission.

between various models of planet formation at wide separations. Although the technique is more direct than other exoplanet detection methods (hence the name) it still relies on accurate characterization of the host star in order to determine the parameters (namely masses) of any companions. However, there is an important difference between direct imaging and other exoplanet detection methods in this regard: masses of directly imaged companions are inferred from stellar ages and while the masses and radii of stars are typically known with adequate precision, ages are not (Figure 1.4 demonstrates this problem for a current census of directly imaged companions). Stars in coeval populations are an exception, and consequently young associations and moving groups have been repeatedly targeted.

Another approach has been to target intermediate-mass stars because (1) they are

intrinsically bright and young (and thus their planets are thought to be in a state of contraction), (2) protoplanetary disks around these stars are presumed to be more massive, and (3) RV surveys have revealed a trend of rising giant planet occurrence with stellar mass (Fischer & Valenti, 2005). The problem is that the youngest intermediate-mass field stars will sit securely on the ZAMS, since it is unlikely to find such a massive pre-MS star not kinematically associated with a known young region. Evolution is slow on the MS, and hence the fractional uncertainties in the ages of such stars are large. These uncertainties translate directly into uncertainties in the masses of directly imaged companions (or in assessments of survey sensitivity if no companion is found). Unfortunately, there are no empirical age relations for intermediate mass stars, owing primarily to the fact that they lack convective envelopes and do not spin down through magnetized winds. Thus, age-dating in an H-R diagram, color-magnitude diagram, or some equivalent is currently the most quantitative method for these stars.

Several recent studies have addressed this problem (Brandt & Huang, 2015a; David & Hillenbrand, 2015; Jones et al., 2015), all reaching one overarching conclusion: the sky-projected rotational velocity is a critical parameter in the age determination of intermediate-mass stars. For the same reason these stars do not spin down in a predictable fashion, they retain rapid rotation rates throughout their main-sequence lifetimes. Rotation has two important effects: (1) rotationally-induced mixing delivers hydrogen to the core and enhances the main-sequence lifetime by $\sim 25\%$ on average, and (2) it induces observable pole-to-equator gradients in temperature and luminosity or surface gravity (Peterson et al., 2006). The first effect must be accounted for by utilizing stellar models which properly treat rotation. The second effect causes rapidly rotating stars to appear older the closer they are to an edge-on orientation (because the star is oblate, the observer is viewing a larger surface area of low-gravity, cool gas). As an aside, because stars are born with a range of rotation rates, rotation can induce color-magnitude (CMD) spreads in the upper main sequence of clusters and mimic genuine age spreads (Brandt & Huang, 2015b). Thus, there is some fundamental limit on the precision with which one can hope to determine the age of an intermediate mass star in a CMD in the absence of detailed knowledge regarding its spin rate, inclination, and metallicity. In Chapter II I present a detailed approach towards the age determination of early-type stars, and apply the method to approximately 3500 nearby stars that are likely targets for direct imaging surveys.

1.2.3 The future of exoplanet science at young ages

Despite the difficulties associated with searching for exoplanets around young stars, there are many reasons to be optimistic about the future of this subfield. Mapping the surfaces of young, spotted stars via Zeeman-Doppler Imaging has proven useful in disentangling radial velocity variability due to stellar surface features from the reflex motions induced by close-in giant planets (see Donati et al., 2016; Yu et al., 2017). New and upcoming precision radial velocity instruments that operate in the near-infrared are ideal for planet searches in young populations: the intrinsic radial velocity variations of spotted stars are of smaller amplitude in the infrared relative to the optical and these instruments are well-suited for red, low-mass stars, constituting the vast majority of stars in coeval populations. These instruments include CARMENES (Quirrenbach et al., 2014), HPF (Mahadevan et al., 2012), the Infrared Doppler (IRD) spectrograph (Tamura et al., 2012), and SPIRou (Artigau et al., 2014). The earliest results from the Atacama Large Millimeter Array are already providing some of our most powerful constraints yet on planet formation at wide separations (ALMA Partnership et al., 2015; Andrews et al., 2016; Pérez et al., 2016). Major advances in coronagraph design and speckle suppression will unlock regions of the planet mass-separation plane that have not yet been probed (see Mawet et al., 2012, for a review), particularly when paired with a space mission such as *WFIRST*. Atmospheres of exoplanets will be revealed in new detail with *JWST*, and young exoplanets may be some of the most intriguing targets if their atmospheres have not yet equilibrated. Finally, TESS will tile nearly all of the sky with a photometric precision similar to that of *K2* (Ricker et al., 2015). The mission will deliver full-frame images at a cadence equivalent to that of *K2*, in the process observing a large number of young stars around which short-period planets may be sought.

Chapter 2

THE AGES OF EARLY-TYPE STARS: STRÖMGREN
PHOTOMETRIC METHODS CALIBRATED, VALIDATED,
TESTED, AND APPLIED TO HOSTS AND PROSPECTIVE
HOSTS OF DIRECTLY IMAGED EXOPLANETS

David, T. J., & Hillenbrand, L. A., 2015, ApJ, 804, 146

ABSTRACT

Age determination is undertaken for nearby early-type (BAF) stars, which constitute attractive targets for high-contrast debris disk and planet imaging surveys. Our analysis sequence consists of: acquisition of $uvby\beta$ photometry from catalogs, correction for the effects of extinction, interpolation of the photometry onto model atmosphere grids from which atmospheric parameters are determined, and finally, comparison to the theoretical isochrones from pre-main sequence through post-main sequence stellar evolution models, accounting for the effects of stellar rotation. We calibrate and validate our methods at the atmospheric parameter stage by comparing our results to fundamentally determined T_{eff} and $\log g$ values. We validate and test our methods at the evolutionary model stage by comparing our results on ages to the accepted ages of several benchmark open clusters (IC 2602, α Persei, Pleiades, Hyades). Finally, we apply our methods to estimate stellar ages for 3493 field stars, including several with directly imaged exoplanet candidates.

2.1 Introduction

In contrast to other fundamental stellar parameters such as mass, radius, and angular momentum – that for certain well-studied stars and stellar systems can be anchored firmly in observables and simple physics – stellar ages for stars other than the Sun have no firm basis. Ages are critical, however, for many investigations involving time scales including formation and evolution of planetary systems, evolution of debris disks, and interpretation of low mass stars, brown dwarfs, and so-called planetary mass objects that are now being detected routinely as faint point sources near bright stars in high contrast imaging surveys.

2.1.1 The Era of Direct Imaging of Exoplanets

Intermediate-mass stars ($1.5 - 3.0 M_{\odot}$) have proven themselves attractive targets for planet search work. Hints of their importance first arose during initial data return from IRAS in the early 1980s, when several A-type stars (notably Vega but also β Pic and Fomalhaut) as well K-star Eps Eri – collectively known as “the fab four” – distinguished themselves by showing mid-infrared excess emission due to optically thin dust in Kuiper-Belt-like locations. Debris disks are signposts of planets, which dynamically stir small bodies resulting in dust production. Spitzer results in the late 2000s solidified the spectral type dependence of debris disk presence (e.g. Carpenter et al. 2006; Wyatt 2008) for stars of common age. For a random sample of field stars, however, the primary variable determining the likelihood of debris is stellar age (Kains et al., 2011).

The correlation in radial velocity studies of giant planet frequency with stellar mass (Fischer & Valenti, 2005; Gaidos et al., 2013) is another line of evidence connecting planet formation efficiency to stellar mass. The claim is that while $\sim 14\%$ of A stars have one or more $> 1M_{\text{Jupiter}}$ companions at < 5 AU, only $\sim 2\%$ of M stars do (Johnson et al. 2010, c.f. Lloyd 2013; Schlaufman & Winn 2013).

Consistently interpreted as indicators of hidden planets, debris disks finally had their long-awaited observational connection to planets with the watershed discovery of *directly imaged* planetary mass companions. These were – like the debris disks before them – found first around intermediate-mass A-type stars, rather than the solar-mass FGK-type stars that had been the subject of much observational work at high contrast during the 2000s. HR 8799 (Marois et al., 2008; Marois et al., 2010) followed by Fomalhaut (Kalas et al., 2008) and β Pic (Lagrange et al., 2009; Lagrange et al., 2010) have had their planets *and indeed one planetary*

system, digitally captured by ground-based and/or space-based high contrast imaging techniques. Of the known *bona fide* planetary mass ($< 10M_{\text{Jup}}$) companions that have been directly imaged, six of the nine are located around the three A-type host stars mentioned above, with the others associated with lower mass stars including the even younger 5-10 Myr old star 1RXS 1609-2105 (Lafrenière et al., 2008; Ireland et al., 2011) and brown dwarf 2MASS 1207-3933 (Chauvin et al., 2004) and the probably older GJ 504 (Kuzuhara et al., 2013). Note that to date these directly imaged objects are all “super-giant planets” and not solar system giant planet analogs (e.g. Jupiter mass or below).

Based on the early results, the major direct imaging planet searches have attempted to optimize success by preferentially observing intermediate-mass, early-type stars. The highest masses are avoided due to the limits of contrast. Recent campaigns include those with all the major large aperture telescopes: Keck/NIRC2, VLT/NACO, Gemini/NICI, and Subaru/HiCAO. Current and near-future campaigns include Project 1640 (P1640; Hinkley et al. 2011) at Palomar Observatory, Gemini Planet Imager (GPI), operating on the Gemini South telescope, VLT/SPHERE, and Subaru/CHARIS. The next-generation TMT and E-ELT telescopes both feature high contrast instruments.

Mawet et al. (2012) compares instrumental contrast curves in their Figure 1. Despite the technological developments over the past decade, given the as-built contrast realities, only the largest, hottest, brightest, and therefore the youngest planets, i.e. those less than a few to a few hundred Myr in age, are still self-luminous enough to be amenable to direct imaging detection. Moving from the 3-10 M_{Jupiter} detections at several tens of AU that are possible today/soon, to detection of lower mass, more Earth-like planets located at smaller, more terrestrial zone, separations, will require pushing to higher contrast from future space-based platforms. The targets of future surveys, whether ground or space, are however not likely to be substantially different from the samples targeted in today’s ground-based surveys.

The most important parameter really is age, since the brightness of planets decreases so sharply with increasing age due to the rapid gravitational contraction and cooling (Fortney et al., 2008; Burrows et al., 2004). There is thus a premium on identifying the closest, youngest stars.

2.1.2 The Age Challenge

Unlike the other fundamental parameters of stellar mass (unambiguously determined from measurements of double-line eclipsing binaries and application of Kepler's laws) and stellar radius (unambiguously measured from interferometric measurements of angular diameters and parallax measurements of distances), there are no directly interpretable observations leading to stellar age.

Solar-type stars ($\sim 0.7 - 1.4M_{\odot}$, spectral types F6-K5) were the early targets of radial velocity planet searches and later debris disk searches that can imply the presence of planets. For these objects, although more work remains to be done, there are established activity-rotation-age diagnostics that are driven by the presence of convective outer layers and can serve as proxies for stellar age (e.g. Mamajek & Hillenbrand, 2008).

For stars significantly different from our Sun, however, and in particular the intermediate-mass stars ($\sim 1.5 - 3.0M_{\odot}$, spectral types A0-F5 near the main sequence) of interest here, empirical age-dating techniques have not been sufficiently established or calibrated. Ages have been investigated recently for specific samples of several tens of stars using color-magnitude diagrams by Nielsen et al. (2013), Vigan et al. (2012), Moór et al. (2006), Su et al. (2006), Rhee et al. (2007), and Lowrance et al. (2000).

Perhaps the most robust ages for young BAF stars come from clusters and moving groups, which contain not only the early-type stars of interest, but also lower mass stars to which the techniques mentioned above can be applied. These groups are typically dated using a combination of stellar kinematics, lithium abundances, rotation-activity indicators, and placement along theoretical isochrones in a color-magnitude diagram. The statistics of these coeval stellar populations greatly reduce the uncertainty in derived ages. However, only four such groups exist within ~ 60 pc of the Sun and the number of early-type members is small.

Field BAF stars having late-type companions at wide separation could have ages estimated using the methods valid for F6-K5 age dating. However, these systems are not only rare in the solar neighborhood, but considerable effort is required in establishing companionship e.g. Stauffer et al. (1995), Barrado y Navascués et al. (1997), and Song et al. (2000). Attempts to derive fractional main sequence ages for A-stars based on the evolution of rotational velocities are ongoing (Zorec & Royer, 2012), but this method is undeveloped and a bimodal distribution in $v \sin i$ for early-type A-stars may inhibit its utility. Another method, asteroseismology, which detects low-order oscillations in stellar interiors to determine the central density and

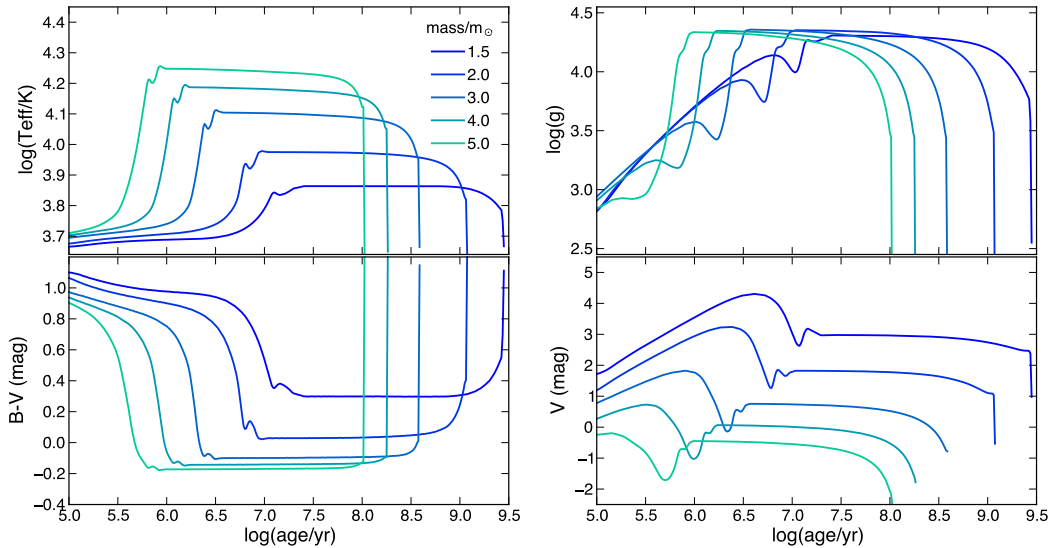


Figure 2.1: *Top panels:* Evolution of $\log T_{\text{eff}}$ and $\log g$ with age for intermediate-mass stars, as predicted by PARSEC evolutionary models (Bressan et al., 2012). *Bottom panels:* Same evolutionary trends for $B - V$ (close to $b - y$) and M_V mag, as might be used to discern ages from color-magnitude diagram evolution (e.g. Nielsen et al., 2013). While the color and temperature trends reflect one another, the absolute magnitude trends are not as strong as the surface gravity trends when the stars are evolving from the main sequence after a few hundred Myr. The PARSEC models predict the precision in $\log g$ needed to distinguish a $1.5M_{\odot}$ star and a $2.0M_{\odot}$ star evolves from 0.0397 dex at ~ 30 Myr to 0.0242 dex at 100 Myr to 0.0378 dex at ~ 300 Myr. The precision in $\log g$ needed to distinguish a $1.5M_{\odot}$ star and a $3.0M_{\odot}$ evolves from 0.0085 dex at ~ 30 Myr to 0.0694 dex at 100 Myr to 0.5159 dex at ~ 300 Myr. The precision in $\log g$ needed to distinguish a $2.0M_{\odot}$ star and a $3.0M_{\odot}$ evolves from 0.0312 dex at ~ 30 Myr to 0.0936 dex at 100 Myr to 0.4781 dex at 300 Myr.

hence age, is a heavily model-dependent method, observationally expensive, and best suited for older stars with denser cores.

The most general and quantitative way to age-date A0-F5 field stars is through isochrone placement. As intermediate-mass stars evolve quickly along the H-R diagram, they are better suited for age-dating via isochrone placement relative to their low-mass counterparts which remain nearly stationary on the main sequence for many Gyr (Soderblom, 2010). Indeed, the mere presence of an early-type star on the main sequence suggests moderate youth, since the hydrogen burning phase is relatively short-lived. However, isochronal ages are obviously model-dependent and they do require precise placement of the stars on an H-R diagram implying a parallax. The major uncertainties arise from lack of information regarding metallicity (Nielsen et al., 2013), rotation (Collins & Smith, 1985) and multiplicity (De Rosa et al., 2014).

2.1.3 Our Approach

Despite that many nearby BAF stars are well-studied, historically, there is no modern data set leading to a set of consistently derived stellar ages for this population of stars. Here we apply Strömgren photometric techniques, and by combining modern stellar atmospheres and modern stellar evolutionary codes, we develop the methods for robust age determination for stars more massive than the Sun. The technique uses specific filters, careful calibration, definition of photometric indices, correction for any reddening, interpolation from index plots of physical atmospheric parameters, correction for rotation, and finally Bayesian estimation of stellar ages from evolutionary models that predict the atmospheric parameters as a function of mass and age.

Specifically, our work uses high-precision archival $uvby\beta$ photometry and model atmospheres so as to determine the fundamental stellar atmospheric parameters T_{eff} and $\log g$. Placing stars accurately in an $\log T_{\text{eff}}$ vs. $\log g$ diagram leads to derivation of their ages and masses. We consider Bressan et al. (2012) evolutionary models that include pre-main sequence evolutionary times (2 Myr at $3 M_{\odot}$ and 17 Myr at $1.5 M_{\odot}$), which are a significant fraction of any intermediate mass star’s absolute age, as well as Ekström et al. (2012) evolutionary models that self-consistently account for stellar rotation, which has non-negligible effects on the inferred stellar parameters of rapidly rotating early-type stars. Figure 2.1 shows model predictions for the evolution of both physical and observational parameters.

The primary sample to which our technique is applied in this work consists of 3499 BAF field stars within 100 pc and with $uvby\beta$ photometry available in the Hauck & Mermilliod (1998) catalog, hereafter HM98. The robustness of our method is tested at different stages with several control samples. To assess the uncertainties in our atmospheric parameters we consider (1) 69 T_{eff} standard stars from Boyajian et al. (2013) or Napiwotzki et al. (1993); (2) 39 double-lined eclipsing binaries with standard $\log g$ from Torres et al. (2010); (3) 16 other stars from Napiwotzki et al. (1993), also for examining $\log g$. To examine isochrone systematics, stars in four open clusters are studied (31 members of IC 2602, 51 members of α Per, 47 members of the Pleiades, and 47 members of the Hyades). Some stars belonging to sample (1) above are also contained in the large primary sample of field stars.

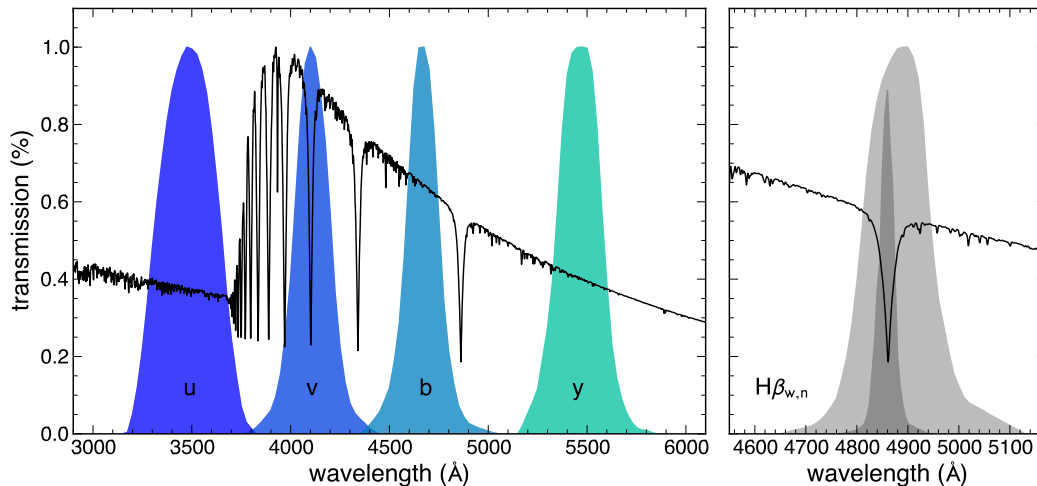


Figure 2.2: The *u*, *v*, *b*, *y*, $H\beta_{\text{wide}}$ and $H\beta_{\text{narrow}}$ passbands. Overplotted on an arbitrary scale is the synthetic spectrum of an A0V star generated by Munari et al. (2005) from an ATLAS9 model atmosphere. The *uvby* filter profiles are those of Bessell (2011), while the $H\beta$ filter profiles are those originally described in Crawford (1966) and the throughput curves are taken from Castelli & Kurucz (2006).

2.2 The Strömgren Photometric System

Historical use of Strömgren photometry methods indeed has been for the purpose of determining stellar parameters for early-type stars. Recent applications include work by Nieva (2013), Dalle Mese et al. (2012), Önehag et al. (2009), and Allende Prieto & Lambert (1999). An advantage over more traditional color-magnitude diagram techniques (Nielsen et al., 2013; De Rosa et al., 2014) is that distance knowledge is not required, so the distance-age degeneracy is removed. Also, metallicity effects are relatively minor (as addressed in the Appendix) and rotation effects are well-modelled and can be corrected for (§ 2.3.3).

2.2.1 Description of the Photometric System

The *uvby β* photometric system is comprised of four intermediate-band filters (*uvby*) first advanced by Strömgren (1966) plus the $H\beta$ narrow and wide filters developed by Crawford (1958); see Figure 2.2. Together, the two filter sets form a well-calibrated system that was specifically designed for studying earlier-type BAF stars, for which the hydrogen line strengths and continuum slopes in the Balmer region rapidly change with temperature and gravity.

From the fluxes contained in the six passbands, five *uvby β* indices are defined. The color indices, $(b - y)$ and $(u - b)$, and the β -index,

$$\beta = H\beta_{\text{narrow}} - H\beta_{\text{wide}}, \quad (2.1)$$

are all sensitive to temperature and weakly dependent on surface gravity for late A- and F-type stars. The Balmer discontinuity index,

$$c_1 = (u - v) - (v - b), \quad (2.2)$$

is sensitive to temperature for early type (OB) stars and surface gravity for intermediate (AF) spectral types. Finally, the metal line index,

$$m_1 = (v - b) - (b - y), \quad (2.3)$$

is sensitive to the metallicity $[M/H]$.

For each index, there is a corresponding intrinsic, dereddened index denoted by a naught subscript with e.g c_0 , $(b - y)_0$, and $(u - b)_0$, referring to the intrinsic, dereddened equivalents of the indices c_1 , $(b - y)$, and $(u - b)$, respectively. Furthermore, although reddening is expected to be negligible for the nearby sources of primary interest to us, automated classification schemes that divide a large sample of stars for analysis into groups corresponding to earlier than, around, and later than the Balmer maximum will sometimes rely on the reddening-independent indices defined by Crawford & Mandwewala (1976) for A-type dwarfs:

$$[c_1] = c_1 - 0.19(b - y) \quad (2.4)$$

$$[m_1] = m_1 + 0.34(b - y) \quad (2.5)$$

$$[u - b] = [c_1] + 2[m_1]. \quad (2.6)$$

Finally, two additional indices useful for early A-type stars, a_0 and r^* , are defined as follows:

$$a_0 = 1.36(b - y)_0 + 0.36m_0 + 0.18c_0 - 0.2448 \quad (2.7)$$

$$= (b - y)_0 + 0.18[(u - b)_0 - 1.36], \quad (2.8)$$

$$r^* = 0.35c_1 - 0.07(b - y) - (\beta - 2.565). \quad (2.9)$$

Note that r^* is a reddening free parameter, and thus indifferent to the use of reddened or unreddened photometric indices.

2.2.2 Extinction Correction

Though the sample of nearby stars to which we applying the Strömgren methodology are assumed to be unextincted or only lightly extincted, interstellar reddening is significant for the more distant stars including those in the open clusters used in § 2.6 to test the accuracy of the ages derived using our $uvby\beta$ methodology. In the cases where extinction is thought to be significant, corrections are performed using the UVBYBETA¹ and DEREDD² programs for IDL.

These IDL routines take as input $(b - y)$, m_1 , c_1 , β , and a class value (between 1-8) that is used to roughly identify what region of the H-R diagram an individual star resides in. For our sample, stars belong to only four of the eight possible classes. These classes are summarized as follows: (1) B0-A0, III-V, $2.59 < \beta < 2.88$, $-0.20 < c_0 < 1.00$, (5) A0-A3, III-V, $2.87 < \beta < 2.93$, $-0.01 < (b - y)_0 < 0.06$, (6) A3-F0, III-V, $2.72 < \beta < 2.88$, $0.05 < (b - y)_0 < 0.22$, and (7) F1-G2, III-V, $2.60 < \beta < 2.72$, $0.22 < (b - y)_0 < 0.39$. The class values in this work were assigned to individual stars based on their known spectral types (provided in the XHIP catalog (Anderson & Francis, 2011)), and β values where needed. In some instances, A0-A3 stars assigned to class (5) with values of $\beta < 2.87$, the dereddening procedure was unable to proceed. For these cases, stars were either assigned to class (1) if they were spectral type A0-A1, or to class (6), if they were spectral type A2-A3.

Depending on the class of an individual star, the program then calculates the dereddened indices $(b - y)_0$, m_0 , c_0 , the color excess $E(b - y)$, δm_0 , the absolute V magnitude, M_V , the stellar radius and effective temperature. Notably, the β index is unaffected by reddening as it is the flux difference between two narrow band filters with essentially the same central wavelength. Thus, no corrections are performed on β and this index can be used robustly in coarse classification schemes.

To transform $E(b - y)$ to A_V , we use the extinction measurements of Schlegel et al. (1998) and to propagate the effects of reddening through to the various $uvby\beta$ indices we use the calibrations of Crawford & Mandwewala (1976):

¹<http://idlastro.gsfc.nasa.gov/ftp/pro/astro/uvbybeta.pro>

²<http://idlastro.gsfc.nasa.gov/ftp/pro/astro/deredd.pro>

$$E(m_1) = -0.33E(b - y) \quad (2.10)$$

$$E(c_1) = 0.20E(b - y) \quad (2.11)$$

$$E(u - b) = 1.54E(b - y). \quad (2.12)$$

From these relations, given the intrinsic color index $(b - y)_0$, the reddening free parameters m_0 , c_0 , $(u - b)_0$, and a_0 can be computed.

In § 2.4.3 we quantify the effects of extinction and extinction uncertainty on the final atmospheric parameter estimation, T_{eff} , $\log g$.

2.2.3 Utility of the Photometric System

From the four basic Strömgren indices – $b - y$ color, β , c_1 , and m_1 – accurate determinations of the stellar atmospheric parameters T_{eff} , $\log g$, and $[M/H]$ are possible for B, A, and F stars. Necessary are either empirical (e.g. Crawford, 1979; Lester et al., 1986; Olsen, 1988; Smalley, 1993; Smalley & Dworetsky, 1995; Clem et al., 2004), or theoretical (e.g. Balona, 1984; Moon & Dworetsky, 1985; Napiwotzki et al., 1993; Balona, 1994; Lejeune et al., 1999; Castelli & Kurucz, 2006; Castelli & Kurucz, 2004; Önehag et al., 2009) calibrations. Uncertainties of 0.10 dex in $\log g$ and 260 K in T_{eff} are claimed as achievable and we reassess these uncertainties ourselves § 2.4.3.

2.3 Determination of Atmospheric Parameters T_{eff} , $\log g$

2.3.1 Procedure

Once equipped with $uvby\beta$ colors and indices and understanding the effects of extinction, arriving at the fundamental parameters T_{eff} and $\log g$ for program stars, proceeds by interpolation among theoretical color grids (generated by convolving filter sensitivity curves with model atmospheres) or explicit formulae (often polynomials) that can be derived empirically or using the theoretical color grids. In both cases, calibration to a sample of stars with atmospheric parameters that have been independently determined through fundamental physics is required. See e.g. Figueras et al. (1991) for further description.

Numerous calibrations, both theoretical and empirical, of the $uvby\beta$ photometric system exist. For this work we use the Castelli & Kurucz (2006) and Castelli & Kurucz (2004) color grids generated from solar metallicity ($Z=0.017$, in this case) ATLAS9 model atmospheres using a microturbulent velocity parameter of $\xi = 0$

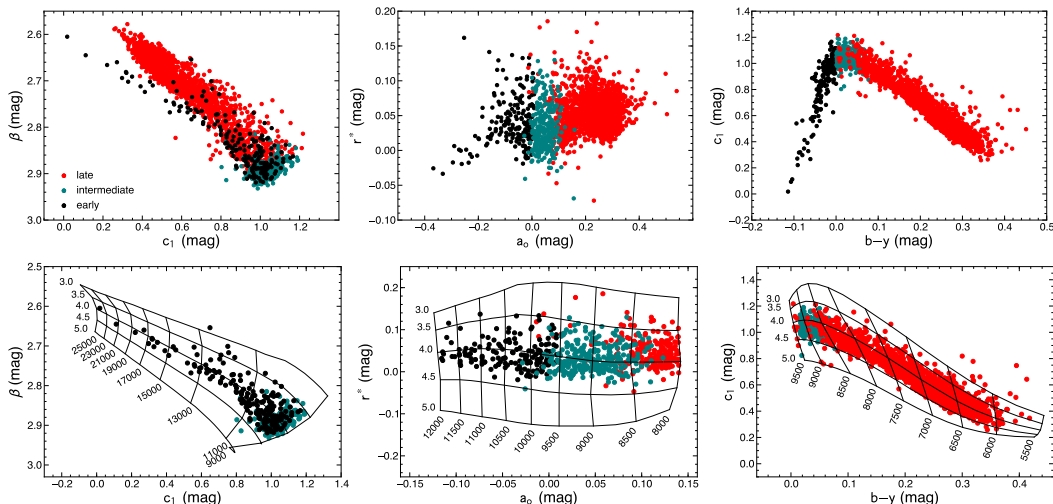


Figure 2.3: *Top*: Three relevant $uvby\beta$ spaces for atmospheric parameter determination of our sample of BAF stars with $uvby\beta$ photometry in the HM98 catalog, and located within 100 pc of the Sun. Two stars were excluded from these figures for favorable scaling: Castor, which is an outlier in all three planes ($\beta < 2.4$, $a_0 > 1$, $b - y > 0.6$), and HD 17300, a poorly studied F3V star with $b - y > 0.6$. *Bottom*: The same plots as above, with the model color grids of Castelli & Kurucz (2006) and Castelli & Kurucz (2004) overlaid in the relevant regions of parameter space. The lines of constant T_{eff} (largely vertical) and of constant $\log g$ (largely horizontal) are annotated with their corresponding values. Some outliers have been pruned, and irrelevant groups of stars eliminated, for clarity in this second plot.

km s^{-1} and the new ODF. We do not use the alpha-enhanced color grids. The grids are readily available from F. Castelli³ or R. Kurucz⁴.

Prior to assigning atmospheric parameters to our program stars directly from the model grids, we first investigated the accuracy of the models on samples of BAF stars with fundamentally determined T_{eff} (through interferometric measurements of the angular diameter and estimations of the total integrated flux) and $\log g$ (from measurements of the masses and radii of double lined eclipsing binaries). We describe these validation procedures in § 2.4.1 and § 2.4.2.

Atmospheric parameter determination occurs in three different observational Strömgren planes depending on the temperature regime (see Figure 2.3); this is in order to avoid the degeneracies that are present in all single observational planes when mapped onto the physical parameter space of $\log T_{\text{eff}}$ and $\log g$.

Building off of the original work of e.g. Strömgren (1951) and Strömgren (1966), Moon & Dworetzky (1985), and later Napiwotzki et al. (1993), suggested assigning

³<http://wwwuser.oats.inaf.it/castelli>

⁴<http://kurucz.harvard.edu/grids/gridP00ODFNEW/uvbyp00k0odfnew.dat>

physical parameters in the following three regimes: for cool stars ($T_{\text{eff}} \leq 8500$ K), β or $(b - y)$ can be used as a temperature indicator and c_0 is a surface gravity indicator; for intermediate temperature stars ($8500 \text{ K} \leq T_{\text{eff}} \leq 11000$ K), the temperature indicator is a_0 and surface gravity indicator r^* ; finally, for hot stars ($T_{\text{eff}} \gtrsim 11000$ K), the c_0 or the $[u - b]$ indices can be used as a temperature indicator while β is a gravity indicator (note that the role of β is reversed for hot stars compared to its role for cool stars). We adopt here c_1 vs. β for the hottest stars, a_0 vs. r^* for the intermediate temperatures, and $(b - y)$ vs. c_1 for the cooler stars.

Choosing the appropriate plane for parameter determination effectively means establishing a crude temperature sequence prior to fine parameter determination; in this, the β index is critical. Because the β index switches from being a temperature indicator to a gravity indicator in the temperature range of interest to us (spectral type B0-F5, luminosity class IV/V stars), atmospheric parameter determination proceeds depending on the temperature regime. For the T_{eff} and $\log g$ calibrations described below, temperature information existed for all of the calibration stars, though this is not the case for our program stars. In the general case we must rely on photometric classification to assign stars to the late, intermediate, and early groups, and then proceed to determine atmospheric parameters in the relevant $uvby\beta$ planes.

Moon (1985) provides a scheme, present in the UVBYBETA IDL routine, for roughly identifying the region of the H-R diagram in which a star resides. However, because our primary sample of field stars are assumed to be unextincted, and because the UVBYBETA program relies on user-inputted class values based on unverified spectral types from the literature, we opt for a classification scheme based solely on the $uvby\beta$ photometry.

Mongi o et al. (2014), hereafter M14, designed a sophisticated classification scheme, based on the work of Str omgren (1966). The M14 scheme places stars into early (B0-A0), intermediate (A0-A3), and late (later than A3) groups based solely on β , the reddened color $(b - y)$, and the reddening-free parameters $[c_1]$, $[m_1]$, $[u - b]$. The M14 scheme improves upon the previous method of Figueras et al. (1991) by imposing two new conditions (see their Figure 2 for the complete scheme) intended to prevent the erroneous classification of some stars. For our sample of 3499 field stars (see § 2.7), there are 699 stars lacking β photometry, all but three of which cannot be classified by the M14 scheme. For such cases, we rely on supplementary spectral type information and manually assign these unclassified stars to the late group. Using the M14 scheme, the final makeup of our field star sample is 85.9%

late, 8.4% intermediate, and 5.7% early.

2.3.2 Sample and Numerical Methods

For all stars in this work, $uvby\beta$ photometry is acquired from the Hauck & Mermilliod (1998) compilation (hereafter HM98), unless otherwise noted. HM98 provides the most extensive compilation of $uvby\beta$ photometric measurements, taken from the literature and complete to the end of 1996 (the photometric system has seen less frequent usage/publication in more modern times). The HM98 compilation includes 105,873 individual photometric measurements for 63,313 different stars, culled from 533 distinct sources, and are presented both as individual measurements and weighted means of the literature values.

The HM98 catalog provides $(b - y)$, m_1 , c_1 , and β and the associated errors in each parameter if available. From these indices a_0 and r^* are computed according to Equations (7), (8) & (9). The ATLAS9 $uvby\beta$ grids provide a means of translating from $(b - y, m_1, c_1, \beta, a_0, r^*)$ to a precise combination of $(T_{\text{eff}}, \log g)$. Interpolation within the model grids is performed on the appropriate grid: $((b - y)$ vs. c_1 for the late group, a_0 vs. r^* for the intermediate group, and c_1 vs. β for the early group).

The interpolation is linear and performed using the SciPy routine `griddata`. Importantly, the model $\log g$ values are first converted into linear space so that g is determined from the linear interpolation procedure before being brought back into log space. The model grids used in this work are spaced by 250 K in T_{eff} and 0.5 dex in $\log g$. To improve the precision of our method of atmospheric parameter determination in the future, it would be favorable to use model color grids that have been calculated at finer resolutions, particularly in $\log g$, directly from model atmospheres. However, the grid spacings stated above are fairly standardized among extant $uvby\beta$ grids.

2.3.3 Rotational Velocity Correction

Early-type stars are rapid rotators, with rotational velocities of $v \sin i \gtrsim 150 \text{ km s}^{-1}$ being typical. For a rotating star, both surface gravity and effective temperature decrease from the poles to the equator, changing the mean gravity and temperature of a rapid rotator relative to a slower rotator (Sweet & Roy, 1953). Vega, rotating with an inferred equatorial velocity of $v_{\text{eq}} \sim 270 \text{ km s}^{-1}$ at a nearly pole-on inclination, has measured pole-to-equator gradients in T_{eff} and $\log g$ that are $\sim 2400 \text{ K}$ and ~ 0.5 dex, respectively (Peterson et al., 2006). The apparent luminosity change due to rotation depends on the inclination: a pole-on ($i = 0^\circ$) rapid rotator appears more

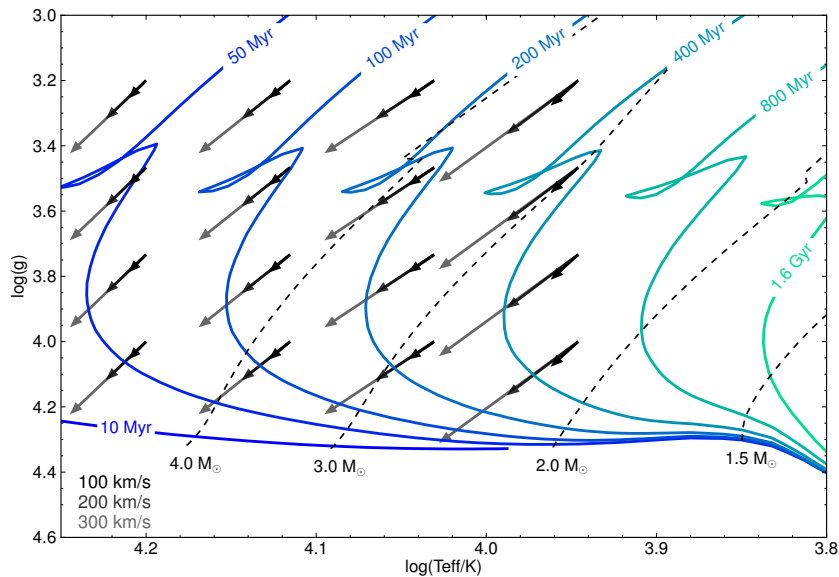


Figure 2.4: Vectors showing the magnitude and direction of the rotational velocity corrections at 100 (black), 200, and 300 (light grey) km s^{-1} for a grid of points in $\log(\text{Teff})$ - $\log g$ space, with PARSEC isochrones overlaid for reference. While typical A-type stars rotate at about 150 km s^{-1} , high-contrast imaging targets are sometimes selected for slow rotation and hence favorable inclinations, typically $v \sin i < 50 \text{ km s}^{-1}$ or within the darkest black vectors. For rapid rotators, a 100% increase in the inferred age due to rotational effects is not uncommon.

luminous than a nonrotating star of the same mass, while an edge-on ($i = 90^\circ$) rapid rotator appears less luminous than a nonrotating star of the same mass. Sweet & Roy (1953) found that a $(v \sin i)^2$ correction factor could describe the changes in luminosity, gravity, and temperature.

The net effect of stellar rotation on inferred age is to make a rapid rotator appear cooler, more luminous, and hence older when compared to a nonrotating star of the same mass (or more massive when compared to a nonrotating star of the same age). Optical colors can be affected since the spectral lines of early type stars are strong and broad. Kraft & Wrubel (1965) demonstrated specifically in the Strömgren system that the effects are predominantly in the gravity indicators (c_1 , which then also affects the other gravity indicator r^*) and less so in the temperature indicators ($b - y$, which then affects a_0).

Figueras & Blasi (1998), hereafter FB98, used Monte-Carlo simulations to investigate the effect of rapid rotation on the measured $uvby\beta$ indices, derived atmospheric parameters, and hence isochronal ages of early-type stars. Those authors concluded

that stellar rotation conspires to artificially enhance isochronal ages derived through $uvby\beta$ photometric methods by 30-50% on average.

To mitigate the effect of stellar rotation on the parameters T_{eff} and $\log(g)$, FB98 presented the following corrective formulae for stars with $T_{\text{eff}} > 11000$ K:

$$\Delta T_{\text{eff}} = 0.0167(v \sin i)^2 + 218, \quad (2.13)$$

$$\Delta \log g = 2.10 \times 10^{-6}(v \sin i)^2 + 0.034. \quad (2.14)$$

For stars with $8500\text{K} \leq T_{\text{eff}} \leq 11000\text{K}$, the analogous formulae are

$$\Delta T_{\text{eff}} = 0.0187(v \sin i)^2 + 150, \quad (2.15)$$

$$\Delta \log g = 2.92 \times 10^{-6}(v \sin i)^2 + 0.048. \quad (2.16)$$

In both cases, ΔT_{eff} and $\Delta \log g$ are *added* to the T_{eff} and $\log g$ values derived from $uvby\beta$ photometry.

Notably, the rotational velocity correction is dependent on whether the star belongs to the early, intermediate, or late group. Specifically, FB98 define three regimes: $T_{\text{eff}} < 8830$ K (no correction), $8830 \text{ K} < T_{\text{eff}} < 9700$ K (correction for intermediate A0-A3 stars), $T_{\text{eff}} > 9700$ K (correction for stars earlier than A3).

Song et al. (2001), who performed a similar isochronal age analysis of A-type stars using $uvby\beta$ photometry, extended the FB98 rotation corrections to stars earlier and later than B7 and A4, respectively. In the present work, a more conservative approach is taken and the rotation correction is applied only to stars in the early or intermediate groups, as determined by the classification scheme discussed in § 2.3.1. This decision was partly justified by the abundance of late-type stars that fall below the ZAMS in the open cluster tests (§ 2.6), for which the rotation correction would have a small (due to the lower rotational velocities of late-type stars) but exacerbating effect on these stars whose surface gravities are already thought to be overestimated.

We include these corrections and, as illustrated in Figure 2.4, emphasize that in their absence we would err on the side of over-estimating the age of a star, meaning conservatively overestimating rather than underestimating companion masses based on assumed ages. As an example, for a star with $T_{\text{eff}} \approx 13,275$ K and $\log g \approx 4.1$,

assumed to be rotating edge-on at 300 km s^{-1} , neglecting to apply the rotation correction would result in an age of $\sim 100 \text{ Myr}$. Applying the rotation correction to this star results in an age of $\sim 10 \text{ Myr}$.

Of note, the FB98 corrections were derived for atmospheric parameters determined using the synthetic $uvby\beta$ color grids of Moon & Dworetzky (1985). It is estimated that any differences in derived atmospheric parameters resulting from the use of color grids other than those of Moon & Dworetzky (1985) are less than the typical measurement errors in those parameters. In § 2.4.3 we quantify the effects of rotation and rotation correction uncertainty on the final atmospheric parameter estimation, T_{eff} , $\log g$.

2.4 Calibration and Validation Using the HM98 Catalog

In this section we assess the effective temperatures and surface gravities derived from atmospheric models and $uvby\beta$ color grids relative to fundamentally determined temperatures (§ 2.4.1) and surface gravities (§ 2.4.2).

2.4.1 Effective Temperature

A fundamental determination of T_{eff} is possible through an interferometric measurement of the stellar angular diameter and an estimate of the total integrated flux. We gathered 69 stars (listed in Table 2.1) with fundamental T_{eff} measurements from the literature and determine photometric temperatures for these objects from interpolation of $uvby\beta$ photometry in ATLAS9 model grids.

Fundamental T_{eff} values were sourced from Boyajian et al. (2013), hereafter B13, and Napiwotzki et al. (1993), hereafter N93. Several stars have multiple interferometric measurements of the stellar radius, and hence multiple fundamental T_{eff} determinations. For these stars, identified as those objects with multiple radius references in Table 2.1, the mean T_{eff} and standard deviation were taken as the fundamental measurement and standard error. Among the 16 stars with multiple fundamental T_{eff} determinations by between 2 and 5 authors, there is a scatter of typically several percent (with 0.1-4% range).

Additional characteristics of the T_{eff} “standard” stars are summarized as follows: spectral types B0-F9, luminosity classes III-V, $2 \text{ km s}^{-1} \leq v \sin i \leq 316 \text{ km s}^{-1}$, mean and median $v \sin i$ of 58 and 26 km s^{-1} , respectively, $2.6 \text{ pc} \leq d \leq 493 \text{ pc}$, and a mean and median $[\text{Fe}/\text{H}]$ of -0.08 and -0.06 dex, respectively. Line-of-sight rotational velocities were acquired from the Glebocki & Gnacinski (2005) compila-

tion and $[\text{Fe}/\text{H}]$ values were taken from SIMBAD. Variability and multiplicity were considered, and our sample is believed to be free of any possible contamination due to either of these effects.

From the HM98 compilation we retrieved $uvby\beta$ photometry for these “effective temperature standards.” The effect of reddening was considered for the hotter, statistically more distant stars in the N93 sample. Comparing mean $uvby\beta$ photometry from HM98 with the dereddened photometry presented in N93 revealed that nearly all of these stars have negligible reddening ($E(b - y) \leq 0.001$ mag). The exceptions are HD 82328, HD 97603, HD 102870, and HD 126660 with color excesses of $E(b - y) = 0.010, 0.003, 0.011,$ and 0.022 mag, respectively. Inspection of Table 2.1 indicates that despite the use of the reddened HM98 photometry the T_{eff} determinations for three of these four stars are still of high accuracy. For HD 97603, there is a discrepancy of > 300 K between the fundamental and photometric temperatures. However, the $uvby\beta$ T_{eff} using reddened photometry for this star is actually hotter than the fundamental T_{eff} . Notably, the author-to-author dispersion in multiple fundamental T_{eff} determinations for HD 97603 is also rather large. As such, the HM98 photometry was deemed suitable for all of the “effective temperature standards.”

For the sake of completeness, different model color grids were investigated, including those of Fitzpatrick & Massa (2005), which were recently calibrated for early group stars, and those of Önehag et al. (2009), which were calibrated from MARCS model atmospheres for stars cooler than 7000 K. We found the grids that best matched the fundamental effective temperatures were the ATLAS9 grids of solar metallicity with no alpha-enhancement, microturbulent velocity of 0 km s^{-1} , and using the new opacity distribution function (ODF). The ATLAS9 grids with microturbulent velocity of 2 km s^{-1} were also tested, but were found to worsen both the fractional T_{eff} error and scatter, though only nominally (by a few tenths of a percent).

For the early group stars, temperature determinations were attempted in both the $c_1 - \beta$ and $[u - b] - \beta$ planes. The c_1 index was found to be a far better temperature indicator in this regime, with the $[u - b]$ index underestimating T_{eff} relative to the fundamental values $> 10\%$ on average. Temperature determinations in the $c_1 - \beta$ plane, however, were only $\approx 1.9\%$ cooler than the fundamental values, regardless of whether c_1 or the dereddened index c_0 was used. This is not surprising as the $c_1 - \beta$ plane is not particularly susceptible to reddening.

At intermediate temperatures, the $a_0 - r^*$ plane is used. In this regime, the ATLAS9

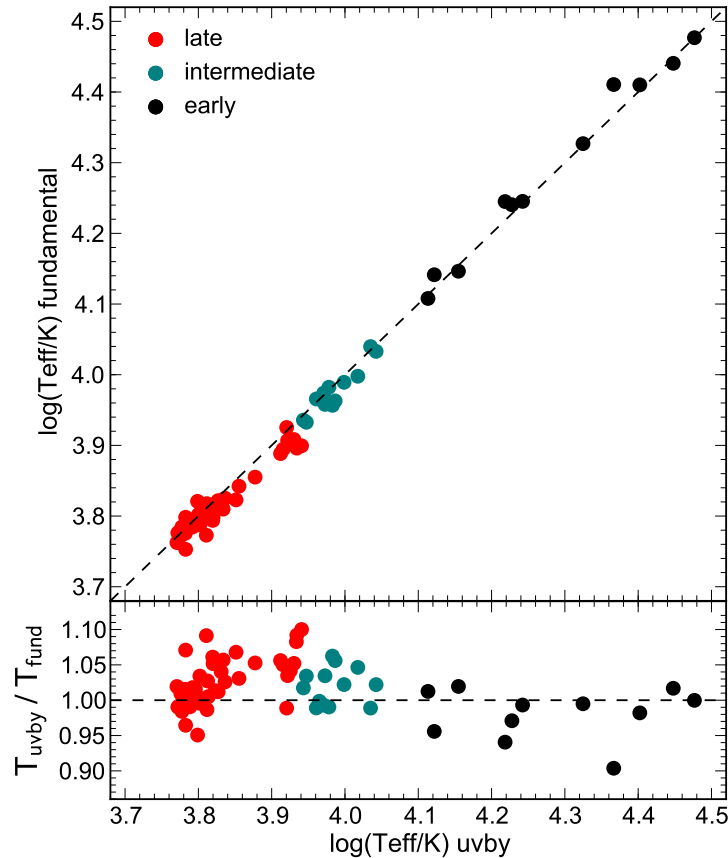


Figure 2.5: *Top:* Comparison of the temperatures derived from the ATLAS9 $uvby\beta$ color grids (T_{uvby}) and the fundamental effective temperatures (T_{fund}) taken from B13 and N93. *Bottom:* Ratio of $uvby\beta$ temperature to fundamental temperature, as a function of T_{uvby} . For the majority of stars, the $uvby\beta$ grids can predict T_{eff} to within $\sim 5\%$ without any additional correction factors.

grids were found to overestimate T_{eff} by $\approx 2.0\%$ relative to the fundamental values.

Finally, for the late group stars temperature determinations were attempted in the $(b - y) - c_1$ and $\beta - c_1$ planes. In this regime, $(b - y)$ was found to be a superior temperature indicator, improving the mean fractional error marginally and reducing the RMS scatter by more than 1% . In this group, the model grids overpredict T_{eff} by $\approx 2.4\%$ on average, regardless of whether the reddened or dereddened indices are used.

Figure 2.5 shows a comparison of the temperatures derived from the ATLAS9 $uvby\beta$ color grids and the fundamental effective temperatures given in B13 and N93. For the majority of stars the color grids can predict the effective temperature to within about 5% . A slight systematic trend is noted in Figure 2.5, such that the model color grids overpredict T_{eff} at low temperatures and underpredict T_{eff} at

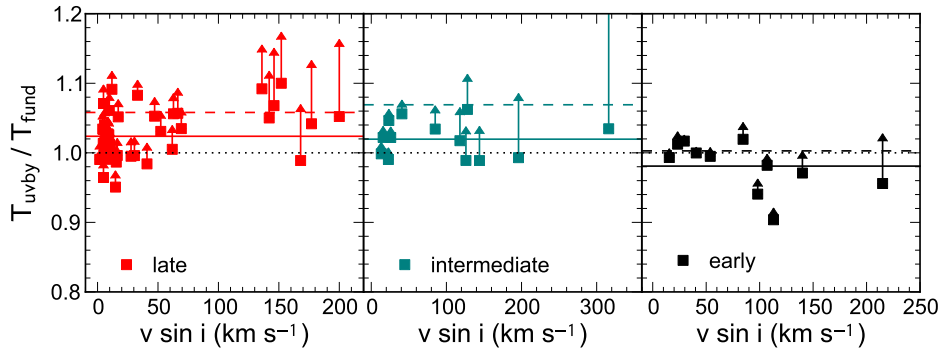


Figure 2.6: Ratio of the $uvby\beta$ temperature to fundamental temperature as a function of $v \sin i$, for the late (left), intermediate (middle), and early (right), group stars. The solid horizontal colored lines indicate the mean ratios in each case. The arrows represent both the magnitude and direction of change to the ratio T_{uvby}/T_{fund} after applying the FB98 rotation corrections. The dashed horizontal colored lines indicate the mean ratios after application of the rotation correction. The rotation correction appears to improve temperature estimates for early group stars, but worsen estimates for the late and intermediate groups. Notably, however, the vast majority of T_{eff} standards are slowly rotating ($v \sin i < 150 \text{ km s}^{-1}$). Note one rapidly rotating intermediate group star extends beyond the scale of the figure, with a rotation corrected T_{uvby}/T_{fund} ratio of ≈ 1.26 .

high temperatures. We attempt to correct for this systematic effect by applying T_{eff} offsets in three regimes according to the mean behavior of each group: late and intermediate group stars were shifted to cooler temperatures by 2.4% and 2.0%, respectively, and early group stars were shifted by 1.9% toward hotter temperatures. After offsets were applied, the remaining RMS error in temperature determinations for these “standard” stars was 3.3%, 2.5%, and 3.5% for the late, intermediate, and early groups, respectively, or 3.1% overall.

Taking the uncertainties or dispersions in the fundamental T_{eff} determinations as the standard error, there is typically a 5-6 σ discrepancy between the fundamental and photometric T_{eff} determinations. However, given the large author-to-author dispersion observed for stars with multiple fundamental T_{eff} determinations, it is likely that the formal errors on these measurements are underestimated. Notably, N93 does not publish errors for the fundamental T_{eff} values, which are literature means. However, those authors did find fractional errors in their photometric T_{eff} ranging from 2.5-4% for BA stars.

In § 2.6, we opted not to apply systematic offsets, instead assigning T_{eff} uncertainties in three regimes according to the average fractional uncertainties noted in each group. In our final T_{eff} determinations for our field star sample (§ 2.7) we attempted to correct

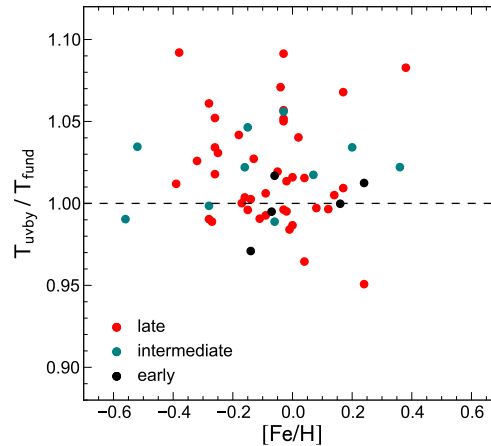


Figure 2.7: Ratio of the $uvby\beta$ temperature to fundamental temperature as a function of $[\text{Fe}/\text{H}]$. There is no indication that the grids systematically overestimate or underestimate T_{eff} for different values of $[\text{Fe}/\text{H}]$.

for the slight temperature systematics and applied offsets, using the magnitude of the remaining RMS error (for all groups considered collectively) as the dominant source of uncertainty in our T_{eff} measurement (see § 2.4.3).

As demonstrated in Figure 2.6, rotational effects on our temperature determinations for the T_{eff} standards were investigated. Notably, the FB98 $v \sin i$ corrections appear to enhance the discrepancy between our temperature determinations and the fundamental temperatures for the late and intermediate groups, while moderately improving the accuracy for the early group. For the late group this is expected, as the correction formulae were originally derived for intermediate and early group stars. Notably, however, only two stars in the calibration sample exhibit projected rotational velocities $> 200 \text{ km s}^{-1}$. We examine the utility of the $v \sin i$ correction further in § 2.4.2 & § 2.6.

The effect of metallicity on the determination of T_{eff} from the $uvby\beta$ grids is investigated in Figure 2.7 showing the ratio of the grid-determined temperature to the fundamental temperature as a function of $[\text{Fe}/\text{H}]$. The sample of temperature standards spans a large range in metallicity, yet there is no indication of any systematic effect with $[\text{Fe}/\text{H}]$, justifying our choice to assume solar metallicity throughout this work (see further discussion of metallicity effects in the Appendix).

The effect of reddening on our temperature determinations was considered but since the vast majority of sources with fundamental effective temperatures are nearby, no significant reddening was expected. Indeed, no indication of a systematic trend of

the temperature residuals as a function of distance was noted.

In summary our findings that the ATLAS9 predicted T_{eff} values are $\sim 2\%$ hotter than fundamental values for AF stars are consistent with the results of Bertone et al. (2004), who found 4-8% shifts warmer in T_{eff} from fits of ATLAS9 models to spectrophotometry relative to T_{eff} values determined from the infrared flux method (IRFM). We attempt systematic corrections with offsets of magnitude $\sim 2\%$ according to group, and the remaining RMS error between $uvby\beta$ temperatures and fundamental values is $\sim 3\%$.

Table 2.1: Stars with fundamental determinations of T_{eff} through Interferometry

HD	Sp. Type	T_{fund} (K)	Radius Ref. ^a	$T_{uvby\beta}$ (K)	$\log g_{uvby\beta}$ (dex)	[Fe/H] (dex)	$v \sin i$ (km s ⁻¹)	$(b - y)$ (mag)	m_1 (mag)	c_1 (mag)	β (mag)
4614	F9V	5973 ± 8	3	5915	4.442	-0.28	1.8	0.372	0.185	0.275	2.588
5015	F8V	5965 ± 35	3	6057	3.699	0.04	8.6	0.349	0.174	0.423	2.613
5448	A5V	8070	18	8350	3.964	...	69.3	0.068	0.189	1.058	2.866
6210	F6Vb	6089 ± 35	1	5992	3.343	-0.01	40.9	0.356	0.183	0.475	2.615
9826	F8V	6102 ± 75	2,4	6084	3.786	0.08	8.7	0.346	0.176	0.415	2.629
16765	F7V	6356 ± 46	1	6330	4.408	-0.15	30.5	0.318	0.160	0.355	2.647
16895	F7V	6153 ± 25	3	6251	4.118	0.00	8.6	0.325	0.160	0.392	2.625
17081	B7V	12820	18	12979	3.749	0.24	23.3	-0.057	0.104	0.605	2.717
19994	F8.5V	5916 ± 98	2	5971	3.529	0.17	7.2	0.361	0.185	0.422	2.631
22484	F9IV-V	5998 ± 39	3	5954	3.807	-0.09	3.7	0.367	0.173	0.376	2.615
30652	F6IV-V	6570 ± 131	3,6	6482	4.308	0.00	15.5	0.298	0.163	0.415	2.652
32630	B3V	17580	18	16536	4.068	...	98.2	-0.085	0.104	0.318	2.684
34816	B0.5IV	27580	18	28045	4.286	-0.06	29.5	-0.119	0.073	-0.061	2.602
35468	B2III	21230	18	21122	3.724	-0.07	53.8	-0.103	0.076	0.109	2.613
38899	B9IV	10790	18	11027	3.978	-0.16	25.9	-0.032	0.141	0.906	2.825
47105	AOIV	9240	18	9226	3.537	-0.28	13.3	0.007	0.149	1.186	2.865
48737	F5IV-V	6478 ± 21	3	6510	3.784	0.14	61.8	0.287	0.169	0.549	2.669
48915	A0mA1Va	9755 ± 47	7,8,9,10,11	9971	4.316	0.36	15.8	-0.005	0.162	0.980	2.907
49933	F2Vb	6635 ± 90	12	6714	4.378	-0.39	9.9	0.270	0.127	0.460	2.662
56537	A3Vb	7932 ± 62	3	8725	4.000	...	152	0.047	0.198	1.054	2.875
58946	F0Vb	6954 ± 216	3,18	7168	4.319	-0.25	52.3	0.215	0.155	0.615	2.713
61421	F5IV-V	6563 ± 24	11,13,14,15,18	6651	3.983	-0.02	4.7	0.272	0.167	0.532	2.671
63922	BOIII	29980	18	29973	4.252	0.16	40.7	-0.122	0.043	-0.092	2.590
69897	F6V	6130 ± 58	1	6339	4.290	-0.26	4.3	0.315	0.149	0.384	2.635
76644	A7IV	7840	18	8232	4.428	-0.03	142	0.104	0.216	0.856	2.843
80007	A2IV	9240	18	9139	3.240	...	126	0.004	0.140	1.273	2.836
81937	F0IVb	6651 ± 27	3	7102	3.840	0.17	146	0.211	0.180	0.752	2.733

Table 2.1 Continued: Stars with fundamental determinations of T_{eff} through Interferometry

82328	F5.5IV-V	6299 ± 61	3,18	6322	3.873	-0.16	7.1	0.314	0.153	0.463	2.646
90839	F8V	6203 ± 56	3	6145	4.330	-0.11	8.6	0.341	0.171	0.333	2.618
90994	B6V	14010	18	14282	4.219	...	84.5	-0.066	0.111	0.466	2.730
95418	A1IV	9181 ± 11	3,18	9695	3.899	-0.03	40.8	-0.006	0.158	1.088	2.880
97603	A5IV(n)	8086 ± 169	3,6,18	8423	4.000	-0.18	177	0.067	0.195	1.037	2.869
102647	A3Va	8625 ± 175	5,6,18	8775	4.188	0.07	118	0.043	0.211	0.973	2.899
102870	F8.5IV-V	6047 ± 7	3,18	6026	3.689	0.12	5.4	0.354	0.187	0.416	2.628
118098	A2Van	8097 ± 43	3	8518	4.163	-0.26	200	0.065	0.183	1.006	2.875
118716	B1III	25740	18	23262	3.886	...	113	-0.112	0.058	0.040	2.608
120136	F7IV-V	6620 ± 67	2	6293	3.933	0.24	14.8	0.318	0.177	0.439	2.656
122408	A3V	8420	18	8326	3.500	-0.27	168	0.062	0.164	1.177	2.843
126660	F7V	6202 ± 35	3,6,18	6171	3.881	-0.02	27.7	0.334	0.156	0.418	2.644
128167	F4Vkf2mF1	6687 ± 252	3,18	6860	4.439	-0.32	9.3	0.254	0.134	0.480	2.679
130948	F9IV-V	5787 ± 57	1	5899	4.065	-0.05	6.3	0.374	0.191	0.321	2.625
136202	F8IV	5661 ± 87	1	6062	3.683	-0.04	4.9	0.348	0.170	0.427	2.620
141795	kA2hA5mA7V	7928 ± 88	3	8584	4.346	0.38	33.1	0.066	0.224	0.950	2.885
142860	F6V	6295 ± 74	3,6	6295	4.130	-0.17	9.9	0.319	0.150	0.401	2.633
144470	B1V	25710	18	25249	4.352	...	107	-0.112	0.043	-0.005	2.621
162003	F5IV-V	5928 ± 81	3	6469	3.916	-0.03	11.9	0.294	0.147	0.497	2.661
164259	F2V	6454 ± 113	3	6820	4.121	-0.03	66.4	0.253	0.153	0.560	2.690
168151	F5Vb	6221 ± 39	1	6600	4.203	-0.28	9.7	0.281	0.143	0.472	2.653
169022	B9.5III	9420	18	9354	3.117	...	196	0.016	0.102	1.176	2.778
172167	AOVa	9600	18	9507	3.977	-0.56	22.8	0.003	0.157	1.088	2.903
173667	F5.5IV-V	6333 ± 37	3,18	6308	3.777	-0.03	16.3	0.314	0.150	0.484	2.652
177724	A0IV-Vnn	9078 ± 86	3	9391	3.870	-0.52	316	0.013	0.146	1.080	2.875
181420	F2V	6283 ± 106	16	6607	4.187	-0.03	17.1	0.280	0.157	0.477	2.657
185395	F3+V	6516 ± 203	3,4	6778	4.296	0.02	5.8	0.261	0.157	0.502	2.688
187637	F5V	6155 ± 85	16	6192	4.103	-0.09	5.4	0.333	0.151	0.380	2.631
190993	B3V	17400	18	16894	4.195	-0.14	140	-0.083	0.100	0.295	2.686
193432	B9.5V	9950	18	10411	3.928	-0.15	23.4	-0.021	0.134	1.015	2.852

Table 2.1 Continued: Stars with fundamental determinations of T_{eff} through Interferometry

193924	B2IV	17590	18	17469	3.928	...	15.5	-0.092	0.087	0.271	2.662
196867	B9IV	10960	18	10837	3.861	-0.06	144	-0.019	0.125	0.889	2.796
209952	B7IV	13850	18	13238	3.913	...	215	-0.061	0.105	0.576	2.728
210027	F5V	6324 ± 139	6	6496	4.187	-0.13	8.6	0.294	0.161	0.446	2.664
210418	A2Vb	7872 ± 82	3	8596	3.966	-0.38	136	0.047	0.161	1.091	2.886
213558	A1Vb	9050 ± 157	3	9614	4.175	...	128	0.002	0.170	1.032	2.908
215648	F6V	6090 ± 22	3	6198	3.950	-0.26	7.7	0.331	0.147	0.407	2.626
216956	A4V	8564 ± 105	5,18	8857	4.198	0.20	85.1	0.037	0.206	0.990	2.906
218396	F0+(λ Boo)	7163 ± 84	17	7540	4.435	...	47.2	0.178	0.146	0.678	2.739
219623	F8V	6285 ± 94	1	6061	3.85	0.04	4.9	0.351	0.169	0.395	2.624
222368	F7V	6192 ± 26	3	6207	3.988	-0.14	6.1	0.330	0.163	0.399	2.625
222603	A7V	7734 ± 80	1	8167	4.318	...	62.8	0.105	0.203	0.891	2.826

^a Interferometric radii references: (1) Boyajian et al. (2013), (2) Baines et al. (2008), (3) Boyajian et al. (2012), (4) Ligi et al. (2012), (5) Di Folco et al. (2004), (6) van Belle & von Braun (2009), (7) Davis et al. (2011), (8) Hanbury Brown et al., 1974, (9) Davis & Tango (1986), (10) Kervella et al. (2003), (11) Mozurkewich et al. (2003), (12) Bigot et al. (2011), (13) Chiavassa et al. (2012), (14) Nordgren et al. (2001), (15) Kervella et al. (2004), (16) Huber et al. (2012), (17) Baines et al. (2012), (18) Napiwotzki et al. (1993). Note, that (18) simply provides means of the T_{eff} values published by Code et al. (1976), Beeckmans (1977), and Malagnini et al. (1986), all three of which used the radii of (9).

2.4.2 Surface Gravity

To assess the surface gravities derived from the $uvby\beta$ grids, we compare to results on both double-lined eclipsing binary and spectroscopic samples.

2.4.2.1 Comparison with Double-Lined Eclipsing Binaries

Torres et al. (2010) compiled an extensive catalog of 95 double-lined eclipsing binaries with fundamentally determined surface gravities for all 180 individual stars. Eclipsing binary systems allow for dynamical determinations of the component masses and geometrical determinations of the component radii. From the mass and radius of an individual component, the Newtonian surface gravity, $g = GM/R^2$ can be calculated.

From these systems, 39 of the primary components have $uvby\beta$ photometry available for determining surface gravities using our methodology. The spectral type range for these systems is O8-F2, with luminosity classes of IV, V. The mass ratio (primary/secondary) for these systems ranges from ≈ 1.00 -1.79, and the orbital periods of the primaries range from ≈ 1.57 -8.44 days. In the cases of low mass ratios, the primary and secondary components should have nearly identical fundamental parameters, assuming they are coeval. In the cases of high mass ratios, given that the individual components are presumably unresolved, we assume that the primary dominates the $uvby\beta$ photometry. For both cases (of low and high mass ratios), we assume that the photometry allows for accurate surface gravity determinations for the primary components and so we only consider the primaries from the Torres et al. (2010) sample.

It is important to note that the eclipsing binary systems used for the surface gravity calibration are more distant than the stars for which we can interferometrically determine angular diameters and effective temperatures for. Thus, for the surface gravity calibration it was necessary to compute the dereddened indices $(b-y)_0$, m_0 , c_0 in order to obtain the highest accuracy possible for the intermediate-group stars, which rely on a_0 (an index using dereddened colors) as a temperature indicator. Notably, however, we found that the dereddened photometry actually worsened $\log g$ determinations for the early and late groups. Dereddened colors were computed using the IDL routine UVBYBETA.

The results of the $\log g$ calibration are presented in Table 2.2 and Figure 2.8. As described above, for the late group stars. ($T_{\text{eff}} < 8500$ K), $\log g$ is determined in the $(b-y) - c_1$ plane. The mean and median of the $\log g$ residuals (in the sense of

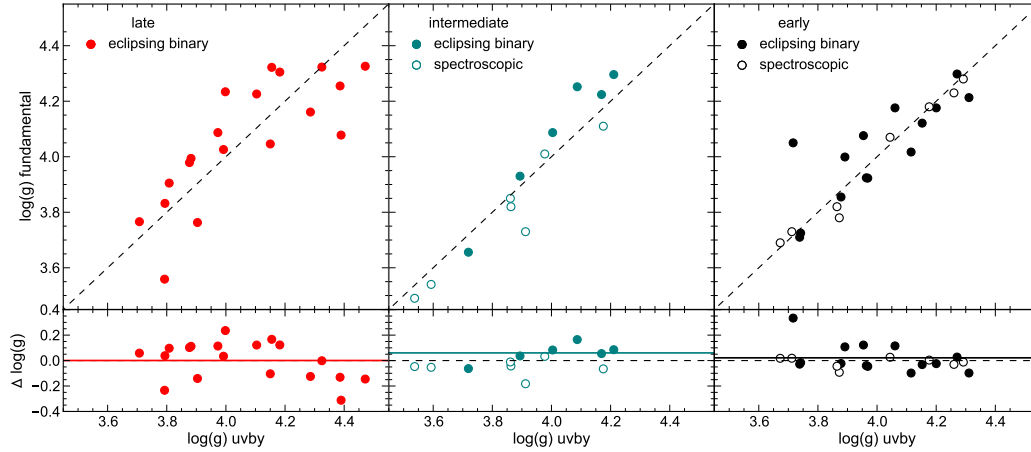


Figure 2.8: Comparison of the $uvby\beta$ derived $\log g$ values with fundamental values for the primary components of the double lined eclipsing binaries compiled in Torres et al. (2010). Red, teal, and black points represent late, intermediate, and early group stars, respectively. In each case the solid colored line represents the mean of the residuals, $\Delta \log g$ (in the sense of fundamental- $uvby\beta$). As can be seen, the mean offsets for the late and early groups is negligible. For the intermediate group, however, while only five stars were used for calibration, the $uvby\beta$ $\log g$ values are about 0.13 dex lower than the fundamental values on average.

grid-fundamental) are -0.001 dex and -0.038 dex, respectively, and the RMS error 0.145 dex. As in § 2.4.1, we found that the $\beta - c_1$ plane produced less accurate atmospheric parameters, relative to fundamental determinations, for late group stars.

For the intermediate group stars ($8500 \text{ K} \leq T_{\text{eff}} \leq 11000 \text{ K}$), $\log g$ is determined in the $a_0 - r^*$ plane. The mean and median of the $\log g$ residuals are -0.060 dex and -0.069 dex, respectively with RMS error 0.091 dex. For the early group stars ($T_{\text{eff}} > 11000 \text{ K}$), $\log g$ is determined in the $c_1 - \beta$ plane. The mean and median of the $\log g$ residuals are -0.0215 dex and 0.024 dex, respectively, with RMS error 0.113 dex. The $[u - b] - \beta$ plane was also investigated for early group stars, but was found to produce $\log g$ values of lower accuracy relative to the fundamental determinations.

When considered collectively, the mean and median of the $\log g$ residuals for all stars are -0.017 dex and -0.034 dex, and the RMS error 0.127 dex. The uncertainties in our surface gravities that arise from propagating the photometric errors through our atmospheric parameter determination routines are of the order ~ 0.02 dex, significantly lower than the uncertainties demonstrated by the comparison to fundamental values of $\log g$.

As stated above, the main concern with using double-lined eclipsing binaries as surface gravity calibrators for our photometric technique is contamination from

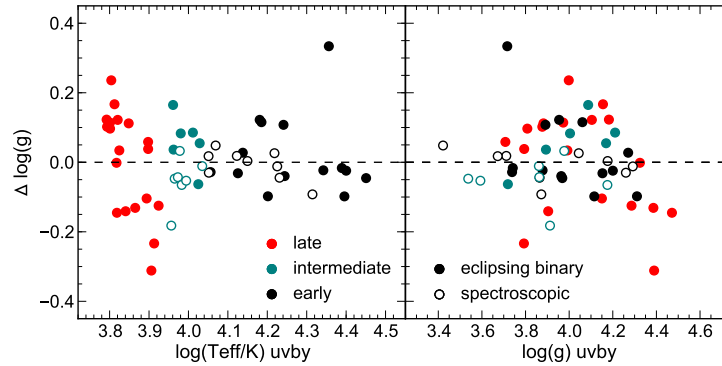


Figure 2.9: Surface gravity residuals, $\Delta \log g$ (in the sense of fundamental- $uvby\beta$), as a function of $uvby\beta$ -determined $\log(T_{\text{eff}})$ (left) and $\log g$ (right). Solid points represent eclipsing binary primaries from Torres et al. (2010) and open circles are stars with spectroscopic $\log g$ determinations in N93. Of the 39 eclipsing binaries, only six have residuals greater than 0.2 dex in magnitude. This implies that the $uvby\beta$ grids determine $\log g$ to within 0.2 dex of fundamental values $\sim 85\%$ of the time. Surface gravity residuals are largest for the cooler stars. Photometric surface gravity measurements are in better agreement with spectroscopic determinations than the eclipsing binary sample. There is no indication for a global systematic offset in $uvby\beta$ -determined $\log g$ values as a function of either T_{eff} or $\log g$.

the unresolved secondary components. The $\log g$ residuals were examined as a function of both mass ratio and orbital period. While the amplitude of the scatter is marginally larger for low mass ratio or short period systems, in all cases our $\log g$ determinations are within 0.2 dex of the fundamental values $\approx 85\%$ of the time.

To assess any potential systematic inaccuracies of the grids themselves, the surface gravity residuals were examined as a function of T_{eff} and the grid-determined $\log g$. Figures 2.9 show the $\log g$ residuals as a function of T_{eff} and $\log g$, respectively. No considerable systematic effects as a function of either effective temperature or $\log g$ were found in the $uvby\beta$ determinations of $\log g$.

The effect of rotational velocity on our $\log g$ determinations was considered. As before, $v \sin i$ data for the surface gravity calibrators was collected from Glebocki & Gnacinski (2005). As seen in Figure 2.10, the majority of the $\log g$ calibrators are somewhat slowly rotating ($v \sin i \leq 150 \text{ km s}^{-1}$). While the $v \sin i$ correction increases the accuracy of our $\log g$ determinations for the early-group stars in most cases, the correction appears to worsen our determinations for the intermediate group, which appear systematically high to begin with.

The potential systematic effect of metallicity on our $\log g$ determinations is considered in Figure 2.11, showing the surface gravity residuals as a function of $[\text{Fe}/\text{H}]$.

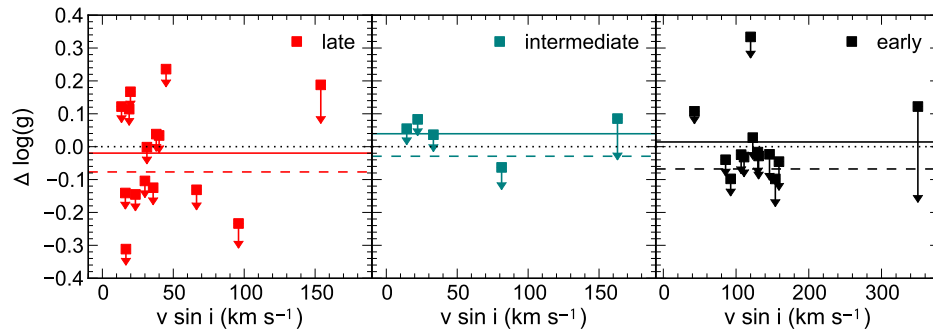


Figure 2.10: Surface gravity residuals, $\Delta \log g$ (in the sense of fundamental- $uvby\beta$), of eclipsing binary primaries as a function of $v \sin i$. Arrows indicate the locations of points after application of the Figueras & Blasi (1998) $v \sin i$ correction, where in this case late group stars received the same correction as the intermediate group.

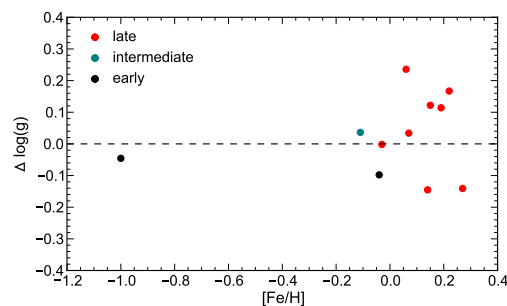


Figure 2.11: Surface gravity residuals, $\Delta \log g$ (in the sense of fundamental- $uvby\beta$), as a function of $[\text{Fe}/\text{H}]$. The metallicity values have been taken primarily from Ammons et al. (2006), with additional values coming from Anderson & Francis (2012). While metallicities seem to exist for very few of the surface gravity calibrators used here, there does not appear to be a systematic trend in the residuals with $[\text{Fe}/\text{H}]$. There is a larger amount of scatter for the more metal-rich late-type stars, however the scatter is confined to a relatively small range in $[\text{Fe}/\text{H}]$ and it is not clear that this effect is due to metallicity effects.

Metallicity measurements were available for very few of these stars, and were primarily taken from Ammons et al. (2006) and Anderson & Francis (2012). Nevertheless, there does not appear to be a global systematic trend in the surface gravity residuals with metallicity. There is a larger scatter in $\log g$ determinations for the more metal-rich, late-type stars, however it is not clear that this effect is strictly due to metallicity.

In summary, for the open cluster tests we assign $\log g$ uncertainties in three regimes: ± 0.145 dex for stars belonging to the late group, ± 0.091 dex for the intermediate group, and ± 0.113 dex for the early group.

For our sample of nearby field stars we opt to assign a uniform systematic uncertainty

of ± 0.116 dex for all stars. We do not attempt to correct for any systematic effects by applying offsets in $\log g$, as we did with T_{eff} . As noted in discussion of the T_{eff} calibration, we do apply the $v \sin i$ correction to both intermediate and early group stars, as these corrections permit us to better reproduce open cluster ages (as presented in § 2.6).

Table 2.2: Primary Components of Double-lined Eclipsing Binaries with fundamental determinations of $\log g$

Star	Sp. Type	T_{eff} (K)	T_{uvby} (K)	$\log g_{\text{EB}}$ (dex)	$\log g_{\text{uvby}}$ (dex)	$v \sin i$ (km s ⁻¹)	[Fe/H] (dex)	$(b - y)$ (mag)	m_1 (mag)	c_1 (mag)	β (mag)
EM Car	O8V	34000 ± 2000	21987	3.855 ± 0.016	3.878	146.0	...	0.279	-0.042	0.083	2.617
V1034 Sco	O9V	33200 ± 900	28228	3.923 ± 0.008	3.969	159.0	-1.0	0.190	-0.024	-0.068	2.587
AH Cep	B0.5Vn	29900 ± 1000	24867	4.017 ± 0.009	4.115	154.0	...	0.290	-0.064	0.003	2.611
V578 Mon	B1V	30000 ± 740	25122	4.176 ± 0.015	4.200	107.0	...	0.206	-0.024	-0.003	2.613
V453 Cyg	B0.4IV	27800 ± 400	24496	3.725 ± 0.006	3.742	130.0	...	0.212	-0.004	-0.004	2.590
CW Cep	B0.5V	28300 ± 1000	22707	4.050 ± 0.019	3.716	120.0	...	0.355	-0.077	0.050	2.601
V539 Ara	B3V	18100 ± 500	17537	3.924 ± 0.016	3.964	85.6	...	-0.033	0.089	0.268	2.665
CV Vel	B2.5V	18100 ± 500	17424	3.999 ± 0.008	3.891	42.8	...	-0.057	0.083	0.273	2.659
AG Per	B3.4V	18200 ± 800	15905	4.213 ± 0.020	4.311	92.6	-0.04	0.048	0.079	0.346	2.708
U Oph	B5V	16440 ± 250	15161	4.076 ± 0.004	3.954	350.0	...	0.081	0.050	0.404	2.695
V760 Sco	B4V	16900 ± 500	15318	4.176 ± 0.019	4.061	0.169	0.023	0.392	2.701
GG Lup	B7V	14750 ± 450	13735	4.298 ± 0.009	4.271	123.0	...	-0.049	0.115	0.514	2.747
ζ Phe	B6V	14400 ± 800	13348	4.121 ± 0.004	4.153	111.0	...	-0.039	0.118	0.559	2.747
χ ² Hya	B8V	11750 ± 190	11382	3.710 ± 0.007	3.738	131.0	...	-0.020	0.110	0.841	2.769
V906 Sco	B9V	10400 ± 500	10592	3.656 ± 0.012	3.719	81.3	...	0.039	0.101	0.996	2.805
TZ Men	A0V	10400 ± 500	10679	4.224 ± 0.009	4.169	14.4	...	0.000	0.142	0.918	2.850
V1031 Ori	A6V	7850 ± 500	8184	3.559 ± 0.007	3.793	96.0	...	0.076	0.174	1.106	2.848
β Aur	A1m	9350 ± 200	9167	3.930 ± 0.005	3.894	33.2	-0.11	0.017	0.173	1.091	2.889
V364 Lac	A4m:	8250 ± 150	7901	3.766 ± 0.005	3.707	0.107	0.168	1.061	2.875
V624 Her	A3m	8150 ± 150	7902	3.832 ± 0.014	3.794	38.0	...	0.111	0.230	1.025	2.870
V1647 Sgr	A1V	9600 ± 300	9142	4.252 ± 0.008	4.087	0.040	0.174	1.020	2.899
VV Pyx	A1V	9500 ± 200	9560	4.087 ± 0.008	4.004	22.1	...	0.028	0.161	1.013	2.881
KW Hya	A5m	8000 ± 200	8053	4.078 ± 0.006	4.390	16.6	...	0.122	0.232	0.832	2.827
WW Aur	A5m	7960 ± 420	8401	4.161 ± 0.005	4.286	35.8	...	0.081	0.231	0.944	2.862
V392 Car	A2V	8850 ± 200	10263	4.296 ± 0.011	4.211	163.0	...	0.097	0.108	1.019	2.889
RS Cha	A8V	8050 ± 200	7833	4.046 ± 0.022	4.150	30.0	...	0.136	0.186	0.866	2.791
MY Cyg	F0m	7050 ± 200	7054	3.994 ± 0.019	3.882	0.219	0.226	0.709	2.756

Table 2.2 Continued: Primary Components of Double-lined Eclipsing Binaries

El Cep	F3V	6750 ± 100	6928	3.763 ± 0.014	3.904	16.2	0.27	0.234	0.199	0.658	2.712
FS Mon	F2V	6715 ± 100	6677	4.026 ± 0.005	3.992	40.0	0.07	0.266	0.148	0.594	2.688
PV Pup	A8V	6920 ± 300	7327	4.255 ± 0.009	4.386	66.4	...	0.200	0.169	0.636	2.722
HD 71636	F2V	6950 ± 140	6615	4.226 ± 0.014	4.104	13.5	0.15	0.278	0.157	0.496	...
RZ Cha	F5V	6450 ± 150	6326	3.905 ± 0.006	3.808	...	0.02	0.312	0.155	0.482	...
BW Aqr	F7V	6350 ± 100	6217	3.979 ± 0.018	3.877	0.328	0.165	0.432	2.650
V570 Per	F3V	6842 ± 50	6371	4.234 ± 0.019	3.998	44.9	0.06	0.308	0.165	0.441	...
CD Tau	F6V	6200 ± 50	6325	4.087 ± 0.007	3.973	18.9	0.19	0.314	0.178	0.436	...
V1143 Cyg	F5V	6450 ± 100	6492	4.322 ± 0.015	4.155	19.8	0.22	0.294	0.165	0.451	2.663
VZ Hya	F3V	6645 ± 150	6199	4.305 ± 0.003	4.182	...	-0.22	0.333	0.145	0.370	2.629
V505 Per	F5V	6510 ± 50	6569	4.323 ± 0.016	4.325	31.4	-0.03	0.287	0.142	0.435	2.654
HS Hya	F4V	6500 ± 50	6585	4.326 ± 0.005	4.471	23.3	0.14	0.287	0.160	0.397	2.648

Spectral type, temperature, and fundamental $\log g$ information originate from Torres et al. (2010). The $uvby\beta \log g$ values are from this work. Projected rotational velocities are from Glebocki & Gnacinski (2005), [Fe/H] from Anderson & Francis (2012) and Ammons et al. (2006), and the $uvby\beta$ photometry are from HM98. The surface gravities in the column $\log g_{uvby}$ are derived together with T_{uvby} , and not for the T_{eff} values given by Torres et al. (2010).

2.4.2.2 Comparison with Spectroscopic Measurements

The Balmer lines are a sensitive surface gravity indicator for stars hotter than $T_{\text{eff}} \gtrsim 9000$ K and can be used as a semi-fundamental surface gravity calibration for the early- and intermediate-group stars. The reason why surface gravities derived using this method are considered semi-fundamental and not fundamental is because the method still relies on model atmospheres for fitting the observed line profiles. Nevertheless, surface gravities determined through this method are considered of high fidelity and so we performed an additional consistency check, comparing our $uvby\beta$ values of $\log g$ to those with well-determined spectroscopic $\log g$ measurements.

N93 fit theoretical profiles of hydrogen Balmer lines from Kurucz (1979) to high resolution spectrograms of the $H\beta$ and $H\gamma$ lines for a sample of 16 stars with $uvby\beta$ photometry. The sample of 16 stars was mostly drawn from the list of photometric β standards of Crawford (1966). We compared the $\log g$ values we determined through interpolation in the $uvby\beta$ color grids to the semi-fundamental spectroscopic values determined by N93. The results of this comparison are presented in Table 2.3.

Though N93 provide dereddened photometry for the spectroscopic sample, we found using the raw HM98 photometry produced significantly better results (yielding an RMS error that was three times lower). For the early group stars, the atmospheric parameters were determined in both the $c_0 - \beta$ plane and the $[u - b] - \beta$ plane. In both cases, β is the gravity indicator, but we found that the $\log g$ values calculated when using c_0 as a temperature indicator for hot stars better matched the semi-fundamental spectroscopic $\log g$ values. This result is consistent with the result from the effective temperature calibration that suggests c_0 better predicted the effective temperatures of hot stars than $[u - b]$. As before, $\log g$ for intermediate group stars is determined in the $a_0 - r^*$ plane.

We tested $uvby\beta$ color grids of different metallicity, alpha-enhancement, and microturbulent velocity and determined that the non-alpha-enhanced, solar metallicity grids with microturbulent velocity $v_{\text{turb}} = 0 \text{ km s}^{-1}$ best reproduced the spectroscopic surface gravities for the sample of 16 early- and intermediate-group stars measured by N93.

The $\log g$ residuals, in the sense of (spectroscopic – grid), as a function of the grid-calculated effective temperatures are plotted in Figure 2.9. There is no evidence for a significant systematic offset in the residuals as a function of either the $uvby\beta$ -determined T_{eff} or $\log g$. For the early group, the mean and median surface gravity

Table 2.3: Stars with semi-fundamental determinations of $\log g$ through Balmer-line fitting

HR	Sp. Type	T_{eff} (K)	T_{uvby} (K)	$\log g_{\text{spec}}$ (dex)	$\log g_{uvby}$ (dex)	$(b - y)$ (mag)	m_1 (mag)	c_1 (mag)	$[u - b]$ (mag)	β (mag)
63	A2V	8970	9047	3.73	3.912	0.026	0.181	1.050	1.425	2.881
153	B2IV	20930	20635	3.78	3.872	-0.090	0.087	0.134	0.264	2.627
1641	B3V	16890	16528	4.07	4.044	-0.085	0.104	0.319	0.485	2.683
2421	AOIV	9180	9226	3.49	3.537	0.007	0.149	1.186	1.487	2.865
4119	B6V	14570	14116	4.18	4.176	-0.062	0.111	0.481	0.673	2.730
4554	AOVe	9360	9398	3.82	3.863	0.006	0.155	1.112	1.425	2.885
5191	B3V	17320	16797	4.28	4.292	-0.080	0.106	0.297	0.470	2.694
6588	B3IV	17480	17025	3.82	3.864	-0.065	0.079	0.292	0.418	2.661
7001	AOVa	9540	9508	4.01	3.977	0.003	0.157	1.088	1.403	2.903
7447	B5III	13520	13265	3.73	3.712	-0.016	0.088	0.575	0.743	2.707
7906	B9IV	10950	10838	3.85	3.861	-0.019	0.125	0.889	1.130	2.796
8585	A1V	9530	9615	4.11	4.175	0.002	0.170	1.032	1.373	2.908
8634	B8V	11330	11247	3.69	3.672	-0.035	0.113	0.868	1.077	2.768
8781	B9V	9810	9868	3.54	3.593	-0.011	0.128	1.129	1.380	2.838
8965	B8V	11850	11721	3.47	3.422	-0.031	0.100	0.784	0.969	2.725
8976	B9IVn	11310	11263	4.23	4.260	-0.035	0.131	0.831	1.076	2.833

Note: Spectral type, T_{eff} , and spectroscopic $\log g$ originate from N93. The $uvby\beta$ T_{eff} and $\log g$ values are from this work. Though N93 does not provide formal errors on the atmospheric parameters, those authors estimate uncertainties of ~ 0.03 dex in their spectroscopically determined $\log g$. The fractional errors in their photometrically derived T_{eff} range from 2.5% for stars cooler than ≈ 11000 K to 4% for stars hotter than ≈ 20000 K. The photometry is from HM98.

residuals are -0.007 dex and 0.004 dex, respectively, with RMS 0.041 dex. For the intermediate group, the mean and median surface gravity residuals are -0.053 dex and -0.047 dex, respectively, with RMS 0.081 dex. Considering both early and intermediate group stars collectively, the mean and median surface gravity residuals are -0.027 dex and -0.021 dex, and the RMS 0.062 dex.

One issue that may cause statistically larger errors in the $\log g$ determinations compared to the T_{eff} determinations is the linear interpolation in a low resolution logarithmic space (the $uvby\beta$ colors are calculated at steps of 0.5 dex in $\log g$). In order to mitigate this effect one requires either more finely gridded models or an interpolation scheme that takes the logarithmic gridding into account.

2.4.3 Summary of Atmospheric Parameter Uncertainties

Precise and accurate stellar ages are the ultimate goal of this work. The accuracy of our ages is determined by both the accuracy with which we can determine atmospheric parameters and any systematic uncertainties associated with the stellar evolutionary models and our assumptions in applying them. The precision, on the other hand, is determined almost entirely by the precision with which we determine atmospheric parameters and, because there are some practical limits to how well we may ever determine T_{eff} and $\log g$, the location of the star in the H-R diagram (e.g.

stars closer to the main sequence will always have more imprecise ages using this method).

It is thus important to provide a detailed accounting of the uncertainties involved in our atmospheric parameter determinations, as the final uncertainties quoted in our ages will arise purely from the values of the $\sigma_{T_{\text{eff}}}$, $\sigma_{\log g}$ used in our χ^2 calculations. Below we consider the contribution of the systematics already discussed, as well as the contributions from errors in interpolation, photometry, metallicity, extinction, rotational velocity, multiplicity, and spectral peculiarity.

Systematics: The dominant source of uncertainty in our atmospheric parameter determinations are the systematics quantified in § 2.4.1 and § 2.4.2. All systematic effects inherent to the $uvby\beta$ method, and the particular model color grids chosen, which we will call σ_{sys} , are embedded in the comparisons to the stars with fundamentally or semi-fundamentally determined parameters, summarized as approximately $\sim 3.1\%$ in T_{eff} and ~ 0.116 dex in $\log g$. We also found that for stars with available $[\text{Fe}/\text{H}]$ measurements, the accuracy with which we can determine atmospheric parameters using $uvby\beta$ photometry does not vary systematically with metallicity, though we further address metallicity issues both below and in an Appendix.

Interpolation Precision: To estimate the errors in atmospheric parameters due to the numerical precision of the interpolation procedures employed here, we generated 1000 random points in each of the three relevant $uvby\beta$ planes. For each point, we obtained ten independent T_{eff} , $\log g$ determinations to test the repeatability of the interpolation routine. The scatter in independent determinations of the atmospheric parameters were found to be $< 10^{-10}$ K, dex, and thus numerical errors are assumed zero.

Photometric Errors: Considering the most basic element of our approach, there are uncertainties due to the propagation of photometric errors through our atmospheric parameter determination pipeline. As discussed in § 2.7, the photometric errors are generally small (~ 0.005 mag in a given index). Translating the model grid points in the rectangular regions defined by the magnitude of the mean photometric error in a given index, and then interpolating to find the associated atmospheric parameters of the perturbed point, we take the maximum and minimum values for T_{eff} and $\log g$ to calculate the error due to photometric measurement error.

To simplify the propagation of photometric errors for individual stars, we performed simulations with randomly generated data to ascertain the mean uncertainty in T_{eff} ,

$\log g$ that results from typical errors in each of the $uvby\beta$ indices.

We begin with the HM98 photometry and associated measurement errors for our sample (3499 stars within 100 pc, B0-F5, luminosity classes IV-V). Since the HM98 compilation does not provide a_0 or r^* , as these quantities are calculated from the four fundamental indices, we calculate the uncertainties in these parameters using the crude approximation that none of the $uvby\beta$ indices are correlated. Under this assumption, the uncertainties associated with a_0 and r^* are as follows:

$$\sigma_{a_0} = \sqrt{1.36^2 \sigma_{b-y}^2 + 0.36^2 \sigma_{m_1}^2 + 0.18^2 \sigma_{c_1}^2} \quad (2.17)$$

$$\sigma_{r^*} = \sqrt{0.07^2 \sigma_{b-y}^2 + 0.35^2 \sigma_{c_1}^2 + \sigma_{\beta}^2}. \quad (2.18)$$

A model for the empirical probability distribution function (hereafter PDF) for the error in a given $uvby\beta$ index is created through a normalized histogram with 25 bins. From this empirical PDF, one can randomly draw values for the error in a given index. For each $uvby\beta$ plane, 1,000 random points in the appropriate range of parameter space were generated with photometric errors drawn as described above. The eight (T_{eff} , $\log g$) values corresponding to the corners and midpoints of the “standard error rectangle” centered on the original random data point are then evaluated. The maximally discrepant (T_{eff} , $\log g$) values are saved and the overall distributions of $\Delta T_{\text{eff}}/T_{\text{eff}}$ and $\Delta \log g$ are then analyzed to assess the mean uncertainties in the atmospheric parameters derived in a given $uvby\beta$ plane due to the propagation of typical photometric errors.

For the late group, points were generated in the range of $(b - y) - c_1$ parameter space bounded by $6500 \text{ K} \leq T_{\text{eff}} \leq 9000 \text{ K}$ and $3.0 \leq \log g \leq 5.0$. In this group, typical photometric uncertainties of $\langle \sigma_{b-y} \rangle = 0.003 \text{ mag}$ and $\langle \sigma_{c_1} \rangle = 0.005 \text{ mag}$ lead to average uncertainties of 0.6 % in T_{eff} and 0.055 dex in $\log g$. For the intermediate group, points were generated in the range of $a_0 - r^*$ parameter space bounded by $8500 \text{ K} \leq T_{\text{eff}} \leq 11000 \text{ K}$ and $3.0 \leq \log g \leq 5.0$. In this group, typical photometric uncertainties of $\langle \sigma_{a_0} \rangle = 0.005 \text{ mag}$ and $\langle \sigma_{r^*} \rangle = 0.005 \text{ mag}$ lead to average uncertainties of 0.8 % in T_{eff} and 0.046 dex in $\log g$. For the early group, points were generated in the range of $c_1 - \beta$ parameter space bounded by $10000 \text{ K} \leq T_{\text{eff}} \leq 30000 \text{ K}$ and $3.0 \leq \log g \leq 5.0$. In this group, typical photometric uncertainties of $\langle \sigma_{c_1} \rangle = 0.005 \text{ mag}$ and $\langle \sigma_{\beta} \rangle = 0.004 \text{ mag}$ lead to average uncertainties of 1.1 % in T_{eff} and 0.078 dex in $\log g$. Across all three

groups, the mean uncertainty due to photometric errors is $\approx 0.9\%$ in T_{eff} and ≈ 0.060 dex in $\log g$.

Metallicity Effects: For simplicity and homogeneity, our method assumes solar composition throughout. However, our sample can more accurately be represented as a Gaussian centered at -0.109 dex with $\sigma \approx 0.201$ dex. Metallicity is a small, but non-negligible, effect and allowing $[M/H]$ to change by ± 0.5 dex can lead to differences in the assumed T_{eff} of $\sim 1\text{-}2\%$ for late-, intermediate-, and some early-group stars, or differences of up to 6% for stars hotter than ~ 17000 K (of which there are few in our sample). In $\log g$, shifts of ± 0.5 dex in $[M/H]$ can lead to differences of ~ 0.1 dex in the assumed $\log g$ for late- or early-group stars, or ~ 0.05 dex in the narrow region occupied by intermediate-group stars.

Here, we estimate the uncertainty the metallicity approximation introduces to the fundamental stellar parameters derived in this work. We begin with the actual $uvby\beta$ data for our sample, and $[\text{Fe}/\text{H}]$ measurements from the XHIP catalog (Anderson & Francis, 2012), which exist for approximately 68% of our sample. Those authors collected photometric and spectroscopic metallicity determinations of Hipparcos stars from a large number of sources, calibrated the values to the high-resolution catalog of Wu et al. (2011) in an attempt to homogenize the various databases, and published weighted means for each star. The calibration process is described in detail in §5 of Anderson & Francis (2012).

For each of the stars with available $[\text{Fe}/\text{H}]$ in our field star sample, we derive T_{eff} , $\log g$ in the appropriate $uvby\beta$ plane for the eight cases of $[M/H]=\{-2.5, -2.0, -1.5, -1.0, -0.5, 0.0, 0.2, 0.5\}$. Then, given the measured $[\text{Fe}/\text{H}]$, and making the approximation that $[M/H]=[\text{Fe}/\text{H}]$, we perform a linear interpolation to find the most accurate values of T_{eff} , $\log g$ given the color grids available. We also store the atmospheric parameters a given star would be assigned assuming $[M/H]=0.0$. Figure 2.12 shows the histograms of $T_{\text{eff}}/T_{\text{eff},[M/H]=0}$ and $\log g - \log g_{[M/H]=0}$. We take the standard deviations in these distributions to reflect the typical error introduced by the solar metallicity approximation. For T_{eff} , there is a 0.8% uncertainty introduced by the true dispersion of metallicities in our sample, and for $\log g$, the uncertainty is 0.06 dex. These uncertainties in the atmospheric parameters are naturally propagated into uncertainties in the age and mass of a star through the likelihood calculations outlined in § 2.5.2.1.

Reddening Effects: For the program stars studied here, interstellar reddening is assumed negligible. Performing the reddening corrections (described in § 2.2.2)

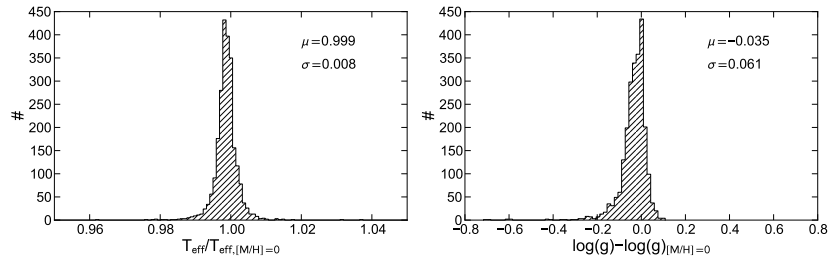


Figure 2.12: Distributions of the true variations in T_{eff} (left) and $\log g$ (right) caused by our assumption of solar metallicity. The “true” T_{eff} and $\log g$ values are determined for the $\sim 68\%$ of our field star sample with $[\text{Fe}/\text{H}]$ measurements in XHIP and from linear interpolation between the set of atmospheric parameters determined in eight ATLAS9 grids (Castelli & Kurucz, 2006; Castelli & Kurucz, 2004) that vary from -2.5 to 0.5 dex in $[\text{M}/\text{H}]$.

on our presumably unreddened sample of stars within 100 pc, we find for the $\sim 80\%$ of stars for which dereddening proved possible, that the distribution of A_V values in our sample is approximately Gaussian with a mean and standard deviation of $\mu = 0.007$, $\sigma = 0.125$ mag, respectively (see Figure 2.19). Of course, negative A_V values are unphysical, but applying the reddening corrections to our $uvby\beta$ photometry and deriving the atmospheric parameters for each star in both the corrected and uncorrected cases gives us an estimate of the uncertainties in those parameters due to our assumption of negligible reddening out to 100 pc. The resulting distributions of $T_{\text{eff},0}/T_{\text{eff}}$ and $\log g_0 - \log g$, where the naught subscripts indicate the dereddened values, are sharply peaked at 1 and 0, respectively. The FWHM of these distributions indicate an uncertainty $< 0.2\%$ in T_{eff} and ~ 0.004 dex in $\log g$. For the general case of sources at larger distances that may suffer more significant reddening, the systematic effects of under-correcting for extinction are illustrated in Figure 2.13.

Uncertainties in Projected Rotational Velocities: The Glebocki & Gnacinski (2005) compilation contains mean $v \sin i$ measurements, as well as individual measurements from multiple authors. Of the 3499 stars in our sub-sample of the HM98 catalog, 2547 stars have $v \sin i$ values based on 4893 individual $v \sin i$ measurements, 1849 of which have an accompanying measurement error. Of these measurements, 646 are for intermediate or early groups, for which rotation corrections are performed in our method. The mean fractional error in $v \sin i$ for this subset of measurements is $\sim 13\%$. Calculating the atmospheric parameters for these stars, then performing the FB98 $v \sin i$ corrections using v_{rot} and $v_{\text{rot}} \pm \sigma_{v_{\text{rot}}}$ allows us to estimate the magnitude of the uncertainty in T_{eff} , $\log g$ due to the uncertainties in $v \sin i$ measurements.

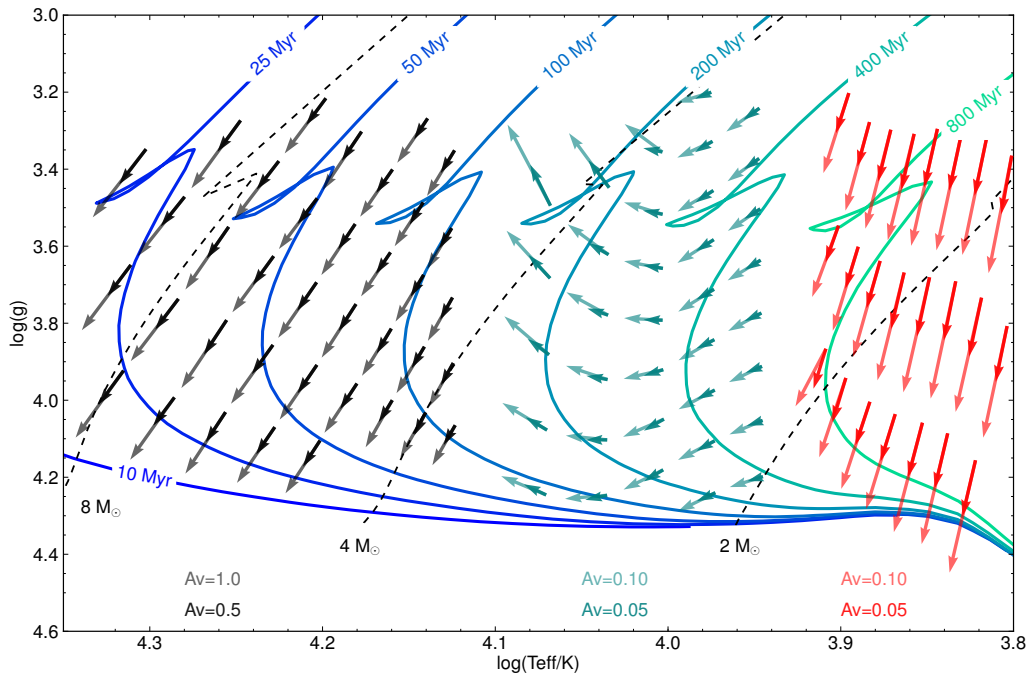


Figure 2.13: The effect of interstellar reddening on atmospheric parameters derived from $uvby\beta$ photometry. The isochrones and mass tracks plotted are those of Bressan et al. (2012). The tail of each vector represents a given point in a specific photometric plane ($(b - y) - c_1$ for the late group stars in red, $a_0 - r^*$ for the intermediate group stars in teal, and $c_1 - \beta$ for the early group stars in black) and its corresponding value in $[T_{\text{eff}}, \log g]$. The tip of the vector points to the new value of $[T_{\text{eff}}, \log g]$ after each point in photometric space has been “dereddened” assuming arbitrary values of A_V . The shifts in $uvby\beta$ space have been computed according to the extinction measurements of Schlegel et al. (1998) and Crawford & Mandwewala (1976), assuming $A_V \approx 4.237E(b - y)$. The magnitudes of A_V chosen for this figure represent the extremes of values expected for our sample of nearby stars and are meant to illustrate the directionality of the effects of reddening as propagated through the $uvby\beta$ planes. Finally, note for the early group (black vectors), the A_V values are an order of magnitude larger and much higher than expected for our sample. Again, this is to illustrate the directionality of the reddening effect, which is particularly small for the early group which rely on c_1 , the Balmer discontinuity index, for temperature, and β , a color between two narrow-band filters with nearly the same central wavelength, for $\log g$.

The resulting RMS errors in T_{eff} , $\log g$ are 0.7% and 0.01 dex, respectively. When $v \sin i$ measurements are not available, an average value based on the spectral type can be assumed, resulting in a somewhat larger error. The systematic effects of under-correcting for rotation are illustrated in Figure 2.4.

Influence of Multiplicity: In a large study such as this one, a high fraction of stars are binaries or higher multiples. Slightly more than 30% of our sample stars are known as members of multiple systems. We choose not to treat these stars differently, given the unknown multiplicity status of much of the sample, and caution our readers to use due care regarding this issue.

Influence of Spectral peculiarities: Finally, early-type stars possess several peculiar subclasses (e.g. Ap, Bp, Am, etc. stars) for which anomalous behavior has been reported in the $uvby\beta$ system with respect to their “normal-type” counterparts. Some of these peculiarities have been linked to rotation, which we do account for. We note that peculiar subclasses constitute $\sim 4\%$ of our sample and these stars could suffer unquantified errors in the determination of fundamental parameters when employing a broad methodology based on calibrations derived from mostly normal-type stars (see Tables 2.1 & 2.2 for a complete accounting of the spectral types used for calibrations). As these subclasses were included in the atmospheric parameter validation stage (§ 2.3), and satisfactory accuracies were still obtained, we chose not to adjust our approach for these stars and estimate the uncertainties introduced by their inclusion is negligible.

Final Assessment: Our final atmospheric parameter uncertainties are dominated by the systematic effects quantified in § 2.4.1 and § 2.4.2, with the additional effects outlined above contributing very little to the total uncertainty. The largest additional contributor comes from the photometric error. Adding in quadrature the sources σ_{sys} , σ_{num} , σ_{phot} , $\sigma_{[\text{Fe}/\text{H}]}$, $\sigma_{v \sin i}$ and σ_{A_V} results in final error estimates of 3.4% in T_{eff} and 0.14 dex in $\log g$.

The use of $uvby\beta$ photometry to determine fundamental stellar parameters is estimated in previous literature to lead to uncertainties of just 2.5% in T_{eff} and 0.1 dex in $\log g$ (Asiain et al., 1997), with our assessment of the errors somewhat higher.

The uncertainties that we derive in our Strömgen method work can be compared with those given by other methods. The Geneva photometry system (U , $B1$, $B2$, $V1$, G filters), like the Strömgen system, has been used to derive T_{eff} , $\log g$, and $[\text{M}/\text{H}]$ values based on atmospheric grids (Kobi & North, 1990; Kunzli et al., 1997), with

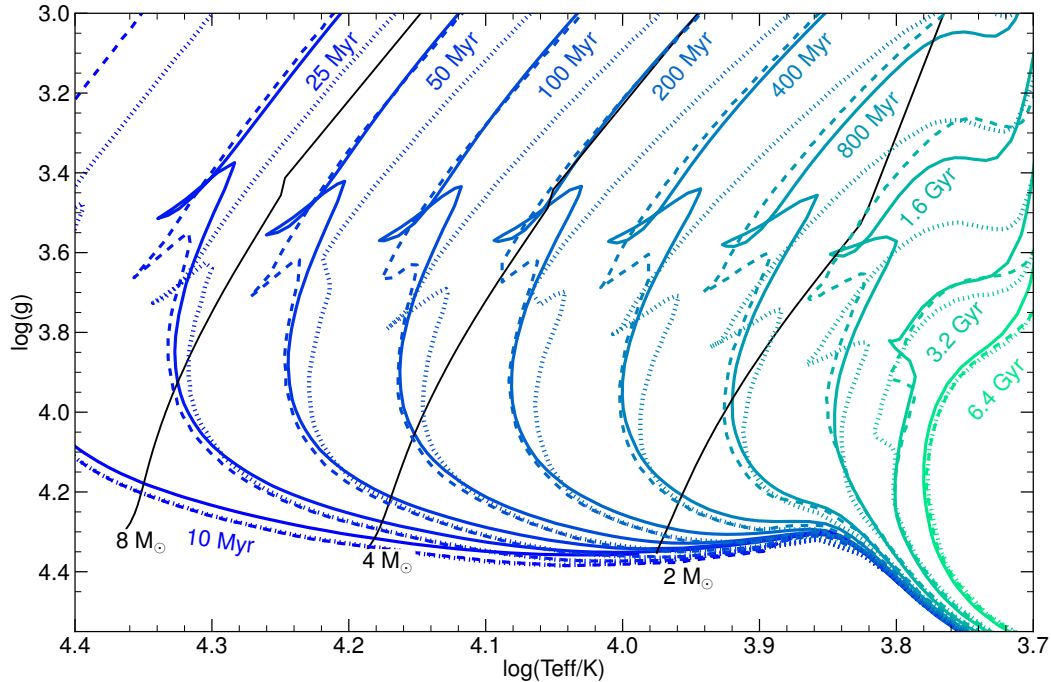


Figure 2.14: Comparison of PARSEC isochrones (solid lines), Ekström isochrones in the rotating case (dashed lines), and Ekström isochrones in the non-rotating case (dotted lines). The solid black lines are evolutionary tracks for stars of intermediate-mass, from the PARSEC models. All evolutionary tracks plotted are for solar metallicity.

Kunzli et al. (1997) finding 150-250 K (few percent) errors in $\log T_{\text{eff}}$ and 0.1-0.15 dex errors in $\log g$, comparable to our values. From stellar model atmosphere fitting to high dispersion spectra, errors of 1-5% in T_{eff} and 0.05-0.15 dex (typically 0.1 dex) in $\log g$ are quoted for early type stars (e.g. Nieva & Simón-Díaz, 2011), though systematic effects in $\log g$ on the order of an additional 0.1 dex may be present. Wu et al. (2011) tabulate the dispersions in atmospheric parameters among many different studies, finding author-to-author values that differ for OBA stars by 300-5000 K in T_{eff} (3-12%) and 0.2-0.6 dex in $\log g$ (cm/s^2), and for FGK stars 40-100 K in T_{eff} and 0.1-0.3 dex in $\log g$ (cm/s^2).

2.5 Age Estimation from Isochrones

2.5.1 Selection of Evolutionary Models

Once T_{eff} and $\log g$ have been established, ages are determined through a Bayesian grid search of the fundamental parameter space encompassed by the evolutionary models. In this section we discuss the selection of evolution models, the Bayesian approach, numerical methods, and resulting age/mass uncertainties.

Two sets of isochrones are considered in this work. The model families are compared

in Figure 2.14. The PARSEC solar-metallicity isochrones of Bressan et al. (2012), hereafter B12, take into account in a self-consistent manner the pre-main-sequence phase of evolution. The PARSEC models are the most recent iteration of the Padova evolutionary models, with significant revisions to the major input physics such as the equation of state, opacities, nuclear reaction rates and networks, and the inclusion of microscopic diffusion. The models are also based on the new reference solar composition, $Z = 0.01524$ from Caffau et al. (2011), but can be generated for a wide range of metallicities. The B12 models cover the mass range $0.1 - 12M_{\odot}$.

PARSEC isochrones are attractive because early-type dwarfs have relatively rapid evolution with the pre-main-sequence evolution constituting a significant fraction of their lifetimes, i.e. $\tau_{\text{PMS}}/\tau_{\text{MS}}$ is larger compared to stars of later types. For stars with effective temperatures in the range 6500 K - 25000 K (approximately spectral types B0-F5), the B12 models predict pre-main sequence lifetimes ranging from $\sim 0.2\text{-}40$ Myr, main-sequence lifetimes from ~ 14 Myr - 2.2 Gyr, and the ratio $\tau_{\text{PMS}}/\tau_{\text{MS}} \sim 1.6\text{-}2.4\%$. A star of given initial mass thus can be followed consistently through the pre-MS, MS, and post-MS evolutionary stages. As a consequence, most points in $T_{\text{eff}}\text{-}\log g$ space will have both pre-ZAMS and post-ZAMS ages as possible solutions. Figure 2.1 illustrates the evolution of atmospheric and corresponding photometric properties according to the PARSEC models.

The solar-metallicity isochrones of Ekström et al. (2012), hereafter E12, also use updated opacities and nuclear reaction rates, and are the first to take into account the effects of rotation on global stellar properties at intermediate masses. They are available for both non-rotating stars and stars that commence their lives on the ZAMS with a rotational velocity of 40% their critical rotational velocity ($v_{\text{rot,i}}/v_{\text{crit}} = 0.4$); however, the Ekström et al. (2012) models do not take the pre-main sequence phase into account. The E12 models currently exist only for solar metallicity ($Z=0.014$ is used), but cover a wider range of masses ($0.8 - 120M_{\odot}$).

The E12 models are attractive because they explicitly account for rotation, though at a fixed percentage of breakup velocity. All output of stellar evolutionary models (e.g. lifetimes, evolution scenarios, nucleosynthesis) are affected by axial stellar rotation which for massive stars enhances the MS lifetime by about 30% and may increase isochronal age estimates by about 25% (Meynet & Maeder, 2000). In terms of atmospheres, for A-type stars, stellar rotation increases the strength of the Balmer discontinuity relative to a non-rotating star with the same color index (Maeder & Peytremann, 1970). In the E12 models, the convective overshoot parameter was

selected to reproduce the observed main sequence width at intermediate masses, which is important for our aim of distinguishing the ages of many field stars clustered on the main sequence with relatively large uncertainties in their surface gravities. Figure 2.14 shows, however, that there is close agreement between the B12 and the rotating E12 models. Thus, there is not a significant difference between the two models in regards to the predicted width of the MS band.

It should be noted that the $uvby\beta$ grids of Castelli & Kurucz (2006) and Castelli & Kurucz (2004) were generated assuming a solar metallicity value of $Z=0.017$. As discussed elsewhere, metallicity effects are not the dominant uncertainty in our methods and we are thus not concerned about the very small metallicity differences between the two model isochrone sets nor the third metallicity assumption in the model atmospheres.

In matching data to evolutionary model grids, a general issue is that nearly any given point in an H-R diagram (or equivalently in $T_{\text{eff}}\text{-}\log g$ space), can be reproduced by multiple combinations of stellar age and mass. Bayesian inference can be used to determine the relative likelihoods of these combinations, incorporating prior knowledge about the distributions of the stellar parameters being estimated.

2.5.2 Bayesian Age Estimation

A simplistic method for determining the theoretical age and mass for a star on the Hertzsprung-Russell (H-R) diagram is interpolation between isochrones or evolutionary models. Some problems with this approach, as pointed out by Takeda et al., 2007; Pont & Eyer, 2004, is that interpolation between isochrones neither accounts for the nonlinear mapping of time onto the H-R diagram nor the non-uniform distribution of stellar masses observed in the galaxy. As a consequence, straightforward interpolation between isochrones results in an age distribution for field stars that is biased towards older ages compared to the distribution predicted by stellar evolutionary theory.

Bayesian inference of stellar age and mass aims to eliminate such a bias by accounting for observationally and/or theoretically motivated distribution functions for the physical parameters of interest. As an example, for a given point with error bars on the H-R diagram, a lower stellar mass should be considered more likely due to the initial mass function. Likewise, due to the longer main-sequence timescales for lower mass stars, a star that is observed to have evolved off the main sequence should have a probability distribution in mass that is skewed towards higher masses, i.e.

because higher mass stars spend a more significant fraction of their entire lifetime in the post-MS stage.

2.5.2.1 Bayes Formalism

Bayesian estimation of the physical parameters can proceed from comparison of the data with a selection of models. Bayes' Theorem states:

$$P(\text{model}|\text{data}) \propto P(\text{data}|\text{model}) \times P(\text{model}) \quad (2.19)$$

The probability of a model given a set of data is proportional to the product of the probability of the data given the model and the probability of the model itself. In the language of Bayesian statistics, this is expressed as:

$$\text{posterior} \propto \text{likelihood} \times \text{prior}. \quad (2.20)$$

Our model is the set of stellar parameters, age (τ) and mass (M_*), and our data are the measured effective temperature, T_{eff} , and surface gravity, $\log g$, for a given star. At any given combination of age and mass, the predicted T_{eff} and $\log g$ are provided by stellar evolutionary models. The χ^2 statistic for an individual model can be computed as follows:

$$\chi^2(\tau, M_*) = \sum \frac{(O - E)^2}{\sigma^2} \quad (2.21)$$

$$= \frac{[(T_{\text{eff}})_O - (T_{\text{eff}})_E]^2}{\sigma_{T_{\text{eff}}}^2} + \frac{[(\log g)_O - (\log g)_E]^2}{\sigma_{\log g}^2}, \quad (2.22)$$

where the subscripts O and E refer to the observed and expected (or model) quantities, respectively, and σ is the measurement error in the relevant quantity.

Assuming Gaussian statistics, the relative likelihood of a specific combination of (T_{eff} , $\log g$) is:

$$P(\text{data}|\text{model}) = P(T_{\text{eff,obs}}, \log g_{\text{obs}}|\tau, M_*) \quad (2.23)$$

$$\propto \exp \left[-\frac{1}{2} \chi^2(\tau, M_*) \right]. \quad (2.24)$$

Finally, the joint posterior probability distribution for a model with age τ and mass M_* , is given by:

$$P(\text{model}|\text{data}) = P(\tau, M_* | T_{\text{eff,obs}}, \log g_{\text{obs}}) \quad (2.25)$$

$$\propto \exp \left[-\frac{1}{2} \chi^2(\tau, M_*) \right] P(\tau) P(M_*), \quad (2.26)$$

where $P(\tau)$ and $P(M_*)$ are the prior probability distributions in age and mass, respectively. The prior probabilities of age and mass are assumed to be independent such that $P(\tau, M_*) = P(\tau)P(M_*)$.

2.5.2.2 Age and Mass Prior Probability Distribution Functions

Standard practice in the Bayesian estimation of stellar ages is to assume an age prior that is uniform in linear age, e.g. Pont & Eyer (2004), Jørgensen & Lindegren (2005), Takeda et al. (2007), and Nielsen et al. (2013). There are two main justifications for choosing a uniform age prior: 1) it is the least restrictive choice of prior and 2) at this stage the assumption is consistent with observations that suggest a fairly constant star formation rate in solar neighborhood over the past 2 Gyr (Cignoni et al., 2006).

Since the evolutionary models are logarithmically gridded in age, the relative probability of age bin i is given by the bin width in linear age divided by the total range in linear age:

$$P(\log(\tau_i) \leq \log(\tau) < \log(\tau_{i+1})) = \frac{\tau_{i+1} - \tau_i}{\tau_n - \tau_0}, \quad (2.27)$$

where τ_n and τ_0 are the largest and smallest allowed ages, respectively. This weighting scheme gives a uniform probability distribution in linear age.

As noted by Takeda et al. (2007), it is important to understand that assuming a flat prior in linear age corresponds to a highly non-uniform prior in the measured quantities of $\log T_{\text{eff}}$ and $\log g$. This is due to the non-linear mapping between these measurable quantities and the physical quantities of mass and age in evolutionary models. Indeed, the ability of the Bayesian approach to implicitly account for this effect is considered one of its main strengths.

As is standard in the Bayesian estimation of stellar masses, an initial mass function (IMF) is assumed for the prior probability distribution of all possible stellar masses.

Several authors point out that Bayesian estimates of physical parameters are relatively insensitive to the mass prior (i.e. the precise form of the IMF assumed), especially in the case of parameter determination over a small or moderate range in mass space. For this work considering BAF stars, the power law IMF of Salpeter (1955) is assumed for the mass prior, so that the relative probability of mass bin i is given by the following expression:

$$P(M_i \leq M < M_{i+1}) \propto M_i^{-2.35}. \quad (2.28)$$

2.5.2.3 Numerical Methods

As Takeda et al. (2007) point out, in Bayesian age estimation interpolation should be performed only along isochrones and not between them. To avoid biasing our derived physical parameters from interpolating between isochrones, we generated a dense grid of PARSEC models. The evolutionary models were acquired with a spacing of 0.0125 dex in $\log(\text{age}/\text{yr})$ and $0.0001 M_\odot$ in mass. All probabilities were then computed on a 321×321 grid ranging from $\log(\text{age}/\text{yr})=6$ to 10 and from $1-10 M_\odot$.

2.5.2.4 Age and Mass Uncertainties

Confidence intervals in age and mass are determined from the one-dimensional marginalized posterior probability distributions for each parameter. Since the marginalized probability distributions can often be asymmetric, the region chosen for determining confidence intervals is that of the Highest Posterior Density (HPD). This method selects the smallest range in a parameter that encompasses $N\%$ of the probability. The HPD method is discussed in more detail in the appendix.

Notably, uncertainties in the ages depend on where in the $\log g$ and $\log T_{\text{eff}}$ parameter space the star is located, and whether a pre-main sequence or a post-zero-age-main sequence age is more appropriate. In the pre-main sequence phase, both atmospheric parameters are important in age determination. For post-ZAMS stars, however, the relative importance of the two parameters changes. When stars are just bouncing back from the ZAMS and are starting to evolve through the MS phase, $\log g$ must be known precisely (within the range of ~ 4.3 to 4.45) in order to derive a good age estimate. The age at which this bounce occurs will be a function of mass (earlier for more massive stars). Otherwise, once late B, A, and early F stars are comfortably settled on the MS, their evolution is at roughly constant temperature (see Figure

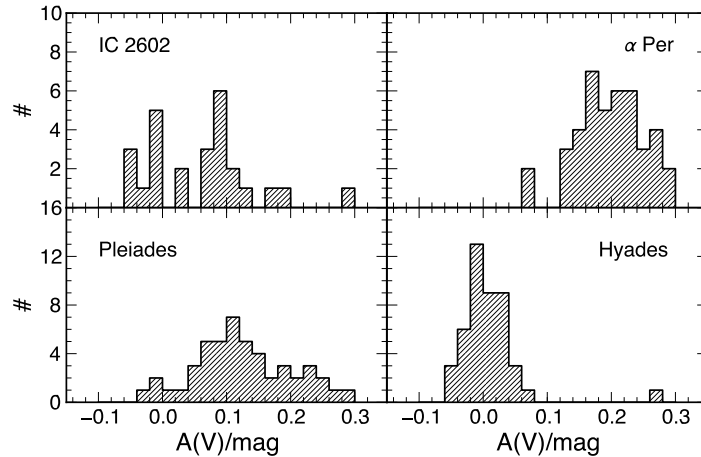


Figure 2.15: Histograms of the visual extinction, A_V , in magnitudes for individual members of the four open clusters considered here. The extinction values are calculated using the relation $A_V = 4.237E(b - y)$, with the $(b - y)$ color excesses computed as described in § 2.2.2.

2.14) and so the gravity precision becomes far less important, with temperature precision now critical.

2.6 The Methodology Tested on Open Clusters

An important test of our methods is to assess the ages derived from our combination of $uvby\beta$ photometry, atmospheric parameter placement, and comparison to evolutionary models relative to the accepted ages for members of well-studied open clusters. We investigate four such clusters with rigorous age assessment in previous literature: IC 2602, α Persei, the Pleiades, and the Hyades.

The youngest ($\lesssim 20 - 30$ Myr) open clusters may be age-dated kinematically, by tracing the space motions of individual members back to the time when the stars were in closest proximity to one another (Soderblom, 2010). After $\lesssim 1$ galactic rotation period, however, individual member motions are randomized to the extent of limiting the utility of the kinematic method. Beyond $\sim 20 - 30$ Myr, the most precise open cluster ages come from the lithium depletion boundary (LDB) technique. This method uses the lithium abundances, which diminish predictably with time, of the lowest mass cluster members to converge on precise ($\sim 10\%$) ages. LDB ages are available for IC 2602: $\tau = 46_{-5}^{+6}$ Myr (Dobbie et al., 2010), α Per: $\tau = 90 \pm 10$ Myr (Stauffer et al., 1999), and the Pleiades: $\tau = 125 \pm 8$ Myr (Stauffer et al., 1998). The LDB technique does not work past ~ 250 Myr, so the Hyades is dated based on isochrone fitting in the H-R diagram using stars with high precision distance

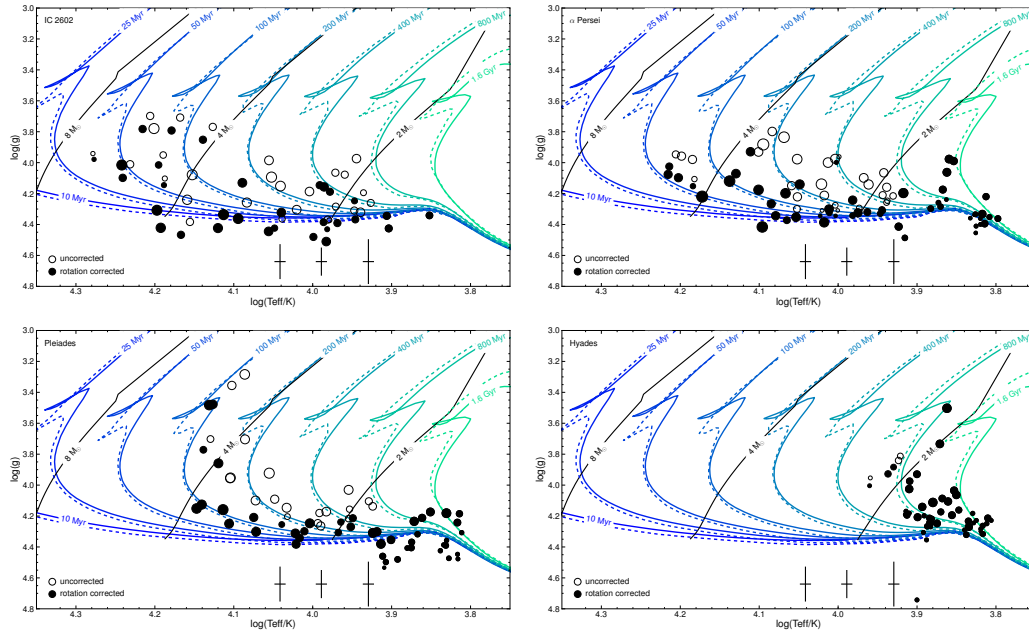


Figure 2.16: PARSEC isochrones and mass tracks (Bressan et al., 2012) in $\log T_{\text{eff}}\text{-}\log g$ space and the isochrones of Ekström et al. (2012) (including rotation, plotted as dashed lines) with our $uvby\beta$ photometric determinations of the atmospheric parameters. For early and intermediate group stars, the black filled circles represent the $v \sin i$ corrected atmospheric parameters (using the FB98 formulae), while the open circles represent the uncorrected parameters. Note that the late-group stars do not receive a $v \sin i$ correction but are still plotted as filled circles. In both cases the point sizes are $\propto v \sin i$. The typical uncertainties in our $\log T_{\text{eff}}$ and $\log g$ determinations are represented by the error bars at the bottom of the figure. These uncertainties correspond to 1.6% or ≈ 0.007 dex in $\log T_{\text{eff}}$ and 0.091 dex (intermediate), and 0.145 dex (late) in $\log g$, corresponding to the RMS errors as determined in the effective temperature and surface gravity calibrations. *Top left:* IC 2602 members; the currently accepted age of IC 2602 is $\tau = 46_{-5}^{+6}$ Myr (Dobbie et al., 2010). *Top right:* Members of the α Persei cluster, which has a currently accepted age of $\tau = 90 \pm 10$ Myr (Stauffer et al., 1999). *Bottom left:* Pleiades members where the currently accepted age of the Pleiades is $\tau = 125 \pm 8$ Myr Stauffer et al., 1998. Of the ~ 20 Pleiads that sit below the zero age main sequence, 5 are known pulsators of the δ Scu or γ Dor variety. Additionally, there is an excess of slow rotators sitting below the ZAMS. Possible reasons for this observed behavior include systematics of the atmospheric models (several authors have noted problems with the treatment of convection in ATLAS9 models at this mass range), failure of the evolutionary models to predict the true width of the main sequence (though this effect is unlikely to be as large as the scatter seen here), and overaggressive dereddening procedures. *Bottom right:* Hyades cluster members where the currently accepted age of the Hyades is $\tau = 625 \pm 50$ Myr Perryman et al. (1998). Note the far left outlier, HD 27962, is a known blue straggler (Abt, 1985; Eggen, 1995) and was excluded by Perryman et al. (1998) in their isochrone-fitting analysis. The outlier far below the ZAMS, HD 27268, is a spectroscopic binary (Debernardi et al., 2000).

measurements, with currently accepted age 625 ± 50 Myr (Perryman et al., 1998).

2.6.1 Process

Membership probabilities, $uvby\beta$ photometry, and projected rotational velocities are obtained for members of these open clusters via the WEBDA open cluster database⁵. For the Pleiades, membership information was augmented and cross-referenced with Stauffer et al. (2007). Both individual $uvby\beta$ measurements and calculations of the mean and scatter from the literature measurements are available from WEBDA in each of the photometric indices. As the methodology requires accurate classification of the stars according to regions of the H-R diagram, we inspected the spectral types and β indices and considered only spectral types B0-F5 and luminosity classes III-V for our open cluster tests.

In contrast to the field stars studied in the next section, the open clusters studied here are distant enough for interstellar reddening to significantly affect the derived stellar parameters. The photometry is thus dereddened as described in § 2.2.2. Figure 2.15 shows the histograms of the visual extinction A_V for each cluster, with the impact of extinction on the atmospheric parameter determination illustrated above in Figure 2.13.

In many cases, individual cluster stars have multiple measurements of $v \sin i$ in the WEBDA database and we select the measurement from whichever reference is the most inclusive of early-type members. In very few cases does a cluster member have no rotational velocity measurement present in the database; for these stars we assume the mean $v \sin i$ according to the $T_{\text{eff}} - v \sin i$ relation presented in Appendix B of Gray (2005).

Atmospheric parameters are determined for each cluster member, as described in § 2.3. Adopting our knowledge from the comparison to fundamental and semi-fundamental atmospheric parameters (§ 2.4.1 & § 2.4.2), a uniform 1.6% shift towards cooler T_{eff} was applied to all temperatures derived from the model color grids to account for systematic effects in those grids. The FB98 $v \sin i$ corrections were then applied to the atmospheric parameters. The $v \sin i$ corrections prove to be a crucial step in achieving accurate ages for the open clusters (particularly for the Pleiades).

⁵<http://www.univie.ac.at/webda/>

2.6.2 Results

The results of applying our procedures to open cluster samples appear in Figure 2.16. While the exact cause(s) of the remaining scatter observed in the empirical isochrones for each cluster is not known, possible contributors may be systematic or astrophysical in nature, or due to incorrect membership information. Multiplicity, variability, and spectral peculiarities were among the causes investigated for this scatter, but the exclusion of objects on the basis of these criteria did not improve age estimation for any individual cluster. The number of stars falling below the theoretical ZAMS, particularly for stars with $\log T_{\text{eff}} \lesssim 3.9$, is possibly systematic and may be due to an incomplete treatment of convection by the ATLAS9 models. This source of uncertainty is discussed in further detail in § 2.8.2.

For each cluster, we publish the individual stars considered, along with relevant parameters, in Tables 2.8, 2.9, 2.10, & 2.11. In each table, the spectral types and $v \sin i$ measurements are from WEBDA, while the dereddened $uvby\beta$ photometry and atmospheric parameters are from this work.

2.6.2.1 Ages from Bayesian Inference

Once atmospheric parameters have been determined, age determination proceeds as outlined in § 2.5. For each individual cluster member, the χ^2 , likelihood, and posterior probability distribution are calculated for each point on a grid ranging from $\log(\text{age}/\text{yr})=6.5$ to 10, with masses restricted to $1 \leq M/M_{\odot} \leq 10$. The resolution of the grid is 0.0175 dex in $\log(\text{age}/\text{yr})$ and $0.045 M_{\odot}$ in mass. The 1-D marginalized posterior PDFs for each individual cluster member are normalized and then summed to obtain an overall posterior PDF in age for the cluster as a whole. This composite posterior PDF is also normalized prior to the determination of statistical measures (mean, median, confidence intervals). Additionally, the posterior PDFs in $\log(\text{age})$ for each member are multiplied to obtain the total probability in each $\log(\text{age})$ bin that all members have a single age. While the summed PDF depicts better the behavior of individual stars or groups of stars, the multiplied PDF is best for assigning a single age to the cluster and evaluating any potential systematics of the isochrones themselves.

As shown in Figure 2.17, the summed age PDFs for each cluster generally follow the same behavior: (1) the peaks are largely determined by the early group (B-type) stars which have well-defined ages due to their unambiguous locations in the $T_{\text{eff}} - \log g$ diagram; (2) examining the age posteriors for individual stars, the intermediate

group stars tend to overpredict the cluster age relative to the early group stars, and the same is true for the late group stars with respect to the intermediate group stars, resulting in a large tail at older ages for each of the summed PDFs due to the relatively numerous and broad PDFs of the later group stars. For IC 2602 and the Pleiades, the multiplied PDFs have median ages and uncertainties that are in close agreement with the literature ages. Notably, the results of the open cluster tests favor an age for the Hyades that is older (~ 800 Myr) than the accepted value, though not quite as old as the recent estimate of 950 ± 100 Myr from Brandt & Huang (2015a). The Bayesian age analysis also favors an age for α Per that is younger (~ 70 Myr) than the accepted value based on lithium depletion, but older than the canonical 50 Myr from the Upper Main Sequence Turnoff Mermilliod (1981). In an appendix, we perform the same analysis for the open clusters on $p(\tau)$ rather than $p(\log \tau)$, yielding similar results.

The results of the open cluster test are presented in Table 2.4. It is noted that all statistical measures of the marginalized age PDFs quoted hereafter are from PDFs normalized in $\log(\text{age})$, as opposed to converting to linear age and then normalizing. This choice was made due to the facts that 1) the isochrones are provided in uniform logarithmic age bins, and 2) the marginalized PDFs of individual stars are more symmetric (and thus better characterized by traditional statistical measures) in $\log(\text{age})$ than in linear age. Notably, the median age is equivalent regardless of whether one chooses to analyze $\text{prob}(\log \tau)$ or $\text{prob}(\tau)$. This issue is discussed further in an appendix. In general, there is very close agreement in the Bayesian method ages between B12 and rotating E12 models. For IC 2602 and the Pleiades, our analysis yields median cluster ages (as determined from the multiplied PDFs) that are within $1-\sigma$ of accepted values, regardless of the evolutionary models considered. The Bayesian analysis performed with the PARSEC models favor an age for α Persei that is $\sim 20\%$ younger than the currently accepted value, or $\sim 20\%$ older for the Hyades.

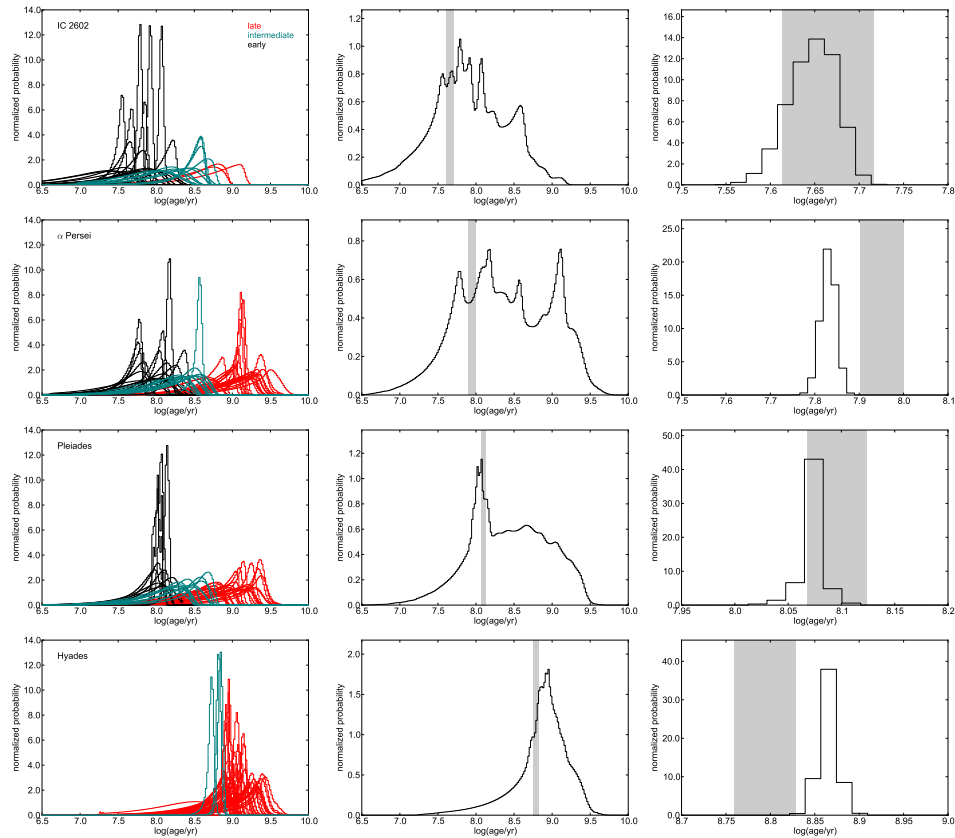


Figure 2.17: *Left panels:* 1D marginalized, normalized posterior PDFs in age, calculated from Bressan et al. (2012) evolutionary models, for individual open cluster members. Black, teal, and red histograms represent early, intermediate, and late group stars, respectively. *Middle panels:* Sums of the individual PDFs depicted on the left. This figure shows the total probability associated with the 200 age bins between $\log(\text{age}/\text{yr})=6.5$ to 10. The grey shaded regions indicate the currently accepted ages of IC 2602 (46^{+6}_{-5} Myr), α Per (90 ± 10 Myr), the Pleiades (125 ± 8 Myr), and the Hyades (625 ± 50 Myr). *Right panels:* Products of the individual PDFs depicted in the left panels. The grey shaded regions again depict the accepted literature age ranges of each cluster.

Table 2.4: Open Cluster Ages.

Cluster	Lit. Age (Myr)	Models	Summed PDF	Summed PDF	Multiplied PDF	Multiplied PDF	χ^2_{\min}
			Median (Myr)	68% C.I. (Myr)	Median (Myr)	68% C.I. (Myr)	
IC 2602	46^{+6}_{-5}	Ekström et al. (2012)	80	32-344	42	41-46	39
		Bressan et al. (2012)	79	27-284	46	44-50	37
α Persei	90^{+10}_{-10}	Ekström et al. (2012)	234	83-1618	71	68-74	50
		Bressan et al. (2012)	226	74-1500	70	69-74	48
Pleiades	125^{+8}_{-8}	Ekström et al. (2012)	277	81-899	128	126-130	126
		Bressan et al. (2012)	271	85-948	123	121-126	115
Hyades	625^{+50}_{-50}	Ekström et al. (2012)	872	518-1940	827	812-837	631
		Bressan et al. (2012)	844	487-1804	764	747-780	501

Note: Literature ages (column 2) come from the sources referenced in § 2.6. For each set of evolutionary models, the median and 68% confidence interval are computed for both the summed PDF (columns 4,5) and multiplied PDF (columns 6,7). The final column indicates the best-fit isochrone found through χ^2 -minimization of all cluster members in $\log(T_{\text{eff}}) - \log g$ space. Note, the Hyades analysis includes the blue straggler HD 27962 and the spectroscopic binary HD 27268. Excluding these outliers results in a median and 68% confidence interval of 871 Myr [517-1839 Myr] of the summed PDF or 832 Myr [812-871 Myr] of the multiplied PDF, using the B12 models.

2.6.2.2 Ages from Isochrone Fitting

As a final test of the two sets of evolutionary models, we used χ^2 -minimization to find the best-fitting isochrone for each cluster. By fitting all members of a cluster simultaneously, we are able to assign a single age to all stars, test the accuracy of the isochrones for stellar ensembles, and test the ability of our $uvby\beta$ method to reproduce the shapes of coeval stellar populations in $T_{\text{eff}} - \log g$ space. For this exercise, we did not interpolate between isochrones, choosing instead to use the default spacing for each set of models (0.1 dex and 0.0125 dex in $\log(\text{age}/\text{yr})$ for the E12 and B12 models, respectively). For the best results, we consider only the sections of the isochrones with $\log g$ between 3.5 and 5.0 dex. The results of this exercise are shown in Figure 2.18. The best-fitting E12 isochrone (including rotation) is consistent with accepted ages to within 1% for the Pleiades and Hyades, $\sim 15\%$ for IC 2602, and $\sim 44\%$ for α -Per. For the B12 models, the best-fit isochrones are consistent with accepted ages to $\sim 8\%$ for the Pleiades, $\sim 20\%$ for the Hyades and IC 2602, and $\sim 47\%$ for α -Per. The B12 models produce systematically younger ages than the E12 models, by a fractional amount that increases with absolute age.

As detailed above, the open cluster tests revealed that our method is able to distinguish between ensembles of differing ages, from tens to hundreds of Myr, at least in a statistical sense. For individual stars, large uncertainties may remain, particularly for the later types, owing almost entirely to the difficulty in determining both precise and accurate surface gravities. The open cluster tests also demonstrate the importance of a $v \sin i$ correction for early (B0-A0) and intermediate (A0-A3) group stars in determining accurate stellar parameters. While the $v \sin i$ correction was not applied to the late group (A3-F5 in this case) stars, it is likely that stars in this group experience non-negligible gravity darkening. The typically unknown inclination angle, i , also contributes significant uncertainties in derived stellar parameters and hence ages.

2.7 The Methodology Applied to Nearby Field Stars

As an application of our developed, calibrated, validated, and tested methodology, we consider the complete HM98 photometric catalog of 63,313 stars. We are interested only in nearby stars that are potential targets for high contrast imaging campaigns, and for which interstellar extinction is negligible. We thus perform a distance cut at 100 pc, using distances from the XHIP catalog (Anderson & Francis, 2012). We perform an additional cut in spectral type (using information from XHIP),

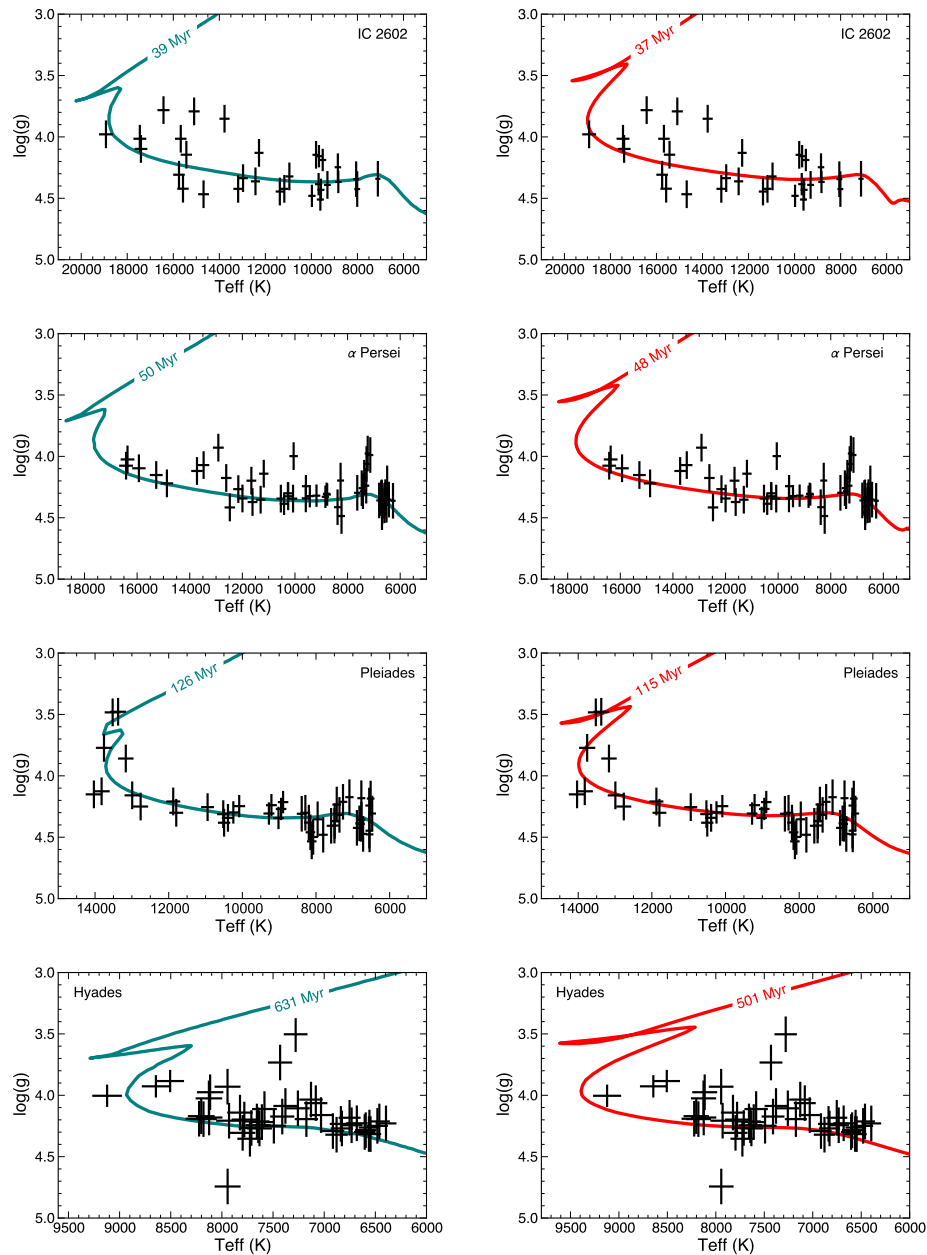


Figure 2.18: Best fitting isochrones found through χ^2 -minimization for four open clusters, with atmospheric parameters determined through $uvby\beta$ photometry. Left panels are the fully rotating Ekström et al. (2012) evolutionary models while right panels are the Bressan et al. (2012) models. For the Pleiades, the best fitting isochrone age (126 Myr) from the E12 models is within the currently accepted range of 125 ± 8 Myr. The B12 models give a best-fit age of 115 Myr, representing a fractional error of $\sim 8\%$ (or 1.25σ) relative to the accepted age. In the case of the Hyades (lower panels), the low and far left outliers are a spectroscopic binary and a blue straggler, respectively. Excluding these stars yields no change in the best-fitting isochrone for the E12 models and only moderately increases the best-fitting B12 model to 530 Myr.

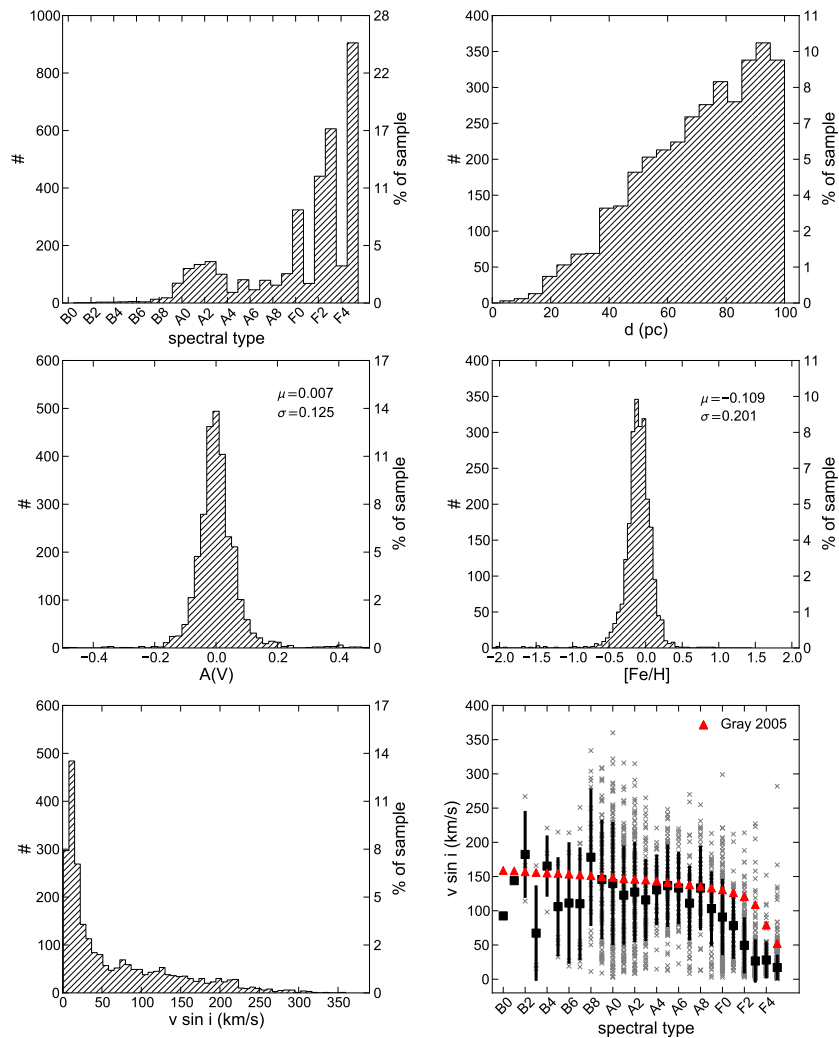


Figure 2.19: Characterization of our sample of 3499 nearby field stars. *Upper panels:* histograms of the spectral types (left) and distances (right) of stars in our sample, taken from Anderson & Francis (2012). *Middle panels:* histograms of the V-band extinction in magnitudes (left), as derived by the IDL program described in § 2.2.2, and the $[\text{Fe}/\text{H}]$ values in dex from Anderson & Francis (2012). *Lower panels:* histogram of the projected rotational velocities in our sample (left), with data taken from Glebocki & Gnacinski (2005), and $v \sin i$ as a function of spectral type (right) with grey x's indicating individual stars and black squares representing the mean $v \sin i$ in each spectral type bin. The error bars represent the standard deviation in $v \sin i$ values for each bin. The red triangles indicate the empirical $T_{\text{eff}}-v \sin i$ relation of Gray (2005) using the spectral-type- T_{eff} relation of Habets & Heintze (1981).

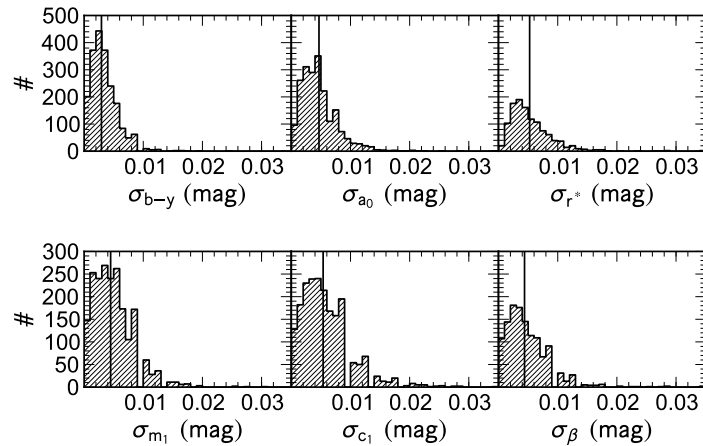


Figure 2.20: Histograms of the uncertainties (in mag) for different $uvby\beta$ indices for the sample of ~ 3500 field stars discussed in § 2.7. The solid lines in each plot indicate the position of the mean uncertainty in that parameter. Uncertainties in a_0 and r^* are calculated according to Eqns. (13) & (14).

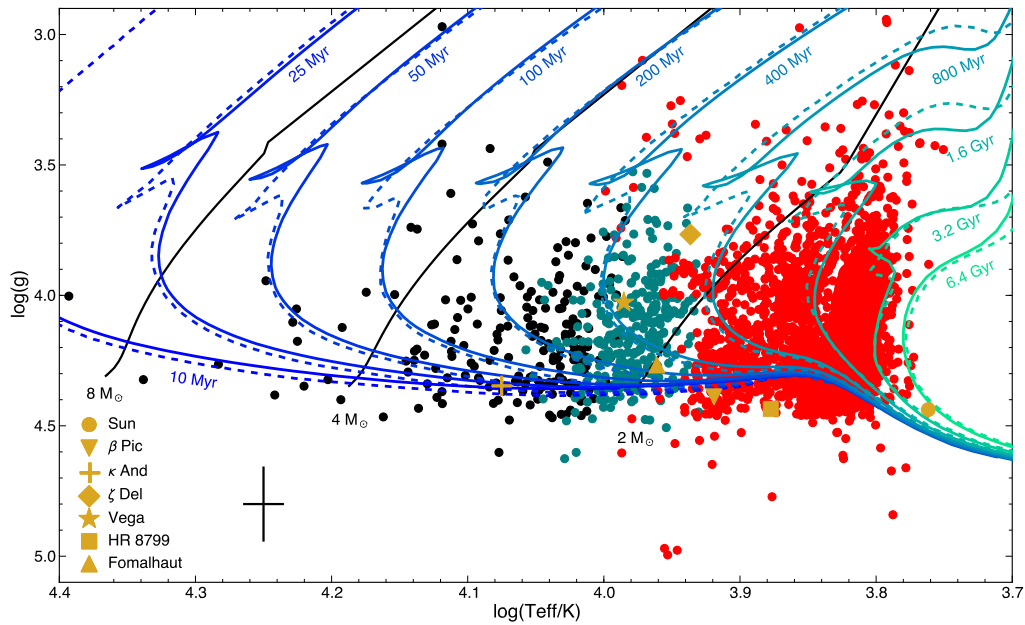


Figure 2.21: H-R diagram for our sample of B0-F5 field stars within 100 pc. Thirteen stars with $\log g < 2.9$ are excluded in this figure. Several stars of interest are plotted in gold. As before, red, teal, and black scatter points correspond to late, intermediate, and early group stars, respectively. Values for the Sun are also plotted for reference. Of note, ~ 770 of the stars plotted are subgiants according to their XHIP luminosity classes, while only ~ 250 stars have $\log g < 3.8$, suggesting some spectral types are in error.

considering only B0-F5 stars belonging to luminosity classes IV,V, because this is the range for which our method has been shown to work with high fidelity and additionally these are the primary stars of interest to near-term high-contrast imaging surveys. In total, we are left with 3499 stars. Figure 2.19 shows the distribution of our field star sample in spectral type, distance, A_V , $[\text{Fe}/\text{H}]$, and $v \sin i$. The distributions of photometric errors in given $uvby\beta$ indices are shown in Figure 2.20, and the mean errors in each index are summarized as follows: $\langle \sigma_{b-y} \rangle, \langle \sigma_{m_1} \rangle, \langle \sigma_{c_1} \rangle, \langle \sigma_{\beta} \rangle, \langle \sigma_{a_0} \rangle, \langle \sigma_{r^*} \rangle = 0.003, 0.004, 0.005, 0.004, 0.005, 0.005$ mag.

Projected rotational velocities for the sample of nearby field stars are sourced from the Glebocki & Gnacinski (2005) compilation, which contains $v \sin i$ measurements for 2874 of the stars, or $\sim 82\%$ of the sample. For an additional 8 stars $v \sin i$ measurements are collected from Zorec & Royer (2012), and for another 5 stars $v \sin i$ values come from Schröder et al. (2009). For the remaining stars without $v \sin i$ measurements, a projected rotational velocity is assumed according to the mean $v \sin i - T_{\text{eff}}$ relation from Appendix B of Gray (2005). Atmospheric parameters are corrected for rotational velocity effects as outlined in § 2.3.3.

Atmospheric parameter determination was not possible for six stars, due to discrepant positions in the relevant $uvby\beta$ planes: HIP 8016 (a B9V Algol-type eclipsing binary), HIP 12887 (a poorly studied F3V star), HIP 36850 (a well-studied A1V+A2Vm double star system), HIP 85792 (a well-studied Be star, spectral type B2Vne), HIP 97962 (a moderately studied B9V star), and HIP 109745 (an A0III star, classified in XHIP as an A1IV star). Consequently, ages and masses were not computed for these stars.

An H-R diagram of the entire sample is shown in Figure 2.21, with the evolutionary models of Bressan et al. (2012) overlaid. Equipped with atmospheric parameters for the remaining 3493 stars, and assuming uniform uncertainties of 3.4% and 0.14 dex in T_{eff} and $\log g$, respectively, ages and masses were computed via the process outlined in § 2.5. Posterior probabilities were calculated on a uniform 321×321 grid of the Bressan et al. (2012) models, gridded from 1 Myr-10 Gyr in steps of 0.0125 dex in $\log(\text{age})$, and from $1-10M_{\odot}$ in steps of $0.028M_{\odot}$. As the Bressan et al. (2012) models exist for high resolution timesteps, no interpolation between isochrones was required.

From the 2D joint posterior PDF, we obtain the marginalized 1D PDFs in age and mass, from which we compute the mean (expected value), median, mode (most probable value), as well as 68% and 95% confidence intervals. Interpolated ages

and masses are also included, and these values may be preferred, particularly for objects with an interpolated age $\lesssim 10^8$ yr and a $\log g$ placing it near the ZAMS (see § 2.8.2 for more detail). The table of ages and masses for all 3943 stars, including our newly derived atmospheric parameters, are available as an electronic table and a portion (sorted in ascending age) is presented here in Table 2.5. In rare instances (for $\sim 5\%$ of the sample), true 68% and 95% confidence intervals were not obtained due to numerical precision, the star's location near the edge of the computational grid, or some combination of the two effects. In these cases the actual confidence interval quoted is noted as a flag in the electronic table.

Table 2.5: Ages, Masses, and Atmospheric Parameters of Nearby B0-F5 Field Stars

HIP	T_{eff}	$\log g$	Mean Age	Median Age	Mode Age	68% Age	95% Age	Interp. Age	Mean Mass	Median Mass	Mode Mass	68% Mass	95% Mass	Interp. Mass
	(K)	(dex)	(Myr)	(Myr)	(Myr)	(Myr)	(Myr)	(Myr)	(M_{\odot})	(M_{\odot})	(M_{\odot})	(M_{\odot})	(M_{\odot})	(M_{\odot})
65474	24718	4.00	6	7	9	5-12	2-14	13	9.59	9.61	9.62	9.4-9.9	9.2-10.0	10.26
61585	21790	4.32	6	7	11	4-18	1-21	1	7.53	7.52	7.48	7.3-7.7	7.1-8.0	7.34
61199	16792	4.18	18	22	33	13-53	3-60	36	4.84	4.83	4.78	4.6-5.0	4.5-5.2	4.95
60718	16605	4.35	19	23	35	13-55	3-61	1	4.75	4.74	4.70	4.6-4.9	4.4-5.1	4.58
60000	15567	4.12	21	26	40	14-65	4-77	60	4.27	4.26	4.22	4.1-4.4	4.0-4.6	4.48
100751	17711	3.94	23	29	43	20-50	5-52	48	5.41	5.42	5.35	5.1-5.6	5.0-5.9	5.91
23767	16924	4.10	23	30	44	18-56	4-61	46	4.96	4.95	4.92	4.7-5.2	4.5-5.4	5.14
92855	19192	4.26	24	29	34	23-38	8-40	8	6.39	6.37	6.25	6.0-6.6	5.8-7.1	5.95
79992	14947	3.99	26	31	48	18-78	4-89	88	4.01	4.00	3.97	3.8-4.1	3.7-4.3	4.45

Note: The fractional uncertainty in our T_{eff} determinations is 3.4% and the uncertainty in our $\log g$ determinations is 0.14 dex. All ages and masses are computed from the Bressan et al. (2012) models. Statistical measures are quoted for marginalized PDFs in $\log(\text{age})$ rather than age, e.g. column 4 is $10^{\langle \log(\tau) \rangle}$ rather than $\langle \tau \rangle$. Confidence intervals are computed via the HPD method. The full table containing ages, masses, and atmospheric parameters for all 3493 stars is available electronically. Table 2.5 is published in its entirety in the electronic edition of *ApJ*. A portion is shown here for guidance regarding its form and content.

Table 2.6: Statistics of Composite Age PDFs.

Sp. Types	Mean Age (Myr)	Median Age (Myr)	Mode Age (Myr)	68% C.I. (Myr)	95% C.I. (Myr)
B0-B9	93	122	147	56-316	8-410
A0-A4	296	365	392	200-794	39-1090
A5-A9	572	750	854	434-1372	82-1884
F0-F5	1554	1884	2024	1000-4217	307-6879

As with the open clusters, we can sum the individual, normalized PDFs in age to produce composite PDFs for various subsets of our sample. Figure 2.22 depicts the composite age PDF for our entire sample, as well as age PDFs for the subsets of B0-B9, A0-A4, A5-A9, and F0-F5 stars. From these PDFs we can ascertain the statistical properties of these subsets of solar neighborhood stars, which are presented in Table 2.6.

2.7.1 Empirical Mass-Age Relation

From our newly derived set of ages and masses of solar-neighborhood B0-F5 stars, we can determine an empirical mass-age relation. Using the mean ages and masses for all stars in our sample, we performed a linear least squares fit using the NumPy polyfit routine, yielding the following relation, valid for stars $1.04 < M/M_{\odot} < 9.6$:

$$\log(\text{age}/\text{yr}) = 9.532 - 2.929 \log\left(\frac{M}{M_{\odot}}\right). \quad (2.29)$$

The RMS error between the data and this relation is a fairly constant 0.225 dex as a function of stellar mass.

2.7.2 Empirical Spectral-Type-Age/Mass Relations

We can also derive empirical spectral-type-age and spectral-type-mass relations for the solar neighborhood, using the mean masses derived from our 1D marginalized posterior PDFs in age, and spectral type information from XHIP. These relations are plotted in Figure 2.23, and summarized in Table 2.7.

2.8 Discussion

The precision of the age-dating method described here relies on the use of Strömgren $ubvy\beta$ photometry to finely distinguish stellar atmosphere parameters and compare them to isochrones from stellar evolution models. For ages ≤ 10 Myr and $\gtrsim 100$ Myr, in particular, there is rapid evolution of $\log T_{\text{eff}}$ and $\log g$ for intermediate-mass stars (see Figure 2.1). This enables greater accuracy in age determination through

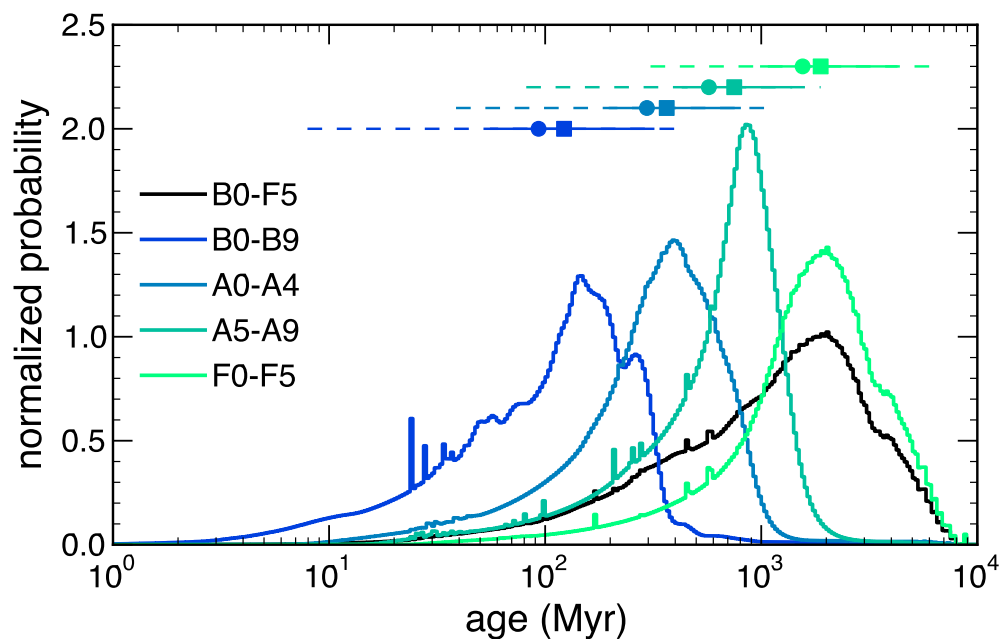


Figure 2.22: Normalized composite age PDFs for our sample of field B0-F5 stars within 100 pc. The normalized composite PDFs are created by summing the normalized, 1D marginalized age PDFs of individual stars in a given spectral type grouping. The black curve represents the composite pdf for all spectral types, while the colored curves represent the composite PDFs for the spectral type groups B0-B9, A0-A4, A5-A9, F0-F5 (see legend). Circles represent the expectation values of the composite PDFs, while squares represent the medians. The solid and dashed lines represent the 68% and 95% confidence intervals, respectively, of the composite PDFs. The statistical measures for these composite PDFs are also presented in Table 2.6.

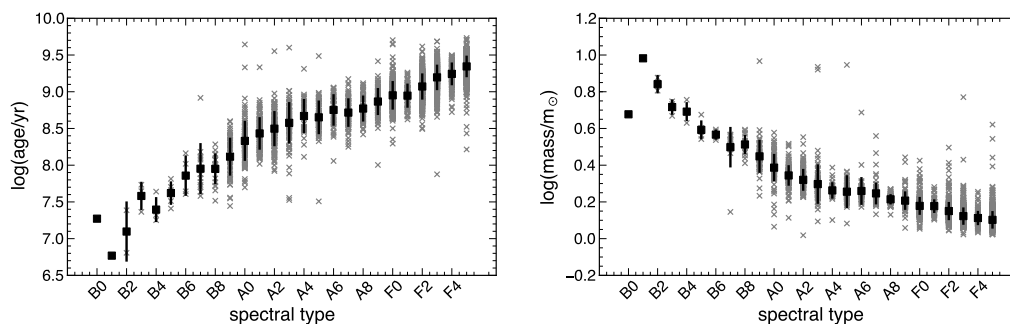


Figure 2.23: Empirical spectral-type-age relation (left) and spectral-type-mass relation (right) for solar neighborhood B0-F5 stars. Grey x's represent individual stars, while the black scatter points represent the mean value in a given spectral type bin and the error bars represent the scatter in a that bin.

Table 2.7: Empirical Spectral-Type Relations for Main Sequence B0-F5 Stars.

Sp. Type	$\langle\tau\rangle$ (Myr)	σ_τ (Myr)	$\langle M\rangle$ (M_\odot)	σ_M (M_\odot)	No. of Stars
B0	19	—	4.75	—	1
B1	6	—	9.59	—	1
B2	15	13	6.96	0.81	2
B3	41	16	5.22	0.50	3
B4	26	12	4.94	0.59	4
B5	44	16	3.94	0.49	5
B6	84	51	3.69	0.23	4
B7	140	209	3.23	0.60	13
B8	99	43	3.28	0.38	18
B9	154	86	2.88	0.88	67
A0	285	437	2.47	0.40	120
A1	313	217	2.23	0.29	132
A2	373	320	2.11	0.30	144
A3	462	412	2.07	0.96	100
A4	540	333	1.84	0.19	37
A5	514	350	1.86	0.81	81
A6	628	265	1.85	0.49	46
A7	574	262	1.78	0.30	79
A8	642	272	1.64	0.11	62
A9	800	339	1.62	0.21	102
F0	994	544	1.52	0.19	324
F1	948	352	1.51	0.13	68
F2	1280	526	1.42	0.19	441
F3	1687	633	1.34	0.23	605
F4	1856	600	1.30	0.12	129
F5	2326	697	1.27	0.18	905

isochrone placement for stars in this mass and age range. Fundamentally, our results rely on the accuracy of both the stellar evolution models and the stellar atmosphere models that we have adopted. Accuracy is further set by the precision of the photometry, the derived atmospheric parameters, the calibration of the isochrones, and the ability to determine whether an individual star is contracting onto the main sequence or expanding off of it. By using isochrones that include both pre-MS and post-MS evolution in a self-consistent manner (Bressan et al., 2012), we can determine pre-ZAMS in addition to post-ZAMS ages for every data point in $(T_{\text{eff}}, \log g)$.

Above, we have described our methodology in detail, including corrections for reddening and rotation, and we have presented quality control tests that demonstrate the precision and accuracy of our ages. In the section we describe several aspects of our analysis of specific interest, including the context of previous estimates of stellar ages for early type stars (§ 2.8.1), how to treat stars with locations apparently below the ZAMS (§ 2.8.2), and discussion of notable individual objects (§ 2.8.3). We will in the future apply our methods to new spectrophotometry.

2.8.1 Methods Previously Employed in Age Determination for Early Type Stars

In this section we place our work on nearby open cluster stars and approximately 3500 nearby field stars in the context of previous age estimation methods for BAF stars.

Song et al. (2001) utilized a method quite similar to ours, employing $uvby\beta$ data from the catalogs of Hauck & Mermilliod (1980), Olsen (1983), and Olsen & Perry (1984), the color grids of Moon & Dworetzky (1985) including a temperature-dependent gravity modification suggested by Napiwotzki et al. (1993), and isochrones from Schaller et al. (1992), to determine the ages of 26 Vega-like stars.

For A-type stars, Vican (2012) determined ages for *Herschel* DEBRIS survey stars by means of isochrone placement in $\log(T_{\text{eff}})$ - $\log(g)$ space using Li & Han (2008) and Pinsonneault et al. (2004) isochrones, and atmospheric parameters from the literature. Rieke et al. (2005) published age estimates for 266 B- & A-type main sequence stars using cluster/moving group membership, isochrone placement in the H-R diagram, and literature ages (mostly coming from earlier application of $uvby\beta$ photometric methods).

Among later type F dwarfs, previous age estimates come primarily from the Geneva-Copenhagen Survey (Casagrande et al., 2011), but their reliability is caveated by the substantially different values published in various iterations of the catalog (Nordström et al., 2004; Holmberg et al., 2007; Holmberg et al., 2009; Casagrande et al., 2011) and the inherent difficulty of isochrone dating these later type dwarfs.

More recently, Nielsen et al. (2013) applied a Bayesian inference approach to the age determination of 70 B- & A-type field stars via M_V vs $B - V$ color-magnitude diagram isochrone placement, assuming a constant star formation rate in the solar neighborhood and a Salpeter IMF. De Rosa et al. (2014) estimated the ages of 316 A-type stars through placement in a M_K vs $V - K$ color-magnitude diagram. Both of these broad-band photometric studies used the theoretical isochrones of Siess et al. (2000).

Considering the above sources of ages, the standard deviation among them suggests scatter among authors of only 15% for some stars up to 145%, with a typical value of 40%. The full range (as opposed to the dispersion) of published ages is 3-300%, with a peak around the 80% level. The value of the age estimates presented here resides in the large sample of early type stars and the uniform methodology applied

to them.

2.8.2 Stars Below the Main Sequence

In Figure 2.21 it may be noted that many stars, particularly those with $\log T_{\text{eff}} \leq 3.9$, are located well below the model isochrones. Using rotation-corrected atmospheric parameters, ~ 540 stars or $\sim 15\%$ of the sample, fall below the theoretical ZAMS.

Prior studies also faced a similarly large fraction of stars falling below the main sequence. Song et al. (2001) arbitrarily assigned an age of 50 Myr to any star lying below the 100 Myr isochrone used in that work. Tetzlaff et al. (2011) arbitrarily shifted stars towards the ZAMS and treated them as ZAMS stars.

Several possibilities might be invoked to explain the large population of stars below the $\log g - \log T_{\text{eff}}$ isochrones: (1) failure of evolutionary models to predict the true width of the MS, (2) spread of metallicities, with the metal-poor MS residing beneath the solar-metallicity MS, (3) overaggressive correction for rotational velocity effects, or (4) systematics involved in surface gravity or luminosity determinations. Of these explanations, we consider (4) the most likely, with (3) also contributing somewhat. Valenti & Fischer (2005) found a 0.4 dex spread in $\log g$ among their main sequence FGK stars along with a 0.1 dex shift downward relative to the expected zero metallicity main sequence.

The Bayesian age estimates for stars below the MS are likely to be unrealistically old, so we compared the ages for these stars with interpolated ages. Using the field star atmospheric parameters and Bressan et al. (2012) models, we performed a 2D linear interpolation with the SciPy routine `griddata`. Stars below the main sequence could be easily identified by selecting objects with $\log(\text{age}/\text{yr})_{\text{Bayes}} - \log(\text{age}/\text{yr})_{\text{interp}} > 1.0$. Notably, for these stars below the MS, the linear interpolation produces more realistic ages than the Bayesian method. A comparison of the Bayesian and interpolated ages for all stars is presented in Figure 2.24. Of note, there is closer agreement between the Bayesian and interpolation methods in regards to estimating masses.

Figure 2.24 further serves to illustrate the difference between the Bayesian ages and the interpolated ages, which scatters over an order magnitude from a 1:1 relationship. A number of stars that fall below the MS and have independently constrained ages are examined in detail in n § 2.8.3. These stars have interpolated ages that are more in line with prior studies, and in light of this, we publish the interpolated ages in addition to the Bayesian ages in the final electronic table.

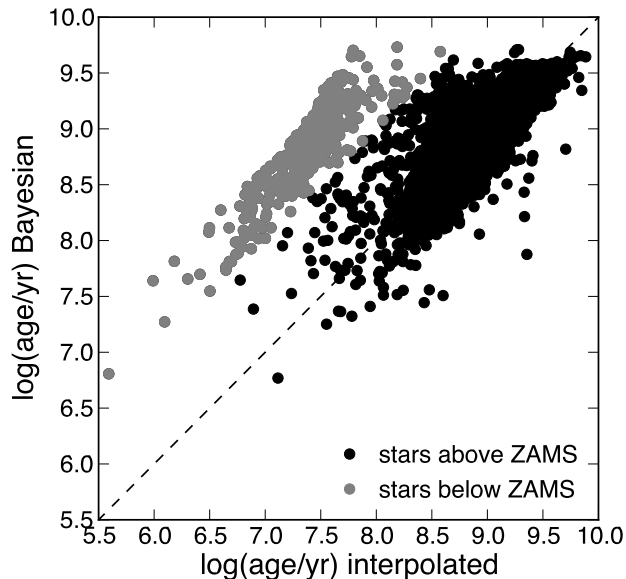


Figure 2.24: Comparison of ages for BAF field stars derived through 2D linear interpolation and Bayesian inference. Grey points represent those stars with $\Delta \log \text{age/yr} > 1$ (in the sense of Bayesian minus interpolated), which coincide with the same stars that reside below the MS.

2.8.3 Stars of Special Interest

In this section we discuss stars of particular interest given that they have either spatially resolved debris disks, detected possibly planetary mass companions, or both. As a final test of the Bressan et al. (2012) evolutionary models and our Bayesian age and mass estimation method, we performed our analysis on these stars, including the Sun.

2.8.3.1 Sun

The atmospheric parameters of our Sun are known with a precision that is orders of magnitude higher than what is obtainable for nearby field stars. One would thus expect the assumed priors to have a negligible influence on the Bayesian age and mass estimates.

The effective temperature of the Sun is calculated to be $T_{\text{eff}} = 5771.8 \pm 0.7$ K from the total solar irradiance (Kopp & Lean, 2011), the solar radius (Haberreiter et al., 2008), the IAU 2009 definition of the AU, and the CODATA 2010 value of the Stefan-Boltzmann constant. The solar surface gravity is calculated to be $\log g = 4.43812 \pm 0.00013$ dex from the IAU 2009 value of GM_{\odot} and the solar radius (Haberreiter et al., 2008). Using these values, our Bayesian analysis yields a median age of 5.209 ± 0.015

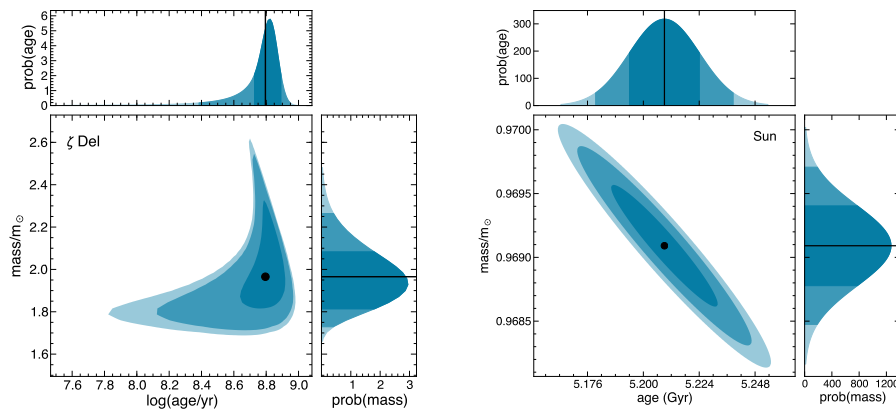


Figure 2.25: 2D joint posterior PDFs in age and mass for an early-type star with typical atmospheric parameter uncertainties (*left*) and the Sun (*right*), for which T_{eff} and $\log g$ are known to high precision. The dark, medium, and light blue shaded regions indicate the 68%, 95%, and 99% confidence contours. Above, 1D marginalized and normalized posterior PDF in age, with the shaded regions representing the same corresponding confidence intervals. Right, the same as above for mass.

Gyr. The Bayesian estimation also yields a mass estimate of $0.9691 \pm 0.0003 M_{\odot}$. Performing a 2D linear interpolation yields a slightly older age of 5.216 Gyr and slightly lower mass of $0.9690 M_{\odot}$. As expected, the precise solar values lead to an elliptical joint posterior PDF in age and mass, and symmetric 1D marginalized PDFs. The difference between the Bayesian age estimate and interpolated age is negligible in this regime of extremely small uncertainties. This test also demonstrates that the Bressan et al. (2012) evolutionary models may introduce a systematic overestimation of ages and underestimation of masses towards cooler temperatures, though because the Sun is substantially different from our sample stars we do not extrapolate this conclusion to our sample.

2.8.3.2 HR 8799

HR 8799 is located near the ZAMS and is metal-poor with $[\text{Fe}/\text{H}] = -0.47 \pm 0.10$ dex (Gray & Kaye, 1999). However, because HR 8799 is a λ Boo peculiar-type star, its photospheric metallicity may not reflect the global stellar metal abundance. The age of HR 8799 is believed to be 30_{-10}^{+20} Myr based on its proposed membership to the Columba association (Zuckerman et al., 2011).

Figure 2.21 shows that HR 8799 lays well below the theoretical ZAMS. This location is well-documented from other spectroscopic and photometric analyses

of the star, and is likely due to a combination of its genuine youth and subsolar metallicity. Consistent with the discussion in §8.2 and as illustrated in Figure 2.24, our Bayesian age analysis leads to an unrealistically old age for the star, with a median age of 956 Myr and a 68% confidence interval of 708-1407 Myr. The Bayesian approach also seems to overestimate the mass, with a median mass of $1.59M_{\odot}$ and 68% confidence interval of $1.49 - 1.68M_{\odot}$. Notably, however, 2D linear interpolation leads to more reasonable age estimates: 26 Myr assuming our newly derived atmospheric parameters ($T_{\text{eff}}=7540$ K, $\log g = 4.43$), or 25 Myr using $T_{\text{eff}}=7430$ K and $\log g = 4.35$ from Gray & Kaye (1999).

2.8.3.3 β Pic

Zuckerman (2001) assigned an age of 12 Myr to β Pic based on its proposed membership to the moving group of the same name. Isochronal age estimates for the star have ranged from the ZAMS age to 300 Myr (Barrado y Navascués et al., 1999). Nielsen et al. (2013) performed a Bayesian analysis concluding a median age of 109 Myr with a 68% confidence interval of 82-134 Myr. Although barely below the ZAMS, β Pic in our own Bayesian analysis has a much older median age of 524 Myr with a 68% confidence interval of 349-917 Myr. Prior authors also have noted that β Pic falls below the ZAMS on a color-magnitude diagram. As was the case for HR 8799, we conclude that our erroneous age for β Pic is due to the dominance of the prior assumption/s in exactly such a scenario.

However, the interpolated age using our atmospheric parameters of $T_{\text{eff}}=8300$ K, $\log g=4.389$, is 20 Myr. Using the Gray et al. (2006) values of $T_{\text{eff}}=8052$ K (within 1σ of our determination), $\log g=4.15$ ($> 1.5\sigma$ away from our surface gravity) we obtain an interpolated age of 308 Myr.

2.8.3.4 κ And

κ Andromedae is another proposed member of the Columba association (Zuckerman et al., 2011). Using the nominal 30 Myr age, Carson et al. (2013) suggested a companion discovered via direct imaging is of planetary mass ($12 - 13M_{\text{Jup}}$). Hinkley et al. (2013) refuted this claim, concluding an age of 220 ± 100 Myr from multiple isochronal analyses in §3.2 of that work. This older age estimate leads to a model-dependent companion mass of $50^{+16}_{-13}M_{\text{Jup}}$. Our Bayesian analysis allows us to nearly rule out a 30 Myr age with a 95% confidence interval of 29-237 Myr. The mean, median, mode, and 68% confidence interval of the 1D marginalized

posterior PDF in age for κ And are 118, 150, 191, and 106-224 Myr, respectively. Notably, κ And has a projected rotational velocity of $v \sin i \sim 160 \text{ km s}^{-1}$ (Glebocki & Gnacinski, 2005), and we find its rotation corrected atmospheric parameters ($T_{\text{eff}} = 11903 \pm 405 \text{ K}$, $\log g = 4.35 \pm 0.14 \text{ dex}$) produce an interpolated age of 16 Myr. Using uncorrected atmospheric parameters ($T_{\text{eff}} = 11263 \pm 383 \text{ K}$, $\log g = 4.26 \pm 0.14 \text{ dex}$) leads to an interpolated age of 25 Myr.

2.8.3.5 ζ Delphini

De Rosa et al. (2014) recently published the discovery of a wide companion to ζ Delphini (HIP 101589). Those authors estimated the age of the system as 525 ± 125 Myr, from the star's positions on a color-magnitude and a temperature-luminosity diagram, leading to a model-dependent companion mass of $50 \pm 15 M_{\text{Jup}}$. Our method yields a mean age of 552 Myr, with 68% and 95% confidence intervals of 531-772 Myr, and 237-866 Myr, respectively. Our revised age is in agreement with the previous estimate of De Rosa et al. (2014), although favoring the interpretation of an older system and thus more massive companion. The interpolated ages for ζ Del are somewhat older: 612 Myr for the rotation-corrected atmospheric parameters $T_{\text{eff}}=8305 \text{ K}$, $\log g=3.689$, or 649 Myr for the uncorrected parameters $T_{\text{eff}}=8639 \text{ K}$, $\log g=3.766$. Note, in this case moderate rotation ($v \sin i = 99.2 \text{ km s}^{-1}$) leads to a discrepancy of only $\approx 6\%$ in the derived ages.

2.8.3.6 49 Ceti

49 Ceti does not have a known companion at present, but does possess a resolved molecular gas disk (Hughes et al., 2008). The star is a proposed member of the 40 Myr Argus association, which would require cometary collisions to explain the gaseous disk that should have dissipated by ~ 10 Myr due to radiation pressure (Zuckerman et al., 2012). With a mean rotational velocity of $\sim 190 \text{ km s}^{-1}$ (Glebocki & Gnacinski, 2005), and evidence that the star is highly inclined to our line of sight, rotational effects on photometric H-R diagram placement are prominent. Our $uvby\beta$ atmospheric parameters for 49 Ceti are $T_{\text{eff}} = 10007 \pm 340 \text{ K}$, $\log g = 4.37 \pm 0.14 \text{ dex}$, after rotational effects were accounted for. These parameters place the star essentially on the ZAMS, with an interpolated age of 9 Myr, and calling into question the cometary genesis of its gaseous disk. However, the uncorrected atmospheric parameters ($T_{\text{eff}} = 9182 \pm 309 \text{ K}$, $\log g = 4.22 \pm 0.14 \text{ dex}$) are more consistent with the A1 spectral type and produces an interpolated age of 57 Myr, which seems to

support the cometary collision hypothesis. This case illustrates the importance of high-precision atmospheric parameters.

2.9 Conclusions

In the absence of finely calibrated empirical age indicators, such as the rotation-activity-age relation for solar-type stars (e.g. Mamajek & Hillenbrand, 2008), ages for early spectral type stars typically have come from open cluster and moving group membership, or through association with a late-type companion that can be age-dated through one of the applicable empirical methods. Because of their rapid evolution, early type stars are amenable to age dating via isochrones. In this paper we have investigated the use of Strömngren photometric techniques for estimating stellar atmospheric parameters, which are then compared to isochrones from modern stellar evolution models.

Bayesian inference is a particularly useful tool in the estimation of parameters such as age and mass from evolutionary models for large samples that span considerable ranges in temperature, luminosity, mass, and age. The Bayesian approach produces unbiased ages relative to a straightforward interpolation among isochrones which leads to age estimates that are biased towards older ages. However, as noted earlier, stars located beyond the range of the theory (below the theoretical ZAMS in our case) are assigned unreasonably old ages with the Bayesian method. This presumably is due to the clustering of isochrones and the dominance of the prior in inference scenarios in which the prior probability is changing quickly relative to the magnitude of the uncertainty in the atmospheric parameters. Linear interpolation for stars apparently below the MS may produce more reasonable age estimates.

The most important parameter for determining precise stellar ages near the ZAMS is the luminosity or surface gravity indicator. Effective temperatures, or observational proxies for temperature, are currently estimated with suitable precision. However, $\log g$, luminosity, or absolute magnitude (requiring a precise distance as well), are not currently estimated with the precision needed to meaningfully constrain the ages of field stars near the ZAMS. This effect is particularly pronounced for lower temperature stars where, for a given shift in $\log g$, the inferred age can change by many orders of magnitude. Our open cluster tests indicated that the age uncertainties due to the choice of evolutionary models are not significant compared to those introduced by the uncertainties in the surface gravities.

We have derived new atmospheric parameters (taking stellar rotation into account)

and model-dependent ages and masses for 3493 BAF stars within 100 pc of the Sun. Our method of atmospheric parameter determination was calibrated and validated to stars with fundamentally determined atmospheric parameters. We further tested and validated our method of age estimation using open clusters with well-known ages. In determining the uncertainties in all of our newly derived parameters we conservatively account for the effects of systematics, metallicity, numerical precision, reddening, photometric errors, and uncertainties in $v \sin i$ as well as unknown rotational velocities.

Field star ages must be considered with caution. At minimum, our homogeneously derived set of stellar ages provides a relative youth ordering. For those stars below the MS we encourage the use of interpolated ages rather than Bayesian ages, unless more precise atmospheric parameters become available. Using the new set of ages, we presented an empirical mass-age relation for solar neighborhood B0-F5 stars. We also presented empirical relations between spectral type and age/mass and we discussed ages in detail for several famous low mass companion and/or debris disk objects. An anticipated use of our catalog is in the prioritization of targets for direct imaging of brown dwarf and planetary mass companions. David & Hillenbrand (2015b, *in preparation*) will explore how ages derived using this methodology can be applied to investigations such as debris disk evolution.

The authors wish to thank John Stauffer for his helpful input on sources of $uvby\beta$ data for open clusters and Timothy Brandt for helpful discussions during the proof stage of this work regarding the open cluster analysis, resulting in the appendix material concerning logarithmic versus linear approaches and a modified version of Figure 17. This material is based upon work supported in 2014 and 2015 by the National Science Foundation Graduate Research Fellowship under Grant No. DGE 1144469. This research has made use of the WEBDA database, operated at the Institute for Astronomy of the University of Vienna, as well as the SIMBAD database and VizieR catalog access tool, operated at CDS, Strasbourg, France.

APPENDIX

2.A Metallicity Effects

We do not account explicitly for metallicity in this study, having assumed solar values in both our atmospheric models and our evolutionary grids. Our analysis in the T_{eff} and $\log g$ calibrations found that for stars with fundamentally determined atmospheric parameters and available $[\text{Fe}/\text{H}]$ measurements, the accuracy with which we can determine atmospheric parameters using $uvby\beta$ photometry does not vary systematically with metallicity.

The effects of different metallicity assumptions on the Strömngren index atmospheric grids is illustrated in Figure 2.26. Moving from the atmospheric grid to the evolutionary grid, Figure 17 of Valenti & Fischer (2005) illustrates that for the coolest stars under consideration here, which were the focus of their study, variation of metallicity from +0.5 to -0.5 dex in $[\text{Fe}/\text{H}]$ corresponds to a +0.1 to -0.1 dex shift in $\log g$ of an evolutionary isochrone. Among hotter stars, Figure 2.26 shows that metallicity uncertainty affects temperatures only minorly, and gravities not at all or minimally.

We similarly calculated the effect on atmospheric parameter determination when allowing the model color grids to vary from +0.5 to -0.5 dex in $[\text{M}/\text{H}]$, which notably represent the extremes of the metallicity range included in our sample (less than 1% of stars considered here have $|[\text{Fe}/\text{H}]| > 0.5$ dex). Figures 2.27 & 2.28 examine in detail the effects of metallicity on T_{eff} , $\log g$ determinations in the relevant $uvby\beta$ planes. In summary, T_{eff} variations of up to $\sim 1\%$ in the $(b - y) - c_1$ plane, $\sim 2\%$ in the $a_0 - r^*$ plane, and 6% in the $c_1 - \beta$ plane are possible with shifts of ± 0.5 dex in $[\text{M}/\text{H}]$. Notably, however, T_{eff} variations above the 2% level are only expected in the $c_1 - \beta$ plane for stars hotter than ~ 17000 K, or roughly spectral type B4, of which there are very few in our sample. Similarly metallicity shifts of ± 0.5 dex can cause variations of ~ 0.1 dex in $\log g$ in the $(b - y) - c_1$ and $c_1 - \beta$ planes, while the same variation in the $a_0 - r^*$ plane produces surface gravity shifts closer to ~ 0.05 dex.

By contrast, metallicity effects are more prominent in color-magnitude techniques. Recently, Nielsen et al. (2013) executed a Bayesian analysis of the locations in the M_V vs $B - V$ diagram of Gemini/NICI targets to derive their ages including confidence contours for the stellar masses, ages, and metallicities. The work demonstrates

correlation in this particular color-magnitude diagram of increasing mass and decreasing age with higher metallicity. Metal poor stars will have erroneously young ages attributed to them when solar metallicity is assumed.

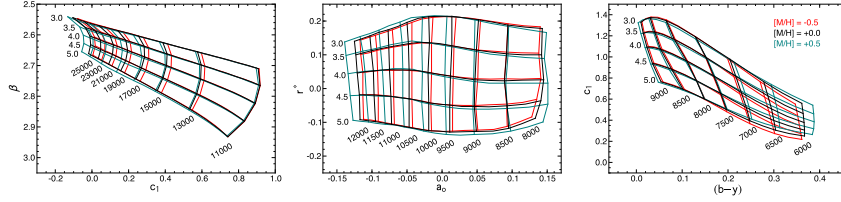


Figure 2.26: Comparison of ATLAS9 color grids for different metallicities.

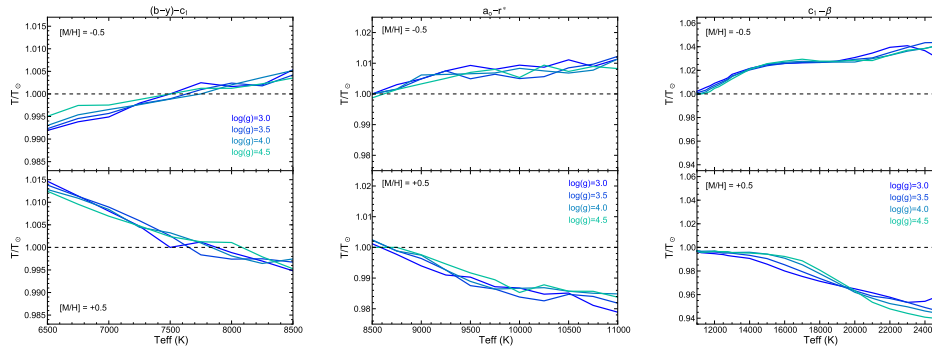


Figure 2.27: The effect of metallicity on $uvby\beta$ determinations of temperature, as predicted by model grids of Castelli & Kurucz (2006) and Castelli & Kurucz (2004). In the left-most figure, for given values of T_{eff} , or $(b-y)$, the ratio of the temperature given by the grid of metallicity $[M/H]=-0.5$ to the solar metallicity grid is depicted in the top panel. The bottom panel shows the ratio of the temperature given by a grid of metallicity $[M/H]=+0.5$ to the temperature given by the solar metallicity grid. In the temperature range of interest ($\approx 6500\text{K}-8500\text{K}$, or spectral types F5-A4), a shift of 0.5 dex in $[M/H]$ can produce variations up to $\sim 1\%$ in T_{eff} , with the smallest discrepancies occurring at approximately the F0-A9 boundary. The middle figure is analogous to the left figure, for the $a_0 - r^*$ grids which are used for stars between $\approx 8500\text{K}-11000\text{K}$ (A3-B9). In this regime, shifts of 0.5 dex in metallicity can produce variations up to $\sim 2\%$ in temperature. Finally, for the hottest stars ($T_{\text{eff}} > 11000\text{K}$, spectral types B9 and earlier), a 0.5 dex shift in metallicity can produce variations up to $\sim 6\%$ in effective temperature.

2.B Confidence Intervals

All confidence intervals in age and mass quoted in this work are the bounds of the Highest Posterior Density (HPD) Region. For a given posterior probability density, $p(\theta|x)$, the $100(1 - \alpha)\%$ HPD region is defined as the subset, C , of θ values:

$$C = \{\theta : p(\theta|x) \geq p^*\}, \quad (2.30)$$

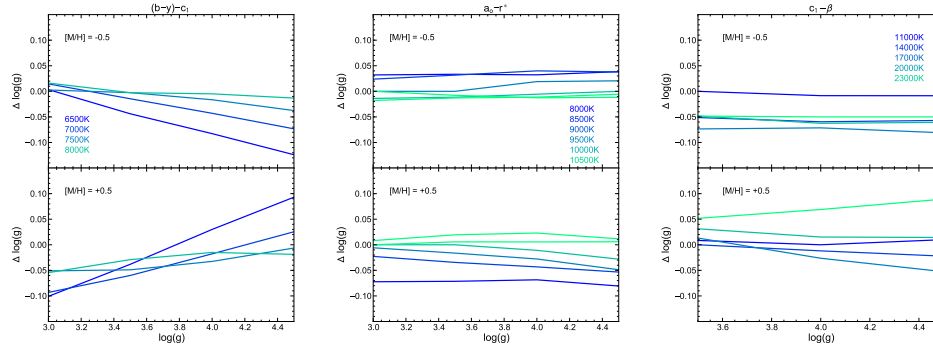


Figure 2.28: The effect of metallicity on $uvby\beta$ determinations of surface gravity, as predicted by model grids of Castelli & Kurucz (2006) and Castelli & Kurucz (2004). In the left-most figure, for given values of $\log g$, or c_1 , the ratio of the temperature given by the grid of metallicity $[M/H]=-0.5$ to the solar metallicity grid is depicted in the top panel. The bottom panel shows the ratio of the temperature given by a grid of metallicity $[M/H]=+0.5$ to the temperature given by the solar metallicity grid. In the temperature range of interest ($\approx 6500\text{K}-8500\text{K}$, or spectral types F5-A4), a shift of 0.5 dex in $[M/H]$ can produce variations up to ~ 0.1 dex in $\log g$. The middle figure is analogous to the left figure, for the $a_0 - r^*$ grids which are used for stars between $\approx 8500\text{K}-11000\text{K}$ (A3-B9). In this regime, the gravity indicator r^* is particularly insensitive to metallicity, with shifts of 0.5 dex in metallicity producing variations of only ~ 0.05 dex or less in $\log g$. Finally, for the hottest stars ($T_{\text{eff}} > 11000$ K, spectral types B9 and earlier), a 0.5 dex shift in metallicity can produce variations up to ~ 0.1 dex in $\log g$.

where p^* is the largest number such that

$$\int_{\theta: p(\theta|x) \geq p^*} p(\theta|x) d\theta = 1 - \alpha. \quad (2.31)$$

In other words, the HPD region is the set of most probable values (corresponding to the smallest range in θ) that encloses $100(1 - \alpha)\%$ of the posterior mass. The HPD method is particularly suited for finding confidence intervals of skewed probability distributions, such as the stellar age posteriors studied in this work. To find the highest posterior density (HPD) region numerically, a function is created that iteratively integrates a normalized posterior PDF above a test value of p^* while the area/volume under the PDF is less than the desired confidence interval.

2.C Open Cluster Tables

Table 2.8: IC 2602 members dereddened $uvby\beta$ photometry and atmospheric parameters.

Star	Sp. Type	$(b - y)_0$ (mag)	m_0 (mag)	c_0 (mag)	β (mag)	T_{eff} (K)	$\log g$ (dex)	$v \sin i$ (km s^{-1})
HD 91711	B8 V	-0.062	0.146	0.457	2.745	14687 ± 235	4.467 ± 0.113	153
HD 91839	A1 V	0.025	0.178	1.033	2.904	9509 ± 152	4.188 ± 0.091	146
HD 91896	B7 III	-0.081	0.093	0.346	2.660	16427 ± 263	3.782 ± 0.113	155
HD 91906	A0 V	0.016	0.177	1.005	2.889	9799 ± 157	4.146 ± 0.113	149
HD 92275	B8 III/IV	-0.056	0.125	0.562	2.709	13775 ± 220	3.852 ± 0.113	153
HD 92467	B95III	-0.026	0.168	0.833	2.851	11178 ± 179	4.423 ± 0.113	110
HD 92478	A0 V	0.010	0.183	0.978	2.925	9586 ± 153	4.431 ± 0.091	60
HD 92535	A5 V n	0.104	0.194	0.884	2.838	8057 ± 129	4.344 ± 0.145	140
HD 92536	B8 V	-0.043	0.131	0.705	2.795	13183 ± 211	4.423 ± 0.113	250
HD 92568	A M	0.209	0.237	0.625	2.748	7113 ± 114	4.341 ± 0.145	126
HD 92664	B8 III P	-0.083	0.118	0.386	2.702	15434 ± 247	4.145 ± 0.113	65
HD 92715	B9 V nn	-0.027	0.136	0.882	2.836	12430 ± 199	4.362 ± 0.113	290
HD 92783	B85V nn	-0.033	0.124	0.835	2.804	12278 ± 196	4.130 ± 0.113	230
HD 92837	A0 IV nn	-0.007	0.160	0.953	2.873	10957 ± 175	4.322 ± 0.113	220
HD 92896	A3 IV	0.114	0.193	0.838	2.831	8010 ± 128	4.425 ± 0.145	139
HD 92938	B3 V n	-0.075	0.105	0.384	2.690	15677 ± 251	4.015 ± 0.113	120
HD 92966	B95V nn	-0.019	0.158	0.930	2.878	11372 ± 182	4.445 ± 0.113	225
HD 92989	A05Va	0.008	0.180	0.982	2.925	9979 ± 160	4.480 ± 0.091	148
HD 93098	A1 V s	0.017	0.180	0.993	2.915	9688 ± 155	4.385 ± 0.091	135
HD 93194	B3 V nn	-0.078	0.105	0.357	2.668	17455 ± 279	4.015 ± 0.113	310
HD 93424	A3 Va	0.060	0.197	0.950	2.890	8852 ± 142	4.247 ± 0.113	95
HD 93517	A1 V	0.052	0.196	0.976	2.919	9613 ± 154	4.510 ± 0.091	220
HD 93540	B6 V nn	-0.065	0.116	0.476	2.722	15753 ± 252	4.308 ± 0.113	305
HD 93549	B6 V	-0.066	0.123	0.454	2.729	15579 ± 249	4.422 ± 0.113	265
HD 93607	B25V n	-0.084	0.102	0.292	2.675	17407 ± 279	4.098 ± 0.113	160
HD 93648	A0 V n	0.041	0.188	1.025	2.890	9672 ± 155	4.157 ± 0.091	215
HD 93714	B2 IV-V n	-0.092	0.100	0.201	2.647	18927 ± 303	3.979 ± 0.113	40
HD 93738	A0 V nn	-0.027	0.158	0.842	2.817	12970 ± 208	4.336 ± 0.113	315
HD 93874	A3 IV	0.071	0.203	0.947	2.896	8831 ± 141	4.367 ± 0.091	142
HD 94066	B5 V n	-0.068	0.117	0.439	2.680	15096 ± 242	3.792 ± 0.113	154
HD 94174	A0 V	0.046	0.193	0.946	2.907	9305 ± 149	4.391 ± 0.113	149

Table 2.9: α Persei members dereddened $uvby\beta$ photometry and atmospheric parameters.

Star	Sp. Type	$(b - y)_0$ (mag)	m_0 (mag)	c_0 (mag)	β (mag)	T_{eff} (K)	$\log g$ (dex)	$v \sin i$ (km s^{-1})
BD+49 868	F5 V	0.261	0.165	0.459	2.683	6693 \pm 107	4.455 \pm 0.145	20
HD 19767	F0 V N	0.176	0.178	0.756	2.765	7368 \pm 118	4.174 \pm 0.145	140
HD 19805	A0 Va	-0.000	0.161	0.931	2.887	10073 \pm 161	4.344 \pm 0.113	20
HD 19893	B9 V	-0.031	0.131	0.850	2.807	12614 \pm 202	4.176 \pm 0.113	280
HD 19954	A9 IV	0.150	0.200	0.794	2.792	7632 \pm 122	4.297 \pm 0.145	85
HD 20135	A0 P	-0.011	0.186	0.970	2.848	10051 \pm 161	3.998 \pm 0.113	35
BD+49 889	F5 V	0.292	0.156	0.418	2.656	6430 \pm 103	4.352 \pm 0.145	65
BD+49 896	F4 V	0.261	0.168	0.472	2.686	6686 \pm 107	4.410 \pm 0.145	30
HD 20365	B3 V	-0.079	0.103	0.346	2.681	16367 \pm 262	4.025 \pm 0.113	145
HD 20391	A1 Va n	0.026	0.179	1.006	2.901	10415 \pm 167	4.386 \pm 0.091	260
HD 20487	A0 V N	-0.016	0.151	0.976	2.856	11659 \pm 187	4.198 \pm 0.113	280
BD+47 808	F1 IV N	0.183	0.179	0.759	2.763	7281 \pm 116	4.062 \pm 0.145	180
BD+48 892	F3 IV-V	0.246	0.167	0.524	2.696	6800 \pm 109	4.359 \pm 0.145	20
BD+48 894	F0 IV	0.174	0.202	0.734	2.770	7416 \pm 119	4.284 \pm 0.145	75
HD 20809	B5 V	-0.074	0.109	0.395	2.696	15934 \pm 255	4.097 \pm 0.113	200
HD 20842	A0 Va	-0.005	0.157	0.950	2.886	10258 \pm 164	4.325 \pm 0.113	85
HD 20863	B9 V	-0.034	0.134	0.810	2.813	12154 \pm 194	4.267 \pm 0.113	200
BD+49 914	F5 V	0.281	0.170	0.431	2.664	6520 \pm 104	4.395 \pm 0.145	120
HD 20919	A8 V	0.168	0.191	0.757	2.775	7463 \pm 119	4.259 \pm 0.145	50
BD+49 918	F1 V N	0.186	0.183	0.770	2.755	7235 \pm 116	3.977 \pm 0.145	175
HD 20931	A1 Va	0.018	0.174	0.979	2.911	9588 \pm 153	4.342 \pm 0.113	85
BD+47 816	F4 V	0.271	0.155	0.452	2.672	6600 \pm 106	4.399 \pm 0.145	28
HD 20961	B9.5V	-0.019	0.163	0.920	2.875	10537 \pm 169	4.344 \pm 0.113	25
BD+46 745	F4 V	0.274	0.169	0.462	2.674	6566 \pm 105	4.332 \pm 0.145	160
HD 20969	A8 V	0.186	0.192	0.715	2.758	7291 \pm 117	4.239 \pm 0.145	20
HD 20986	A3 V N	0.046	0.190	1.004	2.896	9584 \pm 153	4.243 \pm 0.091	210
HD 21005	A5 V N	0.074	0.189	0.987	2.862	8266 \pm 132	4.197 \pm 0.145	250
HD 21091	B9.5IV nn	-0.019	0.152	0.938	2.856	12477 \pm 200	4.416 \pm 0.113	340
HD 21092	A5 V	0.054	0.218	0.938	2.893	8775 \pm 140	4.311 \pm 0.091	75
TYC 3320-1715-1	F4 V	0.281	0.153	0.469	2.663	6495 \pm 104	4.220 \pm 0.145	110
HD 21152	B9 V	-0.018	0.158	0.943	2.868	11306 \pm 181	4.353 \pm 0.113	225
HD 232793	F5 V	0.311	0.172	0.377	2.645	6274 \pm 100	4.362 \pm 0.145	93
HD 21181	B8.5V N	-0.038	0.122	0.784	2.766	13726 \pm 220	4.119 \pm 0.113	345
HD 21239	A3 V N	0.045	0.190	0.997	2.910	9182 \pm 147	4.320 \pm 0.091	145
HD 21278	B5 V	-0.073	0.111	0.398	2.705	15274 \pm 244	4.152 \pm 0.113	75
HD 21302	A1 V N	0.022	0.177	0.989	2.888	10269 \pm 164	4.301 \pm 0.091	230
BD+48 923	F4 V	0.270	0.153	0.464	2.673	6603 \pm 106	4.362 \pm 0.145	20
HD 21345	A5 V N	0.051	0.208	0.969	2.893	9435 \pm 151	4.324 \pm 0.091	200
HD 21398	B9 V	-0.030	0.145	0.825	2.837	11615 \pm 186	4.372 \pm 0.113	135
HD 21428	B3 V	-0.077	0.105	0.363	2.686	16421 \pm 263	4.076 \pm 0.113	200
HD 21481	A0 V N	-0.013	0.164	0.993	2.858	11187 \pm 179	4.141 \pm 0.113	250
HD 21527	A7 IV	0.093	0.231	0.855	2.856	8231 \pm 132	4.486 \pm 0.145	80
HD 21551	B8 V	-0.048	0.118	0.673	2.746	14869 \pm 238	4.220 \pm 0.113	380
HD 21553	A6 V N	0.072	0.206	0.921	2.872	8381 \pm 134	4.414 \pm 0.145	150
HD 21619	A6 V	0.052	0.221	0.935	2.894	8843 \pm 141	4.329 \pm 0.091	90
BD+49 957	F3 V	0.258	0.168	0.500	2.687	6699 \pm 107	4.334 \pm 0.145	56
HD 21641	B8.5V	-0.042	0.131	0.721	2.747	12914 \pm 207	3.929 \pm 0.113	215
BD+49 958	F1 V	0.198	0.188	0.732	2.739	7137 \pm 114	3.989 \pm 0.145	155
HD 21672	B8 V	-0.050	0.119	0.649	2.747	13473 \pm 216	4.071 \pm 0.113	225
BD+48 944	A5 V	0.063	0.220	0.931	2.886	8799 \pm 141	4.305 \pm 0.091	120
HD 21931	B9 V	-0.029	0.147	0.835	2.829	11998 \pm 192	4.343 \pm 0.113	205

Table 2.10: Pleiades members dereddened $uvby\beta$ photometry and atmospheric parameters.

HD	Sp. Type	$(b-y)_0$ (mag)	m_0 (mag)	c_0 (mag)	β (mag)	T_{eff} (K)	$\log g$ (dex)	$v \sin i$ (km s $^{-1}$)
HD 23157	A9 V	0.168	0.190	0.725	2.778	7463 \pm 121	4.369 \pm 0.145	100
HD 23156	A7 V	0.111	0.215	0.815	2.837	8046 \pm 130	4.498 \pm 0.145	70
HD 23247	F3 V	0.237	0.174	0.527	2.704	6863 \pm 111	4.424 \pm 0.145	40
HD 23246	A8 V	0.170	0.184	0.758	2.773	7409 \pm 120	4.234 \pm 0.145	200
HD 23288	B7 V	-0.051	0.120	0.636	2.747	13953 \pm 226	4.151 \pm 0.113	280
HD 23302	B6 III	-0.054	0.098	0.638	2.690	13308 \pm 216	3.478 \pm 0.113	205
HD 23289	F3 V	0.244	0.164	0.521	2.699	6796 \pm 110	4.387 \pm 0.145	40
HD 23326	F4 V	0.250	0.164	0.514	2.691	6741 \pm 109	4.358 \pm 0.145	40
HD 23324	B8 V	-0.052	0.116	0.634	2.747	13748 \pm 223	4.126 \pm 0.113	255
HD 23338	B6 IV	-0.061	0.104	0.553	2.702	13696 \pm 222	3.772 \pm 0.113	130
HD 23351	F3 V	0.249	0.176	0.507	2.695	6755 \pm 109	4.391 \pm 0.145	80
HD 23361	A25Va n	0.069	0.201	0.959	2.872	8356 \pm 135	4.309 \pm 0.145	235
HD 23375	A9 V	0.180	0.187	0.710	2.765	7336 \pm 119	4.318 \pm 0.145	75
HD 23410	A0 Va	0.004	0.164	0.975	2.899	10442 \pm 169	4.382 \pm 0.113	200
HD 23409	A3 V	0.070	0.202	0.980	2.892	8903 \pm 144	4.270 \pm 0.091	170
HD 23432	B8 V	-0.039	0.127	0.758	2.793	12695 \pm 206	4.250 \pm 0.113	235
HD 23441	B9 V N	-0.029	0.135	0.858	2.822	11817 \pm 191	4.209 \pm 0.113	200
HD 23479	A9 V	0.188	0.166	0.716	2.755	7239 \pm 117	4.212 \pm 0.145	150
HD 23489	A2 V	0.033	0.183	1.012	2.907	9170 \pm 149	4.239 \pm 0.091	110
HD 23512	A2 V	0.057	0.196	1.035	2.909	8852 \pm 143	4.214 \pm 0.091	145
HD 23511	F5 V	0.279	0.174	0.412	2.674	6521 \pm 106	4.477 \pm 0.145	28
HD 23514	F5 V	0.285	0.179	0.443	2.668	6450 \pm 104	4.307 \pm 0.145	40
HD 23513	F5 V	0.278	0.170	0.423	2.673	6528 \pm 106	4.447 \pm 0.145	30
HD 23568	B95Va n	-0.024	0.139	0.914	2.847	11731 \pm 190	4.301 \pm 0.113	240
HD 23567	F0 V	0.159	0.196	0.735	2.788	7560 \pm 122	4.407 \pm 0.145	50
HD 23585	F0 V	0.168	0.185	0.713	2.780	7472 \pm 121	4.405 \pm 0.145	100
HD 23608	F5 V	0.278	0.177	0.482	2.673	6492 \pm 105	4.185 \pm 0.145	110
HD 23607	F0 V	0.108	0.203	0.814	2.841	8085 \pm 131	4.534 \pm 0.145	12
HD 23629	A0 V	-0.001	0.163	0.986	2.899	10340 \pm 168	4.342 \pm 0.113	170
HD 23632	A0 Va	0.006	0.167	1.009	2.899	10461 \pm 169	4.312 \pm 0.113	225
HD 23628	A4 V	0.090	0.189	0.904	2.853	8163 \pm 132	4.381 \pm 0.145	215
HD 23643	A35V	0.079	0.194	0.943	2.862	8258 \pm 134	4.301 \pm 0.145	185
HD 23733	A9 V	0.207	0.177	0.672	2.736	7066 \pm 114	4.174 \pm 0.145	180
HD 23732	F5 V	0.258	0.172	0.460	2.688	6695 \pm 108	4.473 \pm 0.145	50
HD 23753	B8 V N	-0.046	0.113	0.712	2.736	13096 \pm 212	3.859 \pm 0.113	240
HD 23791	A9 V+	0.139	0.214	0.758	2.811	7776 \pm 126	4.480 \pm 0.145	85
HD 23850	B8 III	-0.048	0.102	0.701	2.695	13446 \pm 218	3.483 \pm 0.113	280
HD 23863	A8 V	0.116	0.201	0.857	2.826	7926 \pm 128	4.354 \pm 0.145	160
HD 23872	A1 Va n	0.032	0.182	1.013	2.894	10028 \pm 162	4.247 \pm 0.091	240
HD 23873	B95Va	-0.023	0.143	0.907	2.852	10897 \pm 177	4.255 \pm 0.113	90
HD 23886	A4 V	0.068	0.214	0.915	2.880	8974 \pm 145	4.343 \pm 0.091	165
HD 23912	F3 V	0.274	0.154	0.481	2.671	6531 \pm 106	4.242 \pm 0.145	130
HD 23924	A7 V	0.100	0.223	0.852	2.852	8121 \pm 132	4.460 \pm 0.145	100
HD 23923	B85V N	-0.033	0.124	0.839	2.794	12911 \pm 209	4.159 \pm 0.113	310
HD 23948	A1 Va	0.033	0.191	0.984	2.905	9237 \pm 150	4.307 \pm 0.091	120
HD 24076	A2 V	0.008	0.168	0.923	2.867	10196 \pm 165	4.298 \pm 0.091	155
HD 24132	F2 V	0.245	0.149	0.597	2.692	6744 \pm 109	4.182 \pm 0.145	230

Table 2.11: Hyades members dereddened $uvby\beta$ photometry and atmospheric parameters.

HD	Sp. Type	$(b - y)_0$ (mag)	m_0 (mag)	c_0 (mag)	β (mag)	T_{eff} (K)	$\log g$ (dex)	$v \sin i$ (km s ⁻¹)
HD 26015	F3 V	0.252	0.174	0.537	2.693	6732 ± 109	4.244 ± 0.145	25
HD 26462	F1 IV-V	0.230	0.165	0.596	2.710	6916 ± 112	4.291 ± 0.145	30
HD 26737	F5 V	0.274	0.168	0.477	2.674	6558 ± 106	4.263 ± 0.145	60
HD 26911	F3 V	0.258	0.176	0.525	2.690	6682 ± 108	4.228 ± 0.145	30
HD 27176	A7 m	0.172	0.187	0.785	2.767	7380 ± 120	4.087 ± 0.145	125
HD 27397	F0 IV	0.171	0.194	0.770	2.766	7410 ± 120	4.173 ± 0.145	100
HD 27429	F2 VN	0.240	0.171	0.588	2.693	6828 ± 111	4.270 ± 0.145	150
HD 27459	F0 IV	0.129	0.204	0.871	2.812	7782 ± 126	4.198 ± 0.145	35
HD 27524	F5 V	0.285	0.161	0.461	2.656	6461 ± 105	4.213 ± 0.145	110
HD 27561	F4 V	0.270	0.162	0.482	2.677	6594 ± 107	4.284 ± 0.145	30
HD 27628	A2 M	0.133	0.225	0.707	2.756	7944 ± 129	4.743 ± 0.145	30
HD 27819	A7 IV	0.080	0.209	0.982	2.857	8203 ± 133	4.170 ± 0.145	35
HD 27901	F4 V N	0.238	0.178	0.597	2.704	6837 ± 111	4.233 ± 0.145	110
HD 27934	A5 IV-V	0.064	0.201	1.053	2.867	8506 ± 138	3.884 ± 0.091	90
HD 27946	A7 V	0.149	0.192	0.840	2.783	7584 ± 123	4.112 ± 0.145	210
HD 27962	A3 V	0.020	0.193	1.046	2.889	9123 ± 148	4.004 ± 0.091	30
HD 28024	A9 IV- N	0.165	0.175	0.947	2.753	7279 ± 118	3.503 ± 0.145	215
HD 28226	A M	0.164	0.213	0.771	2.775	7493 ± 121	4.248 ± 0.145	130
HD 28294	F0 IV	0.198	0.173	0.694	2.745	7174 ± 116	4.194 ± 0.145	135
HD 28319	A7 III	0.097	0.198	1.011	2.831	7945 ± 129	3.930 ± 0.145	130
HD 28355	A7 m	0.112	0.226	0.908	2.832	7930 ± 128	4.207 ± 0.145	140
HD 28485	F0 V+ N	0.200	0.192	0.717	2.740	7129 ± 115	4.035 ± 0.145	150
HD 28527	A5 m	0.085	0.218	0.964	2.856	8180 ± 133	4.194 ± 0.145	100
HD 28546	A7 m	0.142	0.234	0.796	2.809	7726 ± 125	4.354 ± 0.145	30
HD 28556	F0 IV	0.147	0.202	0.814	2.795	7645 ± 124	4.244 ± 0.145	140
HD 28568	F5 V	0.274	0.168	0.466	2.676	6564 ± 106	4.315 ± 0.145	55
HD 28677	F2 V	0.214	0.176	0.654	2.725	7032 ± 114	4.161 ± 0.145	100

Table 2.11 Continued: Hyades members dereddened $uvby\beta$ photometry and atmospheric parameters.

HD 28911	F5 V	0.283	0.163	0.459	2.663	6481 ± 105	4.249 ± 0.145	40
HD 28910	A9 V	0.144	0.200	0.830	2.796	7659 ± 124	4.213 ± 0.145	95
HD 29169	F2 V	0.236	0.183	0.567	2.708	6880 ± 111	4.321 ± 0.145	80
HD 29225	F5 V	0.276	0.171	0.461	2.675	6547 ± 106	4.316 ± 0.145	45
HD 29375	F0 IV-V	0.187	0.187	0.740	2.754	7257 ± 118	4.106 ± 0.145	155
HD 29388	A5 IV-V	0.062	0.199	1.047	2.870	8645 ± 140	3.927 ± 0.091	115
HD 29499	A M	0.140	0.231	0.826	2.810	7713 ± 125	4.266 ± 0.145	70
HD 29488	A5 IV-V	0.080	0.196	1.017	2.852	8127 ± 132	4.025 ± 0.145	160
HD 30034	A9 IV-	0.150	0.195	0.813	2.791	7610 ± 123	4.218 ± 0.145	75
HD 30210	A5 m	0.091	0.252	0.955	2.845	8126 ± 132	4.181 ± 0.145	30
HD 30780	A9 V+	0.122	0.207	0.900	2.813	7823 ± 127	4.141 ± 0.145	155
HD 31845	F5 V	0.294	0.165	0.439	2.658	6396 ± 104	4.229 ± 0.145	25
HD 32301	A7 IV	0.079	0.202	1.034	2.847	8116 ± 131	3.975 ± 0.145	115
HD 33254	A7 m	0.132	0.251	0.835	2.824	7797 ± 126	4.306 ± 0.145	30
HD 33204	A7 m	0.149	0.245	0.803	2.796	7634 ± 124	4.270 ± 0.145	30
HD 25202	F4 V	0.206	0.172	0.695	2.724	7082 ± 115	4.064 ± 0.145	160
HD 28052	F0 IV-V N	0.153	0.183	0.934	2.767	7431 ± 120	3.733 ± 0.145	170
HD 18404	F5 IV	0.269	0.169	0.481	2.680	6605 ± 107	4.299 ± 0.145	0
HD 25570	F4 V	0.249	0.147	0.557	2.688	6752 ± 109	4.183 ± 0.145	34
HD 40932	A2 M	0.079	0.205	0.978	2.853	8224 ± 133	4.191 ± 0.145	18

2.D Alternative Treatment of Open Clusters

As described in § 2.5.2.3 The 1-D marginalized PDF in age for an individual star is computed on a model grid that is uniformly spaced in $\log(\text{age})$. As such, the prior probability of each bin is also encoded in $\log(\text{age})$ (see § 2.5.2.2). Thus, the resultant PDF is naturally in the units of $d p(\log \tau)/d \log \tau$, where p is probability and τ is age.

In order to transform $p(\log \tau)$ to $p(\tau)$ one uses the conversion $p(\tau) = p(\log \tau)/\tau$. Statistical measures *other than the median*, such as the mean, mode, confidence intervals, etc. will be different depending on whether the PDF being quantified is $p(\log \tau)$ or $p(\tau)$. For example, $10^{\langle \log \tau \rangle} \neq \langle \tau \rangle$. Strictly speaking, however, both values are meaningful and authors frequently choose to report one or the other in the literature. In the case at hand, $p(\log \tau)$ for an individual star is more symmetric than the linear counterpart, $p(\tau)$. As such, one could reasonably argue that $10^{\langle \log \tau \rangle}$ is a more meaningful metric than $\langle \tau \rangle$.

In either case, because the PDFs in age or $\log(\text{age})$ are both skewed, the median (which, again, is equal regardless of whether $p(\tau)$ or $p(\log \tau)$ is under consideration), is actually the most meaningful quantification of the PDF since it is less susceptible to extreme values than either the mean or mode.

With respect to the open clusters, regardless of whether our analyses are performed in logarithmic or linear space, our results favor ages that are younger and older than accepted values for α Per and the Hyades, respectively.

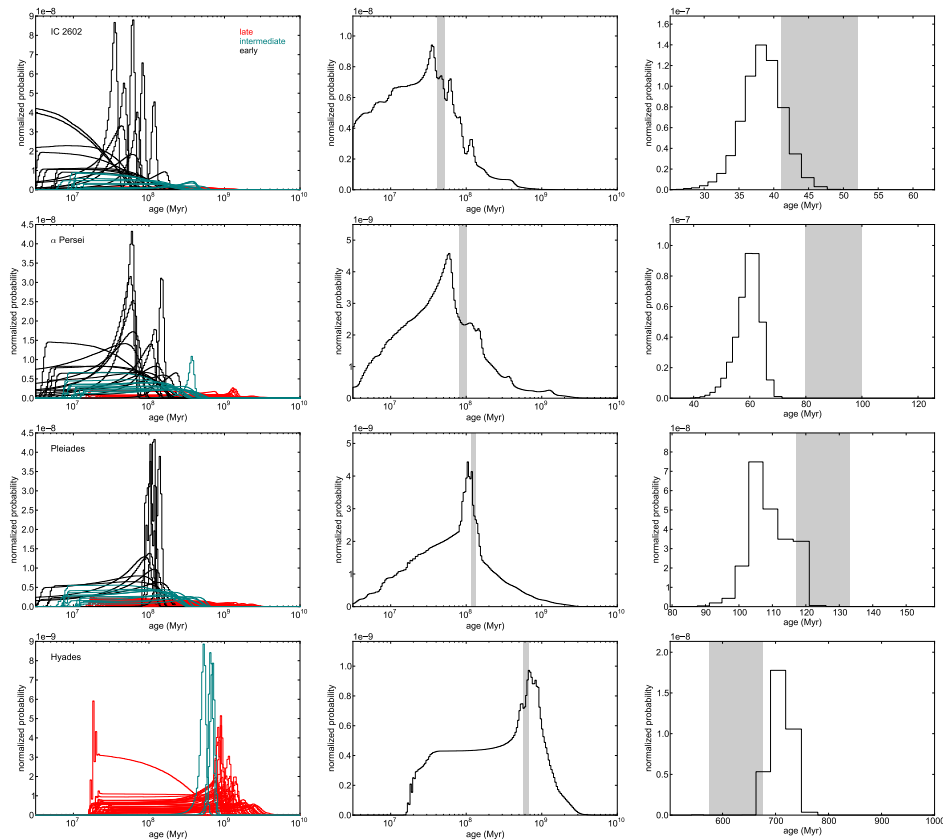


Figure 2.29: *Left panels:* 1D marginalized, normalized posterior PDFs in age, calculated from Bressan et al. (2012) evolutionary models, for individual open cluster members. Black, teal, and red histograms represent early, intermediate, and late group stars, respectively. *Middle panels:* Sums of the individual PDFs depicted on the left. This figure shows the total probability associated with the 200 age bins between $\log(\text{age}/\text{yr})=6.5$ to 10. The grey shaded regions indicate the currently accepted ages of IC 2602 (46^{+6}_{-5} Myr), α Per (90 ± 10 Myr), the Pleiades (125 ± 8 Myr), and the Hyades (625 ± 50 Myr). *Right panels:* Products of the individual PDFs depicted in the left panels. The grey shaded regions again depict the accepted literature age ranges of each cluster.

Table 2.12: Open Cluster Ages: Analysis in Linear Age.

Cluster	Lit. Age (Myr)	Models	Summed PDF Median (Myr)	Summed PDF 68% C.I. (Myr)	Multiplied PDF Median (Myr)	Multiplied PDF 68% C.I. (Myr)
IC 2602	46^{+6}_{-5}	Ekström et al. (2012)	22	3-39	41	41-42
		Bressan et al. (2012)	24	3-40	40	37-43
α Persei	90^{+10}_{-10}	Ekström et al. (2012)	41	3-68	63	61-68
		Bressan et al. (2012)	45	3-71	62	58-66
Pleiades	125^{+8}_{-8}	Ekström et al. (2012)	61	3-113	125	122-131
		Bressan et al. (2012)	77	3-117	112	107-120
Hyades	625^{+50}_{-50}	Ekström et al. (2012)	118	3-403	677	671-690
		Bressan et al. (2012)	288	17-593	738	719-765

Note: Literature ages (column 2) come from the sources referenced in § 2.6. For each set of evolutionary models, the median and 68% confidence interval are computed for both the summed PDF (columns 4,5) and multiplied PDF (columns 6,7). Note, the Hyades analysis includes the blue straggler HD 27962 and the spectroscopic binary HD 27268. Excluding these outliers results in a median and 68% confidence interval of 322 Myr [17-650 Myr] of the summed PDF or 784 Myr [749-802 Myr] of the multiplied PDF, using the B12 models.

*Chapter 3***HII 2407: AN ECLIPSING BINARY REVEALED BY K2
OBSERVATIONS OF THE PLEIADES**

David, T. J., Stauffer, J., Hillenbrand, L. A., et al., 2015, ApJ, 814, 62

ABSTRACT

The star HII 2407 is a member of the relatively young Pleiades star cluster and was previously discovered to be a single-lined spectroscopic binary. It is newly identified here within *Kepler/K2* photometric time series data as an eclipsing binary system. Mutual fitting of the radial velocity and photometric data leads to an orbital solution and constraints on fundamental stellar parameters. While the primary has arrived on the main sequence, the secondary is still pre-main-sequence and we compare our results for the M/M_{\odot} and R/R_{\odot} values with stellar evolutionary models. We also demonstrate that the system is likely to be tidally synchronized. Follow-up infrared spectroscopy is likely to reveal the lines of the secondary, allowing for dynamically measured masses and elevating the system to benchmark eclipsing binary status.

3.1 Introduction

Binary stars, notably double-lined eclipsing binaries, are fundamental astrophysical systems whose study is key to obtaining accurate empirical measurements of stellar radii, masses, and temperatures. These precisely derived quantities are necessary for calibrating theoretical models of stars, and understanding stellar evolution. Particularly valuable are well-characterized systems in either the pre-main sequence or post-main sequence phases where stellar evolution is more rapid, and fundamental calibrators correspondingly more rare relative to the main sequence. Among pre-main-sequence stars, fewer than 10 systems with masses below $1.5 M_{\odot}$ have published orbital solutions and fundamentally derived stellar parameters; see Stassun et al. (2014) and Ismailov et al. (2014) for reviews.

The Pleiades cluster ($d = 136.2 \pm 1.2$ pc; Melis et al., 2014 and age = 125 ± 8 Myr; Stauffer et al., 1998) is well-studied and has sizable membership. At the upper end of the mass distribution the stars are slightly evolved, with a well-populated main sequence between ~ 0.5 and $\sim 3 M_{\odot}$ (or M0 through B8 spectral types), and at lower masses the stars are still contracting as pre-main sequence objects. The *K2* phase of the Kepler mission (Howell et al., 2014) has observed ~ 800 bona fide and candidate Pleiads.

We report here the detection of Pleiades member HII 2407 as an eclipsing binary system, and make use of *K2* photometry and existing radial velocity measurements from the literature to derive an orbital solution and constrain the stellar parameters. Mutual fitting of the data combined with assumptions based on available information about the early-K type primary suggests a mid-M type secondary. At the Pleiades age, the primary has arrived on the main sequence while the secondary is still pre-main-sequence. Future observations will be needed in order to detect the spectrum of the secondary distinctly from that of the primary, rendering it a double-lined system and enabling a unique solution for the masses of the individual components.

3.2 K2 Observations and Analysis

The observations took place during *K2* Campaign 4 which ran from 2015-02-08 through 2015-04-20 UTC¹. Although we also produced our own light curve from aperture photometry, in our final analysis, we use the Simple Aperture Photometry (SAP) light curve available from the Mikulski Archive for Space Telescopes (MAST), which we corrected for systematics and intrinsic stellar variability.

¹Data release notes available at <http://keplerscience.arc.nasa.gov/K2/C4drn.shtml>

The dominant characteristic of the *K2* light curve of HII 2407 is a variability pattern of $\sim 2\%$ amplitude caused by rotational modulation of star spots. Primary eclipses of $\sim 5\%$ depth were detected by inspection of the raw light curve. Following removal of the spot modulation pattern, a Lomb-Scargle periodogram analysis of the corrected light curve yielded an orbital period of 7.05 days. Phase-folding the corrected light curve on this period then revealed secondary eclipses of depth $< 0.5\%$. The light curve extends over ~ 71 days, with ~ 30 minute cadence, yielding ten 2015 epochs.

In addition to the eclipses and star spot variability pattern, the light curve displays a saw-tooth-like pattern induced by the roll angle variations of the satellite. Following Aigrain et al. (2015), we model the spot- and roll- induced variations jointly, using a Gaussian process (GP) model with three components: a time-dependent term to represent the spot modulation, a term depending on the star's position on the CCD (as measured via the centroid) to represent the systematics, and a white noise term. This enables us to subtract the systematics and, where appropriate, the spot-induced variability in order to study the eclipses.

A detailed description of GP regression applied to *K2* light curve modelling is beyond the scope of this paper; we refer the interested reader to Aigrain et al. (2015) and restrict ourselves here to the differences between the present analysis and that paper. The position component was two-dimensional, depending on the centroid x and y , rather than on a 1-D estimate of the roll-angle variations. The time component was modelled as quasi-periodic to reflect the periodic but evolving nature of the spot-induced variations (see § 7.2 for further discussion of the spot variability modeling). The eclipses were excluded when training the model, but we did use the model to predict and correct for the systematics and spot-modulations across the eclipses. Finally, we included two change-points in the position component (at $\text{BJD}-2454833 = 2240$ and 2273 , each time the direction of the roll angle variations reverses): the systematics are treated as correlated between each pair of change points, but not across a change-point.

We fit for the characteristic amplitude and length scales of the systematics and spot component, the period and evolutionary timescale of the latter, as well as the white noise standard deviation, by maximizing the likelihood subject to log-normal priors on the length scales and log-uniform priors on the other parameters. The priors used were broad enough that they do not affect the fit, merely restricting the model to physically plausible values. Once the covariance parameters are set, we compute, for each cadence, the mean and standard deviation of the predictive distribution of

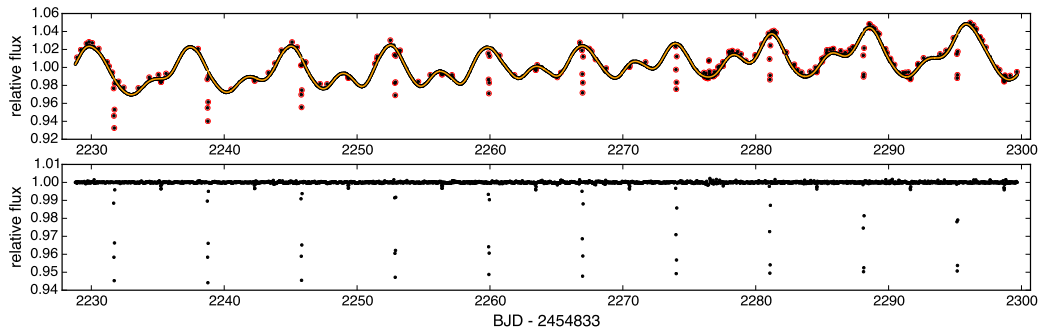


Figure 3.1: Top panel: Systematics corrected *K2* SAP light curve with our GP stellar variability fit in orange. Observations circled in red were excluded from the variability fit. Bottom panel: Corrected light curve obtained from dividing out the variability fit and excluding outliers.

the GP conditioned on the observations. We flag any observations lying more than three standard deviations away from the mean as outliers and repeat the fitting and prediction procedure to ensure the outliers did not affect the fit. The mean of the predictive distribution for the full (systematics + spot) model was subtracted from the data in order to model the eclipses, with the standard deviation of the same predictive distribution serving as our estimate of the photometric errors. These include the white noise term, plus additional errors arising from imperfections in the GP model’s ability to reproduce the data. As one would expect, the errors are slightly larger during the eclipses, where the data was not used to constrain the fit. We also evaluated the individual systematic and spot components separately in order to produce a systematics-corrected light curve that preserves astrophysical variability. The systematics-corrected light curve, variability fit, and final light curve used in eclipse modeling are presented in Figure 5.2.

3.3 HII 2407

The star is a classical member of the Pleiades² with Trumpler (1921), van Maanen (1945) and Hertzsprung (1947) designations; the last is the name by which it is most well known: Hz or HII 2407. The *K2* identifier is EPIC 211093684.

A spectral type of G5 is reported in (but not derived by) Mermilliod et al. (1992), which differs from the previous spectral type of K3 presented by Herbig (1962). The star has a *V* magnitude of 12.19, and *J* – *K* color of 0.572. An $R \approx 60,000$ spectrum from $\sim 3800 - 8000 \text{ \AA}$ of HII 2407 was obtained on UT 9-20-2015 using HIRES

²Its categorization in SIMBAD as an RS CVn star is not the correct interpretation of source properties.

(Vogt et al., 1994) on the Keck I telescope. The estimated spectral type is K1-K1.5 based on the line ratios discussed by Basri & Batalha (1990). For comparison, a spectral type of K1 corresponds to $T_{\text{eff}} = 5170$ K according to the Pecaut & Mamajek (2013) temperature scale.

Independent analysis of an $R \approx 20,000$ spectrum over the range of 6450-6850 Å taken with WIYN/Hydra in December 1999 produces an effective temperature estimate $T_{\text{eff}} = 4970 \pm 95$ K. This result is based on measurement of 51 lines using the ARES program³, and is consistent with a K2 spectral type from the empirical relations of Pecaut & Mamajek (2013).

The star is known as a variable, and was identified by Soderblom et al. (1993a) and Soderblom et al. (1993b) to have Li I 6707 Å absorption as well as weak H α and Ca II triplet core emission, and as a weak x-ray emitter by Stauffer et al. (1994) – all signs of youth that are consistent with the properties of many other low mass Pleiades members. From the HIRES spectrum, we measure $\text{EW}(\text{Li}) = 43.8 \pm 5.2$ mÅ.

Color-magnitude diagrams show the star to sit firmly on the main sequence with no photometric excess indicative of multiplicity. Observations conducted with the Palomar 60" telescope and the Robo-AO instrument (Baranec et al., 2014) confirm that HII 2407 is an apparently single star at wide separations. No far-red optical companions are detected brighter than the 5σ contrast limits of 2 mag, 4.25 mag, and 5.5 mag fainter than the star at separations from the star of 0.5", 1.5" and 3.5", respectively. We use this information below to rule out any “third light” contamination in the eclipse fitting part of our analysis.

The star was classified as spotted by Norton et al. (2007) from analysis of its WASP light curve (designation 1SWASP J034942.26+242746.8), but the eclipses were not identified by those authors. Our reanalysis of the WASP light curve using the WASP transit-search algorithm confirmed the eclipses and yielded the following orbital ephemeris:

$$P = 7.05046 \pm 0.00003 \text{ days}$$

$$\text{HJD}_0 = 2455302.0983 \pm 0.0019,$$

consistent with our *K2*-derived ephemeris, presented in Table 3.1.

However, HII 2407 was reported as a single-line spectroscopic binary by Mermilliod et al. (1992), who derived a 7.05 day orbital period with zero eccentricity. This

³<http://www.astro.up.pt/~sousasag/ares/>

period is the same as the 7.05 day eclipse period reported above from the *K2* analysis. Below we combine absolute radial velocity measurements from Table 7 of Mermilliod et al. (1992) with the *K2* photometry to fit for the system orbital and stellar parameters. Analysis of the HIRES spectrum revealed no signs of a secondary set of lines brighter than a few percent of the primary at wavelengths shorter than $\sim 8000 \text{ \AA}$, with this limit applicable for radial velocity separations of $> 10 \text{ km s}^{-1}$ between the primary and any putative secondary.

We evaluated the rotation period by modelling the out-of-eclipse light curve using a Gaussian process (GP) model with likelihood:

$$\mathcal{L} = \frac{1}{\sqrt{(2\pi)^n |K|}} \exp\left(-\frac{1}{2} \mathbf{y}^T K^{-1} \mathbf{y}\right), \quad (3.1)$$

where \mathbf{y} is a vector of n (normalised) flux measurements, and the elements of the covariance matrix K are given by

$$\begin{aligned} K_{ij} &= k(t_i, t_j) \\ &= A^2 \exp\left\{-\Gamma \sin^2\left[\frac{\pi}{P}|t_i - t_j|\right] - \frac{(t_i - t_j)^2}{2L^2}\right\} \\ &\quad + \sigma^2 \delta(t_i - t_j), \end{aligned} \quad (3.2)$$

where A is an amplitude, Γ an inverse length scale, P a period, L an evolutionary time-scale, and σ represents the white noise standard deviation, while $\delta(x)$ is the Kronecker delta function. This covariance function gives rise to a family of functions which display periodic but slowly evolving behaviour, and has previously been used to model the light curve of active stars (e.g. Aigrain et al., 2012). The GP model was implemented in PYTHON using the GEORGE package (Ambikasaran et al., 2014). To speed up the computation, the light curve was sub-sampled by selecting 500 data points at random. The posterior distribution for P was then evaluated (while marginalizing over the other parameters) using an affine-invariant Markov Chain Monte Carlo (MCMC) implemented in the EMCEE package (Foreman-Mackey et al., 2013). The priors used were uniform in natural log between -10 and 10 for all parameters, and we ran 36 parallel chains of 700 steps each, discarding the first 200 as burn-in. The resulting estimate of the rotation period is $P_{\text{rot}} = 7.45 \pm 0.07$.

Our value is inconsistent with both the 7.291 day period previously reported by Hartman et al. (2010) from HATNET and the 7.748 day period reported by Norton et al. (2007) from a Fourier periodogram analysis of the SuperWASP archive. We note that a separate Lomb-Scargle periodogram analysis of the *K2* light curve yielded a rotation period of 7.28 ± 0.30 days (where this approximate uncertainty is estimated from the full-width half-maximum of the oversampled periodogram peak), consistent with the HATNET value. We ultimately adopt the rotation period from the GP modeling in our final analysis.

The *K2*-derived photospheric rotation period can be considered in combination with $v \sin i$ values from the literature. Mermilliod et al. (2009) measured $5.2 \pm 0.9 \text{ km s}^{-1}$ while Queloz et al. (1998) tabulated $6.3 \pm 0.8 \text{ km s}^{-1}$. From these two values we calculate a primary radius of $R_1 = 0.77 \pm 0.13 R_\odot$ in the first case or $R_1 = 0.93 \pm 0.12 R_\odot$ in the second. Notably, the radius calculated from the Stefan-Boltzmann law ($\sim 0.72 R_\odot$) assuming our measured T_{eff} and a luminosity from the literature is consistent within error with the smaller radius estimate above, but not the larger value. We note that the large uncertainty in the primary radius is dominated by the $v \sin i$ measurement error.

For comparison, from the evolutionary models of Siess et al. (2000) and assumed values of $T_{\text{eff}} = 4764 \text{ K}$ and $L = 0.29 L_\odot$, Wright et al. (2011) estimated a radius of $0.74 R_\odot$ and a mass of $0.83 M_\odot$ for HII 2407. Hartman et al. (2010) reported $0.717 R_\odot$ and $0.817 M_\odot$ from the K-band magnitude and Yi et al. (2001) isochrones while Bouvier et al. (1998) and Bouvier (1998) found $0.81 M_\odot$ from the *I* magnitude, an assumed age of 120 Myr, and Baraffe et al. (1998) models.

Ultimately, we adopt the following as the final primary parameters: spectral type of $K2 \pm 1$, $T_{\text{eff},1} = 4970 \pm 95 \text{ K}$, $\log(L_1/L_\odot) = -0.54$, $M_1 = 0.81 \pm 0.08 M_\odot$, and $R_1 = 0.77 \pm 0.13 R_\odot$. Our adopted values for HII 2407 are mostly consistent with the highly precise measurements of well-studied double-lined eclipsing binaries. Among comparable main sequence systems compiled by Torres et al. (2010), K1-K3 types have masses in the range $0.764\text{--}0.934 M_\odot$, radii of $0.768\text{--}0.906 R_\odot$, T_{eff} in the range $4720\text{--}5220 \text{ K}$, and luminosities of $\log(L/L_\odot)$ -0.515 to -0.303 . We note our mass uncertainty of 10% is arbitrary and intended to be conservative. For comparison, there is a $\sim 7\%$ dispersion in the masses of K1-K3 benchmarks discussed above. HII 2407 has a luminosity slightly lower than typical, perhaps owing to the presence of spots given its relatively young age.

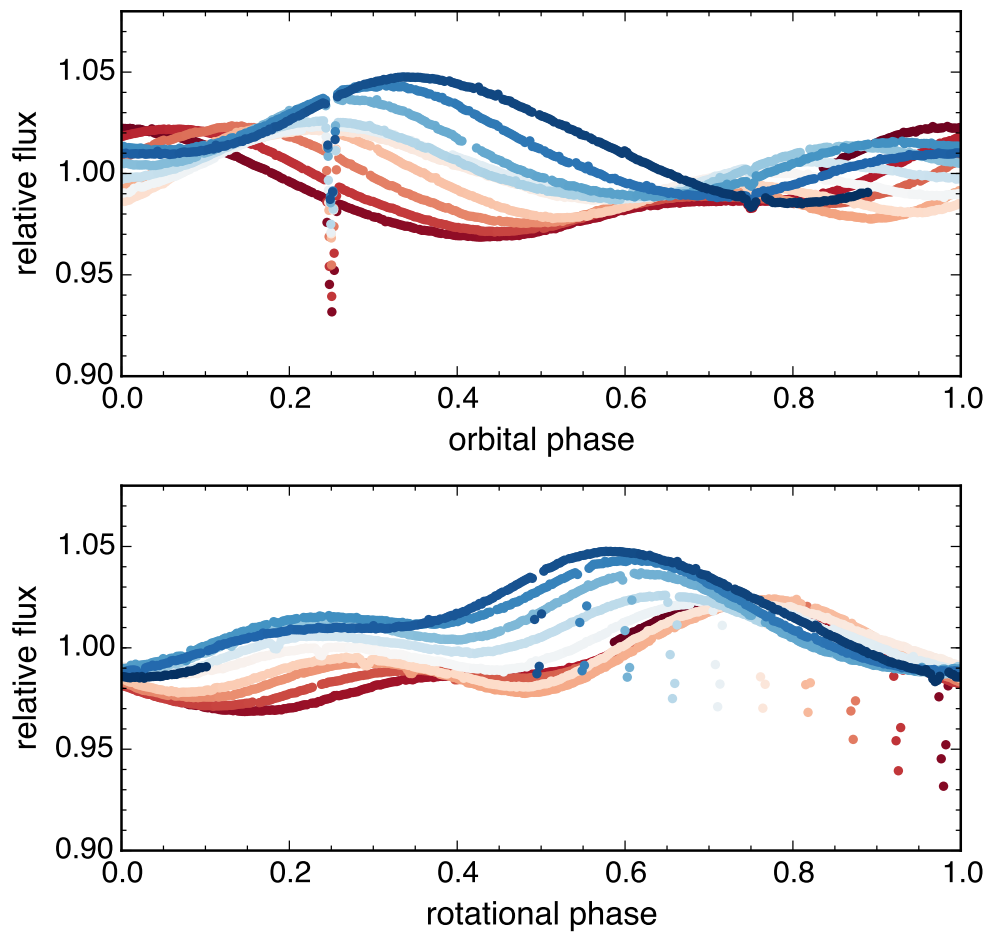


Figure 3.2: Systematics-corrected *K2* light curve phase-folded on the orbital period (top) and on the rotational period (bottom). Points are colored according to the time of observation. Rotational modulation of starspots is clearly demonstrated. The variable amplitude of the spot signature suggests a changing spot fraction. Though the eclipses are clearly not in phase with the rotational period, we discuss in § 7.7 the likelihood that the system is tidally synchronized with the difference in spot and orbital periods due to a latitudinal gradient in the rotation rate.

3.4 Orbital Parameter Fitting

We used the JKTEBOP⁴ orbit-fitting code (Southworth, 2013, and references therein) to derive the orbital and stellar parameters for the HII 2407 system. The code is based on the Eclipsing Binary Orbit Program (Popper & Etzel, 1981; Etzel, 1981), which relies on the Nelson-Davis-Etzel biaxial ellipsoidal model for well-detached EBs (Nelson & Davis, 1972; Etzel, 1975). JKTEBOP models the two components as biaxial spheroids for the calculation of the reflection and ellipsoidal effects, and as spheres for the eclipse shapes.

Our procedure of removing the out-of-eclipse variability also eliminates gravity darkening, reflected light, and ellipsoidal effects from the light curves. As such, parameters related to these effects are not included in the JKTEBOP modeling. Additionally, out-of-eclipse observations are excluded in order to reduce the effect these observations have on the χ^2 calculation and to expedite the fitting process. The observational errors were iteratively scaled by JKTEBOP to find a χ^2_{red} close to 1. A single outlier towards the center of secondary eclipse, located more than $3\text{-}\sigma$ above the eclipse minimum, was deemed systematic in nature and was excluded from further analysis.

The integration times of *Kepler* long cadence data are comparable to the eclipse durations, resulting in “phase-smearing” of the light curve. The long exposure times were accounted for in JKTEBOP by numerically integrating the model light curves at ten points in a total time interval of 1766 seconds, corresponding to the *Kepler* long cadence duration.

The code finds the best-fit model to a light curve through Levenberg-Marquardt (L-M) optimization. The initial L-M fitting procedure requires reasonable estimates of the orbital parameters to be determined. Period estimates were obtained using Lomb-Scargle (Lomb, 1976; Scargle, 1982) periodogram analysis. Approximations of the ephemeris timebase, T_0 , were obtained by manually phase-folding the light curves on the periodogram period.

Holding the period and ephemeris timebase fixed, initial L-M fits are performed in succession for the remaining orbital parameters: the central surface brightness ratio, $J = (T_{\text{eff},2}/T_{\text{eff},1})^4$ (which can be approximated by the ratio of the eclipse depths for circular orbits), the sum of the relative radii, $(R_1 + R_2)/a$, the ratio of the radii, $k = R_2/R_1$, the orbital inclination, i , and the quantities $e \cos \omega$ and $e \sin \omega$,

⁴<http://www.astro.keele.ac.uk/jkt/codes/jktebop.html>

where e and ω are the eccentricity and periastron longitude, respectively. We find an initial estimate for J from the ratio of secondary to primary eclipse depths, which is $\approx 1/13$. For circular orbits this ratio approximately corresponds to a temperature ratio of ~ 0.53 between the secondary and primary, or a central surface brightness ratio of ~ 0.08 . We find the data to be consistent with a circular orbit, but also explore the possibility of a nonzero eccentricity. Additionally, we incorporate radial velocities (RVs) in the fitting procedure, introducing free parameters corresponding to the RV semi-amplitudes of the primary, v_r , and the systemic RV, γ .

After successively increasing the number of free parameters in the fit, a final L-M fit was performed allowing all relevant parameters to be free. In modeling each system, we assumed a linear limb-darkening law for both components and held the limb-darkening coefficients fixed at 0.7, corresponding to the mean value tabulated by Sing (2010) for the *Kepler* bandpass and solar metallicity stellar atmospheres with $3500 \leq T_{\text{eff}} \leq 5500$, $4.0 \leq \log g \leq 4.5$.

We also explored a quadratic limb-darkening law, adopting limb darkening coefficients of $a_1, b_1 = 0.70, 0.04$ for the primary (corresponding to the mean values tabulated by Claret et al. (2012) for solar metallicity atmospheres with $4400 \text{ K} \leq T_{\text{eff}} \leq 4800 \text{ K}$, $\log g=4.5$) and $a_2, b_2 = 0.41, 0.29$ for the secondary (corresponding to the mean values for $3000 \text{ K} \leq T_{\text{eff}} \leq 4000 \text{ K}$, $\log g=5.0$). Using a quadratic limb-darkening law in this case provided essentially no improvement to the quality of the light curve fit. We suggest that grazing eclipses, spot activity, the quality of the *K2* photometry, and the light curve processing procedures may all contribute to some degree in making it difficult to constrain limb-darkening parameters for this system.

Robust statistical errors on the best-fit model parameters are then found through repeated Monte Carlo (MC) simulations in which Gaussian white noise commensurate to the observational errors is added to the best-fit model. A new L-M fit is performed on the perturbed best-fit model and the new parameters are saved as links in the MC chain. The final orbital parameters for each system are then given by the original L-M best-fit, with uncertainties given by the standard deviations determined from the MC parameter distributions.

The best-fit JKTEBOP model light curve and radial velocity curve are presented in Figure 3.3 with details given in Table 3.1. The χ_{red}^2 of the best fit is 1.04 for the light curve with out of eclipse observations removed. We also present in Table 3.1 the best-fit parameters in the case of an eccentric orbit (where $e \cos \omega$ and $e \sin \omega$ are

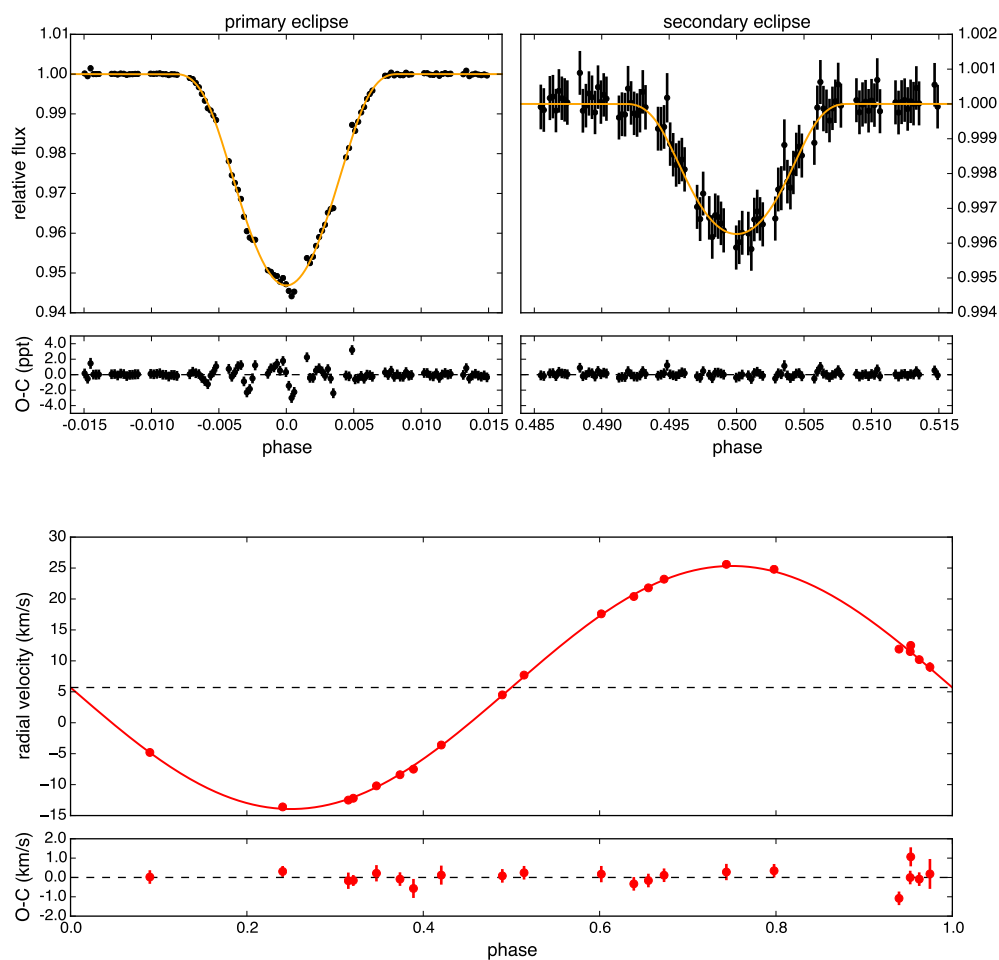


Figure 3.3: Best-fit JKTEBOP model to the *K2* photometry (top panels) and the Mermilliod et al. (1992) radial velocities (bottom panel). For each panel the residuals of the best fit model are plotted below. Measurement uncertainties in the top left and bottom panels are smaller than the points themselves. The increased scatter seen in primary eclipse is potentially due to spot activity and/or artifacts from the *Kepler* data reduction pipeline. The horizontal dashed line in the bottom panel indicates the best-fit systemic radial velocity.

allowed free), which are completely consistent with the corresponding parameters in the circular orbit solution. The best-fit eccentricity in this case was $e=0.0044 \pm 0.0049$, consistent with zero. We thus adopt the circular orbit solution for the analysis that follows.

Table 3.1: Best-fit Orbital Parameters

Parameter	Symbol	Value	1- σ Error	Units
Central surface brightness ratio	J	0.0602	± 0.0024	
Sum of fractional radii	$(R_1 + R_2)/a$	0.0590	± 0.0018	
Ratio of radii	R_2/R_1	0.268	$\pm 0.025^a$	
Inclination	i	87.69	± 0.14	deg
Period	P	7.0504829	± 0.0000047	days
Time of primary minimum	T_0	2456916.65777	± 0.00014	BJD
Radial velocity amplitude	v_r	19.64	± 0.11	km s ⁻¹
Systemic radial velocity	γ	5.695	± 0.084	km s ⁻¹
<i>Eccentric Orbit Parameters</i>				
Central surface brightness ratio	J	0.0589	± 0.0031	
Sum of fractional radii	$(R_1 + R_2)/a$	0.0587	± 0.0018	
Ratio of radii	R_2/R_1	0.268	± 0.023	
Inclination	i	87.72	± 0.13	deg
Eccentricity, periastron longitude combination	$e \cos \omega$	0.00006	± 0.00025	
Eccentricity, periastron longitude combination	$e \sin \omega$	-0.0044	± 0.0068	
Period	P	7.0504823	± 0.0000049	days
Time of primary minimum	T_0	2456916.65778	± 0.00015	BJD
Radial velocity amplitude	v_r	19.60	± 0.13	km s ⁻¹
Systemic radial velocity	γ	5.707	± 0.084	km s ⁻¹

^a The statistical uncertainty in R_2/R_1 is not reliable in the absence of a flux ratio measurement due to the intrinsic degeneracies of EB lightcurves, particularly for circular orbits (see § 7.7). The HIRES spectrum provides an upper limit to the flux ratio of $\sim 5\%$, which corresponds to an upper limit for the radius ratio of ~ 0.9 using the ЖКТЕВОР temperature ratio or ~ 0.6 from the PHOEBE temperature ratio, as discussed in § 3.4.

Note: Orbital parameters determined from a simultaneous fit of the corrected *K2* light curve and Mermilliod et al. (1992) radial velocities. Statistical parameter uncertainties are 1- σ errors determined from 10,000 Monte Carlo simulations with ЖКТЕВОР . Parameters in the eccentric orbit case were determined from 5,000 Monte Carlo simulations. All parameters in the eccentric case are consistent within error with the circular orbit fit.

Notably, the minimum of primary eclipse is poorly fit by the model, primarily due to the three lowest flux observations. These data correspond to the first three eclipse minima, suggestive of an intrinsic variability origin to the outlying points. However, we can not rule out the possibility that the low fluxes are systematic in nature.

A battery of tests were performed to assess how the quality of fit changed with the inclusion/exclusion of these outliers and neighboring points. Keeping the observational errors fixed, the best-fit χ_{red}^2 is minimized by excluding the three low flux outliers. Moreover, exclusion of the entire bottom of primary eclipse (defined here as those observations with relative flux values lower than 0.955) leads to a best-fit with parameters more similar to those found when excluding just the three low flux outliers. Finally, a higher χ_{red}^2 is found by forcing the fit to pass through the low flux outliers through excluding only the cluster of observations occurring just prior to the primary eclipse minimum in phase.

However, given that we know the primary exhibits significant spot activity with periodicity similar to that of the binary orbit, we consider the removal of these outliers a contrived choice. Furthermore, given the youth of the system, it is likely that the low-mass secondary is also spotted. In such instances, complicated patterns may arise during eclipses with contributions from both the background and foreground stars (e.g. Gillen et al., 2014). As such, we choose to include all observations from primary eclipse in our final fit and suggest that the increased scatter is likely due to spots. We note that excluding these three observations changes the best-fit temperature ratio by $<1\%$, the inclination by ~ 0.2 deg, the sum of fractional radii by $\sim 4\%$ (or $<1.5\sigma$), and the ratio of radii by $\sim 12\%$ (or $<1.5\sigma$).

Independent of the JKTEBOP analysis, we also modeled the light curve and radial velocities with PHOEBE (Prša & Zwitter, 2005). Based on the fact that we could not detect the secondary component in the HIRES spectrum, we can place an upper limit on the optical flux ratio of $\sim 5\%$. After creating an initial model in PHOEBE, we ran an MCMC fitting routine using both the SB1 radial velocities and the detrended *K2* light curve with the following free parameters: mass ratio, semi-major axis, inclination, effective temperature of the secondary component, potentials of both the primary and secondary components, and light and third-light levels. We set priors on the mass ratio and semi-major axis such that resulting masses would be consistent with the estimated values, but generally left them free to explore the degenerate parameter space. We then introduced a penalty in the likelihood function to forbid any models that resulted in the secondary contributing more than 5% of

the flux.

We then derived the values and posteriors of the quantities which can actually be constrained by this system by propagating the values for the MCMC chains and fitting a Gaussian to the resulting distributions. Assuming a circular orbit, the PHOEBE analysis yields the following values: $(R_1 + R_2)/a = 0.0506 \pm 0.0006$, $a_1 \sin i = 2.69 \pm 0.05 R_\odot$, $i = 88.09 \pm 0.04$ deg, and a temperature ratio of $T_{\text{eff},2}/T_{\text{eff},1} = 0.612 \pm 0.005$. This temperature ratio, combined with the assumed primary temperature, implies $T_{\text{eff},2} = 3040 \pm 60$ K. These values are close to those found by JKTEBOP, though there is a $\sim 15\%$ difference in the sum of fractional radii and a $\sim 20\%$ discrepancy between the temperature ratios favored by the two different codes. These differences suggest the statistical uncertainties we report in Table 3.1 may not reflect the true uncertainties. A possible etiology of this behavior is the reliance of PHOEBE on stellar atmospheres to convert surface brightness to T_{eff} at cool temperatures, in contrast to JKTEBOP which does not rely on such models. We consider the results of both modeling efforts in the analysis that follows.

3.5 Discussion

Simultaneous fitting of the light curve and primary radial velocities yield an RV semi-amplitude of the primary, systemic RV, and binary mass function that are entirely consistent with the values reported in Mermilliod et al. (1992). We find a binary mass function $f(M_2) = 0.005521 \pm 0.000097 M_\odot$, providing an absolute lower limit of $\sim 6 M_{\text{Jup}}$ to the mass of the secondary.

Since HII 2407 is an SB1 binary, the radial velocities contain information only about the projected orbit of the primary component (i.e. $a_1 \sin i$) and fail to provide us information about the separation between the two stars or the mass ratio, as would be the case in an SB2 binary. Without significant ellipsoidal variations, the light curve can not constrain the mass ratio and, since the eclipses are merely grazing, does not provide a strong constraint on the radius ratio either. Instead, the light curve contains robust information only about the sum of fractional radii $(R_1 + R_2)/a$, the inclination, and the temperature ratio.

Nevertheless, auxiliary information about the system allows for coarse characterization of the secondary. The broad-band photometry places HII 2407 close to the Pleiades single star locus, which provides a rough constraint on the mass ratio of $q \lesssim 0.3 - 0.4$. This upper limit, combined with the lower limit from the precisely measured mass function, places the companion firmly in the $\sim 0.006-0.4$

M_{\odot} mass range. This, of course, assuming the primary mass from photometry, which again is consistent with benchmark K dwarfs. Moreover, the inclination is robustly constrained and given the well-defined range of dynamical masses for K1-K3 type benchmark double-lined EBs, one can use the radial velocity equation (Lehmann-Filhés, 1894) to obtain a reasonable, and more precise, approximation for the secondary mass.

As noted in Table 3.1, the upper limit on the flux ratio from the HIRES spectrum can be used to place an upper limit on the radius ratio. However, significantly different limits arise from the different temperature ratios favored by JKTEBOP and PHOEBE. An upper limit of $R_2/R_1 < 0.9$ is obtained from the JKTEBOP best-fit J value, while PHOEBE favors a higher temperature ratio that implies $R_2/R_1 < 0.6$.

Based on assumed parameters for the primary of $R_1 = 0.77 \pm 0.13 R_{\odot}$ and $M_1 = 0.81 \pm 0.08 M_{\odot}$ (§ 7.2), the companion to HII 2407 has the following properties: $R_2 \approx 0.21 \pm 0.04 R_{\odot}$, $M_2 \approx 0.18 \pm 0.02 M_{\odot}$ (given the primary mass, and the best-fit radial velocity semi-amplitude and inclination). For these parameters and an assumed age of 120 Myr, interpolation of Baraffe et al., 2015, hereafter BHAC15 models predicts temperatures of $T_1 = 4975$ K and $T_2 = 3120$ K. The predicted flux ratio of this configuration is thus $F_2/F_1 \sim 0.1$ at 8000 \AA or ~ 0.3 at $1.55 \mu\text{m}$ (L. Prato, private communication). Detection of spectral lines from the secondary is likely possible in the infrared.

JKTEBOP modeling suggests a luminosity ratio $L_2/L_1 \approx k^2 J \approx 0.004$, which is consistent with the HIRES-determined upper limit on the optical flux ratio. For comparison, assuming an age of 120 Myr and $M_1 = 0.81 M_{\odot}$, the luminosity ratio suggests $M_2 \approx 0.11 M_{\odot}$, from interpolation among either BHAC15 or Siess et al. (2000) isochrones. We caution that this ratio is strongly dependent on the poorly constrained ratio of radii. The best-fit central surface brightness ratio corresponds to a temperature ratio of $T_{\text{eff},2}/T_{\text{eff},1} = 0.4953 \pm 0.0049$. This ratio suggests a secondary temperature of $T_{\text{eff},2} = 2460 \pm 90$, assuming a $3\text{-}\sigma$ error in the surface brightness ratio. We note this temperature is ~ 500 K cooler than predictions from BHAC15 or Siess et al. (2000) models for a star with the assumed secondary mass. The temperature ratio favored by PHOEBE, however, produces a secondary temperature that is in much better agreement with models.

The position of the secondary in the mass-radius plane relative to Siess et al. (2000), BHAC15, and PARSEC v1.1 (Bressan et al., 2012) models (see Figure 5.8) is consistent in each case with an age older than the nominal cluster age of 120 Myr,

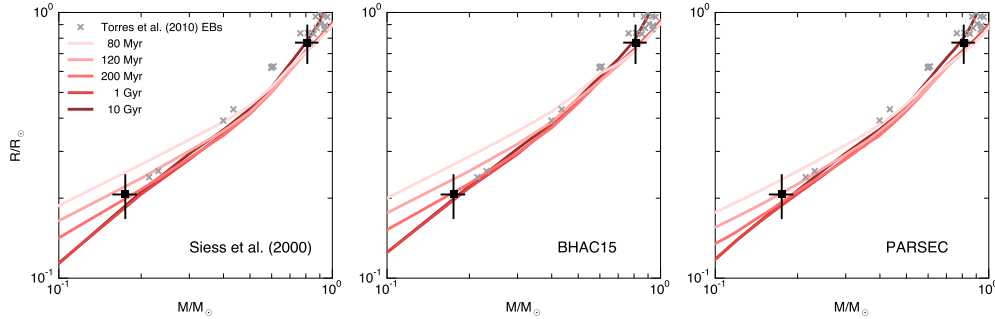


Figure 3.4: Isochrones in the mass-radius plane with the components of HII 2407 and benchmark EBs from Torres et al. (2010) overplotted. From left to right, the evolutionary models depicted are from Siess et al. (2000), Baraffe et al. (2015), and Bressan et al. (2012). All models plotted are for solar metallicity ($Z=0.02$). Unlike the Torres et al. (2010) sample, the masses and radii of the HII 2407 components are model-dependent.

but within error of the accepted value. The largest discrepancy is present in the BHAC15 models, which imply a significantly older age for the secondary (in other words, the BHAC15 models overpredict the radius at a given mass, if the mass and radius are assumed correct). For the assumed cluster age, the PARSEC models provide the closest match to our estimates of the secondary parameters. However, we note that given the large uncertainties, meaningful constraints on evolutionary models will be obtained only when secondary lines are detected and thus precise masses and radii for both components are measured directly.

Regarding the near-coincidence of the binary orbital and the stellar rotational periods, the ~ 7 day rotation period of the primary is typical of single Pleiads with masses in the range $0.6\text{-}0.8 M_{\odot}$ (Hartman et al., 2010). The ~ 0.4 day difference between the rotational and orbital frequencies corresponds to 0.048 radian/day. This is comparable to the equator-to-pole difference in rotational frequency found in Doppler imaging studies of differential rotation in young K dwarfs of similar effective temperature (Barnes et al., 2005). In other words, the frequency difference is small enough that if the surface rotation of the primary is locked to the orbit at low latitude, and the spot activity is confined to higher latitudes, the observed frequency difference could arise from surface differential rotation.

Using equation 4.12 from Zahn (1977) for tidal synchronization due to eddy viscosity in a convective star with a tidal Love number of order unity, we obtain a synchronization timescale $\approx 3 \times 10^7$ years for the primary's rotation. While this estimate is somewhat uncertain, it indicates that the synchronization timescale for such a system should exceed the age of the cluster at rotation periods longer than

10 days. This is consistent with the studies of Meibom et al. (2006) and Marilli et al. (2007), who found synchronized binaries in clusters of comparable age only at periods less than ten days.

We conclude that there is good theoretical and observational support for the interpretation that the similarity between the orbital and photometric periods is causal rather than coincidental, and that the primary's rotation is tidally locked to the orbit.

3.6 Summary

We report the discovery of Pleiades member HII 2407 as an eclipsing binary. The star was known previously as a spectroscopic binary, and we used the literature radial velocities combined with new *K2* photometry to constrain the fundamental parameters of the system. We revised the spectral type of the primary, provided a new measurement of the rotation period, and demonstrated that the system is likely tidally synchronized. The companion is likely to be a mid-M type, and thus still a contracting pre-main-sequence star given the nominal cluster age. It is the first fundamental calibrator available in this mass and age range. Follow-up infrared spectroscopy, where the flux ratio is more favorable relative to optical spectroscopy, is likely to reveal the lines of the secondary, allowing for dynamically measured masses and elevating the system to benchmark EB status.

ACKNOWLEDGMENTS

We thank the referee for suggestions that led to significant improvements in this paper. We thank Lisa Prato for her estimate of the infrared flux ratio and look forward to a direct detection of the secondary. The material presented herein is based upon work supported in 2015 by the National Science Foundation Graduate Research Fellowship under Grant No. DGE1144469. T.J.D. gratefully acknowledges support from France Córdova through the Neugebauer Scholarship. This research was partially supported by an appointment to the NASA Postdoctoral Program at the Ames Research Center, administered by Oak Ridge Associated Universities through a contract with NASA. Support for this work was provided by NASA via grant NNX15AV62G. This paper includes data collected by the Kepler mission. Funding for the Kepler mission is provided by the NASA Science Mission directorate. Some of the data presented in this paper were obtained from the Mikulski Archive for Space Telescopes (MAST). STScI is operated by the Association of Universities for Research in Astronomy, Inc., under NASA contract NAS5-26555. Support for MAST for non-HST data is provided by the NASA Office of Space Science via grant NNX09AF08G and by other grants and contracts. Some of the data presented herein were obtained at the W.M. Keck Observatory, which is operated as a scientific partnership among the California Institute of Technology, the University of California and the National Aeronautics and Space Administration. The Observatory was made possible by the generous financial support of the W.M. Keck Foundation. The authors wish to recognize and acknowledge the very significant cultural role and reverence that the summit of Mauna Kea has always had within the indigenous Hawaiian community. We are most fortunate to have the opportunity to conduct observations from this mountain. The Robo-AO system was developed by collaborating partner institutions, the California Institute of Technology and the Inter-University Centre for Astronomy and Astrophysics, and supported by the National Science Foundation under Grant Nos. AST-0906060, AST-0960343 and AST-1207891, the Mt. Cuba Astronomical Foundation and by a gift from Samuel Oschin. C.B. acknowledges support from the Alfred P. Sloan Foundation. A.C.C. acknowledges support from STFC grant ST/M001296/1. Funding for WASP comes from consortium universities and from UK's Science and Technology Facilities Council.

*Chapter 4***NEW PLEIADES ECLIPSING BINARIES AND A HYADES
TRANSITING SYSTEM IDENTIFIED BY K2**

David, T. J., Conroy, K. E., Hillenbrand, L. A., et al., 2016, AJ, 151, 112

ABSTRACT

We present the discovery in *Kepler*'s *K2* mission observations and our follow-up radial velocity observations from Keck/HIRES for four eclipsing binary (EB) star systems in the young benchmark Pleiades and Hyades clusters. Based on our modeling results, we announce two new low mass ($M_{tot} < 0.6 M_{\odot}$) EBs among Pleiades members (HCG 76 and MHO 9) and we report on two previously known Pleiades binaries that are also found to be EB systems (HII 2407 and HD 23642). We measured the masses of the binary HCG 76 to $\lesssim 2.5\%$ precision, and the radii to $\lesssim 4.5\%$ precision, which together with the precise effective temperatures yield an independent Pleiades distance of 132 ± 5 pc. We discuss another EB towards the Pleiades that is a possible but unlikely Pleiades cluster member (AK II 465). The two new confirmed Pleiades systems extend the mass range of Pleiades EB components to $0.2\text{--}2 M_{\odot}$. Our initial measurements of the fundamental stellar parameters for the Pleiades EBs are discussed in the context of the current stellar models and the nominal cluster isochrone, finding good agreement with the stellar models of Baraffe et al (2015) at the nominal Pleiades age of 120 Myr.

Finally, in the Hyades, we report a new low mass eclipsing system (vA 50) that was concurrently discovered and studied by Mann et al. (2016b). We confirm that the eclipse is likely caused by a Neptune-sized transiting planet, and with the additional radial velocity constraints presented here we improve the constraint on the maximum mass of the planet to be $\lesssim 1.2 M_{\text{Jup}}$.

4.1 Introduction

Clusters provide a unique opportunity to study stellar evolution by assuming coevality among their members. Eclipsing Binaries (EBs) have historically been used as a primary tool to measure masses, radii, and temperatures of stars. Combining these together, EBs in clusters are essential to calibrating these relations. Furthermore, EBs in clusters can be used to directly determine the distance to the cluster, providing a distance determination independent of parallax (see e.g. Milone & Schiller, 2013).

The *Kepler* space satellite provided unprecedented precision photometry for $\sim 150,000$ stars over a 4 year mission. With a primary purpose to discover earth-like planets, *Kepler* also allowed identification of nearly 2500 EBs (Prša et al., 2011; Slawson et al., 2011; Kirk et al., 2016). Now that *Kepler's* primary mission has reached an end, its repurposed *K2* mission is now observing fields along the ecliptic with similar precision in ~ 80 d timespans called “campaigns” (Howell et al., 2014). *K2* has already resulted in the discovery of over 100 EBs (Conroy et al., 2014; LaCourse et al., 2015; Armstrong et al., 2015).

The *K2* Campaign 4 included the Pleiades and the Hyades, two of the most well-studied clusters in the literature, providing a unique opportunity to identify and characterize future benchmark EBs at moderately young ages. The *K2* Campaign 4 pointing encompassed more than 900 confirmed or candidate members of the Pleiades and 80 confirmed or candidate members of the Hyades. The field was monitored continuously between UT 2015-02-08 and UT 2015-04-20¹.

The canonical age of the Pleiades cluster is $\tau = 125 \pm 8$ Myr, measured using the lithium depletion boundary technique (Stauffer et al., 1998). A more recent analysis by Dahm (2015) using the same method and updated evolutionary models favors a slightly younger age of $\tau = 112 \pm 5$ Myr, but is statistically consistent with the canonical value above. The distance to the Pleiades was the subject of a long-term controversy due to discrepant parallaxes measured by the *Hipparcos* satellite, but several independent studies have since resolved this issue; the best current estimate of $d = 136.2 \pm 1.2$ pc comes from very long baseline radio interferometry (Melis et al., 2014). The Pleiades age is such that the lowest mass members (i.e., later than a spectral type of K2, roughly) are still contracting down to the main sequence, while the intermediate mass stars are steadily burning hydrogen, and the highest

¹Data release notes are available at <http://keplerscience.arc.nasa.gov/K2/C4drn.shtml>

mass members have begun evolution off of the main sequence. Thus, the Pleiades represents a critical test for any stellar evolution model that aims to reproduce the fundamental parameters of stars from the pre-main sequence to post-main sequence phases of evolution. Fundamental calibrators, such as benchmark EBs, across a large range in mass are needed to place stringent constraints on these models.

The traditional Hyades age and distance are $\tau = 625 \pm 50$ Myr and $d = 46.34 \pm 0.27$ pc (Perryman et al., 1998), though more recent analyses suggest a substantially older age ~ 800 Myr (David & Hillenbrand, 2015; Brandt & Huang, 2015a). Unlike the Pleiades, all Hyades age estimates result from Hertzsprung-Russell diagram (HRD) analysis. EBs may help to resolve the age disagreement for this cluster, which serves as a critically important benchmark for many stellar evolution studies.

With its high-precision and high-cadence photometry for targets covering large portions of the Pleiades and Hyades clusters (Fig. 4.1), *K2* serves as a perfect opportunity to identify and characterize EBs in these clusters and both test and refine isochrone models, particularly the pre-main sequence (PMS) locus at 125 Myr for the Pleiades and the zero-age main sequence (ZAMS) locus for the Hyades (Schiller & Milone, 1987).

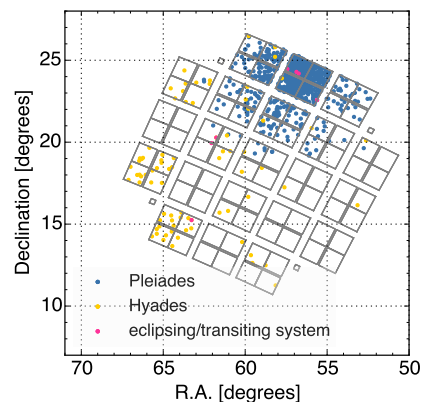


Figure 4.1: *K2* Campaign 4 pointing (grey) with observed Pleiades and Hyades members overlaid. Eclipsing or transiting systems discussed in this paper are indicated by pink points.

Before *K2* there were two EBs known in the Hyades. HD 27130 is a ~ 5.6 day, $\sim 1.8M_{\odot}$ system (McClure, 1980; McClure, 1982; Schiller & Milone, 1987) but was not observed by *K2*. V471 Tauri (Guinan & Ribas, 2001; Vaccaro et al., 2015) is a ~ 0.5 day main sequence - white dwarf binary and was a *K2* target (EPIC 210619926) but is not re-analyzed in this work.

In the Pleiades cluster, before *K2* there was only a single known EB: HD 23642

(Torres, 2003). The EB aspect of an additional, previously known, binary HII 2407 was recently discovered from *K2* and presented in detail by David et al. (2015). The Pleiades EB population is valuable to establish, given the cluster age, and particularly so at low masses given the rarity of fundamental calibrators at the lowest stellar masses at any age (Stassun et al., 2014).

Here we present two new low mass EBs with certain membership in the Pleiades, one solar-mass EB with possible membership in the Pleiades, and a candidate EB in the Hyades that is solar-type with a likely substellar companion (see also Mann et al., 2016b). We also present updated models for the known EB Pleiades member HD 23642 using *K2* data.

In Section 4.2 we describe the data that we use, including the *K2* light curves, photometry from the literature, and newly obtained spectroscopy. We describe our analysis procedures, including estimation of stellar properties and light-curve modeling, in Section 4.3. The results for the five EBs studied in this paper, including modeling results and initial physical parameters, are presented in Section 4.4. Finally, we briefly discuss the measured physical parameters in the context of stellar models in Section 4.5 and conclude with a summary in Section 4.6.

4.2 Data

As a part of the *K2* Campaign 4 guest observer program (Fig. 4.1), targets from Stassun et al. (2007) and Sarro et al. (2014) were included in the proposed target list as long as they fell within reasonable brightness cuts. Known members of the Hyades were included from historical proper motion surveys (van Bueren, 1952; van Altena, 1969; Hanson, 1975) as well as more recent surveys (Röser et al., 2011; Goldman et al., 2013).

The *K2* light curves for all Pleiades and Hyades members were examined by eye to identify potential EBs, and the membership of the detected EBs was then re-examined and confirmed using both archival and followup observations as described below. The EB cluster members newly reported here and their ephemerides are summarized in Table 4.1. Two previously known Pleiades EBs are summarized in Table 4.2, one of which (HII 2407) was presented in detail in David et al. (2015).

Table 4.1: Newly identified eclipsing binaries

EPIC	Coordinates (J2000.0)	Common ID	Cluster	Period (d)	BJD_0 (BJD-2450000)
210974364	03 42 27.30 +22 34 24.8	HCG 76	Pleiades	32.747	7068.748
211075914	03 46 55.31 +24 11 16.8	MHO 9	Pleiades	42.8	7099.2
210490365	04 13 05.60 +15 14 52.0	vA 50	Hyades	3.48451	7062.5801

Table 4.2: Previously known eclipsing binaries

EPIC	Common ID	Cluster	Period (d)	BJD_0 (BJD-2450000)	Reference
211082420	HD 23642	Pleiades	$2.46113412 \pm 0.00000052$	7119.522069 ± 0.00002	Torres, 2003
211093684	HII 2407	Pleiades	7.0504829 ± 0.0000047	6916.65777 ± 0.00014	David et al., 2015

Table 4.3: Photometric magnitudes in V and K_s bands for reported EBs

EPIC	Common ID	Cluster	V	Reference	K_s	Reference
210974364	HCG 76	Pleiades	17.04	Stassun et al. (2007)	11.86	Cutri & et al. (2012)
211075914	MHO 9	Pleiades	19.02	Stauffer et al. (1998)	12.88	Cutri & et al. (2012)
210490365	vA 50	Hyades	15.81	Ugoren et al. (1985)	10.44	Cutri & et al. (2012)

4.2.1 *K2* Photometry and Detrending

Long-cadence (~ 30 min exposure) *Kepler* photometry was obtained for all requested targets. Several different methods of data reduction and systematic removal were employed. Source photometry included the Simple Aperture Photometry (SAP) provided by the *Kepler* project and available through MAST, as well as custom aperture photometry from the *Kepler* target pixel files. The details of our custom aperture photometry procedure are discussed in David et al. (2016b) and will be presented in detail in Cody et al. (2016, *in prep*). Removal, or “detrending”, of systematic trends related to jitter in the spacecraft pointing was achieved through the Gaussian process regression algorithm of Aigrain et al. (2015), the Pre-search Data Conditioning (PDC) procedure applied to the SAP flux, or a modified version of the Self-Flat-Fielding method (Vanderburg & Johnson, 2014) which is described in detail in David et al. (2016b).

Our experience is that no one photometry method and no one detrending method can be considered best for all sources. Thus our analysis makes use of the best available combination, chosen on a source-by-source basis. These decisions are based on an assessment of the photometric precision on 6.5 hour timescales (using the “quasi-CDPP” metric defined in Aigrain et al., 2015, the median value of the standard deviation in a moving window of a given duration) as well as visual inspection of the detrended light curves for the presence of remaining sawtooth-like systematic features related to spacecraft pointing. In particular, for HCG 76 and MHO 9, the analyzed light curves were obtained from the Aigrain et al. (2015) method of detrending applied to the SAP time series. For HD 23642, we used the PDC detrended SAP light curve, publicly available through MAST². Finally, for vA 50, we again used the PDC light curve, subject to additional detrending using the procedure described in David et al. (2016b).

4.2.2 Photometric Colors

$V - K$ colors were assembled for each cluster target observed with *K2*. The K_s magnitudes are adopted from 2MASS (Cutri & et al., 2012). The V magnitudes are adopted from various sources for both the Pleiades (Stauffer et al., 1998; Stauffer et al., 2007; Kamai et al., 2014) and Hyades (Ungren & Weis, 1977; Weis et al., 1979; Weis, 1983; Ungren et al., 1985; Weis & Hanson, 1988). Figure 4.2 shows color-magnitude diagrams for the Pleiades and Hyades, respectively, with our newly

²Mikulski Archive for Space Telescopes - available at <http://archive.stsci.edu/index.html>

reported EBs highlighted, and Table 4.3 lists the adopted V and K_s magnitudes.

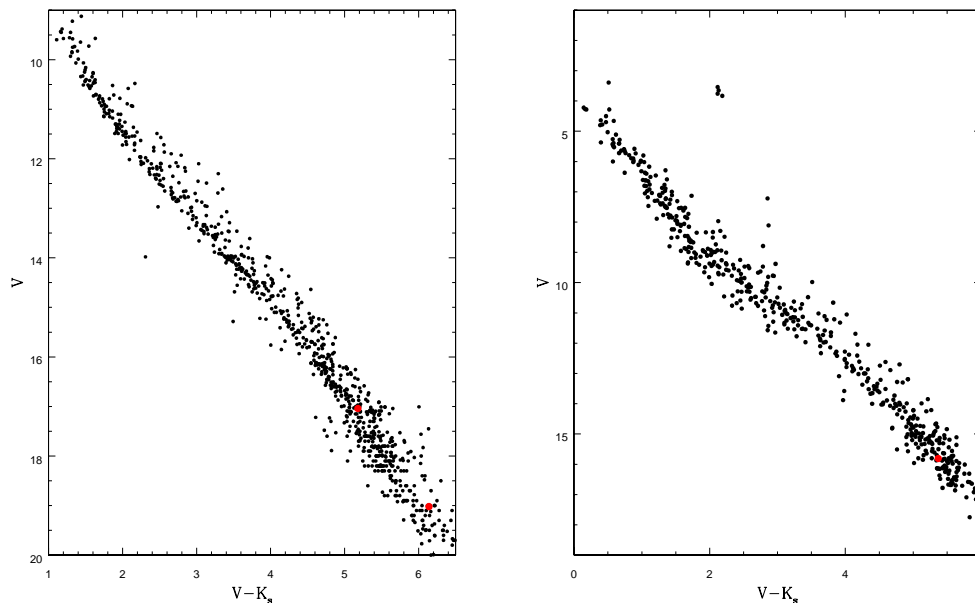


Figure 4.2: V vs $V - K_s$ photometric color magnitude diagram for the observed known members of the Pleiades (left) and Hyades (right) clusters. The red highlighted points are the EBs reported in this paper.

4.2.3 Spectroscopy

Follow-up spectroscopy was obtained for all targets that were identified as potential new EB cluster members. These spectra served to confirm membership in the cluster by verifying the systemic velocity as consistent with that of the cluster. They also verify that the identified source is a spectroscopic binary, either right away for double-lined systems or following the acquisition of a time series for single-lined systems, and therefore exclude the possibility of a background EB contaminating the $K2$ light curve. Finally the spectra provide constraints on the physical properties of each system such as the primary spectral type and rotational velocity, and the primary (and secondary for double-lined systems) velocity amplitudes.

Keck/HIRES (Vogt et al., 1994) spectra were collected at the epochs listed in Table 8.2. The images were processed and spectra extracted using either the California Planet Search (CPS) pipeline, requiring subsequent heliocentric correction, or the `MAKEE` package written by Tom Barlow. Radial velocities (RVs) were derived from Gaussian fitting to cross correlation peaks using the routine `fxcor` within `IRAF`. Absolute calibration was achieved for the M-type stars by baselining from Gl 176

Table 4.4: Keck-I/HIRES Radial Velocities and Flux Ratios

Proper Name	Epoch (UT Date)	Epoch (BJD-2450000)	v_1 (km s ⁻¹)	σ_{v_1} (km s ⁻¹)	v_2 (km s ⁻¹)	σ_{v_2} (km s ⁻¹)	F_2/F_1
vA 50	20150925	7291.036879681	37.74	0.93	<0.1
...	20151003	7299.036548298	38.90	0.72	<0.1
...	20151027	7322.880052281	37.60	1.21	<0.1
...	20151031	7327.047595191	38.77	0.67	<0.1
...	20151113	7339.967314662	38.74	0.67	<0.1
...	20151128	7354.985788494	39.02	0.61	<0.1
...	20151129	7355.958388342	38.51	0.59	<0.1
HCG 76	20150925	7291.026244638	-24.41	0.68	37.29	1.24	1.04 ± 0.20
...	20151001	7297.048107753	-3.78	0.98	14.35	0.85	0.96 ± 0.08
...	20151003	7299.045895660	7.12	0.66 [†]
...	20151027	7322.865231574	-23.31	0.48	35.76	0.27	1.04 ± 0.06
...	20151031	7327.039266404	-18.94	0.69	31.42	0.89	0.95 ± 0.06
...	20151128	7354.992645023	-20.65	0.69	35.37	0.66	0.94 ± 0.06
...	20151129	7355.949031859	-23.24	0.73	37.07	0.63	0.88 ± 0.07
...	20151221	7377.834221745	19.73	0.37	-10.39	0.37	0.92 ± 0.05
...	20151224	7380.724124841	4.67	0.44 [†]
...	20151229	7385.918133654	-14.21	0.47	27.51	0.43	0.96 ± 0.04
MHO 9	20151027	7322.900583908	-7.19	2.52	32.12	4.41	0.75 ± 0.17
...	20151221	7377.788149023	10.23	1.83
...	20151224	7380.878626538	12.64	2.21
...	20151229	7385.786528022	14.72	2.05	-21.85	5.13	0.39 ± 0.12
...	20160124	7411.775413410	-0.67	1.63
AK II 465	20151027	7323.164355309	57.18	0.59	0.25	0.52	0.76 ± 0.09
...	20151221	7377.933238088	-27.34	0.84	73.68	0.57	0.75 ± 0.12
...	20151224	7381.023604991	97.07	0.72	-35.90	0.38	0.70 ± 0.10
...	20151229	7385.935177983	-28.34	0.53	77.19	0.52	0.76 ± 0.11
HD 23642*	20151224	7381.026716140	-90.44	4.58	147.75	3.30	...

Note: Quoted radial velocities are weighted means across several spectral orders within a single epoch, with each measurement weighted inversely to the variance. The uncertainties used in the orbital parameter fitting procedure are the root-mean-square errors between individual measurements. The final column lists flux ratios, measured from the relative peak heights in the cross-correlation functions. [†]In the orbit fitting of HCG 76 we used an *ad hoc* uncertainty of 3 km s⁻¹ for the 20151003 and 20151224 epochs, believing the formal values in the table to be an underestimate due to the small velocity separation between components relative to the spectrograph resolution. *Though we report a single epoch of RVs here for HD 23642 we did not include these measurements in the analysis that follows. The data are consistent with our solution, however.

and adopting the RV from Nidever et al. (2002); GJ 105B was used as a secondary standard. For the earlier type stars, a suite of GK-type reference stars from Nidever et al. (2002) was used. The derived radial velocities and measured flux ratios are listed in Table 8.2.

4.3 Analysis

Our analysis consists of measuring or estimating properties of the primary star in each EB, and fitting the combined photometric and RV time-series data in order to derive the properties of the secondaries. Here we briefly describe some of the general analysis methods that were used in common to all EB systems. Individualized analysis for specific EBs appears below.

4.3.1 Estimation of Primary Star Properties

We determine the absolute V and K_s magnitudes from the measured or adopted apparent magnitudes and colors (see Section 4.2.2) using bolometric corrections from Pecaut & Mamajek (2013), assuming a distance of 136.2 pc for the Pleiades (Melis et al., 2014) and ~ 45 pc for the Hyades (Perryman et al., 1998; de Bruijne et al., 2001). Effective temperatures are estimated from the adopted $V - K_s$ colors (see Section 4.2.2) using the following relations, derived empirically by fitting polynomials to color and temperature data from Pecaut & Mamajek (2013), valid for $0.3 < V - K_s < 7.0$:

$$T_{\text{eff}}[\text{K}] = \frac{5000.0}{\Theta}, \quad (4.1)$$

where

$$\begin{aligned} \Theta = & 0.51903 + 0.24918(V - K_s) - 0.02160(V - K_s)^2 \\ & + 0.00415(V - K_s)^3 - 0.000359(V - K_s)^4. \end{aligned} \quad (4.2)$$

Radii of the primary stars can then be estimated using the Stefan-Boltzman law, adopting $T_{\text{eff},\odot} = 5770$ K.

Masses of the primary stars can be estimated from empirical relations. For the lowest mass stars with $V - K > 4.0$, we adopt the relation derived by Delfosse et al. (2000) for $4.0 < V - K < 7.0$:

$$\begin{aligned} \log(M/M_{\odot}) = & 0.001 \times [7.4 + 17.61(V - K_s) + 33.216(V - K_s)^2 + 34.222(V - K_s)^3 \\ & - 27.1986(V - K_s)^4 + 4.94747(V - K_s)^5 - 0.27454(V - K_s)^6]. \end{aligned} \quad (4.3)$$

Note that these estimates are approximations only. These empirical relations are nominal for main sequence stars with solar metallicity. The Hyades is slightly metal rich and the Pleiades, although essentially at solar metallicity, is still pre-main sequence at the lowest stellar masses.

4.3.2 Light Curve Modeling

Modeling of the EB light curves was performed with the publicly available code JKTEBOP³ (Southworth, 2013, and references therein). JKTEBOP is based on the Eclipsing Binary Orbit Program (Popper & Etzel, 1981; Etzel, 1981), which relies

³<http://www.astro.keele.ac.uk/jkt/codes/jktebop.html>

on the Nelson-Davis-Etzel biaxial ellipsoidal model for well-detached EBs (Nelson & Davis, 1972; Etzel, 1975). JKTEBOP models the two components as biaxial spheroids for the calculation of the reflection and ellipsoidal effects, and as spheres for the eclipse shapes. JKTEBOP finds the best-fit model to a light curve through Levenberg-Marquardt (L-M) optimization. Robust statistical errors on the best-fit model parameters are then found through repeated Monte Carlo (MC) simulations in which Gaussian white noise commensurate to the observational errors is added to the best-fit model. A new L-M fit is performed on the perturbed best-fit model and the new parameters are saved as links in the MC chain. The final orbital parameters for each system are then given by the original L-M best-fit, with uncertainties given by the standard deviations determined from the MC parameter distributions.

All modeling in this work took into account the effect of the ≈ 30 min *Kepler K2* cadence by numerically integrating model light curves at ten points in a total time interval of 1766 seconds, corresponding to the integration time of Kepler long cadence data.

4.4 Results

4.4.1 HCG 76

HCG 76 (V 612 Tau, EPIC 210974364) was first identified as a probable Pleiades member, and given the HCG designation, when it was detected as a flare star (Haro et al., 1982). In a proper motion membership study of HCG stars, Stauffer et al. (1991) found HCG 76 to have a membership probability of 90%. Subsequent proper motion surveys of the Pleiades re-identified HCG 76 as a member and provided the alternate designations of HHJ 294 and DH 224 (Hambly et al., 1993; Deacon & Hambly, 2004). The spectral type estimate based on colors is $\sim M3$.

The *K2* light curve (Fig. 4.3) used in our analysis was corrected for systematics from the raw SAP flux using the algorithm described in Aigrain et al. (2015). The light curve is characterized by a beating spot pattern, likely due to the different rotation periods of the primary and secondary. A Lomb-Scargle periodogram analysis on the systematics-corrected photometry identifies significant periodicity at 1.524 ± 0.028 d and 1.978 ± 0.051 d (see Fig. 4.4). In each case, the rotational period uncertainty has been coarsely approximated from the full width at half maximum (FWHM) of the corresponding periodogram peak. The variability was then iteratively fit with a cubic B-spline, using breakpoints every 12 cadences or ~ 6 hr, and $2\text{-}\sigma$ low or $4\text{-}\sigma$ high outlier exclusion upon each iteration, using the method described in David

et al. (2016b).

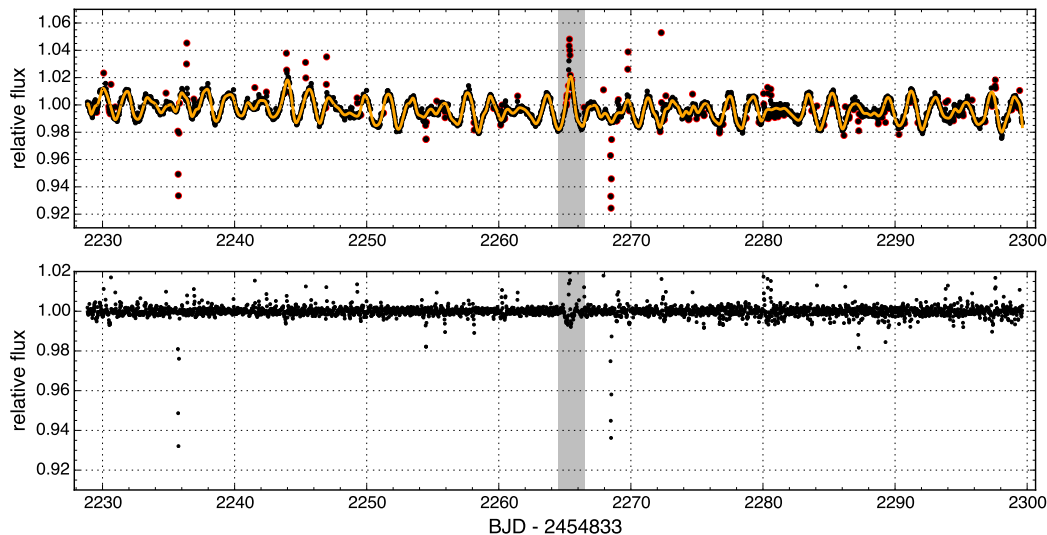


Figure 4.3: Top panel: The systematics corrected *K2* light curve for HCG 76 with our variability fit indicated by the orange curve. Outlier points excluded from this fit are marked by the red circles. Bottom panel: The rectified light curve, from dividing out the variability fit above, upon which we performed our fitting procedure. In both panels the gray shaded region highlights a portion of the light curve that is poorly modeled by the variability fit, leading to the introduction of systematics in the rectified light curve.

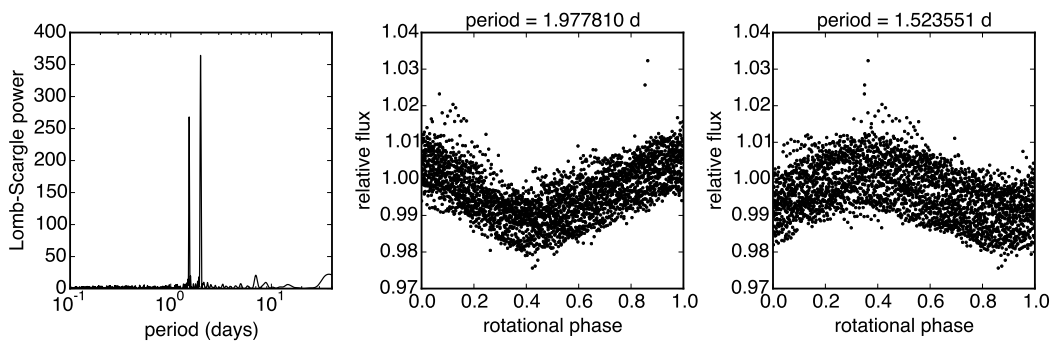


Figure 4.4: Lomb-Scargle periodogram of the variable light curve for HCG 76 (left) and the *K2* light curve for the object phase folded on the two strong rotational periods detected in the periodogram (middle and right panels). Outliers (both flares and eclipses) have been removed from the light curves in these figures for the purposes of illustrating the sinusoidal rotation signals.

The light curve shows two primary eclipses with depth $\sim 7\%$, plus two secondary eclipses with depth $\sim 2\%$ slightly offset from phase = 0.5. The eclipses are of short duration, with only a few points in eclipse. Due to these factors, a periodogram analysis fails; the initial period estimate by eye is ≈ 33 d and that from the orbital fit below is 32.7 d.

The corrected *K2* light curve and follow-up Keck/HIRES RVs (Table 8.2) were used to determine a best-fit JKTEBOP model of the system. We assumed a linear limb darkening law with coefficient $u=0.6$ for each component, though because the eclipses are only partial and the ingress and egress are sparsely sampled, limb darkening cannot be strongly constrained with current data. Table 4.5 lists the best-fit parameters from the model shown in Fig. 4.5. The uncertainty in the ratio of the radii is large, despite the spectroscopic light ratio constraints imposed, due to the fact that the eclipses are grazing and e and ω are currently poorly constrained. Additional RVs covering the first half of the orbit, as well as high cadence photometry of the eclipses to fill out the light curve, will help to further constrain the masses and radii of this system.

The Monte Carlo distributions in mass and radius for the binary components include solutions for which the system is highly non-coeval, with the less massive component falling below the main sequence of solar metallicity BHAC15 models. This tail of physically implausible solutions could be cleanly separated from the densely populated and more likely region of parameter space by considering only those solutions with $R_1/R_2 < 1.4$. Excluding the implausible solutions, we obtain $\lesssim 4.5\%$ precision in the component radii. Specifically, we find $M_1 = 0.3019 \pm 0.0070 M_\odot$, $M_2 = 0.2767 \pm 0.0068 M_\odot$, $R_1 = 0.341 \pm 0.016 R_\odot$, and $R_2 = 0.319 \pm 0.013 R_\odot$. In Table 4.5, we thus report all relevant parameter values both including and excluding these implausible solutions. Notably, the dynamical masses are $\sim 30\%$ larger than the value predicted by the combined light $V - K_s$ color and the Delfosse et al. (2000) relation presented in § 4.3.1. The mass- K_s relation for M-dwarfs presented in Mann et al., 2015 is slightly more consistent with our dynamical masses, predicting a mass that is $\sim 10\text{-}20\%$ smaller than our fundamental values, after correcting the absolute K_s magnitude for binarity. We note that the Mann et al. (2015) relation was derived for main-sequence stars, while HCG 76 is still pre-main-sequence and thus more luminous compared to their MS counterparts.

In Figures 4.6 and 4.7 we compare the JKTEBOP derived parameters for this system with solar metallicity ($Z=0.02$) Baraffe et al. (2015) evolutionary models, hereafter BHAC15. Figure 4.6 shows that the components are similar in mass and are both consistent with the slope of the isochrones in the mass-radius and temperature-gravity planes, but preferring a slightly younger age than 120 Myr as suggested by Dahm (2015). The component ages derived using the `griddata` routine in PYTHON are $\tau_1 = 106_{-13}^{+18}$ Myr and $\tau_2 = 102_{-22}^{+24}$ Myr, where the median and 68% confidence

intervals are quoted. The two stars are thus consistent with being coeval within the uncertainties. A more precise system age can be determined using the assumption of coevality from the product of the two age distribution functions. The resulting system age is $\tau=103_{-10}^{+7}$ Myr. If we again assume coevality and age-date the system in the $T_{\text{eff}}\text{-log } g$ plane, we find a mode age of 93 Myr, with a median and 68% confidence interval of 102_{-14}^{+112} Myr. The long tail towards older ages is due to the clustering of isochrones towards the main sequence.

Figure 4.7 illustrates inconsistencies between the observations and the BHAC15 models; specifically, at a fixed age, the models are unable to simultaneously reproduce mass, radius, T_{eff} , and luminosity. We suggest that these discrepancies can be largely resolved, at least in this narrow mass range, by shifting the models by 200 K towards cooler temperatures. It is possible that the models are incorrectly predicting T_{eff} , or that there is a systematic offset in the adopted empirical color- T_{eff} or spectral type- T_{eff} conversions, or some combination of both effects. Such a temperature shift would likewise improve the agreement among the panels in Figure 4.6.

Finally, we can use the highly precise stellar parameters that we have determined for HCG 76 to make an independent measurement of the distance to the Pleiades. We used the broadband catalog photometry assembled by Sarro et al. (2014) and supplemented these with the available WISE photometry. In total, the observed broadband spectral energy distribution (SED) spans a wavelength range of 0.35–12 μm . The SED was fit by the sum of two NextGen stellar atmosphere models (Hauschildt et al., 1999a) of solar metallicity, interpolated to the respective HCG 76 component T_{eff} and $\log g$, and scaled by the respective radii squared. We adopted the canonical Pleiades extinction of $A_V = 0.12$. We varied the component T_{eff} 's and radii within their uncertainties (Table 4.5) but enforcing the directly measured T_{eff} ratio and sum of radii. The observed u -band flux exhibits a strong excess over the nominal SED, not surprising considering the identification of HCG 76 as an active flaring star (Kazarovets, 1993). Excluding the u -band flux, the resulting SED fit is excellent, with reduced χ^2 of 2.4. The corresponding distance is 132 ± 5 pc, consistent with most recent determinations of the Pleiades distance (see Table 8 in Southworth et al., 2005) including their results on the massive Pleiades EB HD 23642 that is also discussed below, and the VLBI distance to a different Pleiades member of 136.2 ± 1.2 pc (Melis et al., 2014).

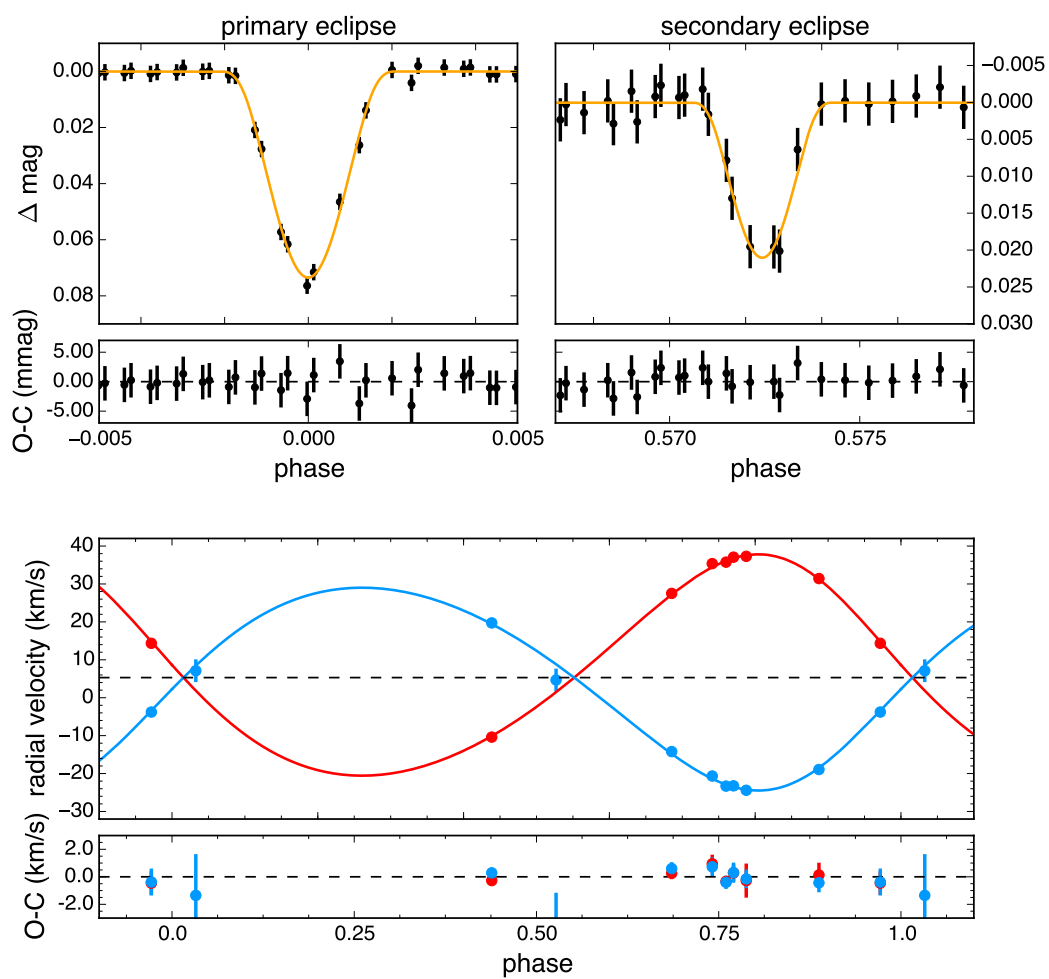


Figure 4.5: Best-fit JKTEBOP model to the *K2* photometry (top) and Keck/HIRES RVs (bottom) for HCG 76.

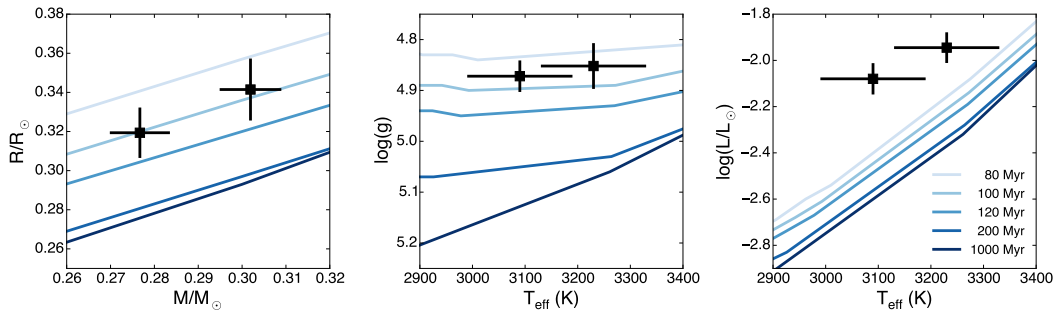


Figure 4.6: The positions of HCG 76 components relative to BHAC15 isochrones in the mass-radius plane (left), $T_{\text{eff}} - \log g$ plane (middle), and $T_{\text{eff}} - \log L/L_{\odot}$ plane (right). Square points represent best-fit values and errorbars indicate 1- σ uncertainties. We assumed 100 K uncertainties in the temperatures and propagated these through in determining the luminosity uncertainties. The two components are consistent within error of being coeval in the mass-radius plane at ~ 100 Myr, though they appear younger in the $T_{\text{eff}} - \log g$ plane. The luminosities calculated from the Stefan-Boltzmann law, the measured radii, and photometric temperatures, are significantly larger than the model predictions.

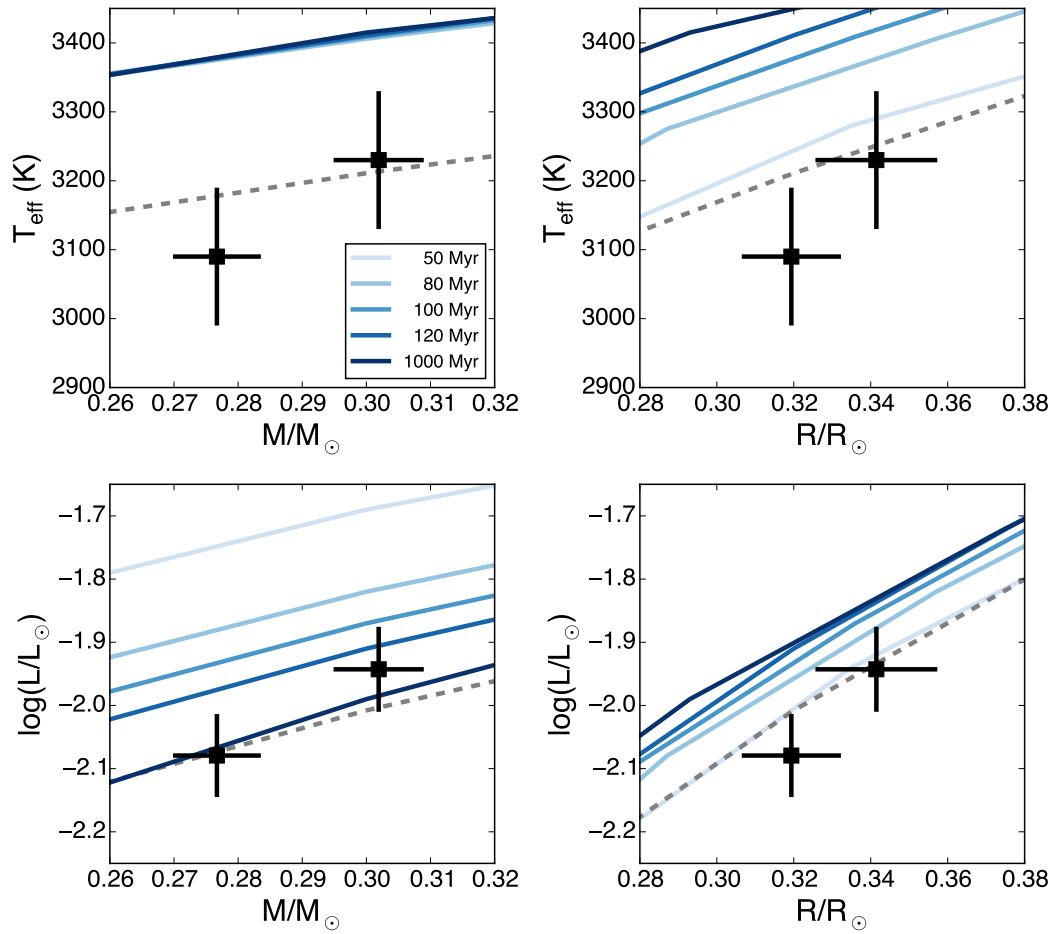


Figure 4.7: BHAC15 isochrones in the mass-temperature, radius-temperature, mass-luminosity, and radius-luminosity planes (clockwise from upper left panel) compared to the derived parameters for the HCG 76 components. In each panel, the dashed line indicates the 120 Myr isochrone shifted by 200 K towards cooler effective temperatures (or the luminosities resulting from such a shift).

Table 4.5: System Parameters of HCG 76

Parameter	Symbol	JKTEBOP Value	Adopted Value	Units
Orbital period	P	32.7470 ± 0.0013	32.7470 ± 0.0013	days
Ephemeris timebase - 2457000	T_0	68.7480 ± 0.0010	68.748 ± 0.0010	BJD
Surface brightness ratio	J	0.84 ± 0.34	0.84 ± 0.12	
Sum of fractional radii	$(R_1 + R_2)/a$	0.0184 ± 0.0022	0.01842 ± 0.00050	
Ratio of radii	k	0.93 ± 0.23	0.938 ± 0.065	
Orbital inclination	i	89.13 ± 0.17	89.126 ± 0.029	deg
Combined eccentricity, periastron longitude	$e \cos \omega$	0.1138 ± 0.0040	0.1137 ± 0.0011	
Combined eccentricity, periastron longitude	$e \sin \omega$	0.0682 ± 0.0087	0.0681 ± 0.0085	
Primary radial velocity amplitude	K_1	26.75 ± 0.31	26.75 ± 0.30	km s^{-1}
Secondary radial velocity amplitude	K_2	29.19 ± 0.30	29.19 ± 0.29	km s^{-1}
Systemic radial velocity	γ	5.31 ± 0.17	5.31 ± 0.17	km s^{-1}
Fractional radius of primary	R_1/a	0.0095 ± 0.0030	0.00952 ± 0.00047	
Fractional radius of secondary	R_2/a	0.00890 ± 0.00099	0.00890 ± 0.00033	
Luminosity ratio	L_2/L_1	0.950 ± 0.022	0.951 ± 0.022	
Eccentricity	e	0.1326 ± 0.0049	0.1328 ± 0.0043	
Periastron longitude	ω	30.9 ± 3.7	30.8 ± 3.2	deg
Impact parameter of primary eclipse	b_1	1.80 ± 0.65	1.807 ± 0.068	
Impact parameter of secondary eclipse	b_2	1.57 ± 0.58	1.577 ± 0.077	
Orbital semi-major axis	a	35.88 ± 0.29	35.88 ± 0.27	R_\odot
Mass ratio	q	0.917 ± 0.013	0.917 ± 0.013	
Primary mass	M_1	0.3020 ± 0.0073	0.3019 ± 0.0070	M_\odot
Secondary mass	M_2	0.2768 ± 0.0072	0.2767 ± 0.0068	M_\odot
Primary radius	R_1	0.34 ± 0.11	0.341 ± 0.016	R_\odot
Secondary radius	R_2	0.319 ± 0.036	0.319 ± 0.013	R_\odot
Primary surface gravity	$\log g_1$	4.85 ± 0.22	4.852 ± 0.045	cgs
Secondary surface gravity	$\log g_2$	4.87 ± 0.11	4.872 ± 0.031	cgs
Primary mean density	ρ_1	7.7 ± 3.2	7.7 ± 1.3	ρ_\odot

Table 4.5 Continued: HCG 76

Parameter	Symbol	JKTEBOP Value	Adopted Value	Units
Secondary mean density	ρ_2	8.5 ± 4.4	8.56 ± 0.95	ρ_\odot
Temperature ratio	T_2/T_1	0.957 ± 0.099	0.957 ± 0.034	
Primary temperature	T_1	...	3230 ± 100	K
Secondary temperature	T_2	...	3090 ± 100	K
Reduced chi-squared of light curve fit	χ_{red}^2	0.412	...	
RMS of best fit light curve residuals		1.627	...	mmag
Reduced chi-squared of primary RV fit	χ_{red}^2	0.007	...	
RMS of primary RV residuals		0.438	...	km s ⁻¹
Reduced chi-squared of secondary RV fit	χ_{red}^2	0.025	...	
RMS of secondary RV residuals		1.439	...	km s ⁻¹

Note: The JKTEBOP best-fit orbital parameters and 1- σ uncertainties result from 5,000 Monte Carlo simulations. The primary temperature is calculated from the $V - K_s$ color, as described in § 4.3.1. The adopted value column indicates the mean and 1- σ errors of the Monte Carlo parameter distributions after excluding those physically implausible solutions with $R_1/R_2 > 1.4$. See § 4.4.1 for details.

4.4.2 MHO 9 (BPL 116)

MHO 9 (BPL 116, EPIC 211075914) was first identified as a candidate Pleiades member of very low mass in Stauffer et al. (1998), based on V and I photometry obtained with the Mt. Hopkins 48" telescope, and on proper motion consistent with the Pleiades derived from UK Schmidt plates⁴. An independent combined photometric (I Z) and proper motion survey also identified it as a probable very low mass Pleiades member, under the designation BPL 116 (Pinfield et al., 2000). The star was later confirmed as a Pleiades proper motion member by Deacon & Hambly (2004). The spectral type estimate based on colors is \sim M4.5.

The detrended $K2$ light curve exhibits periodic, low amplitude undulations, which we interpret as due to spot rotation with a single period of $P_{\text{rot}} = 0.2396 \pm 0.0008$ d (see Fig. 4.9). The uncertainty in P_{rot} has been coarsely approximated from the FWHM of the Lomb-Scargle periodogram peak.

The Keck/HIRES spectrum reveals a double-lined system with the individual RVs reported in Table 8.2. The rotational velocity can be estimated by broadening standard star templates that are then added together with the measured RV difference and the inferred flux ratio from the cross correlation analysis. The resulting estimate of $v \sin i \approx 42 \pm 1 \text{ km s}^{-1}$ assumes that the two components of the binary have the same projected velocity, as the lines are close enough together that it is not possible to fit separately for each component. Combining this $v \sin i$ estimate with our P_{rot} estimate above, and assuming the rotational axis of the primary is perpendicular to our line-of-sight, we arrive at an approximation of $R_1 \approx 0.199 \pm 0.005 R_{\odot}$ for the primary radius, where the uncertainty is the formal statistical error.

The $K2$ light curve exhibits a single primary eclipse (at BJD 2457099 with a depth of $\sim 24\%$), and two shallow events of similar widths and shapes (at BJD 2457070 and 2457113 with depths of $\sim 5\%$). Assuming that these two events are both secondary events of the same system, then we can determine the period to be ~ 42.8 d (see Fig. 4.10). Note that all of the following analysis depends upon this assumption; further follow-up is necessary to confirm both the period of this system and the presence of these shallow secondary events.

From the phase separation between the primary and secondary eclipses, we can constrain the value for $e \cos \omega$ to be approximately -0.29 . The durations of the

⁴We caution the reader that there is another star in Taurus with the designation MHO 9, not to be confused with the Pleiades EB discussed here. Identified in Briceño et al. (1998), that star is a pre-MS weak-lined T-Tauri star, also of moderately late M type.

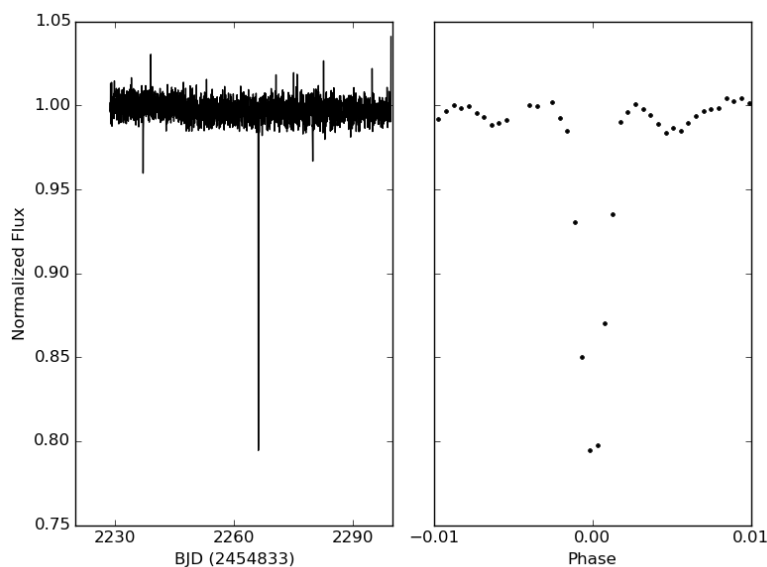


Figure 4.8: Detrended normalized light curve for MHO 9 (BPL 116). The full unphased light curve is shown on the left with the phased light curve zoomed in on the primary eclipse shown on the right.

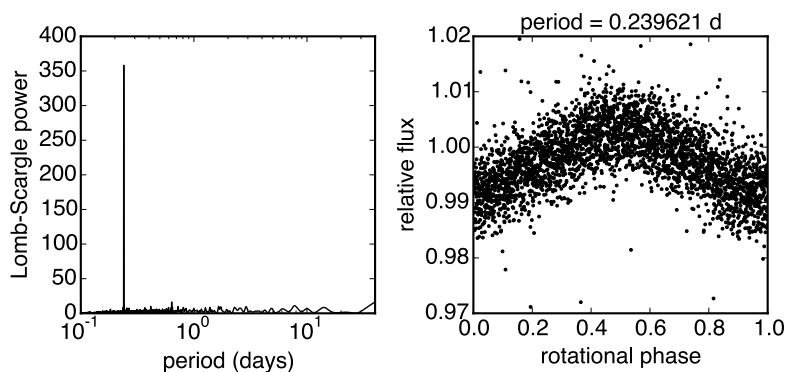


Figure 4.9: Lomb-Scargle periodogram for the systematics corrected light curve of MHO 9 (left), phased at the inferred rotation period (right). Eclipses are excluded in the scaling of this figure for clarity.

eclipses can be measured only approximately given the single primary event and poor signal-to-noise. However, doing so yields a constraint on $e \sin \omega$ and gives an estimate for eccentricity ($e \sim 0.29$) and argument of periastron ($\omega \sim 3.2$).

We used JKTEBOP to fit the *K2* photometry and all RV measurements. For two epochs, the velocity separation between components was small enough that two peaks were not distinguishable in the CCF. In such cases, we take the derived velocity to be the RV of the primary and do not include any secondary velocities in the RV fitting procedure. We assumed a linear limb darkening law with coefficient $u=0.6$ for each

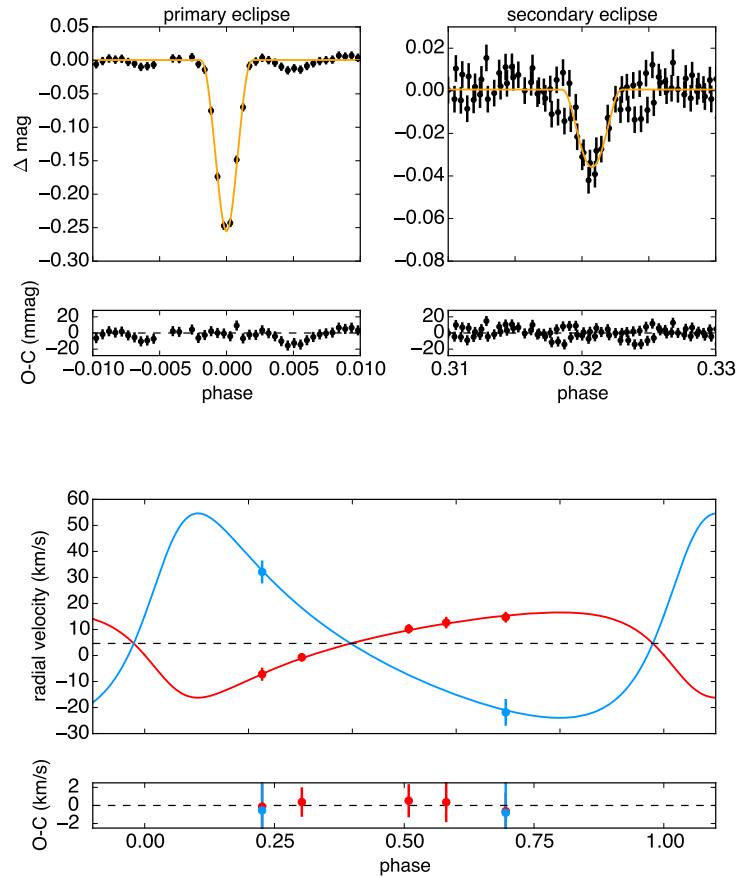


Figure 4.10: JKTEBOP fit to the *K2* light curve and RVs for MHO 9. The RV point near phase of 0.3 (corresponding to the UT 2016-01-24 observation) was not included in this analysis but is entirely consistent with our best fit.

component, though because the eclipses are only partial and the ingress and egress are sparsely sampled, limb darkening can not be strongly constrained with current data. The resulting physical parameters are summarized in Table 4.6 and the best-fit model shown in Figure 4.10.

We note that there is an apparent discrepancy between the positions of MHO 9 relative to HCG 76 in the color-magnitude diagram compared to the positions of these objects in the mass-radius diagram; while the nearly identical components of HCG 76 occupy a position of higher mass in the $(V - K_s)$ - V diagram (see Fig. 4.2), the primary of MHO 9 appears to be more massive than either of the components of HCG 76 in the mass-radius diagram (see Fig. 4.18). Furthermore, the components of MHO 9 appear younger (i.e. larger) in the mass-radius diagram.

We do not have a satisfactory explanation for this, though we do note that substantial uncertainties remain in the masses and radii for the MHO 9 system, owing to incom-

plete phase coverage in the RV curves, difficulties in extracting the secondary RVs due to small velocity separations relative to the spectrograph resolution, and only a single primary eclipse and two presumed secondary eclipses in the *K2* photometry due to the long period of the system. Thus, within these large uncertainties the system is consistent with Pleiades age in the mass-radius diagram, and the primary is still possibly less massive than either of the components of HCG 76 at one end of its uncertainty range, and the secondary is possibly quite close to the hydrogen-burning limit (as shown in Fig. 4.18). However, an alternate solution that forces the fit to produce a primary mass for MHO 9 that is lower than the primary mass for HCG 76 yields masses for MHO 9 of $M_1, M_2 = 0.26, 0.12 M_\odot$ with $\sim 20\text{-}25\%$ uncertainty, and radii of $R_1 = 0.37, 0.29 R_\odot$ with $\sim 15\%$ uncertainty.

4.4.3 HD 23642

HD 23642 (HII 1431, EPIC 211082420) is a known double-lined EB that has been well characterized in the literature, and in fact has been used to provide highly precise distances to the Pleiades (e.g. Munari et al., 2004; Southworth et al., 2005; Groenewegen et al., 2007). The system was first noted to be a double-lined spectroscopic binary by Pearce (1957) and was discovered to be eclipsing by Torres (2003) from Hipparcos epoch photometry. The primary spectral type from Abt & Levato (1978) is A0vp(Si)+Am. Though high quality ground-based photometric time series exist for this system, *K2* has delivered the most extensive (covering 29 complete orbital phases) and precise light curve to date, despite being clearly saturated on the detector. With a period of $P \approx 2.46$ d, the system clearly exhibits ellipsoidal modulation and reflection effects in the raw *K2* photometry.

We used JKTEBOP to mutually fit the new *K2* photometry and literature radial velocities, providing direct determinations of the masses and radii. The photometry used for this purpose was the PDC SAP flux from the publicly available files on MAST. No additional treatment of the light curve was performed for this analysis. The 6.5-hr pseudo-CDPP⁵ (combined differential photometric precision) across the entire light curve was taken as the constant observational error for each measurement. RVs were adopted from Munari et al. (2004) and Groenewegen et al. (2007). The Groenewegen et al. (2007) RVs in their Table 2 are *relative to systemic*, so to each measurement we added the final best-fit systemic RV from the PHOEBE fit presented in their Table 5. Additional RVs for this system exist in Pearce (1957) and Abt (1958), but were excluded here due to their lower precision, following

⁵See Aigrain et al. (2015) for a detailed definition of the pseudo-CDPP.

Table 4.6: System Parameters of MHO 9 (BPL 116)

Parameter	Symbol	JKTEBOP Value	Units
Orbital period	P	42.80 (fixed)	days
Ephemeris timebase - 2454833	T_0	2266.21943 ± 0.00064	BJD
Surface brightness ratio	J	1.04 ± 0.42	
Sum of fractional radii	$(R_1 + R_2)/a$	0.0181 ± 0.0011	
Ratio of radii	k	0.70 ± 0.20	
Orbital inclination	i	89.278 ± 0.094	deg
Combined eccentricity, periastron longitude	$e \cos \omega$	-0.272 ± 0.019	
Combined eccentricity, periastron longitude	$e \sin \omega$	0.302 ± 0.083	
Primary radial velocity amplitude	K_1	16.4 ± 3.0	km s^{-1}
Secondary radial velocity amplitude	K_2	39.3 ± 6.8	km s^{-1}
Systemic radial velocity	γ	4.6 ± 1.3	km s^{-1}
Fractional radius of primary	R_1/a	0.0106 ± 0.0016	
Fractional radius of secondary	R_2/a	0.00746 ± 0.00095	
Luminosity ratio	L_2/L_1	0.510 ± 0.097	
Eccentricity	e	0.406 ± 0.056	
Periastron longitude	ω	132.0 ± 9.8	deg
Impact parameter of primary eclipse	b_1	0.76 ± 0.26	
Impact parameter of secondary eclipse	b_2	1.41 ± 0.28	
Orbital semi-major axis	a	43.0 ± 5.7	R_\odot
Mass ratio	q	0.417 ± 0.075	
Primary mass	M_1	0.41 ± 0.18	M_\odot
Secondary mass	M_2	0.172 ± 0.069	M_\odot
Primary radius	R_1	0.46 ± 0.11	R_\odot
Secondary radius	R_2	0.321 ± 0.060	R_\odot
Primary surface gravity	$\log g_1$	4.73 ± 0.12	cgs
Secondary surface gravity	$\log g_2$	4.66 ± 0.14	cgs
Primary mean density	ρ_1	4.3 ± 2.4	ρ_\odot
Secondary mean density	ρ_2	5.2 ± 1.6	ρ_\odot
Temperature ratio	T_2/T_1	1.01 ± 0.10	
Primary temperature	T_1	2970	K
Secondary temperature	T_2	3000	K
Reduced chi-squared of light curve fit	χ_{red}^2	1.038	
RMS of best fit light curve residuals		6.320	mmag
RMS of primary RV residuals		0.451	km s^{-1}
RMS of secondary RV residuals		0.693	km s^{-1}

Note: The JKTEBOP best-fit orbital parameters and $1\text{-}\sigma$ uncertainties result from 1,000 Monte Carlo simulations. The primary temperature is calculated from the $V - K_s$ color, as described in § 4.3.1.

Southworth et al. (2005).

In order to better constrain the ratio of radii, we imposed the following light ratio: $l_2/l_1 = 0.354 \pm 0.035$. We calculated this light ratio for the *Kepler* bandpass by convolving the *Kepler* throughput curve⁶ with ATLAS9 model atmospheres of temperatures $T_1 = 9750$ K, $T_2 = 7600$ K (Southworth et al., 2005), $\log g = 4.5$ dex, $Z=0$, and scaling the flux ratio to equal the Torres (2003) value of $l_2/l_1 = 0.31 \pm 0.03$ for a 45 \AA window centered on 5187 \AA . The uncertainty in our light ratio comes from assuming that the 10% error measured by Torres (2003) is preserved when we

⁶The *Kepler* response function is available at http://keplergo.arc.nasa.gov/kepler_response_hires1.txt

calculated our synthetic value from model atmospheres.

We hold the eccentricity fixed at zero in our fit, consistent with prior studies of this system and with expectations of the tidal circularization timescale compared to the system age. The mass ratio used by JKTEBOP to calculate the out-of-eclipse variability due to ellipsoidal modulation was held fixed at the spectroscopic value obtained from an initial fit of the RVs, $q = 0.7030$. As also noted by Southworth et al. (2005), inclusion of the reflection effect was required to obtain a good fit in the out-of-eclipse portions of the light curve. Initial estimates for the primary and secondary reflection coefficients were found by manually adjusting these parameters in the initial fitting stages until an acceptable fit was found. The reflection coefficients were then left as free parameters in the final fit. As prior authors have done, we fixed the gravity darkening exponent, β , to 1 for each component. This value is expected for such hot stars with radiative envelopes, but we note that our final solution favors oblateness values very close to zero (i.e., consistent with spherical stars) which is also supported by the modest $v \sin i$ values ($< 40 \text{ km s}^{-1}$) measured for both components.

A linear limb darkening law for both components was assumed, and we allowed the limb darkening coefficient, u , to be a free parameter for both stars, using appropriate values from Claret & Bloemen (2011) as initial estimates. Prior authors have not been able to constrain limb darkening in this system due to lower fidelity ground-based light curves. To account for the relatively long integration time of the photometry compared to the orbital period, we numerically integrated the models at 10 points in 1766 second intervals, corresponding to the length of *Kepler* long cadence observations.

The best-fitting JKTEBOP model to the *K2* photometry and literature RVs are depicted in Figures 4.11–4.12 and the resulting parameters listed in Table 4.7. For comparison, in Table 4.8 we provide parameters from the literature for each study that has characterized this system in detail. We find masses for both components that are consistent with prior determinations in the literature. For the radii, we find a secondary radius that is consistent with the literature, but a primary radius that is $\sim 5\%$ smaller than previously reported values. Additionally, we find a temperature ratio that is higher than previous authors have found, though the absolute temperature of the secondary is consistent within error with prior determinations, assuming the primary temperature and uncertainty from Southworth et al. (2005).

While it is surprising to find a radius for the primary star that is so discrepant from

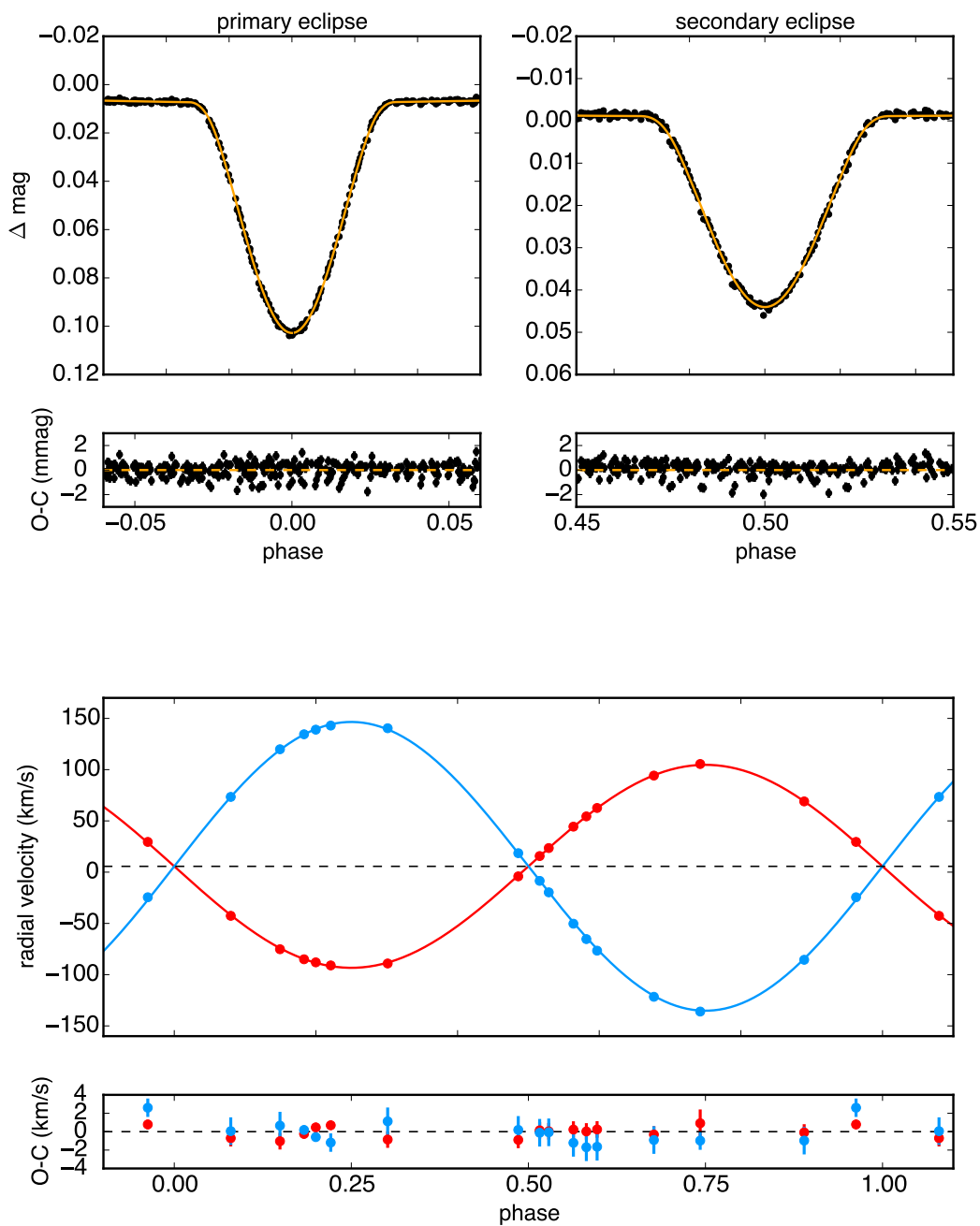


Figure 4.11: Top panels: *K2* PDC SAP light curve for HD 23642 phase folded on the orbital period of ≈ 2.46 days, with the best-fit JKTEBOP model plotted in orange. Bottom panel: Literature radial velocities from Munari et al. (2004) and Groenewegen et al. (2007) with the best-fit JKTEBOP models indicated by the red and blue curves. In each panel the best-fit residuals are plotted below.

prior determinations, we show in Fig. 4.13 that in this case the primary is much closer to the Pleiades age isochrone in the mass-radius plane when compared to the Bressan et al. (2012) PARSEC v1.2S isochrones assuming the recently revised

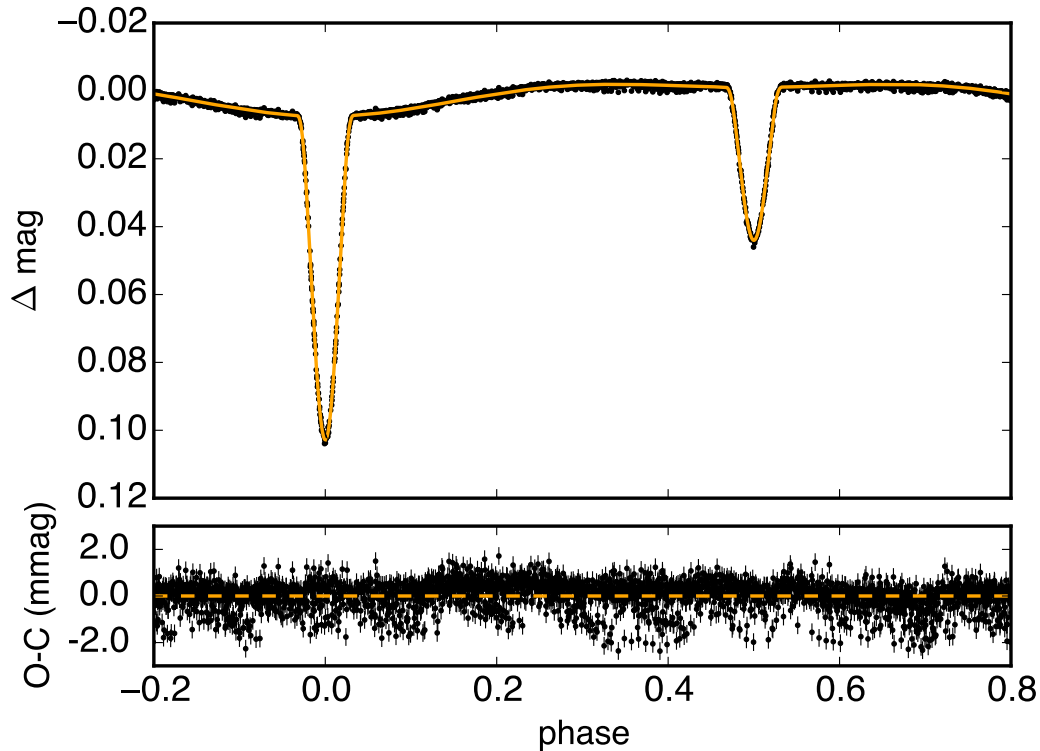


Figure 4.12: The complete *K2* light curve for HD 23642, phase folded on the best period and showing the best-fit JKTEBOP model in orange. The best fit residuals are plotted below.

solar metallicity ($Z_{\odot}=0.015$) of Caffau et al. (2011). In fact, the primary parameters are entirely consistent with the accepted Pleiades age in both planes. All prior determinations of the primary parameters suggest the star is roughly a factor of two or more older than Pleiades age using this metallicity value. We also note that the fractional uncertainties in our mass and radius determinations are $\sim 2\text{--}4\%$, which are consistent with Munari et al. (2004) and Southworth et al. (2005) but inconsistent with Groenewegen et al. (2007). We suggest these last authors likely underestimated their mass and radius uncertainties. In all determinations, there is a significant degree of apparent non-coevality between the primary and secondary components, but is greatly ameliorated with our updated parameters and the degree of which is also somewhat lessened by adopting super-solar metallicities.

The positions of these stars in the mass-radius plane relative to evolutionary models has been studied previously in Southworth et al. (2005). Those authors invoked super-solar metallicities ($0.02 < Z < 0.03$) to reconcile the large radii with the Pleiades age. Groenewegen et al. (2007) also made comparisons with evolutionary models, using a value of $[\text{Fe}/\text{H}]=+0.058$ dex. However, Soderblom et al. (2009)

measured the metallicity of the Pleiades from high-resolution echelle spectroscopy of 20 members, finding $[\text{Fe}/\text{H}] = +0.03 \pm 0.02 \pm 0.05$ dex (statistical and systematic errors quoted), which they compared to the average across previously published values of $[\text{Fe}/\text{H}] = +0.042 \pm 0.021$ dex. Thus, the evolution models employed by prior authors to demonstrate the positions of these stars relative to Pleiades age isochrones may have represented the metal rich end of the true Pleiades metallicity distribution.

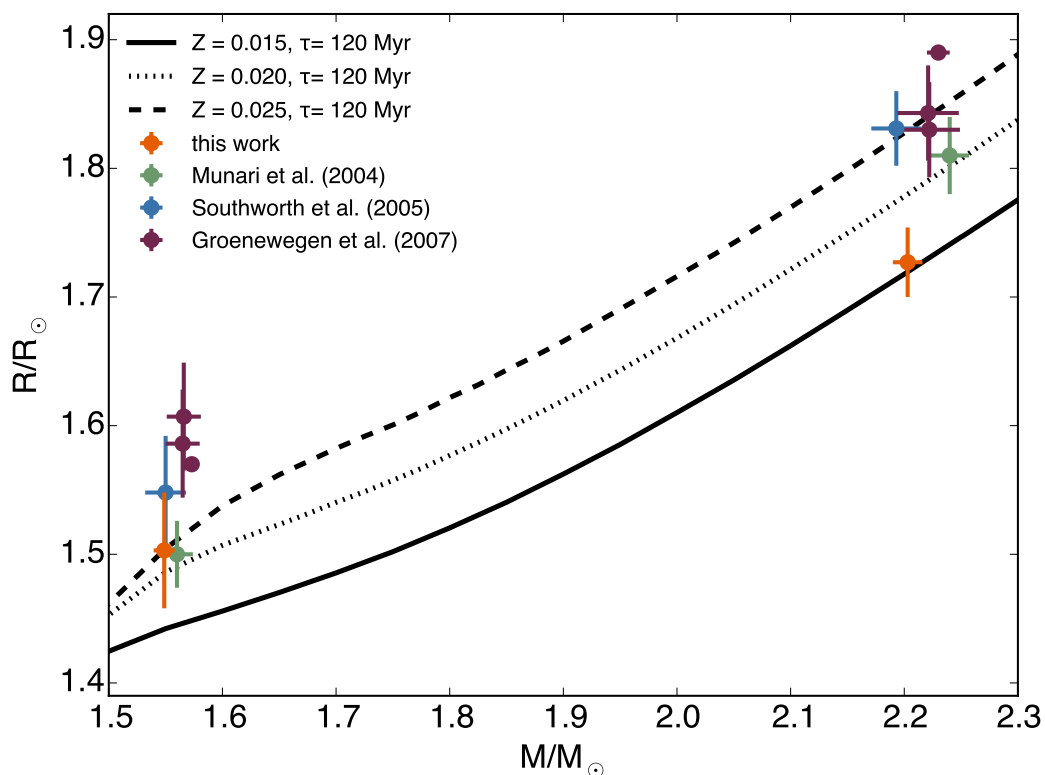


Figure 4.13: PARSEC v1.2S 120 Myr isochrones (Bressan et al., 2012; Chen et al., 2015) in the mass-radius plane, of different metallicities. Several direct determinations of the masses and radii of the double-lined EB HD 23642 from the literature are indicated, along with our new determinations from the highly precise *K2* light curve and literature RVs.

Table 4.7: System Parameters of HD 23642

Parameter	Symbol	ЖКТЕБОР Value	Units
Orbital period	P	$2.46113408 \pm 0.00000050$	days
Ephemeris timebase - 2457000	T_0	119.522070 ± 0.000021	BJD
Surface brightness ratio	J	0.4859 ± 0.0068	
Sum of fractional radii	$(R_1 + R_2)/a$	0.2712 ± 0.0014	
Ratio of radii	k	0.870 ± 0.039	
Orbital inclination	i	78.21 ± 0.11	deg
Primary limb darkening coefficient	u_1	0.412 ± 0.032	
Secondary limb darkening coefficient	u_2	0.510 ± 0.034	
Primary geometric reflection coefficient	r_1	0.00246 ± 0.00015	
Secondary geometric reflection coefficient	r_2	0.00648 ± 0.00015	
Primary radial velocity amplitude	K_1	99.02 ± 0.27	km s^{-1}
Secondary radial velocity amplitude	K_2	140.86 ± 0.36	km s^{-1}
Systemic radial velocity	γ	5.68 ± 0.16	km s^{-1}
Fractional radius of primary	R_1/a	0.1450 ± 0.0023	
Fractional radius of secondary	R_2/a	0.1262 ± 0.0037	
Luminosity ratio	L_2/L_1	0.355 ± 0.035	
Impact parameter of primary eclipse	b_1	1.409 ± 0.036	
Impact parameter of secondary eclipse	b_2	1.409 ± 0.036	
Orbital semi-major axis	a	11.915 ± 0.023	R_\odot
Mass ratio	q	0.7030 ± 0.0027	
Primary mass	M_1	2.203 ± 0.013	M_\odot
Secondary mass	M_2	1.5488 ± 0.0093	M_\odot
Primary radius	R_1	1.727 ± 0.027	R_\odot
Secondary radius	R_2	1.503 ± 0.045	R_\odot
Primary surface gravity	$\log g_1$	4.306 ± 0.014	cgs
Secondary surface gravity	$\log g_2$	4.274 ± 0.025	cgs
Primary mean density	ρ_1	0.427 ± 0.020	ρ_\odot
Secondary mean density	ρ_2	0.456 ± 0.040	ρ_\odot
Reduced chi-squared of light curve fit	χ_{red}^2	2.59	
RMS of best fit light curve residuals		0.61	mmag
Reduced chi-squared of primary RV fit	χ_{red}^2	0.63	
RMS of primary RV residuals		0.59	km s^{-1}
Reduced chi-squared of secondary RV fit	χ_{red}^2	0.95	
RMS of secondary RV residuals		1.12	km s^{-1}

Note: Best-fit orbital parameters and their uncertainties resulting from 1,000 Monte Carlo simulations with ЖКТЕБОР. For this fit the eccentricity was fixed at zero, and the gravity darkening exponents for both the primary and secondary were fixed at one.

Table 4.8: Parameters derived for HD 23642 from the literature

Parameter	Groenewegen et al. (2007)	Southworth et al. (2005)	Munari et al. (2004)	Torres (2003)
P (d)	$2.46113358 \pm 0.00000015$	fixed at M04 value	$2.46113400 \pm 0.00000034$	$2.46113329 \pm 0.00000066$
T_0 (HJD)	$2452903.60002 \pm 0.00014$	fixed at M04 value	2452903.5981 ± 0.0013	2436096.5204 ± 0.0040
γ (km s $^{-1}$)	5.39 ± 0.04	6.07 ± 0.39	5.17 ± 0.24	6.1 ± 1.7
q	0.7054 ± 0.0006	0.7068 ± 0.0050	0.6966 ± 0.0034	0.6934 ± 0.0077
i (deg)	76.63 ± 0.02	77.78 ± 0.17	78.10 ± 0.21	~ 78
a (R $_{\odot}$)	11.959 ± 0.0052	11.906 ± 0.041	11.956 ± 0.030	~ 11.82
e	0.0 (fixed)	0.0 (fixed)	0.0 ± 0.002	0 (fixed)
T_1 (K)	9950 (fixed)	9750 ± 250	9671 (fixed)	
T_2 (K)	7281 ± 9	7600 ± 400	7500 ± 61	
R_1 (R $_{\odot}$)	1.890 ± 0.003	1.831 ± 0.029	1.81 ± 0.030	
R_2 (R $_{\odot}$)	1.570 ± 0.003	1.548 ± 0.044	1.50 ± 0.026	
M_1 (M $_{\odot}$)	2.230 ± 0.010	2.193 ± 0.022	2.24 ± 0.017	
M_2 (M $_{\odot}$)	1.573 ± 0.002	1.550 ± 0.018	1.56 ± 0.014	
$\log g_1$ (cgs)	4.2331 ± 0.0024	4.254 ± 0.014	4.27 ± 0.015	
$\log g_2$ (cgs)	4.2426 ± 0.0018^a	4.249 ± 0.025	4.28 ± 0.016	

^a We calculated the surface gravity of the primary and secondary based on the masses and radii of the final fit from Groenewegen et al. (2007), as those authors did not report the values. The uncertainties come from Monte Carlo error propagation of the associated uncertainties in mass and radius.

4.4.4 HII 2407

HII 2407 (EPIC 211093684) is a recently recognized EB in the Pleiades, consisting of a K2 type primary and likely M-type secondary. The system was found to be a single-lined spectroscopic binary by Mermilliod et al. (1992). It was discovered as eclipsing in the *K2* data and has been recently analyzed and discussed in David et al. (2015). The *K2* light curve is suggestive of a radius ratio of 0.27 and a large ΔT_{eff} between the primary and secondary, consistent with the non-detection of secondary lines in optical spectra to date. Follow-up spectroscopy in the infrared, where the flux ratio between the primary and secondary is more favorable, is underway (L. Prato, private communication) and should allow for the unique determination of the masses and radii of this system.

4.4.5 AK II 465

The star AK II 465 (EPIC 210822691) is an EB with possible membership to the Pleiades. The star was first mentioned, and given the AK classification, in the Artiukhina & Kalinina (1970) proper motion survey of the Pleiades. Mermilliod et al. (1997) classified the source as a non-member based on two RV measurements separated by 1065 days, yielding a mean RV of $23.4 \pm 0.4 \text{ km s}^{-1}$, compared to the mean Pleiades systemic radial velocity of $\sim 5 \text{ km s}^{-1}$. Mermilliod et al. (2009) again asserted non-membership based on the same data, and additionally provided a $v \sin i$ measurement of $3.9 \pm 1.9 \text{ km s}^{-1}$. However, given the binary nature of this system and short orbital period implied by the *K2* light curve, two epochs may not be enough to invalidate membership on the basis of mean RV alone. The source is not discussed elsewhere in the literature.

Proper motion measurements for this source are inconsistent with Pleiades membership, as detailed in Table 4.9. For reference, the Pleiades mean proper motion is $\mu_{\alpha}, \mu_{\delta} = 20.10, -45.39 \text{ mas yr}^{-1}$ (van Leeuwen, 2009). In particular, Bouy et al. (2015) assigned membership probabilities to the source of $\lesssim 1\%$ based on the proper motions measured from either DANCe or Tycho-2 data sets. In addition, in a V versus $V - K$ CMD the source falls slightly below the Pleiades single star main sequence. The primary and secondary eclipse depths are similar, suggesting a temperature ratio (and thus mass ratio) close to unity. Thus, one would expect this system to be overluminous for its position in a CMD. Furthermore, the out-of-eclipse *K2* light curve for the source is much less variable than any of the well-known Pleiades members of a similar V magnitude. The evidence above is suggestive that AK II 465 is most likely a non-member.

Table 4.9: Literature proper motion measurements for AK II 465

μ_α (mas yr ⁻¹)	μ_δ (mas yr ⁻¹)	Note	Source
9.0±5.5	-28.6±5.5	URAT1	Zacharias et al. (2015)
3.59±6.07	-22.05±6.07	DANCe	Bouy et al. (2015)
4.8±0.7	-37.5±0.7	UCAC4	Zacharias et al. (2013)
7.0±1.3	-38.5±1.4	PPMXL	Roeser et al., 2010
8.3±1.4	-39.3±1.5	Tycho-2	Høg et al., 2000

Table 4.10: Keck/HIRES equivalent widths for AK II 465

Component	EW(Li I 6707.8) [Å]	EW(Ca I 6717) [Å]
A	0.05	0.04
B	0.03	0.02

Keck/HIRES spectra revealed the source to be double-lined, and from these spectra we estimate a G0 spectral type. Both components possess lithium absorption (see Table 4.10), normally an indicator of extreme stellar youth; however, lithium may be removed from the stellar photosphere either via convective transport to depths hot enough for burning (the dominant mechanism for late G and K dwarfs) or due to gravitational settling (which is thought to be the case for F dwarfs). Around a spectral type of G0, neither process works significantly, and one expects lithium abundances that nearly reflect the local interstellar medium values for a wide range of ages (see e.g. Soderblom et al., 1999; Jones et al., 1999). Thus, at this temperature or mass, lithium is not a useful youth diagnostic. Furthermore, Barrado y Navascues & Stauffer (1996) showed that tidally locked binaries (as AK II 465 is expected to be) tend to retain lithium longer than both single stars or more widely separated binaries of the same age.

From simultaneous fitting of the *K2* photometry and four epochs of double-lined RV measurements, we confirmed that the systemic velocity of AK II 465 ($\gamma \sim 20$ km s⁻¹) is inconsistent with the mean Pleiades motion. Furthermore, the derived masses and radii are consistent with an age of ~ 4 -5 Gyr when compared to BHAC15 models. Thus, we conclude that this EB is unlikely to be a true member of the Pleiades and indeed likely not a system of Pleiades age despite the appearance of modest Li in the spectrum. We provide the best fit parameters in Appendix 4.A for completeness but do not discuss this EB further in the context of the Pleiades or Hyades below.

4.4.6 vA 50 (HAN 87)

vA 50 (HAN 87, EPIC 210490365) was first identified as a proper motion member of the Hyades by van Altena (1966), under the name vA 50, using photographic plates from the Lick Observatory 20" astrographic telescope. A subsequent proper motion survey, also using Lick plates, reconfirmed it as a candidate Hyades member based on its proper motion, with the additional name of HAN 87 (Hanson, 1975). Concurrent with our identification and follow-up of the system, Mann et al. (2016b) recently reported vA 50 to harbor a Neptune-sized planet.

We estimated the physical parameters of the primary star as described in Section 4.3.1. Reid (1993) lists vA 50 as having an absolute V magnitude of 15.70 and $V - I_C$ color of 2.91. Uggren et al. (1985) lists an absolute V magnitude of 15.80 and a $V - I_K$ color of 2.87 which converts to $V - I_C$ of 2.95. Adopting $V = 15.80$ and $V - I_C = 2.93$ gives $V - K = 5.36$ and $T_{\text{eff}} = 3170$ K and a spectral type of $\sim M4$.

From a measured secular parallax of 22.3 mas (Röser et al., 2011) based on proper motions from PPMXL (Roeser et al., 2010), the distance can be estimated to be ≈ 44.8 pc. We also find an estimated mass of $0.261 M_{\odot}$ and estimated radius of $0.321 R_{\odot}$ (see Section 4.3.1). These values may be compared with those determined in the analysis by Mann et al. (2016b), which estimates the host star to have a mass of $M_* = 0.294 \pm 0.021 M_{\odot}$, a radius of $R_* = 0.295 \pm 0.020 R_{\odot}$, and $T_{\text{eff}} = 3180 \pm 60$ K.

From the BLS periodogram of the rectified light curve, we find that vA 50 exhibits a triangular eclipse shape every ~ 3.48 d with a width of approximately 0.04 d and a depth of 1%. It is not clear from the light curve alone if these events are transits, primary eclipses alone, or primary and secondary eclipses. If this system is a stellar binary, then the period could be either ~ 3.48 d or ~ 6.97 d. RV measurements or confirmation that the companion is indeed sub-stellar is necessary to distinguish between these two possibilities.

From the PDC light curve and a Lomb-Scargle periodogram analysis, we also measured the rotation period of the primary star from the repeating spot pattern (Figure 4.14). We find $P_{\text{rot}} = 1.88 \pm 0.05$ d, where the uncertainty has been approximated from the FWHM of the periodogram peak. Our rotation period is in agreement with the value reported in Mann et al. (2016b). Those authors also reported a $v \sin i$ measurement of 7.8 ± 0.5 km s $^{-1}$. Assuming an edge-on inclination, the rotational velocity and period imply a stellar radius of $R_* \approx 0.29 \pm 0.02 R_{\odot}$, which is consistent with the Mann et al. (2016b) value, but slightly smaller than the

value based on photometry quoted above.

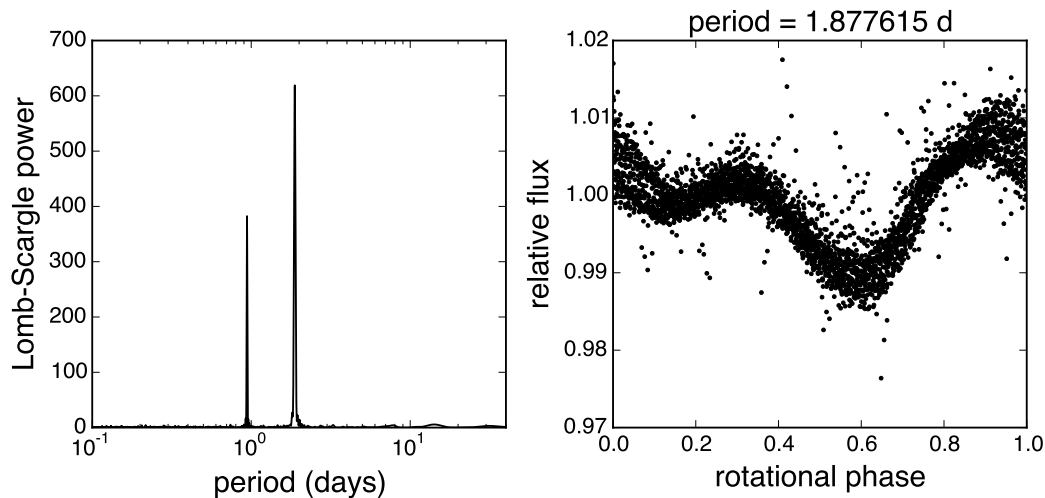


Figure 4.14: Lomb-Scargle periodogram (left) and *K2* PDC light curve phase folded on the favored rotation period of vA 50 (right). The other significant peak in the periodogram is at the half-period alias.

Mann et al. (2016b) report 10 single-lined RV measurements using the IGRINS infrared spectrometer from the 2.7m Harlan J. Smith telescope at McDonald Observatory. These measurements in addition to our 5 Keck single-lined RV measurements (Table 8.2) result in full phase-coverage at either potential period that restricts the RV amplitude to be less than 0.3 km s^{-1} (Figure 4.15). If we take the color-estimated mass of $0.261 M_{\odot}$ to be the mass of the primary component of the system, then we can use this estimated maximum RV amplitude to constrain the mass of the companion. Kepler’s Third Law with either of the two possible periods constrains the semi-major axis of the system to be dependent only on the mass of the companion. If we then assume a circular orbit and the most conservative case of an edge-on system ($i = 90^{\circ}$), then we can investigate the dependence of the RV semi-amplitude on the mass of the companion.

Figure 4.16 shows this relation along with the maximum amplitude consistent with the existing RV observations. For either period, the mass of the companion must not be over $0.0011 M_{\odot}$ ($1.15 M_{\text{jup}}$). Furthermore, since this would imply a sub-stellar companion, then the existence of a secondary eclipse is unlikely, strengthening the claim that we are seeing transits, rather than eclipses, at a period of $\sim 3.48 \text{ d}$.

Under the assumption of a sub-stellar object transiting, a JKTEBOP model was fit to the light curve data alone. Though originally designed to model EB light curves, JKTEBOP has also been demonstrated to reliably model exoplanet transits (see e.g.

Southworth, 2012, and references therein). The results and error estimates are shown in Table 4.11 with the best-fit model shown in Fig. 4.17. Most notably, the ratio of radii is estimated to be $R_p/R_* = 0.111$. This along with the estimated radius of the host star of $R_* = 0.32R_\odot$, gives the planetary companion a radius of $R_p = 0.035R_\odot = 0.354R_{\text{Jup}} = 1.01R_{\text{Nep}}$. Under the assumption that this planetary companion has a density comparable to that of Neptune ($0.287M_\odot/R_\odot^3$), its mass would be approximately $1.05M_{\text{Nep}}$. This mass would give a RV semi-amplitude of $< 0.019 \text{ km s}^{-1}$ which is consistent with the measured RV observations (Figs. 4.15–4.16). Mann et al. (2016b) also explore several possibilities besides a transiting Neptune, and also conclude that all scenarios involving an EB (blend, grazing, or companion EB) are inconsistent with the data. We note that the MCMC fitting results do admit solutions with companion radii as large as $\sim 0.2 R_\odot$ or $\sim 2 R_{\text{Jup}}$. However, at the nominal age of the Hyades such a large radius would put the companion in the stellar mass regime, which is ruled out by the RVs.

We used the PDC light curve, subject to additional custom detrending via the procedure outlined in David et al. (2016b), for the purposes of fitting the *K2* transits of vA 50b. We performed two fits, using JKTEBOP to model the transit curves in both cases. In the first fit, we used the JKTEBOP Levenberg-Marquardt fitting routine to find a best fit, determining parameter uncertainties through 1000 Monte Carlo simulations, as described in § 4.3.2. For the second fit, we employed the exact approach described in Crossfield et al. (2015), which uses standard minimization routines and the emcee Markov Chain Monte-Carlo (MCMC) implementation in Python (Foreman-Mackey et al., 2013) to generate and assess the likelihoods of JKTEBOP model light curves, more fully exploring the degenerate parameter space (see Crossfield et al., 2015, for further details regarding burn-in treatment, chain initialization, and convergence testing). For the MCMC fit, we assumed a Gaussian prior on the linear limb darkening parameter u , with $\mu = 0.6$, $\sigma = 0.1$, encompassing any reasonable value predicted by Claret et al. (2012) for a star with temperature and surface gravity similar to vA 50. In the MCMC fit, we also allowed for modest eccentricity by imposing a Gaussian prior on e with $\mu=0.0$, $\sigma=0.01$. Mann et al. (2016b) explored a solution with eccentricity as a free parameter, but in general the resulting parameters were consistent within error with the circular solution, and moreover the eccentricity is poorly constrained given the RV precision is not high enough to detect orbital motion at this stage. Thus, we report only a circular solution in our transit modeling analysis.

Table 4.11: Fit to the K2 transits of vA 50b

Parameter	JKTEBOP value	MCMC fit value
P (days)	3.48451 ± 0.00004	$3.484505^{+0.000049}_{-0.000049}$
T_0 (BJD-2457000)	62.5801 ± 0.0005	$62.58012^{+0.00056}_{-0.00053}$
$(R_P + R_*)/a$	$0.0474^{+0.0099}_{-0.0082}$	$0.047^{+0.039}_{-0.006}$
R_P/R_*	$0.111^{+0.020}_{-0.016}$	$0.120^{+0.598}_{-0.006}$
i ($^\circ$)	$88.10^{+0.63}_{-0.44}$	$88.0^{+0.4}_{-2.5}$
$e \cos \omega$	0 (fixed)	$0.0009^{+0.0087}_{-0.0113}$
$e \sin \omega$	0 (fixed)	$0.0007^{+0.0010}_{-0.0105}$
χ^2_{red}	1.295	
σ_{rms} (mmag)	1.074	

Note: The JKTEBOP parameters quoted are median values and 68% confidence intervals from 1000 Monte Carlo simulations. The MCMC parameters assumed a Gaussian prior on eccentricity with $\mu=0.0$, $\sigma=0.01$, as well as for the linear limb darkening parameter, with $\mu=0.6$, $\sigma=0.1$.

Our upper limit for the companion mass is consistent with both observational evidence and theoretical considerations that suggest Jovian mass planets should be rare around M-dwarfs; RV surveys have found that giant planets ($m \sin i \sim 0.3\text{--}3 M_{\text{Jup}}$) with orbital periods between 1–10 d are extremely scarce around M-dwarfs (Bonfils et al., 2013), and core accretion is believed to be ineffective at forming such massive planets around low-mass stars, though Neptunes and super-Earths are thought to be more common (Laughlin et al., 2004). For comparison, the MEarth project measured the occurrence rate of warm Neptunes transiting mid-to-late M dwarfs to be <0.15 per star (Berta et al., 2013).

From the orbital period and the stellar mass adopted above, using Kepler’s third law we estimate the separation of this putative planet to be $a \sim 0.03$ AU, well within the predicted location of the snow line (~ 1 AU) for a low-mass star at the time of gas disk dispersal (Kennedy et al., 2007). If validated, this system would make an excellent target for future transit transmission spectroscopy studies, which would allow for a direct measurement of the C/O ratio in the planetary atmosphere, indicating where in the protoplanetary disk the planet may have formed (Öberg et al., 2011).

4.5 Test of Model Isochrones at Pleiades Age

Our resulting models for each of the Pleiades EBs above allows us to examine all of the stellar components at once in a single mass-radius diagram, spanning a large range of masses, in comparison to the predictions of stellar evolution models. Figure 4.18 shows the mass-radius relations of all known Pleiades EB components,

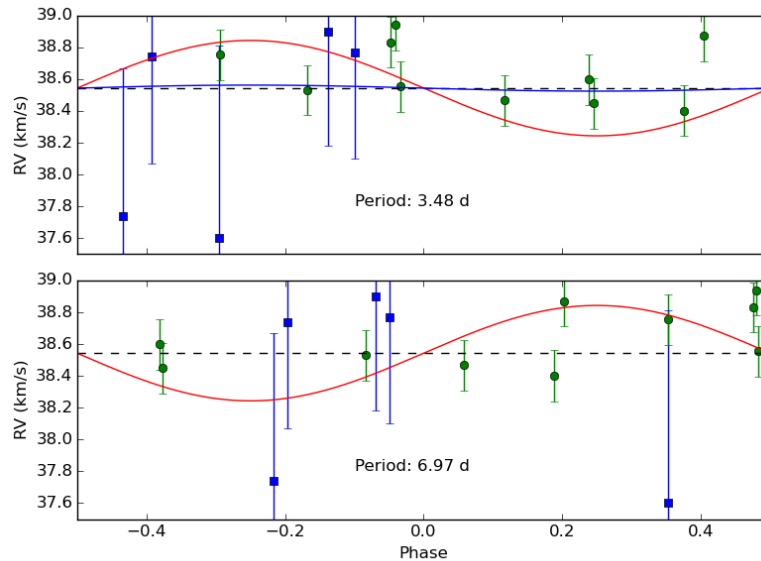


Figure 4.15: Measured RVs of vA 50 (HAN 87, EPIC 210490365) folded on the two possible periods of ~ 3.48 and ~ 6.97 days, respectively. RVs from Mann et al. (2016b) are plotted with green circles while our reported RVs are plotted with blue squares. The dashed horizontal lines represent the median velocity of all RVs and is therefore assumed as the systemic velocity. The red curve represents a circular orbit with an amplitude of 0.3 km/s. This is not a fit, but rather a representative of the approximate maximum amplitude allowed by an RV curve to still be consistent with observations. This limit is used in Figure 4.16 to constrain the maximum mass of the companion for each of these periods and ultimately rule out a stellar companion. The blue curve on the left panel represents the maximum amplitude of the estimated mass of the planetary companion.

both previously published and reported here. Neither the PARSEC v1.2S nor the BHAC15 isochrones extend across the entire mass range probed by these EBs, so we show both sets of isochrones at 80, 120, and 400 Myr for solar metallicity ($Z=0.02$). We note again that the currently accepted age of the Pleiades is 125 ± 8 Myr (Stauffer et al., 1998) though with recent suggestions of a slightly younger age (112 ± 5 Myr; Dahm, 2015).

The three EB components at masses $\gtrsim 0.5 M_{\odot}$ appear to be largely consistent with both sets of isochrones at 120 Myr. As discussed in Sec. 4.4.3 and shown in Fig. 4.13, our updated parameters for HD 23642 largely resolve discrepancies for this system from previous works.

At low masses our measurements for the EB components agree better with the 120 Myr isochrone from BHAC15 than the same isochrone from PARSEC. This is most apparent for the lowest mass object, HII 2407B at a mass of $\sim 0.2 M_{\odot}$, which clearly prefers the BHAC15 isochrone at 120 Myr and is inconsistent with

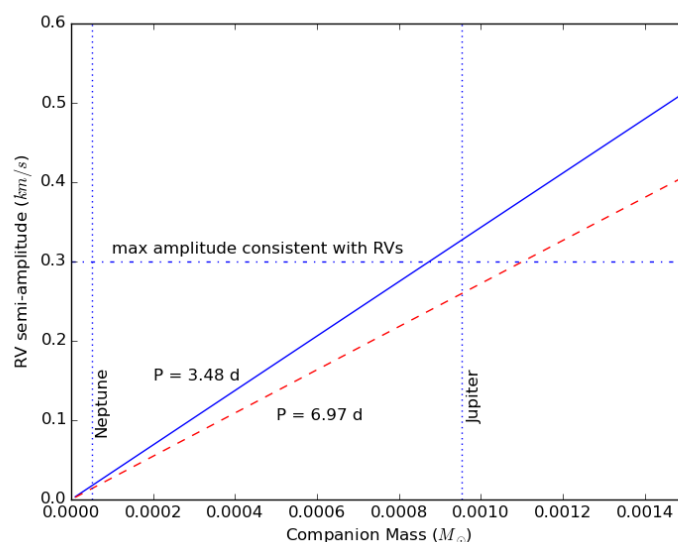


Figure 4.16: Expected RV semi-amplitude as a function of the mass of the companion, assuming $M_1 = 0.261M_\odot$ and $i = 90^\circ$, for both possible periods (3.48 days shown as a solid blue line, 6.97 days shown as a dashed red line). Dotted vertical lines represent the masses of Neptune and Jupiter, respectively. The dot-dashed horizontal line depicts the approximate maximum amplitude that would be consistent with the measured RVs shown in Figure 4.15. This clearly rules out a stellar-companion, which also implies that the true period is in fact 3.48 d.

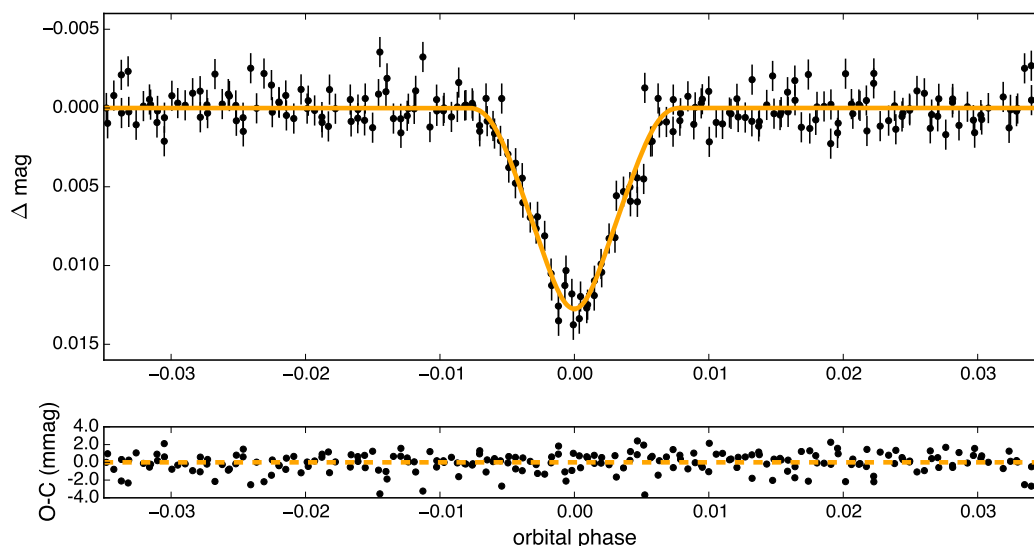


Figure 4.17: Phase folded *K2* light curve of vA 50 with the best-fitting JKTEBOP transit model shown in orange. The fit residuals are shown in the bottom panel.

the PARSEC isochrone at 120 Myr by $2\text{--}3\sigma$. The exception at low masses is BPL 116B, however its mass uncertainty is large and therefore the discrepancy with the

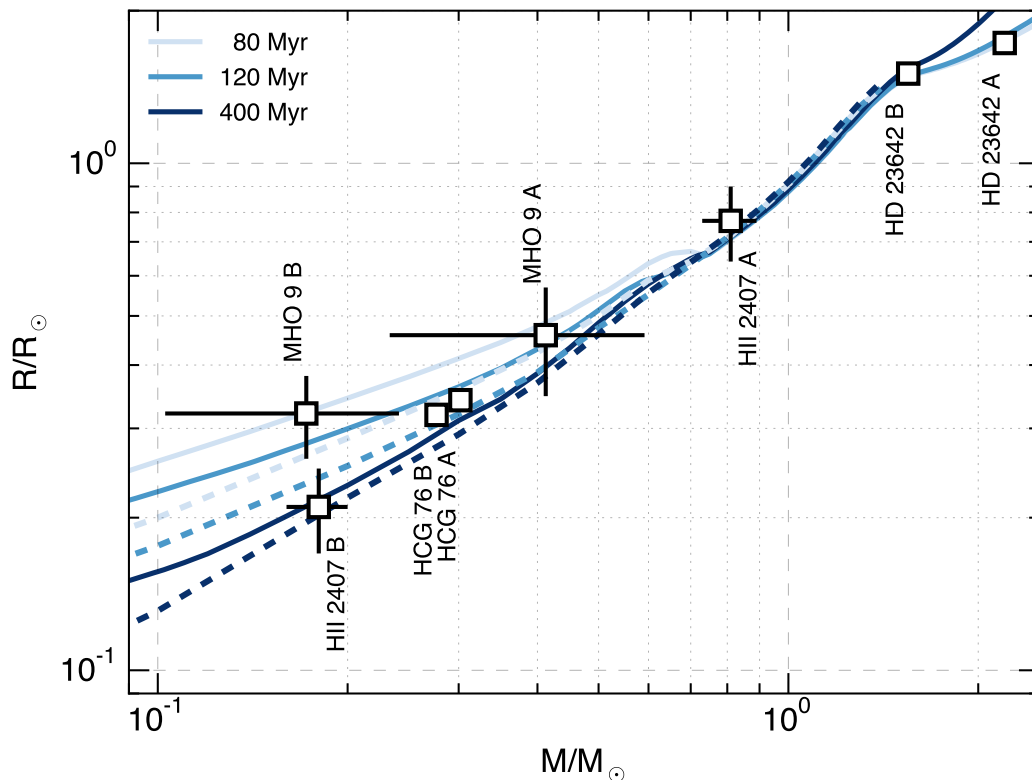


Figure 4.18: Mass-radius diagram for all currently known eclipsing binaries in the Pleiades star cluster. With the exception of HII 2407 which is single-lined, each system is double-lined with dynamically determined masses. The solid and dashed curves show PARSEC v1.2S and BHAC15 isochrones for solar metallicity ($Z=0.02$).

BHAC15 isochrone at 120 Myr is only $\sim 1\sigma$.

As noted in Sec. 4.4.1 and shown in Fig. 4.6, our current best-fit constraints on HCG 76 suggest a modest preference for the slightly younger Pleiades age of Dahm (2015). However, the radius ratio for HCG 76 is currently poorly constrained, and moreover the lowest mass component of HII 2407 is more consistent with the age of 120 Myr (Stauffer et al., 1998) than with the younger age of Dahm (2015). Thus, overall the collective assessment of the Pleiades EBs spanning masses $0.2\text{--}2 M_{\odot}$ is to clearly prefer the BHAC15 models over the PARSEC models at a Pleiades age of ≈ 120 Myr.

4.6 Summary and Conclusions

We report the discovery of two new eclipsing binaries in the Pleiades cluster from inspection of *K2* data, doubling the total number of known EBs in the cluster. These two systems have the lowest primary masses of the known EBs in the cluster, and thus

all four of the stellar components are still in the pre-main-sequence phase of evolution at Pleiades age. With follow-up studies they may be elevated to benchmark status, becoming critically important anchors for evolution models that aim to reproduce both bulk stellar parameters and radiative properties at fixed ages. Importantly, both of the new EB systems have relatively large separations between components, reducing the likelihood that their individual properties are corrupted by interaction effects and increasing their value as calibrators.

As these two new Pleiades EBs have long orbital periods relative to the *K2* campaign duration, the ephemerides of both still have large uncertainties. Thus, follow-up radial velocities and eclipse photometry are critically needed to better characterize these systems. Even so, we have measured the masses of the components of HCG 76 to $\lesssim 2.5\%$ precision, the radii of these stars to $\lesssim 4.5\%$ precision, and have determined masses and radii for all four of the newly discovered Pleiades EB components. The highly precise parameters for HCG 76 further permit us to determine an independent Pleiades distance of 132 ± 5 pc. In addition, we have newly measured the masses and radii of the components of the previously known Pleiades EB HD 23642, with updated stellar radii that largely resolve discrepant radii for this system relative to the Pleiades isochrone. Finally, together with a fourth Pleiades EB discovered in the *K2* data and analyzed by David et al. (2015), we assess the overall agreement of stellar model isochrones at Pleiades ages over the mass range $0.2\text{--}2 M_{\odot}$, finding broad agreement for the BHAC15 stellar models at an age of 120 Myr.

In addition, we characterized a likely planetary mass companion in the Hyades, vA 50b, concurrently discovered and studied by Mann et al. (2016b). We confirm the finding of those authors of a Neptune sized transiting object. With the additional radial velocity measurements presented here, we are able to improve the constraint on the maximum mass of the planet, yielding a maximum mass of $1.15 M_{\text{Jup}}$. Extrasolar planets with well-constrained ages are extremely scarce, making this system valuable for constraining planet formation, migration, and evolution theories that aim to explain planetary and orbital parameters as a function of age. Most interesting about this planet is that it has a short orbital period and a relatively large size, which is particularly well constrained because of the host star's membership to a cluster with an extensively studied distance and age. Holding the radius fixed, we estimate that a planet mass of $1 M_{\text{Jup}}$ would yield a bulk density an order of magnitude more dense than any of the terrestrial planets, while a mass of $1 M_{\oplus}$ would imply a density a factor of ~ 4 less dense than Saturn. We consider either of these two extremes to

be unlikely. In any case, the existence of such a large planet on a short orbital period at ~ 600 Myr can be used in the future to place constraints on theories of planet formation and migration.

The upcoming *K2* Campaign 13 will also target the Hyades cluster, allowing for the opportunity to discover new EBs and planets among members that were not included in the Campaign 4 pointing.

ACKNOWLEDGMENTS

We thank the referee for helpful comments which led to significant improvement in the quality of this work. T.J.D. thanks J. Southworth for helpful discussions regarding the use of JKTEBOP, and I. Crossfield for providing his MCMC transit fitting routine which was used to fit vA 50b. Support for this work was provided by NASA via grant NNX15AV62G. Some of the material presented herein is based upon work supported in 2015 by the National Science Foundation Graduate Research Fellowship under Grant DGE1144469. T.J.D. gratefully acknowledges research activities support from F. Córdova through the Neugebauer Scholarship. Some of the data presented in this paper were obtained from the Mikulski Archive for Space Telescopes. STScI is operated by the Association of Universities for Research in Astronomy, Inc., under NASA contract NAS5-26555. Support for MAST for non-HST data is provided by the NASA Office of Space Science via grant NNX09AF08G and by other grants and contracts. This paper includes data collected by the Kepler mission. Funding for the Kepler mission is provided by the NASA Science Mission directorate. Some of the data presented herein were obtained at the W.M. Keck Observatory, which is operated as a scientific partnership among the California Institute of Technology, the University of California and the National Aeronautics and Space Administration. The Observatory was made possible by the generous financial support of the W.M. Keck Foundation. The authors wish to recognize and acknowledge the very significant cultural role and reverence that the summit of Mauna Kea has always had within the indigenous Hawaiian community. We are most fortunate to have the opportunity to conduct observations from this mountain.

APPENDIX

4.A Model results for Pleiades non-member EB AK II 465

The best-fit parameters of the EB AK II 465 are summarized in Table 4.12 and the solution displayed in Figure 4.19.

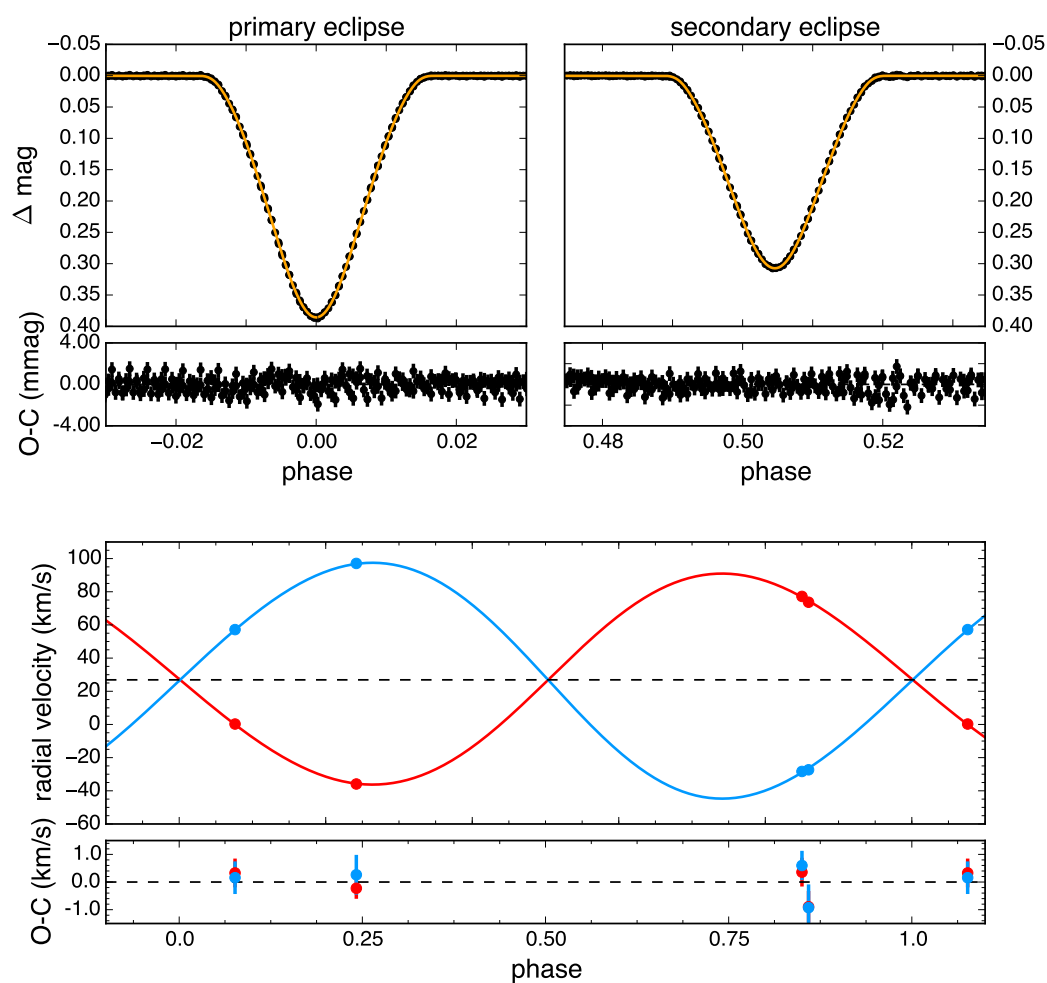


Figure 4.19: Top panels: *K2* PDC SAP light curve for AK II 465 phase folded on the orbital period, with the best-fit JKTEBOP model plotted in orange. Bottom panel: Radial velocities with the best-fit JKTEBOP models indicated by the red and blue curves. In each panel the best-fit residuals are plotted below. The structure in the residuals to the fit of the primary eclipse is likely due to inadequate modeling of limb darkening.

Table 4.12: System Parameters of AK II 465

Parameter	Symbol	JKTEBOP Value	Units
Orbital period	P	8.0746423 ± 0.0000067	days
Ephemeris timebase - 2457000	T_0	72.234969 ± 0.000030	BJD
Surface brightness ratio	J	0.760 ± 0.014	
Sum of fractional radii	$(R_1 + R_2)/a$	0.10077 ± 0.00038	
Ratio of radii	k	0.797 ± 0.016	
Orbital inclination	i	87.987 ± 0.034	deg
Primary limb darkening coefficient	u_1	0.541 ± 0.037	
Secondary limb darkening coefficient	u_2	0.438 ± 0.052	
Combined eccentricity, periastron longitude	$e \cos \omega$	0.0072303 ± 0.0000069	
Combined eccentricity, periastron longitude	$e \sin \omega$	-0.0358 ± 0.0018	
Primary radial velocity amplitude	K_1	63.61 ± 0.31	km s^{-1}
Secondary radial velocity amplitude	K_2	71.09 ± 0.44	km s^{-1}
Systemic radial velocity	γ	26.89 ± 0.19	km s^{-1}
Fractional radius of primary	R_1/a	0.05608 ± 0.00035	
Fractional radius of secondary	R_2/a	0.04469 ± 0.00064	
Luminosity ratio	L_2/L_1	0.503 ± 0.019	
Eccentricity	e	0.0365 ± 0.0017	
Periastron longitude	ω	281.42 ± 0.55	deg
Impact parameter of primary eclipse	b_1	0.649 ± 0.014	
Impact parameter of secondary eclipse	b_2	0.604 ± 0.014	
Orbital semi-major axis	a	21.488 ± 0.088	R_\odot
Mass ratio	q	0.8947 ± 0.0067	
Primary mass	M_1	1.079 ± 0.015	M_\odot
Secondary mass	M_2	0.965 ± 0.011	M_\odot
Primary radius	R_1	1.2051 ± 0.0097	R_\odot
Secondary radius	R_2	0.960 ± 0.014	R_\odot
Primary surface gravity	$\log g_1$	4.3087 ± 0.0058	cgs
Secondary surface gravity	$\log g_2$	4.458 ± 0.013	cgs
Primary mean density	ρ_1	0.617 ± 0.011	ρ_\odot
Secondary mean density	ρ_2	1.090 ± 0.047	ρ_\odot
Reduced chi-squared of light curve fit	χ_{red}^2	1.078	
RMS of best fit light curve residuals		0.720	mmag
Reduced chi-squared of primary RV fit	χ_{red}^2	0.63	
RMS of primary RV residuals		0.521	km s^{-1}
Reduced chi-squared of secondary RV fit	χ_{red}^2	0.95	
RMS of secondary RV residuals		0.572	km s^{-1}

Note: Best-fit orbital parameters and their uncertainties resulting from 1,000 Monte Carlo simulations with JKTEBOP.

Chapter 5

**K2 DISCOVERY OF YOUNG ECLIPSING BINARIES IN UPPER
SCORPIUS: DIRECT MASS AND RADIUS DETERMINATIONS
FOR THE LOWEST MASS STARS AND INITIAL
CHARACTERIZATION OF AN ECLIPSING BROWN DWARF
BINARY**

David, T. J., Hillenbrand, L. A., Cody, A. M., Carpenter, J. M., & Howard, A. W.,
2016, *ApJ*, 816, 21

ABSTRACT

We report the discovery of three low-mass double-lined eclipsing binaries in the pre-main sequence Upper Scorpius association, revealed by *K2* photometric monitoring of the region over ~ 78 days. The orbital periods of all three systems are < 5 days. We use the *K2* photometry plus multiple Keck/HIRES radial velocities and spectroscopic flux ratios to determine fundamental stellar parameters for both the primary and secondary components of each system, along with the orbital parameters. We present tentative evidence that EPIC 203868608 is a hierarchical triple system comprised of an eclipsing pair of $\sim 25 M_{\text{Jup}}$ brown dwarfs with a wide M-type companion. If confirmed, it would constitute only the second double-lined eclipsing brown dwarf binary system discovered to date. The double-lined system EPIC 203710387 is composed of nearly identical M4.5-M5 stars with fundamentally determined masses and radii measured to better than 3% precision ($M_1 = 0.1183 \pm 0.0028 M_{\odot}$, $M_2 = 0.1076 \pm 0.0031 M_{\odot}$ and $R_1 = 0.417 \pm 0.010 R_{\odot}$, $R_2 = 0.450 \pm 0.012 R_{\odot}$) from combination of the light curve and radial velocity time series. These stars have the lowest masses of any stellar mass double-lined eclipsing binary to date. Comparing our derived stellar parameters with evolutionary models suggest an age of ~ 10 -11 Myr for this system, in contrast to the canonical age of 3-5 Myr for the association. Finally, EPIC 203476597 is a compact single-lined system with a G8-K0 primary and a likely mid-K secondary whose lines are revealed in spectral ratios. Continued measurement of radial velocities and spectroscopic flux ratios will better constrain fundamental parameters and should elevate the objects to benchmark status. We also present revised parameters for the double-lined eclipsing binary UScoCTIO 5 ($M_1 = 0.3336 \pm 0.0022 M_{\odot}$, $M_2 = 0.3200 \pm 0.0022 M_{\odot}$ and $R_1 = 0.862 \pm 0.012$, $R_2 = 0.852 \pm 0.013 R_{\odot}$), which are suggestive of a system age younger than previously reported. We discuss the implications of our results on these ~ 0.1 -1.5 M_{\odot} stars for pre-main-sequence evolutionary models.

5.1 Introduction

In the aftermath of the loss of two of its reaction wheels, the *Kepler* spacecraft was reoriented to observe fields along the ecliptic plane for consecutive campaigns of ~ 75 days in duration and designated as the *K2* extended mission (Howell et al., 2014). The *K2* Field 2 pointing encompasses the Upper Scorpius region of recent star formation (see Preibisch & Mamajek, 2008, for a review) and the molecular cloud near ρ Ophiuchus in which star formation is ongoing (see Wilking et al., 2008, for a review).

Extinction is quite high towards the “ ρ Oph” molecular cloud, but some cluster members (typically those of higher mass) are bright enough for study with *K2*. The sizable “Upper Sco” association by contrast is essentially gas free, though there is a small amount of dust extinction ($A_V < 1$). The association samples a wide range in mass – from mid-B type stars having several to ten solar masses, all the way down to late M-type, very low mass stars and sub-stellar mass objects, the majority of which are bright enough for *K2* photometry.

Census work in the Upper Sco region has established over 1500 secure and candidate members, with a major compilation of candidates appearing in Lodieu (2013). Notable studies include the early kinematic work that culminated in Preibisch et al. (2002) as well as contemporaneous x-ray (e.g. Köhler et al., 2000) and wide-field optical (e.g. Ardila et al., 2000) studies, through to the most recent additions to the stellar population by e.g. Rizzuto et al. (2011) and Rizzuto et al. (2015) and Gagné et al. (2015). The traditional age of the association is 3-5 Myr (e.g. de Geus et al., 1989; Preibisch et al., 2002; Slesnick et al., 2008) which is reinforced in the analysis of Herczeg & Hillenbrand, 2015, hereafter HH15, using modern pre-main sequence tracks and a sample of several hundred GKM stars, but challenged by Pecaution et al., 2012 who argue for an age of 11 Myr based on an assessment of 5-6 post-main sequence stars and several tens of AFG stars near the main sequence. The ρ Oph region is significantly younger at $< 1-2$ Myr and features self-embedded protostars, classical T Tauri disks in various stages of evolution, and disk-free young stars; Wilking et al. (2008) provide a compilation of accepted members.

Notably, in the short but exciting time span between the age of younger active star-forming regions such as ρ Oph and the only somewhat older Upper Sco region, definitive changes are taking place in both the stars and their circumstellar environments. Most relevant for this paper is that the stars will have contracted by a mass-dependent factor of 50% to 250%, making the existing *K2* data a valuable

resource for measuring the pre-main sequence evolution of stellar radii.

Pre-main-sequence eclipsing binaries (EBs) are particularly valuable for calibrating pre-main sequence evolutionary models which show large discrepancies when compared with EB measurements and remain poorly constrained at the very lowest masses ($M < 0.3 M_{\odot}$), as reviewed by Stassun et al. (2014). Only a small number of such pre-main sequence EB systems are known. Here, we report the discovery of three new pre-main sequence EBs, two secure members and one likely member of Upper Sco, and all with short periods (< 5 days).

In § 5.2 we discuss characteristics of the *K2* observations as well as our procedures for light curve extraction and subsequent removal of intrinsic and systematic variability. We discuss our spectroscopic observations, which we use to measure radial velocities, establish spectral types, and confirm membership, in § 7.5. The procedures for determination of orbital and stellar parameters are described in § 5.4 and § 5.5, respectively. Finally, we discuss the individual EB systems and our results on fundamentally determined radii and masses in § 5.6.

5.2 *K2* Observations and Analysis

A field covering the Upper Sco region was observed by *K2* in 2014 between BJD 2456894 - 2456970. The modified observing configuration of *K2* has the telescope pitch and yaw confined using the two remaining reaction wheels, while the roll along the boresight is partially balanced by solar radiation pressure with thruster firings every ~ 6 hours to correct for the remaining azimuthal drift. As a result of the roll axis drift and intrinsic flat field variations, *K2* light curves possess significant systematic noise correlated with the telescope pointing. After correcting for this systematic noise, the photometric precision of *K2* light curves over typical transit timescales of ~ 6 hours has been measured to be a magnitude-dependent factor of 2-3 lower than that of *Kepler* data (Vanderburg, 2014; Aigrain et al., 2015).

The precision of *Kepler* light curves can be quantified by the metric of Combined Differential Photometric Precision (CDPP) originally described by Christiansen et al. (2012). We use a quasi-CDPP, defined as the median of the standard deviation in a running bin of a fixed duration. For this work, we choose 6.5-hour as the time frame over which to calculate the quasi-CDPP which is used as our light curve precision metric.

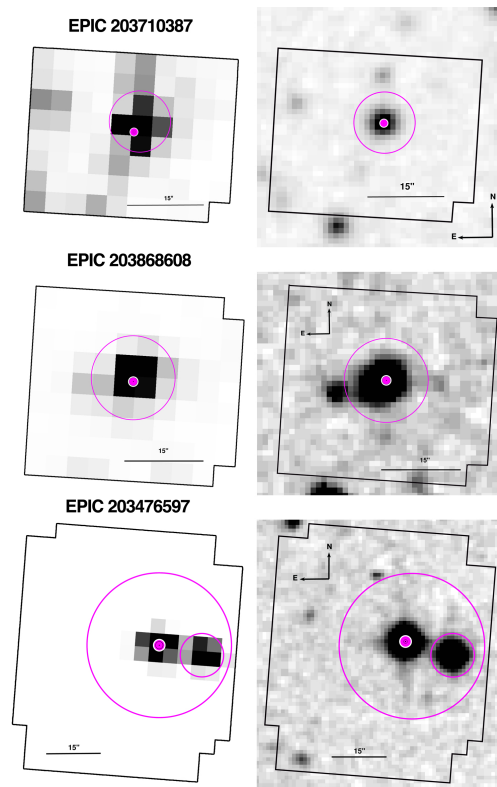


Figure 5.1: *Left column:* *K2* postage stamps showing the regions around the three EB systems. Orientation is such that north is up and east is left. The *K2* plate scale is $\sim 4''$ /pixel. The magenta circles indicate the photometric apertures used for light curve extraction. The points represent the nominal locations of the sources from the target pixel file header information and may not be centered on the star due to small errors in the WCS (World Coordinate System). For EPIC 203476597, the second, smaller aperture around the neighboring star to the west was used to compute the time-averaged flux which was ultimately subtracted from the raw EB light curve. *Right column:* DSS2 “infrared” views of the corresponding regions presented on the left. The potential for contamination in the *K2* photometry due to either unresolved or spatially resolved nearby sources is discussed in the text individually for each EB system.

5.2.1 Light Curve Extraction

In *K2* Field 2, we extracted photometry for objects identified as being members or candidate members of Upper Sco and the slightly younger ρ Ophiuchus complex, which is nearby and somewhat overlapping in projection on the sky. Aperture photometry was performed with the PYTHON `photutils` package on background-subtracted images using a range of aperture radii from 1.5 to 5 pixels. Unlike the *Kepler* pipeline and recently publicized reductions of *K2* data (e.g. Vanderburg, 2014; Foreman-Mackey et al., 2015), we vary aperture placement with the stellar centroid position. We computed a flux-weighted centroid in a 7×7 pixel box centered on the location of each star, as specified by the target pixel file header information.

Stellar flux within the aperture was computed using the `photutils` “exact” setting, in which the intersection of the circular aperture with the square pixels is calculated. The *K2* regions used for aperture photometry, and corresponding “infrared” views of the regions from DSS2¹, are shown in Figure 5.1.

Depending on detector position, we find that source centroids move at up to 0.03 pixel (i.e., 0.12”) per hour due to instability of the telescope’s pointing. Approximately every six hours, a correction is applied to return pointing to the nominal position. Since intrapixel sensitivity can vary at the few percent level, even small centroid movements can contribute systematic effects to *K2* photometry. Shifting the aperture according to centroid position partially mitigates these effects. For light curves with significant pointing related systematics, we also applied a detrending procedure to recover the intrinsic variability pattern (see § 5.2.2).

For many stars, signatures are present in the raw photometric extractions of behavior associated with e.g. young star accretion or circumstellar obscuration, starspots and stellar rotation, chromospheric flaring, and binary eclipses. However, both the light curves with these types of large amplitude variations, and those light curves with more subtle variations, can benefit from attention to so-called de-trending, which aims to remove prominent systematic effects and restore the innate photometric precision of the *Kepler* spacecraft CCDs.

5.2.2 Detrending Procedure

Multiple techniques for detrending *K2* light curves have emerged in the literature (e.g. Vanderburg, 2014; Aigrain et al., 2015; Lund et al., 2015; Huang et al., 2015). Foreman-Mackey et al. (2015) advocate fitting systematic effects simultaneously with the astrophysical signals sought to be quantified (e.g. transits). This approach, as those authors point out, mitigates the risk of distorting the astrophysical signal in question through under- or over-fitting.

In this work, the raw light curves are corrected for systematic and astrophysical variability through a principal component analysis procedure based on that of Vanderburg & Johnson, 2014 and Vanderburg, 2014, hereafter V14. The approach employed here differs from that of V14 in the following ways:

1. We opted to detrend data from the entire campaign at once, as opposed to dividing the campaign into smaller sets of observations.

¹<http://archive.stsci.edu/dss/acknowledging.html>

2. We removed outlier points with nonzero quality flags, corresponding to e.g. attitude tweaks and observations taken in coarse pointing mode, except those observations with the detector anomaly flag raised as these are fairly common. We also discarded any observations that were simultaneous $3\text{-}\sigma$ outliers in both x and y centroid coordinates.
3. We considered photometry generated from four possible apertures of radii 1.5, 2, 3 and 5 pixels, selecting the raw light curve with the lowest 6.5 hr quasi-CDPP.
4. Principle component analysis is used to transform the x, y centroid positions to a new coordinate space, x', y' , in which the positions drift primarily along one axis. A polynomial fit to the new x', y' coordinates is then performed in order to determine the ‘arclength’ (defined in V14) at each position. Instead of only a degree 5 fit to the transformed coordinates, we perform polynomial fits of degrees 1 through 5, and select the best-fitting curve (after ten iterations of $3\text{-}\sigma$ outlier exclusion) according to a Spearman test.
5. The raw photometry is corrected for the centroid position variability effects via the process above, which produces a “low-pass filtered” flux (i.e. corrected for trends on timescales <6 hours).

In some instances, this step of the detrending procedure can introduce additional noise to the raw photometry (as was the case for the three EBs discussed here). This is partially due to the fact that we detrend the entire campaign of data at once, and the pointing-related trends are often of shorter duration (on the order of days). It is also likely that allowing the photometric aperture to shift with centroid position, as we do, partially mitigates pointing-induced trends. Thus, at this stage, the 6.5 hour quasi-CDPP of the raw photometry is compared with that of the low-pass flux and the higher quality light curve is selected for “long-term” variability correction.

6. As a final step, we correct for variability on timescales longer than 6 hours. The source of variability on these timescales can be a combination of astrophysical (as is the case with EPIC 203476597, seen in Figure 5.2), pointing-related effects, and long-term systematic trends (such as a general decline in overall flux levels seen from the first to second halves of the campaign). V14 correct for long-term systematic variability via an iterative spline fit, with knots every 1.5 days and 3-sigma outlier rejection to ensure that transit signals do not drag

down the spline fit thus resulting in distorted transit signals in the corrected light curve. In our iterative intrinsic variability fitting, we allow a much more flexible spline with knots every 12 cadences (~ 6 hours) and up to 10 iterations with $2\text{-}\sigma$ outlier rejection at each stage. This approach appropriately fits and removes the intrinsic variability exhibited by these young stars, which can be significant over short timescales similar to the timescales expected for eclipse/transit durations. Our aggressive approach to outlier rejection ensures that any eclipse/transit signals are excluded from the variability fit. The `splrep` and `splev` tasks in the `scipy.interpolate` package were used to perform the spline fit in PYTHON.

The raw *K2* and corrected light curves for each of the EB systems are depicted in Figure 5.2.

5.3 Spectroscopic Observations and Analysis

We obtained initial high dispersion spectra for the three EBs on 1 and 2 June 2015, UT using Keck I and HIRES (Vogt et al., 1994). The instrument was configured to produce spectra from $\sim 4800\text{-}9200 \text{ \AA}$ using the C5 decker which provides spectral resolution $\sim 36,000$. Additional HIRES spectra were obtained using the setup of the California Planet Search covering $\sim 3600\text{-}8000 \text{ \AA}$ at $R\sim 48,000$ with the C2 decker, on the six additional nights listed in Table 8.2. Figure 5.3 shows for all three stars a photospheric region of spectrum along with the profiles of $H\alpha$ and Li I 6707.8 \AA .

We use the spectra to assess spectral types, to confirm membership through detection of $H\alpha$ emission and Li I absorption, and to measure systemic radial velocities from binary orbit fitting. The equivalent widths are given in Table 5.2; line strengths are consistent with the expectations for young active low mass stars with some variation observed among the epochs in the $H\alpha$ strengths. We note that our measurements for EPIC 203476597 match within expectations the values reported by Rizzuto et al. (2015) from lower resolution spectra.

The FXCOR task within IRAF² was used to measure relative velocities, using selected spectral orders with sufficient S/N, and spectral ranges with abundant photospheric features and minimal atmospheric contamination. FXCOR implements the Tonry & Davis (1979) method of cross correlation peak finding; a Gaussian

²IRAF is distributed by the National Optical Astronomy Observatory, which is operated by the Association of Universities for Research in Astronomy (AURA) under a cooperative agreement with the National Science Foundation

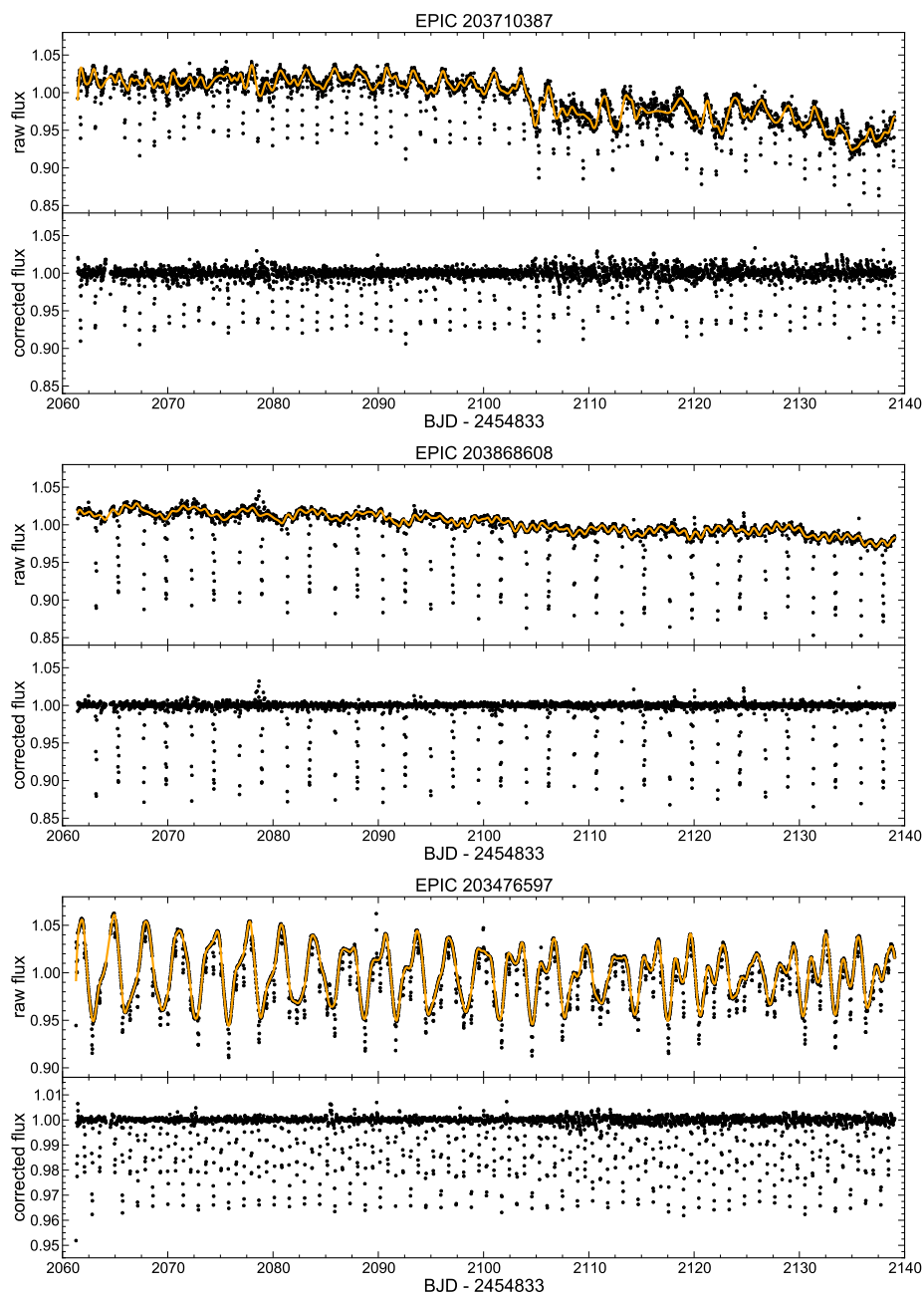


Figure 5.2: For each of the three eclipsing binary systems, raw *K2* (top panels) and corrected (bottom panels) light curves. All fluxes are median normalized. The orange line indicates the cubic B-spline fits to the raw photometry used to produce the corrected fluxes. A noticeable change in the data quality between the first and second halves of Campaign 2 is seen in these sources (most prominently EPIC 203710387) as well as many others.

profile was used to interactively fit for the velocity shift and errors for individual components of each binary at each epoch. The measured velocities were calibrated to radial velocity standard stars as detailed below, with each spectrum first corrected to the heliocentric frame. The final velocities at each epoch are derived as weighted means from among the individual orders. The results on radial velocities are discussed below in the sections on the individual EB systems, and are presented in Table 8.2.

At any given epoch, the relative heights of the cross correlation peaks for the two components of a double-lined binary system can be used as an approximation of the flux ratio, with final values again taken as means among the measured orders.

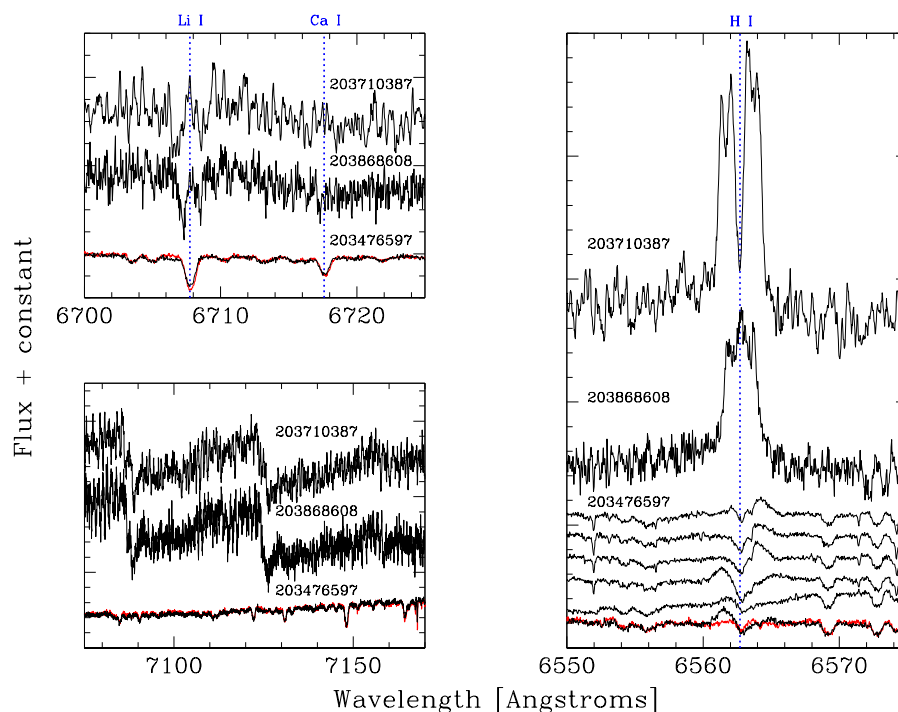


Figure 5.3: Sections of the HIRES spectra showing a photospheric region (lower left), the Li I 6707.8 Å and Ca I 6717 Å lines (upper left) and the H α line profiles (right). All three stars show H α activity and have Li I absorption. The spectra of EPIC 203710387 and EPIC 203868608 are clearly double-lined, as seen most prominently in the two components of H α emission (each of which is double-peaked) and in the doubled Li I absorption, but also in the TiO bandhead regions. The red line indicates a second spectrum of EPIC 203476597, which differs from the black (first) that it overlays in its H α profile and in the Li I line, where a small absorption blueward of line center moves to become enhanced absorption redward of line center. The full time series of spectra is shown for EPIC 203476597 in the H α panel; we interpret the profile variations as due to orbital motion of a faint young H α emitting secondary, which is indeed revealed in the absorption lines from differences and ratios of the spectra.

Table 5.1: Keck-I/HIRES Radial Velocities and Flux Ratios

EPIC identifier	Epoch (BJD-2450000)	v_1 (km s ⁻¹)	σ_{v_1} (km s ⁻¹)	v_2 (km s ⁻¹)	σ_{v_2} (km s ⁻¹)	F_2/F_1
203710387	7174.83185	38.98 ± 0.31	0.69	-51.31 ± 0.37	0.86	0.939 ± 0.175
...	7175.83303	-26.03 ± 0.45	0.69	19.40 ± 0.44	1.04	0.976 ± 0.139
...	7176.02710	-38.94 ± 0.39	1.27	35.29 ± 0.38	1.13	0.937 ± 0.198
...	7217.80815	-10.14 ± 0.20	0.35	5.87 ± 0.25	0.91	0.947 ± 0.055
...	7254.84470	-45.77 ± 0.07	1.01	42.36 ± 0.08	0.93	0.951 ± 0.093
...	7255.82026	14.23 ± 0.14	0.90	-21.49 ± 0.14	1.26	0.971 ± 0.057
203868608	7175.92133	-5.24 ± 0.12	0.42
...	7217.81681	16.51 ± 0.01	0.25	-29.5 ± 0.01	0.47	0.980 ± 0.037
...	7255.82988	-26.39 ± 0.03	1.62	14.51 ± 0.03	0.51	1.075 ± 0.056
...	7262.79913	21.87 ± 0.04	0.80	-25.48 ± 0.06	1.19	1.120 ± 0.100
...	7265.79721	-4.66 ± 0.02	0.23
...	7290.72899	15.79 ± 0.03	0.19	-29.26 ± 0.03	0.26	0.955 ± 0.071
203476597	7175.84692	-1.66 ± 0.33	0.67
...	7176.05433	-0.12 ± 0.29	0.95
...	7217.82236	-0.72 ± 0.19	0.56
...	7254.83534	-0.44 ± 0.11	0.51
...	7255.81131	0.02 ± 0.12	0.38
...	7262.79242	-0.47 ± 0.13	0.64
...	7265.79154	-1.29 ± 0.13	0.42

Note: Quoted radial velocities are weighted means across several spectral orders within a single epoch, with each measurement weighted inversely to the variance. Formal errors on the weighted mean are quoted to the right of each measurement, where the errors are defined as the square root of the variance of the weighted mean (defined as $\sigma^2 = 1/\sum_{i=1}^n \sigma_i^{-2}$). The uncertainties actually used in the orbital parameter fitting procedure, σ_v , are the root-mean-square errors between individual measurements. The final column lists flux ratios, measured from the relative peak heights in the cross-correlation functions of double-lined systems.

Table 5.2: Keck-I/HIRES Equivalent Widths

EPIC identifier	EW(H α) (\AA)	EW(Li I 6707.8) (m \AA)
203710387A	-2.9	150
203710387B	-2.4	420
203868608A	-1.8	260
203868608B	-1.4	310
203476597A	weak abs.	360
203476597B	-0.2:	95:

Note: Numbers correspond to the spectra shown in Figure 5.3. The H α measurements have $\sim 0.1 \text{ \AA}$ measurement accuracy but up to 30% variation among epochs, and the Li I measurement error is estimated at $< 5\text{-}10\%$.

5.4 Orbital Parameter Fitting

Orbital parameters were determined from the detrended light curves using the JKTEBOP³ orbit-fitting code (Southworth et al., 2004a; Southworth et al., 2007). The code is based on the Eclipsing Binary Orbit Program (Popper & Etzel, 1981; Etzel, 1981), which relies on the Nelson-Davis-Etzel biaxial ellipsoidal model for well-detached EBs (Nelson & Davis, 1972; Etzel, 1975). JKTEBOP models the two components as biaxial spheroids for the calculation of the reflection and ellipsoidal effects, and as spheres for the eclipse shapes.

Our procedure of removing the out-of-eclipse variability also eliminates gravity darkening, reflected light, and ellipsoidal effects from the light curves. As such, parameters related to these effects are not included in the JKTEBOP modeling. Additionally, out-of-eclipse observations are masked in order to reduce the effect these observations have on the χ^2 calculation and to expedite the fitting process. The RMS in the out of eclipse observations is taken as the constant observational error.

The code finds the best-fit model to a light curve through Levenberg-Marquardt (L-M) optimization. The initial L-M fitting procedure requires reasonable estimates of the orbital parameters to be determined. Period estimates were obtained using Lomb-Scargle (Lomb, 1976; Scargle, 1982) and Box-fitting Least Squares (Kovács et al., 2002) periodogram analyses. Approximations of the ephemeris timebase, T_0 , were obtained by manually phase-folding the light curves on the periodogram period.

³<http://www.astro.keele.ac.uk/jkt/codes/jktebop.html>

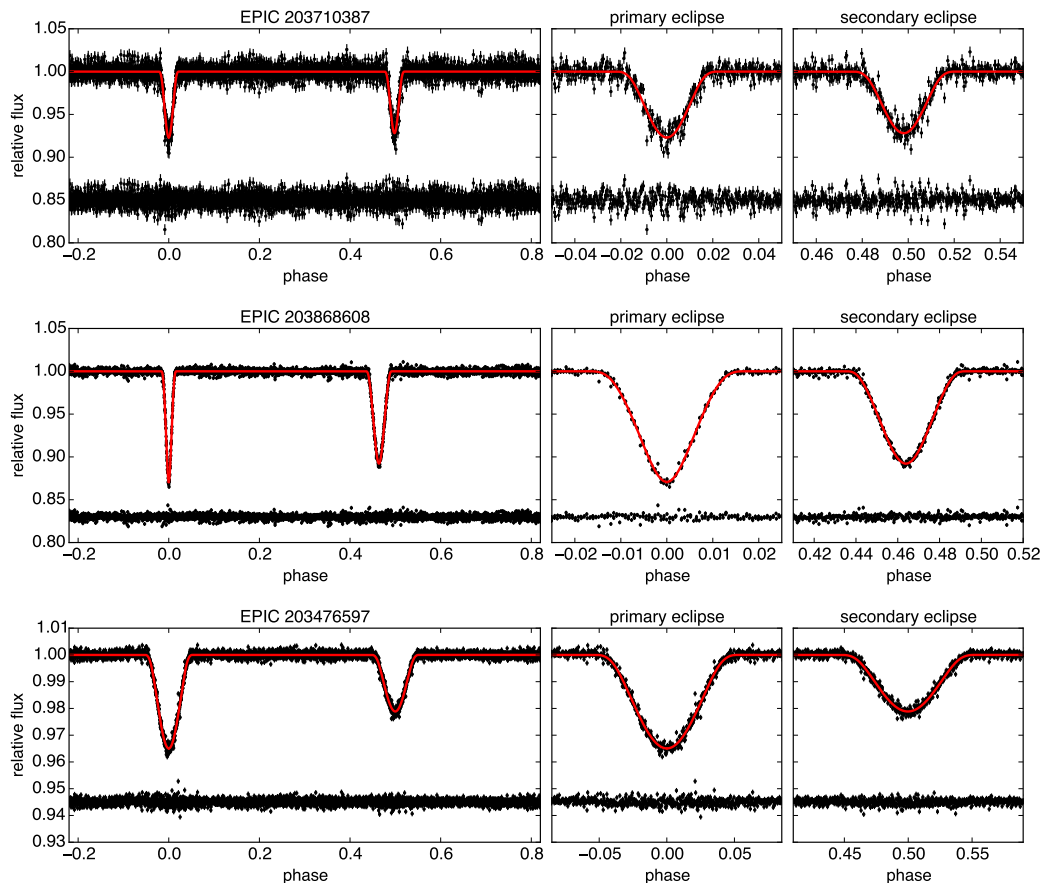


Figure 5.4: Phased *K2* light curves (black points) with best-fitting JKTEBOP models (red curves). Residuals are plotted below the model fits. Observational errors are determined by the RMS scatter in the out-of-eclipse portions of the light curves. From top to bottom, the periods of these three EBs are approximately 2.8 d, 4.5 d, and 1.4 d.

Holding the period and ephemeris timebase fixed, initial L-M fits are performed in succession for the remaining orbital parameters: the surface brightness ratio, $J = (T_{\text{eff},2}/T_{\text{eff},1})^4$ (which can be approximated by the ratio of the eclipse depths for circular orbits), the sum of the relative radii, $(R_1 + R_2)/a$, the ratio of the radii, $k = R_2/R_1$, the orbital inclination, i , and the quantities $e \cos \omega$ and $e \sin \omega$, where e and ω are the eccentricity and periastron longitude, respectively. In systems where contaminating light from neighboring stars is suspected, the so-called “third light” parameter, l_3 , is also investigated as a free parameter. The third light parameter is defined as a constant, such that the sum of the total system light is unity in the out-of-eclipse portions of the light curve. Additionally, in § 5.6.1, we incorporate radial velocities (RVs) in the fitting procedure, introducing free parameters corresponding to the RV semi-amplitudes of each star in an EB (K_1 , K_2), and the systemic RV, γ . Analysis of the RVs produces a precise estimate of the mass ratio, $q = M_2/M_1$.

After successively increasing the number of free parameters in the fit, a final L-M fit was performed allowing all relevant parameters to be free. In modeling each system, we assumed a linear limb-darkening law for both components and held the limb-darkening coefficients fixed at reasonable values, discussed further in § 5.6.

The integration times of *Kepler* long cadence data are comparable to the eclipse durations, resulting in “phase-smearing” of the light curve. The long exposure times were accounted for in *JKTEBOP* by numerically integrating the model light curves at ten points in a total time interval of 1766 seconds, corresponding to the *Kepler* long cadence duration.

Robust statistical errors on the best-fit model parameters are then found through repeated Monte Carlo (MC) simulations in which Gaussian white noise commensurate to the observational errors is added to the best-fit model. A new L-M fit is performed on the perturbed best-fit model and the new parameters are saved as links in the MC chain. The final orbital parameters for each system are then given by the original L-M best-fit, with uncertainties given by the standard deviations determined from the MC parameter distributions.

Figure 5.4 shows the detrended and phased *K2* photometry and the best-fit *JKTEBOP* models, while Tables 5.3, 5.4, and 5.5 present final values and uncertainties for the fitted orbital parameters derived from corresponding parameter distributions. We note that there are many plausible and excellent fits to the light curves from a statistical robustness perspective, and the L-M approach constrains the parameter combinations based on mutual satisfaction of standard χ^2 constraints.

5.5 Overview of System and Primary/Secondary Parameter Estimation

For each of our eclipsing binary systems we have collected available catalog and literature data to assess membership and stellar/disk parameters, as reported in Tables 5.3, 5.4, and 5.5 and in the discussion below. Spectral energy distributions (SEDs) constructed from broadband photometry for each system are presented in Figure 7.1. We supplement the literature data with our own spectroscopic observations which allow us to establish or validate spectral type, and confirm membership.

An important discriminant between likely members and probable non-members in young clusters and moving groups is kinematic information. Lodieu (2013) derived a mean proper motion for the previously claimed Upper Sco cluster members of $\mu_\alpha = -8.6 \text{ mas yr}^{-1}$ and $\mu_\delta = -19.6 \text{ mas yr}^{-1}$, which they noted as a relative value that differs somewhat from the de Zeeuw et al. (1999) Hipparcos value on an

absolute astrometric frame of $\mu_\alpha = -11 \text{ mas yr}^{-1}$ and $\mu_\delta = -25 \text{ mas yr}^{-1}$. To assess membership likelihood we made use of proper motions reported in the UCAC4 (Zacharias et al., 2013) and/or PPMXL (Roeser et al., 2010) catalogs. We further assess membership based on radial velocities from the HIRES data. The details for the individual EB systems are discussed below.

Finally, for all three EB systems, the $H\alpha$ emission and Li I 6707.8 Å absorption line strengths illustrated in Figure 5.3, discussed above, are consistent with the expectations for young active low mass stars.

Having assessed membership, we used literature and our own HIRES-derived spectral types to estimate effective temperature based on empirical calibrations for pre-MS stars, and then incorporated 2MASS photometry to calculate combined system luminosities. The near-infrared colors of all three sources are slightly redder than expected from young star intrinsic colors, suggesting a modest amount ($A_V \sim 1\text{-}3$ mag) of reddening. From the spectral type and broadband SED we calculated the extinction, and then the corresponding J -band based luminosity (which also assumes the cluster distance, here assumed to be the de Zeeuw et al. (1999) value of 145 ± 13 pc). For those systems in which we could measure the radial velocities of both eclipsing components (EPIC 203710387 and EPIC 203868608), we directly determined the masses and radii through mutual fitting of the light curves, radial velocity time series, and spectroscopic flux ratios. In these cases, distance-independent luminosities are determined from the temperatures (based on spectral types) and radii using the Stefan-Boltzmann law and an assumed value of $T_\odot = 5771.8 \pm 0.7 \text{ K}$ ⁴. For EPIC 203476597, in which the secondary lines were too weak to measure reliable radial velocities, we estimated the primary radius from its projected rotational velocity, $v \sin i$, and rotational period. The secondary radius is then determined from the orbit-fitting results. Model-dependent masses for the components of this system are derived from interpolation between PARSEC models (Bressan et al., 2012). We used either PARSEC or Baraffe et al. (2015), hereafter BHAC15, pre-main sequence evolutionary models to also estimate the ages of each system.

5.6 Results and Discussion of Individual Eclipsing Binaries

For each system we now discuss characteristics of the raw $K2$ photometry, the details of the light curve detrending procedure, and the results of the orbital and stellar parameter determinations using methods described above. In each case,

⁴From the total solar irradiance (Kopp & Lean, 2011), the solar radius (Haberreiter et al., 2008), the IAU 2009 definition of the AU, and the CODATA 2010 value of the Stefan-Boltzmann constant.

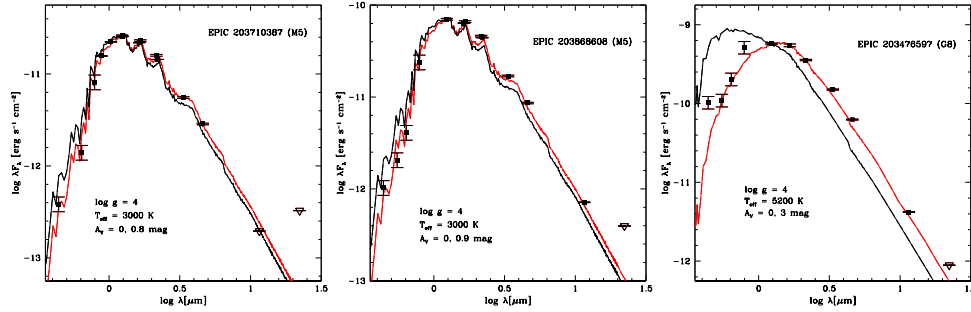


Figure 5.5: Available USNO *BV*, 2MASS *JHK*, UKIDSS *ZYJHK*, and WISE *W1, W2, W3, W4* photometry or 1σ upper limits (downward pointing triangles) compared to NextGen2 model atmospheres. For both EPIC 203710387 and EPIC 203868608, a model atmosphere with $T_{\text{eff}} = 3000$ K and $\log g = 4.0$ fits the photometry well. Adopting $A_V = 0.9$ mag (red line) produces a better fit to the photometry than an unreddened photosphere (black line). Although the stars have the same spectral type, and EPIC 203710387 is a clear double-line system with approximately equal size/temperature and therefore presumably luminosity components, EPIC 203868608 is the brighter source. For EPIC 203476597 a 5200 K model is adopted, requiring $A_V = 3.0$ mag (red line) to match the SED. The A_V values illustrated here are refined in the text based on a match to $J - H$ colors.

we have sampled a range of possible orbital parameter fits and assessed Monte Carlo parameter distributions of all fitted parameters, in some cases needing to constrain or fix certain parameters in order to produce physically reasonable overall solutions. For each fitted parameter, uncertainties are derived from Monte Carlo error propagation after including the uncertainties in anchoring stellar properties.

5.6.1 EPIC 203710387

This system is comprised of nearly identical M4.5 or M5 components in a circular orbit with period ≈ 2.8 d. Separated by $\sim 5 R_{\odot}$, or ~ 11 stellar radii, and inclined $\sim 83^{\circ}$ to our line-of-sight, the stars undergo partial or grazing eclipses of nearly equal depths. As noted earlier, the system is double-lined, and radial velocity measurements indicate approximately equal mass components.

A 1.5-pixel radius aperture was found to produce the highest quality *K2* light curve. Primary and secondary eclipses of $\sim 7\%$ depth each are notable in the raw photometry (see Fig. 5.2). The low-pass flux is a significant improvement over the raw flux, but only in the first half of the campaign where the centroid drifts are smaller. Over the entire campaign, the low-pass flux has a higher noise level than the raw photometry, so in this instance the raw photometry was selected for further correction.

After applying the detrending procedure, the phased light curve was divided into 100 bins. In each phase bin the mean flux and standard deviation were computed and $3\text{-}\sigma$

outliers were identified, resulting in the exclusion of an additional 38 observations across the entire campaign.

The 2.5 hr and 6.5 hr quasi-CDPP of the detrended light curve (including in-transit observations) are 1313 ppm and 886 ppm, respectively. In this case, the detrending provides a $\sim 20\%$ improvement over the raw photometry on 6.5 hr timescales or $\sim 5\%$ improvement on 2.5 hr timescales. Inspection of the broader dataset revealed that hundreds of other light curves from Campaign 2 display the same variation in quality between the first and second halves of the time series. Though considering only observations from the first half yields a more precise light curve, we opted to include all of the observations for the benefit of sampling additional transits.

The star is included in Table 1 of Luhman & Mamajek (2012), which lists properties of known Upper Sco members, however, there is a lack of literature on this source prior to that work. The star was then identified as a candidate member by Lodieu (2013) based on both its proper motion and location in an infrared color-magnitude diagram. The two independent measurements of the proper motion, $(\mu_\alpha, \mu_\delta = -11.8 \pm 5.1, -28.0 \pm 5.1 \text{ mas yr}^{-1})$ from Roeser et al. (2010) and $(\mu_\alpha, \mu_\delta = -12.30 \pm 1.82, -19.96 \pm 1.82 \text{ mas yr}^{-1})$ from Lodieu (2013),⁵ are consistent with one another, and with the mean values among Upper Sco members with $\chi^2 < 1-2$ (depending on which values are adopted). There is no evidence for circumstellar material around EPIC 203710387, with the object too faint for WISE in its two longest bands. The location is south and west of the main ρ Oph cluster, in a relatively lower extinction region.

An M5 spectral type was reported by Luhman & Mamajek (2012). From our HIRES spectrum we estimate a spectral type of M4.5 and report both H α emission and lithium absorption, confirming the youth of EPIC 203710387 (see Fig. 5.3). As an external consistency check, we constructed an SED from the available broadband photometry and compared it with artificially reddened NextGen2 model atmospheres based on Hauschildt et al. (1999b) to find plausible combinations of spectral type and A_V (see Fig. 7.1). We found that a model atmosphere having $T_{\text{eff}} = 3000 \text{ K}$ (corresponding to approximately spectral type M5), $\log g = 4.0$, and $A_V = 0.8 \text{ mag}$ provides a good match to the broadband photometry, though we refine both the temperature and extinction below.

We also compared broadband colors with the empirical spectral type - color - temper-

⁵Notably, proper motion measurements for EPIC 203710387 are not included in UCAC4 (Zacharias et al., 2013) or URAT1 (Zacharias et al., 2015).

ature relations of HH15 and Pecaut & Mamajek (2013), hereafter PM13. The $J - H$ color evolves rapidly in the pre-main sequence and is not well-reproduced by evolutionary models. The 2MASS $J - H = 0.655 \pm 0.033$ mag color of EPIC 203710387 is consistent on the HH15 color scale with an M4 spectral type if similar to ‘young’ 3-8 Myr old moving group members, but an M0-M3 spectral type if more similar to ‘old’ 20-30 Myr moving group members. On the PM13 color scale appropriate for 5-30 Myr old stars, the $J - H$ color suggests an M2-M4 star. The quoted UKIDSS photometry produces $J - H = 0.567 \pm 0.002$, more consistent with a young M5 star according to both HH15 and PM13. Allowance for a small amount of reddening would argue for earlier spectral types on these color scales.

We conclude that the near-infrared photometry as well as the broader SED are consistent with the previously determined M5 spectral type for a young pre-main sequence age, so we adopt this spectral type in what follows. The corresponding effective temperature from HH15 (their Table 2) is $T_{\text{eff}} = 2980$ K, or from PM13 $T_{\text{eff}} = 2880$ K. We adopt the former along with an uncertainty of ± 75 K in T_{eff} to account for a possible 0.5 subclass error in the spectral type, as suggested by Herczeg & Hillenbrand (2015).

We find from the photometry that $A_V = 1.2 \pm 0.3$ mag and the J -band based system luminosity $\log(L/L_{\odot}) = -1.64 \pm 0.08$, where the error terms come from Monte Carlo sampling of the allowed error in temperature, but for luminosity are dominated by the uncertainty in the distance. This calculation places the object in the middle of the Upper Sco temperature-luminosity sequence, reaffirming its presumed youth and membership. From the luminosity estimates and the plausible effective temperature range, and assuming equal luminosity components (consistent with the nearly equal mass components), we estimate the individual stellar radii at $0.40 \pm 0.04 R_{\odot}$ each. Direct radii measurements are derived later from combination of the light curve and RVs, but are broadly consistent with this approximation.

The M4.5 radial velocity standard GJ388 (Nidever et al., 2002), was used to measure absolute RVs from the HIRES spectrum. Several spectral orders with high signal-to-noise were chosen to produce multiple measurements per observation. In the orbital parameter fitting, an individual RV measurement for each epoch was derived from a weighted average of individual measurements from separate orders of the spectrograph. The JKTEBOP code is capable of fitting light curves and RV curves simultaneously, but only considering one RV curve at a time. The systemic velocities for each component were forced to be equal, and the resulting best-fit value ($\gamma \sim -3$

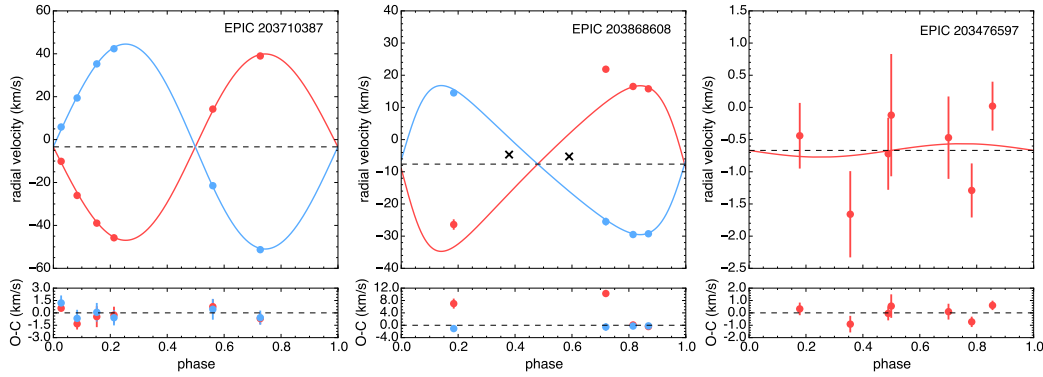


Figure 5.6: For each EB studied here, the radial velocity curve (upper panel) and best-fit residuals (lower panel). The measurements are phase-folded on the best-fit period from simultaneous fitting of RVs and the *K2* light curve with JKTEBOP. The red and blue points and curves are the observations and best-fit model, for the primary and secondary components, respectively. Each point indicates the weighted mean radial velocity derived from measurements over several spectral orders within a single spectrum. Each measurement receives a weight equal to the inverse of the variance. The error bars represent the corresponding standard deviation between the multiple measurements, which in the top panel are smaller than the points themselves. In the case of EPIC 203868608, which is a triple system, two measurements at essentially the mean systemic velocity of Upper Sco ($\sim -4 \text{ km s}^{-1}$) are indicated by the black crosses. These measurements are likely compromised due to the low expected velocity separation that is comparable to the spectrograph resolution, and were consequently excluded from the RV fits in order to obtain a good fit.

km s^{-1}) is consistent with values typical of Upper Sco members (de Zeeuw et al., 1999; Mohanty et al., 2004; Kurosawa et al., 2006). The radial velocity curves for both components and best-fitting models are shown in Figure 5.6.

It is typically considered good practice to allow limb darkening coefficients to be free parameters when fitting light curves, given that these coefficients are largely uncalibrated (Southworth et al., 2007). However, as noted by Gillen et al. (2014), JKTEBOP is susceptible to allowing non-physical limb-darkening parameters to find a good fit. Furthermore, grazing eclipses do not contain enough information to constrain the limb-darkening coefficients. We find that allowing the limb-darkening parameters to vary does not change the other fitted parameters significantly, so we hold the limb-darkening coefficients fixed. We assumed a linear limb-darkening law for both components, setting the coefficient $u = 0.888$, corresponding to the mean of all values calculated by Claret et al. (2012) satisfying $2780 \text{ K} \leq T_{\text{eff}} \leq 3180 \text{ K}$ and $4.0 \text{ dex} \leq \log g \leq 4.5 \text{ dex}$, appropriate for an M4.5-M5 PMS star.

Initial attempts to fit the photometry to model light curves revealed strong degeneracies between the stellar radii related parameters, inclination, and surface brightness

ratio, in large part due to the quite poorly constrained parameter, $k = R_2/R_1$. This is expected: for detached EBs with similar components in a grazing configuration, the sum of the fractional radii is well-defined (depending mainly on the inclination and eclipse durations), but the eclipse shapes are relatively insensitive to the ratio of the radii (Andersen et al., 1980; Southworth et al., 2007).

The degeneracy is so strong that allowing R_2/R_1 to be a free parameter resulted in a best-fit that suggested nearly equal mass components ($< 10\%$ difference in the masses, which are well constrained by the RVs) but with a $\sim 35\%$ difference in the radii, such that the more massive component was smaller. Although this solution provided a good fit, it implied a physically unlikely scenario in which the more massive component would be nearly a factor of 10 older than the secondary when compared to BHAC15 mass-radius isochrones. Notably, however, the large uncertainties did admit that the radii were consistent within 2σ with being equal size.

From the HIRES spectra, we measured spectroscopic flux ratios at each epoch from the relative heights of the two distinct cross-correlation function peaks (presented in Table 8.2). We provide these flux ratio time series data as input in the final modeling with JKTEBOP which effectively breaks the degeneracy in the ratio of radii noted above. The final orbital parameters (including masses and radii, given the presence of RVs), which are the result of 5,000 MC simulations with JKTEBOP are presented in Table 5.3. Figure 5.7 shows distributions of selected parameters derived from the MC fitting procedure.

We explored a solution to the light curve and radial velocities in which $e \cos \omega$ and $e \sin \omega$ were adjusted parameters, as well as one in which the eccentricity is assumed zero. These two solutions (presented in Table 5.3) show very good agreement in most adjusted and derived parameters, and indeed the best-fit eccentricity is within $2\text{-}\sigma$ of zero. However, the χ_{red}^2 is significantly lower in the eccentric case, and close inspection of light curve (see Fig. 5.2) confirms that the secondary eclipse occurs just slightly before phase=0.5. As such, we ultimately adopt the eccentric orbital parameters and subsequently derived quantities in our final analysis. Though, it is interesting to note that the circular orbit solution leads to a temperature ratio much closer to unity, $T_{\text{eff},2}/T_{\text{eff},1} = 0.984 \pm 0.004$, relative to the temperature ratio favored by the eccentric solution, $T_{\text{eff},2}/T_{\text{eff},1} = 0.953 \pm 0.019$. Both solutions suggest the secondary is larger than the primary, though the circular solution favors a ratio of radii very close to one, $k = 1.009 \pm 0.017$, compared with the eccentric

solution value of $k = 1.077 \pm 0.045$. Notably, with such a short orbital period and well-constrained age, this system should be quite valuable for studies of pre-MS circularization timescales.

The final masses and radii of the two components of EPIC 203710387, resulting from the equal-radii light curve solution, suggest an age of ~ 10 -11 Myr for the system when adopting the BHAC15 models and circular solution parameters (the median ages and $1\text{-}\sigma$ errors are 11.6 ± 0.4 Myr for the primary, and 9.9 ± 0.3 Myr for the secondary, from interpolation between isochrones in the mass-radius plane). If we consider a more traditional age for Upper Sco of 5 Myr, the implication is that the BHAC15 models over-predict the radii by $\sim 25 - 35\%$ for a given mass and age.

From the bolometric luminosity, the best-fit luminosity ratio ($L_2/L_1 \approx k^2J$, for circular orbits), and the directly determined stellar radii we can compute the effective temperatures of each component. We calculated $T_{\text{eff},1} = 2940 \pm 150$ K and $T_{\text{eff},2} = 2800 \pm 150$ K, where the uncertainties come from standard error propagation. The placement of each component in $T_{\text{eff}}\text{-log } g$ space relative to BHAC15 isochrones is consistent with an age of ~ 11 -14 Myr, though the corresponding model masses are underestimated by a factor of 2. Allowing for temperatures ~ 175 -200 K hotter, while holding $\log g$ fixed, brings the model-predicted masses into better agreement with the dynamical measurements and lowers the age of each component by ~ 1 Myr. If we instead assume a primary temperature from the spectral type, we obtain temperatures of $T_{\text{eff},1} = 2980 \pm 75$ K and $T_{\text{eff},2} = 2840 \pm 90$ K, which helps to resolve some of the model discrepancies in mass and age noted above. Assuming these temperatures and the directly measured radii, we then calculate *distance-independent* luminosities of $L_1 = 0.0124 \pm 0.0014 L_{\odot}$ and $L_2 = 0.0119 \pm 0.0016 L_{\odot}$. We ultimately adopt the temperatures based on the spectral type and the distance-independent luminosities in our final analysis.

With a period of approximately 2.8 d and a separation of only ~ 11 stellar radii, the system is quite compact. However, it still meets the criterion for detachment. Using the precise mass ratio derived from RVs, we calculate the effective Roche lobe radius for the system to be $\approx 37\%$ of the separation, or $\approx 1.9 R_{\odot}$, from the formula of Eggleton (1983).

Eclipsing binary light curves, and thus the parameters derived from them, are susceptible to the level of extraneous light from other stars in the photometric aperture. This contamination from nearby sources, whether associated or not, is known as third light in the EB literature. The effect of third light on EB light curves is

to decrease the depths of eclipses and mimic a system with lower inclination (Kallrath & Milone, 2009). To assess potential sources of contamination, EPIC 203710387 was imaged with Keck/NIRC2 in a K_p ($2.12 \mu\text{m}$) filter on May 27, 2015 UT. The dithered mosaic covered a $15'' \times 15''$ region, but due to the dither pattern used, the upper $\sim 5.8'' \times 5.8''$ region in the northeast quadrant of the mosaic was not covered. A star was detected that is 3.6 mag fainter than EPIC 203710387, at a position angle of $\sim 332^\circ$ measured east of north and separation of $1.6''$. This nearby source is unaccounted for in the light curve modeling, but likely contaminates the $K2$ photometry at the few percent level.

We explored the possibility of fixing the third light parameter at 3.6%, corresponding to the contamination in K_p . This trial resulted in a slightly higher χ_{red}^2 than our best-fit solution presented in Table 5.3, and masses and radii that change within error of our reported values. As such, we choose to ignore third light for this system but note it may indeed introduce an additional few percent uncertainty in the absolute radii, though not nearly enough to favor an age as young as 5 Myr in the mass-radius plane.

5.6.2 EPIC 203868608

High-angular resolution imaging revealed that this system is likely a hierarchical triple, with the EB components in an eccentric 4.5 d orbit and an M-type companion within 20 AU. Orbital motion of tens of km s^{-1} was detected with six epochs of Keck-I/HIRES spectroscopy, indicating the M4.5-M5 type which dominates the spectrum must be the primary component of the EB. The system is double-lined, and though we find a good model fit for only one of the RV curves (see Fig. 5.6), there is compelling evidence that the sum of the RV semi-amplitudes is $< 60 \text{ km s}^{-1}$, corresponding to a total system mass of $M_1 + M_2 \lesssim 0.1 M_\odot$. If confirmed, this would constitute only the second double-lined eclipsing brown dwarf binary to date, the first being 2MASS J05352184-0546085 in Orion (Stassun et al., 2006; Stassun et al., 2007).

A 2-pixel aperture produced the highest quality $K2$ photometry, and the raw flux (rather than the low-pass flux) was selected for further correction. The light curve exhibits both narrower 12.5% primary and broader 10% secondary eclipses, indicating a non-negligible eccentricity, with period 4.54 days. There is also a superposed sinusoidal pattern likely due to rotation with a period just over 1 day, as well as longer time scale variations.

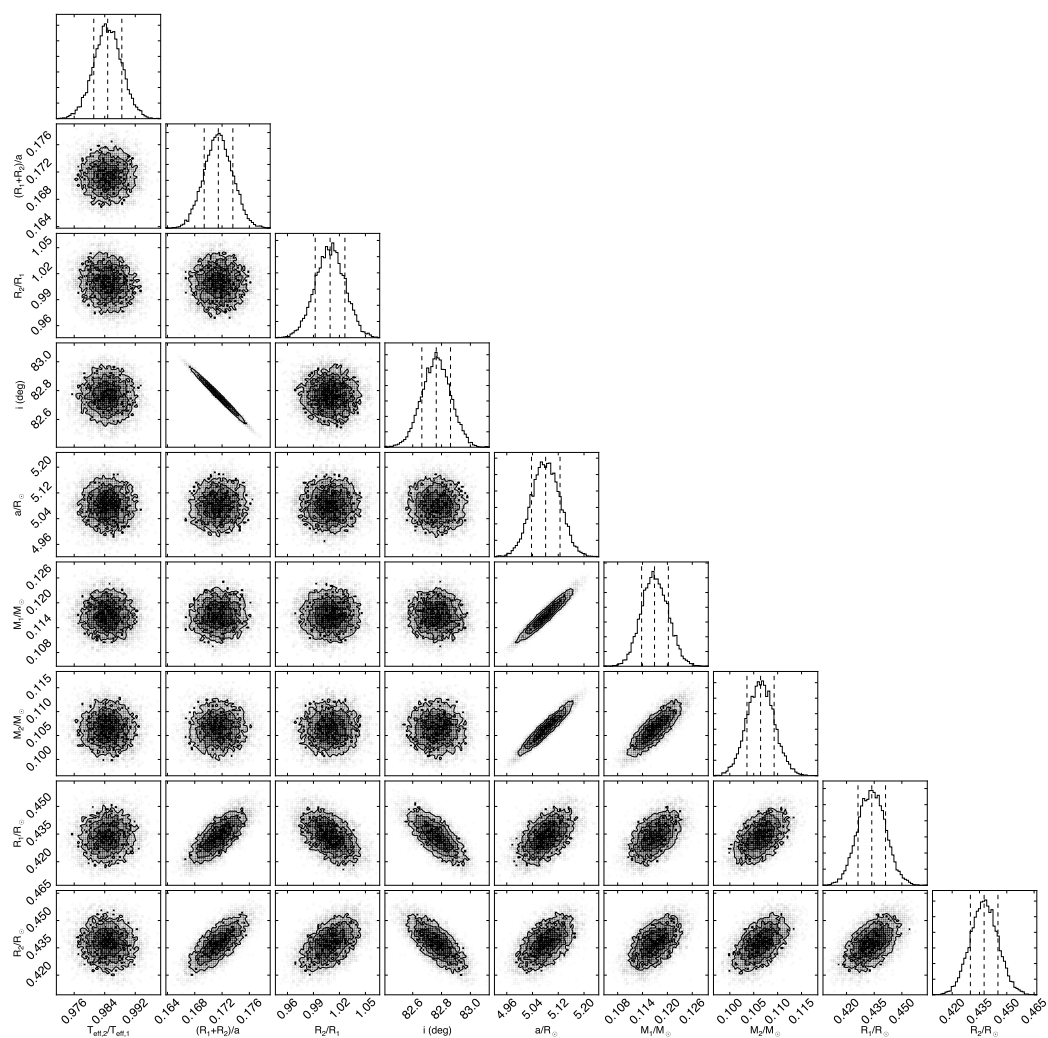


Figure 5.7: Distributions of selected free and derived parameters and their pairs from the MC fitting procedure in the circular orbit fit for EPIC 203710387. The 0.5-, 1.0-, 1.5-, and 2.0- σ contours are drawn. The dashed lines in the 1D parameter distributions represent the median and 68% confidence intervals of the distribution. This plot was created using the `triangle` PYTHON code (Foreman-Mackey et al. 2014, DOI:10.5281/zenodo.11020).

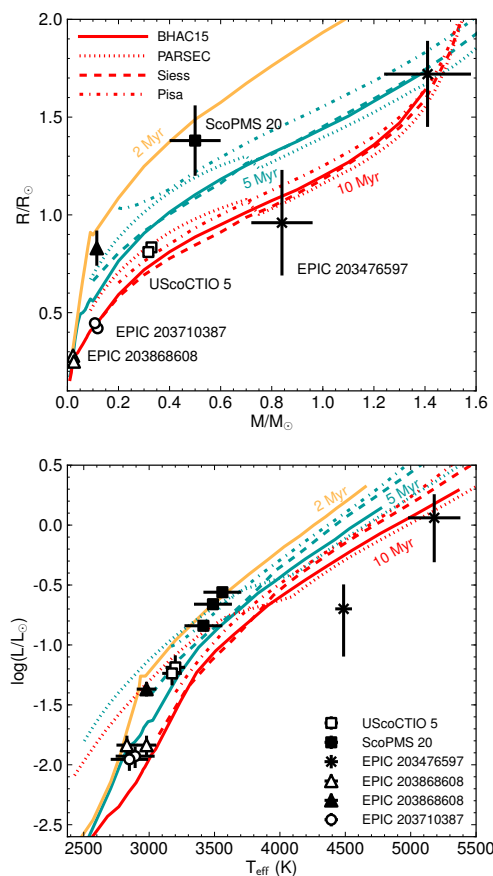


Figure 5.8: Isochrones in the mass-radius (top) and temperature-luminosity (bottom) planes with the three EBs discussed here and two other low-mass systems in Upper Sco: both components of UScoCTIO 5 (Kraus et al., 2015) and the primary of the triple system ScoPMS 20 (Mace et al., 2012). The BHAC15, PARSEC v1.2s (Bressan et al., 2012; Chen et al., 2014), Siess et al. (2000), and Pisa (Tognelli et al., 2011) pre-MS evolutionary models at solar metallicity ($Z=0.02$) are considered for comparison. The two components of EPIC 203710387 are overlapping in the mass-radius plane. UScoCTIO 5 and EPIC 203710387 have fundamentally determined masses and radii; errors are smaller than the points themselves. The eclipsing components of EPIC 203868608 also have fundamentally determined masses and radii, though large uncertainties remain for this system, particularly in the luminosities, for the reasons discussed in § 5.6.2. The tertiary of this system does not have fundamentally determined parameters and hence is represented by the filled black triangle. All other systems have parameters that depend on models and/or empirical relations. In the lower panel, the equal-temperature, equal-luminosity components of UScoCTIO 5 are offset for clarity. No single isochrone can reproduce the fundamentally determined masses and radii of both the EPIC 203710387 and the UScoCTIO 5 systems.

After applying the detrending procedure, the phased light curve was divided into 100 bins. In each phase bin the mean flux and standard deviation were computed and $3\text{-}\sigma$ outliers were identified, resulting in the exclusion of an additional 54 observations across the entire campaign. The observational errors were determined from the RMS scatter of the out-of-eclipse observations taken during the first half of the campaign, which have a slightly higher noise level than the second half for this particular system.

The colors of the primary are quite red, corresponding to a late M spectral type, with an M5 star consistent with the HIRES spectrum. Proper motion is not available in UCAC4 but the values in PPMXL ($\mu_\alpha, \mu_\delta = 1.3, -19.6 \text{ mas yr}^{-1}$) are inconsistent with Sco membership at the $> 3.5\sigma$ level, perhaps due to astrometric contamination from the faint closely projected companion. Nevertheless, our detection of Li absorption and $\text{H}\alpha$ emission confirm the youth of the system. The source is located due west of the embedded ρ Oph cluster, close to EPIC 203710387 in fact.

As with EPIC 203710387, we adopt an effective temperature of $T_{\text{eff}}=2980\pm 75 \text{ K}$, from the empirical calibration of HH15. Monte Carlo error propagation of 50,000 points drawn from a normal distribution in T_{eff} was used to determine A_V and bolometric luminosity.

We adopt the same analysis approach used for EPIC 203710387 and assume a linear limb-darkening law for both EB components, setting the coefficient $u = 0.888$, corresponding to the mean of all values calculated by Claret et al. (2012) satisfying $2780 \text{ K} \leq T_{\text{eff}} \leq 3180 \text{ K}$ and $4.0 \text{ dex} \leq \log g \leq 4.5 \text{ dex}$, appropriate for an M4.5-M5 PMS star.

Radial velocities were acquired over six epochs with HIRES. Though the system is double-lined, only one velocity component (at roughly -5 km s^{-1}) could be extracted from the spectra at two epochs, corresponding to phases ~ 0.4 and 0.6 . Somewhat conspicuously, these two epochs are approximately equidistant in phase from the predicted time of secondary eclipse, as demonstrated in Figure 5.6. The expected velocity separation at these epochs is only a few times the resolution of the spectrograph and we were unable to distinguish two peaks in the cross-correlation function, only a single peak with the quoted velocity, which is near systemic for the binary. In our final mutual fit of the *K2* light curve and HIRES RVs, we exclude these two discrepant observations, which are not obviously associated with either component. We also measured spectroscopic flux ratios from the HIRES data for each of the four epochs included in the radial velocity fitting. We estimated the flux

ratios from the relative heights of the two distinct cross-correlation function peaks. These flux ratios were included as input in the JKTEBOP modeling and helped to constrain the ratio of radii.

The total system luminosity is $\log(L_{\text{bol}}/L_{\odot}) = -1.14 \pm 0.08$, where the uncertainty is dominated by the uncertainty in distance. Despite their similar spectral types, EPIC 203868608 has a luminosity that is larger by a factor of ~ 3 than that of EPIC 203710387. The cluster distance was assumed in the luminosity calculations, and given the significant cluster depth ($\sigma_d/d \approx 9\%$), we considered the possibility that different distances could account for some of the luminosity discrepancy. If we allow for a $2\text{-}\sigma_d$ separation in the line-of-sight distance between the two systems, EPIC 203868608 is still more than twice as luminous as EPIC 203710387. We therefore conclude that differing distances is unlikely to account for the entire luminosity discrepancy between the two systems.

High angular resolution imaging of the system revealed nearby sources which partially resolves the luminosity discrepancy noted above. A snapshot image taken on July 14, 2015 UT with the MAGIQ guide camera on Keck/HIRES revealed a fainter source with $\Delta m = 3.58 \pm 0.10$ mag that at $\sim 4''$ separation is blended with EPIC 203868608 in the $K2$ aperture. Additionally, there is a source $< 15''$ to the southeast with $\Delta m = 1.45 \pm 0.01$ mag fainter than EPIC 203868608 that is partially enclosed by the $K2$ aperture (see the middle right panel of Fig. 5.1, in which this source is resolved in DSS2).

Keck/NIRC2 images obtained on July 25, 2015 UT then revealed a nearly equal brightness ($\Delta J = 0.278 \pm 0.034$ mag, $\Delta K_p = 0.316 \pm 0.021$ mag) companion at a projected separation of $0.12''$. At the distance of Upper Sco, this corresponds to a separation of < 20 AU, indicating the second source is likely a bound companion. We then propose that the eclipses provide evidence that EPIC 203868608 is a hierarchical triple system. Additionally, there exists a more widely separated source to the southeast with $\Delta K_p = 5.11 \pm 0.021$ mag fainter than the brighter component of the nearly equal-brightness pair.

For the remaining discussion, we will assume a primary is being eclipsed by a secondary to remain consistent with the language used to this point. We then designate the third more distant, and presumably single, companion as the tertiary. The NIRC2 imaging indicates a flux (and thus luminosity) ratio between the two near-equal-brightness components of $\sim 0.75\text{-}0.80$ in J -band or $\sim 0.73\text{-}0.76$ in K_p . For the remaining discussion, we will approximate the NIRC2 flux ratio as 0.765 ± 0.035 ,

the mean of the lower limit set by the K_p band and the J -band upper limit. At present, however, we can not say with certainty which component of the pair is the presumably single star and which is the EB. Thus, we consider two general scenarios: (1) in which the tertiary is more luminous than the combined luminosities of the EB components, and (2) in which the tertiary is fainter than the combined EB luminosity.

For each of the two scenarios above, we calculate the expected third light parameters given the measured flux ratios of the tertiary and all other contaminating sources within the aperture. We consider the contributions from all of the blended sources discussed above, as well as the relatively bright source that is only partially enclosed by the $K2$ aperture. For this partially enclosed source, we consider a range of values for the fraction of light enclosed by the aperture. In the absence of other data, we assume the contamination from the tertiary in the *Kepler* bandpass is equal to the measured NIRC2 contamination.

In the first scenario, in which the tertiary luminosity exceeds the EB combined luminosity, the EB contributes approximately 40% of the total system light in the $K2$ light curve, accounting for both the tertiary and fainter contaminating sources in the aperture. This implies a third light parameter of $l_3 = 0.59$, if only 5% of the light from the partially enclosed source is contaminating the aperture, or as high as $l_3 = 0.63$ if half of the light from this source is enclosed.

When allowing the third light parameter to be free, the light curve fitting favors the first scenario, settling on a best fit with a third light parameter of $l_3 = 0.684 \pm 0.016$. Assuming $L_{\text{bol}} = L_1 + L_2 + L_3$ (with no additional sources of contamination), and using the NIRC2 measured flux ratio, and EB luminosity ratio, L_2/L_1 , that arise from the best fit model, we determine EB component luminosities of $L_1 = 0.0146 \pm 0.0029 L_{\odot}$, $L_2 = 0.0146 \pm 0.0029 L_{\odot}$, and a tertiary luminosity of $L_3 = 0.0428 \pm 0.0060 L_{\odot}$. From combination of the light curve and radial velocities, this fit results in EB component masses and radii of $M_1 = 0.02216 \pm 0.00045 M_{\odot}$, $M_2 = 0.02462 \pm 0.00055 M_{\odot}$, $R_1 = 0.2823 \pm 0.0051 R_{\odot}$, $R_2 = 0.2551 \pm 0.0036 R_{\odot}$. We note that the luminosities calculated above are overluminous by a factor of three given the measured effective temperatures and radii. For the radii favored by the fit, and the temperatures we measure from the spectral type and J , the implied luminosities are $L_1 = 0.0046 \pm 0.0005 L_{\odot}$ and identically $L_2 = 0.0046 \pm 0.0005 L_{\odot}$.

However, this scenario, in which the tertiary is more than twice as luminous as either the primary or secondary, is incongruous with the detection of orbital motion

of tens of km s^{-1} in the Keck-I/HIRES spectra. If the tertiary was so luminous, contributing more than half the total system light, it should be readily detectable as a distinct component from the M4.5-M5 primary which exhibits the large radial velocity shifts.

Nevertheless, for completeness, we calculate the EB parameters implied by the best-fit light curve model in this first scenario. Notably, the best-fit model suggests a “secondary” that is slightly hotter, more massive, but smaller than the primary. However, we stress that there are unquantifiable uncertainties due to the fact that the RVs for only one component are well fit by the models. If we assume the HH15 M5 temperature of $T_{\text{eff},1} = 2980 \pm 75$ K for the primary in this scenario, then the radius implied by the luminosity is $R_1 \approx 0.40 \pm 0.04 R_{\odot}$, consistent with the radii of the components of EPIC 203710387, but discrepant at the $3\text{-}\sigma$ level with the radius implied by our light curve and radial velocity fit. We note that the spectral type we find is earlier than the M6.5 spectral type of the eclipsing brown dwarf binary found in the younger Orion Nebula (Stassun et al., 2006; Stassun et al., 2007). For comparison, the primary of that system has a mass of $M=0.054\pm 0.005 M_{\odot}$ and temperature of $T_{\text{eff}}=2650\pm 100$ K (from the spectral type).

Meanwhile, the HIRES spectrum shows no evidence for a component earlier than M4.5. Thus, the tertiary must have a similar temperature and, given its large luminosity, a radius of $R_3 \approx 0.83 \pm 0.09 R_{\odot}$. However, we again emphasize that if the tertiary is indeed so luminous it should have been detected as a distinct peak in the cross-correlation functions.

Evidence in favor of this first scenario is found when comparing the near-IR brightnesses predicted by models for brown dwarfs and stellar mass M-types, with the measured NIRC2 magnitude differences. If we assume the system is composed of a single M5 star (the wide tertiary at ~ 20 AU) with an eclipsing pair that are equal in brightness to each other in either K - or J -band, we can use the K - and J -band magnitude differences from NIRC2 to interpolate between evolutionary models and estimate the masses of the eclipsing pair. For example, BHAC15 models predict an M5 star (here approximated as a $0.1 M_{\odot}$ star) at 10 Myr should have $K=6.60$ mag, $J=7.44$ mag. Holding the age fixed, two brown dwarfs of $\sim 0.03 M_{\odot}$ could reproduce the NIRC2 magnitude differences in either J or K . Allowing the age to be as young as 3 Myr would imply an eclipsing pair of $\sim 0.04 M_{\odot}$ brown dwarfs.

In the second scenario, the EB combined luminosity is greater than the tertiary luminosity. In this case, the EB contributes approximately 50% of the total system

light in the *K2* light curve, depending on the fraction of light included from the partially enclosed source. The range of third light parameters corresponding to 5-50% containment of the partially enclosed source is $l_3 = 0.46 - 0.52$.

In this scenario, we can no longer rely on a light curve model that has a third light parameter $> 55\%$. We perform a new light curve fit using 1,000 MC simulations and fixing third light to $l_3 = 0.50$. Possibly supporting this scenario are the NIRC2 $J - K_p$ colors of the components in the equal-brightness pair, which are 1.064 ± 0.033 and 1.073 ± 0.023 (both uncorrected for reddening). Such similar colors suggest the tertiary and the EB primary have quite similar temperatures. However, we note that the BHAC15 models predict $J - K$ colors that change very little (< 0.1 mag) with either mass or age in the mass range of 0.1-0.3 M_\odot and the age range 1-15 Myr.

The best fit light curve in the second scenario has a reduced- χ^2 that is slightly higher than that of the first scenario (1.24 compared to 1.18, for the masked light curve). In this second case, the EB radii ratio is significantly smaller ($k = 0.6825 \pm 0.0081$), while the temperature ratio is $T_{\text{eff},2}/T_{\text{eff},1} \sim 1.22$, from $J = 2.187 \pm 0.015$. The component luminosities are such that $L_1 = L_2 = 0.018 \pm 0.004 L_\odot$, and $L_3 = 0.036 \pm 0.007 L_\odot$. Since the “secondary” and tertiary have similar NIRC2 colors, we will assume they have equal temperatures in order to calculate the EB radii. The implied radii are then $R_1, R_2, R_3 = 0.746 \pm 0.082, 0.506 \pm 0.055, 0.712 \pm 0.078 R_\odot$, respectively. The primary effective temperature in this case is $T_{\text{eff},1} = 2440 \pm 60$ K. This scenario is also somewhat difficult to imagine, given that it implies the “primary” is ~ 500 K cooler than the secondary, but with a radius that is $\sim 50\%$ larger due to the fact that the spectroscopic flux ratios provide a strong constraint that the EB components have nearly equal luminosities. We also explored fits with lower levels of contamination, and note that the χ_{red}^2 of these fits increased monotonically with lower third light values.

Ultimately, we adopt parameters assuming the first scenario ($L_{\text{EB}} < L_3$), using the HH15 temperature for an M5 star for the “secondary”, and allowing the third light parameter to be free. The best-fit orbital parameters and their uncertainties, derived from 1,000 MC simulations with JKTEBOP, as well as derived parameters for all three components are presented in Table 5.4. We do not attempt to finely characterize the tertiary, due to the numerous intermediate assumptions required in doing so. We note that the most robust information we have for the third component is that it has a similar brightness to the unresolved EB in J and K , has a similar $J - K$ color, and

is undetected in all epochs of our optical spectra.

We consider an alternative explanation for the simultaneous presence of a bright companion in the NIRC2 AO imaging and non-detection of a distinct third component in the HIRES spectra. If the closely projected source discovered in the AO images is not associated but instead a background M-giant, it may have a similar brightness and colors in the near-IR but be too faint to contribute significantly to the optical HIRES spectra. There are two primary difficulties in accepting this scenario: 1) at such a small projected separation ($\sim 0.1''$), the probability that the source is unassociated is finite but low, and 2) the light curve modeling is highly suggestive that there is significant third light in the *Kepler* bandpass, which is primarily optical but does extend to $\sim 0.9 \mu\text{m}$.

We stress that unquantifiable uncertainties remain for the EB parameters of EPIC 203868608, and that the quoted uncertainties are merely formal errors. In particular, the masses are highly uncertain due to the fact that only one component has RVs that are well fit by the model. As illustrated above, uncertainties in the radii-related parameters on the order of a few to tens of percent may also remain due to faulty assumptions regarding the precise optical third light value. However, we again emphasize that there is compelling evidence that the sum of the RV semi-amplitudes is $< 60 \text{ km s}^{-1}$, which at the period implied by the light curve implies a total system mass $< 0.1 M_{\odot}$, placing the components firmly in the brown dwarf mass regime. Furthermore, if the masses are indeed as low as $\sim 20 M_{\text{Jup}}$, and if the tertiary is in fact associated, this system constitutes a unique and intriguing comparison to the population of brown dwarfs and high mass giant planets on wide orbits (tens of AU) that are routinely imaged around young, mostly early-type stars.

Comparing EPIC 203868608 with the compilation of pre-MS EBs and SBs presented in Ismailov et al. (2014), we note that independent of our difficulties above in determining the component parameters, this young system has the highest eccentricity for any pre-MS EB/SB system with a period below 10 days. However, the high eccentricity must also be considered in the context of the potential hierarchical triple nature of the system.

5.6.3 EPIC 203476597

This system is comprised of a late-G type primary, with a likely mid-K-type secondary in a close circular orbit of period 1.4 d. The low inclination indicates grazing eclipses (and thus a poorly constrained radius ratio), and there is some evidence that

the system is semi-detached.

A 5-pixel aperture produced the highest quality *K2* photometry, which was selected for further correction. The raw light curve exhibits both $\sim 3.5\%$ primary and $\sim 2\%$ secondary eclipses with period 1.44 days (see Fig. 5.2). In addition, there is a roughly sinusoidal pattern due to rotation with a 3.21 day period. The 5-pixel aperture also contains a nearby star contributing $\sim 25\%$ of the total flux. Consequently, we subtracted the time-averaged flux from a 1.5-pixel aperture centered on the neighboring star. In principle, this subtraction removes dilution effects, restoring eclipses to their true depths. We note the eclipses became $\sim 1\%$ deeper after this subtraction. For each of the two stars, photometry was extracted from 1.5-pixel apertures to confirm EPIC 203476597 is the eclipsing source.

Twenty-two observations were discarded due to being flux outliers with quality flags indicating the spacecraft was in coarse pointing mode. The stellar variability was removed via four iterations of the cubic B-spline fit with $2\text{-}\sigma$ outlier rejection upon each iteration. After removing the variability, an additional thirteen observations with flux levels $1\text{-}\sigma$ above the median were noted to be artifacts of the detrending procedure and were subsequently discarded. After the detrending procedure was applied, the phased light curve was divided into 100 bins. In each phase bin the mean and standard deviation were computed and $3\text{-}\sigma$ outliers were identified, resulting in the exclusion of an additional 55 observations across the entire campaign.

According to Rizzuto et al. (2015), the primary is a G8 lithium-rich star with weak $H\alpha$ emission and a small amount of reddening ($A_V = 1.3$ mag). Our spectrum is consistent with this type, though a K0 might be more appropriate for the line ratios seen in the HIRES spectrum. In order to fit the SED a higher value of the reddening is found, $A_V \sim 3.0$ mag, which can be lower if a small infrared excess is permitted beyond $2\ \mu\text{m}$, and drops to no less than 2 mag allowing for a spectral type as late as K2. The considerable extinction is consistent with the star's location towards optical nebulosity in the vicinity of ρ Oph, just southwest of the main embedded cluster.

The proper motion measurements reported in UCAC4 ($\mu_\alpha, \mu_\delta = -7.9, -19.9$ mas yr^{-1}) and PPMXL are consistent with membership in Upper Sco within $\chi^2 < 0.1 - 2.5$ (depending on which measurements and which mean cluster values are adopted). Aiding membership confirmation is the detection of both Li I absorption and weak $H\alpha$ emission.

As noted in Figure 5.3, there are obvious changes in $H\alpha$ line profiles among spectra

of this eclipsing system. Examining the difference and ratio of the spectra reveals the change in the lines more clearly, and suggests that the secondary possesses weak H α and Ca II triplet core emission as well as Li I absorption. It is challenging to infer an accurate spectral type from the spectral subtractions or ratios, but a mid-K (K2-K5) type is consistent with the data. Radial velocities obtained over seven epochs never exceeded 1.5 km s^{-1} in magnitude, despite extensive coverage in orbital phase. However, we do note that from epoch to epoch, a large velocity shift is noted in the H α emission component: a positive $10 \pm 2 \text{ km s}^{-1}$ shift was measured between the first and third epochs, separated by only a small phase difference, and a positive $98 \pm 2 \text{ km s}^{-1}$ shift between the first and second epochs which differed by almost 0.2 in phase. These measurements seem to suggest that while the primary shifted by only $\sim 2 \text{ km s}^{-1}$, from the first to second epochs, the secondary moved by $\approx 100 \text{ km s}^{-1}$. The RVs are presented in Table 8.2, and the primary RV curve is presented in Fig. 5.6. Though a fit is not found to the RVs, we can use the non-detection of orbital motion in the lines of the primary to place an upper limit on the mass ratio of $q \sim 0.03$, which would place the secondary in the substellar mass regime. This scenario is seemingly inconsistent with inferences from the HIRES spectra.

One possible explanation for the non-detection of orbital motion greater than a few km s^{-1} in the primary is that the eclipses are due to an unassociated, young EB with low-mass components that are not detectable in the HIRES spectra, except for in H α emission, due to a low optical flux ratio with the G8-K0 star. In this scenario, dilution from the G8-K0 star would dilute the eclipse depths of the EB and mimic a low inclination orbital configuration. More complete phase coverage is needed in the RV curve, but current observations imply a smaller mass ratio than the analysis below suggests.

At the model light curve fitting stage, we adopted a linear limb darkening law for both the primary and secondary. We fixed the limb darkening coefficients for both components to $u = 0.7$, corresponding to the mean of all the tabulated values from Sing (2010) with $3.5 \leq \log g \leq 4.0$, $3500 \text{ K} \leq T_{\text{eff}} \leq 5500 \text{ K}$, and $-0.1 \leq [M/H] \leq 0.1$.

From the effective temperature of $5180 \pm 200 \text{ K}$ derived from the spectral type and HH15 calibration plus recommended error, we find from the photometry that $A_V = 2.4 \pm 0.2 \text{ mag}$ and a J -band based system luminosity $\log(L/L_{\odot}) = 0.13 \pm 0.11 \text{ dex}$, where the error terms come from Monte Carlo sampling of the allowed error in temperature, but for luminosity are dominated by the uncertainty in the distance.

The light curve modeling produces a luminosity ratio which is in good agreement with PARSEC model predictions of the luminosity ratio expected between $0.8 M_{\odot}$ and $1.4 M_{\odot}$ stars at 10 Myr.

From the primary temperature and luminosity we calculated the primary radius to be $R_1 = 1.33 \pm 0.38 R_{\odot}$. The primary radius can be better constrained, however, through combination of the rotational period and projected rotational velocity. The raw *K2* light curve possesses variability due to rotational modulation of star spots. We performed a Lomb-Scargle periodogram analysis on the raw light curve for 10,000 periods between 1 and 4 days. The periodogram peak suggests a rotation period of $P_{\text{rot}} = 3.21 \pm 0.12$ days, where the uncertainty is estimated from the full-width half-maximum (FWHM) of a Gaussian fit to the oversampled periodogram peak. Figure 5.9 shows the periodogram described above along with the raw light curve phase folded on the rotational period. From the HIRES spectrum, we then measured a projected rotational velocity of $v \sin i = 25 \pm 2 \text{ km s}^{-1}$. Combined with the rotational period, we calculate $R_1 \sin i = 1.59 \pm 0.14 R_{\odot}$. Thus, we derive a lower limit of $R_1 > 1.45 R_{\odot}$ and for the range of inclinations favored by the light curve modeling, we find $R_1 = 1.72^{+0.17}_{-0.27} R_{\odot}$.

Combining the primary radius with the best-fit ratio of radii we obtain a secondary radius of $R_2 = 0.96 \pm 0.27 R_{\odot}$, where the large uncertainty is due to the grazing nature of the eclipses. At presumed ages of 5-10 Myr (consistent with the star's location in both the mass-radius and temperature-luminosity planes), this range of radii corresponds to a late-K to mid-M type secondary according to the BHAC15 models, consistent with the inference from the HIRES spectrum. The expected RV semi-amplitude in the primary of this configuration is $\sim 70\text{-}100 \text{ km s}^{-1}$, or $130\text{-}160 \text{ km s}^{-1}$ for the secondary depending on the broad ranges in plausible component masses. From the primary effective temperature and best-fit surface brightness ratio, J , we estimate the secondary temperature, $T_{\text{eff},2} = 4490 \pm 60 \text{ K}$. This value is consistent with a K3-K4 spectral type on the HH15 and PM13 scales.

The best-fit JKTEBOP model has an average fractional radius greater than 0.3, indicating the system may be semi-detached. JKTEBOP treats proximity effects (such as ellipsoidal modulation) in an approximate manner, and is best suited for modeling detached EBs. In such cases, the uncertainty in the derived radii may be as high as 5% (North & Zahn, 2004), though the uncertainty in the ratio of radii we derived is much greater than 5% due to the grazing configuration of the system. The best-fit model light curve and phase-folded *K2* photometry are presented in Fig. 5.4. Best-

fit orbital parameters and their uncertainties, derived from 10,000 MC simulations with JKTEBOP, are presented in Table 5.5.

From the primary radius and R_1/a from the light curve solution, we computed the semi-major axis, $a = 5.8 \pm 0.9 R_\odot$. However, this separation implies a total system mass which is lower than the presumed primary mass, given the period. We obtained lower and upper limits on the semi-major axis by considering the range in system mass corresponding to $M_{\text{tot}} = M_1$ to $M_{\text{tot}} = 2M_1$, also accounting for the uncertainty on the mass. The corresponding range in semi-major axis is 5.8-7.9 R_\odot , or $\sim 3 - 5.5$ times the primary radius. Note that this range assumes the model-dependent primary mass. Kallrath & Milone (2009) suggest that stars with radii greater than ~ 10 -15% of their separation no longer meet the criterion for detachment, providing further support that this system is likely to be semi-detached.

The 2D parameter distributions resulting from the MC fit showed high degrees of correlation between the inclination, surface brightness ratio, and radii related parameters. Nevertheless, the total range in each of these parameters was deemed acceptable. We investigated an alternative solution, holding eccentricity fixed at zero, and fixing the period and ephemeris timebase. This solution yielded very similar results to those from allowing these same parameters to be free.

We note that the presence of both eclipses and a spot modulation pattern in the light curve of EPIC 203476597 may allow for determination of the direction of orbital motion. Eclipse timing variations induced by star spots, combined with measurements of the local slope in the variable light curve of the primary during eclipses, can allow one to distinguish between prograde and retrograde motion (Mazeh et al., 2015; Holczer et al., 2015).

5.7 General Discussion

The young eclipsing binaries identified here are a significant contribution to the pre-main sequence eclipsing binary population below $1 M_\odot$. We have added two EB systems with M-type primary stars and one EB system with a late G primary star to the $< 15 - 20$ EB systems already known at ages less than a few Myr (see Ismailov et al. (2014) and Stassun et al. (2014) for compilations of pre-main sequence EBs and SBs). Quantitative information for each system is provided in Tables 5.3, 5.4, and 5.5.

Our best determinations of the fundamental parameters for the components of the three systems are illustrated Figure 5.8, in comparison to two other multiple systems

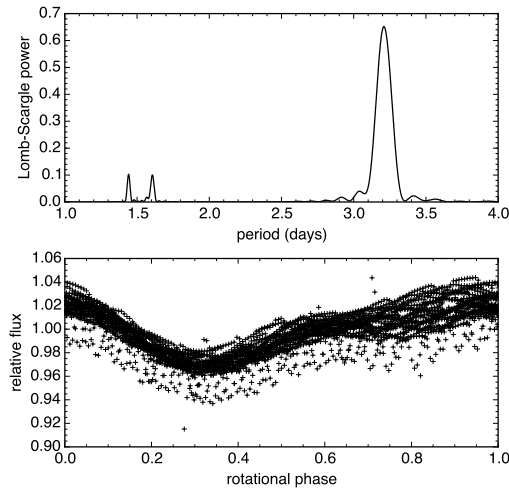


Figure 5.9: *Above*: A Lomb-Scargle periodogram analysis of the EPIC 203476597 raw light curve for 10,000 periods between 1 and 4 days, using the `lombscargle` routine in the `scipy.signal` PYTHON package. The peak at 3.21 days is the rotational period of the primary, while the peaks at 1.4 and 1.6 days represent the orbital period and half the rotational period, respectively. *Below*: The raw K2 light curve phase folded on the rotational period.

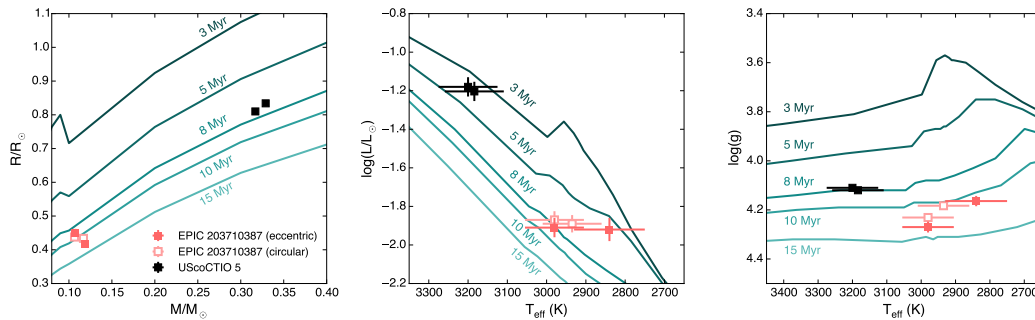


Figure 5.10: BHAC15 isochrones showing an enhanced view of the mass-radius plane (left), as well as the $T_{\text{eff}}-\log(L/L_{\odot})$ (middle), and $T_{\text{eff}}-\log g$ (right) planes. In each case the 3, 5, 8, 10, and 15 Myr isochrones are plotted, from darkest to lightest. The red points indicate the positions of both components of EPIC 203710387, while the black scatter points represent the components of UScoCTIO 5. The dark red shaded squares indicate the parameters of EPIC 203710387 from the eccentric orbit solution, while the light red open squares show the circular solution values. The components of UScoCTIO5 are assumed to have equal temperatures and luminosities, but are offset for clarity here. For both systems, the uncertainties in mass, radius, and $\log g$ are smaller than the points themselves.

in the same Upper Sco association with well-determined parameters.

Each of the three EBs considered in this work have periods < 5 days – even though the *K2* data stream is sensitive to periods as long as 37 days (and up to 75 days if single eclipses are deemed significant). While the periods sample a range of parameter space occupied by other known low-mass EBs⁶, short period orbits are generally attributed to observational biases (Ribas, 2006), which are not present in the case of the *K2* data given its continuous cadence over the 75 days. The period distribution of the newly discovered systems can be further compared to that for previously known pre-main sequence EBs with good orbital solutions, which span the range 2-14 days plus the recent 34 day system characterized by Kraus et al. (2015).

Two of our systems (EPIC 203476597 and EPIC 203710387) appear to be on highly circular orbits, while EPIC 203868608 has a non-negligible eccentricity of $e \approx 0.3$. This last system has the longest period at 4.5 d and is likely part of a hierarchical triple. However, according to Zahn & Bouchet (1989), circularization is expected to occur within < 1 Myr for periods shorter than about 7 days. Melo et al. (2001) seems to have a different view on the necessary timescales, and as noted by Zahn (2008), the pre-MS circularization timescale is a topic of ongoing research.

EPIC 203710387 constitutes the lowest *stellar* mass double-lined EB discovered to date. With masses between the $\sim 0.17M_{\odot} + 0.18M_{\odot}$ JW 380 pair of stars and the $\sim 0.04M_{\odot} + 0.06M_{\odot}$ 2MASS J0535-0546 pair of brown dwarfs, both systems located in Orion, the older $\sim 0.12M_{\odot} + 0.11M_{\odot}$ EPIC 203710387 pair in Upper Sco provides a critical anchor near the substellar boundary for pre-MS evolution models.

5.7.1 Comparing EPIC 203710387 and UScoCTIO 5

With very few low-mass, pre-MS EBs currently known, EPIC 203710387 and UScoCTIO 5, which as double-lined EB systems both have fundamentally determined masses and radii measured to $\lesssim 3\%$ precision, are extremely valuable for testing both model predictions and empirical relations. Interestingly, EPIC 203710387 is a slightly lower-mass analog to UScoCTIO 5 (Kraus et al., 2015, see also the current Appendix) in that it has a mass ratio close to 1 (though it has a much shorter orbital period, 2.8 d compared to 34 d). These systems are especially significant because at the lowest stellar masses, discrepancies between observations of eclipsing binaries and theoretical models are most prominent.

⁶<http://www.astro.keele.ac.uk/~jkt/debcats/>

For example, main sequence EBs with M-type components have been observed to have radii that are 5-15% larger than model predictions (Ribas, 2006). Though, those authors do point out models seem to perform better below $\sim 0.30-0.35 M_{\odot}$ (near the limit between fully convective stars and those with radiative cores). Magnetic activity is one possible explanation invoked to account for the inflated radii of low-mass EBs. In principle, this is a testable prediction since the model-observation discrepancies should become larger at shorter periods due to the facts that (1) at short periods the rotational and orbital periods are expected to be synchronized and (2) activity is expected to increase with increasing rotational velocity (Feiden, 2015).

For pre-MS evolution, starspots have also been advanced as a means of producing inflated radii for low-mass stars. Recently, Somers & Pinsonneault (2015) studied the effect of starspots on pre-MS evolution for stars of $0.1-1.2 M_{\odot}$. They found that pre-MS models accounting for starspots leads to radii that are enhanced by up to 10%, consistent with observations of active EBs. Spotted stars also have a decreased luminosity and T_{eff} , leading to systematic underestimation of both masses (by a factor of 2) and ages (by factors of 2-10) derived from evolutionary models that do not take spots into account.

Kraus et al. (2015) used USco-CTIO 5 to test various pre-main-sequence evolutionary models. For an assumed cluster age of 11 Myr, those authors found BHAC15 and several other models under-predict the fundamentally determined radius at the fundamentally determined mass (with Padova models working in the opposite direction). For the more traditional cluster age of 5 Myr, the models over-predict the radius. The results are consistent in the older age scenario with the so-called "radius inflation" found among many main sequence eclipsing binary systems.

We also find for the components of EPIC 203710387 that for the canonical 3-5 Myr age, the models significantly over-predict the fundamentally determined radii. However, we find that for an assumed cluster age of 10-11 Myr, the BHAC15 models quite accurately predict the radii at the masses of the components of EPIC 203710387. Thus, if the older age is assumed accurate, we find no evidence for radius inflation in this lower mass, shorter period analog to UScoCTIO 5.

In comparing the two systems, we also noted significant temperature discrepancies for what is reportedly only a 0.5 subclass difference in spectral type. Kraus et al. (2015) determined an $M4.5 \pm 0.5$ spectral type for UScoCTIO 5 based on comparison of a low-resolution spectrum with field M dwarf spectra, simultaneously constraining

spectral type and extinction. While this result is consistent with the M4 spectral type for UScoCTIO 5 originally reported by Ardila et al. (2000), there is evidence favoring an earlier type. Reiners et al. (2005) found that discrepancies between the dynamically measured system mass and masses predicted by models could be rectified by considering a spectral type that is half a subclass or more earlier than M4.

Indeed, the “geometric” temperature derived by Kraus et al. (2015) for both components of UScoCTIO 5 (from the sum of the radii, total system luminosity, and assuming equal-luminosity components) is $T_{\text{eff,geom}} = 3235_{-200}^{+160}$ K, which is slightly higher than the empirical temperatures of young M4 stars on both the HH15 ($T_{\text{eff}} = 3190$ K) and PM13 ($T_{\text{eff}} = 3160$ K) scales. By comparison, the effective temperatures for the components of EPIC 203710387 based on the total system luminosity, luminosity ratio, and the radii (assumed to be equal), are more in line with an M6 type for both the primary and secondary on the HH15 scale. In other words, the components of EPIC 203710387 are ~ 100 K cooler than the predicted M5 temperature on the HH15 scale, but in good agreement with the analogous PM13 prediction.

If we assume equal-luminosity components of EPIC 203710387 and calculate the “geometric” effective temperature implied by the total system luminosity and the sum of the radii, as Kraus et al. (2015) did, we obtain $T_{\text{eff,geom}} \approx 2410 \pm 120$ K, or more than 500 K cooler than the empirical temperature of a young M5 star. This discrepancy becomes larger if we assume the radii have been underestimated. In fact, assuming the M5 spectral type and temperature are correct, then the system luminosity implies a sum of radii of $R_1 + R_2 = 0.568 \pm 0.057 R_{\odot}$, or component radii of only $\sim 0.284 R_{\odot}$.

One possible explanation for this discrepancy is starspots. The “geometric” temperature assumes the measured luminosity is the intrinsic luminosity. However, for a spotted star the measured luminosity is actually the product of the intrinsic luminosity and the factor $(1 - \beta)$, where β is the equivalent spot covering fraction, which Jackson & Jeffries (2014) suggest may be as high as ~ 0.35 - 0.51 for M-type pre-MS stars.

Thus, assuming the measured luminosity is the intrinsic luminosity leads to an anomalously low temperature when holding the radius fixed, or conversely an erroneously small radius when the temperature is held fixed. We estimate the average spot covering fraction for the components of EPIC 203710387 from the ratio of the “emitting” surface area to the measured surface area, which implies an average spot

covering fraction of $\sim 60\%$.

In Appendix 5.A, we present our independent analysis of UScoCTIO 5 from our own detrended *K2* light curve combined with the radial velocities and spectroscopic flux ratios published in Kraus et al. (2015). We find masses that are consistent with K15, but radii that are significantly larger. Our revised parameters help somewhat to resolve the discrepancies noted above for the age of the system as determined in different theoretical planes. We find the system age to be consistent with ~ 6 Myr.

5.7.2 On the Age of Upper Scorpius

Disagreement about the age of Upper Sco stems from different studies of distinct stellar populations, such that the more massive stars appear older (~ 10 Myr) and the less massive stars appear younger (~ 3 -5 Myr). Several possible “simple” explanations for this observed discrepancy exist: (1) the evolutionary models are inadequate, and the degree to which they diverge from observations is mass-dependent (this explanation includes the failure of models to properly include magnetic fields and spot-related effects), (2) the binary fraction at low masses is underestimated such that isochrone ages for these stars are anomalously young, having neglected the companion’s luminosity, (3) there is a genuine dispersion of roughly a few Myr in the ages of Upper Sco members, indicating extended star formation.⁷

Notably, the age we find for EPIC 203710387 in the fundamental mass-radius plane is ~ 10 -11 Myr (using the circular orbit solution), older than the canonical 3-5 Myr age for Upper Sco. While large uncertainties remain for EPIC 203476597 (grazing and possibly semi-detached) and EPIC 203868608 (a triple system), starB and UScoCTIO 5 are well-characterized and provide reliable anchors with which to investigate the cluster age at the lowest stellar masses.

In Figure 5.10, we show the positions of these two double-lined EBs in different planes with BHAC15 isochrones overplotted. In each plane, no single isochrone can match the observed parameters of both EBs. However, an even larger discrepancy becomes apparent when comparing the ages of a single EB system derived in different planes. For example, while the components of EPIC 203710387 rest near the 10 Myr isochrone in mass-radius space, the same stars suggest an age of $\sim 7 \pm 3$ Myr in the temperature-luminosity plane. A similar trend is true of UScoCTIO 5, the components of which lie closest to the 8 Myr mass-radius isochrone, but appear

⁷Evidence for luminosity spreads, potentially due to an age dispersion of several Myr, is well-documented in the pre-MS Orion Nebula Cluster (Hillenbrand, 1997; Da Rio et al., 2010).

more consistent with the canonical 3-5 Myr age in temperature-luminosity space. It is noteworthy that the $T_{\text{eff}}\text{-log}(L/L_{\odot})$ ages for both systems are in broad agreement with the widely accepted cluster age of 3-5 Myr which is also based on H-R diagram (HRD) analyses of low-mass members. The ages in $T_{\text{eff}}\text{-log } g$ space for each system, however, are in closer agreement with those ages from the mass-radius plane.

As reviewed by Kraus et al. (2015), considering different sets of pre-MS models does not alleviate the discrepancies noted above. These results indicate that (1) no set of models is able to predict the ensemble of fundamental parameters for pre-MS stars in this mass range, and/or (2) there is a systematic bias in one or more observationally determined parameters. For example, if current empirical SpT- T_{eff} or color- T_{eff} scales systematically underestimate T_{eff} by a couple hundred K, the HRD-derived ages of the hundreds of low-mass members would shift closer to 10 Myr. However, in the $T_{\text{eff}}\text{-log } g$ plane it is not possible to shift the systems along the temperature axis in order to obtain a match to the canonical 3-5 Myr age. This indicates there is some minimal “age” spread if it is believed that radii contract and masses remain constant during pre-MS evolution.

The stellar bulk parameters of mass and radius for double-lined EBs are directly determined with exquisite precision based on firmly understood physics. Meanwhile, the photospheric parameters of T_{eff} and luminosity are generally less well-determined. In principle, this suggests that ages derived for double-lined EBs in the mass-radius diagram should be considered more fundamental than HRD ages. However, few pre-MS EBs with well-determined radii exist, and so evolution models at these ages are uncalibrated.

If the masses and radii of EPIC 203710387 and UScoCTIO 5 are assumed accurate, then the models must overpredict the radii by $\sim 10\text{-}25\%$ for 5 Myr to be the true age. Interestingly, this implies stellar evolution models are not contracting quickly enough at these masses to match observations. Future iterations of stellar models at these masses will include magnetic fields and starspots, two phenomena which are intrinsically linked and both act to *slow* contraction through inhibiting convection and decreasing the emergent flux (Feiden, 2016b). Thus, as models evolve to include these effects, the discrepancy between the canonical age of 3-5 Myr and the ages implied for these two systems in the mass-radius plane will likely *widen*. If current mass-radius isochrones are assumed correct, then these two double-lined EBs favor an older (8-10 Myr) age for Upper Sco.

5.7.3 Coevality Within and Between Systems

With multiple EBs in the same star forming region, and the additions of UScoCTIO 5 and HD 144548, it is possible to study the degree of coevality within individual systems (intra-coevality) and between distinct EBs (inter-coevality). Stassun et al. (2014) found that, among PMS EBs in Orion, the components within a given EB appear significantly more coeval than do the EBs relative to one another. In other words, EBs in Orion display a higher degree of intra-coevality than inter-coevality. A possible explanation for this behavior could be genuine age dispersion in a presumably coeval population, as mentioned in § 5.7.2.

As mentioned in § 5.7.5, the more massive component of the triple system HD 144548 appears to be several Myr younger than lower mass eclipsing pair. However, due to the difficulty of characterizing triple systems, it is possible that this apparent non-coevality within a single system is artificial in nature. Nevertheless, an empirical mass-radius isochrone at the age of Upper Sco is beginning to emerge from the components of EPIC 203710387, UScoCTIO 5, and the lower mass components of HD 144548 (see Fig. 5.11). Each of these systems have mass ratios close to 1, making it difficult to draw meaningful conclusions about the intra-coevality of any particular system. However, there is an interesting trend in which the higher mass EBs of Upper Sco appear *younger* than their lower mass counterparts.

From our comparison of EPIC 203710387 and UScoCTIO 5 (see Fig. 5.10), it is also apparent that there is a higher degree of coevality within each of these systems than between them. Specifically, there is a $\lesssim 1$ Myr discrepancy between the ages of the primary and secondary of EPIC 203710387 (in the circular orbit case) and similarly for the two components of UScoCTIO 5. However, despite the fact that both systems belong to the presumably coeval population in Upper Sco, EPIC 203710387 appears to be 3-4 Myr older than UScoCTIO 5. Preliminary results from modeling the pre-main-sequence evolution of low-mass stars indicate that including magnetic fields may significantly help to resolve the discrepancies noted above (G. Feiden, private communication). We note that the eccentric orbit solution for EPIC 203710387 leads to primary and secondary parameters that appear significantly less coeval relative to the circular solution in all of the parameter planes featured in Fig. 5.10. However, we caution that this discrepancy is possibly due to a degeneracy between the temperature ratio and ratio of radii. More precise spectroscopic flux ratios may help to resolve this issue in the future.

5.7.4 Chromospheric Activity Effects

The correlation between chromospheric activity and the temperatures, radii, and subsequently derived masses of main-sequence stars is well-established (e.g. López-Morales, 2007). Due to the paucity of pre-MS benchmark systems, however, the effect of activity on the fundamental parameters of pre-MS stars has not been rigorously tested. For field age low-mass stars and brown dwarfs, Stassun et al. (2012) derived an empirical relation to correct for such activity effects based on the $H\alpha$ equivalent width (see §2.1 of that work), among other measures. Using our $EW(H\alpha)$ measurements from the HIRES spectra (see Table 5.2), we calculated that the fractional change in the radii and temperatures for the two components of EPIC 203710387 are approximately:

$$\Delta R_1/R_1 = 2.0 \pm 0.9\%$$

$$\Delta R_2/R_2 = 2.7 \pm 1.3\%$$

$$\Delta T_{\text{eff},1}/T_{\text{eff},1} = -1.3 \pm 0.4\%$$

$$\Delta T_{\text{eff},2}/T_{\text{eff},2} = -1.6 \pm 0.6\%.$$

Thus, in agreement with the findings of Stassun et al. (2014), we determine that the effect of chromospheric activity on the temperatures, radii, and masses of EPIC 203710387 is small enough that it can not resolve the apparent discrepancies between the positions in the mass-radius diagram compared with the positions in $T_{\text{eff}}-L$ space, as discussed in § 5.7.1 and illustrated in Fig. 5.10. We note, however, that a temperature suppression of $\sim 2\%$ does help to partially resolve the discrepancies noted above, leading to inferred ages closer to those implied by the well-determined masses and radii.

We find for the eclipsing components of EPIC 203868608 that the corrections in the radii and temperatures due to activity are approximately $\Delta R/R \sim 4 \pm 2\%$, and $\Delta T_{\text{eff}}/T_{\text{eff}} \sim 2 \pm 1\%$. This level of temperature suppression could potentially explain the apparent reversal in T_{eff} between the primary and secondary components, given that the primary is apparently more active. Similar behavior was observed in the other known eclipsing brown dwarf system discovered in Orion (Stassun et al., 2006; Stassun et al., 2007). We note, however, even larger uncertainties may remain in the parameters of this system due to its triple nature and the subsequent complexity of its analysis.

5.7.5 Triple Systems in Upper Sco

In comparison with binaries, Stassun et al. (2014) found that benchmark pre-MS triple systems have apparently corrupted properties in both the mass-radius and T_{eff} -luminosity planes. Recently, Alonso et al. (2015) characterized the young triply eclipsing system HD 144548 (EPIC 204506777) in Upper Sco. As seen in Figure 5.11, the system is composed of an eclipsing pair of $\sim 1.0 M_{\odot}$ stars, which in turn eclipse a $\sim 1.5 M_{\odot}$ tertiary host. While the less massive pair have masses and radii that are in broad agreement with the emerging empirical mass-radius isochrone from EPIC 203710387 and UScoCTIO 5 (i.e. located between the 5 and 10 Myr BHAC15 isochrones), the massive tertiary has a highly discrepant mass and radius suggestive of a 1-2 Myr age.

ScoPMS 20 is another triple system in Upper Sco, characterized by Mace et al. (2012). As seen in Figure 5.8, this system also presents a challenge to the conventional notion of a coeval stellar population within Upper Sco. Only one component of ScoPMS 20 has a published mass and radius, which places it between 2-5 Myr in widely used pre-MS models. This is in contrast to EPIC 203710387, UScoCTIO 5, and the two less massive components of HD 144548, which are all suggestive of an age between 5-10 Myr according to BHAC15 mass-radius isochrones. The three components of ScoPMS 20 present a slightly more coherent picture in the temperature-luminosity plane, though the positions are suggestive of a somewhat younger age relative to the lower mass systems mentioned above.

Finally, for EPIC 203868608, the uncertainties intrinsic to the analysis of this system make it difficult to comment on the quality of derived parameters relative to binary counterparts. With our current knowledge, it is not possible to determine the radius of the tertiary, since there is no eclipse information and even if the orbit is highly inclined, the period implied by the separation is unfavorably long. Moreover, it is not yet clear whether the tertiary is indeed associated. Resolved spectroscopy of the closely projected companion could be used to test the scenario that it is a background M-giant. If the companion is associated, it is possible, however, that radial velocity time series over a sufficiently long time baseline could allow for dynamical mass measurements of all three components. The radii are uncertain due to the uncertain nature of the contamination in the *K2* bandpass. Optical AO imaging of the system would provide a direct measurement of this quantity, and further test the background M-giant scenario described above. Furthermore, the EB components appear to be in a mass regime where the pre-MS evolutionary tracks are closely clustered and

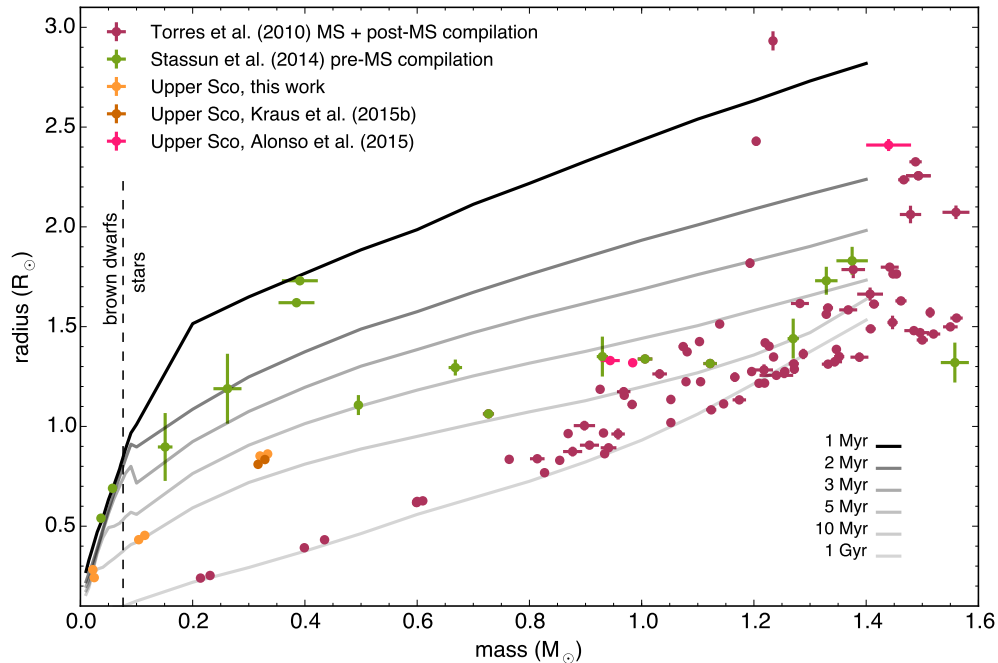


Figure 5.11: BHAC15 isochrones in the mass-radius plane. Overplotted are compilations of double-lined EBs with fundamentally determined masses and radii, either in the pre-MS phase of evolution (Stassun et al., 2014) or MS/post-MS phases of evolution (Torres et al., 2010). At a fixed mass, the radius evolves vertically downward in this diagram. We include recently characterized, double-lined eclipsing members of Upper Sco. For UScoCTIO 5, first characterized by Kraus et al. (2015), we overplot our revised parameters. We additionally input small offsets to our derived parameters for EPIC 203710387 and EPIC 203868608 for visual clarity. We do not include the tertiary for this latter system since a fundamental determination of the mass and radius for that component was not possible. We stress that unquantifiable uncertainties remain for EPIC 203868608, but we include the EB components here for illustrative purposes. The pink points correspond to the triply eclipsing system HD 144548 (Alonso et al., 2015).

largely vertical (see Figure 5.11), implying that a broad range of radii are feasible for current mass determinations and the relatively uncertain age of Upper Sco.

5.8 Conclusion

We report the discovery of three new pre-MS EBs. Two systems (EPIC 203476597 and EPIC 203710387) are secure members of the Upper Sco association, while the third (EPIC 203868608) is certainly young but has a discrepant proper motion. All three systems are located in the southern part of the association, relatively close to but west of the ρ Oph molecular cloud.

The system EPIC 203710387 was observed to be double-lined, allowing model-independent masses and radii to be measured through combination of the light curve

and the radial velocities. With near-equal mass $0.12+0.11 M_{\odot}$ components, it is the lowest-mass stellar double-lined EB discovered to date.⁸ The mass measurements of both components have $\sim 2\%$ precision, while the radii were fixed as equal in order to obtain a reasonable solution for the ensemble of parameters. The positions of both components in the fundamental mass-radius plane are consistent with a ~ 10 Myr age according to both the BHAC15 and Siess et al. (2000) isochrones.

We provide tentative evidence that the system EPIC 203868608 is an eclipsing system of $\sim 25+25 M_{\text{Jup}}$ brown dwarfs in a potential hierarchical triple configuration with a wide M-type companion. If confirmed, this would be only the second double-lined eclipsing brown dwarf system discovered to date (see Stassun et al., 2006; Stassun et al., 2007). This system also constitutes the most eccentric pre-MS binary system having an orbital period < 10 days (c.f. Ismailov et al., 2014), though a stellar-mass companion interior to 20 AU also contributes to the dynamical evolution of this system. Such a system presents a unique data point for studies concerning pre-MS circularization timescales. The triple nature of the system also makes it interesting for investigations of dynamical effects in hierarchical triples such as the Kozai-Lidov mechanism. This system is also significantly more luminous than EPIC 203710387 while sharing the same combined light spectral type. Follow-up studies, notably optical AO imaging and resolved near-IR spectroscopy could shed light on the nature of the AO companion. Additional radial velocities will also help to more accurately constrain the EB component masses and separation, and hence radii through combination of RVs and the light curve.

EPIC 203476597 has a roughly $1.4 M_{\odot}$ primary with a likely early-M to mid-K type secondary. The extremely short period suggests this system may be semi-detached, and there is possible evidence for ellipsoidal modulation in the raw *K2* light curve. If ellipsoidal modulation is recovered from the light curve, re-analysis with software suitable for semi-detached EBs could produce a highly precise mass ratio for this system (Wilson, 1994). Follow-up infrared spectroscopy, where the flux ratio is more favorable relative to optical, could reveal secondary lines and allow for dynamical mass measurements and directly measured radii. The positions of the primary in both the mass-radius and temperature-luminosity planes are consistent with an age of ~ 10 Myr, though we note that the mass determination is model-dependent and the large parameter uncertainties do admit ages < 5 Myr.

⁸The pre-MS system reported by Stassun et al. (2006) and Stassun et al. (2007) has lower mass components with masses just below the stellar-brown dwarf boundary.

We have characterized the components of the three EB systems presented here based on the information available, acknowledging that future spectroscopic studies will greatly refine the parameters. These three newly identified EB systems, in addition to the recently fully characterized (Kraus et al., 2015) UScoCTIO 5 system, are valuable assets for constraining pre-MS evolutionary models at the age of Upper Sco.

ACKNOWLEDGMENTS

We thank the referee for many helpful comments, which greatly improved the quality and rigor of this work. We thank Ian Crossfield for lending his Python MCMC wrapper for the `JKTEBOP` orbit fitting code and for consultation regarding its use, which aided our analysis. We thank Erik Petigura for helpful discussions regarding eclipse model fitting practices. We thank Howard Isaacson, Geoff Marcy, Erik Petigura and the CPS group for acquiring additional HIRES spectra and providing MAGIQ snapshots for the three systems. We thank Christoph Baranec for acquiring Keck/NIRC2 images of EPIC 203476597 and EPIC 203868608, and Brendan Bowler for performing the reductions of these data. We thank Jessie Christiansen for early advice regarding *Kepler* telescope data products, photometry techniques, and detrending strategies. We thank Avi Shporer for suggesting the possibility of measuring the direction of orbital motion for EPIC 203476597. We thank Jonathan Swift for lending his transit analysis routines, which aided our analysis. We thank Ross Fredella for his assistance in creating Figure 1.

The material presented herein is based upon work supported in 2015 by the National Science Foundation Graduate Research Fellowship under Grant No. DGE1144469. T. J. D. gratefully acknowledges research activities support from France Córdoba through the Neugebauer Scholarship. This research was partially supported by an appointment to the NASA Postdoctoral Program at the Ames Research Center, administered by Oak Ridge Associated Universities through a contract with NASA. This research has made use of the NASA Exoplanet Archive, which is operated by the California Institute of Technology, under contract with the National Aeronautics and Space Administration under the Exoplanet Exploration Program. This research has also made use of the SIMBAD database and VizieR catalog access tool, operated at CDS, Strasbourg, France, and NASA's ADS and IPAC/IRSA services. Some of the data presented in this paper were obtained from the Mikulski Archive for Space Telescopes (MAST). STScI is operated by the Association of Universities for Research in Astronomy, Inc., under NASA contract NAS5-26555. Support for MAST for non-HST data is provided by the NASA Office of Space Science via grant NNX09AF08G and by other grants and contracts. This paper includes data collected by the Kepler mission. Funding for the Kepler mission is provided by the NASA Science Mission directorate. Some of the data presented herein were obtained at the W.M. Keck Observatory, which is operated as a scientific partnership among

the California Institute of Technology, the University of California and the National Aeronautics and Space Administration. The Observatory was made possible by the generous financial support of the W.M. Keck Foundation. The authors wish to recognize and acknowledge the very significant cultural role and reverence that the summit of Mauna Kea has always had within the indigenous Hawaiian community. We are most fortunate to have the opportunity to conduct observations from this mountain.

Table 5.3: System Parameters of EPIC 203710387

Parameter	Symbol or Prefix	Value	Units	Source
<i>Identifying Information</i>				
Right ascension	α J2000.	16:16:30.681	hh:mm:ss	Roeser et al. (2010)
Declination	δ J2000.	-25:12:20.20	dd:mm:ss	Roeser et al. (2010)
K2 ID	EPIC	203710387		Huber & Bryson 2015
2 Micron All Sky Survey ID	2MASS	J16163068-2512201		Cutri et al. (2003)
Wide-field Infrared Survey Explorer ID	AllWISE	J161630.66-251220.3		Cutri & et al., 2014
UKIRT Infrared Deep Sky Survey ID	UGCS	J161630.67-251220.2		Lawrence et al., 2013
<i>Photometric Properties</i>				
	J	12.932 ± 0.023	mag	2MASS
	H	12.277 ± 0.024	mag	2MASS
	K_s	11.907 ± 0.023	mag	2MASS
	$W1$	11.748 ± 0.023	mag	AllWISE
	$W2$	11.483 ± 0.022	mag	AllWISE
	$W3$	>11.559	mag	AllWISE; S/N < 2
	$W4$	>8.846	mag	AllWISE; S/N < 2
	KEPMAG	14.268	mag	K2 EPIC
<i>Best-Fitting Adjusted Parameters (Eccentric Solution)</i>				
Orbital period	P	2.808849 ± 0.000024	days	this work
Ephemeris timebase - 2456000	T_0	894.71388 ± 0.00051	BJD	this work
Surface brightness ratio	J	0.825 ± 0.065		this work

Table 5.3 Continued: System Parameters of EPIC 203710387

Sum of fractional radii	$(R_1 + R_2)/a$	0.1700 ± 0.0021		this work
Ratio of radii	k	1.077 ± 0.045		this work
Orbital inclination	i	82.84 ± 0.10	deg	this work
Combined eccentricity, periastron longitude	$e \cos \omega$	-0.00298 ± 0.00029		this work
Combined eccentricity, periastron longitude	$e \sin \omega$	-0.0153 ± 0.0091		this work
Primary radial velocity amplitude	K_1	43.43 ± 0.60	km s^{-1}	this work
Secondary radial velocity amplitude	K_2	47.77 ± 0.43	km s^{-1}	this work
Systemic radial velocity	γ	-3.38 ± 0.22	km s^{-1}	this work
Mass ratio	q	0.909 ± 0.014		this work
Reduced chi-squared of light curve fit	χ_{red}^2	1.060		this work
RMS of best fit light curve residuals		6.76	ppt	this work
Reduced chi-squared of primary RV fit	χ_{red}^2	1.363		this work
RMS of primary RV residuals		0.75	km s^{-1}	this work
Reduced chi-squared of secondary RV fit	χ_{red}^2	0.522		this work
RMS of secondary RV residuals		0.68	km s^{-1}	this work

Best-Fitting Derived Parameters (Eccentric Solution)

Orbital semi-major axis	a	5.100 ± 0.043	R_{\odot}	this work
Fractional radius of primary	R_1/a	0.0818 ± 0.0020		this work
Fractional radius of secondary	R_2/a	0.0882 ± 0.0021		this work
Luminosity ratio	L_2/L_1	0.957 ± 0.034		this work
Primary mass	M_1	0.1183 ± 0.0028	M_{\odot}	this work
Secondary mass	M_2	0.1076 ± 0.0031	M_{\odot}	this work
Primary radius	R_1	0.417 ± 0.010	R_{\odot}	this work
Secondary radius	R_2	0.450 ± 0.012	R_{\odot}	this work
Primary surface gravity	$\log g_1$	4.270 ± 0.022	cgs	this work
Secondary surface gravity	$\log g_2$	4.164 ± 0.021	cgs	this work
Primary mean density	ρ_1	1.63 ± 0.12	ρ_{\odot}	this work
Secondary mean density	ρ_2	1.184 ± 0.088	ρ_{\odot}	this work

Table 5.3 Continued: System Parameters of EPIC 203710387

Impact parameter of primary eclipse	b_1	1.547 ± 0.047		this work
Impact parameter of secondary eclipse	b_2	1.500 ± 0.021		this work
Eccentricity	e	0.0156 ± 0.0087		this work
Periastron longitude	ω	259.0 ± 9.3	deg	this work
<i>Best-Fitting Adjusted Parameters (Circular Solution)</i>				
Orbital period	P	2.808862 ± 0.000024	days	this work
Ephemeris timebase - 2456000	T_0	894.71117 ± 0.00043	BJD	this work
Surface brightness ratio	J	0.940 ± 0.014		this work
Sum of fractional radii	$(R_1 + R_2)/a$	0.1715 ± 0.0021		this work
Ratio of radii	k	1.009 ± 0.017		this work
Orbital inclination	i	82.76 ± 0.10	deg	this work
Primary radial velocity amplitude	K_1	43.28 ± 0.52	km s^{-1}	this work
Secondary radial velocity amplitude	K_2	47.55 ± 0.57	km s^{-1}	this work
Systemic radial velocity	γ	-3.26 ± 0.23	km s^{-1}	this work
Mass ratio	q	0.910 ± 0.015		this work
Reduced chi-squared of light curve fit	χ_{red}^2	1.173		this work
RMS of best fit light curve residuals		7.08	ppt	this work
Reduced chi-squared of primary RV fit	χ_{red}^2	1.423		this work
RMS of primary RV residuals		0.80	km s^{-1}	this work
Reduced chi-squared of secondary RV fit	χ_{red}^2	0.766		this work
RMS of secondary RV residuals		0.85	km s^{-1}	this work
<i>Best-Fitting Derived Parameters (Circular Solution)</i>				
Orbital semi-major axis	a	5.044 ± 0.037	R_{\odot}	this work
Fractional radius of primary	R_1/a	0.0854 ± 0.0013		this work
Fractional radius of secondary	R_2/a	0.0861 ± 0.0013		this work

Table 5.3 Continued: System Parameters of EPIC 203710387

Luminosity ratio	L_2/L_1	0.957 ± 0.034		this work
Primary mass	M_1	0.1169 ± 0.0031	M_\odot	this work
Secondary mass	M_2	0.1065 ± 0.0027	M_\odot	this work
Primary radius	R_1	0.4338 ± 0.0071	R_\odot	this work
Secondary radius	R_2	0.4377 ± 0.0080	R_\odot	this work
Primary surface gravity	$\log g_1$	4.231 ± 0.013	cgs	this work
Secondary surface gravity	$\log g_2$	4.183 ± 0.013	cgs	this work
Primary mean density	ρ_1	1.433 ± 0.062	ρ_\odot	this work
Secondary mean density	ρ_2	1.270 ± 0.058	ρ_\odot	this work
Impact parameter of primary eclipse	b_1	1.4694 ± 0.0030		this work
Impact parameter of secondary eclipse	b_2	1.4694 ± 0.0030		this work
<i>Final Adopted Stellar Parameters</i>				
Primary spectral type	SpT ₁	M4.5-M5		this work, spectroscopy
Secondary spectral type	SpT ₂	M4.5-M5		this work, spectroscopy
Extinction	A_V	1.22 ± 0.31	mag	this work, SpT, photometry
Bolometric luminosity	$\log(L_{\text{bol}}/L_\odot)$	-1.64 ± 0.08	dex	this work, SpT, photometry, A_V , d
Primary luminosity	L_1	0.0124 ± 0.0014	L_\odot	this work, $T_{\text{eff},1}$, R_1
Secondary luminosity	L_2	0.0119 ± 0.0016	L_\odot	this work, $T_{\text{eff},2}$, R_2
Orbital semi-major axis	a	5.100 ± 0.043	R_\odot	this work, fundamental determination
Primary mass	M_1	0.1183 ± 0.0028	M_\odot	this work, fundamental determination
Secondary mass	M_2	0.1076 ± 0.0031	M_\odot	this work, fundamental determination
Primary radius	R_1	0.417 ± 0.010	R_\odot	this work, fundamental determination
Secondary radius	R_2	0.450 ± 0.012	R_\odot	this work, fundamental determination
Primary surface gravity	$\log g_1$	4.270 ± 0.022	cgs	this work, M_1 , R_1
Secondary surface gravity	$\log g_2$	4.164 ± 0.021	cgs	this work, M_2 , R_2
Primary mean density	ρ_1	1.63 ± 0.12	ρ_\odot	this work, M_1 , R_1
Secondary mean density	ρ_2	1.184 ± 0.088	ρ_\odot	this work, M_2 , R_2
Primary effective temperature	$T_{\text{eff},1}$	2980 ± 75	K	this work, SpT, HH15

Table 5.3 Continued: System Parameters of EPIC 203710387

Secondary effective temperature	$T_{\text{eff},2}$	2840 ± 90	K	this work, $J, T_{\text{eff},1}$
Primary age	τ_1	11.6 ± 0.4	Myr	this work
Secondary age	τ_2	9.9 ± 0.3	Myr	this work

Best-fit orbital parameters and their uncertainties resulting from 10,000 Monte Carlo simulations with JKTEBOP in the circular case and 5,000 simulations in the eccentric case. The χ_{red}^2 values quoted above were computed over the light curve with out-of-eclipse observations removed. Both the primary and secondary ages are determined from interpolation of the MC distributions in mass and radius between the BHAC15 isochrones.

Table 5.4: System Parameters of EPIC 203868608

Parameter	Symbol or Prefix	Value	Units	Source
<i>Identifying Information</i>				
Right ascension	α J2000.	16:17:18.992	hh:mm:ss	Roeser et al. (2010)
Declination	δ J2000.	-24:37:18.75	dd:mm:ss	Roeser et al. (2010)
K2 ID	EPIC	203868608		Huber & Bryson 2015
2 Micron All Sky Survey ID	2MASS	J16171898-2437186		Cutri et al. (2003)
Wide-field Infrared Survey Explorer ID	AllWISE	J161718.97-243718.9		Cutri & et al. (2014)
UKIRT Infrared Deep Sky Survey ID	UGCS	J161718.97-243718.7		Lawrence et al. (2013)
<i>Photometric Properties</i>				
	J	11.858 ± 0.026	mag	2MASS
	H	11.137 ± 0.024	mag	2MASS
	K_s	10.760 ± 0.021	mag	2MASS
	$W1$	10.535 ± 0.023	mag	AllWISE
	$W2$	10.286 ± 0.020	mag	AllWISE
	$W3$	10.150 ± 0.078	mag	AllWISE
	$W4$	8.638 ± 0.416	mag	AllWISE
	KEPMAG	13.324	mag	K2 EPIC
<i>Best-Fitting Adjusted Parameters</i>				
Orbital period	P	4.541710 ± 0.000019	days	this work
Ephemeris timebase - 2456000	T_0	896.19699 ± 0.00019	BJD	this work

Table 5.4 Continued: System Parameters of EPIC 203868608

Surface brightness ratio	J	1.223 ± 0.066		this work
Sum of fractional radii	$(R_1 + R_2)/a$	0.12930 ± 0.00073		this work
Ratio of radii	k	0.904 ± 0.026		this work
Third light	l_3	0.684 ± 0.016	L_{tot}	this work
Orbital inclination	i	87.77 ± 0.18	deg	this work
Combined eccentricity, periastron longitude	$e \cos \omega$	-0.05377 ± 0.00011		this work
Combined eccentricity, periastron longitude	$e \sin \omega$	0.3182 ± 0.0042		this work
Primary radial velocity amplitude	K_1	25.74 ± 0.31	km s^{-1}	this work
Secondary radial velocity amplitude	K_2	23.17 ± 0.28	km s^{-1}	this work
Systemic radial velocity	γ	-7.62 ± 0.25	km s^{-1}	this work
Mass ratio	q	1.111 ± 0.024		this work
<i>Best-Fitting Derived Parameters</i>				
Orbital semi-major axis	a	4.157 ± 0.025	R_{\odot}	this work
Fractional radius of primary	R_1/a	0.0679 ± 0.0012		this work
Fractional radius of secondary	R_2/a	0.06138 ± 0.00071		this work
Luminosity ratio	L_2/L_1	0.999 ± 0.027		this work
Primary mass	M_1	0.02216 ± 0.00045	M_{\odot}	this work
Secondary mass	M_2	0.02462 ± 0.00055	M_{\odot}	this work
Primary radius	R_1	0.2823 ± 0.0051	R_{\odot}	this work
Secondary radius	R_2	0.2551 ± 0.0036	R_{\odot}	this work
Primary surface gravity	$\log g_1$	3.882 ± 0.017	cgs	this work
Secondary surface gravity	$\log g_2$	4.015 ± 0.011	cgs	this work
Primary mean density	ρ_1	0.985 ± 0.054	ρ_{\odot}	this work
Secondary mean density	ρ_2	1.482 ± 0.052	ρ_{\odot}	this work
Impact parameter of primary eclipse	b_1	0.389 ± 0.024		this work
Impact parameter of secondary eclipse	b_2	0.751 ± 0.051		this work
Eccentricity	e	0.3227 ± 0.0042		this work
Periastron longitude	ω	99.59 ± 0.14	deg	this work

Table 5.4 Continued: System Parameters of EPIC 203868608

Reduced chi-squared of light curve fit	χ_{red}^2	1.185		this work
RMS of best fit light curve residuals		2.48	ppt	this work
Reduced chi-squared of primary RV fit	χ_{red}^2	47.04		this work
RMS of primary RV residuals		6.21	km s ⁻¹	this work
Reduced chi-squared of secondary RV fit	χ_{red}^2	1.381		this work
RMS of secondary RV residuals		0.63	km s ⁻¹	this work
<i>Other Adopted Stellar Parameters</i>				
Spectral Type	SpT	M5±0.5		this work, spectroscopy
Extinction	A_V	2.04 ± 0.31	mag	this work, SpT, photometry
Bolometric luminosity	$\log(L_{\text{bol}}/L_{\odot})$	-1.14 ± 0.08	dex	this work, SpT, photometry, A_V , d
Primary effective temperature	$T_{\text{eff},1}$	2830 ± 80	K	this work, $T_{\text{eff},2}$, J
Secondary effective temperature	$T_{\text{eff},2}$	2980 ± 75	K	this work, SpT, HH15

Best-fit orbital parameters and their uncertainties are the result of 1,000 Monte Carlo simulations with JKTEBOP. The χ_{red}^2 quoted above was computed for the light curve with out-of-eclipse observations removed, and is reduced to 1.052 over the full light curve.

Table 5.5: System Parameters of EPIC 203476597

Parameter	Symbol or Prefix	Value	Units	Source
<i>Identifying Information</i>				
Right ascension	α J2000.	16:25:57.915	hh:mm:ss	Zacharias et al. (2013)
Declination	δ J2000.	-26:00:37.35	dd:mm:ss	Zacharias et al. (2013)
K2 ID	EPIC	203476597		Huber & Bryson (2015)
2 Micron All Sky Survey ID	2MASS	J16255790-2600374		Cutri et al. (2003)
Wide-field Infrared Survey Explorer ID	AllWISE	J162557.90-260037.5		Cutri & et al. (2014)
UKIRT Infrared Deep Sky Survey ID	UGCS	J162557.91-260037.5		Lawrence et al. (2013)
<i>Photometric Properties</i>				
	J	9.575 ± 0.024	mag	2MASS
	H	8.841 ± 0.044	mag	2MASS
	K_s	8.535 ± 0.021	mag	2MASS
	$W1$	8.161 ± 0.019	mag	AllWISE
	$W2$	8.130 ± 0.017	mag	AllWISE
	$W3$	8.230 ± 0.023	mag	AllWISE
	$W4$	7.757 ± 0.172	mag	AllWISE
	KEPMAG	9.575	mag	K2 EPIC
<i>Best-Fitting Adjusted Parameters</i>				
Orbital period	P	1.4408031 ± 0.0000050	days	this work
Ephemeris timebase - 2456000	T_0	894.37787 ± 0.00016	BJD	this work

Table 5.5 Continued: System Parameters of EPIC 203476597

Surface brightness ratio	J	0.563 ± 0.032		this work
Sum of fractional radii	$(R_1 + R_2)/a$	0.462 ± 0.014		this work
Ratio of radii	k	0.56 ± 0.13		this work
Orbital inclination	i	67.5 ± 1.2	deg	this work
Combined eccentricity, periastron longitude	$e \cos \omega$	-0.00035 ± 0.00017		this work
Combined eccentricity, periastron longitude	$e \sin \omega$	0.0029 ± 0.0030		this work
Primary radial velocity amplitude	K_1	0.10 ± 0.27	km s ⁻¹	this work
Systemic radial velocity	γ	-0.67 ± 0.22	km s ⁻¹	this work
Reduced chi-squared of light curve fit	χ_{red}^2	1.46		this work
RMS of best fit light curve residuals		1.06	ppt	this work
<i>Best-Fitting Derived Parameters</i>				
Fractional radius of primary	R_1/a	0.296 ± 0.016		this work
Fractional radius of secondary	R_2/a	0.166 ± 0.030		this work
Luminosity ratio	L_2/L_1	0.176 ± 0.090		this work
Impact parameter of primary eclipse	b_1	1.29 ± 0.13		this work
Impact parameter of secondary eclipse	b_2	1.30 ± 0.13		this work
Eccentricity	e	0.0029 ± 0.0027		this work
Periastron longitude	ω	97.0 ± 14.1	deg	this work
<i>Other Adopted Stellar Parameters</i>				
Spectral Type	SpT	G8-K0		this work
Extinction	A_V	2.42 ± 0.52	mag	this work
Primary effective temperature	$T_{\text{eff},1}$	5180 ± 200	K	this work, SpT, HH15
Secondary effective temperature	$T_{\text{eff},2}$	4490 ± 60	K	this work, $T_{\text{eff},1}$, J
Bolometric luminosity	$\log(L_{\text{bol}}/L_{\odot})$	0.13 ± 0.11	dex	this work, SpT, photometry, A_V , d
Primary luminosity	L_1	1.15 ± 0.66	L_{\odot}	this work, L_{bol} , L_2/L_1
Secondary luminosity	L_2	0.20 ± 0.12	L_{\odot}	this work, L_{bol} , L_2/L_1

Table 5.5 Continued: System Parameters of EPIC 203476597

Primary rotation period	P_{rot}	3.21 ± 0.12	days	this work
Projected rotational velocity	$v \sin i$	25 ± 2	km s^{-1}	this work
Primary radius	R_1	$1.72^{+0.17}_{-0.27}$	R_{\odot}	this work, $P_{\text{rot}}, v \sin i$
Secondary radius	R_2	0.96 ± 0.27	R_{\odot}	this work, R_1, k
Primary mass	M_1	1.41 ± 0.17	M_{\odot}	this work, $T_{\text{eff},1}, R_1, \text{PARSEC}$
Secondary mass	M_2	0.84 ± 0.12	M_{\odot}	this work, $T_{\text{eff},2}, R_2, \text{PARSEC}$
Primary age	τ_1	$6.6^{+2.4}_{-3.6}$	Myr	this work, $T_{\text{eff},1}, R_1, \text{PARSEC}$

Best-fit orbital parameters and their uncertainties are the result of 1,000 Monte Carlo simulations with JKTEBOP. We note that the χ_{red}^2 of the model light curve fit was computed with out-of-eclipse observations removed, and becomes <1 when computed over the entire light curve.

APPENDIX

5.A Revised Parameters for UScoCTIO 5

We independently characterized the double-lined eclipsing system UScoCTIO 5 (EPIC 205030103), using our own detrended *K2* light curve and the radial velocities and spectroscopic flux ratios published in Table 1 of Kraus et al. (2015), hereafter K15. We used a 3-pixel aperture to extract photometry from the target pixel files, and detrended the raw light curve using our procedure described in § 5.2.2. Following the same approach for EPIC 203710387 (which has similar spectral type components), we assumed a linear limb-darkening law for both components, fixing the coefficient u to 0.888 for each. Consistent with our analysis above, we also account for the *Kepler* long cadence integration time through numerical integration of the models at ten points across intervals of 1766 seconds. Because we used a larger photometric aperture than employed in K15, we investigated the possibility of contamination by allowing third light as a free parameter in a JKTEBOP trial fit. The resulting best-fit third light value was consistent with zero and so this parameter was fixed at zero for the final fit. We also excluded three clear outliers during secondary eclipse in our final fit, which we note were also excluded from the fitting procedure in K15. These outliers are possibly systematic artifacts intrinsic to the data, or perhaps related to the detrending procedure, though given the fact that they are seen in independently detrended light curves it is also possible there is modulation of the eclipse morphology due to star spots. As initial parameter estimates for the final fit, we used the best-fit values found by K15 as input for 10,000 MC simulations with JKTEBOP. We present our newly derived best-fit parameters in Table 5.6, and show the best-fit models to the photometry and radial velocities in Figure 5.12.

We find component masses that are consistent at the $2 - \sigma$ level with those published in K15. However, we find radii that are discrepant with those in K15 at the $> 4.5 - \sigma$ level for the primary and the $7 - \sigma$ level for the secondary (where we take the uncertainties from K15 as $1 - \sigma$ in a given parameter), such that our radii are larger. The implication of this finding is that the UScoCTIO 5 component positions in the mass-radius plane are consistent with an age slightly younger than the age implied by the K15 parameters.

Combining the bolometric luminosity from K15, with our radii determinations and the luminosity ratio implied by our best-fit model, we find temperatures of $T_{\text{eff},1} = 3180 \pm 180$ K and $T_{\text{eff},2} = 3140 \pm 180$ K, consistent with K15. The large tem-

perature uncertainties are dominated by the large uncertainty in the bolometric luminosity. These temperatures are consistent with matching M4 spectral types on both the HH15 and PM13 empirical scales. For completeness, we also investigated the possible effect of chromospheric activity on the temperatures and radii for UScoCTIO 5. Using the empirical relations of Stassun et al. (2012) and the H α equivalent widths published in K15, we estimate that activity may account for an additional $\sim 1\%$ change in the temperatures and radii for this system.

Most notably, our revised radii for the components of UScoCTIO 5 help to resolve the discrepancies noted in § 5.7.1, in that the K15 parameters produce an age in the H-R diagram that is nearly a factor of two younger than the age implied in the mass-radius plane, when using BHAC15 models. Using our newly derived parameters, there is better agreement in the age of the system as derived in the mass-radius, $T_{\text{eff}}\text{-}\log(L/L_{\odot})$, and $T_{\text{eff}}\text{-}\log(g)$ planes with BHAC15 models.

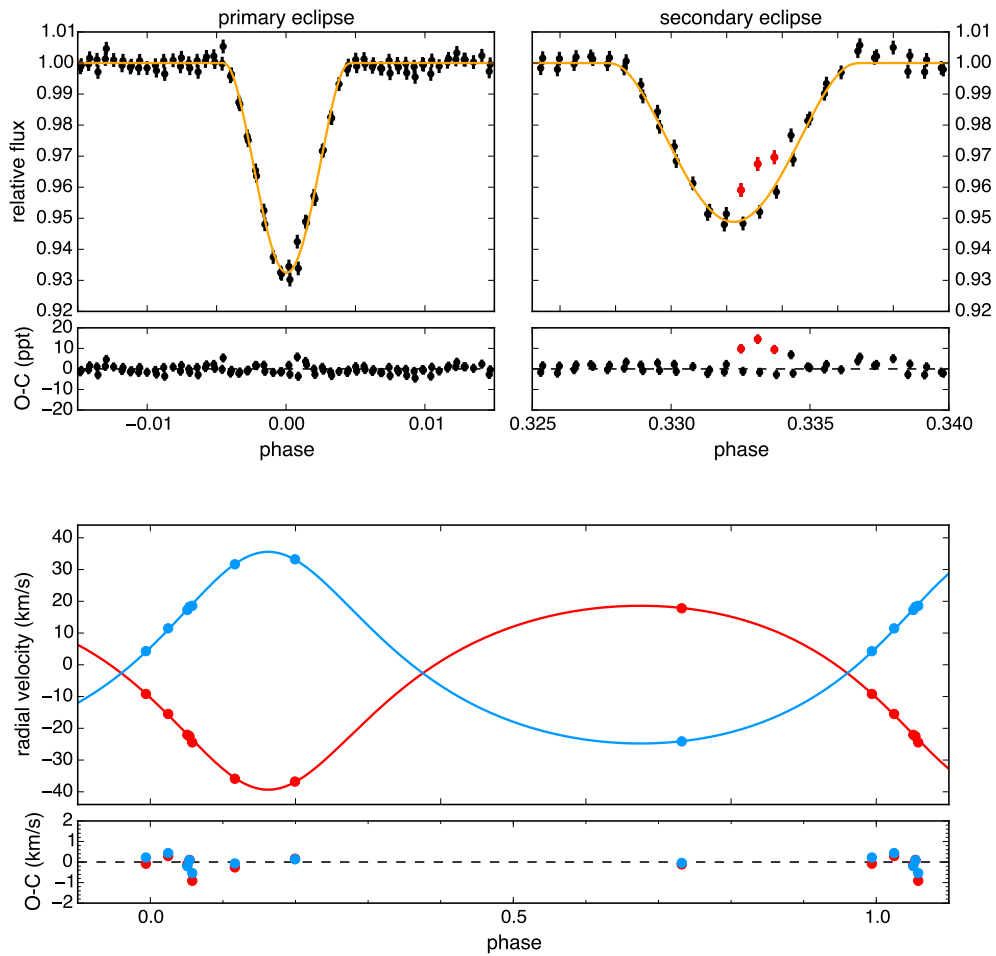


Figure 5.12: Best-fit JKTEBOP models to our detrended *K2* light curve for UScoCTIO 5 (top panels) and the radial velocities published by K15 (bottom panel). The three red points in secondary eclipse (upper right), were excluded from the fitting procedure. These points, as well as others, were also excluded in the K15 analysis.

Table 5.6: System Parameters of UScoCTIO 5

Parameter	Symbol or Prefix	Value	Units	Source
Orbital period	P	34.000703 ± 0.000089	days	this work
Ephemeris timebase - 2456000	T_0	909.25110 ± 0.00085	BJD	this work
Surface brightness ratio	J	0.955 ± 0.035		this work
Sum of fractional radii	$(R_1 + R_2)/a$	0.04473 ± 0.00048		this work
Ratio of radii	k	0.989 ± 0.018		this work
Orbital inclination	i	87.880 ± 0.025	deg	this work
Combined eccentricity, periastron longitude	$e \cos \omega$	-0.266564 ± 0.000071		this work
Combined eccentricity, periastron longitude	$e \sin \omega$	0.0191 ± 0.0031		this work
Primary radial velocity amplitude	K_1	28.962 ± 0.090	km s^{-1}	this work
Secondary radial velocity amplitude	K_2	30.185 ± 0.085	km s^{-1}	this work
Systemic radial velocity	γ	-2.651 ± 0.043	km s^{-1}	this work
Fractional radius of primary	R_1/a	0.02249 ± 0.00031		this work
Fractional radius of secondary	R_2/a	0.02224 ± 0.00032		this work
Luminosity ratio	L_2/L_1	0.9343 ± 0.0074		this work
Eccentricity	e	0.26725 ± 0.00022		this work
Periastron longitude	ω	175.90 ± 0.67	deg	this work
Impact parameter of primary eclipse	b_1	1.498 ± 0.019		this work
Impact parameter of secondary eclipse	b_2	1.557 ± 0.011		this work
Orbital semi-major axis	a	38.313 ± 0.083	R_\odot	this work
Mass ratio	q	0.9595 ± 0.0039		this work
Primary mass	M_1	0.3336 ± 0.0022	M_\odot	this work, fundamental determination
Secondary mass	M_2	0.3200 ± 0.0022	M_\odot	this work, fundamental determination
Primary radius	R_1	0.862 ± 0.012	R_\odot	this work, fundamental determination
Secondary radius	R_2	0.852 ± 0.013	R_\odot	this work, fundamental determination
Primary surface gravity	$\log g_1$	4.090 ± 0.012	cgs	this work, M_1, R_1
Secondary surface gravity	$\log g_2$	4.082 ± 0.012	cgs	this work, M_2, R_2
Primary mean density	ρ_1	0.521 ± 0.022	ρ_\odot	this work, M_1, R_1
Secondary mean density	ρ_2	0.517 ± 0.022	ρ_\odot	this work, M_2, R_2
Reduced chi-squared of light curve fit	χ_{red}^2	1.020		this work
RMS of best fit light curve residuals		2.08	ppt	this work
Reduced chi-squared of primary RV fit	χ_{red}^2	5.58		this work
RMS of primary RV residuals		0.36	km s^{-1}	this work
Reduced chi-squared of secondary RV fit	χ_{red}^2	2.64		this work
RMS of secondary RV residuals		0.27	km s^{-1}	this work

Note: Best-fit orbital parameters and their uncertainties resulting from 10,000 Monte Carlo simulations with JKTEBOP. For this analysis we mutually fit our own detrended K2 light curve with the radial velocities and spectroscopic flux ratios published in Table 1 of Kraus et al. (2015).

*Chapter 6***A PRE-MAIN-SEQUENCE MASS-RADIUS RELATION AND THE AGE OF UPPER SCORPIUS FROM ECLIPSING BINARIES**

Prior to the *K2* mission (Howell et al., 2014), there were no published eclipsing binaries (EBs) in the Upper Scorpius OB association. From the second campaign of that mission, nine EBs with secure membership have been discovered, representing a significant contribution to the number of known EBs with pre-MS components. To date, only five of these systems have been published (Kraus et al., 2015; Alonso et al., 2015; Lodieu et al., 2015a; David et al., 2016b). Here, we present preliminary analyses of the unpublished systems and updated interpretations of previously published systems in light of new radial velocities from Keck/HIRES. We consider the implications of these initial results for the age of the Upper Scorpius OB association and present a preliminary mass-radius relation appropriate for stars in the 0.1–1 M_{\odot} mass range.

6.1 Introduction

There are presently five double-lined EBs with well-determined masses and radii in Upper Sco, which we considered in this analysis. One system, HD 144548, is triply eclipsing and has masses and radii determined for each component. Thus, there are eleven stars for which the mass-radius relation in Upper Sco can be reliably mapped over a wide range of masses. We note, however, that for three systems we choose to present solutions in which the ratio of radii were fixed to unity. The reasons for this are because (1) the sum of the radii are more robustly determined than the ratio of radii in EB modeling, and (2) the mass ratio in each of these three systems is close to unity, so that large differences in radii between components are not expected. While forcing the radii to be equal in a nearly equal-mass EB will result in a slightly non-coeval solution, allowing the ratio of radii to be a free parameter in some cases results in even more non-coeval solutions. In such cases it is not clear whether the parameters of one component are to be trusted over the other, and the EBs thus become less useful in assessing ages from the mass-radius diagram. We expect, then, that fixing this parameter allows us to determine the average radii and effectively marginalize over the degeneracies that light curve fitting is susceptible to when the ratio of radii are poorly constrained.

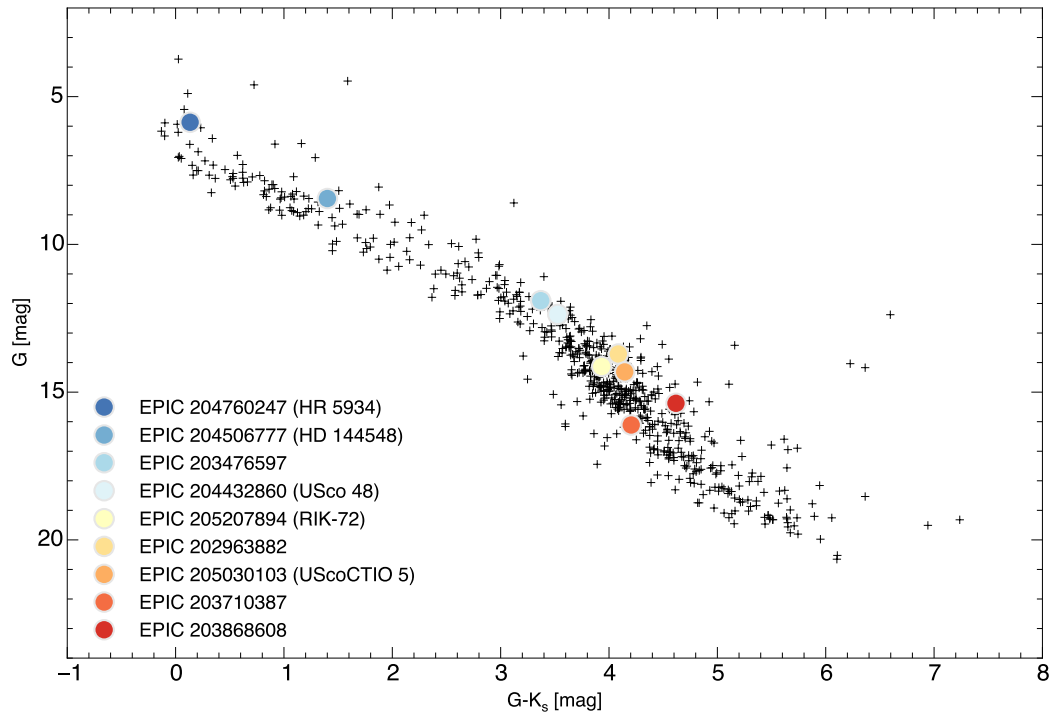


Figure 6.1: Color-magnitude diagram for Upper Sco, with EBs discovered in *K2* data highlighted by the colored points. The black points are members suggested in Luhman & Mamajek (2012). We have not applied any corrections to the photometry based on our knowledge of the mass or flux ratios of the binaries and higher order multiples studied here.

6.2 Observations

We briefly describe the primary data analyzed for each system here, and leave a more detailed discussion of the observations for a future work. Generally, our analysis steps closely follow those presented in David et al. (2016b) and David et al. (2016a). Notably, in our present analysis we use *K2* photometry detrended using the EVEREST 2 algorithm (Luger et al., 2016; Luger et al., 2017), except in the case of the USco 48 system where we use the $\kappa 2_{\text{PHOT}}$ light curve publicly available on the ExoFOP webpage. The EVEREST 2 pipeline uses the pixel-level decorrelation method of Deming et al. (2015) to remove pointing-related systematic artifacts present in *K2* data. We also present new radial velocity (RV) and optical flux ratio measurements from Keck-I/HIRES spectroscopy. These measurements are recorded in Table 8.2. RV determination is achieved through cross-correlation (CCF) with RV standard stars, and flux ratios determined from the ratio of CCF peak heights. For four of the EBs studied here, we also acquired optical speckle imaging using the DSSI camera at Gemini South Observatory or the NESSI camera on the WIYN telescope (Figure 6.2). These high resolution images allow us to

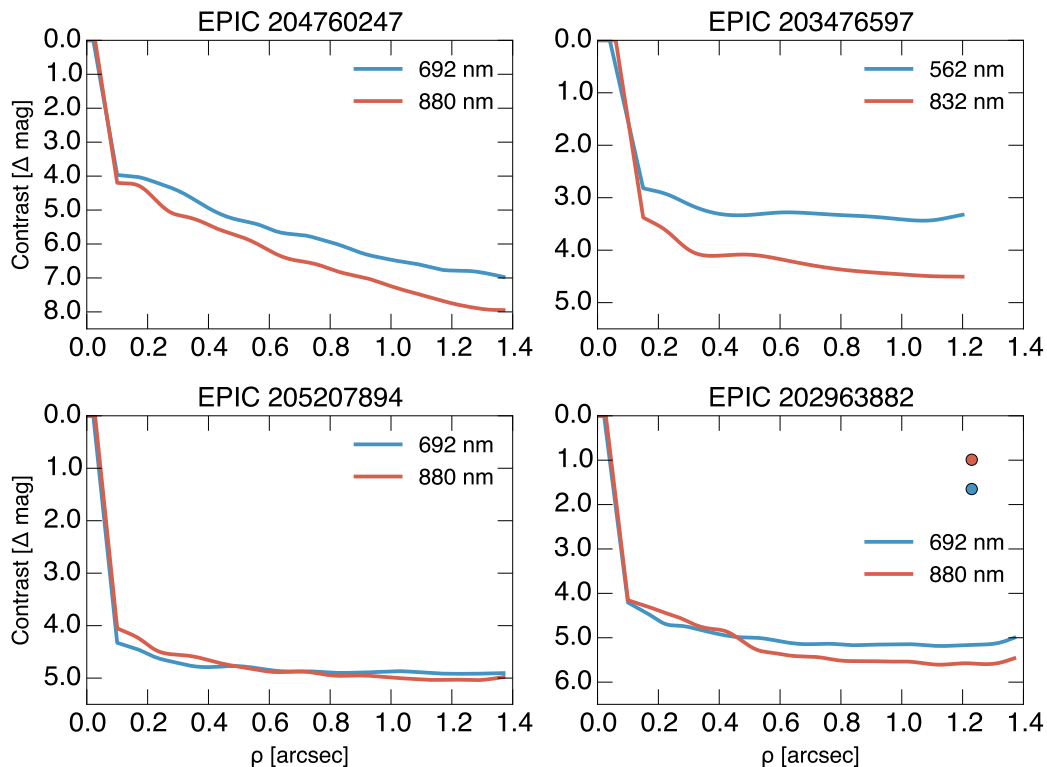


Figure 6.2: Speckle imaging results for four of the EBs discussed here. The data for EPIC 203476597 originate from the NESSI instrument on the WIYN telescope. For the rest, the speckle data were acquired with the DSSI instrument at Gemini South Observatory. EPIC 202963882 has a companion at $1.23''$, and its contrast at 692 nm and 880 nm are represented as the red and blue points respectively. We determined from Keck/HIRES spectroscopy that this companion is the EB.

assess whether there are additional stars in the system that require us to account for flux dilution at the EB light curve fitting stage.

Table 6.1: Keck-I/HIRES radial velocities

System	UT Date	BJD	v_1 km s ⁻¹	σ_1 km s ⁻¹	v_2 km s ⁻¹	σ_2 km s ⁻¹	F_2/F_1	σ_{F_2/F_1}
HR 5934	2016 May 17	2457525.847810	44.6	4.0	-109.9	2.5
	2016 May 20	2457528.830532	8.3	2.0	-33.1	3.4	0.41	0.17
	2017 Jul 08	2457942.810159	6.2	2.5	-37.5	1.4	0.46	0.11
	2017 Jul 09	2457943.807572	-32.3	2.4	49.1	5.5
	2017 Jul 10	2457944.873724	-62.6	2.6	126.2	4.7
	2017 Jul 11	2457945.862162	-63.3	2.5	127.9	3.9
USco 48	2015 Jun 02	2457175.820325	-87.3	1.1	79.4	1.9	1.020	0.030
	2016 May 20	2457529.019142	-61.3	2.0	56.1	1.5	0.894	0.073
	2017 Jul 08	2457942.780202	-42.9	2.3	31.1	1.6	0.866	0.069
	2017 Jul 09	2457943.775365	-45.8	2.7	32.1	2.9	1.019	0.019
	2017 Jul 10	2457944.786688	74.5	2.7	-88.7	1.5	0.933	0.094
	2017 Jul 11	2457945.764455	-57.6	1.8	50.5	2.1	0.889	0.068
RIK-72	2015 Jun 02	2457175.872713	-1.50	0.47
	2016 May 17	2457525.841835	-8.73	0.21
	2016 May 20	2457528.839284	-7.89	0.21
	2016 Jun 15	2457554.965238	-2.46	0.22
	2017 Jul 08	2457942.790311	-5.45	0.41
	2017 Jul 09	2457943.782008	-4.76	0.41
	2017 Jul 10	2457944.822261	-3.81	0.39
	2017 Jul 11	2457945.840403	-3.33	0.40
UScoCTIO 5	2017 Jul 08	2457942.829644	0.27	0.43	-7.12	0.45	0.830	0.039
	2017 Jul 09	2457943.819253	4.77	0.41	-10.89	0.48	0.771	0.050
	2017 Jul 10	2457944.917664	9.13	0.41	-14.05	0.46	0.836	0.051
	2017 Jul 11	2457945.779752	11.48	0.46	-16.73	0.49	0.840	0.034

Table 8.2 Continued: Keck-I/HIRES radial velocities

System	UT Date	BJD	v_1 km s ⁻¹	σ_1 km s ⁻¹	v_2 km s ⁻¹	σ_2 km s ⁻¹	F_2/F_1	σ_{F_2/F_1}
EPIC 203868608 A	2015 Jun 02	2457175.921333	-4.72	0.60
	2015 Jul 14	2457217.816800	16.51	0.25	-29.50	0.47
	2015 Aug 21	2457255.829930	14.51	0.51	-26.39	1.62
	2015 Aug 28	2457262.799230	-25.48	1.19	21.87	0.80
	2015 Aug 31	2457265.797000	-4.66	0.23
	2015 Sep 25	2457290.729400	15.79	0.19	-29.26	0.26
	2016 May 17	2457526.116009	7.18	0.31	-19.57	0.37
	2016 May 20	2457528.959473	-30.40	0.30	27.90	0.34
	2016 Jun 15	2457555.031623	7.25	0.34	-16.44	0.37
	2017 Jul 08	2457942.801689	-37.57	0.49	32.42	0.56
	2017 Jul 09	2457943.795450	-31.46	0.43	28.49	0.46
	2017 Jul 10	2457944.858624	-23.82	0.48	18.77	0.86
	2017 Jul 11	2457945.824092	-15.91	0.44	10.07	0.65

6.3 Discussion of individual systems

6.3.1 EPIC 204760247 / HD 142883 / HR 5934

HR 5934 (also HD 142883 and EPIC 204760247) is a B3 type member of Upper Sco that has been studied extensively in the literature.¹ With an optical magnitude of 5.8, the star is visible to the unaided eye from dark sites and one of the brightest EBs in the sky. The star was not included in the pioneering work of Blaauw (1946) on the region, but was first proposed as a possible member by Bertiau (1958). The distance to the system from trigonometric parallax and its proper motions, both measured by *Gaia*, are consistent with cluster membership. The systemic radial velocity, measured from a joint fit of the *K2* light curve and RV time series, further secures the membership status of these stars.

The system was previously known to be a spectroscopic binary, with radial velocities measured for both components in Andersen & Nordstrom (1983), though subsequent studies published radial velocities for only the primary component (Levato et al., 1987; Jilinski et al., 2006). Prior studies of the primary radial velocities erroneously assumed an eccentric orbit and a period of 10.5 days but the *K2* light curve shows eclipses and unambiguously defines the true orbital period of 9.2 days with no appreciable eccentricity. This period, and the eclipsing nature of the system, were previously noted by Wraight et al. (2011) but a complete solution for the masses and radii have not been published. We present the literature radial velocities, which we used in fitting an orbital solution for the system, in Table 6.2.

The angular diameter has been previously estimated indirectly from the intrinsic brightness and color as 0.16 mas (Wesselink et al., 1972) and 0.19 mas (Morossi & Malagnini, 1985). Notably, these studies neglected the binarity of the source. A previous speckle interferometry study did not resolve the binary (Mason et al., 1999). This is not surprising, as the binary separation is approximately 0.2 AU, which at the distance measured by *Gaia* corresponds to a projected angular separation of 1.1–1.4 mas. The binary separation may therefore be resolvable with the CHARA array.

The sky projected rotational velocity has been reported variously as $v \sin i = 5 \text{ km s}^{-1}$ (Abt et al., 2002; Strom et al., 2005) and 14 km s^{-1} (Brown & Verschueren, 1997; Wolff et al., 2007). While this is a modest rotational velocity for an early-type stars such as HR 5934 A, the eclipses are deep enough that the spin-orbit alignment of the system could be studied through the Rossiter-McLaughlin effect.

¹The star is misclassified as a Cepheid variable in SIMBAD

Table 6.2: Literature radial velocities of HR 5934

HJD	v_1 km s ⁻¹	σ_1 km s ⁻¹	v_2 km s ⁻¹	σ_2 km s ⁻¹	Reference
2442671.5311	4.4	1.2	a
2442876.8905	-58.3	1.9	154.1	11.3	a
2442881.8234	48.1	1.3	-129.3	8.1	a
2442179.737	23.3	1.7	b
2442180.676	44.5	2.3	b
2442174.817 [†]	-51.8	6.1	b
2442176.897	-61.4	2.6	b
2442178.643	-37.1	2.1	b
2442921.746	-59.5	0.9	b
2443297.555	-14.1	2.9	b
2443300.566	-41.8	3.7	b
2452415.3002	-54.3	0.5	c

REFERENCES. — a: Andersen & Nordstrom (1983); b: Levato et al. (1987); c: Jilinski et al. (2006)

[†] The RV at this epoch was discrepant by >10 km s⁻¹ from the best-fit orbital solution and was thus excluded from our final analysis.

Speckle imaging observations of HR 5934 at 692 nm and 880 nm were acquired at Gemini South Observatory with the DSSI instrument (P.I. Steve Howell). We found no evidence for companions brighter than $\Delta m \lesssim 3.97$ mag at 692 nm, or $\Delta m \lesssim 4.2$ mag at 880 nm, in the angular separation range of 0.1–1.37". We show the contrast curves from speckle imaging observations for HR 5934 and three other systems in Figure 6.2.

In Table 6.3, we present parameters of the HR 5934 system culled from the literature and resulting from our joint fit of the *K2* light curve, literature RVs, and new RVs determined from Keck/HIRES spectra. We find no evidence for eccentricity from the light curve or radial velocities, and accordingly we jointly fit the data assuming a circular orbit. In fitting the eclipses, we assumed linear limb darkening with coefficients of $u_1 = 0.3026$ and $u_2 = 0.4411$ for the primary and secondary, respectively. The limb darkening coefficients were calculated from interpolation of the Sing (2010) tables for stars of appropriate temperature and surface gravity.

The resulting solution helps to constrain the age of the system. Both components of the binary appear to be securely on (or in the case of the primary, perhaps slightly evolved off of) the ZAMS. If the system were younger than 3 Myr, one might expect the secondary to have a much larger radius, because of its proximity to a prominent feature in the mass-radius diagram, discussed in detail below.

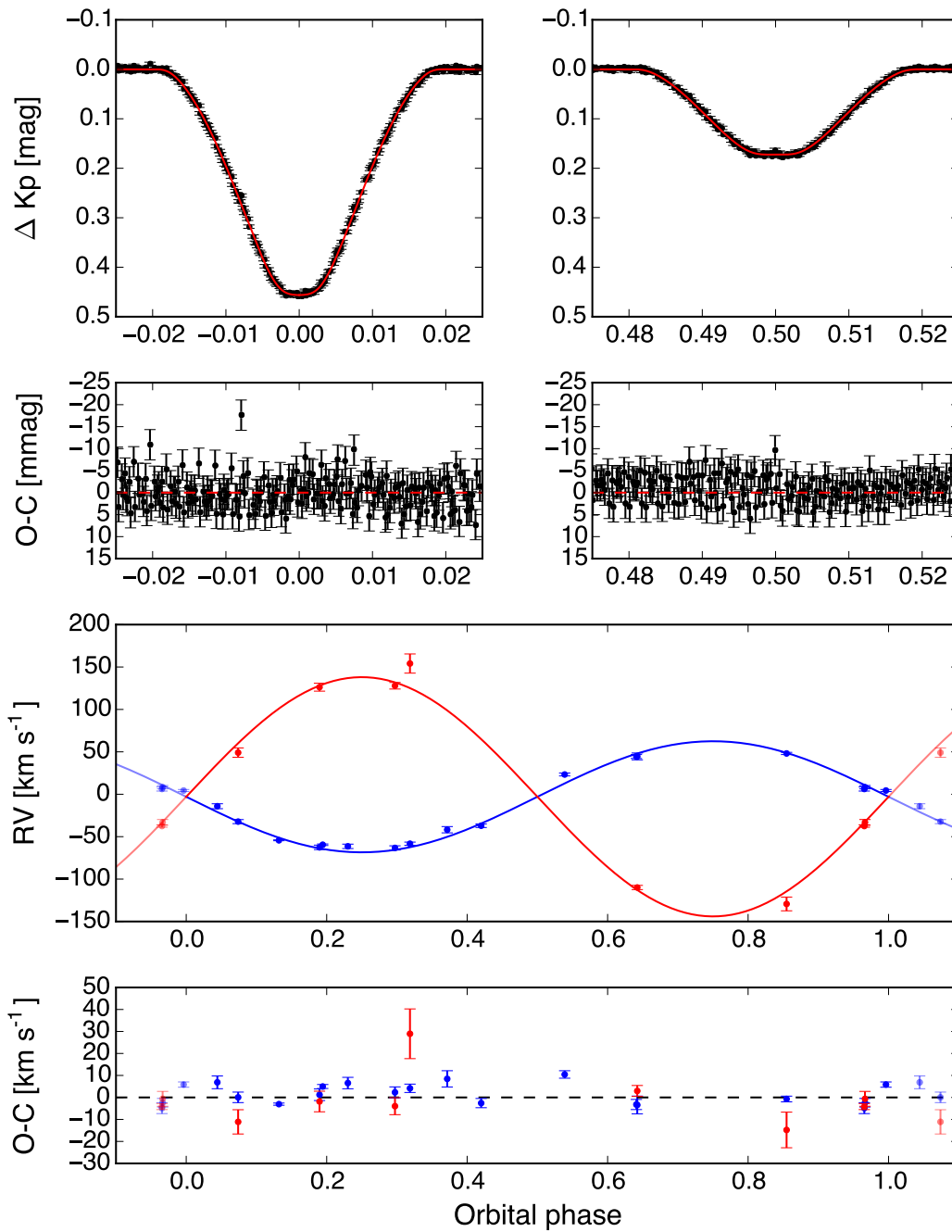


Figure 6.3: Joint fits to the *K2* photometry and radial velocity time series of HR 5934. The two most discrepant secondary radial velocities, with large errors, originate from Andersen & Nordstrom (1983).

Table 6.3: System Parameters of HR 5934

Parameter	Symbol	Value	Units	Source
<i>Literature parameters</i>				
Right ascension, R.A. (J2000)	α	15:57:40.46	hh mm ss	
Declination, Dec. (J2000)	δ	-20:58:59.09	dd mm ss	
Proper motion, R.A.	μ_α	-9.66 ± 0.04	mas yr ⁻¹	Gaia Collaboration et al. (2016)
Proper motion, Dec.	μ_δ	-21.67 ± 0.01	mas yr ⁻¹	Gaia Collaboration et al. (2016)
Distance	d	158^{+25}_{-19}	pc	Gaia Collaboration et al. (2016)
<i>Gaia</i> G magnitude	G	5.868	mag	Gaia Collaboration et al. (2016)
Primary spectral type	SpT ₁	B2.5Vn		Carpenter et al. (2006)
		B3±1		Hernández et al. (2005)
Combined bolometric luminosity	$\log(L_{\text{bol}}/L_\odot)$	2.88	dex	Hohle et al. (2010)
		2.91	dex	Hernández et al. (2005)
Primary effective temperature	$T_{\text{eff},1}$	18700	K	Hohle et al. (2010)
		20350	K	Carpenter et al. (2006)
		18620	K	Hernández et al. (2005)
Extinction	A_V	0.6	mag	Carpenter et al. (2006)
		0.62 ± 0.14	mag	Hernández et al. (2005)
<i>Directly measured parameters</i>				
Orbital period	P	9.199736 ± 0.000010	days	this work
Ephemeris timebase - 2456000	T_0	894.357695 ± 0.000098	BJD	this work
Surface brightness ratio	J	0.4727 ± 0.0013		this work
Sum of fractional radii	$(R_1 + R_2)/a$	0.11857 ± 0.00019		this work
Ratio of radii	k	0.61840 ± 0.00070		this work
Orbital inclination	i	88.570 ± 0.016	deg	this work
Primary radial velocity amplitude	K_1	65.47 ± 0.60	km s ⁻¹	this work
Secondary radial velocity amplitude	K_2	141.0 ± 2.0	km s ⁻¹	this work
Systemic radial velocity	γ	-2.97 ± 0.42	km s ⁻¹	this work

Table 6.3 Continued: HR 5934

Parameter	Symbol	Value	Units	Source
Mass ratio	q	0.4642 ± 0.0076		this work
Orbital semi-major axis	a	37.54 ± 0.39	R_{\odot}	this work
Fractional radius of primary	R_1/a	0.07326 ± 0.00011		this work
Fractional radius of secondary	R_2/a	0.045307 ± 0.000092		this work
Luminosity ratio	L_2/L_1	0.17147 ± 0.00058		this work
Primary mass	M_1	5.74 ± 0.20	M_{\odot}	this work
Secondary mass	M_2	2.664 ± 0.070	M_{\odot}	this work
Primary radius	R_1	2.751 ± 0.029	R_{\odot}	this work
Secondary radius	R_2	1.701 ± 0.018	R_{\odot}	this work
Primary surface gravity	$\log g_1$	4.3175 ± 0.0063	cgs	this work
Secondary surface gravity	$\log g_2$	4.4017 ± 0.0043	cgs	this work
Primary mean density	ρ_1	0.2757 ± 0.0018	ρ_{\odot}	this work
Secondary mean density	ρ_2	0.5412 ± 0.0071	ρ_{\odot}	this work
Impact parameter of primary eclipse	b_1	0.3407 ± 0.0036		this work
Impact parameter of secondary eclipse	b_2	0.3407 ± 0.0036		this work
Reduced chi-squared of joint fit	χ_{red}^2	1.36		this work
Reduced chi-squared of light curve fit	$\chi_{\text{red,LC}}^2$	0.93		this work
Residuals of light curve fit	rms _{LC}	3.32	mmag	this work
Reduced chi-squared of primary RV fit	$\chi_{\text{red,RV1}}^2$	9.54		this work
Residuals of primary RV fit	rms _{RV1}	4.98	km s^{-1}	this work
Reduced chi-squared of secondary RV fit	$\chi_{\text{red,RV2}}^2$	12.37		this work
Residuals of primary RV fit	rms _{RV2}	3.21	km s^{-1}	this work
Reduced chi-squared of light ratio fit	$\chi_{\text{red,LR}}^2$	4.47		this work
Residuals of light ratio fit	rms _{LR}	0.26		this work

6.3.2 EPIC 204506777 / HD 144548

HD 144548 is a triply eclipsing system with masses and radii that have been determined for all three components (Alonso et al., 2015). Modeling this system is a complex task, and we do not duplicate the efforts of those authors here. Four new epochs of radial velocities have been acquired with Keck/HIRES, for which the data will be made publicly available. It is worth noting that the most massive component of this system has a location in the mass-radius diagram that provides powerful constraints on the age of Upper Sco. This feature of the mass-radius diagram is discussed in further detail below.

6.3.3 EPIC 203476597

This apparently single-lined system was originally published in David et al. (2016b). The star exhibits no detectable RV variations above the $\sim 1 \text{ km s}^{-1}$ level, although in some epochs there appears to be an emission component that is shifting by $\sim 100 \text{ km s}^{-1}$ on short timescales. It is possible that this is H α emission from a faint secondary in the EB, but it is also possible that the source is a triple or higher order multiple. In this scenario, the eclipsing component may be at a wide separation from the star which contributes most to the optical spectra. This may explain why no orbital motion is detected in the most luminous star.

Speckle imaging observations of EPIC 203476597 were obtained using the NESSI instrument on the WIYN telescope on UT 2017 May 11. NESSI observes targets at two wavelengths simultaneously, at 562 nm (in a 44 nm wide filter) and 832 nm (in a 40 nm wide filter). The data were processed according to the procedures described in Howell et al. (2011) and Horch et al. (2017). These observations exclude additional companions to the system brighter than $\Delta m \gtrsim 3.0 \text{ mag}$ at 832 nm or $\Delta m \gtrsim 2.6 \text{ mag}$ at 562 nm in the angular separation range of 0.14–1.2".

The fact that no additional source could be detected from speckle imaging calls into question the scenario in which EPIC 203476597 is a higher order multiple, e.g. a triple, in which the eclipsing pair is at a wide separation from the primary star. However, the imaging observations do not formally exclude this scenario, as there are regions of parameter space in which a hypothetical binary pair could remain undetected within our data.

6.3.4 EPIC 204432860 / RIK-60 / USco 48

USco 48 is an M1 type post T-Tauri star located in the Upper Scorpius A region of the association. It was first noted for its X-ray emission from *ROSAT* observations,

and consequently given the designation USco 48 (Sciortino et al., 1998). It was later included in Preibisch & Zinnecker (1999), a classic reference on the association. There is no evidence for infrared excesses at $8\ \mu\text{m}$ or $16\ \mu\text{m}$ (Carpenter et al., 2006), but there is a modest $24\ \mu\text{m}$ excess at approximately the 50% level (Carpenter et al., 2009). There is no observed excess at longer wavelengths (in the $W2$, $W3$, or $W4$ bands), leading Luhman & Mamajek (2012) to suggest the system hosts a debris or evolved/transitional disk. Barenfeld et al. (2016) studied the source with ALMA, determining an upper limit to the mass of dust in any putative disk of $M_{\text{dust}}/M_{\oplus} < 0.11$.

Several multiplicity studies have targeted USco 48, searching for both close and wide companions, and all have resulted in null detections (Köhler et al., 2000; Kraus & Hillenbrand, 2007; Kraus et al., 2008; Ireland et al., 2011; Lafrenière et al., 2014). Köhler et al. (2000) searched for but did not detect companions to this source with speckle interferometry and direct imaging. Those authors excluded companions with K -band flux ratios $F_2/F_1 > 0.12$ ($\Delta K < 2.30$ mag) at $0.13''$ or $F_2/F_1 > 0.05$ ($\Delta K < 3.25$ mag) at $0.5''$. Searches for wide companions in 2MASS (Kraus & Hillenbrand, 2007) as well as close companions from Br γ imaging at Keck (Kraus et al., 2008) also resulted in null detections. Given the apparent lack of a relatively bright, closely-projected companion we choose to ignore third light in the eclipse modeling of this system.

The $K2$ light curve of USco 48 is characterized by a semi-sinusoidal waveform of approximately 10% in amplitude and period of $P_{\text{rot}} = 2.8745 \pm 0.0028$ days, presumably due to rotational modulation of starspots.² In phase with this rotation signal are grazing eclipses of $\sim 1\%$ depth (primary eclipse) and $\sim 0.5\%$ depth (secondary eclipse). The orbit of the binary is thus inferred to be tidally synchronized (see Figure 6.4).

From Keck/HIRES spectra emission is noted in $H\alpha$, $H\beta$, and the cores of the Ca II triplet, and lithium absorption is also present, confirming the system's youth. The system is double-lined, including the emission components. We present a preliminary solution for the masses and radii of this system in Table 6.4. In this initial fit, we have fixed the radius ratio to unity in order to avoid degeneracies of EB light curve fitting. With a mass ratio of $q \approx 0.96$ it is likely that equal radii is a reasonable assumption, but we will relax this assumption in a future work. We

²Kiraga (2012) previously identified this period from ASAS photometry.

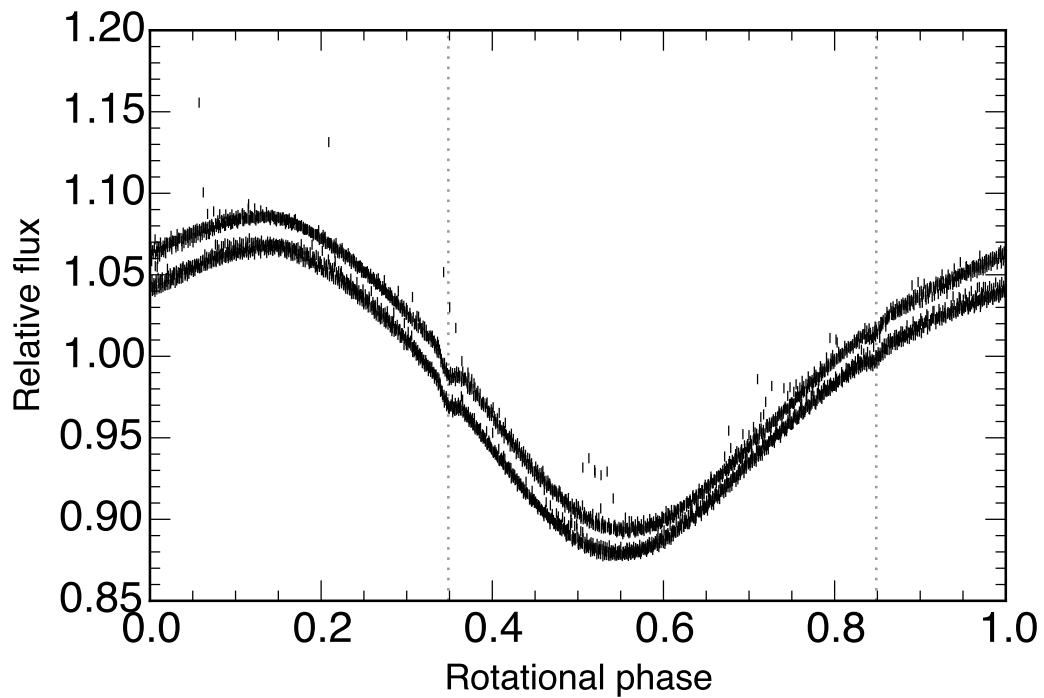


Figure 6.4: *K2* photometry of USco 48 phase-folded on the rotational modulation period, which is commensurate with the binary orbital period. The shallow, grazing eclipses are highlighted by dotted lines.

present our preliminary joint fit of the *K2* photometry and HIRES RVs for USco 48 in Figure 6.5.

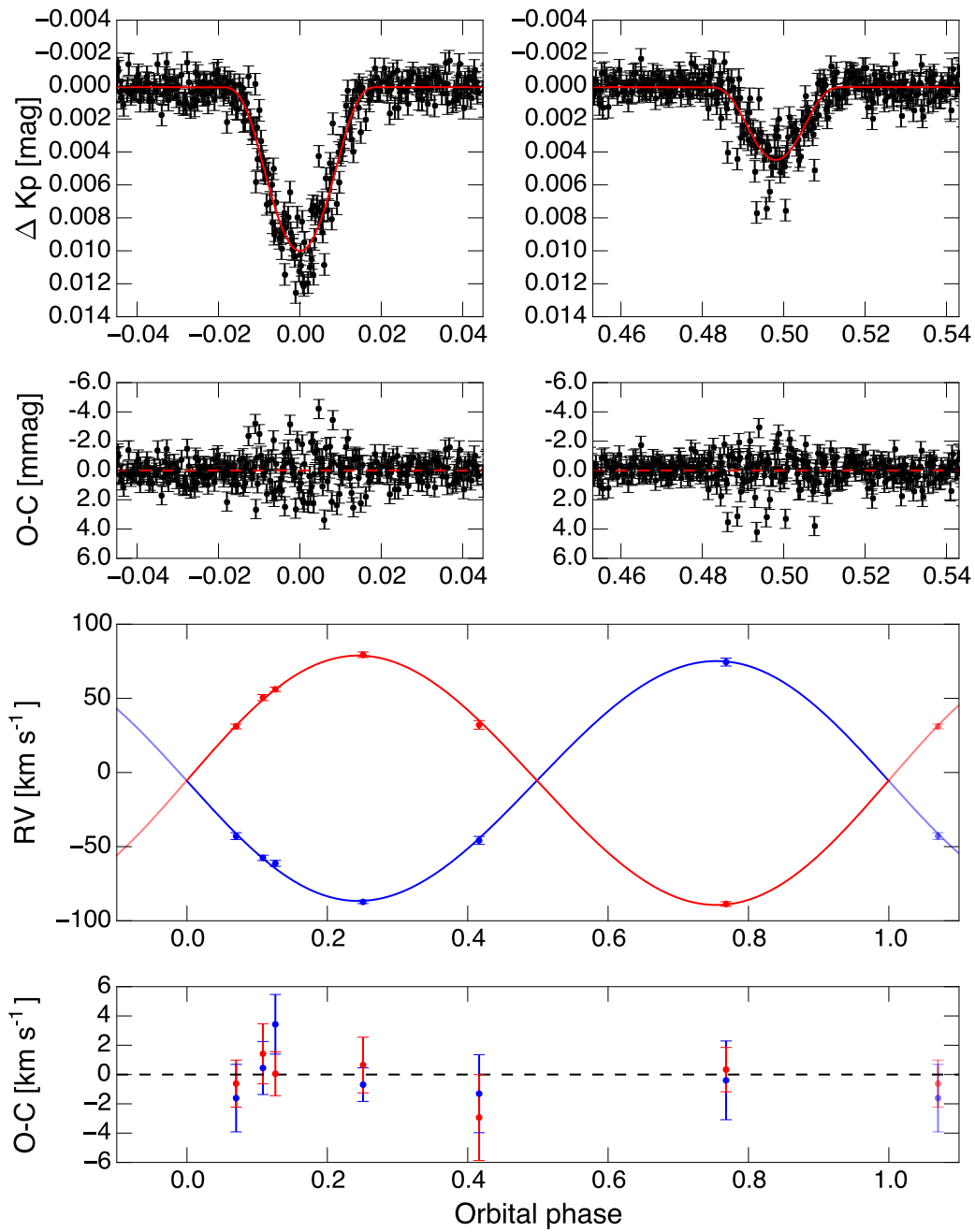


Figure 6.5: Joint fit of *K2* photometry and HIRES RVs for USco 48. In this fit the radius ratio was fixed at unity.

Table 6.4: System Parameters of USco 48

Parameter	Symbol	Value	Units	Source
<i>Literature parameters</i>				
Right ascension, R.A. (J2000)	α	16:02:00.39	hh mm ss	
Declination, Dec. (J2000)	δ	-22:21:23.74	dd mm ss	
Proper motion, R.A.	μ_α	-12.0 ± 0.9	mas yr ⁻¹	Zacharias et al. (2015)
Proper motion, Dec.	μ_δ	-23.8 ± 0.9	mas yr ⁻¹	Zacharias et al. (2015)
<i>Gaia</i> G magnitude	G	12.369	mag	Gaia Collaboration et al. (2016)
APASS V magnitude	V	13.582	mag	Henden et al. (2016)
Primary spectral type	SpT ₁	M1		Rizzuto et al. (2015)
Primary effective temperature	$T_{\text{eff},1}$	3720 ± 75	K	this work, Herczeg & Hillenbrand (2015)
		3630 ± 70	K	this work, Pecaut & Mamajek (2013)
Extinction	A_V	0.7 ± 0.5	mag	Barenfeld et al. (2016)
		0.7	mag	Rizzuto et al. (2015)
		1.1	mag	Carpenter et al. (2009)
<i>Directly measured parameters</i>				
Orbital period	P	2.874456 ± 0.000014	days	this work
Ephemeris timebase - 2456000	T_0	904.90027 ± 0.00030	BJD	this work
Surface brightness ratio	J	0.986 ± 0.015		this work
Sum of fractional radii	$(R_1 + R_2)/a$	0.2410 ± 0.0031		this work
Ratio of radii	k	1.0 (fixed)		this work
Orbital inclination	i	77.00 ± 0.18	deg	this work
Combined eccentricity, periastron longitude	$e \cos \omega$	-0.00300 ± 0.00033		this work
Combined eccentricity, periastron longitude	$e \sin \omega$	0.01628 ± 0.00051		this work
Primary radial velocity amplitude	K_1	80.9 ± 1.1	km s ⁻¹	this work
Secondary radial velocity amplitude	K_2	84.1 ± 1.0	km s ⁻¹	this work
Systemic radial velocity	γ	-5.50 ± 0.67	km s ⁻¹	this work
Mass ratio	q	0.962 ± 0.018		this work
Orbital semi-major axis	a	9.617 ± 0.081	R _☉	this work

Table 6.4 Continued: USco 48

Parameter	Symbol	Value	Units	Source
Fractional radius of primary	R_1/a	0.1205 ± 0.0016		this work
Fractional radius of secondary	R_2/a	0.1205 ± 0.0016		this work
Luminosity ratio	L_2/L_1	0.995 ± 0.015		this work
Primary mass	M_1	0.737 ± 0.020	M_\odot	this work
Secondary mass	M_2	0.709 ± 0.021	M_\odot	this work
Primary radius	R_1	1.159 ± 0.020	R_\odot	this work
Secondary radius	R_2	1.159 ± 0.020	R_\odot	this work
Primary surface gravity	$\log g_1$	4.177 ± 0.012	cgs	this work
Secondary surface gravity	$\log g_2$	4.160 ± 0.012	cgs	this work
Primary mean density	ρ_1	0.473 ± 0.019	ρ_\odot	this work
Secondary mean density	ρ_2	0.455 ± 0.018	ρ_\odot	this work
Impact parameter of primary eclipse	b_1	1.8365 ± 0.0013		this work
Impact parameter of secondary eclipse	b_2	1.8972 ± 0.0015		this work
Eccentricity	e	0.01655 ± 0.00050		this work
Periastron longitude	ω	100.4 ± 1.1	deg	this work
Reduced chi-squared of joint fit	χ_{red}^2	1.978		this work
Reduced chi-squared of light curve fit	$\chi_{\text{red,LC}}^2$	1.974		this work
Residuals of light curve fit	rms_{LC}	0.92	mmag	this work
Reduced chi-squared of primary RV fit	$\chi_{\text{red,RV1}}^2$	0.669		this work
Residuals of primary RV fit	rms_{RV1}	1.68	km s^{-1}	this work
Reduced chi-squared of secondary RV fit	$\chi_{\text{red,RV2}}^2$	0.298		this work
Residuals of primary RV fit	rms_{RV2}	1.39	km s^{-1}	this work
Reduced chi-squared of light ratio fit	$\chi_{\text{red,LR}}^2$	1.755		this work
Residuals of light ratio fit	rms_{LR}	0.085		this work

6.3.5 EPIC 205207894 / RIK-72

RIK-72 was first identified and spectroscopically confirmed as a member of Upper Sco in Rizzuto et al. (2015). Those authors assigned a spectral type of M2.5. The *K2* light curve of RIK-72 is characterized by a semi-sinusoidal waveform of 2% semi-amplitude, presumably due to rotational modulation of starspots on the primary. Assuming this interpretation is correct, the rotation period of the primary is $P_{\text{rot}} = 10.47 \pm 0.04$ days, where the period was measured from the peak in a Lomb-Scargle periodogram and the uncertainty was determined using the method of Mighell & Plavchan (2013). The waveform evolves throughout the campaign, perhaps indicating differential rotation, evolution of the spot distribution, or beating due to contributions from the secondary to the light curve. There is a single primary eclipse of $\sim 10\%$ depth and a single secondary eclipse of $\sim 2\%$ depth. As a result, the period is poorly constrained from the light curve alone. The secondary eclipse is flat-bottomed, indicating a total eclipse of the secondary by the primary star³.

Our Keck/HIRES spectra show emission in $H\alpha$, $H\beta$, and the cores of the Ca II triplet, as well as strong lithium absorption. The system is single-lined in our optical spectra. Radial velocity monitoring on four consecutive nights in July 2017 revealed an RV trend with an apparent period in the ~ 20 d range. We performed a fit to all RV measurements using the `RADVEL` code⁴ written by B.J. Fulton and Erik Petigura. The RVs are well fit by modestly eccentric ($e \approx 0.13$) Keplerian orbit with period 17.1 d. The fit is improved by including a long-term linear trend, possibly due to the wide companion detected with *K2*. The period of the SB1 is distinct, clearly, from the period of the EB (> 78 d) as well as the rotation period of the primary. We conclude the most likely explanation is that RIK-72 is at least a triple. Given the Doppler semi-amplitude of the primary star and a plausible range of masses, the companion in the 17.1 d orbit is likely to be either a brown dwarf or a very low mass star. Speckle imaging with DSSI did not reveal any additional companions to RIK-72, down to contrasts of $\Delta\text{mag} \approx 4\text{--}5$ in the angular separation range 0.1–1.37".

From a preliminary fit to the *K2* photometry, disregarding any potential third light from the companion in the SB2, we find a surface brightness ratio of $s_2/s_1 \approx 0.14$

³We note that, because only one primary eclipse and secondary eclipse were observed by *K2*, it is possible that these are actually transits by two distinct objects on wide orbits. However, in the present study we will consider only the EB scenario and assume the primary and secondary eclipses are associated with the same object.

⁴<http://radvel.readthedocs.io/en/master/>

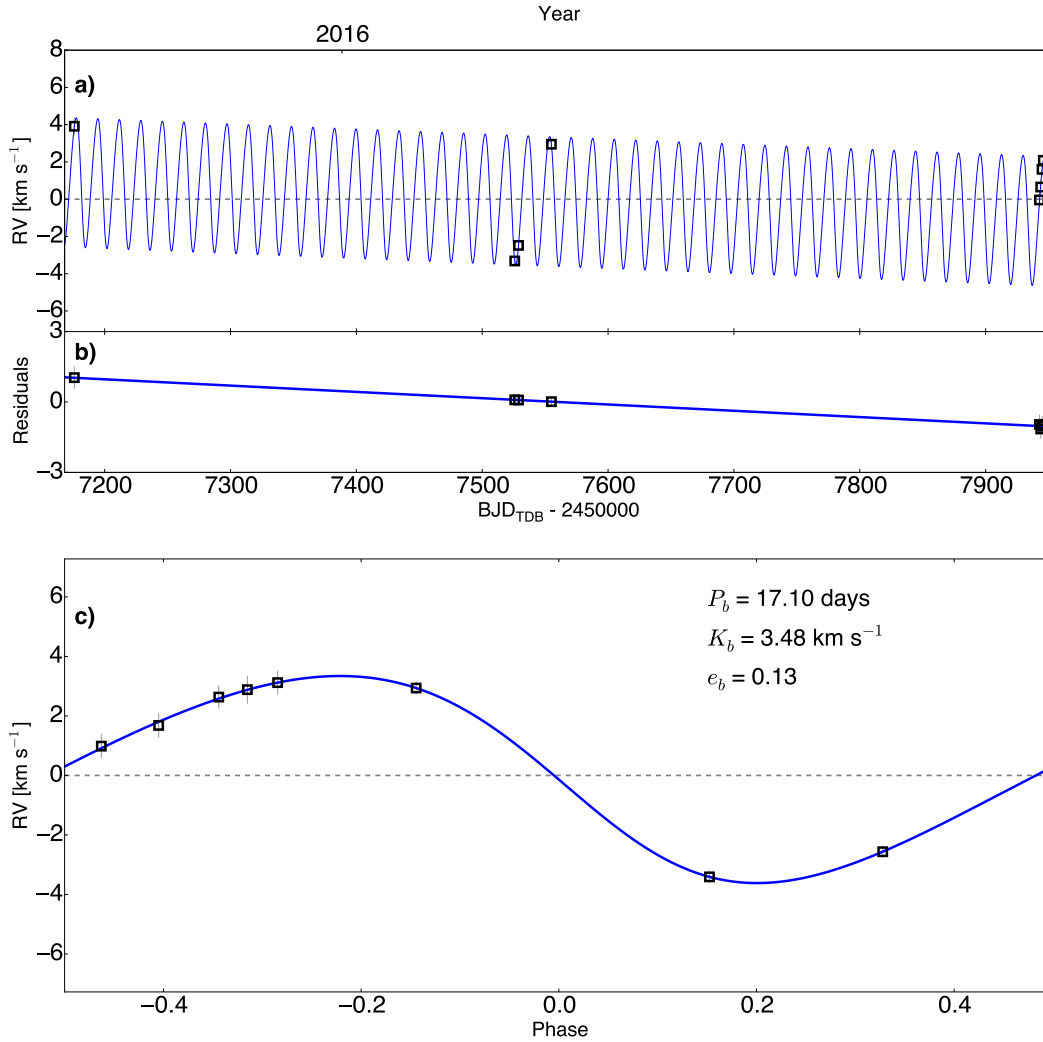


Figure 6.6: Fit to the radial velocities of RIK-72. The 17.1 d orbit is much shorter than the period of the EB, which is longer than the *K2* campaign of 78.8 d. The period is also longer than the 10.5 rotation period inferred from the light curve modulation.

and radius ratio of $R_2/R_1 \approx 0.33$. The temperature of the primary is $T_1 \approx 3485 \pm 75$ K on the Herczeg & Hillenbrand (2015) temperature scale. This implies a secondary temperature of $T_2 \approx 2630$ K. Given that RIK-72 is intermediate to USco 48 and UScoCTIO 5 in spectral type, and presumably mass, we can conservatively assume a range of plausible radii of 0.85–1.15 R_\odot . This implies a secondary radius in the range of 2.7–3.7 R_{Jup} . These parameters would seemingly put the wide companion in the brown dwarf mass regime.

6.3.6 EPIC 202963882

The *K2* photometry for EPIC 202963882 reveals eclipses with a period of 0.63 d. The EB is semi-detached, as revealed by the significant out-of-eclipse variability in the *K2* light curve. The system has not been previously studied in the literature, and we establish its youth from $H\alpha$ and $H\beta$ emission, as well as strong lithium absorption in Keck/HIRES spectra. The system is observed to be double-lined from multiple spectra. The source has a combined light spectral type of M4.5

Keck/HIRES guider camera imaging in 0.4'' seeing revealed the system is a visual binary. For all spectroscopic observations in which the components of this visual binary could be resolved, the slit was rotated to include both components. In good seeing conditions we were able to obtain spatially resolved spectroscopy of the two components in the visual binary. From these observations, we were able to determine that it is the fainter of the pair that is a spectroscopic binary and the EB. The primary component has a systemic radial velocity that is consistent with that of the EB, and with the nominal Upper Sco value. Thus, we define EPIC 202963882 A as the primary star and EPIC 202963882 Ba and EPIC 202963882 Bb as the double-lined EB. Both components of the EB appear to be rapidly rotating, consistent with expectations that the binary is tidally locked.

Speckle imaging with DSSI at Gemini observatory resolved the companion at a separation of 1.23'' and position angle of 295° – 296° , with a contrast of $\Delta m = 1.65$ mag at 692 nm, or $\Delta m = 0.99$ mag at 880 nm. At a nominal association distance of 140 pc, the companion is separated by approximately 172 AU from the EB (ignoring projection effects). Detailed modeling of this system remains to be done and we note that, given the short orbital period and clear out-of-eclipse modulations, it is necessary to use an EB modeling software that properly treats ellipsoidal modulations (unlike JKTEBOP). Also, due to the effect of tides on the sizes of stars in semi-detached binaries, EPIC 202963882 may not be an ideal system for calibrating pre-MS tracks.

6.3.7 EPIC 205030103 / UScoCTIO 5

This system is comprised of two low-mass stars with nearly equal masses and radii, and a full solution was first published by Kraus et al. (2015) using archival radial velocities from Reiners et al. (2005). A parallel analysis was performed by David et al. (2016b) of the system using the same RVs but a different detrending of the *K2* lightcurve. Interestingly, David et al. (2016b) found masses and radii that were

2σ and $2\text{--}3\sigma$ higher, respectively. This disagreement is exacerbated further if the uncertainties quoted in Kraus et al. (2015) are used. This suggests (1) different EB modeling programs can yield different parameters for the same system due to e.g. how stellar surfaces are approximated, or (2) different approaches towards detrending *K2* light curves can result in different eclipse depths. Of course, both possibilities above may be true, and in fact different transit depths obtained from different detrending routines has been observed for at least one exoplanet discovered with *K2* (Petigura et al., 2017). In this analysis, we perform an updated fit using the EVEREST 2 light curve, additional RVs at phases that were previously not covered, and assuming equal radii. This fit is shown in Figure 6.7. We find masses and radii that are broadly consistent with our previous solution.

6.3.8 EPIC 203868608

David et al. (2016b) first published this system as a possible eclipsing brown dwarf binary. Those authors noted residuals of $\sim 10 \text{ km s}^{-1}$ in the RV fits, which led to some trepidation in the interpretation of the system as a pair of eclipsing brown dwarfs in a hierarchical triple (a companion was discovered in NIRC2 imaging at a separation of $\rho = 0.12''$). From sustained radial velocity monitoring with Keck/HIRES we are able to confirm that the RVs presented in David et al. (2016b) are in fact due to a spectroscopic binary with an orbital period distinct from that of the eclipsing system.

From resolved infrared spectroscopy using NIRSPEC+AO on the Keck II telescope, we were able to determine that the brighter, eastern component in the system is the doubled-lined spectroscopic binary (Wang et al., *in prep.*). The fainter component to the west is thus the EB. The systemic radial velocity of the EB component in our NIRSPEC observations is approximately $\gamma = -5.2 \pm 1.1 \text{ km s}^{-1}$, consistent with the systemic RV of the SB2 and the mean value for Upper Sco members. The agreement between the systemic velocities of the EB and the SB2, combined with the close angular separation on the sky (see e.g. Hirsch et al., 2017, for discussion of how probability of association varies with angular separation), essentially confirms that all four components are physically associated.

The line profile of the EB pair is broadened to $\sim 20 \text{ km s}^{-1}$ in FWHM, indicating at least one of the components is a fast rotator. From a Lomb-Scargle periodogram analysis of the *K2* lightcurve we find two significant periods, $P_1 = 5.644 \pm 0.004 \text{ d}$ and $P_2 = 1.106 \pm 0.002 \text{ d}$. Neither of these periods correspond to the orbital period

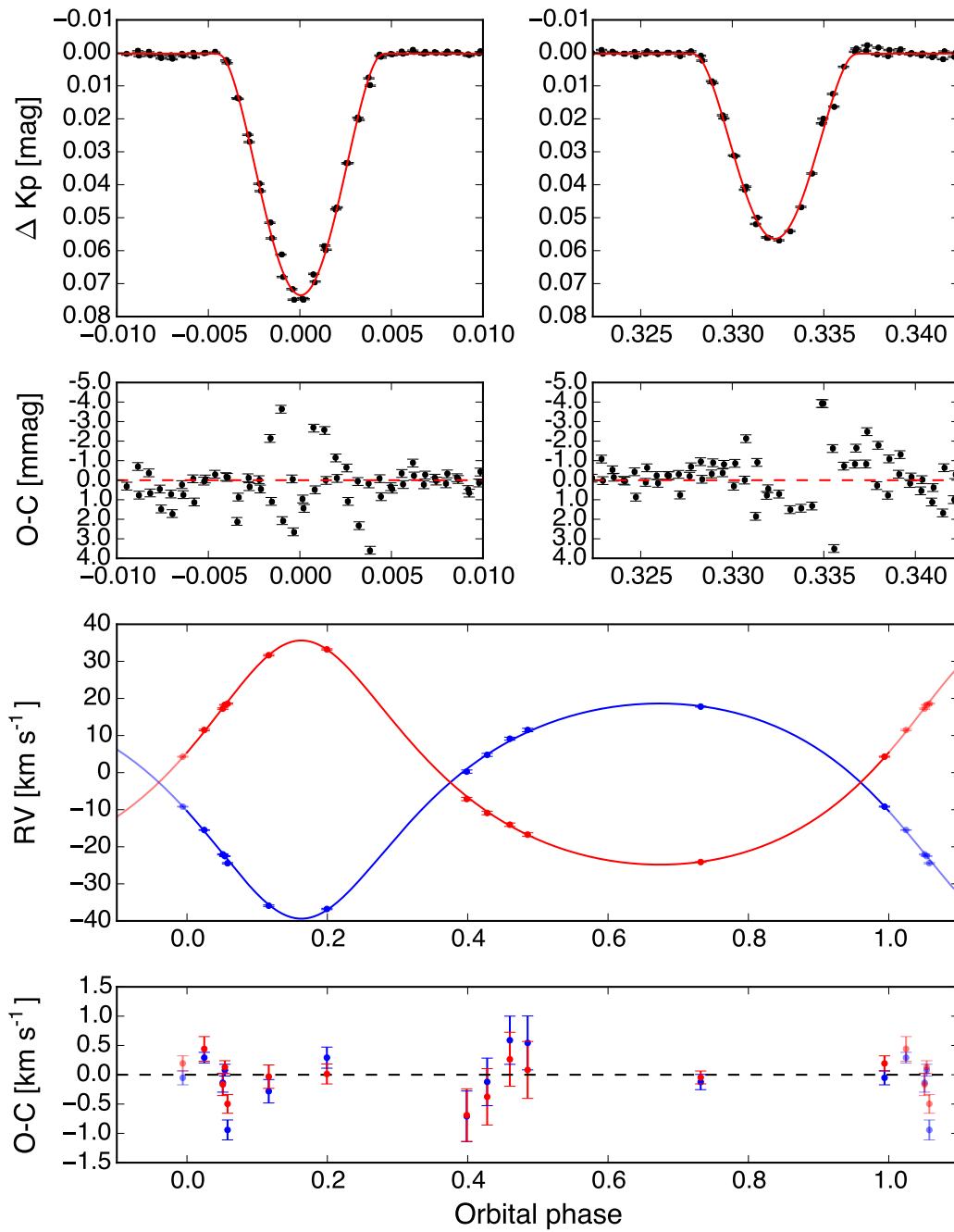


Figure 6.7: Joint fits to the K2 photometry and radial velocity time series of UScoCTIO 5.

Table 6.5: Parameters of the EPIC 203868608 spectroscopic binary

Parameter	Units	Value
<i>Directly measured parameters</i>		
Orbital period, P	days	17.9420 ± 0.0012
Epoch, T_0	BJD	2457175.182 ± 0.031
Primary Doppler semi-amplitude, K_1	km s^{-1}	26.46 ± 0.16
Secondary Doppler semi-amplitude, K_2	km s^{-1}	31.84 ± 0.18
Systemic radial velocity, γ	km s^{-1}	-4.436 ± 0.072
Eccentricity, e		0.2998 ± 0.0041
Longitude of periastron, ω	deg	316.36 ± 0.93
RMS of primary RV fit	km s^{-1}	0.6
RMS of secondary RV fit	km s^{-1}	0.8
χ_{red}^2 of primary RV fit		2.2
χ_{red}^2 of secondary RV fit		2.7
<i>Derived parameters</i>		
Mass ratio, q		0.8309 ± 0.0062
Minimum system mass, $(M_1 + M_2) \sin^3 i$	M_{\odot}	0.3685 ± 0.0050
Orbital separation, a	AU	0.09616 ± 0.00044

Note: Values quoted are best fit parameters and $1-\sigma$ uncertainties from 10,000 Monte Carlo realizations with JKTEBOP.

of the EB, which is $P_{\text{EB}} \approx 4.5$ d, nor do they coincide with the orbital period of the SB2, $P_{\text{SB2}} \approx 17.9$ d. If the smaller of the two rotation periods corresponds to one or both components of the EB, this might explain the apparently rapid rotation of the EB observed in the NIRSPEC+AO data. However, it is also possible that this period is due to a component of the SB2.

With the JKTEBOP software we performed joint fits to the RV time series alone in order to determine orbital and physical parameters of the SB2. We present these parameters in Table 6.5, where the uncertainties were determined from 10,000 Monte Carlo simulations. We show fits to the RV time series and the parameter covariances in Figures 6.8 and 6.9, respectively. We find a minimum system mass of $(M_1 + M_2) \sin^3 i = 0.3685 \pm 0.0050 M_{\odot}$. If one assumes the expected value of $\langle \sin^3 i \rangle = 3\pi/16$, this translates to a system mass of $(M_1 + M_2) \sim 0.63 M_{\odot}$.

More detailed modeling of the NIRSPEC+AO data will be required to interpret the nature of the EB (Wang et al., *in prep.*). Assuming the EB and SB2 are associated, this quadruple system provides an interesting laboratory for testing theories of star formation and dynamical interactions of tightly-packed, hierarchical multiples.

6.3.9 EPIC 203710387

This system was concurrently discovered and published in Lodieu et al. (2015a) and David et al. (2016b). It consists of two stars near the edge of the substellar

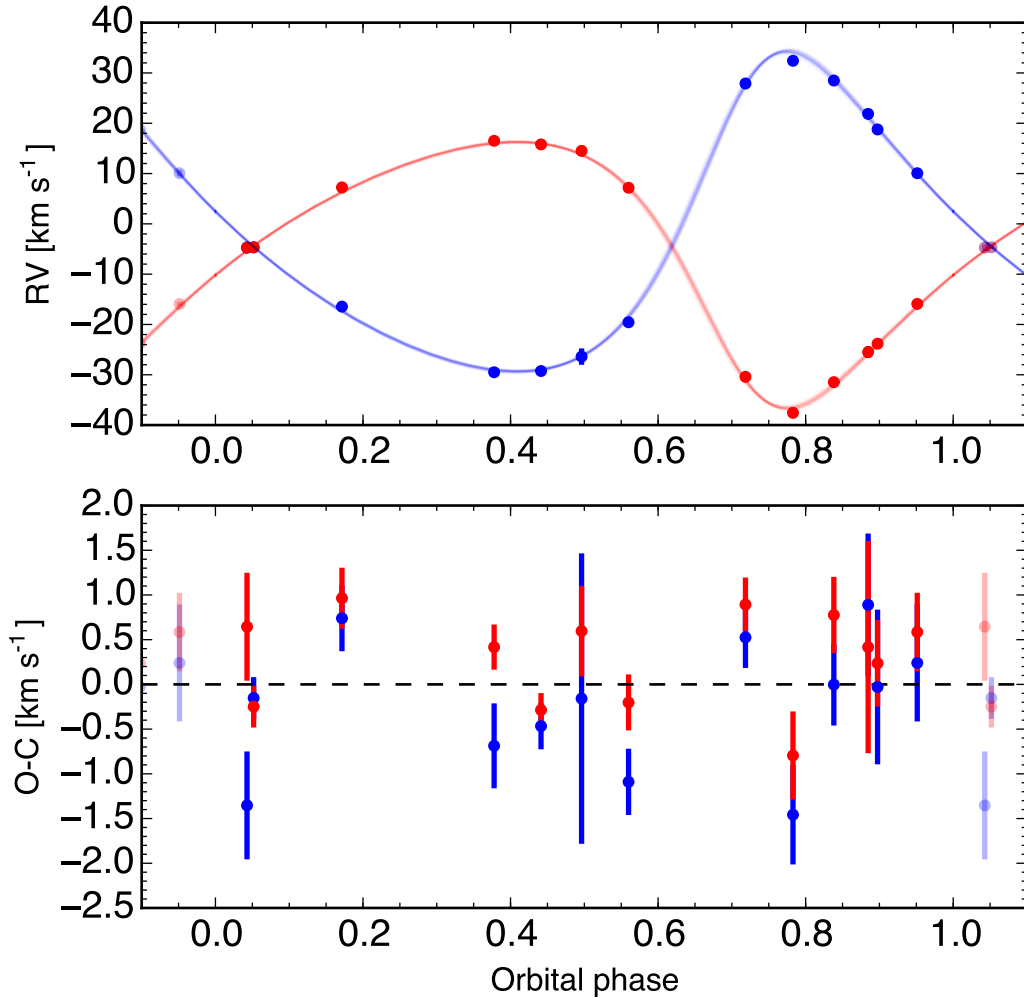


Figure 6.8: Joint fits to the radial velocity time series of the spectroscopic binary component of EPIC 203868608. The curves show fits using parameters from 100 randomly selected links in the Monte Carlo chain.

boundary and thus provides an important anchor to the mass-radius relation of young stars at the very lowest masses. Notably, the masses and radii presented in David et al. (2016b) are $4\text{--}5\sigma$ larger than those published by Lodieu et al. (2015b), i.e. discrepant in the same sense as those of UScoCTIO 5. Both Lodieu et al. (2015b) and Kraus et al. (2015) used custom-written software to fit the EB light curves and RVs, whereas we have used JKTEBOP. For our analysis here, we present a new solution in which the ratio have been assumed equal. Given the mass ratio of the system is close to unity, this assumption is not entirely unreasonable.

From a L-S analysis of the *K2* lightcurve we find a period, which we attribute to rotation, of $P_{\text{rot}} = 2.5479 \pm 0.0026$ d, which is shorter than the orbital period of

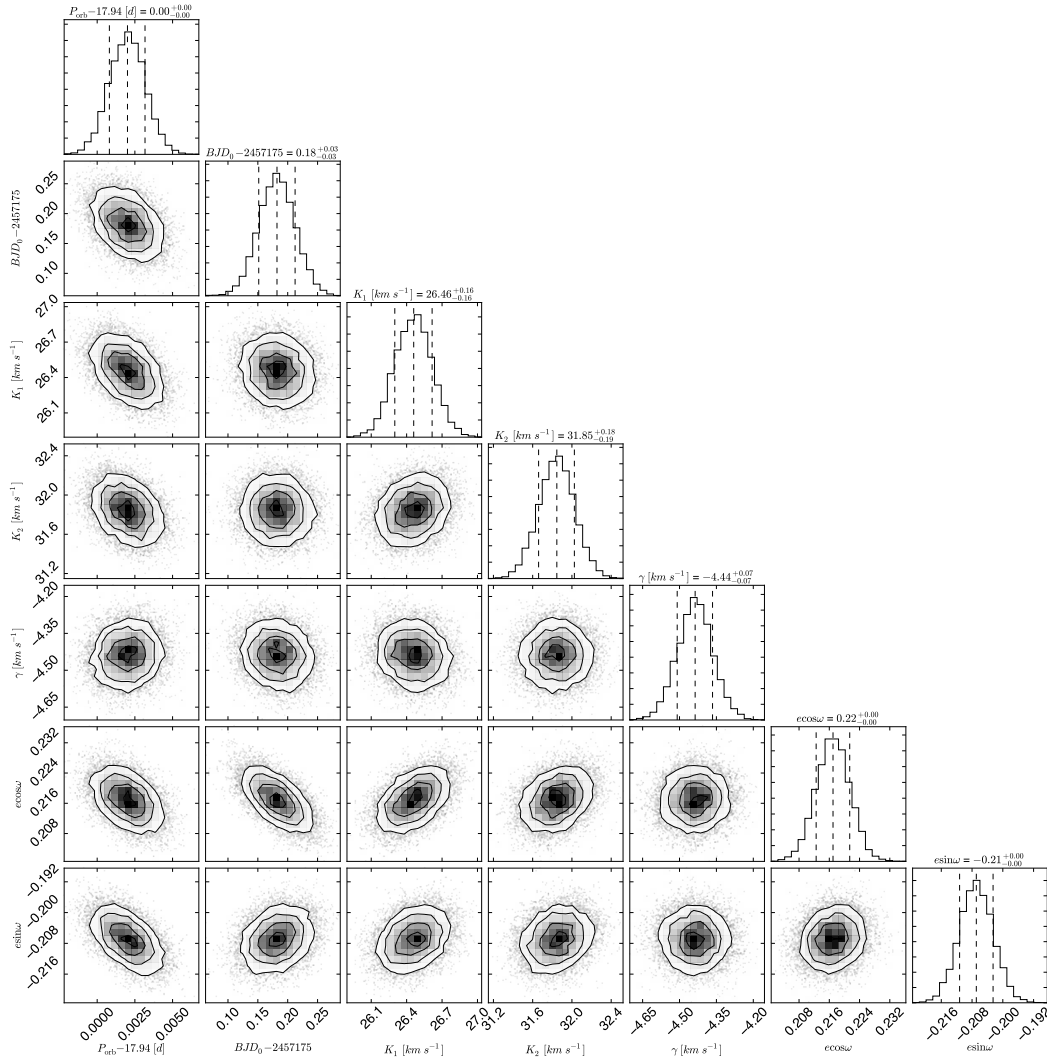


Figure 6.9: Parameter covariances for the joint radial velocity fit of the spectroscopic binary component of EPIC 203868608.

2.8 d. The binary is mildly eccentric, as is most evident from the light curve. It is possible that difference between the rotational and orbital periods indicates the binary is not tidally synchronized. Given the youth of the system, this would not be surprising, and in fact supersynchronous rotation is expected for pre-MS binaries. It is also possible that the binary is in fact in a state of pseudo-synchronous spin in which the rotation rates are synchronized to the orbital speed of the binary at periastron.

6.4 Pre-main-sequence evolution of intermediate-mass stars

During the pre-main-sequence (PMS) phase of evolution low-mass stars ($M_* < 0.5 M_\odot$) evolve nearly vertically along the fully-convective Hayashi track in the H-R

diagram. Stars of higher mass, however, quickly develop a radiative core and depart from the Hayashi track. The subsequent PMS evolution of the star is characterized by a growing radiative core mass, diminishing convective zone, and decreasing opacity. After a temporary decline in luminosity, the star rapidly becomes hotter and more luminous along the nearly horizontal Henyey track in the H-R diagram. Whereas low-mass stars contract continually as they approach the zero-age main-sequence (ZAMS), higher mass stars experience structural changes due to the changing energy output. This is because before the star reaches thermal equilibrium on the ZAMS, a number of nuclear reactions have already commenced. Deuterium, present in small amounts from the interstellar medium, will fuse with normal hydrogen nuclei in what is normally the second reaction in the p-p chain (${}^2\text{H} + {}^1\text{H} \rightarrow {}^3\text{He} + \gamma$). The initial reservoir of deuterium will be depleted by the time the internal temperature reaches 10^6 K, but not before the star's contraction has been halted for a few times $\sim 10^5$ yr. Additionally, the ${}^{12}\text{C}(p,\gamma){}^{13}\text{C}$ reaction is initiated at a lower temperature than is required for the full CNO cycle. As a result, nearly all ${}^{12}\text{C}$ is converted to ${}^{14}\text{N}$ before the star reaches the ZAMS, and this reaction also temporarily halts contraction. In short, as the core contracts and internal temperatures rise, increased energy output from p-p chain reactions increases the ionization of the outer layers and decreases the extent of the outer convective zone. As the star adjusts during these changes there is a brief increase in radius. As a result, there is a prominent peak in the mass-radius diagram for intermediate mass stars at young ages ($\lesssim 20$ Myr).

6.5 The age of Upper Scorpius from eclipsing binaries

We assess the age of Upper Scorpius from comparison of the newly characterized eclipsing binaries with theoretical predictions in the mass-radius diagram. To make this comparison, we select the solar-metallicity MIST isochrones (Choi et al., 2016; Dotter, 2016) which are based on the Modules and Experiments in Stellar Astrophysics (MESA) software (Paxton et al., 2011; Paxton et al., 2013; Paxton et al., 2015). These models are available with and without prescriptions for rotation. In the rotating models, stars are prescribed with solid-body rotation starting on the ZAMS, and the rate of rotation is gradually ramped up from zero to 40% the critical value ($\Omega/\Omega_{\text{crit}} = 0.4$). Because rotation is commenced on the ZAMS in these models, there is no appreciable difference between the rotating and non-rotating models for low- and intermediate-mass stars during the pre-MS stages (Figure 6.10). However, for the more massive stars such as those in the HR 5934 binary, there is a significant

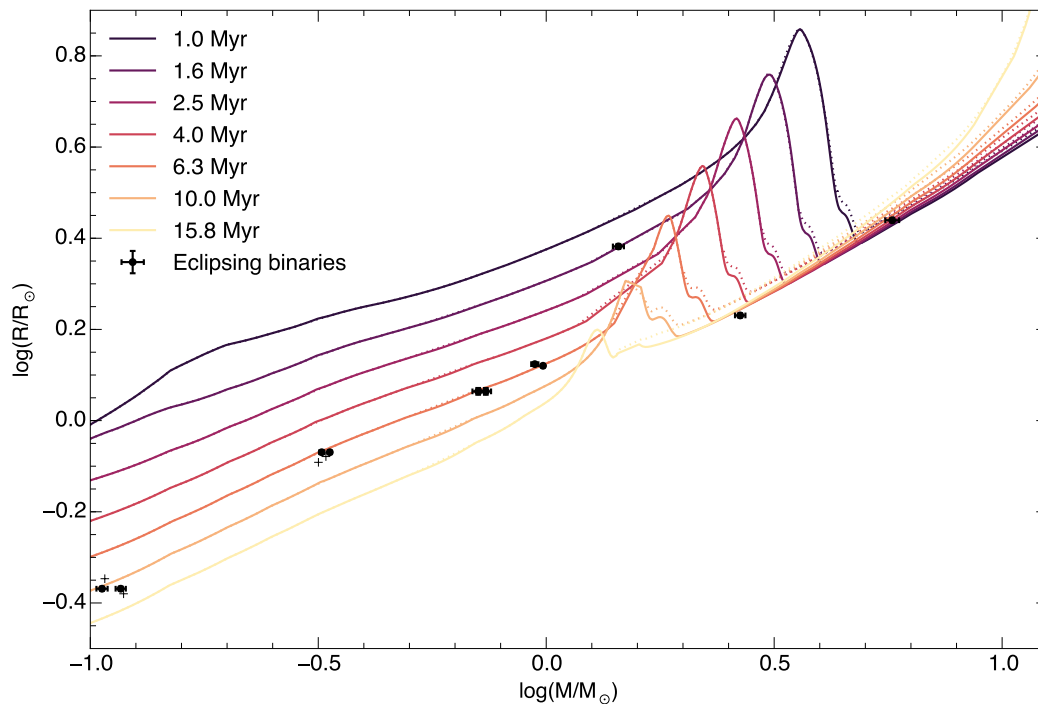


Figure 6.10: Mass-radius diagram. Colored curves are theoretical predictions from the MIST models (Dotter, 2016; Choi et al., 2016) in the non-rotating case (solid) and rotating case (dotted). Eclipsing binaries in the Upper Scorpius OB association are represented by the black points. The black crosses show previously published solutions for EPIC 203710387 (David et al., 2016b) and UScoCTIO5 (Kraus et al., 2015).

difference in the predicted radii on the ZAMS between the two models. We find that the components of HR 5934 fall below the ZAMS in the mass-radius diagram when using the rotating models, but that this problem is alleviated when the non-rotating models are used instead. As such, we use the non-rotating models in the analysis that follows.

For the eclipsing systems shown in Figure 6.10 we evaluated the χ^2 statistic for MIST isochrones over a finely space grid between 0.5–30 Myr. The calculation was performed assuming the EB masses were known perfectly, thus calculating $(O - E)^2$ in the radii at a given age. Figure 6.11 shows the variation of χ^2 with age for this model set, showing a broad minimum between 5–10 Myr. The best-fitting isochrone is one with an age of 7.4 Myr. For each individual component, we also calculated an age based on 2-D linear interpolation between the models, resulting in probability density functions in age (Figure 6.12). The star HR 5934 A has a broad PDF due to the fact that it sits squarely on the ZAMS where the isochrones are clustered. Additionally, the primary in the triply eclipsing system HD 144548

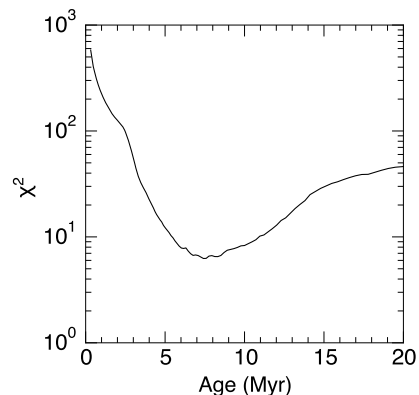


Figure 6.11: Chi-squared statistic as a function of age for non-rotating MIST model fits to the eclipsing binary radii in Upper Scorpius. The χ^2_{\min} age of Upper Scorpius according to this model set is 7.4 Myr

has an anomalously young age. We caution against overinterpreting the age for this star, given the complexities involved in modeling it. Nevertheless, it is notable that the primary appears to be near the prominent peak in the mass-radius diagram and thus in principle can provide a valuable constraint on the age of the association. Finally, the ultra low-mass system EPIC 203710387 appears anomalously old in this and other sets of models. The age of this system is more in line with a recent age estimate of 11 ± 2 Myr (Pecaut et al., 2012). However, the majority of stars show age distributions with well-defined peaks clustered around 7 Myr. This age is intermediate to the canonical age of the association of 5 Myr (e.g. Preibisch et al., 2002) and the recent estimate. We stress these are preliminary results, and in a future work we will carry out the same analyses using different model sets in order to assess the systematic age uncertainty. It is also possible that the kinematic, spatial, and photometric distinctions between the subgroups of Sco-Cen are more complex than traditionally thought.

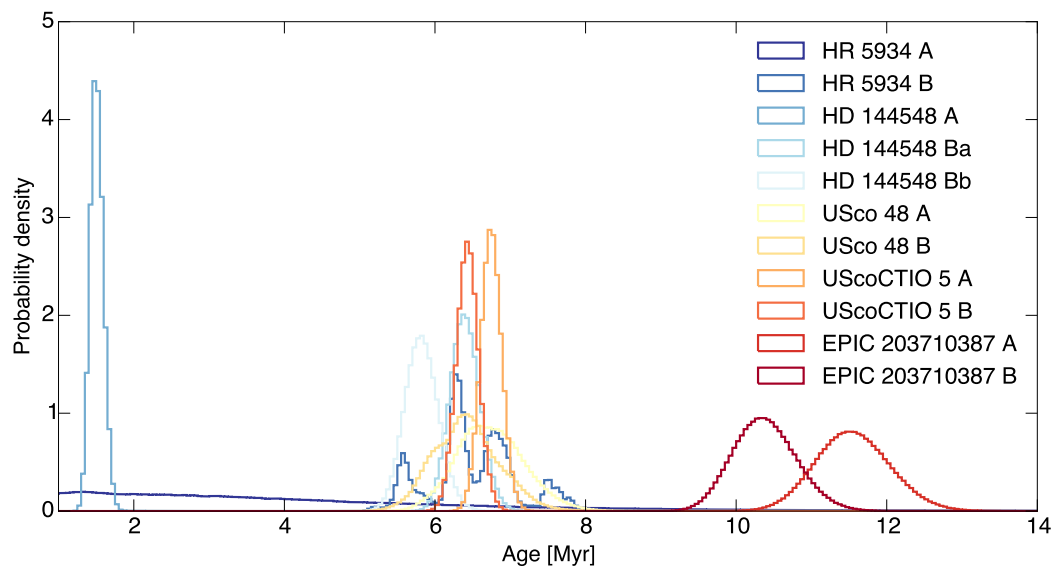


Figure 6.12: Probability density functions in age for individual stars in eclipsing binaries in Upper Scorpius. Ages are derived from interpolation within MIST models.

*Chapter 7***A TRANSIENT TRANSIT SIGNATURE ASSOCIATED WITH
THE YOUNG STAR RIK-210**

David, T. J., Petigura, E. A., Hillenbrand, L. A., et al., 2017, ApJ, 835, 168

ABSTRACT

We find transient, transit-like dimming events within the *K2* time series photometry of the young star RIK-210 in the Upper Scorpius OB association. These dimming events are variable in depth, duration, and morphology. High spatial resolution imaging revealed the star is single, and radial velocity monitoring indicated that the dimming events can not be due to an eclipsing stellar or brown dwarf companion. Archival and follow-up photometry suggest the dimming events are transient in nature. The variable morphology of the dimming events suggests they are not due to a single, spherical body. The ingress of each dimming event is always shallower than egress, as one would expect for an orbiting body with a leading tail. The dimming events are periodic and synchronous with the stellar rotation. However, we argue it is unlikely the dimming events could be attributed to anything on the stellar surface based on the observed depths and durations. Variable obscuration by a protoplanetary disk is unlikely on the basis that the star is not actively accreting and lacks the infrared excess associated with an inner disk. Rather, we explore the possibilities that the dimming events are due to magnetospheric clouds, a transiting protoplanet surrounded by circumplanetary dust and debris, eccentric orbiting bodies undergoing periodic tidal disruption, or an extended field of dust or debris near the corotation radius.

7.1 Introduction

Upper Scorpius, hereafter Upper Sco, is the nearest OB association (see Preibisch & Mamajek, 2008, for a review). At an age of 5–10 Myr, the association is at a critical stage of planet formation, when most protoplanetary disks have dissipated. Roughly 20% of the low-mass members of Upper Sco host a protoplanetary disk, indicating that planet formation is ongoing in the region (Luhman & Mamajek, 2012).

Around young ($\lesssim 10$ Myr) planet-forming stars, dimming events of several tens of percent have been explained as obscuration by a circumstellar disk (Cody et al., 2014). Indeed, in Upper Sco itself, dozens of members exhibit such dimming behavior (Ansdell et al., 2016). At the age of Upper Sco, it is also possible to find fully-formed planets at small orbital separations, as evidenced by *K2*–33 b (David et al., 2016c; Mann et al., 2016a), a transiting, Neptune-sized, short-period exoplanet around a low-mass member of Upper Sco.

Transit profiles that are asymmetric and variable in depth and duration may be attributable to disintegrating planetary bodies with trailing or leading tails (Rappaport et al., 2012; Rappaport et al., 2014; Sanchis-Ojeda et al., 2015; Vanderburg et al., 2015), swarms of rocky or cometary debris (Boyajian et al., 2016), circumplanetary rings (Mamajek et al., 2012), or a precessing planet transiting a star with non-uniform surface brightness (Barnes et al., 2013). While this phenomenon has been documented around mature stars and stellar remnants, due to e.g. tidal disruption or photoevaporation, *periodic* examples have not been previously observed around a young star lacking a protoplanetary disk. Here we present evidence of a transient transit-like signature, possibly due to a transiting cloud or an enshrouded protoplanet, around the young star RIK-210.

In §2 we describe existing and new information about the star. In §3 we present the *K2* data and light curve analysis. Archival and follow-up ground-based photometry in multiple filters is presented in §4, time series spectroscopy in §5, and high spatial resolution imaging in §6. §7 discusses the physical interpretation of the variable depth narrow flux dips in RIK-210, including stellar surface activity and several orbiting planet/debris scenarios.

7.2 RIK-210

RIK-210 (also designated 2MASS J16232454-1717270 and EPIC 205483258) was established as a low-mass member of the 5–10 Myr old Upper Scorpius OB association by Rizzuto et al. (2015). Those authors assigned a 95% membership probability

on the basis of hydrogen emission and lithium absorption. Proper motions from the UCAC4 catalog (Zacharias et al., 2013) are consistent with membership (de Zeeuw et al., 1999; Lodieu, 2013). We confirm the youth of the star spectroscopically and through a precise determination of its systemic radial velocity.

7.2.1 Stellar properties

Observed and derived stellar properties for RIK-210 are reported in Table 7.1. For all distance-dependent parameters we assumed $d = 145 \pm 20$ pc, corresponding to the mean distance to Upper Scorpius from *Hipparcos* trigonometric parallaxes of the high-mass members and assuming an uncertainty comparable to the association's width on the sky (de Zeeuw et al., 1999; de Bruijne, 1999). Our spectrum (§6) is consistent with the previously reported spectral type of M2.5 (Rizzuto et al., 2015). Assuming the spectral type and using empirical calibrations valid for young stars (Pecaut & Mamajek, 2013), we derived the effective temperature, bolometric luminosity and visual extinction for RIK-210. We determined the stellar radius from the temperature, luminosity, and the Stefan-Boltzmann law.

The stellar mass was determined from the temperature and luminosity, interpolating between solar metallicity ($Z=0.0152$) PARSEC v1.2s pre-main sequence models (Bressan et al., 2012; Chen et al., 2014). Mass uncertainties were estimated from Monte Carlo sampling assuming normally distributed errors in $\log(T_{\text{eff}})$ and $\log(L/L_{\odot})$. We adopt generous mass uncertainties (the boundaries of the 5% and 95% quantiles, see Table 7.1) due to the incompleteness of models at low stellar masses to include important physics such as the magnetic inhibition of convection (e.g. Feiden, 2016a).

7.2.2 Activity and Possible Disk

RIK-210 shows modest chromospheric emission. $H\alpha$ with a classic double-horn profile, $H\beta$, He I 5876Å, Na I D, the Ca II H&K doublet and the "infrared" triplet, and Fe I 5169 Å are all seen in emission in our spectra (§6). The line strengths are variable over our spectral time series, as discussed in detail below.

Although the star is active, the spectrum indicates that it is not currently accreting. Furthermore, the spectral energy distribution (Figure 7.1) shows that it does not host a primordial protoplanetary disk. However, there is marginal evidence for a 22 μm mid-infrared excess at the 40% level (detected at $\text{SNR} > 3.5$), based on a model atmosphere fit to available broadband catalog photometry. Typical dust masses of low-mass stars with circumstellar disks in Upper Sco are in the range of

Table 7.1: System properties of RIK-210

Parameter	Value	Reference
2MASS designation	J16232454-1717270	
EPIC designation	205483258	
Spectral type	M2.5	this work
d (pc)	145 ± 20	de Zeeuw et al. (1999)
A_V (mag)	0.6 ± 0.2	this work
EW H α (Å)	-3.5 to -6.5	this work
EW He I 5876 (Å)	-0.6 to -1.2	this work
EW Li (Å)	0.54 ± 0.02	this work
$\log(T_{\text{eff}}/\text{K})$	3.54 ± 0.01	this work
$\log L_*/L_\odot$ (dex)	-0.70 ± 0.08	this work
M_* (M_\odot)	$0.53^{+0.13}_{-0.13}$	this work
R_* (R_\odot)	$1.24^{+0.12}_{-0.13}$	this work
γ (km s $^{-1}$)	-4.63 ± 0.07	this work
$v \sin i$ (km s $^{-1}$)	11 ± 1	this work
P_{rot} (d)	5.670 ± 0.004	this work
Kp (mag)	13.7	EPIC
B (mag)	16.213 ± 0.066	APASS DR9
V (mag)	14.630 ± 0.137	APASS DR9
g' (mag)	15.462 ± 0.121	APASS DR9
r' (mag)	14.093 ± 0.118	APASS DR9
i' (mag)	12.862 ± 0.099	APASS DR9
J (mag)	10.61 ± 0.02	2MASS
H (mag)	9.85 ± 0.02	2MASS
K (mag)	9.65 ± 0.02	2MASS
$W1$ (mag)	9.55 ± 0.02	WISE
$W2$ (mag)	9.40 ± 0.02	WISE
$W3$ (mag)	9.19 ± 0.05	WISE
$W4$ (mag)	8.75 ± 0.45	WISE

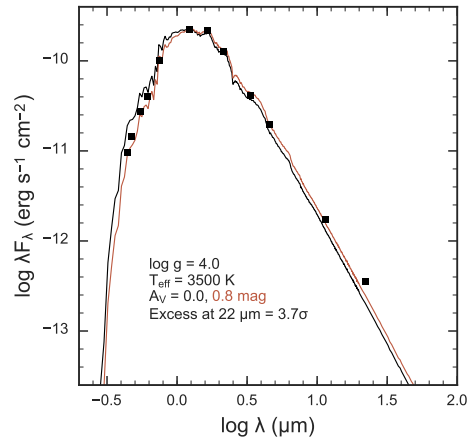


Figure 7.1: Spectral energy distribution of RIK-210 along with a NextGen stellar atmosphere model (Hauschildt et al., 1999b) normalized to the J-band point. Including a small amount of reddening (black) improves the fit over the unreddened model (green).

0.2–20 M_{\oplus} (Barenfeld et al., 2016). As RIK-210 lacks any significant circumstellar disk, we assume the amount of remaining dust in the system is likely below 0.2 M_{\oplus} .

7.3 K2 Light Curve and Analysis

RIK-210 was observed for ~ 77 days at a ≈ 30 minute cadence by the *Kepler* space telescope during Campaign 2 of the *K2* mission (Howell et al., 2014). Systematic artifacts in the photometry due to spacecraft attitude adjustments were corrected for using an established algorithm (Aigrain et al., 2016) and the resulting time series is shown as the top sequence in Figure 7.2. The deep dimming events are superposed on the smooth rotation signature of the spotted star, apparently in phase with the stellar rotation. Figure 7.3 highlights the dimming events in the context of rotation pattern.

Our analysis and interpretation of the dimming events is predicated on the following observations and assumptions, all of which we develop in full below:

1. Dimming events of variable depth, duration, and morphology occur every 5.6685 days, in phase with the stellar rotation.
2. The dimming events are both deep (sometimes greater than 15%) and short in duration relative to the rotational period, and thus unlikely to be due to features on the stellar surface.
3. The morphology of the dimming events is variable over the 77 day campaign, while the starspot modulation pattern remains stable over this timeframe.

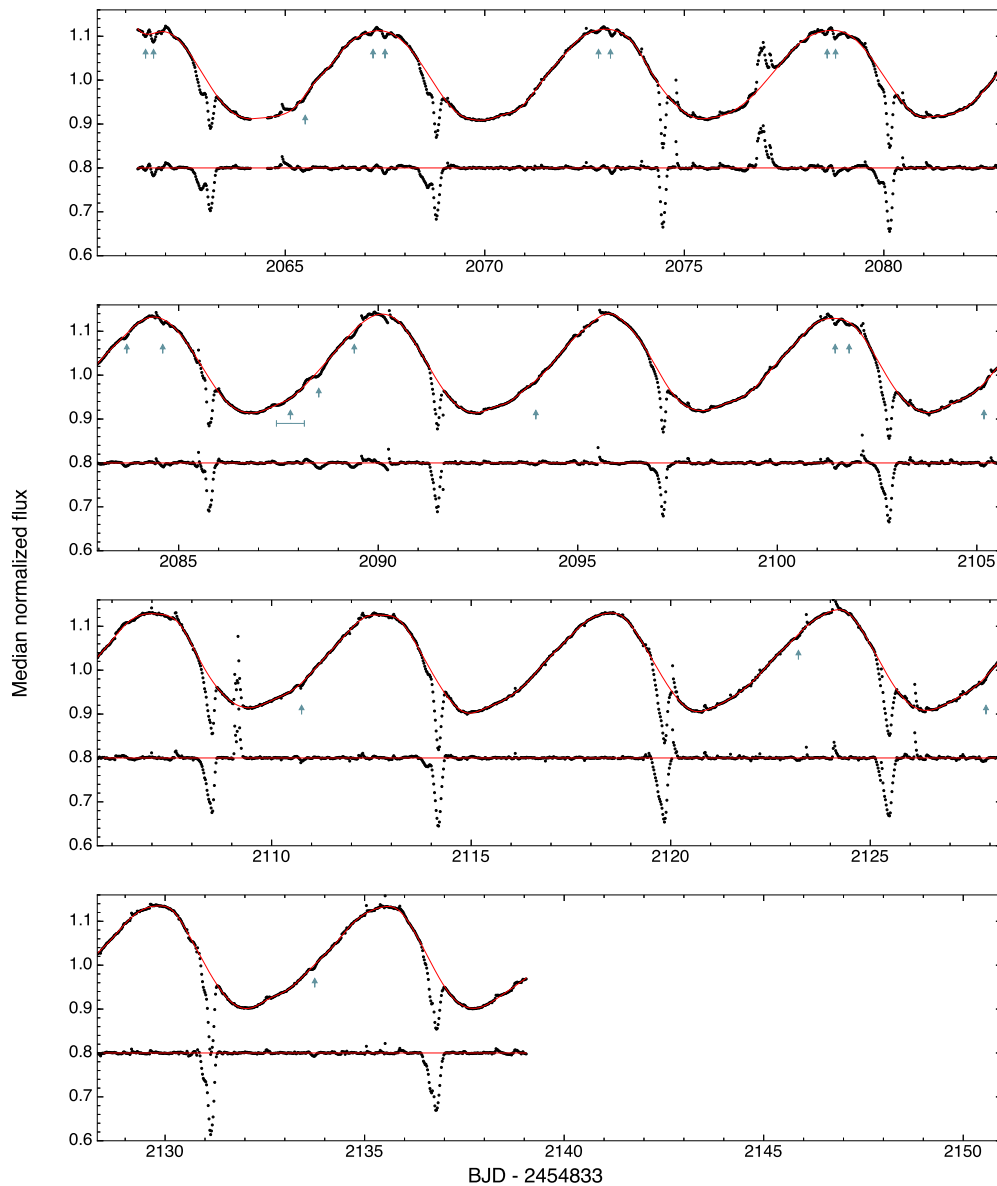


Figure 7.2: *K2* light curve of RIK-210 in 20-day segments (black points). The red curve indicates the iterative spline fit (variability fit A) used to remove the starspot modulation pattern. Blue arrows indicate the approximate positions of shallow dimming events. Below the light curve we plot the residuals of the variability fit, normalized to unity but shifted to a continuum value of 0.8 in this figure. A broad flux dip occurs near $\text{BJD} - 2454833 = 2087.8$, indicated by the arrow and bar in the second panel, however the variability fit shown here passes through it and so it is not apparent in the residuals.

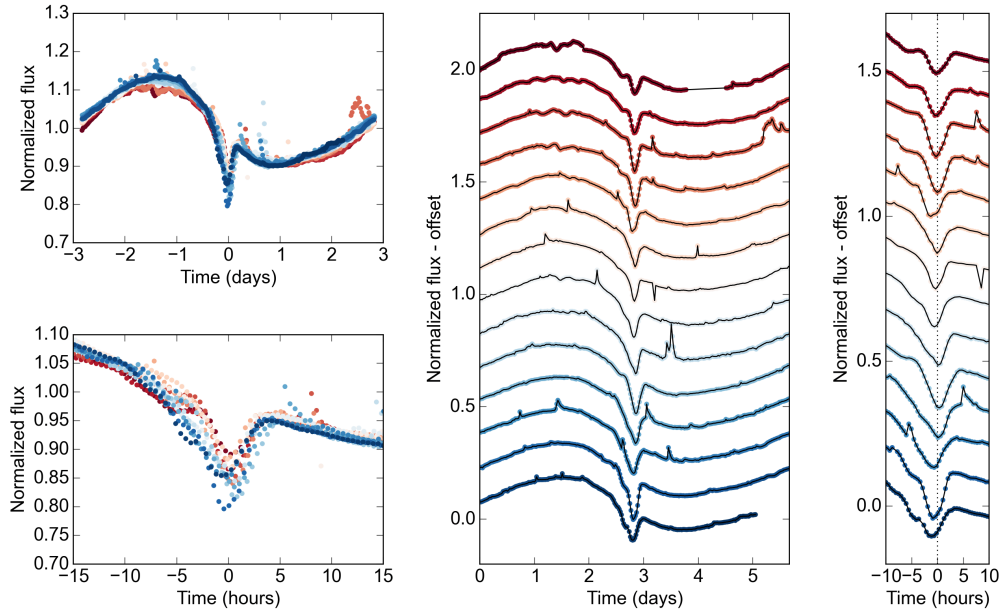


Figure 7.3: *K2* light curve of RIK-210. In each panel, the point color indicates the relative time of observation (with red corresponding to earlier times). Upper left: photometry folded on the rotational/orbital period of 5.67 d. Bottom left: same as above, showing an enhanced view of the dimming events. Middle: Same as the upper left, but with vertical offsets applied after each rotation of the star. Right: Same as middle, showing an enhanced view of the dimming events. There is clear evolution in the depth, duration, and overall morphology of the dimming events, a strong indication against a transit by or eclipse of a single solid body of any size. Some flares appear to occur at approximately the same rotational phase, shortly after the transit events.

4. If the dimming events are due to an object or debris cloud in a Keplerian orbit around the star, the transiting body must be at or near the corotation radius.
5. Assuming the transiting material does not contribute significant flux to the optical light curve, the depth of each transit yields the approximate size of the occulting body or bodies.
6. The facts that the dimming events are periodic yet narrow in rotational phase indicates the occulting material is azimuthally confined within its orbit around the star, else if it is arranged in a torus-like structure its orbital plane is tilted and its distribution vertically above that plane is inhomogeneous.
7. A purely gaseous cloud lacks the requisite opacity in the *Kepler* bandpass to produce the observed transit depths.

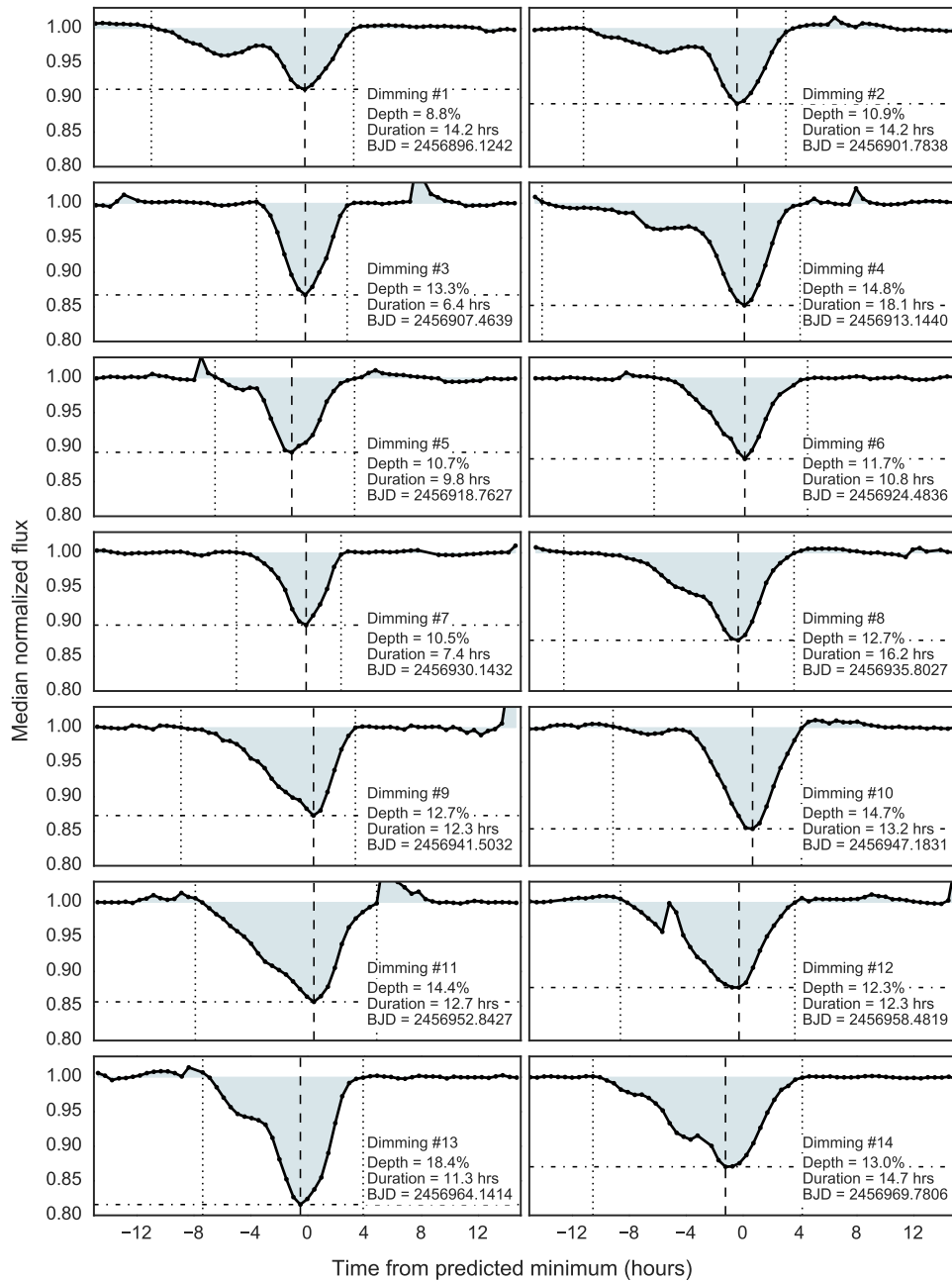


Figure 7.4: Individual dimming events within the *K2* light curve of RIK-210, after removing the starspot modulation. On the abscissa, the data are plotted in terms of time from the predicted minimum as determined from a linear ephemeris. The maximum depth, total duration, and time of minimum light are summarized in the lower right corner of each panel.

7.3.1 Stellar variability fit

At several stages of our analysis, we consider a “flattened” light curve, in which we attempted to remove the underlying starspot modulations whilst excluding dimming events from the fit. We use two fits in this work. The first, which for convenience we call variability fit A, was achieved using a custom, automated routine which iteratively fits the light curve via a cubic basis spline, excluding 2σ outliers upon each iteration (for details see David et al., 2016b). The second, which we call variability fit B, also utilizes a cubic basis spline, though the observations excluded from this fit were manually selected through visual inspection in a cadence-by-cadence manner. We note that fit A is used for quantitative analyses and fit B for qualitative or illustrative purposes. The adopted fit and the residual light curve are displayed as the middle and bottom sequences in Figure 7.2.

7.3.2 Periodicity

A period of 5.670 ± 0.004 d that we associate with the rotation of the star was determined from a Lomb-Scargle periodogram of the systematics-corrected light curve. We note this rotation period is somewhat long for Upper Sco members of comparable color but not outside the distribution, which peaks at periods shorter than 1 d with a long tail out to tens of days (L. Rebull, priv. comm.). The rotation period uncertainty was estimated as $\Delta P = \sigma\sqrt{2/M}$, where $\sigma = dt/2$ is half of the observing cadence and M is the number of rotational cycles contained within the entire light curve (Mighell & Plavchan, 2013). Performing the same periodogram analysis on only the in-transit observations, or on only the out-of-transit observations, yields identical periods within uncertainties. We conclude that the orbital period is indistinguishable from the rotation period of the star, indicating the occulting material is orbiting at or near the corotation radius.

The corotation radius is the separation at which an object in circular orbit around a star has an orbital period equivalent to the stellar rotation period, given by:

$$a_{\text{corot}} = (M_*/M_\odot)^{1/3}(P_{\text{rot}}/\text{yr})^{2/3} \text{ AU}. \quad (7.1)$$

For stars still hosting massive protoplanetary disks, theory predicts truncation of the inner disk near the corotation radius, where ionized material is dragged along magnetospheric field lines and may be accreted onto the stellar surface (Koenigl, 1991; Collier Cameron & Campbell, 1993; Bouvier et al., 1997). For the adopted

stellar mass and the rotation period above, we find $a_{\text{corot}} = 0.050 \pm 0.004$ AU, or approximately $9 R_*$.

7.3.3 Ephemeris

From the *K2* light curve, we determined an ephemeris for the dips from 10^6 bootstrapping simulations of linear fits to the times of minimum light, conservatively assuming 0.5 hr uncertainties and Gaussian errors. The times of minimum light are predicted by:

$$t_n = 2456896.1278(0.011) + n \times 5.6685(0.0014) \text{ BJD.} \quad (7.2)$$

Notably, the time of minimum light deviates from this linear ephemeris within the *K2* campaign, sometimes occurring earlier or later by up to one hour. This is potentially due to morphological changes of the obscuring body itself rather than dynamical effects, as discussed in § 7.3.8.

7.3.4 Durations

Figure 7.4 highlights the individual dimming events during the *K2* campaign. Assuming an edge-on and equatorial transit, the transit duration of a massless, dimensionless particle orbiting with circular velocity v_{circ} and period P_{orb} at a distance a from a star with mass and radius, M_* and R_* , respectively, is given by:

$$t_{\text{cross}} = \frac{2R_*}{v_{\text{circ}}} = \frac{2R_*}{(GM_*/a)^{1/2}} = \frac{P_{\text{orb}}}{\pi} \frac{R_*}{a}. \quad (7.3)$$

For a particle on a circular orbit at the corotation radius, the transit duration is:

$$t_{\text{cross}} = \frac{2R_*}{G^{1/2}(M_*/P_{\text{orb}})^{1/3}}. \quad (7.4)$$

For the stellar mass and radius adopted above, and the presumed orbital period, the expected transit duration is ≈ 5 hours, i.e. slightly less than the minimum observed duration but about three times shorter than the maximum observed duration. A larger transiting object would produce longer durations, though the variable transit duration, depth, and morphology is inconsistent with eclipses by a single spherical body. We conclude that the occulting material must be comprised of, at least in part, an extended distribution of particles with small individual size, but large collective size, relative to the star.

7.3.5 Size of occulting material

A spherical body of radius r transiting the equator of a star with radius R_* has a transverse velocity of

$$v_t = \frac{2(r + R_*)}{t_{\text{dim}}}, \quad (7.5)$$

where t_{dim} is the duration of a transit or eclipse.

If the object is on a circular orbit, the transverse velocity is the circular Keplerian velocity, and the size of the occulting object is given by,

$$r = \frac{t_{\text{dim}}}{2} \left(\frac{GM_*}{a} \right)^{1/2} - R_*. \quad (7.6)$$

From Kepler's third law, assuming the object in orbit has a mass much smaller than the mass of the star, the radius of the occulting body is then,

$$r = \frac{\pi a t_{\text{dim}}}{P_{\text{orb}}} - R_*. \quad (7.7)$$

For the range of dimming durations observed in RIK-210 (≈ 6 – 18 hours), the radius of a putative occulting body would be in the range of ~ 0.3 – $3 R_\odot$ or ~ 3 – $30 R_{\text{Jup}}$, assuming an equatorial orbit. However, we note that the dips with the longest observed durations are always significantly asymmetric. A single, spherical body produces a symmetric transit or eclipse profile (in the absence of spot crossings or precession). Thus, the larger end of the radii quoted above likely represent the size of a putative debris stream or dust cloud rather than any individual occulter.

If instead we assume the occulting material is distributed azimuthally in orbit at the corotation radius around the star, we can calculate its linear size from its arclength as implied by the dimming durations:

$$s = \frac{2\pi a_{\text{cor}} t_{\text{dim}}}{P_{\text{orb}}}, \quad (7.8)$$

from which we found $s \sim 3$ – $9 R_\odot$, i.e. larger than the diameter of the star itself. This would imply the dust or debris covers ~ 4 – 13% of its orbit, or an angle of 0.3 – 0.8 radian, assuming equatorial transits.

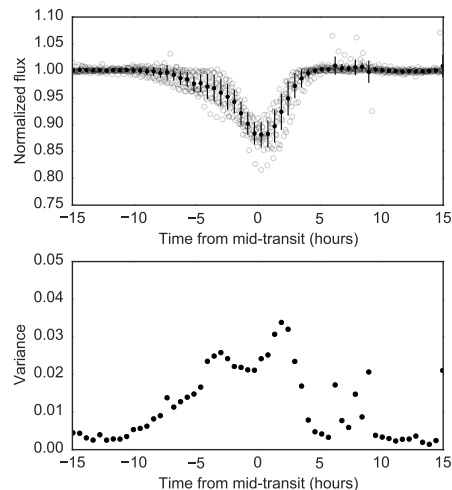


Figure 7.5: Top: Phase folded and binned *K2* light curve of RIK-210 after removing the starspot rotation signal via an iterative spline fit. Bottom: variance in the phased and binned light curve. Variability fit B was used to make this plot.

7.3.6 Dip morphology

The dip morphology continually evolves throughout the *K2* campaign (Figure 7.3 and Figure 7.4). While no two dips have the same morphology, there are common characteristics between all events, which are evident in Figure 7.5. Notably, ingress is often shallower than egress. Such dip morphologies may be produced by a leading tail of debris surrounding a main transiting body, or by a precessing body transiting a star of non-uniform surface brightness. Additionally, the variance in the phase folded light curve shows a double-peaked profile, gradually increasing through ingress before reaching a local minimum at the expected time of mid-transit, a global maximum shortly after the time of mid-transit, and then falling off steeply in egress.

In some individual dips, there are clearly two or even three distinct minima, with the shallower minima always occurring prior to the global minimum (Figure 7.4). Additionally, some dips exhibit either ingress or egress morphologies that are strikingly similar to the morphologies expected from transiting comets (Lecavelier Des Etangs et al., 1999; Lecavelier Des Etangs, 1999).

7.3.7 Bursts, Flares, and Starspots

The out-of-transit light curve is dominated by a semi-sinusoidal waveform of $\sim 20\%$ peak-to-trough amplitude, which we interpret as rotational modulation of starspots. While the starspot modulation amplitude is large even for a young star, it is not unprecedented. For example, a spot modulation amplitude of $\Delta V \approx 0.8$ mag has

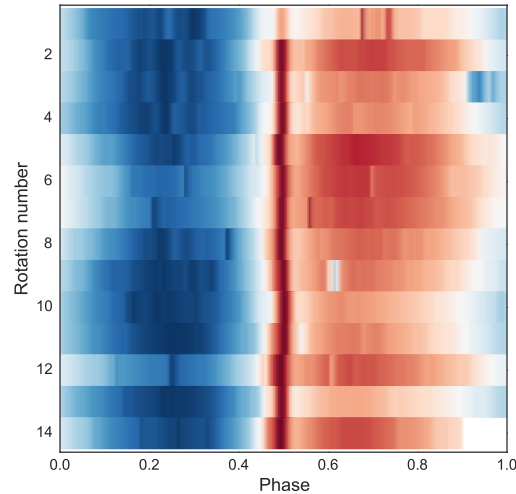


Figure 7.6: Waterfall diagram of RIK-210. Colors represent the *K2* light curve intensity, with blue corresponding to higher flux and red to lower flux. The primary dimming events that are the focus of this work are clearly seen as the dark red stripe, which changes in intensity, duration, and timing. At top left, a series of light blue stripes between phases of 0.2 and 0.3 are observed to apparently drift in phase over the first four cycles. These are some of the shallow flux dips discussed in § 7.3.9. Linear interpolation was performed over data gaps where spacecraft thruster firings were excluded.

been observed in the weak-lined T Tauri star (WTTS) LkCa 4 (Grankin et al., 2008). The brightness difference observed in RIK-210 suggests a $\sim 5\%$ difference in the disk-averaged temperature (i.e. a few hundred Kelvin) between the coolest and hottest hemispheres.

In addition to the flux decrements, there are several flares in the light curve, which are commonly observed in young, low-mass stars. There is marginal evidence that these flares are somewhat confined in rotational phase (see top left panel of Figure 7.3). There is also a large burst, approximately 12 hours in duration, occurring at BJD = 2456909.78 (or BJD - 2454833 = 2076.78, as shown in Fig. 7.2 for example). This burst is different in morphology from the typical flare signature, and could be due to discrete accretion onto the star, possibly a low level form of the events illustrated in Cody et al. (2017) for actively accreting stars observed in the same *K2* campaign. However, as noted above, the star lacks both spectroscopic accretion indicators and an infrared excess indicative of an inner disk. Notably, the end of the burst feature is characterized by two consecutive flare-like decays.

7.3.8 Light curve parameterization

We characterize the *K2* dimming events in terms of eight parameters: maximum depth, total duration, area (the time-integrated extinction), time variation between predicted and observed minimum light, the slopes of ingress and egress, and the durations of ingress and egress (see Table 2).

All parameters were determined from the flattened light curve, using variability fit A (Figure 7.2). No interpolation was performed within individual transits, and as such the maximum depth and time of minimum light were simply determined by the observation with the lowest flux. The total duration was determined by finding the last cadence before mid-transit, and the first cadence after mid-transit, to fluctuate above a median normalized flux of unity. The slope of ingress and egress are determined from the 6 hours preceding, and 3 hours proceeding the time of minimum light, respectively. Often the ingress clearly has multiple minima, which informed the decision to measure the slope for only a portion of ingress.

There is no observed correlation between the depths and durations of dimming events, as was observed for the dips ascribed to a transiting planet around the young star PTFO 8-8695 (Yu et al., 2015). For a single spherical body transiting the disk of a star, both the transit depth and duration depend on the size of the occulting body. Alternatively, if dust is partially contributing to the dimming events in RIK-210, the depths may change independently of the durations due to changing optical depths.

However, there is a correlation between the slope of egress and the timing variation, such that the later the time of minimum light occurs, the steeper the egress (Figure 7.7). The Spearman rank correlation coefficient is $r = 0.617$, with $p < 2\%$. The significance of this correlation increases ($r = 0.65$, $p < 1.2\%$) if variability fit B is used to flatten the light curve. From 10^5 bootstrapping simulations we estimate the correlation to be significant at the $\approx 2.2\sigma$ level, and estimate the true correlation coefficient r to be between 0.4–0.7 at 95% confidence assuming 0.25 hr uncertainties in the timing variations. We note that the correlation strengthens and becomes more significant depending on how the egress slope is measured, and the above estimates are somewhat conservative.

To investigate the significance of the timing variations, we measured the “transit” times using two methods: 1) Gaussian fits to the deepest component of each dip, considering data within 2.4 hours of the faintest cadence, using the Levenberg-Marquardt algorithm, and 2) selecting the cadence with the lowest flux value in each dip. We found that the timing variations with respect to a linear ephemeris agree (in

both magnitude and direction) in most cases to within 0.25 hours, regardless of the technique used to determine the individual “transit” times.

Notably, there is no correlation between the slope of ingress and the timing variation, nor is there one between the egress duration and the timing variation. Timing variations are most typically the result of gravitational interactions between multiple orbiting bodies. However, given the the asymmetries of the dimming events in RIK-210, it is also possible that the observing timing variations are due to the occulting body or bodies changing shape, e.g. variable extinction by a dust cloud. Such a scenario could displace the time of minimum light and mimic timing variations from gravitational interactions.

One possible explanation for the timing variation-egress slope correlation involves a collection of bodies which are gravitationally interacting. A massive body in a trailing orbit with respect to a less massive collection of bodies might pull the leading bodies back in their orbit, causing the configuration to become more spatially compact and delaying the transit time. The more compact the configuration, the less dispersion one expects in stellar disk-crossing times between component bodies and the steeper egress will be. An issue with this explanation is that one might also expect steeper ingress. However, given that some component of the occulting material may be dust, it is not evident whether the timing variations are tracing dynamical evolution or morphological evolution (i.e. due to a variable dust cloud).

It is interesting to note that depth (and apparently morphology) variations which correlate with stellar rotational phase have been observed in the transits of the disintegrating planet KIC 12557548b (Kawahara et al., 2013; Croll et al., 2015). Additionally, Croll et al. (2015) found morphological variations that correlated with the transit timing variations, such that late transits had shallower dips with a more gradual egress relative to the early or on-time transits. Both studies investigated the possibilities that the correlation between transit depth and rotational phase is due to (1) spot-crossing events by the cometary tail (which leads to anomalous brightening if the tail occults a starspot, thereby changing the transit morphology and inducing an apparent timing variation), or (2) periodically modulated mass-loss due to an active region on the star with enhanced X-ray and UV flux.

For RIK-210, the obscuring material, if in orbit about the star, has the same period as the stellar rotation. Thus, while RIK-210 is heavily spotted, spot-crossing anomalies are not a satisfactory answer for the transit variations, unless individual spots are rapidly evolving or different regions of the stellar disk are being occulted from one

transit to the next (perhaps as a result of an obscuring cloud that is evolving in shape or crossing different stellar latitudes as it transits the disk of the star).

Table 7.2: Parameters of the transient transit signature

Event	T_{\min} BJD	Depth (%)	Duration (hrs)	Area (% hrs)	Timing		Ingress slope (%/hr)	Egress slope (%/hr)	Ingress duration (hrs)	Egress duration (hrs)
					variation (hrs)					
1	2456896.1242	8.80	14.22	50.76	0.24	-0.85	2.73	10.79	3.43	
2	2456901.7838	10.89	14.22	56.16	0.03	-1.22	3.29	10.79	3.43	
3	2456907.4639	13.26	6.37	42.47	0.30	-2.38	4.70	3.43	2.94	
4	2456913.1440	14.78	18.14	76.21	0.57	-2.07	5.07	14.22	3.92	
5	2456918.7627	10.74	9.81	41.99	-0.62	-1.87	3.11	5.39	4.41	
6	2456924.4836	11.69	10.79	47.26	0.63	-2.08	4.04	6.37	4.41	
7	2456930.1432	10.46	7.36	32.63	0.41	-1.91	4.01	4.90	2.45	
8	2456935.8027	12.66	16.18	66.04	0.19	-1.72	4.21	12.26	3.92	
9	2456941.5032	12.73	12.26	63.32	0.95	-1.90	4.80	9.32	2.94	
10	2456947.1831	14.65	13.24	63.33	1.23	-2.86	4.67	9.81	3.43	
11	2456952.8427	14.40	12.75	83.37	1.01	-1.88	4.54	8.34	4.41	
12	2456958.4819	12.33	12.26	67.52	0.30	-2.06	3.78	8.34	3.92	
13	2456964.1414	18.44	11.28	88.17	0.08	-2.72	5.41	6.87	4.41	
14	2456969.7806	12.97	14.71	84.57	-0.63	-1.72	2.74	9.32	5.39	

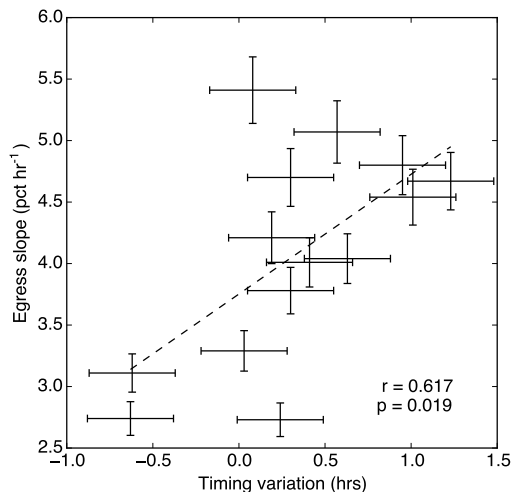


Figure 7.7: Correlation between the dimming timing variations and egress slopes. *Ad hoc* uncertainties of 0.25 hr in timing variation and fractional uncertainties of 10% in slope are assumed.

To qualitatively assess the similarity of individual dimming events to solid-body transits, we performed Levenberg-Marquardt fits to the observations using the JK-TEBOP light curve modeling code (Southworth, 2012, and references therein). All fits presented here assumed a linear limb-darkening coefficient of 0.6 for the primary star, allowing the following parameters to vary: time of mid-transit, inclination, ratio of radii, and the sum of the radii divided by the semi-major axis. These fits typically favor low inclinations ($\sim 81^\circ$), a ratio of radii of ≈ 0.48 , and a sum of fractional radii of ≈ 0.22 . However, these parameters are degenerate and the resulting values are not given significant weight in our interpretation of the data. We also note the size ratio and sum of fractional radii imply conflicting sizes of the occulter. Nevertheless, these models are useful for assessing the symmetry and underlying geometry of the occulting material.

The first dimming event is also the most shallow. Interestingly, by fitting the deepest component of the first dimming event (Figure 7.8), and subsequently fitting this model to the rest of the *K2* data (allowing only the ephemeris timebase, T_0 , and period to vary), we find that essentially all other observations fall *below* this model (Figure 7.9). One might interpret this observation as evidence for a primary occulting body surrounded by an evolving swarm of dust or debris. The residuals of this “minimum-obscuration fit” are quite often double-peaked (Figure 7.10), perhaps suggestive of multiple obscuring bodies or a single, clumpy occulter.

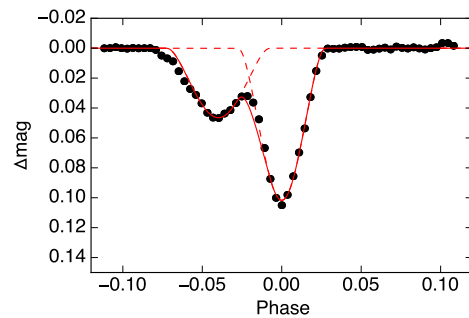


Figure 7.8: Composite of two independent JKTEBOP model fits to the two minima in the first dimming event of RIK-210 in the *K2* photometry. At least some of the individual transits observed by *K2* are reasonably well fit by one to three spherical occulting bodies with large size relative to the star. The fit to the deeper dip alone is referred to later as the “minimum obscuration fit.” Variability fit B was used to make this figure.

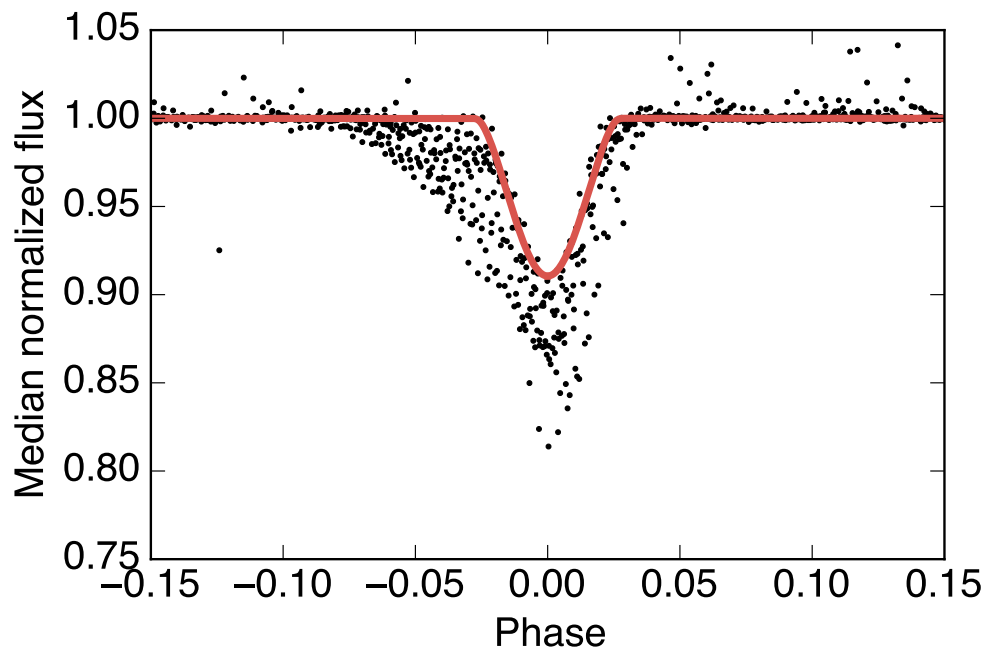


Figure 7.9: JKTEBOP model (red) overplotted on the flattened *K2* light curve of RIK-210 (black points). The model above was fit to the deepest component of the first dimming event in the *K2* campaign, then refit to the entire light curve allowing only the period and time of mid-transit to vary. Few observations lie above this fit, perhaps suggestive of an underlying, spherical occulting body surrounded by a stream of dust or swarm of planetesimals. Variability fit B was used to make this figure, though the conclusions drawn are independent of the fit used.

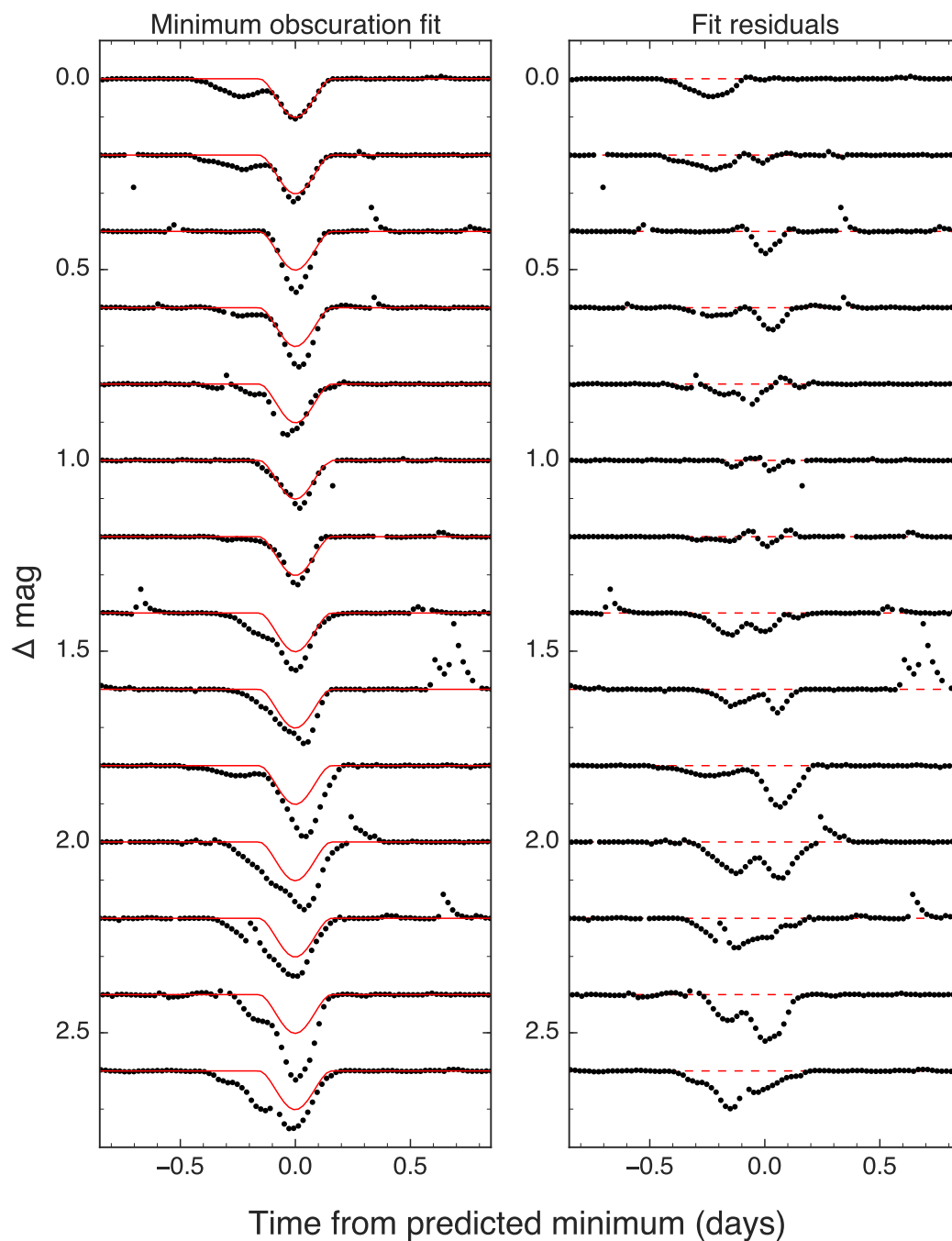


Figure 7.10: Evolution of the primary dips in the *K2* light curve of RIK-210. In both panels, the top row shows data from the first dip, proceeding consecutively downwards to the bottom row, which shows the last observed dip. *Left*: the “minimum obscuration fit,” obtained by fitting a model to the deepest component of the first dimming event, with respect to subsequent individual transits. *Right*: evolution of the residuals to the fits depicted on the left.

7.3.9 Short duration, shallow flux dips

In addition to the main dimming events of several to ~ 20 percent depth, shallower transit-like dips are also apparent in the *K2* light curve (Figures 7.2 and 7.6). In general, these dips are prominent in the beginning of the time series (when the primary dips are generally shallower), and apparently absent by the end of the campaign. These dimming events are typically ~ 5 hrs in duration, consistent with the expected transit duration for an orbiting body at the corotation radius.

In the beginning of the *K2* campaign, there is a grouping of at least four consecutive dips, which persists to some extent for the first four orbits/rotations (Figures 7.2 & 7.12). Over the next four orbits, the spacing between prominent dips appears to increase, somewhat suggestive of bodies that have departed from the original periodicity of ≈ 5.67 days. Finally, over the remainder of the campaign, the number of shallow dips appears to gradually decline. There is at least one dip present in each of the last six orbits/rotations. However, because this dip is not strictly periodic, it is not clear whether this feature is attributed to the same body, or multiple bodies at different semi-major axes. If the former case is true, then the time variations between transits (~ 0.6 d) would represent a fractional transit timing variation of unprecedented amplitude.

In at least one case, a transit of $\approx 0.7\%$ depth appears to recur with a period similar, but not equal to, the deep dimming events (Figure 7.11). Some of the shallow transits appear to have a characteristic *trailing* tail morphology, as opposed to the deep dimming events which possess a morphology reminiscent of a *leading* tail. As Rappaport et al. (2012) points out, in cases such as these the transit depth does not simply reflect the underlying planet size but also the size of a putative cloud of dust. Thus, the transit depth may be expressed as,

$$\delta \sim \left(\frac{f R_{\text{Hill}}}{R_*} \right)^2 \approx \left(\frac{f (M_P / 3M_*)^{1/3} a}{R_*} \right)^2, \quad (7.9)$$

where R_{Hill} is the planetary Hill radius, f is the fraction of the Hill radius that is optically thick, and M_P is the planet mass. Inverting the above equation, we can crudely approximate the planet masses required to create a 1% transit. Assuming $a=0.05$ AU, the planet masses required are: $2.6 M_{\text{Jup}}$ for $f = 0.1$, $6.5 M_{\oplus}$ for $f = 0.5$, or $1.6 M_{\oplus}$ for $f = 0.8$.

It is worth noting that the initial grouping of four or more dips are located near the light curve maximum and approximately 90 degrees out of phase with respect

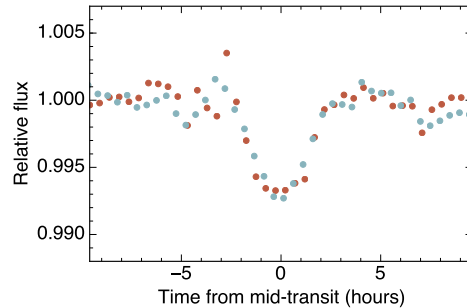


Figure 7.11: Example of shallow dimming events seen late in the *K2* campaign. Here we show two events (indicated by different colored points) separated by 5.888 days with consistent depth, duration, and morphology.

to the primary dimming events. By comparison, Trojans are concentrated around the L4 and L5 Lagrange points, 60 degrees ahead and behind the primary orbiting body, respectively. Trojan populations do have an azimuthal distribution, and some of Jupiter’s Trojans do in fact orbit 90 degrees ahead or behind the giant planet. However, we also note that a stable Trojan population would have the same period as the main occulter, and this does not seem to be the case for the shallow dips which do not exhibit strict periodicity.

In any event, the fact that these shallow dips are not strictly periodic suggests that they are not due to features on the surface of the star nor can they be due to material that is strictly co-rotating with the star or stellar magnetosphere. We posit that these shallow dips are likely related to the deeper dimming events, and speculate that they are due to transiting material in orbit about and nearly corotating with the star.

It is revealing to compare the behavior of these shallow dips to the dips observed around the white dwarf WD 1145+017 (Vanderburg et al., 2015). The current interpretation for that system is of a large asteroid transiting a white dwarf and orbiting near its Roche limit. As a result of tidal disruption, fragments break off from the asteroid, producing distinct flux dips in time series photometry which have been noted to “drift” in phase relative to the transits of the parent body (Rappaport et al., 2016).

7.4 Archival and follow up photometric monitoring

Given the variability in the depth, duration, morphology, and timing of the dimming events observed by *K2*, we sought auxiliary time series photometry to investigate changes over longer time baselines. There is no archival light curve for RIK-210 from HATSouth as that survey avoids crowded fields (G. Bakos, priv. comm.).

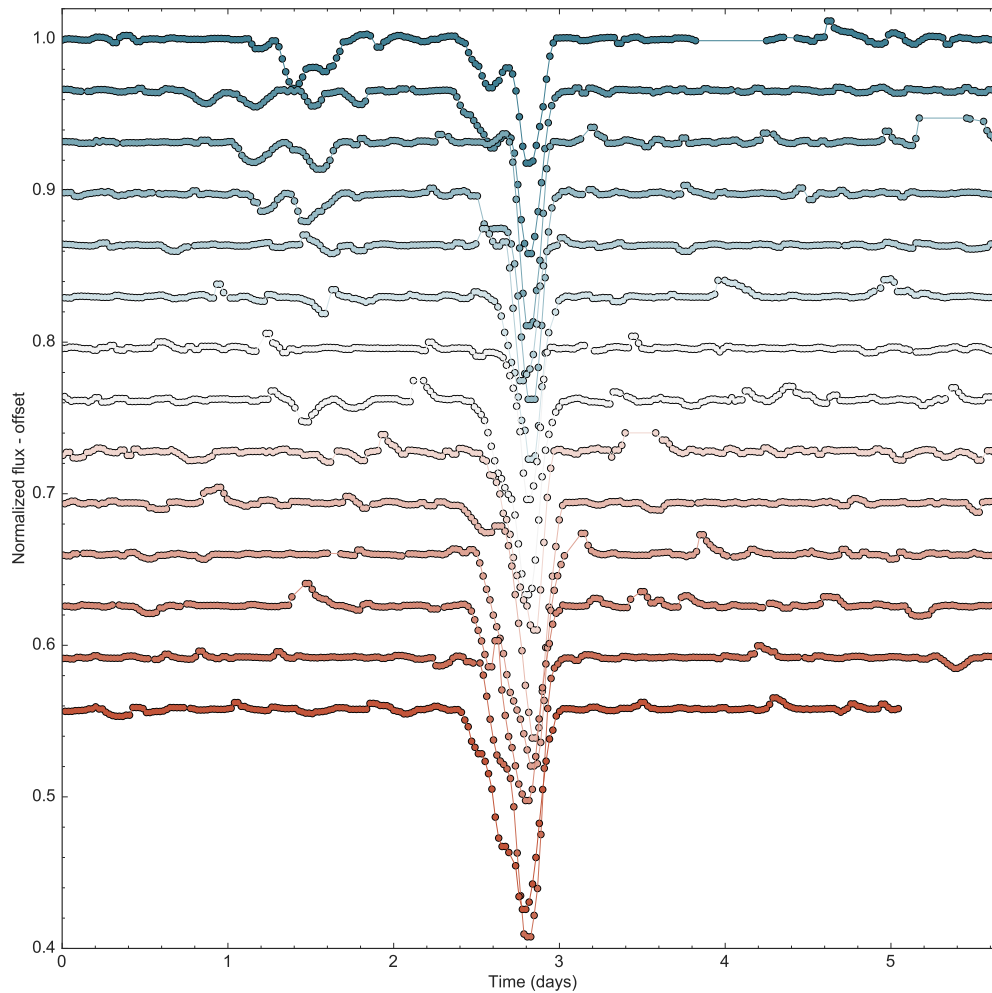


Figure 7.12: Flattened and median filtered *K2* light curve of RIK-210. The data are phase-wrapped on the dip period of 5.6685 days. A grouping of shallow dips preceding the main dip is prominent for the first four rotation periods of the campaign, then largely disappears. Variability fit B was used to make this figure.

Fortunately, there are more than 28,000 individual observations between 2006–2010 from SuperWASP-South (Figure 7.13), hereafter WASP (Pollacco et al., 2006).

A coherent Fourier transform of all the WASP data yields a high-significance peak with only a small first harmonic, indicative of sinusoidal behavior. The period favored by the WASP data is $P=5.6665 \pm 0.0012$ days, within 1.6σ of the period determined from the *K2* data (where σ here represents the uncertainties of the two periods summed in quadrature). Thus, WASP clearly detected the rotation period of the star, but there is mixed evidence regarding the presence of deep flux dips in prior years. A notable feature of the combined WASP light curve, presented in the left panel of Fig. 7.13, is a broad depression at phases earlier than the expected dip

phase from *K2*, seemingly suggestive that the dip was present in previous years but drifted in phase, narrowed, or both. Upon first glance of the annual WASP light curves (right panel of Fig. 7.13), there appear to be some statistically significant dips in previous years (e.g. near phase of 0.65 in 2008). However, further inspection of the WASP data reveals that most of the dip-like structures seen in prior years are the result of data acquired on only one or two nights in that year. The most complete phase coverage was achieved in both 2009 and 2010, but prominent dips are not readily apparent. We conclude that there is no strong evidence for dips in the 2006–2010 WASP data, and suggest the broad trough in the combined light curve may be the result of a spurious dip in 2006 and/or evolution of the spot pattern.

We also acquired follow up ground-based photometry of RIK-210 in the Bessel *V* and Sloan *i'* filters using the Las Cumbres Observatory Global Telescope network, hereafter LCOGT (Brown et al., 2013), between UT 2016-07-06 and 2016-08-10. Raw images were automatically processed using the LCOGT BANZAI pipeline, which performs bad pixel masking, bias and dark subtraction, flat field correction, and provides an astrometric solution. We performed differential photometry from the reduced images with AstroImageJ (Collins et al., 2017), using 2MASS J16234525-1722086 and 2MASS J16230556-1716209 as comparison stars. The color of RIK-210 in these bands is $V - i' = 1.77 \pm 0.17$ mag (uncorrected for reddening, from APASS DR9). This is a bluer color than expected given the M2.5 spectral type, and corresponds more closely to a K9 type photosphere. However, this color discrepancy is not apparent from the SED in Figure 7.1.

Conspicuously, observations from LCOGT at the predicted time of the dimming events (phase=0.5 in Figure 7.13) show that no such dimming events are observed, at least not at the ~ 0.2 mag level observed by *K2*. The absence of a transit or eclipse at the time predicted from a linear ephemeris based on the *K2* data is in tension with the explanation that the dimming events could be due to a solid body with any substantial size relative to the star. We note that because phase coverage is sparse around the predicted time of the dimming events, and due to the precision of our ground-based photometry, we can not rule out the possibility that dimming events of a few percent depth are still occurring.

The LCOGT photometry (Figure 7.13) confirmed the ephemeris of the stellar rotation has remained unchanged more than 2 years after the *K2* observations, though the amplitude of variability in both the *V* and *i'* bands is notably higher than that observed by *K2* (the Kepler bandpass corresponds roughly to the *V* and *R* filters).

Considering the WASP, *K2*, and LCOGT data together (Figure 7.13), the amplitude of variability due to spot modulation appears to have increased monotonically from 2006 to 2016.

The $V - i'$ color varies sinusoidally as a function of rotational phase, with the star becoming bluer when brighter and redder when fainter, as one expects from starspots. The color as a function of rotational phase is used to estimate the temperature contrast between the coolest and hottest hemispheres of the stars. The peak to trough amplitude is ≈ 0.2 mag, corresponding roughly to the $V - i$ color difference between a single spectral type class for M-type pre-main sequence stars (Pecaut & Mamajek, 2013). This corresponds to a temperature difference of ~ 100 – 200 K, which is consistent with spot temperature contrasts published for M-dwarfs of similar temperature (Andersen & Korhonen, 2015). The temperature ratio between the coolest and warmest hemispheres can also be estimated from the peak-to-trough amplitude of the *K2* light curve and the Stefan-Boltzmann law:

$$\frac{L_{\min}}{L_{\max}} = \left(\frac{T_{\min}}{T_{\max}} \right)^{1/4} \sim 0.8, \quad (7.10)$$

consistent with the temperature difference estimated from the $V - i'$ variability amplitude. We note for a given amplitude of photometric modulation, the spot temperature and size are degenerate parameters, but that the above considerations indicate the difference between the average hemisphere temperatures.

7.5 Spectroscopic Observations

We acquired multiple high-dispersion spectra of RIK-210 with Keck-I/HIRES (Vogt et al., 1994), covering either ~ 3600 – 8000 Å or 4800 – 9200 Å depending on the spectrograph settings. These spectra were used to perform a search for secondary lines due to a companion, measure the projected rotational velocity, and monitor variations in the radial velocity and line profiles of RIK-210.

7.5.1 Secondary line search

A search for secondary lines in the spectrum of RIK-210 was performed following the procedure of Kolbl et al. (2015). The method involves fitting template spectra of >600 FGKM stars (mostly dwarfs or subgiants) observed with Keck/HIRES to the continuum-normalized spectrum of RIK-210, then fitting the best-fit residuals to search for a putative secondary, taking possible Doppler shifts into account at both stages. We detected no companions brighter than 3% the brightness of the primary with radial velocity separations >30 km s $^{-1}$ from the primary. In the radial velocity

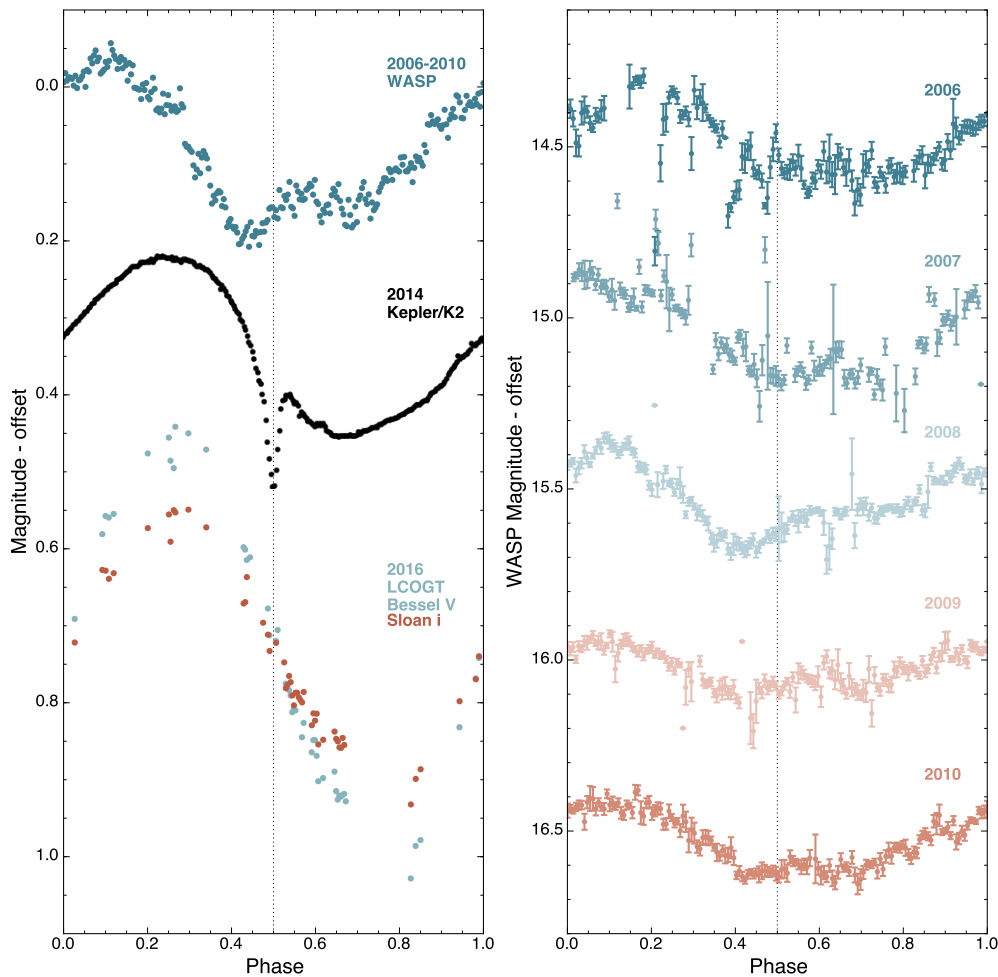


Figure 7.13: Left: Phase-binned and averaged light curves of RIK-210 at three epochs from WASP, *Kepler/K2*, and LCOGT (in both *V* and *i'* filters). Each light curve is phase-folded on the *K2* dip ephemeris. A broad depression in the WASP data between phases 0.3 and 0.5 is suggestive that the dip may have been present in previous years, but drifting in phase, becoming narrower, or both. However, inspection of the WASP data by year suggests this feature in the combined light curve may be due primarily to a combination of a questionable dip in 2006 and evolution of the spot pattern, most notable in the 2008 data. Right: WASP data ordered by year, phase-binned and averaged by weighting data points inversely to their photometric uncertainties. Data are offset vertically from the 2006 median value. Errorbars correspond to the standard deviation in a given phase bin. Only WASP data with photometric errors <0.4 mag were used. There are typically 2500–8000 measurements per year. Although there appear to be dimming events in prior years (e.g. at phases of 0.2 and 0.4 in 2006, phase 0.65 in 2008, or phase 0.45 in 2009), further inspection of the data indicate that many of the narrow structures above result from only one or two nights of observations.

separation range of 10–30 km s⁻¹ our detection limits are less robust, but we do not detect any companions brighter than 5% the brightness of RIK-210. The secondary line search is blind to companions with RV separations <10 km s⁻¹ from the primary. For reference, a velocity separation of 30 km s⁻¹ approximately corresponds to a 0.15M_⊙ companion at the corotation radius.

7.5.2 Projected rotational velocity

The projected rotational velocity was inferred from rotationally broadening the spectrum of GJ 408, an M2.5 dwarf with $v \sin i < 0.97$ km s⁻¹ (Maldonado et al., 2017), to match the spectrum of RIK-210 (Table 7.1). If the *K2* photometric modulation period is assumed to be the stellar rotation period and differential rotation is neglected, an expression for the stellar radius modulated by the sine of the inclination is given by:

$$R_* \sin i = \frac{P_{\text{rot}}}{2\pi} \times v \sin i. \quad (7.11)$$

From this equation we find $R_* \sin i = 1.23 \pm 0.12 R_{\odot}$, in excellent agreement with our radius determined from the Stefan-Boltzmann law, which suggests that the stellar spin axis is nearly perpendicular to our line-of-sight.

7.5.3 Radial velocities

Radial velocities (RVs) were determined via cross-correlation (CCF) with RV standard stars (Nidever et al., 2002) or by using the telluric A and B absorption bands as a wavelength reference (Table 3). For RVs measured via CCF, the mean velocity was determined from cross-correlation in 6 different HIRES orders using between 3–6 (depending on the epoch) M-type RV standards, with the quoted error corresponding to the standard deviation of these 18–36 measurements. Details of telluric-based RV measurements with HIRES, and their uncertainties, are described in Chubak et al. (2012). The quoted RV errors are several times the theoretical best performance for HIRES, which is expected based on the SNR of the data and the modest $v \sin i$ of the star.

We calculated the systemic RV, γ , from a weighted mean of all measurements (Table 7.1). RV variations of $\gtrsim 1.5$ km s⁻¹ were observed among the HIRES spectra (Figure 7.14), with variations of this amplitude observed on consecutive nights in some cases. We consider the possibilities that the RV variability is due to orbital motion of a companion, rotational modulation of starspots, or some combination of the two effects.

The number of measurements is not sufficient to detect a period via Lomb-Scargle periodogram analysis, but the data are used to constrain the masses of putative companions at a range of semi-major axes (Fig. 7.16). From a Fisher matrix analysis of the RVs, we determined a 2σ upper limit to the mass of a putative companion on a circular orbit at the corotation radius of $m \sin i \lesssim 7.6 M_{\text{Jup}}$.

The procedure for determining the upper limit to the mass of a putative companion is described in Boyajian et al. (2016) but we briefly summarize it here. Assuming a circular orbit, the RV measurements were folded on 4×10^5 trial orbital periods between 0.5 d and 3000 d and then fit with a sine and cosine term to represent the reflex motion and systemic RV. The Doppler semi-amplitude, K , and its 2σ uncertainty was determined for each trial period from the fit, then converted to a limit on $m \sin i$ assuming the stellar mass of RIK-210. The constraints are weakest at aliases of the observing cadence, which gives rise to the peaks in the mass limits presented in Fig. 7.16. More stringent mass constraints can be determined by imposing the time of mid-transit be a zero-crossing in the RVs, but given the ambiguous nature of the flux dips and the lack of photometric data concurrent with the spectroscopic observations we elected not to impose such a restriction.

In a separate analysis, we placed constraints on putative wide companions based on the maximum slope implied by the RVs. The RVs cover a period of ~ 100 days, and consequently allow for the detection of a long-term trend due to the gravitational influence of a distant companion. From 10^5 bootstrapping simulations, we determined a 3σ upper limit to the acceleration of RIK-210 of $\dot{\gamma} < 2.2 \text{ km s}^{-1} \text{ yr}^{-1}$. This limit rules out the presence of additional companions more massive than $0.43 M_{\odot}$ interior to 5 AU, or more massive than $0.15 M_{\odot}$ interior to 3 AU. Of course, these limits do not apply interior to ~ 1 AU, where the orbital period of a putative companion is more than 25% the baseline of our measurements. These limits are somewhat more stringent than those implied by the Fisher matrix analysis in the relevant orbital period range.

Spot-induced RV modulations of $\gtrsim 1 \text{ km s}^{-1}$ have previously been observed in weak-lined T Tauri stars, or WTTS (Prato et al., 2008; Huerta et al., 2008; Mahmud et al., 2011). The effect of rotation and spots on RVs is somewhat analogous to the Rossiter-McLaughlin effect, with the important caveats that spots are luminous and can cover a significant fraction of the star. As the most heavily spotted hemisphere rotates into view we receive more flux from the receding hemisphere and we should observe a net redshift. Conversely, as the most spotted hemisphere rotates out of

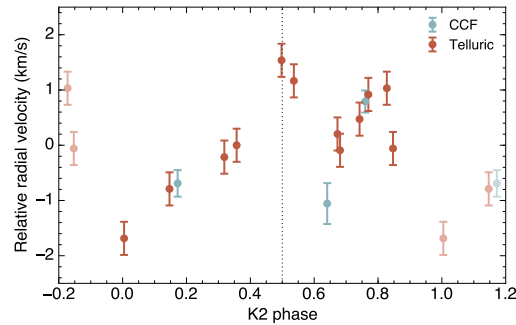


Figure 7.14: Median-subtracted radial velocities for RIK-210 phased on the period of the *K2* light curve. The dotted line indicates the approximate location of the deep dimming events present in *K2* photometry, but absent in ground-based follow-up acquired closer to the time of spectroscopic observations. For illustrative purposes we show redundant phases with lighter shaded points.

view, we should observe a net blueshift. Given the highly spotted nature of RIK-210¹, it is highly likely that the dominant component of the observed RV variability is spot-induced. When phased to the rotation period, however, the RVs appear to deviate slightly from the smooth, semi-sinusoidal variation expected from spots (see e.g. Huerta et al., 2008; Mahmud et al., 2011).

In principle, RV variability from rotation of a spotted star can interfere either constructively or destructively with the reflex motion due to a putative companion at the corotation radius, since both signals would have the same period, a scenario mentioned by van Eyken et al. (2012).

To assess whether the observed RV variability is due to stellar activity or orbital motion, we searched for wavelength-dependent RV trends. RV variations due to surface features on a star are chromatic, inducing apparent Doppler shifts only at wavelengths where the features are optically thick. Doppler shifts due to orbital motion, however, are achromatic. By performing wavelength-restricted cross correlations over 31 orders in the HIRES spectra we find a maximum slope in the RVs as a function of wavelength of $\pm 5 \times 10^{-6} \text{ km s}^{-1} \text{ \AA}^{-1}$. We note that $v \sin i$ is only moderately larger than the spectral resolution of our observations, and so detecting apparent Doppler shifts due to line profile asymmetries is difficult (e.g. Desort et al., 2007).

Aigrain et al. (2012) developed a novel technique (the FF' method) for calculating

¹Spot filling factors in late type stars of up to 50% have been inferred from high-resolution spectroscopy of molecular bands (O’Neal et al., 1998; O’Neal et al., 2004) and in the case of the young weak-line T Tauri star LkCa 4 $\sim 80\%$ (Gully-Santiago et al. 2016, submitted).

the expected radial velocity variability due to stellar surface features from a broad-band light curve alone. We explored modeling the expected RV variability based on the phase-averaged *K2* light curve, confirming in principle that stellar RV variability can mask or enhance the Doppler signal of a body at the corotation radius. We constructed model RV phase curves based on a high-order polynomial fit to the phased *K2* photometry with the flux dips removed, and subsequently fit these models to the RVs allowing the fractional spot coverage to vary. We did not find a good fit, but the χ^2_{\min} model implies a spot covering fraction of $\approx 30\%$. We note, however, that an additional free parameter in the FF' models is the baseline stellar flux level in the absence of spots. This parameter is essentially unknown, but we fixed it to be the maximum of the *K2* light curve.

To avoid overinterpreting the results of the FF' RV modeling, we do not present it in any more detail here and question its utility in this specific instance given (1) the uncertainty in the spot-covering fraction, (2) the lack of simultaneous photometry during the RV acquisition period, (3) the apparent change in spot modulation amplitude from follow-up photometry, and (4) the underlying requirement in the FF' method that the spot-to-photosphere contrast ratio is not close to one, which may not be true for RIK-210.

Ultimately, we conclude that spots induce most but possibly not all of the observed RV variability. While the RVs do exhibit very little scatter when phased to the rotation/orbital period, they are not well fit by either a semi-sinusoidal model (i.e. a sine curve plus harmonics) as one might expect from spots or a Keplerian model. More complete phase coverage is needed to adequately model the RVs, and simultaneous photometric monitoring will greatly help in determining the contribution of spots to the RV variability.

7.5.4 Line profile variations

The chromospheric emission spectrum of RIK-210 is manifest at $H\alpha$ (exhibiting a classic double-horn profile), $H\beta$, He I 5876Å, Na I D, the Ca II H&K doublet and the triplet, and Fe I 5169 Å which are seen at all spectral epochs. All lines are variable in strength over the time series, with the exception of the Ca II triplet which remains constant. At the epoch of strongest emission, Mg Ib triplet and Fe I 5018 Å are also observed.

For the $H\alpha$ line, the measured line strengths range from $W_\alpha = -3.5$ to -6.5 Å. A Gaussian fit results in a $1-\sigma$ line width of 50 km s^{-1} , while the full width at 10% of

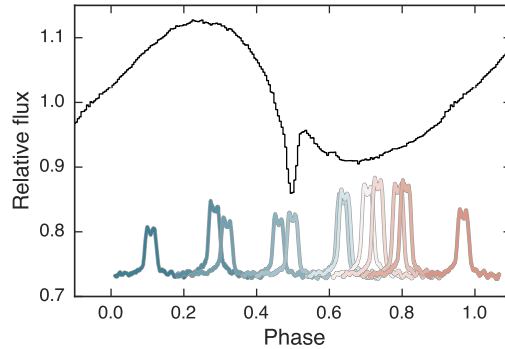


Figure 7.15: Variations of the $H\alpha$ profile (colored curves) as a function of rotational phase, from the Keck-I/HIRES spectra. The black line represents the phase-averaged *K2* light curve. We emphasize that follow-up photometry, acquired around the same time as the spectra, did not show the $\sim 20\%$ dimming at phase = 0.5 observed by *K2*.

peak flux is 120 km s^{-1} . There is a clear trend between the $H\alpha$ equivalent width and rotational phase, such that stronger $H\alpha$ emission is measured when the fractional spot coverage is highest which occurs at the rotational phases where the sinusoidal component of the *K2* lightcurve is faintest (Fig. 7.15). Despite the significant change in line strength, there is no change over phase in the violet-to-red symmetry.

The level of activity in RIK-210 is stronger than the typical M2.5 field dwarf (e.g. Gizis et al., 2002). It is also higher than generally observed for the well-studied active star AD Leo ($W_{H\alpha} = -2.7$ to -4.0 \AA), which was characterized as a high pressure chromosphere by Short & Doyle (1998) based on detailed radiative transfer modelling of various line species. These activity comparisons are as expected given the youth of the star.

7.6 High-resolution Imaging

Speckle imaging observations of RIK-210 were acquired at Gemini South Observatory with the DSSI instrument (P.I. Steve Howell). The speckle observations revealed no companions with $\Delta m \lesssim 4 \text{ mag}$ at separations between $0.1\text{--}1.37''$. Beyond $0.5''$, we obtained more stringent contrast limits of $\Delta m \lesssim 4.8 \text{ mag}$ at 692 nm , or $\Delta m \lesssim 5.4 \text{ mag}$ at 880 nm .

We also obtained near-IR adaptive optics (AO) imaging for RIK-210 on UT 2016 Jul 17 using NIRC2 (P.I. Keith Matthews) with the Keck II Natural Guide Star (NGS) AO system (Wizinowich et al., 2000). We used the narrow camera setting with a plate scale of $10 \text{ mas pixel}^{-1}$. This setting provides a fine spatial sampling of the instrument point spread function. The observing conditions were good with seeing

Table 7.3: Keck-I/HIRES radial velocities of RIK-210

UT Date	JD	RV km s ⁻¹	σ_{RV} km s ⁻¹	Method	Phase
2016-05-12	2457520.930	-4.31	0.30	telluric	0.7357
2016-05-12	2457521.086	-3.86	0.30	telluric	0.7632
2016-05-17	2457526.023	-5.84	0.37	CCF	0.6343
2016-05-20	2457529.035	-5.47	0.24	CCF	0.1656
2016-06-15	2457555.037	-3.99	0.20	CCF	0.7531
2016-07-10	2457579.899	-5.57	0.30	telluric	0.1395
2016-07-13	2457582.927	-4.87	0.30	telluric	0.6738
2016-07-28	2457597.875	-5.00	0.30	telluric	0.3110
2016-07-29	2457598.891	-3.24	0.30	telluric	0.4903
2016-07-30	2457599.884	-4.58	0.30	telluric	0.6655
2016-07-31	2457600.870	-4.84	0.30	telluric	0.8394
2016-08-17	2457617.763	-3.75	0.30	telluric	0.8198
2016-08-18	2457618.766	-6.47	0.30	telluric	0.9968
2016-08-20	2457620.764	-4.78	0.30	telluric	0.3493
2016-08-21	2457621.780	-3.62	0.30	telluric	0.5286

of $0''.5$. RIK-210 was observed at an airmass of 1.29. We used the K_S filter to acquire images with a 3-point dither method. At each dither position, we took an exposure of 0.25 second per coadd and 10 coadds. The total on-source integration time was 7.5 sec.

The raw NIRC2 data were processed using standard techniques to replace bad pixels, flat-field, subtract thermal background, align and co-add frames. We did not find any nearby companions or background sources at the $5\text{-}\sigma$ level. We calculated the $5\text{-}\sigma$ detection limit following Wang et al. (2014). We defined a series of concentric annuli centered on the star. For the concentric annuli, we calculated the median and the standard deviation of flux for pixels within these annuli. We used the value of five times the standard deviation above the median as the $5\text{-}\sigma$ detection limit. The $5\text{-}\sigma$ detection limits are 2.1 mag, 3.6 mag, 5.4 mag, and 5.9 mag for $0''.1$, $0''.2$, $0''.5$, and $1''.0$, respectively.

We combined our high-resolution imaging constraints with the constraints from the secondary spectral line search and lack of a significant RV trend to place limits on putative companions to RIK-210. The combined constraints are depicted in

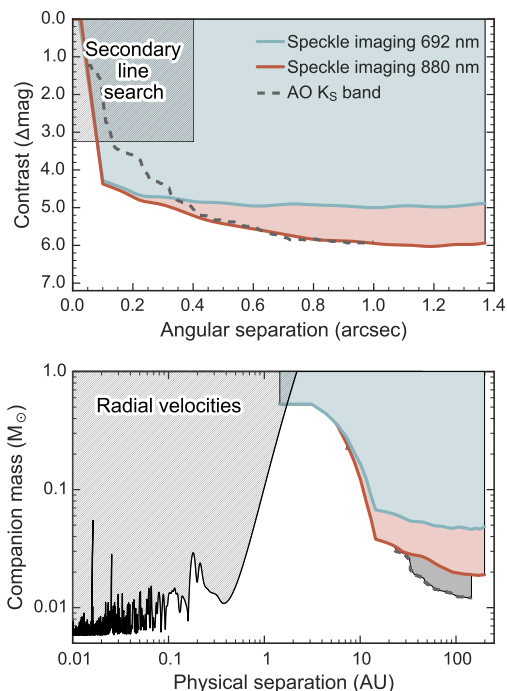


Figure 7.16: Constraints on the brightness (top panel) or mass (lower panel) of putative companions to RIK-210 from optical speckle imaging (blue and red regions), NIRC2 adaptive optics imaging (grey dashed line in top panel, grey region in bottom panel), a HIRES secondary spectral line search, and the RV time series.

Figure 7.16. To convert imaging constraints from Δ mag to companion mass we used the pre-main sequence evolutionary models of Baraffe et al. (2015), using the tabulated R and I magnitudes as proxies for the 692 nm and 880 nm speckle imaging constraints, respectively. In particular, the I band constraints rule out companions down to 20–25 M_{Jup} between 60–200 AU, and 25–40 M_{Jup} between 15–60 AU.

7.7 Discussion

Here we discuss possible explanations for the K2 light curve of RIK-210, in light of its previous and subsequent evolution as observed with WASP and LCOGT, and the spectroscopic monitoring undertaken with Keck-I/HIRES. We consider three general classes of explanations: rotational modulation of stellar surface features, co-rotating circumstellar gas and dust, and phenomena associated with a young, planetary system. In Table 4 we present a broad overview of the most developed theories.

Table 7.4: Proposed explanations for the transient transits of RIK-210

Scenario	Supporting evidence	Conflicting evidence	Plausibility
eclipsing binary or transiting brown dwarf	deep, V-shaped dimmings	inconsistent with RVs, archival/follow-up photometry	ruled out
high-latitude star spot	synchronicity between rotation and dip periods, spotted star	inter-rotation variations and combination of deep depths with short durations	highly unlikely
high-latitude accretion hot spot	synchronicity between rotation and dip periods, modest photometric burst	lack of spectroscopic accretion indicators or IR excess associated with inner disk	highly unlikely
eclipses of prominences	synchronicity between rotation and dip periods, magnetically active star	depths are too deep	highly unlikely
transits of magnetospheric clouds	synchronicity between rotation and dip periods, magnetically active star	does not readily explain the shallow, short-duration flux dips	most likely
dipper	synchronicity between rotation and dip periods, depths and variable morphologies of dimming events	lack of spectroscopic accretion indicators or IR excess associated with inner disk	highly unlikely
transits of an enshrouded protoplanet	RV variability difficult to explain with spots alone	requires extended dusty tail or swarm of satellites to explain long durations, in tension with archival/follow-up photometry, synchronicity between rotation and dip periods not a requirement	somewhat plausible
tidal disruption of planetary or cometary material	variable depths, durations, and morphologies of dimming events, may explain shallow, short-duration dips that appear to drift in phase	does not readily explain synchronicity between rotation and dip periods, requires high eccentricities and/or very low densities of orbiting bodies	somewhat plausible

7.7.1 Rotational modulation of high-latitude spots?

Given the youth of RIK-210 and the large amplitude semi-sinusoidal variability, it is evident that the star is heavily spotted. As the dimming events are essentially in phase with the rotation period of the star, we consider the possibility that the events are due to a spot pattern on the stellar surface. The main difficulties facing a spot-based explanation are that the dimming events are both deep and brief relative to the rotation period. Variability due to any feature on the stellar photosphere typically endures for half of the rotation period, while the dimming events in RIK-210 are always $<15\%$ of the rotational phase.

In principle, a surface feature can rotate into view for less than half of the rotation period if the feature is confined to high latitudes and the stellar rotation axis is tilted modestly away from an equator-on orientation. Thus, a cool spot near the poles, if the rotation axis is tilted slightly away from the observer, could produce a dimming event that endures for less than half the rotation period. Indeed, the existence of polar spots on young, rapidly rotating stars has both theoretical (e.g. Schuessler & Solanki, 1992; Granzer et al., 2000; Yadav et al., 2015) and observational support (e.g. Hatzes, 1995). However, in this scenario it is still difficult to produce sudden or “angular” flux dips because spots are subjected to limb darkening and foreshortening.

The *K2* observations seem to be in tension with a starspot explanation, given how rapidly the depth, duration, and general morphology changes from epoch to epoch. Meanwhile, the globally averaged spot distribution appears to remain stable throughout the *K2* campaign and in fact the follow-up LCOGT photometry confirms the ephemeris and general morphology of the disk-averaged spot pattern more than two years later. Moreover, spots or spot groups on T Tauri stars have measured lifetimes of years or even decades (e.g. Herbst et al., 1994; Bradshaw & Hartigan, 2014).

The maximum depth of the dimming events is $\approx 18\%$. The depth of a dimming event due to starspots is determined by both the opacity and size of the spot(s) at the observed wavelength. The minimum spot size required to produce a given flux decrement is set by the limiting case of a completely opaque spot. In this scenario, the spot size is approximated in the same manner as the size of a transiting planet. Namely, $R_{\text{spot}}/R_* = \sqrt{\delta}$, where δ is the depth of the dimming event. The deepest dimming events observed in RIK-210 would require a *minimum* spot or spot group size of $\sim 0.4R_*$ or $\sim 0.5R_\odot$. This minimum size is so large that it likely could not be confined to the restricted range of latitudes required to get dimming events so brief relative to the rotation period. Furthermore, spots are not opaque and the observed

contrasts around M-type stars correspond to temperature differences of only a few hundred Kelvin (Andersen & Korhonen, 2015).

To have a spot or spot group of sufficient size, contrast, and latitude to produce dimming events of 5 – 15% for only ~ 15% of the star’s rotational phase presents a fine-tuning problem, and is perhaps physically impossible. We conclude that, despite being synchronized with the stellar rotation, the dimming events observed by *K2* are unlikely to be related to spot behavior on the star.

7.7.2 Eclipses of an accretion hotspot?

Although there is no evidence for ongoing accretion analogous to that of classical T Tauri stars, given its youth, RIK-210 could still be experiencing residual gas infall from gaseous and dusty debris in an only recently dispersed circumstellar disk. A star undergoing accretion may develop a hotspot on its surface, as infalling material is deposited onto the star. If the material falls in along magnetic field lines, it should be deposited near one of the magnetic poles. If a star has an accretion hotspot on its surface, the disk averaged brightness will decrease when the hotspot rotates out of view (see e.g. Romanova et al., 2004). Moreover, the magnetic poles need not be coincident with the rotational poles. As such, even a star with its rotational axis aligned perpendicular to the observer’s line-of-sight could host an extended hotspot that is in view for more than half of the rotational phase. This scenario is analogous to the cool starspot scenario, and was considered as a possible explanation for the dimming events seen in PTFO 8-8695 (Yu et al., 2015).

Following the methodology of those authors, one can estimate the mass accretion rate from the depth of flux decrements:

$$L_{\text{acc}} = \frac{GM_*\dot{M}}{R_*} \sim \delta L_{\text{bol}}, \quad (7.12)$$

where \dot{M} is the mass accretion rate and δ is the depth of dimming events. For dimming events of ~9–18% and the derived stellar parameters in Table 7.1, the scenario above would require mass accretion rates of $\dot{M} \sim 1\text{--}3 \times 10^{-9} M_{\odot} \text{ yr}^{-1}$. Despite the modest burst (with flare-like decays) observed in the *K2* light curve, we consider this scenario unlikely as the star lacks both spectroscopic accretion indicators (the enhanced hydrogen emission observed from the spectra is consistent with chromospheric emission) and the infrared excess that would be associated with an inner disk.

7.7.3 Eclipses of prominences?

Some rapidly rotating stars may be surrounded by dense clouds of partially ionized gas (so-called slingshot prominences) at a distance of several stellar radii and co-rotating with the stellar magnetosphere. These clouds may have projected areas as large as 20% of the stellar disk (Collier Cameron & Robinson, 1989a; Collier Cameron & Robinson, 1989b; Collier Cameron et al., 1990). While such clouds have been observed from absorption in the Balmer and Ca II H & K lines, there is no appreciable continuum absorption. Thus, transits of such clouds are not thought capable of producing the deep dips observed in RIK-210. However, if a large prominence contributes significant optical flux relative to the star via Paschen-continuum bound-free emission, it may be possible to produce broadband optical dimmings of a few percent when such a prominence passes *behind* the star. Nevertheless, the dip depths observed in RIK-210 are significantly deeper than a few percent. We conclude that eclipses of slingshot prominences can not produce the 20% dimmings observed in the *Kepler* bandpass.

7.7.4 Transits of magnetospheric clouds?

Transits by circumstellar, magnetospheric clouds have been suggested as a source of photometric variability for high-mass stars (Groote & Hunger, 1982). In particular, the magnetic Be star σ Ori E shows clear, $\sim 5\%$ eclipses twice per rotation period; these eclipses have been attributed to clouds of plasma which are trapped in the magnetosphere and most dense at the corotation radius (Townsend et al., 2013). The phenomenon of a narrow flux dip in phase with, and superposed on, semi-sinusoidal modulation has also been observed in the X-ray light curve of the accreting white dwarf PQ Gem (Mason, 1997; Evans et al., 2006). In that case, the authors attribute the dip to matter from an accretion disk being lifted up out of the plane and into the line-of-sight by the leading edge of the magnetic field lines.

Fully-convective, low-mass pre-main sequence stars have magnetic field strengths typically in the 0.1–1 kG range (e.g. Johns-Krull, 2007; Donati & Landstreet, 2009). Charged material in orbit about the star may become trapped in the magnetosphere at the corotation radius, where closed field lines thread the orbital plane. Magnetized stars may also accrete matter from a circumstellar disk via so-called funnel flows (e.g. Romanova et al., 2002). Such accretion columns, if they contain dust and transit the disk of the star, could lead to optical extinction. Indeed, this idea underpins some explanations for the dipper phenomenon discussed below.

Whether the magnetically entrained material is a cloud of plasma analogous to those observed in high-mass stars, or a dusty accretion column, this model could naturally explain the synchronicity between the rotation period and the dimming events, as the field lines, and thus flows, thread the equatorial plane at corotation. Since the accretion timescale is expected to be of order the free-fall timescale, i.e. much shorter than the orbital period, this model might explain the variable depths and morphologies of dimming events.

The most challenging observation to the accretion column scenario is that RIK-210 lacks spectroscopic accretion indicators. Perhaps we are witnessing the low-level, end state of accretion for a post T Tauri star. Calculations below show that only a modest amount of dust is needed to produce the deep dimming events observed with *K2*. The dust would have to be charged, or coupled to plasma, in order to be dragged by the field lines. The source of such dust close to the star remains a mystery. Moreover, the transient nature of the dimming events would seem to suggest that the dust must be episodically replenished. The modest amount of dust remaining in the system at AU scales may spiral in via P-R drag, but if it is charged one might expect it to be captured by the magnetosphere and subjected to an outward magnetocentrifugal force prior to reaching the inner magnetospheric regions. Regardless of the actual source of the dust, if this model is correct, it reveals a previously unappreciated aspect of the early environments of close-in exoplanets.

We consider this theory quite plausible for the variability observed in RIK-210, however several unanswered questions remain: in the absence of a tilt between the rotation and magnetic axes, how does the cloud remain so compact as to produce dips that are so narrow in rotational phase? How does one explain the inter-rotation variability in morphology, depth, and duration? Perhaps most importantly, the magnetospheric model struggles to explain the short-duration and shallow dips, or at least implies that accretion of the material is clumpy rather than smooth.

7.7.5 Obscuration by a circumstellar disk?

Variable obscuration due to a circumstellar disk has long been an explanation for the photometric variability of some T Tauri stars. For example, UX Ori is the prototype of what Herbst et al., 1994 described as Class III variability within early type T Tauri stars. At lower stellar masses, AA Tau is the archetype for similar variability, which has been attributed to a warped inner disk edge interacting with the stellar magnetosphere (Bouvier et al., 2003, and references therein).

Multi-wavelength observations of this phenomenon in Orion support this hypothesis, showing that the dimming events are deeper in the optical and shallower in the infrared, as one would expect from extinction by dust (Morales-Calderón et al., 2011). The advent of high cadence, precision photometry using space telescopes has revealed an unprecedented level of detail to this general class of variable young stars now called “dippers” (Cody et al., 2014; Stauffer et al., 2015; Ansdell et al., 2016).

In some cases where the stellar rotation is evident, such as the case of Mon 21, the dimming events have been observed to be synchronized with the stellar rotation period (Stauffer et al., 2015). The coincidence between stellar rotation and the orbital period of transiting debris in this model is a natural consequence of disk-locking, where the inner disk edge is truncated near the corotation radius due to interactions with the stellar magnetosphere.

Dippers also exhibit variable depths, but often so variable that the dimming events disappear entirely (EPIC 204137184 is one such quasi-periodic example in Upper Sco). Ansdell et al., 2016 classified the main morphological types of dimming events seen in Upper Sco dippers as: symmetric, trailing tail, and complex. While some of the dimming events in RIK-210 might be classified as symmetric or complex, noticeably absent in that list is the leading tail morphological class, which seems most appropriate for RIK-210.

While some dippers show strong spectroscopic accretion signatures from shocked gas falling onto the star, many exhibit only weak accretion indicators such as those observed in RIK-210. However, within Upper Sco, dipper stars typically have infrared excesses consistent with a protoplanetary disk extending in to $\sim 10 R_*$ (Ansdell et al., 2016). By contrast, RIK-210 has no evidence of an inner disk, yet the obscuring material, if in orbit, rests at a distance of $\sim 9 R_*$. The essential differences between RIK-210 and young dipper stars are that the dimming events in RIK-210 are more constant in depth and shorter in duration, while RIK-210 also lacks evidence for an inner disk.

For the reasons discussed above, it is extremely unlikely that RIK-210 belongs to the class of young dipper stars. However, as we can not completely exclude this scenario, we note that if RIK-210 is indeed a dipper then it would be the first such object with (1) no inner disk, (2) a light curve dominated by rotational modulation of starspots rather than by dimming events, and (3) a relatively high degree of both periodicity and morphological consistency between dimming events.

7.7.6 A co-rotating dust component?

In addition to gas phenomena, dust in the vicinity of the stellar co-rotation radius could be responsible for the narrow dips in RIK-210. Dimming events over $\sim 15\%$ of the rotational phase could be explained by an extended structure of dust obscuring the star and scattering starlight away from the line-of-sight. If this is the case, the existence of such a significant amount of dust close to the star must be explained. For example, the dust could be primordial in origin (i.e. remnants of the late stages of planet formation), the product of a recent major collision, or from sublimation of volatile-rich bodies.

By equating the stellar luminosity with the luminosity of a dust disk extending out to the corotation radius², the temperature of dust at the corotation radius is estimated by,

$$T_{\text{corot}} = 0.34 T_{\text{eff}} \left(\frac{P}{1 \text{ day}} \right)^{-1/3} \left(\frac{R_*}{R_\odot} \right)^{1/2} \left(\frac{M_*}{M_\odot} \right)^{-1/6}. \quad (7.13)$$

Using the Kobayashi et al., 2011 sublimation temperatures for various grain compositions, we inverted the above equation to find the minimum orbital period at which dust of a given composition could exist in the solid phase (Fig. 7.17). The transiting debris around RIK-210 is safely outside the dust sublimation radius for olivine, pyroxene, obsidian, and pure carbon, though it is close to the sublimation radius for pure iron. Note that this analysis assumes a circular orbit.

Dust in orbit about the star will be subjected to radiation pressure and Poynting-Robertson (P-R) drag. The minimum size of dust grains that can survive on circumplanetary orbits is set by the balance of these forces (Burns et al., 1979; Kennedy & Wyatt, 2011).

From Lecavelier Des Etangs et al. (1999), the ratio of radiation pressure to the gravitational force is given by,

$$\beta = 0.2 \left(\frac{L_*/L_\odot}{M_*/M_\odot} \right) \left(\frac{s}{1 \mu\text{m}} \right)^{-1}, \quad (7.14)$$

where s is the grain size. For RIK-210, equilibrium between gravity and radiation pressure is established for grain sizes of $0.075 \mu\text{m}$. For smaller grains, radiation pressure dominates, and for larger grains, gravity dominates.

²We note this equation neglects scattering, self-shielding, or heating by accretion. See Bodman et al. (2016) for details.

From Burns et al. (1979), the timescale for a dust grain to spiral in to the star via P-R drag is,

$$t_{\text{PR}}(r) = \frac{cr^2}{4GM_*\beta}. \quad (7.15)$$

For the parameters of RIK-210, the P-R drag timescale is approximately 2.5 years for $0.1 \mu\text{m}$ grains or 25 years for $1.0 \mu\text{m}$ grains. Thus, if the *K2* extinction events were due to dust grains of $0.1 \mu\text{m}$ in size or smaller, it is plausible that the majority of this dust has since spiraled into the star and thus explain why no such dimming events were detected with follow-up photometry.

One can calculate to first order the mass of dust, M_{dust} , from the maximum depth of a dimming event. From Lecavelier Des Etangs et al. (1999), the maximum extinction due to a cloud of grains is given by,

$$\left(\frac{F_{\text{ext}}}{F_*}\right)_{\text{max}} = \exp\left(-\frac{6M_{\text{dust}} \int s^2 dn(s)}{4\pi\rho R_*^2 \int s^3 dn(s)}\right), \quad (7.16)$$

where s is the grain size, $dn(s)$ is an analytic grain size distribution, and ρ is the dust density. For the grain size distribution adopted by Lecavelier Des Etangs et al. (1999) and a grain density of 3 g cc^{-1} , we find that $\sim 10^{-9} M_{\oplus}$ could extinct RIK-210 by 20%.

Optical attenuation by a transiting dust cloud is primarily the result of scattering of light away from the line-of-sight, rather than absorption. Consequently, at particular orbital phases, a dust cloud may forward scatter starlight into the line-of-sight and contribute observable excess flux to the light curve (Rappaport et al., 2012). For RIK-210, we do not see obvious evidence for forward scattering. However, it is difficult to draw conclusions because such evidence critically depends on how well the stellar continuum level is fit. For example, transits 8 and 10 appear to show modest post-egress flux excesses evocative of forward scattering (see Fig. 7.4), though these features may also be a result of improper continuum fitting. For disintegrating *Kepler* planets on ultra-short-period orbits, the effect of forward scattering is miniscule but statistically significant because of the sheer number of transits over a much longer time baseline.

If there is a significant amount of dust close to the star, the dust will be heated by the star and re-radiate in the near-IR. In § 7.2.2 we showed that RIK-210 lacks

warm dust, but there is marginal evidence for cool dust at AU scales. Thus, if corotating dust is responsible for the dimming events, it must be scarce enough to avoid producing a detectable near-IR excess. We estimated the dust-to-star flux ratio at $24\ \mu\text{m}$, where a putative excess would be most easily be detected, using the following equation:

$$\frac{F_{24,\text{dust}}}{F_{24,*}} = \frac{A_{\text{dust}}}{A_*} \frac{T_{\text{dust}}}{T_*}, \quad (7.17)$$

where A_{dust} is the total cross section of dust grains in the obscuring region and T_{dust} is the dust equilibrium temperature at corotation, here taken to be $\approx 830\ \text{K}$. The implied excess depends on the number of dust grains and their typical geometric cross section. The number of grains, in turn, is highly sensitive to the assumed geometrical distribution. The total cross section of dust is estimated by $A_{\text{dust}} = \langle \tau \rangle A_{\text{geom}} = N(\pi s^2)$, where $\langle \tau \rangle \approx 0.15$ is the average optical depth, A_{geom} is the geometrical area of the dusty region, N is the number of grains, and s is the typical grain size. For $0.1\ \text{mm}$ -sized grains, the implied $24\ \mu\text{m}$ dust-to-star flux ratio is ~ 0.3 assuming the dust is distributed over a thin cylinder centered around the star with radius equal to the corotation radius and height twice the radius of the star. However, assuming the same dust properties, the flux ratio could be doubled if the dust were spread out into an annulus at the corotation radius, or an order of magnitude lower if the dust were arranged in a thin strip as one might expect from an accretion column. Thus, given the uncertainties in dust properties and the geometric distribution of dust in the system, it is difficult to know whether the proposed amount of dust would have been detected in the near-IR. However, we argue there are many plausible geometries and dust properties for which such an excess would have evaded detection.

Dust provides a convenient explanation for the dimming events in that (1) only a modest amount is required to produce deep dimming events, and (2) it can be evacuated somewhat rapidly depending on its size and composition. However, as mentioned at the beginning of the section, the source of such dust must still be explained, given that the star apparently lacks an inner disk. One possibility is a giant impact-type collision between oligarchs.

Some theories predict that collisions between oligarchs on closely packed orbits are a common occurrence in the late stages of planet formation. For example, Chiang & Laughlin (2013) showed that newly-formed, close-in super-Earths lack the energy to scatter each other out of the parent star's gravity well, so planet-planet scattering

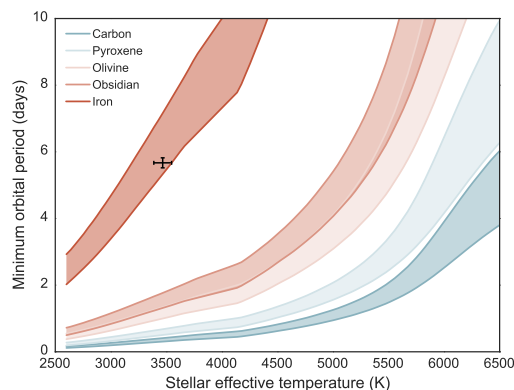


Figure 7.17: Minimum orbital period for grains of varying compositions to exist in the solid phase, as a function of the central star’s effective temperature. Dust sublimation temperatures are taken from Kobayashi et al. (2011), and the stellar parameters needed to calculate the corresponding orbital periods are obtained from the PARSEC v1.2s pre-main sequence models (Bressan et al., 2012; Chen et al., 2014). For each grain composition, the upper and lower boundaries of the shaded regions are set by the 5 and 10 Myr isochrones, respectively. The position of RIK-210 is shown by the black point. Dust grains with compositions ranging from carbon to obsidian could exist in the solid phase at the corotation radius, while iron grains may sublimate.

events instead lead to mergers. Perhaps the dimming events observed in *K2* are the result of a recent collision between two or more protoplanets, which could release a profuse amount of planetary debris. Depending on the energy of the collision, some fraction of material might escape the gravity of the protoplanets, while the remaining material is retained within the combined Hill spheres of the protoplanets. We note that scenarios invoking a collision may be inherently unlikely based on timescale considerations.

Another possible source for dust is a comet or family of comets. The idea of “falling evaporating bodies” has been studied extensively, particularly in the context of the young star β Pic, which exhibits spectroscopic peculiarities ascribed to evaporating exocomets (e.g. Kiefer et al., 2014, and references therein). As we established, the required mass to create such deep dimming events is quite modest, comparable to the mass of Hale-Bopp. What could bring cometary material onto such a short period orbit around the star? One prediction of disk-driven migration is that a migrating planet will trap planetesimals (or comets) in mean motion resonance, allowing them to reach stargazing orbits (Quillen & Holman, 2000; Thébault & Beust, 2001).

7.7.7 Boil-off of a protoplanet atmosphere?

Owen & Wu (2016) predicted that a highly inflated protoplanet newly exposed to vacuum conditions after the confining pressure of the protoplanetary disk has gone will experience profuse atmospheric mass loss via a Parker wind. This mass loss is catalyzed by stellar continuum radiation, as opposed to the EUV/X-ray-driven photoevaporative mass loss that becomes important at later stages. Those authors suggest extraordinary mass loss rates of $\sim 0.01 M_{\oplus} \text{ yr}^{-1}$ may be possible over characteristic timescales of $O(10^3 \text{ yr})$. Clearly, this scenario presents a fine-tuning problem as it requires our observations to be coincident with this relatively short-lived phase of a planet's evolution.

7.7.8 Tidal disruption of a planet?

The leading tail morphology of the RIK-210 dimming events is somewhat suggestive of an orbiting body experiencing Roche lobe overflow. For a body in a circular orbit, the minimum period allowed before tidal disruption is given by equation 2 from Rappaport et al. (2013):

$$P_{\min} \simeq 12.6 \text{ hr} \left(\frac{\rho_p}{1 \text{ g cm}^{-3}} \right)^{-1/2}. \quad (7.18)$$

For typical planetary densities observed in the solar system ($\sim 0.5\text{--}5 \text{ g cc}^{-1}$), this minimum period is on the order of hours, i.e. much shorter than the period of dimming events around RIK-210. In fact, for a body to undergo tidal disruption in a circular orbit of period 5.67 days would require a density of $\lesssim 0.01 \text{ g cc}^{-1}$. This is an order of magnitude lower than the least dense bodies in our solar system, including comets. Planets are presumed to be less dense at young ages, as they are still undergoing Kelvin-Helmholtz contraction, but models of e.g. Jovian-mass planets at an age of 5–10 Myr still predict densities that are $\sim 0.5 \text{ g cc}^{-1}$ (Baraffe et al., 2003; Spiegel & Burrows, 2012).

However, it is possible that a body or collection of bodies are in an eccentric orbit, with a close pericenter passage to the star. In this scenario, the body or bodies undergo periodic tidal disruption upon each crossing of the Roche radius, analogous to the disruption of comets in the solar system. The pericenter distance for an orbit of semi-major axis a and eccentricity e is given by,

$$a_{\text{peri}} = a(1 - e). \quad (7.19)$$

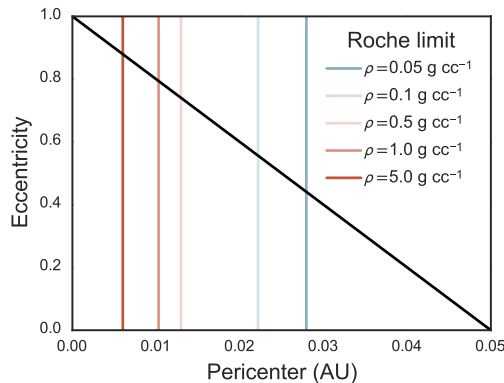


Figure 7.18: Pericenter separation for a range of eccentricities assuming a semi-major axis of 0.05 AU (black line). The colored lines reflect the limiting Roche radius for bodies of varying densities. Eccentricities greater than 0.4 would be required to bring a body interior to its Roche limit for any of the densities plotted here.

The Roche limit for a self-gravitating, incompressible fluid satellite is given by,

$$a_{\text{Roche}} \approx 2.44R_* \left(\frac{\rho_*}{\rho_s} \right)^{1/3}, \quad (7.20)$$

where R_* and ρ_* are the radius and density of the star, respectively, and ρ_s is the density of the satellite.

By setting the Roche limit equal to pericenter, we can estimate the minimum eccentricity needed to bring a planet of a given density interior to its Roche limit (Fig. 7.18). For planet densities $>0.1 \text{ g cc}^{-1}$, an eccentricity $\gtrsim 0.6$ is required. We note that planets that are *both* massive and highly eccentric are seemingly disfavored by the RV measurements which do not exhibit a cusp or variability above the 2 km s^{-1} level.

An appealing aspect of this scenario is that it might naturally explain the changing morphology between consecutive dimming events, as the orbiting body or bodies are disrupted upon each pericenter passage. It might also explain the apparent vanishing of dimming events in follow-up photometry. Complete disruption of a body or bodies could result in a ring of material around the star which would then be subject to radiation pressure and P-R drag. Nevertheless, we consider this scenario unlikely given the high eccentricities and/or low satellite densities required.

7.7.9 Transits of an enshrouded protoplanet?

Any planetary explanation for the dimming events faces the challenge of accounting for the depths of the events. The loss of light during a transit or eclipse depends

on both the size ratio and brightness ratio of the occulting body to the central star. However, the secondary line search and radial velocity time series suggest it is quite unlikely that RIK-210 hosts a companion massive enough to contribute significantly to the total flux received from the system. Furthermore, we find no evidence of secondary eclipses within the *K2* photometry.

The facts that the dimming events are deep and longer than the expected transit duration for a point mass suggest an occulting body (or collection of bodies) that is large relative to the star. On the other hand, the fact that the events are V-shaped, as opposed to flat-bottomed, suggests that if the occulting body is completely opaque, it cannot have *both* an impact parameter close to zero and a size larger than the star itself, else it would produce a total eclipse. Of course, an enshrouded protoplanet need not necessarily fill its Hill sphere (Kennedy & Wyatt, 2011), nor would the material filling such a volume be completely opaque.

The Hill radius is approximately given by,

$$r_{\text{Hill}} \approx a(1 - e) \left(\frac{m_p}{M_*} \right)^{1/3}, \quad (7.21)$$

where a is the semi-major axis, e is the eccentricity, and m_p/M_* is the mass ratio between the planet and star. If a planet were enshrouded in a dusty envelope, the Hill radius sets the maximum extent of that envelope.

For planets in the mass range of $1 M_{\oplus}$ – $10 M_{\text{Jup}}$ orbiting at the corotation radius of RIK-210, the Hill radius is in the range of 0.2 – $2.8 R_{\odot}$. We calculated the transit durations of objects in this size range by inverting eqn. 8. We find transit durations of 5.8 – 16.6 hrs, for an inclination of $i = 90^\circ$ and impact parameter of $b = 0$. Of course, if the enshrouded planet were at the high end of the mass regime above, the Hill radius would be larger than the star itself, and the orientation considered above would result in a total eclipse of the star if the sphere were totally opaque.

A challenge presented to this scenario is accounting for both the depths and durations simultaneously. The maximum durations observed are so long as to require an object with a size larger than the star itself. For example, the Hill radius of a $10M_{\text{Jup}}$ planet is approximately $2.8R_{\odot}$. If transiting the equator of the stellar disk such an object could lead to the maximum observed dimming duration of approximately 16 hours.

In Figure 7.19 we show the expected transit depths and durations of an optically thick Hill sphere in orbit at the corotation radius of RIK-210. Points on the curve

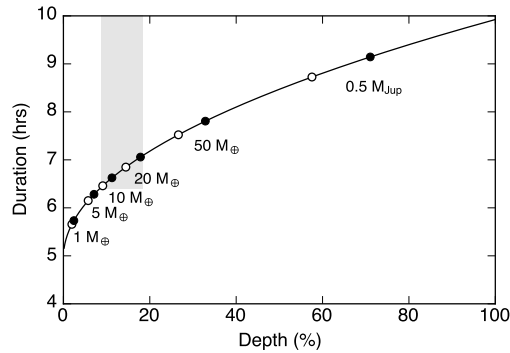


Figure 7.19: Expected depths and durations for equatorial transits of RIK-210 by an optically thick Hill sphere for planets of various masses. Fiducial masses are plotted as black points and annotated with text. However, the planet mass and fraction of the Hill sphere that is optically thick is completely degenerate in this plane. Thus, we show the effect of how these fiducial planet masses move along this curve when only 90% of the Hill sphere is optically thick (open circles). The grey shaded region indicates the range of depths and durations observed in the *K2* light curve.

are degenerate in the parameters of planet mass and the fraction of the Hill sphere that is optically thick. Still, the figure is useful for determining a lower limit to the mass of a hypothetical transiting protoplanet in the scenario described above. In the limit of a completely opaque Hill sphere, a planet mass above $\sim 10 M_{\oplus}$ is required. At high planet masses, a meaningful limit can not be placed since the fraction of the Hill sphere filled with optically thick material can be arbitrarily low. We note that if material were escaping a putative protoplanet, it could of course occupy a larger volume than the Hill sphere and thus lower planet masses may be plausible. In any event, this model can not explain the long durations of the dimming events. An extended tail of optically thick material could be invoked to reconcile this matter.

In this scenario, one must still explain the existence of such a dusty envelope, and also the changing morphologies between transits. If an enshrouded planet is surrounded by a highly non-uniform distribution of dusty material or satellites, perhaps gravitational interactions between the planet and clumps or satellites are reconfiguring the spatial distribution of the bodies on timescales shorter than its orbit.

There is now a wealth of literature on circumplanetary swarms of dust and debris. Current research on this topic is mainly theoretical or the result of numerical simulations and much of it is motivated by the directly imaged planet Fomalhaut b, which is apparently visible in the optical but not the infrared due to scattering by a proposed cloud of dust surrounding the planet (Kalas et al., 2008). Kennedy & Wyatt

(2011) predicted that circumplanetary swarms of irregular satellites may be common around young exoplanets, and proposed this as an explanation for Fomalhaut b. Nesvorný et al. (2007) studied the capture of irregular satellites by Jovian planets migrating within a planetesimal disk, finding many hundreds of such satellites could be captured early in the planet formation process. Additionally, the directly imaged protoplanet LkCa15 b (Kraus & Ireland, 2012; Thalmann et al., 2016) appears to exhibit a tail-like structure, though we note that star is much younger and the protoplanet resides on a much wider orbit.

Finally, we note that the Darwin instability (Darwin, 1879) is a concern for corotational orbits. This occurs when the rotational angular momentum of the primary exceeds one third the orbital angular momentum of the secondary, ultimately leading to spiral-in over the tidal decay timescale. We find for RIK-210 that bodies above a few Earth masses are Darwin stable in a corotational orbit.

7.7.10 Significance of the corotation radius

Conspicuously, the dimming events observed in RIK-210 are essentially synchronous with the stellar rotation. Above, we discussed why it is extremely unlikely that these dimming events could be due to anything on the stellar surface from empirical considerations. Here we provide context, in the form of recent observational and theoretical work, for why planets or planetary material might be *expected* to be found near the corotation radius around stars with ages approximately equal to the disk dispersal time ($\lesssim 10$ Myr). At these ages, the stellar rotation period reasonably tracks the expected location of the inner disk edge. At older ages, the star first spins up as it contracts on to the main sequence (bringing the corotation radius inwards), then spins down as it evolves on and away from the main sequence (causing the corotation radius to be moved outwards).

In a protoplanetary disk, a low-density magnetospheric gap extends from the stellar surface to the inner disk edge. Theoretical investigations and numerical simulations of accretion disks around magnetized stars find the inner disk edge is truncated at the Alfvén radius, where the magnetic energy density in the disk is equivalent to the kinetic energy density. In practice, for T Tauri stars, the Alfvén radius is approximately 20-30% interior to the corotation radius (Long et al., 2005).

Romanova & Lovelace (2006) found the effect of the magnetospheric gap is to greatly reduce the rate of planetary migration through disk interactions. Papaloizou (2007) also studied the orbital evolution of a planet that has migrated through the

disk into the magnetospheric cavity, finding that protoplanet interactions with the stellar magnetosphere should not result in significant orbital evolution after entering the gap. There is also observational support for truncation of the disk at corotation. Meng et al. (2016) recently reported the first measurement of the inner edge of a protoplanetary disk using photo-reverberation mapping. Those authors found a value for the disk edge that is consistent with expectations for the corotation radius.

Of the confirmed or candidate exoplanets around T Tauri stars discovered to date, all are on orbits near the presumed corotation radius. David et al., 2016c pointed out that K2-33 b orbiting slightly interior to the corotation radius, with $P_{\text{orb}}/P_{\text{rot}} \approx 0.86$. The period of the candidate transiting planet around the T Tauri star PTFO 8-8695, also known as CVSO 30, is essentially equivalent to the stellar rotation period (van Eyken et al., 2012; Ciardi et al., 2015; Johns-Krull et al., 2016b). Johns-Krull et al. (2016b) found a period ratio of $P_{\text{orb}}/P_{\text{rot}} \approx 1.23$ for the candidate $\sim 11\text{--}12 M_{\text{Jup}}$ planet around the T Tauri star CI Tau. Lastly, the planet V830 Tau b has a period ratio of $P_{\text{orb}}/P_{\text{rot}} \approx 1.8$ (Donati et al., 2016).

7.7.11 Uniqueness of RIK-210

Inspection of more than 1400 *K2* light curves of secure or likely members of Upper Sco has revealed twelve sources with persistent or transient, short-duration flux dips that in some cases are apparently in phase with the stellar rotation (Stauffer et al. 2017, submitted). It is possible that RIK-210 may belong to this newly discovered class of stars, but we emphasize that RIK-210 is an outlier from these stars in nearly every regard. Namely, it has the longest rotation period by more than a factor of two, it is two spectral classes earlier in type than any of the other mentioned stars, and it has by far the deepest and most variable dimming events. Furthermore, none of the above-mentioned stars have demonstrated shallow, short-duration flux dips that are seemingly out of phase, or drifting in phase with respect to the stellar rotation.

Nevertheless, the physical scenarios explored in this work, and their presumed likelihoods, apply equally well to the population of variables identified in (Stauffer et al. 2017, submitted). Namely, those stars also lack primordial protoplanetary disks or spectroscopic accretion indicators. Those authors conclude the most likely culprits for the variability is material trapped in the magnetosphere or collisional debris.

7.8 Conclusions

We present evidence for transiting gas, dust, or debris around the 5–10 Myr old star RIK-210. Speculative sources of the obscuring material could be a magnetospheric cloud, an accretion flow from residual (yet undetected) gas and dust, remnants of the late stages of planet formation, the product of a giant-impact type collision, an enshrouded protoplanet with an extended tail, or one or more eccentric bodies undergoing periodic tidal disruption upon each periastron passage.

The most important aspect of the dimming events, which must be explained by any successful theory, is that they appear in phase with the stellar rotation. Theories invoking material tied to magnetic field lines at the corotation radius may explain this behavior, but do not readily account for the sub-percent dimmings seen elsewhere in the light curve that are not in phase with the stellar rotation.

The dimming events are variable in depth, duration, and morphology. The depths, while deep ($\sim 5\text{--}20\%$), can be produced by only a modest amount of dust. The durations are long ($\sim 6\text{--}18$ hours), though the minimum duration is only somewhat longer than the expected transit duration at the corotation radius. Nevertheless, the lengthy durations imply a large size for the transiting cloud relative to the star. It is also possible that the occulting material is distributed in a torus which is tilted with respect to our line-of-sight, thereby producing dimmings only when a vertically extended part of the torus crosses the star.

Curiously, archival time series photometry from WASP provide no clear evidence for dimming events in the past. While some $\sim 0.1\text{--}0.2$ mag dimmings are present in previous years they are not at a consistent phase and they are often the result of only one to two nights of data in a given year. We can not conclusively ascribe these dimmings to the same events observed by *K2*. Furthermore, follow-up photometry from LCOGT indicates the dimming events are no longer occurring at the level and phase expected from *K2*. However, our phase coverage in follow-up photometry is rather incomplete. Nevertheless, it is clear the transit signatures are transient in nature.

Follow-up radial velocity monitoring, a secondary spectral line search, and high-resolution imaging place stringent limits on the presence of any putative companions. RIK-210 is an apparently single star, and the upper limit of a companion orbiting at the corotation radius is $\sim 8 M_{\text{Jup}}$. We note RV variability at the level of $\sim 2 \text{ km s}^{-1}$, the dominant component of which is likely induced by starspots. When phased to the *K2* ephemeris, the RVs show small point-to-point scatter in phase but do not exhibit

the sinusoidal variation expected for spot-induced variability. It is possible that orbital motion due to one or more companions may contribute to the RV variability.

RIK-210 is diskless, as implied by its SED and a lack of spectroscopic accretion indicators. A modest amount of dust may remain at AU scales, from a weak $22\ \mu\text{m}$ excess. Close inspection of spectral line profiles reveal a chromospherically active star. No spectroscopic peculiarities are observed at the predicted phase of the dimming events, or elsewhere, though it is not clear the dimming events were still occurring at the time of our spectroscopic observations.

Continued photometric monitoring is needed to ascertain whether the dimmings observed by *K2* have changed depth. High precision photometry is necessary in order to also detect the small, $\lesssim 1\%$ dips. These small dips may hold the clue to the correct physical interpretation of the larger-scale variability. We advocate for continuous or semi-continuous photometric monitoring, not just at the predicted phase of the primary dip.

If the dimming events reappear, or evaded our detection in follow-up photometry, a number of experiments may be conducted to clarify their physical origin. Observations of the Rossiter-McLaughlin effect would conclusively determine whether the flux decrements in RIK-210 are due to material in orbit around the star. For the depths observed by *K2* (though now presumed to be shallower or entirely absent) the expected R-M amplitude is on the order of $1\ \text{km s}^{-1}$. Multi-band photometric monitoring can be used to test whether the dip depths are wavelength-dependent; solid-body transits are achromatic, while extinction by dust is less severe at redder wavelengths. Finally, spectroscopic monitoring while the star is known to be dimming can test whether there is enhanced absorption by a gaseous cloud transiting the star.

ACKNOWLEDGMENTS

The authors thank Todd Boroson for allocation of LCOGT director's discretionary time and Nikolaus Volgenau for assistance scheduling observations. We thank the anonymous referee for a thorough review, Saul Rappaport for helpful comments on an early draft and for providing the Fisher matrix analysis of the RVs, Jim Fuller for bringing σ Ori E to our attention, Eugene Chiang, Konstantin Batygin, Kat Deck, Brad Hansen, and Lee Hartmann for helpful discussions, as well as Norio Narita and John Livingston for attempting follow-up observations. T.J.D. is supported by an NSF Graduate Research Fellowship under Grant DGE1144469. E.A.P. is supported through a Hubble Fellowship. A.M.C.'s research was supported by an appointment to the NASA Postdoctoral Program at the NASA Ames Research Center, administered by Universities Space Research Association under contract with NASA. B.J.F. was supported by the National Science Foundation Graduate Research Fellowship under grant No. 2014184874. Any opinion, findings, and conclusions or recommendations expressed in this material are those of the authors and do not necessarily reflect the views of the National Science Foundation. This paper includes data collected by the *Kepler/K2* mission, funded by the NASA Science Mission directorate and obtained from the Mikulski Archive for Space Telescopes (MAST), supported by the NASA Office of Space Science via grant NNX09AF08G. Some of the data presented herein were obtained at the W.M. Keck Observatory, which is operated as a scientific partnership among the California Institute of Technology, the University of California and the National Aeronautics and Space Administration. The Observatory was made possible by the generous financial support of the W.M. Keck Foundation. The authors wish to recognize and acknowledge the very significant cultural role and reverence that the summit of Mauna Kea has always had within the indigenous Hawaiian community. We are most fortunate to have the opportunity to conduct observations from this mountain.

*Chapter 8***A NEPTUNE-SIZED TRANSITING PLANET CLOSELY
ORBITING A 5-10-MILLION-YEAR-OLD STAR**

David, T. J., Hillenbrand, L. A., Petigura, E. A., et al., 2016, *Nature*, 534, 658

ABSTRACT

Theories of the formation and early evolution of planetary systems postulate that planets are born in circumstellar disks, and undergo radial migration during and after dissipation of the dust and gas disk from which they formed (Kuiper, 1951; Kley & Nelson, 2012). The precise ages of meteorites indicate that planetesimals – the building blocks of planets – are produced within the first million years of a star’s life (Connelly et al., 2012). Fully formed planets are frequently detected on short orbital periods around mature stars. Some theories suggest that the *in situ* formation of planets close to their host stars is unlikely and that the existence of such planets is therefore evidence of large-scale migration (Lin et al., 1996; Rafikov, 2006). Other theories posit that planet assembly at small orbital separations may be common (Hansen & Murray, 2012; Chatterjee & Tan, 2014; Boley et al., 2016). Here we report a newly born, transiting planet orbiting its star with a period of 5.4 days. The planet is 50 per cent larger than Neptune, and its mass is less than 3.6 times that of Jupiter (at 99.7 per cent confidence), with a true mass likely to be similar to that of Neptune. The star is 5–10 million years old and has a tenuous dust disk extending outward from about twice the Earth–Sun separation, in addition to the fully formed planet located at less than one-twentieth of the Earth–Sun separation.

The star [PGZ2001] J161014.7-191909, hereafter K2-33, is an M-type star several million years (Myr) old that was observed by NASA's *Kepler Space Telescope* during campaign 2 of the *K2* mission. The star was identified as one of more than 200 candidate planet hosts in a systematic search for transits in *K2* data (Vanderburg et al., 2016). As part of our ongoing study of the pre-main-sequence population of Upper Scorpius observed by *K2* we independently verified and analysed the planetary transit signal. We acquired radial velocity and high spatial resolution observations at the W. M. Keck Observatory to confirm the detection of the planet, named K2-33 b, and to measure its size and mass.

Within the 77.5-day photometric time series of K2-33 ($K_p = 14.3$ mag), there are periodic dimmings of 0.23% lasting 4.2 h and occurring every 5.4 days (Fig. 1). The ensemble of transits are detected at a combined signal-to-noise ratio of about 32. During the *K2* observations, cool, dark regions on the stellar surface (starspots) rotated in and out of view, producing semi-sinusoidal brightness variations of $\sim 3\%$ peak-to-trough amplitude with a periodicity of 6.3 ± 0.2 days (Extended Data Fig. 1). We removed the starspot variability before modelling the transit events. We fitted the transit profiles using established methods (Crossfield et al., 2015), measuring the planet's size relative to its host star and its orbital geometry (Table 1).

K2-33 is a member of the Upper Scorpius OB association (Preibisch et al., 2001; Preibisch et al., 2002), the nearest site of recent massive star formation (at a distance of 145 ± 20 pc). Approximately 20% of low mass stars in Upper Scorpius host protoplanetary disks (Luhman & Mamajek, 2012), indicating that planet formation is ongoing in the region but in an advanced stage or completed for the majority of stars. The age of the stellar association is 5–10 million years (Myr), as assessed from kinematic, Hertzsprung-Russell (H-R) diagram, and eclipsing binary analyses. The youth of K2-33 itself is based on the spectroscopic indicators of enhanced hydrogen emission and lithium absorption (Preibisch et al., 2001; Preibisch et al., 2002), which we confirm from Keck spectra (Table 1). Furthermore, the stellar rotation rate we measure via broadening of absorption lines in the spectra and via the starspot period (Table 1), is rapid relative to field-age stars of similar mass (McQuillan et al., 2013). We determined the star's systemic radial velocity (Table 1) as consistent with the mean value for Upper Scorpius members (Kurosawa et al., 2006). Previously, proper motions were used to assess the probability of membership in the association at 99.9% (Bouy & Martín, 2009). Finally, the positions of the star in the Hertzsprung-Russell and temperature-density diagrams (Extended Data Fig. 2) are consistent

with the sequence of low mass members of Upper Scorpius (Preibisch et al., 2002). The inferred planet size and mass depend directly upon the host star size and mass. We evaluated the effective temperature and luminosity from our newly determined spectral type (Table 1), extinction-corrected catalogue near-infrared photometry, and empirical pre-main sequence calibrations (Herczeg & Hillenbrand, 2015; Pecauc & Mamajek, 2013). With the temperature and luminosity, we derive a stellar radius from the Stefan-Boltzmann law of $R_* = (1.1 \pm 0.1) R_\odot$, where R_\odot is the radius of the Sun. The radius uncertainty is calculated accounting for recommended errors in temperature (Herczeg & Hillenbrand, 2015), photometric errors, and assuming an association depth comparable to its width on the sky. Combining the stellar radius with the planet-to-star radius ratio determined from the *K2* light curve fit, we infer a planetary radius for the companion $R_P = (5.8 \pm 0.6) R_\oplus$, or about 50% larger than Neptune.

We estimate a stellar mass of $M_* = (0.31 \pm 0.05) M_\odot$ by interpolation among pre-main sequence stellar evolution models (Baraffe et al., 2015), consistent with a previously reported value (Kraus & Hillenbrand, 2007). The mass uncertainty assumes normal error distributions in temperature and luminosity. As there is no evidence for radial velocity variations among four high-dispersion Keck spectra (Extended Data Table 1), the planet mass is constrained from the maximum-amplitude Keplerian curve that is consistent within the errors with all radial velocity measurements (Extended Data Fig. 3). Given the transit ephemeris and assuming a circular, edge-on orbit, the expected stellar reflex velocity is a sinusoid having a single free parameter: the semi-amplitude. Radial velocity semi-amplitudes of $> 900 \text{ m s}^{-1}$ are ruled out at 99.7% confidence, corresponding to a 3σ upper limit on the mass of K2-33 b of $3.6 M_{\text{Jup}}$.

The true mass of K2-33 b is likely to be at least an order of magnitude smaller. There are seven known exoplanets of similar size ($R_P = 4.8\text{--}6.6 R_\oplus$) with densities measured to 50% or better. These planets have masses ranging from $(6.3 \pm 0.8) M_\oplus$ (Kepler-87c) to $(69 \pm 11) M_\oplus$ (CoRoT-8b) owing to varying core masses. Thus, plausible masses of K2-33 b range from about $6 M_\oplus$ to $70 M_\oplus$, corresponding to radial velocity semi-amplitudes of $5\text{--}56 \text{ m s}^{-1}$. An even lower mass may be implied if the young planet is still undergoing Kelvin-Helmholtz radial contraction.

A semi-major axis of 0.04 AU ($\sim 8 R_*$) is measured for K2-33 from the orbital period and Kepler's third law, adopting the value of M_* in Table 1. The orbit is near the silicate dust sublimation radius, as well as the co-rotation radius, where

some protoplanetary disk theories predict a magnetospheric cavity extending to the stellar surface (Armitage, 2011). At this separation, the blackbody equilibrium temperature of the planet is 850 K.

We have interpreted the observed transit as a single planet orbiting K2-33. Other interpretations involving eclipsing stellar binaries residing within the *K2* aperture (Extended Data Fig. 4) would be diluted by the light of K2-33 and could potentially mimic the observed transit. Such a putative eclipsing stellar binary could be associated with (that is, gravitationally bound to) K2-33, or unassociated but aligned by chance. Given constraints from our suite of follow-up observations, we show that the chance of an eclipsing stellar binary producing the observed transit is vanishingly small.

We first consider unassociated eclipsing stellar binaries, which we characterize by their sky-projected separation from K2-33 and their brightness relative to K2-33 in the *Kepler* bandpass, ΔKp . Eclipse depths may not exceed 100%; thus eclipsing stellar binaries with $\Delta Kp > 6.6$ mag cannot account for the 0.23% observed transit depth. We do not detect closely-projected companions in seeing-limited and multi-epoch adaptive optics images (Extended Data Fig. 5), nor in searches for secondary lines in high-resolution optical spectra. These observational constraints, shown in Fig. 2a, eliminate nearly all scenarios involving unassociated eclipsing stellar binaries. The probability of an eclipsing stellar binary lurking in the remaining parameter space is $\ll 4 \times 10^{-6}$ (see Methods).

We now consider associated eclipsing stellar binaries in terms of their physical distance to K2-33, d , and ΔKp . As in the case of unassociated EBs, our imaging and spectroscopic data eliminate the vast majority of associated eclipsing stellar binary configurations. Additionally, the lack of detectable line-of-sight acceleration over the baseline of the observations rules out associated eclipsing stellar binaries in a mass-dependent manner (see Methods). The constraints provided by these complementary observations are depicted in Fig. 2b. However, some scenarios having $d = 1\text{--}3$ AU and $\Delta Kp = 2\text{--}6$ mag, cannot be conclusively eliminated. Nearly all of these scenarios involve a planet orbiting either K2-33 or an undetected companion. If orbiting K2-33, the planet radius is at most 7.6% larger than the value reported in Table 1 (that is, within quoted uncertainties) owing to dilution from a companion. If orbiting a stellar or substellar companion to K2-33, the planet radius is at most $\sim 1.8 R_{\text{Jup}}$, where R_{Jup} is the radius of Jupiter. Only for $\Delta Kp \geq 6$ mag does the radius of the transiting object corresponds to a mass $\gtrsim 13 M_{\text{Jup}}$ at 5–10 Myr.

However, coeval eclipsing brown dwarfs likely would not produce eclipse depths $>50\%$, and thus contrasts of $\Delta Kp \geq 5.8$ mag need not be considered. Furthermore, the low occurrence of brown dwarfs (Bowler et al., 2015) combined with the lack of observed secondary eclipses make such configurations extremely unlikely. Given the *Kepler* photometry and observational constraints, we quantitatively assessed the overall false-positive probability, using an established statistical framework (Morton, 2015) (see Methods). We found scenarios involving a single star and planet are 10^{11} times more likely than scenarios involving eclipsing stellar binaries.

Spitzer Space Telescope observations of K2-33 revealed 24 micron emission in excess of the expected stellar photosphere by 50%, indicating the presence of cool circumstellar dust (Carpenter et al., 2009). There is an absence, however, of warm dust close to the star given the lack of similar infrared excess at wavelengths shorter than $16 \mu\text{m}$ (Carpenter et al., 2006). The spectral energy distribution is best fitted by including a dust component at 122 K having an inner edge at 2.0 AU. These data suggest that the inner regions of the previously present protoplanetary disk have cleared. Supporting this inference is the modest $H\alpha$ signature (Table 1), which is consistent with chromospheric emission and indicates the star is not accreting gas.

At the age of K2-33, it is unclear whether the dust structure consists of debris resulting from the collisional grinding of planetesimals, or if it is a remnant of the initial dust- and gas-rich disk. One possibility is that the inner-disk regions have been cleared of dust by the gravitational influence of one or more planetary mass bodies (Trilling et al., 2008). Our detection of a short-period planet in a transitional disk lends support to this explanation.

A flux upper limit at $880 \mu\text{m}$ from the Atacama Large Millimeter Array combined with the measured *Spitzer* fluxes yields a constraint on the mass of dust remaining in the disk of less than $0.2 M_{\oplus}$ (Barenfeld et al., 2016). Additionally, CO emission, a tracer of molecular hydrogen, was not detected (Barenfeld et al., 2016), indicating the primordial gas disk also has largely or entirely dissipated.

The transiting planet around the young star K2-33 provides direct evidence that large planets can be found at small orbital separations shortly after dispersal of the nebular gas. Migration via tidal circularization of an eccentric planet, through, for example, the Kozai-Lidov mechanism, planet-planet scattering, or secular chaos, proceeds over timescales much greater than disk dispersal timescales, and thus cannot explain the planet's current orbit. *In situ* formation, or formation at a larger separation followed by migration within the gas disk, are permitted scenarios given current

observations.

Interestingly, large planets are rarely found close to mature low mass stars; fewer than 1% of M-dwarfs host Neptune-sized planets with orbital periods <10 days (Dressing & Charbonneau, 2013), while $\sim 20\%$ host Earth-sized planets in the same period range (Dressing & Charbonneau, 2015). This may be a hint that K2-33 b is still contracting, losing atmosphere, or undergoing radial migration. Future observations may test these hypotheses, and potentially reveal where in the protoplanetary disk the planet formed.

8.1 Methods

8.1.1 Stellar Membership and Properties.

The partial kinematics of K2-33 (Table 1) can be combined with the galactic velocity of the Upper Scorpius subgroup to estimate distance and predict radial velocity. We calculated these parameters following established methods (Lépine & Simon, 2009), adopting the mean UVW galactic velocities of the subgroup (Chen et al., 2011), and estimated uncertainties using Monte Carlo sampling. We find $d_{\text{kin}} = 139 \pm 11$ pc, consistent with the mean subgroup distance $d = 145 \pm 2$ pc (de Zeeuw et al., 1999), and $RV = -7.3 \pm 0.5$ km s $^{-1}$, within 2σ of the systemic RV we measure from multiple Keck/HIRES spectra (Extended Data Table 1).

We determined spectral type from the high-dispersion spectra and adopted an empirical spectral type to temperature conversion calibrated for young stars (Herczeg & Hillenbrand, 2015; Pecaut & Mamajek, 2013) to estimate effective temperature (Table 1). From 2MASS photometry and the appropriate intrinsic $J - H$ color for the spectral type (Pecaut & Mamajek, 2013), we calculated the $J - H$ color excess, $E(J - H) = 0.10$ mag. Assuming an extinction law we found visual and J -band extinctions of $A_V = 1.29$ mag and $A_J = 0.30$ mag, respectively. After correcting for extinction, we used the appropriate empirical J -band bolometric correction for the spectral type (Herczeg & Hillenbrand, 2015; Pecaut & Mamajek, 2013) and a distribution of distances to calculate luminosity. While the mean association distance is known precisely, its large sky-projected area (about 150 deg 2) suggests that the association depth is substantial. Results from a secular parallax study indicate an association distance spread <50 pc, with consideration of the angular diameter corresponding to 35-pc spread (de Bruijne, 1999; Preibisch et al., 2002) at the mean distance. In calculating luminosity, we conservatively considered a uniform distribution of distances in a cubic volume 40 pc on each side, centered on the

Table 8.1: System properties of K2-33

Parameter	Value	Uncertainty
Stellar properties		
2MASS designation	J16101473-1919095	
EPIC designation	205117205	
Right ascension (J2000.0)	16 ^h 10 ^m 14.738 ^s	
Declination (J2000.0)	-19°19'09.55''	
Proper motion R.A., μ_α (mas/yr)	-9.8	± 1.7
Proper motion Dec., μ_δ (mas/yr)	-24.2	± 1.8
Kp (mag)	14.3	
Cluster distance, d (pc)	145	± 20
Kinematic distance, d_{kin} (pc)	139	± 11
Spectral type	M3	± 0.5
V-band extinction, A_V (mag)	1.29	
Luminosity, $\log L_*/L_\odot$ (dex)	-0.83	± 0.07
Effective temperature, T_{eff} (K)	3410	± 75
Stellar radius, R_* (R_\odot)	1.1	± 0.1
Stellar mass, M_* (M_\odot)	0.31	± 0.05
Mean stellar density, ρ_* (g/cc)	0.34	± 0.12
Surface gravity, $\log g_*$ (dex)	3.84	± 0.16
Stellar rotation period, P_{rot} (d)	6.3	± 0.2
Systemic radial velocity, γ (km s ⁻¹)	-6.6	± 0.1
Projected rotational velocity, $v \sin i$ (km s ⁻¹)	5-9	
H α equivalent width (\AA)	-1.3	± 0.1
H β equivalent width (\AA)	-1.05	± 0.05
LiI 6708 \AA equivalent width (\AA)	0.60	± 0.05
Light curve modeling parameters		
Orbital period (days)	5.42513	+0.00028 -0.00029
Time of mid-transit, t_0 (BJD _{TDB} ; days)	2,456,936.6665	+0.0012 -0.0012
Transit duration, T_{14} (hours)	4.22	+0.15 -0.10
Planet-to-star radius ratio, R_p/R_*	0.0476	+0.0035 -0.0017
Scaled semi-major axis, R_*/a	0.109	+0.033 -0.012
Impact parameter, b	0.49	+0.26 -0.33
Inclination, i (deg)	86.9	+2.2 -3.1
Mean stellar density, $\rho_{*,\text{circ}}$ (g/cc)	0.49	+0.21 -0.27
Linear limb darkening coefficient, u	0.603	+0.052 -0.053
Planet properties		
Planet radius, R_p (R_\oplus)	5.76	+0.62 -0.58
Planet mass, M_p (M_{Jup})	<3.6	
Semi-major axis, a (AU)	0.0409	+0.0021 -0.0023
Blackbody equilibrium temperature, T_{eq} (K)	850	± 50

Right ascension and declination originate from 2MASS, proper motions from UCAC4, and *Kepler* magnitude from the Ecliptic Plane Input Catalog. The mean cluster distance (de Zeeuw et al., 1999) is assumed, with uncertainty equal to the presumed cluster depth (Preibisch et al., 2002). Quoted transit parameters and uncertainties are medians and 15.87%, 84.13% percentiles of the posterior distributions.

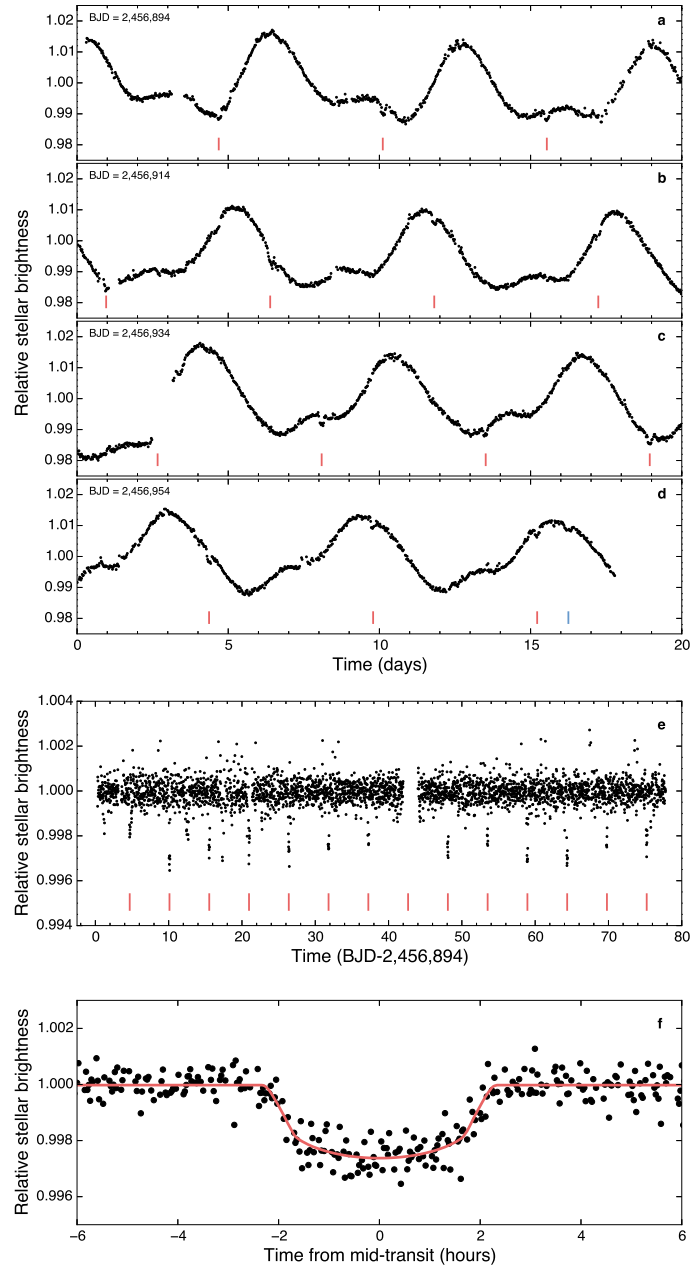


Figure 8.1: Light curve of K2-33. **a-d**, *K2* photometry in twenty-day segments. K2-33 varies in brightness by $\sim 3\%$ every 6.3 days owing to the rotation of its spotted surface. The planet K2-33 b transits its star every 5.4 days (red ticks). Another potential transit (blue tick in d), distinct from the K2-33 b transits, is possibly caused by a second planet with orbital period > 77.5 days. **e**, Stellar variability was removed prior to fitting transits. The data gap is due to excluded observations where the variability fit inadequately captured a systematic artifact in the light curve. **f**, *K2* photometry folded on the planet's orbital period with a transit model fit (red curve). BJD, barycentric Julian date.

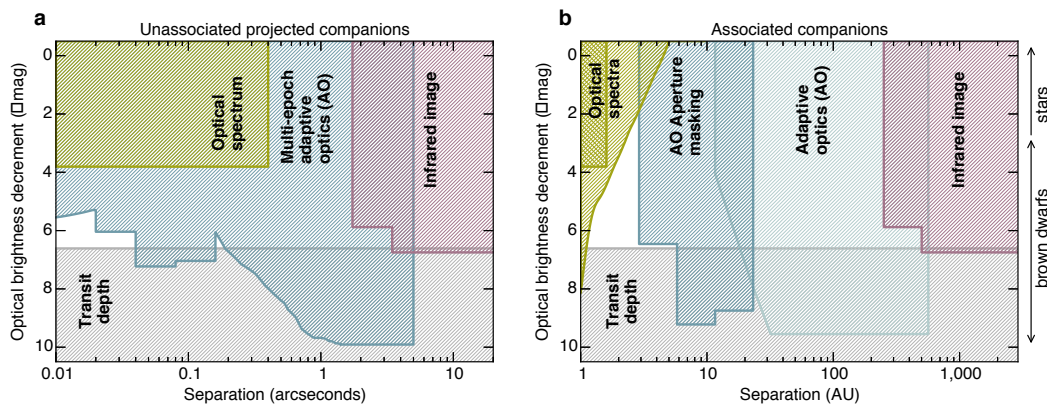


Figure 8.2: Constraints on astrophysical false positive scenarios. To confirm the planetary nature of K2-33 b, we considered and eliminated nearly all false positive scenarios involving eclipsing stellar binaries. **a**, The domain of sky-projected separation and contrast of a putative unassociated eclipsing stellar binary, aligned with K2-33 by chance. The blue hatched region shows eclipsing stellar binaries eliminated using multi-epoch adaptive optics imaging, which leverages stellar proper motion to provide sensitivity at all separations within 5". Green and purple regions represent constraints from optical spectra and seeing-limited imaging, respectively. Finally, eclipsing stellar binaries in the grey region cannot account for the observed transit depth and are eliminated. **b**, Limits on eclipsing stellar binaries associated with (that is, gravitationally bound to) K2-33. Constraints from imaging and spectroscopy are shown as a function of physical separation. The lack of detectable stellar acceleration provides an additional diagonal constraint at top left. Δmag , difference in magnitude.

mean association distance of 145 pc (de Zeeuw et al., 1999). Uncertainty is calculated from Monte Carlo sampling, accounting for photometric errors, recommended errors in temperature (Herczeg & Hillenbrand, 2015), and distance uncertainties. We propagated luminosity and temperature errors through in calculating the radius uncertainties using the Stefan-Boltzmann law.

Detailed modeling of the transit profile provides a constraint on mean stellar density, assuming a circular orbit (Seager & Mallén-Ornelas, 2003). We found a mean stellar density of $\rho_{*,\text{circ}} = 0.49 \text{ g cc}^{-1}$, consistent with the value implied by our adopted M_* and R_* (Table 1). From the posterior distribution of mean stellar densities and a normal distribution in effective temperature, we interpolated between pre-main sequence models (Baraffe et al., 2015) to determine a stellar mass and age of $M_* = 0.30 \pm 0.04 M_\odot$ and $\tau = 5.1^{+1.5}_{-2.6}$ Myr, respectively (Extended Data Fig. 2). However, we conservatively adopt the ensemble age of the association, as we consider it more robust than the age of an individual star.

8.1.2 Stellar Rotation and Independent Assessment of the Stellar Radius.

We measured the stellar rotation period as $P_{\text{rot}} = 6.3 \pm 0.2$ d from a Lomb-Scargle periodogram (Lomb, 1976; Scargle, 1982) of the light curve. Uncertainty was determined from the half width at half maximum of a Gaussian fit to the periodogram peak. Extended Data Fig. 1 depicts the light curve folded on the rotational period.

The stellar rotation speed as projected along the line of sight, $v \sin i_*$, was estimated from the spectra by artificially broadening an absorption spectrum of a slowly rotating stellar template of similar temperature to K2-33, acquired using the same spectrograph and set-up. The range of plausible rotational velocities is constrained through minimization of the residuals between the broadened template and the observed spectrum. We find a most likely projected rotation velocity $v \sin i_* \approx 5\text{--}9$ km s⁻¹. Combined with the rotation period measured from the light curve, we used the projected rotational velocity to determine an independent estimate of the stellar radius modulated by the sine of the stellar inclination of $R_* \sin i_* = v \sin i_* \cdot P_{\text{rot}}/2\pi = (0.85 \pm 0.25) R_{\odot}$, where we quote a 95% confidence interval assuming a uniform distribution in $v \sin i_*$.

Our value for $R_* \sin i_*$ is consistent with the Stefan-Boltzmann radius within $2\text{-}\sigma$. Two effects could bias $R_* \sin i_*$ away from the true value of R_* : (1) the surface features dominating the rotational modulation of the light curve may be confined to a range of stellar latitudes that may not reflect the same velocity field encoded in the rotational broadening of spectral lines, and (2) the star may have an inclination resulting in $\sin i_*$ significantly < 1 . If this is the case, the orbit of K2-33 b is misaligned with the spin of its host star. While $R_* \sin i_*$ provides a valuable consistency check on stellar radius, we use the Stefan-Boltzmann radius given its insensitivity to the unknown stellar inclination.

8.1.3 K2 Time Series Photometry Treatment.

The *K2* mission (Howell et al., 2014) observes fields along the ecliptic plane for approximately 75 days at a time. *K2* photometry possesses percent-level systematic signatures from pointing drift and intra-pixel detector sensitivity variations that must be corrected in order to detect sub-per-cent planet transits. We acquired such a corrected light curve from the Exoplanet Follow-up Observing Program public website (Vanderburg et al., 2016), derived using a $12'' \times 16''$ rectangular aperture (Extended Data Fig. 4).

Before modeling the transit profile, we removed the spot modulation pattern using a

cubic basis spline fit with knots spaced by 12 long-cadence measurements, employing iterative rejection of outliers (David et al., 2016b). We verified that no in-transit observations were included in the spline fit by phasing the flattened light curve on the orbital period and inspecting the points excluded from the fit. An artificial gap in the systematics corrected light curve from the ExoFOP page was not adequately captured by the spline fit and, consequently, we excluded from further analysis those data with BJD values in the range 2,456,936 to 2,456,938 resulting in the loss of a single transit. We assigned a constant observational uncertainty for each *K2* measurement, determined from the standard deviation in the out-of-transit light curve (here defined as observations more than 12 h from either side of the transit centers).

8.1.4 Transit Model Fitting Analysis.

We employed previously established methodology (Crossfield et al., 2015) for fitting transit models to the light curve. The approach uses the BATMAN software (Kreidberg, 2015), based on the Mandel & Agol (2002) analytic light-curve formalism, to generate model transit profiles. Transit models were numerically integrated to match the ≈ 30 minute cadence of *K2* observations. We assumed a linear limb-darkening law for the star, imposing a Gaussian prior on the linear limb-darkening coefficient, u , based on tabulated values (Claret et al., 2012) appropriate for the effective temperature and surface gravity of K2-33. We also allowed for dilution by light from a second star in the fitting. In post-processing, we selected only those samples corresponding to dilution levels consistent with our companion exclusion analysis (Fig. 2).

The directly fitted transit parameters are: scaled semi-major axis (a/R_*), planet-to-star radius ratio (R_p/R_*), orbital period (P), time of mid-transit (t_0), and inclination (i). The multi-dimensional transit parameter space was explored using an affine invariant implementation of the Markov chain Monte Carlo (MCMC) algorithm (Foreman-Mackey et al., 2013) to find the best-fit model and determine parameter uncertainties. Each observation was weighted equally, resulting in a best-fit likelihood of $-\frac{1}{2}\chi^2$. We followed established methods (Crossfield et al., 2015) for MCMC chain initialization, burn-in treatment, rescaling of data weights, and convergence testing. Table 1 quotes median transit model values, with uncertainties determined from the 15.87% and 84.13% percentiles of the parameter posterior distributions.

The scatter in transit is $\sim 15\%$ larger than the scatter in equal duration intervals before and after transit; one possible explanation may be spot-crossing events, given

that the star is expected to have a high spot-covering fraction (Jackson & Jeffries, 2014), supported by the modulation in the unflattened light curve.

Prior to adopting the publicly available light curve (Vanderburg et al., 2016), we independently extracted a light curve from *K2* target pixel files using a different photometric pipeline (Crossfield et al., 2015; Petigura et al., 2015). Performing the same modeling described above on this second light curve produced consistent results.

8.1.5 High Spectral Resolution Observations and Radial Velocities.

We used the HIgh REsolution Spectrograph (Vogt et al., 1994) (HIRES) on the 10-meter Keck-1 telescope to measure the radial velocity of K2-33 relative to the Solar System barycenter (Extended Data Table 1) to confirm its cluster membership, and to constrain the mass of K2-33 b. The resolution of these spectra are $R \approx 50,000$ between $\sim 3600\text{--}8000 \text{ \AA}$ for the 2016 epochs and $R \approx 36,000$ between $\sim 4800\text{--}9200 \text{ \AA}$ for the 2015 epoch.

For the first epoch, velocity was derived by cross-correlating the spectrum with radial velocity standards (Nidever et al., 2002) observed using HIRES in the same spectrograph configuration. Uncertainty is quantified from the dispersion among measurements relative to different standards, and over many different spectral orders. For the three epochs in 2016, systemic radial velocity was measured using the telluric A and B absorption bands as a fiducial wavelength reference. Assessing all measurements, the star’s systemic radial velocity is $-6.6 \pm 0.1 \text{ km s}^{-1}$, where we quote a weighted average and standard deviation.

8.1.6 Limits on Companions from the Spectroscopic Data.

We searched for and excluded distant gravitationally bound companions to K2-33 by looking for trends in the 265-day RV time series. A 3σ upper limit to any possible acceleration is $2.6 \text{ km s}^{-1} \text{ yr}^{-1}$. Following established methods (Montet et al., 2014), the limiting minimum mass detectable from the RV measurements as a function of orbital separation rules out additional companions of $\geq 0.14 M_{\odot}$ at 3 AU and $\geq 0.39 M_{\odot}$ at 5 AU.

We also searched for secondary spectral lines (Kolbl et al., 2015) that would arise from a companion projected within $0''.4$ of the primary. No stars as faint as 3% the brightness of the primary were detected, though we are blind to companion stars with a small ($< 15 \text{ km s}^{-1}$) radial velocity relative to the primary since the spectral

lines of the two stars would not be distinguished.

8.1.7 High-resolution Imaging.

Using adaptive optics at the Keck-2 telescope on UTC 2011 May 15, we obtained ten 9-second exposures of K2-33. A second set of Keck/NIRC2 images was acquired on UTC 2016 February 17 in a three-point dither pattern with 10 second integrations per dither position, repeated three times. For both epochs, the narrow-camera optics were used resulting in a pixel scale of $9.942 \text{ mas pixel}^{-1}$; the final coadded images have resolution $0.07''$ (full-width at half maximum). The observations at the two epochs have the same total integration time, so the final images have comparable depth.

To estimate sensitivity to point sources as a function of radial distance from the star, median flux levels and root-mean-square dispersions (σ) were calculated in incremental annuli centered on the source. An image was constructed with these characteristics and synthetic sources with full width at half maximum equivalent to that of K2-33 were injected into the image at varying positions and brightnesses. The synthetic sources were then measured to determine the 5σ detection limit. Comparing the instrumental magnitude to that of the star produces ΔK for that annulus.

8.1.8 Non-redundant Aperture Masking.

K2-33 was observed using an aperture mask on the same 2011 night as the clear aperture images were taken. Aperture masking interferometry (Tuthill et al., 2000) uses an opaque mask with clear holes such that the baseline between any two samples a unique spatial frequency in the pupil plane, and achieves angular resolution as good as $\frac{1}{3}\lambda/D$ compared to $1.2\lambda/D$ though at the expense of diminished throughput (Baldwin et al., 1986; Readhead et al., 1988).

With the nine-hole mask in the NIRC2 camera, we obtained 40 dithered images using 20-second exposures. Observations of calibrator stars were interspersed with the targets and obtained in an identical manner. In each image, the mask creates a set of 36 overlapping interference fringes on the detector. The bispectrum, the complex triple product of visibilities defined by the three baselines formed from any three subapertures, is then calculated. The phase of this complex quantity is the closure phase, which has the advantage of being largely insensitive to phase delays due to atmospheric effects or residual uncorrected phase aberrations not sensed by the adaptive optics system. We followed established procedures (Kraus et al., 2011;

Hinkley et al., 2015) for calculating the closure phase for calibrator stars.

8.1.9 Limits on Companions from the Imaging Data.

Using all three sets of high-spatial-resolution near-infrared imaging data, we searched for projected companions to K2-33 (either gravitationally bound or foreground / background sources). The two epochs of clear aperture data each achieved $\Delta K > 4.5$ mag of contrast beyond $0''.13$ and $\Delta K > 7.5$ mag beyond $1''$. In the interim between the observations, K2-33 moved on the sky by $0''.1228 \pm 0''.0085$ owing to its parallax and proper motion. The combined set of infrared images thus rules out nearly all unassociated background stars bright enough to produce the transit observed in the optical. The aperture masking observations are sensitive to more closely projected (from $0''.02$ – $0''.16$) companions in the stellar and substellar mass regimes. We use these to rule out potential associated companions larger than 19 Jupiter masses down to orbital separations of 3 AU, and are sensitive to companions with masses as low as 11–12 Jupiter masses from 6–23 AU, where quoted companion masses are model-dependent (Baraffe et al., 2015) conservatively assuming an age of 10 Myr. Finally, a prior analysis of near-infrared photometry ruled out associated companions down to masses of 5%–6% of the primary mass at separations of $1.7''$ – $27.5''$, or approximately 250–4000 AU (Kraus & Hillenbrand, 2012).

The imaging limits constrain the brightnesses of any putative companions in the near-infrared K -band. To approximately convert these contrast limits to constraints in the optical *Kepler* bandpass, K_p , we employed a combination of theoretical evolutionary models and empirical color-color relations. The TRILEGAL simulation discussed below predicts that the mean potential contaminant toward K2-33 would have infrared color $J - K_s = 0.57$ mag, corresponding to a K-type dwarf. From an empirical optical-infrared $K_p - K_s$ conversion (Howell et al., 2012), we conclude that a typical contaminating source would have color $K_p - K_s = 2.00$ mag. We thus gain an additional 2 mag of contrast when converting the NIRC2 contrast curve to the corresponding limits in the *Kepler* bandpass when considering unassociated companions.

For associated companions, the imaging constraints natively derived in the near-infrared were converted to optical limits using pre-main sequence evolutionary models (Baraffe et al., 2015). Putative companion masses can be paired with our assumed primary mass to yield predicted R -band contrasts at 5–10 Myr, where R -band serves as a proxy for the *Kepler* bandpass. Notably, for the clear aperture

AO region of Fig. 2b, the achieved contrast beyond 30 AU is better than represented in the figure due to limitations of the models which do not extend below $10 M_{\text{Jupiter}}$ (corresponding to $\Delta Kp \gtrsim 9.5$ mag).

We rule out nearly all stellar and brown dwarf mass companions to K2-33, with the exception of a narrow swath of parameter space corresponding to ultra-low-mass stars or brown dwarfs separated by 1–3 AU from the primary (Fig. 2). The physically permitted (as opposed to un-excluded) separation range of any hypothetical diluting companion is even smaller, considering the inferred inner edge of the disk at 2 AU.

8.1.10 Galactic Structure Model and Intracluster Contamination.

In addition to searching directly for sources that could contaminate the *K2* light curve, we estimated the expected surface density of such sources as a function of magnitude using the TRILEGAL v1.6 (Girardi et al., 2005; Girardi et al., 2012) model of the Milky Way Galaxy. Notably, TRILEGAL does not include the local extinction due to gas and dust associated with Upper Scorpius itself, and therefore produces an upper limit to the field star source density. We simulated a 1 deg^2 field and scaled the resulting numbers first to the $10 \times 10 \text{ arcsec}^2$ field of view of the Keck/NIRC2 images and the $12 \times 16 \text{ arcsec}^2$ *K2* photometric aperture, and then to the unexcluded regions of parameter space in Fig. 2a. We found the TRILEGAL prediction for the expected surface density of sources to the $K_s < 18.0$ mag limit (5σ) of the NIRC2 data, and translated it to <0.15 sources per NIRC2 field, consistent with our detection of none. Within the *K2* photometry aperture, <0.3 unassociated sources are expected to the same magnitude limit, corresponding to a mean optical brightness $Kp = 18.6$ mag.

By considering the surface density of sources expected from integrating essentially all the way through the galaxy, a maximum of 3 sources are expected in the *K2* aperture, having mean optical brightness $Kp = 23.1$ mag which is too faint to explain the transit depth. Indeed, we have ruled out nearly all companions with projected separations larger than $0.04''$, as well as effectively all of those inside of $0.04''$; fewer than 4×10^{-6} sources are expected in the remaining unexcluded parameter space of Fig. 2a. An even smaller number of sources are expected to be eclipsing stellar binaries. Therefore, in addition to not detecting any contaminants in the high spatial resolution imaging and spectroscopic data, we argue that essentially none are expected.

A similar source density argument can be used to constrain the probability of

contaminants with nearly identical proper motions to K2-33, likely association members that are foreground or background to K2-33. The multi-epoch AO imaging cannot rule out closely-projected sources within $0.02''$ (the inner limit probed by the aperture masking observations) that are also co-moving with K2-33 between 2011–2016. From the observed Upper Scorpius mass function and width of the association on the sky (Preibisch et al., 2002), we estimated a source density of ~ 16 members deg^{-2} . Thus, fewer than 2×10^{-9} co-moving contaminants are expected within $0.02''$ of K2-33.

8.1.11 False Positive Probability Analysis.

Eclipsing stellar binaries when diluted by the light of a third star can produce light curves that masquerade as a planetary transit. These false positives come in three broad classes: (1) undiluted eclipsing stellar binaries, (2) background (and foreground) eclipsing stellar binaries where the eclipses are diluted by the target star (3) bound eclipsing stellar binaries in hierarchical triple systems.

We used the VESPA program (Morton, 2015) to compare the likelihood of each binary scenario against the planetary interpretation. As input for the calculation, we provide the *K2* light curve, the stellar parameters, and to be as conservative as possible, we adopt our least stringent imaging constraints: the 2011 NIRC2 clear contrast curve, and the aperture masking limits. Even in this minimally constraining scenario, we find a false positive probability of $< 1 \times 10^{-11}$ from VESPA, as expected given our exclusion in Fig. 2 of essentially all the modelled scenarios. Notably, however, VESPA does not account for substellar objects, pre-main sequence evolution, or extinction, or the unknown prior probability of planets around 5–10 Myr stars.

8.1.12 Implications of Hierarchical Triple Scenarios.

The conjectured hierarchical triple configuration is argued elsewhere as unlikely based on population statistics; however, we must still consider the possibility that K2-33 b has a larger radius due to dilution of the transit depth by a luminous companion to K2-33. We first consider the case in which the planet orbits K2-33, but the transit depth is diluted by an undetected secondary. In this scenario, the ratio of the true planet radius to the observed planet radius (i.e. not accounting for dilution) is $R_{P,\text{true}}/R_{P,\text{obs}} = \sqrt{1 + F_{\text{sec}}/F_{\text{pri}}}$, where $F_{\text{sec}}/F_{\text{pri}}$ is the optical flux ratio between the secondary and primary. For ΔK_p between 2–6 magnitudes, the true planet radius is at most 7.6% larger, within our quoted uncertainties.

Now, we consider the case in which the planet orbits an undetected companion to K2-33. In this scenario, the planet radius is $R_p = R_{\text{sec}} \sqrt{\delta_0 (1 + F_{\text{pri}}/F_{\text{sec}})}$, where R_{sec} is the secondary radius, and δ_0 is the observed transit depth. Using ΔR as a proxy for ΔKp , we found the secondary radius implied by the optical brightness decrement using evolutionary models valid for 5–10 Myr (Baraffe et al., 2015). For ΔKp between 2–6 magnitudes, we found the implied planet radius is in the range $(0.56\text{--}1.85) R_{\text{Jup}}$. At these ages, such radii correspond to planet masses of $\lesssim 13 M_{\text{Jup}}$. Only for $\Delta Kp \gtrsim 6$ mag does the implied mass exceed the nominal brown dwarf minimum mass. However, coeval eclipsing brown dwarfs are unlikely to produce eclipse depths $>50\%$ (corresponding to contrasts of $\Delta Kp \gtrsim 5.8$ mag). Furthermore, we argue that scenarios involving eclipsing brown dwarfs 1–3 AU from K2-33 are extremely unlikely, due to several compounding reasons: (1) the observed frequency of brown dwarf companions to M-dwarfs is a few percent (Bowler et al., 2015; Dieterich et al., 2012); (2) in the restricted domain of $a = 1 - 3$ AU, the frequency is lower still; and (3) the frequency of eclipsing brown dwarf pairs so similar in size and temperature that primary and secondary eclipse are indistinguishable is smaller still. Finally, the tenuous dust disk with inner edge at 2 AU is further evidence in favor of the single-star scenario.

8.1.13 Cluster Age.

The age of Upper Scorpius is constrained to be between 5–10 Myr from a variety of considerations. Absence of dense molecular gas or protostars in Upper Scorpius implies that star formation has ceased in the region (Preibisch & Mamajek, 2008), while presence of protoplanetary disks around a significant fraction of members indicates that planet formation is ongoing (Luhman & Mamajek, 2012). However, the precise age of the association is currently debated. An early kinematic analysis, in which the motions of high mass members were traced back in time to the point of closest proximity to one another, suggested an age of 5 Myr (Blaauw, 1991). The first H-R diagram analysis of the full stellar population, spanning from the highest to lowest masses, also determined an age of 5 Myr without appreciable dispersion (Preibisch et al., 2002). Most subsequent age determinations using theoretical evolutionary models in the Hertzsprung-Russell diagram arrived at the same consistent age of 5–6 Myr for massive main-sequence turnoff stars (de Zeeuw & Brand, 1985; de Geus et al., 1989), low-mass stars (Preibisch & Zinnecker, 1999; Slesnick et al., 2008; Lodieu et al., 2011a; Herczeg & Hillenbrand, 2015), as well as substellar mass objects (Allen et al., 2003).

Table 8.2: Keck/HIRES radial velocities for K2-33

Epoch (UTC)	BJD	Radial velocity (km s ⁻¹)
2015-06-01 12:57:36.0	2457175.040	-6.61 ± 0.58
2016-02-02 15:30:14.4	2457421.146	-6.66 ± 0.30
2016-02-04 15:23:02.4	2457423.141	-6.60 ± 0.30
2016-02-21 14:29:45.6	2457440.104	-6.40 ± 0.30

Note: Line-of-sight velocities and 1σ uncertainties (standard deviations) with respect to Solar System barycenter.

However, the association age has also been determined to be closer to 10 Myr from analyses of low-mass members (Martín, 1998; Frink, 1999) and the intermediate-mass pre-main-sequence and main-sequence population, main-sequence turn-off stars, and the supergiant Antares (Pecaut et al., 2012). Emerging evidence from double-lined eclipsing binaries also supports an age in the range of 7-11 Myr (Kraus et al., 2015; Lodieu et al., 2015a; David et al., 2016b), as does an updated kinematic analysis (Pecaut et al., 2012). Despite the lack of consensus on the precise age of Upper Scorpius, the full error-inclusive range of estimates in the literature (3-13 Myr) place the association at a critically important stage in the planet formation process – when most primordial disks have dispersed (Wyatt, 2008).

8.1.14 K2-33 b in the Context of Other Claimed Young Planets.

While several secure short-period planets have been found in orbit around stars in benchmark open clusters including the 600-800-Myr-old Hyades (Mann et al., 2016b; David et al., 2016a) and Praesepe (Quinn et al., 2012; Malavolta et al., 2016), the evidence for planets at younger ages is mixed. Direct imaging has revealed (5-10) M_{Jupiter} “planetary mass companions” located at large semi-major axes from several stars having ages a few tens to a few hundred million years. Additionally, there are strong indications of ongoing planet formation in many 1–3 million year old circumstellar disks based on observed radial structure of dust.

However, there are no confirmed planets in the Jupiter or sub-Jupiter mass range with ages less than those corresponding to the late-heavy bombardment era in our own solar system. Both TW Hya and PTFO 8-8695 have been claimed to host hot Jupiter candidates detected via radial velocity or transit methods, but neither object has stood up to scrutiny (Rucinski et al., 2008; Huélamo et al., 2008; Yu et al., 2015). K2-33 b at 5–10 Myr of age, in contrast, is a secure transiting planet. It is slightly larger than Neptune and its mass is probably similar to Neptune’s mass.

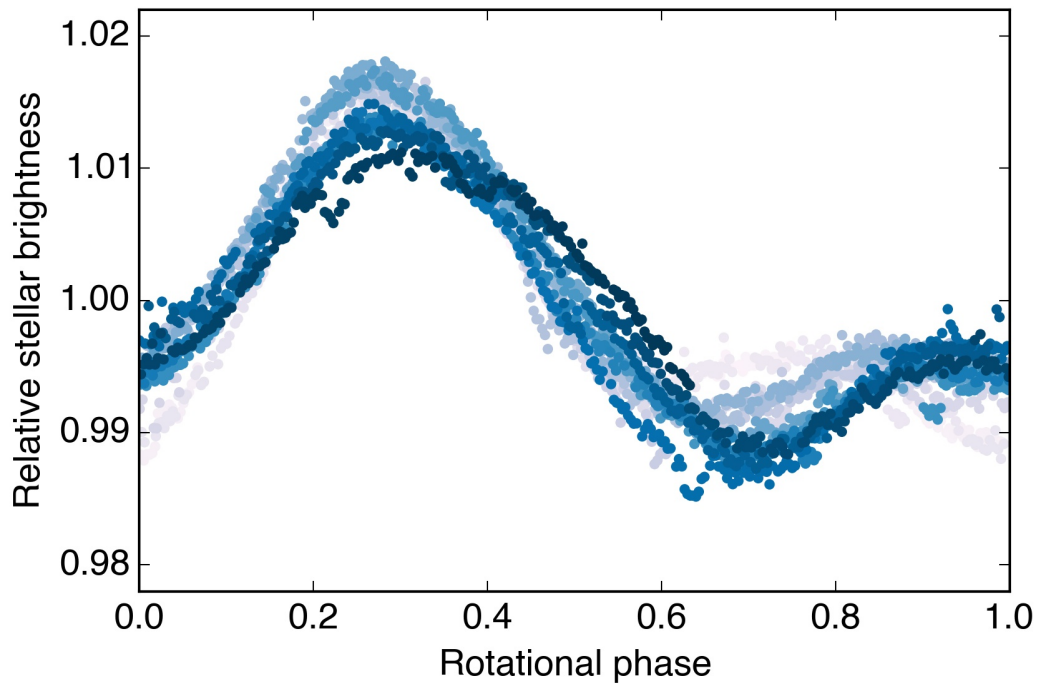


Figure 8.3: Extended Data Figure 1. *K2* light curve for K2-33 phased on the stellar rotation period of 6.3 d. Semi-sinusoidal brightness variations due to rotational modulation of starspots. Point color indicates relative time of observation, with grey corresponding to earlier in the campaign and dark blue corresponding to later times. Brightness is lowest when the most heavily spotted hemisphere of the stellar surface is along the line of sight. The shape and evolution of the variability pattern depends on the number, geometry, distribution, and lifetime of spots, along with any latitudinal gradient in the rotational speed (differential rotation). The transits of K2-33 b are visible by eye in this figure and are too narrow in rotational phase to be attributed to any feature on or near the stellar surface.

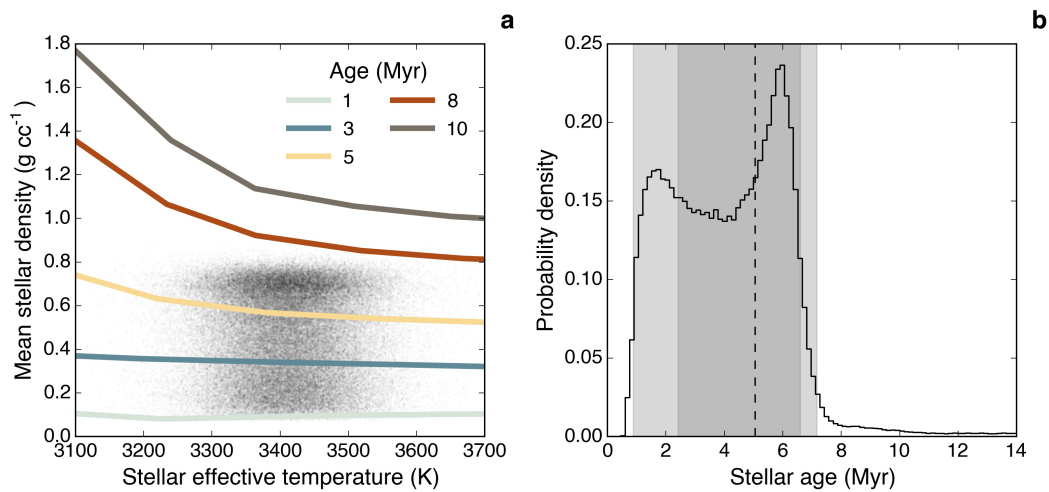


Figure 8.4: Extended Data Figure 2. Model-dependent age of K2-33. **a**, Solid lines show mean stellar density as a function of effective temperature for pre-main-sequence stars having different ages, according to theoretical models (Baraffe et al., 2015). Grey points represent plausible combinations of density and temperature for K2-33 as determined by light-curve fits and stellar spectroscopy. **b**, Distribution of implied stellar age based on temperature, density, and pre-main sequence models. The implied age of 2–7 Myr is consistent with our adopted age of 5–10 Myr, derived independently. Dark and light grey shaded regions indicate 68% and 95% confidence intervals, respectively.

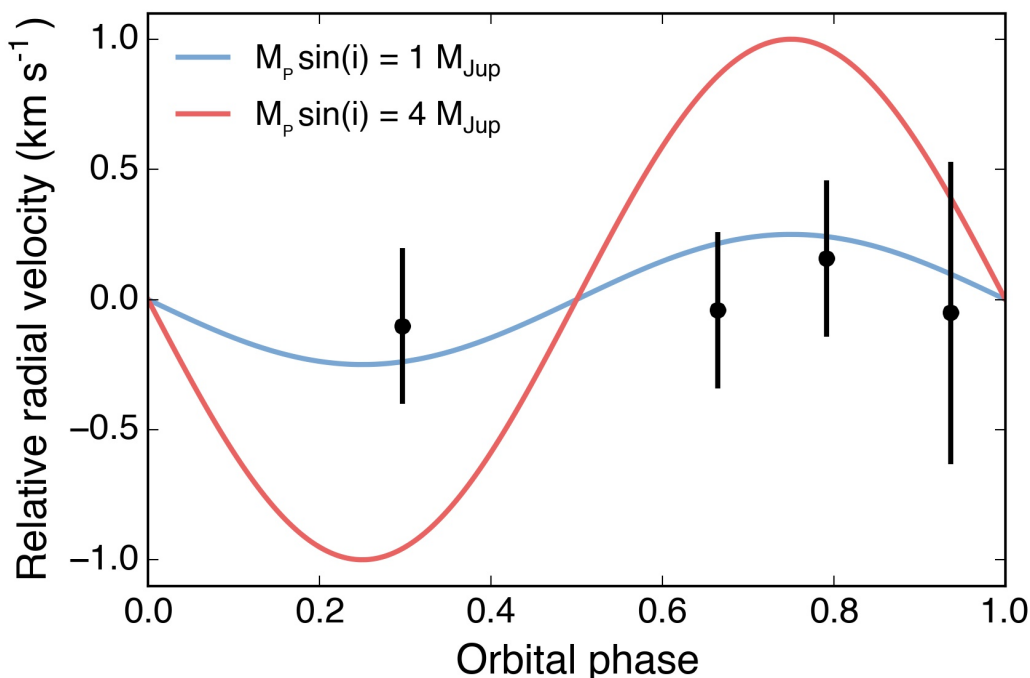


Figure 8.5: Extended Data Figure 3. Apparent radial velocity variations of K2-33. Line-of-sight velocities and 1σ uncertainties (standard deviations) with respect to Solar System barycenter from Keck/HIRES are indicated. Radial velocities (RVs) are mean-subtracted, and the abscissa shows the orbital phase of K2-33 b measured from *K2* photometry (mid-transit occurs at zero orbital phase). We rule out RV variations larger than 300 m s^{-1} at 68.3% confidence, corresponding to a $1.2 M_{\text{Jupiter}}$ planet mass. Curves show the expected radial velocity variations for planets having circular orbits and different masses M_p . Radial velocities due to a 1.0 Jupiter mass planet (blue) are consistent with our observations, while a 4.0 Jupiter-mass planet is ruled out at high confidence.

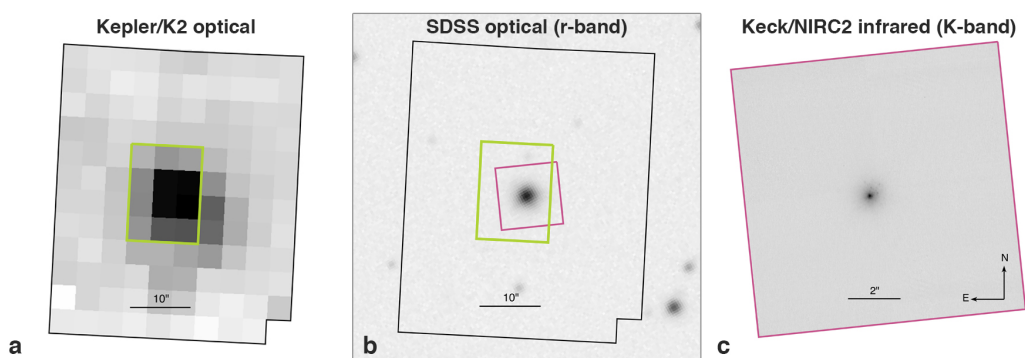


Figure 8.6: Extended Data Figure 4. Images of K2-33. **a**, *K2* target pixel file (TPF). **b**, Sloan Digital Sky Survey (SDSS) optical image. **c**, Keck/NIRC2 *K*-band image. Extents of the *K2* target pixel file, *K2* photometric aperture, and NIRC2 image are shown respectively with black, green, and purple boundaries. In each image, north is up and east is left. Three other sources identified by SDSS reside within the *K2* photometric aperture, one of which is a galaxy. All are 7.3–10.1 magnitudes fainter than K2-33 in the SDSS *r*-filter and below the detection limit of the NIRC2 images, and are thus too faint to produce the observed transits.

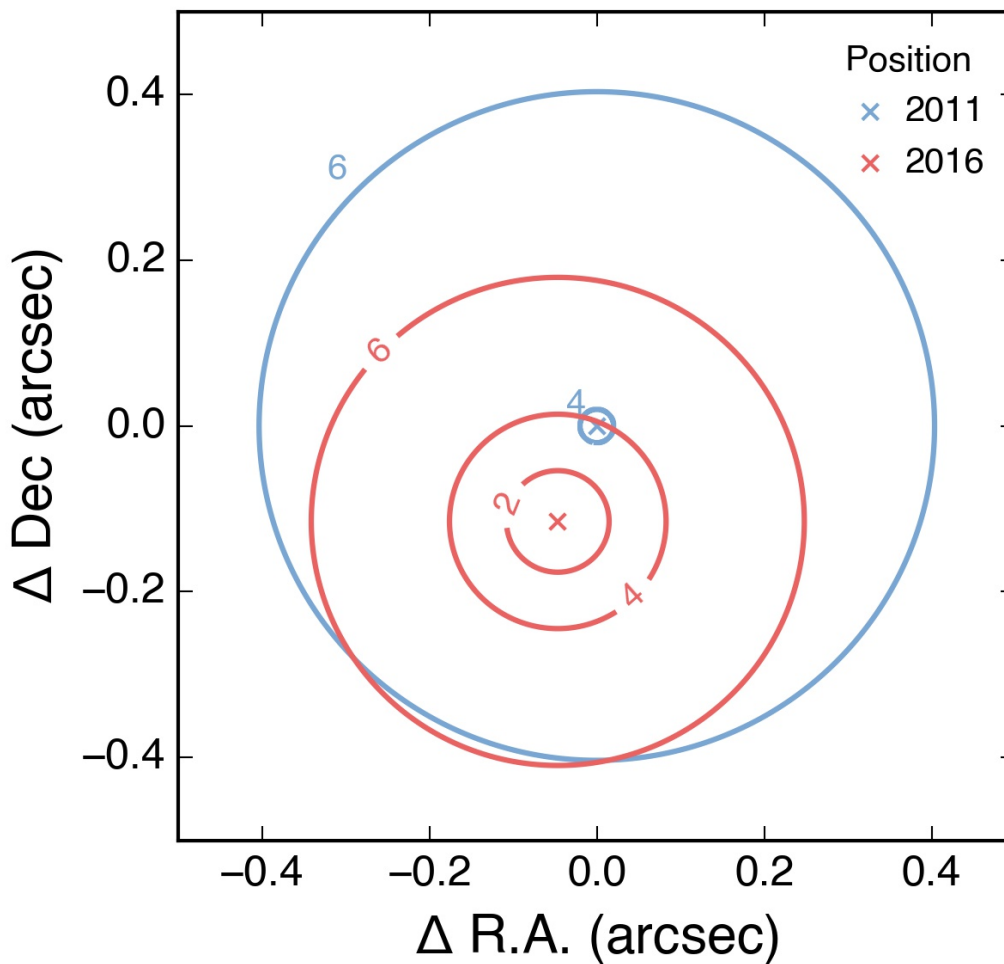


Figure 8.7: Extended Data Figure 5. Sensitivity to non-comoving sources in the vicinity of K2-33. The blue X marks the star's position in 2011. Between 2011 and 2016, the star moved by $0.''1228 \pm 0.''0085$ (red X) owing to proper motion. Contours show *K*-band sensitivity to non-comoving stars from adaptive optics imaging from both epochs. The 2011 data set included non-redundant aperture masking, and provided tighter constraints. The combined sensitivity to non-comoving objects is the maximum contrast achieved for either data set. Owing to stellar proper motion, we achieved *K*-band contrasts of >3.3 mag throughout Δ R.A.– Δ Dec plane, even at the 2011 and 2016 positions of K2-33.

*Chapter 9*THE OCCURRENCE OF CLOSE-IN PLANETS AT THE EPOCH
OF PRIMORDIAL DISK DISPERSAL

ABSTRACT

Low-mass stars, and the tightly arranged planetary systems which orbit them, are abundant throughout the galaxy. How the voluminous population of close-in super-Earths and sub-Neptunes formed is an open question in the field of exoplanets. Whether these planets formed *in situ* or migrated to their present locations has implications for a dominant mode of planet formation. Evidence from the multimodal distribution of planet sizes hints at the importance of photoevaporation in sculpting this observed population of close-in exoplanets. This suggests planets may experience significant atmospheric evolution at early stages in addition to, or perhaps because of, any orbital evolution. The *Kepler* space telescope, in its extended *K2* mission, recently observed the nearby Upper Scorpius OB association, in which a sizable fraction of stars still host protoplanetary disks. Approximately 1000 members were observed by *K2*, constituting the largest, longest duration, highest cadence, and most precise photometric data set for an extremely young stellar population. We use these data to investigate the prevalence of close-in planets at the epoch of primordial disk dispersal, and compare our results with expectations from exoplanet occurrence rates in field stars.

9.1 Introduction

One of the most surprising findings in exoplanets over the past two decades is the abundance of close-in planets, for which our Solar System has no counterpart. Traditional planet formation scenarios suggest these planets could not have formed at their present locations (near where dust sublimates in the protoplanetary disk), and that their existence is evidence for large-scale migration (Lin et al., 1996). However, the *in situ* formation of close-in planets has been revisited by theorists with renewed optimism of late (Hansen & Murray, 2012; Chiang & Laughlin, 2013; Chatterjee & Tan, 2014; Batygin et al., 2016; Boley et al., 2016; Lee & Chiang, 2017).

To test these theories, one must determine the timescales over which close-in exoplanets assemble. If close-in planets with substantial gaseous envelopes formed *in situ* or migrated through disk, one would expect to find the population in place after ~ 10 Myr, when most protoplanetary disks have dispersed. Conversely, if high eccentricity migration channels are important, we expect a dearth of close-in planets within young stellar populations since tidal dissipation acts over longer timescales. It is also possible that both physical processes are important; while some short-period planets form quickly, others may take much longer to reach their current orbits. By comparing the statistical frequencies of close-in planets around stellar populations of different ages, one directly constrains the timescales over which exoplanets settle into short-period orbits.

The *Kepler* spacecraft, in its extended *K2* mission (Howell et al., 2014), has observed and continues to observe several coeval stellar populations ranging in age from ~ 1 Myr to ~ 12 Gyr. *K2* is thus sampling extrasolar planetary systems at critical stages of their formation and evolution. At the ages of ρ Ophiuchi, Taurus, M21, and the Lagoon Nebula (< 5 Myr), one may observe classical T Tauri stars (CTTS) in the throes of planet formation and weak-lined T Tauri stars (WTTS) hosting young fully formed planets. By the age of Upper Sco (5–10 Myr), the majority of gaseous protoplanetary disks have dispersed and giant planet formation is presumed to be complete. Terrestrial planets may very well undergo significant changes long after protoplanetary disks dispersed; the age of M25 (90 Myr), the Pleiades (125 Myr), and NGC 1647 (150 Myr) correspond approximately to the time of the giant impact that has been proposed to explain the formation of the Earth's moon. Similarly, the age of the Hyades and Praesepe (~ 650 – 800 Myr) correspond roughly to the inferred Epoch of Late Heavy Bombardment, as indicated by the cratering records in the Solar System.

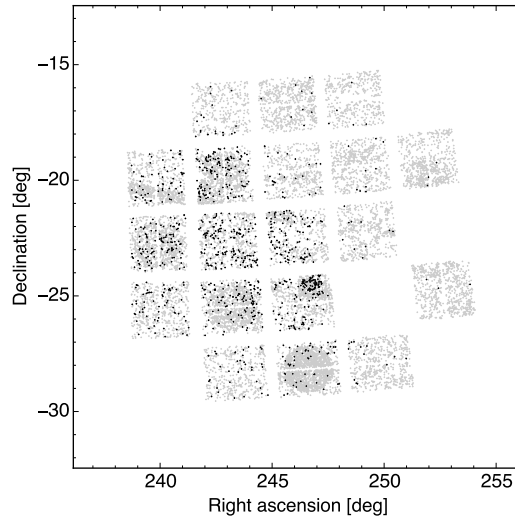


Figure 9.1: Spatial distributions of all stars observed during Campaign 2 of the *K2* mission (grey points) and the subset of young stars considered in this study (black points). The concentration of black points near the middle of the detector mosaic is due to the densely populated ρ Oph cloud. The two blank squares in the mosaic are due to non-operational CCD modules.

Upper Scorpius (hereafter Upper Sco) is a subgroup of the larger Scorpius-Centaurus (Sco-Cen) OB association, the nearest region of recent massive star formation (for a review see Preibisch & Mamajek, 2008). Sco-Cen spans a region of more than 1500 square degrees across the sky. Upper Sco and the foreground ρ Ophiuchi molecular cloud complex constitute the youngest populations in Sco-Cen. The *K2* mission observed approximately 1000 known or candidate members of Upper Sco and ρ Oph during Campaign 2 (hereafter C2) of its mission, between UT 2014 Aug 23 and UT 2014 Nov 13. The dataset constitutes the longest and most sensitive yet for such a large number of young stars, making it ideal to search for transiting planets and setting limits on the occurrence rates of such planets.

9.2 Sample Selection

We selected our sample based primarily on photometry and proper motions, as well as literature membership studies and trigonometric parallaxes when available. During Campaign 2 (hereafter C2) of the *K2* mission, the *Kepler* space telescope observed 13401 unique targets. We queried the 2MASS (Cutri et al., 2003), AllWISE (Cutri & et al., 2013), Gaia DR1 (Gaia Collaboration, 2016), GPS1 (Tian et al., 2017), UCAC5 (Zacharias et al., 2017), UCAC4 (Zacharias et al., 2013), and PPMXL (Roeser et al., 2010) catalogs for the nearest source within a $1''$ radius (compared with the *Kepler* pixel size of $3.98'' \times 3.98''$) of each C2 target position

using the *astroquery* package, part of the *astropy* Python software library¹. For stars missing *Gaia* photometry, we have estimated the *G* magnitude based on the *I* magnitude from the Deep Near Infrared Survey of the Southern Sky² (DENIS), if available, or the *r'* magnitude from the Carlsberg Meridian Catalog (Niels Bohr Institute et al., 2014) otherwise.

Information about the association membership of our sample is incomplete and inhomogeneous. There are several avenues for determining membership and while the youth of some stars has been definitively established by previous authors, there remain many stars for which membership criteria are only partially complete. The observational properties determining membership are as follows:

1. sky position (α, δ)
2. distance (d)
3. proper motions (μ_α, μ_δ)
4. color-magnitude diagram position
5. radial velocity (γ)
6. spectral properties (enhanced hydrogen emission, lithium absorption, surface gravity indicators)

In this case, the size of the association on the sky is comparable to the *Kepler* field-of-view, and the C2 pointing is nearly centered on the association, so the sky position of a source is largely uninformative (although there is a relative dearth of members to the eastern side of the C2 pointing, see Figure 9.1). Distances from trigonometric parallaxes measured by *Gaia* are presently available for only the brightest stars (which for the association members are the highest mass stars), constituting 13% of the stars observed in C2. Proper motions (μ_α, μ_δ) are available for >99% of the sample, and are culled from the following catalogs, in order of preference: *Gaia*, UCAC5, UCAC4, and PPMXL.

¹Every source in our sample with 2MASS and WISE photometry has ‘A’ quality photometry in the *JHK* and *W1, W2* bands. We note that *W2* fluxes are overestimated by 0.2–1.0 mag for saturated (*W2* < 6 mag) stars (Cutri & et al., 2013).

²<http://cds.u-strasbg.fr/denis.html>

Table 9.1: Upper Sco membership studies

Reference	Spectral type	Method	Number of stars
Ardila et al. (2000)	M4–M7	spectroscopic	20
Preibisch et al. (2002)	K5–M6	spectroscopic	166
Slesnick et al. (2006)	M4.5–M8	spectroscopic	43
Lodieu et al. (2008)	M8–L2	spectroscopic	21
Slesnick et al. (2008)	M3–M8	spectroscopic	145
Lodieu et al. (2011b)	M3–L2	spectroscopic	109
Rizzuto et al. (2011)	O9.5–G2	kinematic	436
Luhman & Mamajek (2012)	B0–M9.5	...	863
Rizzuto et al. (2015)	F4.5–M7.5	spectroscopic	257
Pecaut & Mamajek (2016)	B8–M3	spectroscopic	493

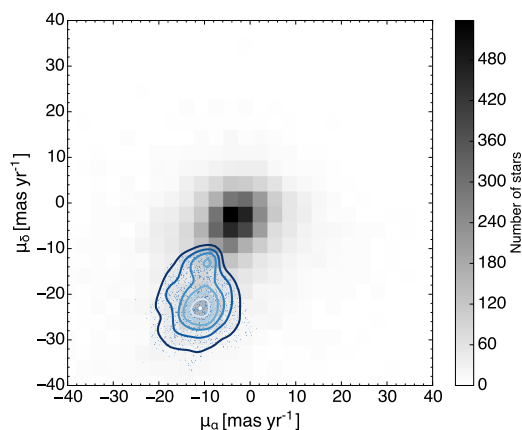


Figure 9.2: Number density of stars in proper motion space observed during Campaign 2 of the *K2* mission. Blue points and contours indicate the region occupied by candidate members of the Upper Sco OB association, as determined with the machine-learning algorithm described in Riedel et al., *in prep.*

9.2.1 Proper motion analysis

Of the 13401 sources in C2, 1741 have proper motions taken from the *Gaia* DR1 catalog, 10083 taken from UCAC5, 452 from UCAC4, 964 from PPMXL, and 161 which lack proper motion measurements from any of the three above catalogs. In short, we used our assembled proper motions and a machine learning algorithm (Riedel et al., *in prep.*) to assign membership probabilities to each source. Probabilities were determined through Monte Carlo sampling of the proper motion errors, and dividing the number of outcomes in which the star was assigned membership by the number of outcomes in which it was not. We describe the details of this procedure below and show distribution of our sample in proper motion space in Figure 9.2.

Our re-derivation of the subgroups of Scorpius-Centaurus is based on a sample of stars culled from an extensive review of the literature. Using the NASA Astrophysics

data system, we have made a thorough survey of all data published since 2010 on the regions of Sco-Cen, plus important extensively-cited papers prior to that date³. In total, there were over 80 papers surveyed for data on Sco OB2, comprising nearly 200 tables. After creating a master table of all members, we pulled data on them from prominent all-sky catalog resources, such as the Two Micron All Sky Survey (2MASS, Cutri et al. 2003, the AllWISE catalog (Wright et al., 2010), American Association of Variable Star Observers (Henden et al., 2016), the USNO Compiled Astrographic Catalog, Fourth Edition (Zacharias et al., 2013) (later changed to UCAC5, Zacharias et al. 2017, after the centers were set), and *Gaia* DR1 (Gaia Collaboration, 2016).

Gaia parallaxes (with an applied 0.3 mas systematic error as recommended by Gaia Collaboration 2016) reveal significant contamination in the proposed US, UCL, and LCC membership lists. While the parallax distribution for the sample is peaked in the expected range of 110-150 pc, examination of *G* mag vs. parallax shows that 41 stars are closer than 100 pc and 250 stars are further than 200 pc, suggesting about 8% contamination in the literature samples from parallax alone. The *G* mag vs *G* – *K* color-magnitude diagram indicates the presence of interloping giants at all spectral types.

We first cleaned our membership lists of the aforementioned stars well outside the established distance range by retaining only those stars with parallax-derived distances between 83 and 205 pc ($\pi = 4.83 - 12$ mas). These objects, despite the large range of distances, are far more likely to be members and therefore trace the actual star-forming region.

We then employed a machine learning algorithm to reconsider the subgroup memberships (Riedel et al., *in prep.*). Machine learning is capable of identifying clusterings of objects based on analysis of a dataset, or classify objects based on a training set that already has labels. They provide a repeatable application of rules decided on by the algorithm, and are thus less prone to human biases.

Visually, it is possible to see clustering that sets US apart from UCL and LCC in spatial distribution plots; and to see a separation of LCC from US and UCL in the proper motion distribution. Accordingly, three regions still appears to be a realistic number of subgroups (though see also the work of Pecaut & Mamajek 2016).

³Papers prior to 1997 were generally not included because their data tables are rarely available in digital form, a small number of works were available from data typed in by various astronomers over the years.

We utilized a K-Means Clustering algorithm from the `scikit-learn` PYTHON package to divide the sample into three groups based solely on RA, DEC, μ_{RA^*} and μ_{DEC} . The algorithm delivered three groups split along lines similar to the classical RA/DEC boundaries, enlarging Upper Scorpius by reassigning it most of the small southern extension of Upper Centaurus Lupus to Upper Scorpius, with only slight overlaps between the groups.

We then took these groups and found new proper motion centers through a process of locating the median. The new centers, in mas yr^{-1} , are:

- Upper Scorpius: -12.9, -24.6
- Upper Centaurus Lupus: -23.4, -22.1
- Lower Centaurus Crux: -33.8, -11.1

With new centers, we can define new high-confidence samples of stars that are both photometrically young as seen on a color-magnitude diagram, and within $2\text{-}\sigma$ of the optimal proper motion center. These high-confidence samples were used to train a Support Vector Machine classifier (again as implemented in `scikit-learn`) to recognize groups entirely based on their proper motions. To properly account for a field star population centered on $\mu_{RA^*,DEC} = (0,0)$ with an enormous proper motion dispersion, we added a fourth group, “Field”, in the form of a random Gaussian distribution of 250 stars centered at $\mu_{RA^*,DEC} = (0,0)$ with standard deviation of 20 mas yr^{-1} in both axes.

To classify individual test stars, we run 1000 Monte Carlo iterations within the standard uncertainties on input stars, and take the mode of the classifications as the correct answer. If a star cannot be uniquely identified in this manner (or has no proper motions to classify), it is assigned to a generic Sco-Cen population.

Because the final classifier relies solely on proper motions, it will find small numbers of stars in every group, everywhere. The K2 C2 field contains only what is classically known as Upper Scorpius, and while the classifier finds an enormous overdensity of Upper Scorpius members in that location (1932 stars out of 13401), it also finds 364 UCL members, and 154 LCC members. We take those 154 LCC members to be field star contamination, representative of our total contamination fraction. This suggests that slightly more than half of the UCL members identified by the classifier are likely to be genuinely young objects, most likely spatially and kinematically at the border between US and UCL.

For the purposes of identifying solely Upper Scorpius members in the *K2* C2 field, we have re-run the classifier without the LCC and UCL training sets. Some 84 stars identified as UCL members are now in the locus of points considered US, but either way they were and are potential young stars of interest to us. The total number of objects of interest identified in this manner is 2120.

9.2.2 Color-magnitude cuts

We define our sample of young stars on the basis of both proper motions and their positions in three color-magnitude diagrams (CMDs). Theoretical pre-main sequence evolution models are inadequate for performing cuts in color-magnitude space as none are able to reproduce the loci of stars in a given association across any appreciable range in mass (see e.g. Herczeg & Hillenbrand, 2015). Instead, we produce empirical isochrones in various color-magnitude planes using a subsample of high confidence Upper Sco members. We constructed this reference sample of members based on the literature sources summarized in Table 9.1. In each of these references, membership is established spectroscopically based on a combination of lithium absorption, enhanced hydrogen emission, low surface gravity indicators, and/or radial velocity. In constructing our reference sample we do not consider references that suggest membership on the basis of proper motions and color-magnitude cuts alone, though many of those stars undoubtedly make it into our final sample. Notably, the Ardila et al. (2000) study includes both photometrically selected and spectroscopically confirmed members, and we consider only the spectroscopic members in our reference sample. Additionally, the exact membership criteria used in Luhman & Mamajek (2012) are not described in that work. Nevertheless, we include these stars in our reference sample because of its size and broad coverage in spectral type. For each reference, only a fraction of members from a given reference were observed by *K2* due to e.g. gaps between CCDs in the *Kepler* mosaic, non-operational detector modules, or sky positions outside of the *K2* C2 pointing. For simplicity, our reference sample is constructed from only those stars observed by *K2*.

Within each CMD, we empirically determined the boundaries of the cluster sequence by fitting the known young star sample using a cubic basis spline with iterative outlier exclusion. As the reference sample is subject to variable extinction and contains a significant number of disk-bearing stars with large infrared excesses, the outlier exclusion is a necessary step to find a fit that adequately depicts the diskless and unreddened cluster sequence. We then applied constant color shifts to the fits

within each CMD to empirically determine the offset required to enclose 95% of the reference sample. We use these offsets later in our CMD selection and exclusion scheme described below. The goal is to find an empirical fit that traces the high gravity boundary of the cluster member sequence, such that candidate members of a given color are included if they are brighter than the shifted fit and excluded otherwise. The CMDs and empirical fits are shown in Figure 9.3.

9.2.3 Disk-hosting stars

Within Upper Sco, a significant fraction of stars retain full or transitional protoplanetary disks. The fraction of disk-hosting stars increases from $\lesssim 10\%$ for the B-G stars to $\sim 25\%$ for M5 and later spectral types (Luhman & Mamajek, 2012; Carpenter et al., 2009). In most cases, the light curves of disk-hosting stars are categorically distinct from those of stars lacking disks. Stars with disks exhibit variability over a wide range of amplitudes and timescales, due either to accretion onto the star (e.g. Cody et al., 2017) or obscuration of the star by the disk (e.g. Cody et al., 2014; Ansdell et al., 2016). Such extreme variability not only hinders automated planet search algorithms, but transits are also not detectable in cases where the star is obfuscated by optically thick gas and dust. Presently, we include disk-bearing stars in our transit injection and recovery tests and in our calculations of occurrence rates. In a future version of this study, we will identify the stars hosting disks through their infrared colors, prior disk classifications in Luhman & Mamajek (2012), and by visual inspection of the light curves contained in our sample. We will then examine how the overall occurrence rates and general conclusions change when the disk-bearing sources are excluded.

9.2.4 Stellar multiplicity

Stellar multiples are problematic for studies of planet occurrence rates for the following reasons: (1) in the case of transiting planet searches, transit depths are diluted by unresolved multiples, (2) they introduce uncertainty in the number of stars surveyed, and (3) there is evidence that planet formation outcomes are different in multiple systems compared to single stars (e.g. Kraus et al., 2016). Inclusion of stellar multiples in a planet occurrence rate study may thus artificially reduce inferred rates if transits are diluted beyond detectability. On the other hand, because rates are often measured in number of planets per star, inclusion of binaries can artificially enhance inferred occurrence rates while obfuscating the meaning of “star,” (that is, assuming one is really attempting to measure the occurrence rate of a certain type

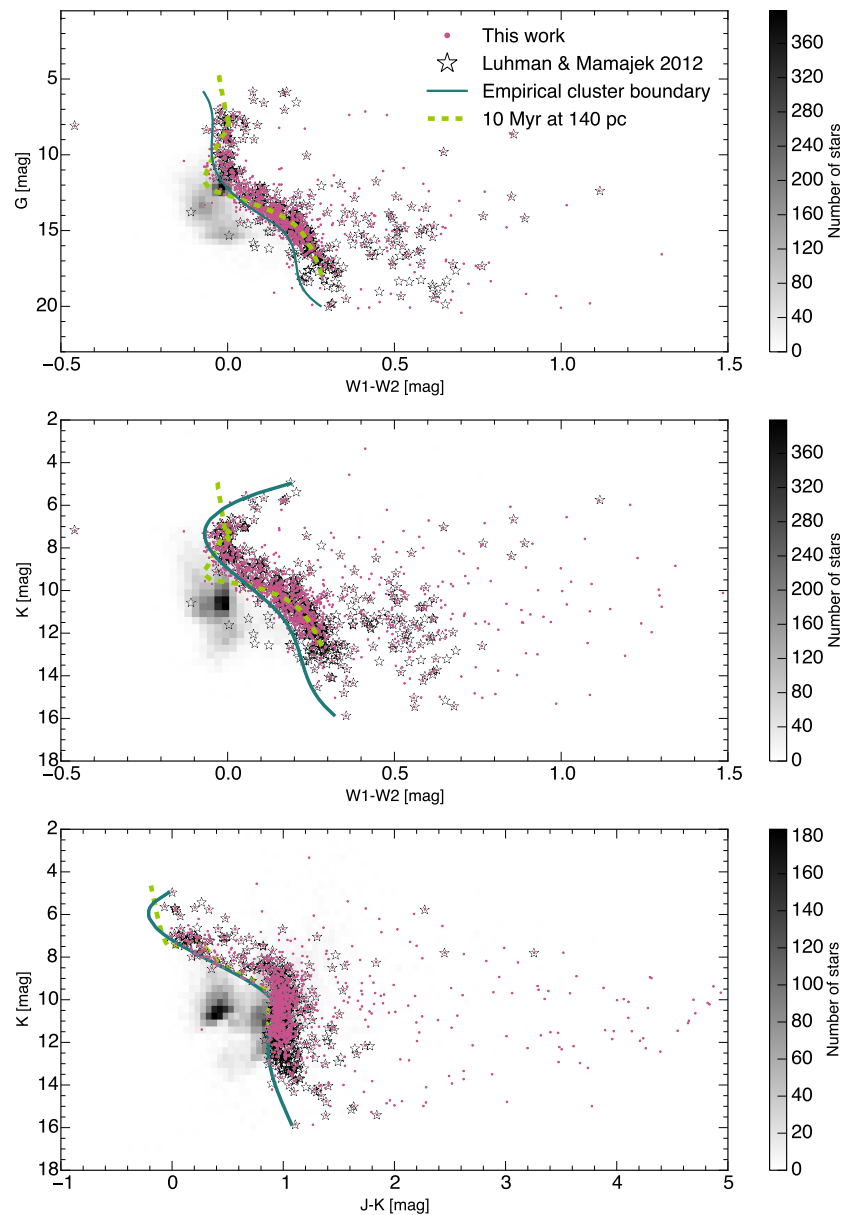


Figure 9.3: Hess diagrams for stars observed during Campaign 2 of the *K2* mission. Overplotted in purple is the sample of young stars considered here, and the Luhman & Mamajek (2012) sample is depicted with black stars. Empirical fits to the cluster sequence in each CMD are shown in blue-green, shifted blueward to encompass 95% of a known young star reference sample. The yellow-green dashed curves show 10 Myr isochrones at 140 pc, illustrating why current models are inadequate for CMD cuts.

of planet around *single* stars). In principle, the prevalence of planets around single stars has implications for planet formation and migration theories that are distinct from the corresponding rates around multiple star systems. Thus, to isolate a single astrophysical question of interest, it is preferable to separate singles and multiples to whatever extent possible.

However, information about the multiplicity of our sample is incomplete. Moreover, binaries with mass ratios close to unity are the most easily detected by any method, so that multiplicity information is highly biased and knowledge about binaries with mass ratios far from unity is most incomplete. While there are avenues for attempting to clean our sample of binaries, especially given the attention paid to the region by direct imaging surveys (e.g. Kraus & Hillenbrand, 2009b) or the possibility to identify binaries within the *K2* data itself (through e.g. the presence of multiple distinct peaks in a periodogram indicating the rotation periods of two stars within the photometric aperture), we leave this effort to a future study. Thus, as other occurrence rate studies utilizing *Kepler* data have done, we ignore the effects of multiplicity for now. It is worth noting however, that the multiplicity characteristics of very young stars may be fundamentally different than those of field stars due to, e.g., early dynamical ejections or disruption by the galactic tidal field at later times (Weinberg et al., 1987). There is mixed evidence that binary fractions in young stars may be higher than the rates measured in the field, but notably these results may depend on stellar mass and the particular star-forming region probed (see Duchêne & Kraus, 2013, for a review).

9.2.5 Crowded fields

It is worth noting that the galactic latitudes observed by *K2* generally have higher surface densities of stars than the original *Kepler* field, which was selected to partially mitigate confusion from neighboring stars. Thus, there is an intrinsic risk to comparing occurrence rates derived from *K2* to those found by *Kepler*, not only because of the reduced sensitivity but also because of the different average amounts of contaminating light from neighboring sources between the two missions. For some stars in our sample, our aperture optimization algorithm will produce apertures containing more than one source. In the present study, we have not treated these cases any differently, but note it here as an additional source of uncertainty. One method to handle such cases, which we intend to explore in a future version of this work, is to prevent the adaptive apertures from growing beyond some threshold number of pixels in order to avoid enclosing flux from a neighbor.

9.2.6 Final selection scheme

For each of the 13401 targets in C2 we made our final determination on whether to include it in our sample of young stars based on the following criteria:

1. The star must have proper motions consistent with membership at $>50\%$ probability.
2. The star must lie above, or within $1 - \sigma$ of, the empirically determined lower boundary to the cluster sequence in all three of the following CMDs: $(W1 - W2)-G$, $(J - K)-K$, and $(W1 - W2)-K$.
3. The star may not have a distance, as determined from its *Gaia* DR1 trigonometric parallax, that is closer than 83 pc or farther than 205 pc.
4. Regardless of proper motions and CMD positions, a star is included if it is in the known young star reference sample described above (i.e. shows spectroscopic youth indicators).

After these selections we are left with a sample of 1070 stars, 547 of which are part of our known young star reference sample.

9.2.7 Stellar characterization

The depth of a transit signal is equal to the relative area of the star blocked by a planet as it crosses the stellar surface. In order to convert a transit depth to a planet size, one must know the size of the star being transited. The sizes of dwarf stars are relatively well known, with a multitude of reliable empirical relations between observable quantities (e.g. colors) and stellar radii in the literature that are calibrated using benchmark stars with directly measured radii from interferometry or eclipsing binaries. For the young stars in our sample, no such empirical relations exist, evolutionary models are largely uncalibrated (see Chapters III–VI), and thus the uncertainties on stellar radii are significantly larger than those for dwarfs.

The factors potentially impacting the accurate determination of stellar radii at the age of Upper Sco are many. Large luminosity spreads ($\gtrsim 1$ dex) for stars of a given mass (and particularly low-mass stars) are frequently observed in pre-MS populations (e.g. Herczeg & Hillenbrand, 2015, and see Figure 9.4). Some have suggested the spreads may represent intrinsic age spreads, i.e. distinct star formation episodes, and it has been shown for the Orion Nebula Cluster that luminosity spreads can not

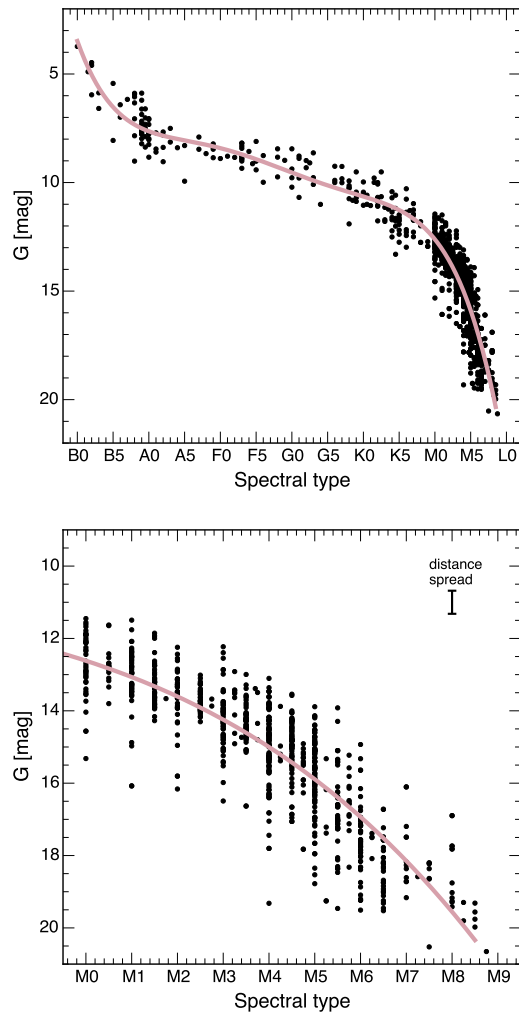


Figure 9.4: *Gaia* G magnitude as a function of spectral type for Upper Sco members across a wide mass range (top) and for M-type stars only (bottom). Spectral types have been source from Preibisch et al. (2002), Slesnick et al. (2008), Luhman & Mamajek (2012), and Rizzuto et al. (2015). A 5th order polynomial fit is shown by the pink line. The standard error in the distance modulus from a normal distribution of distances with center 140 pc and width 20 pc is shown by the errorbar.

be explained through distance effects, unresolved binaries, or variable extinction alone (Da Rio et al., 2010). Photometric variability, which is relatively large for pre-MS stars, is also incapable of reproducing the magnitudes of observed luminosity spreads (Burningham et al., 2005). There is evidence that the more rapidly a pre-MS star rotates the more overluminous it appears relative to the cluster sequence (Littlefair et al., 2011). As such, even at a fixed stellar mass, our sensitivity to planets of a given size and period is a complicated function of brightness, rotation rate, and photometric variability amplitude.

Moreover, the physical extent of Upper Sco is considerable (perhaps as large as 30% the mean distance), based on the width of the association on the sky. As a result, the distance to any individual star in the cluster carries significant uncertainty so that determining radii by assuming the mean cluster distance and calculating luminosities does not alleviate the issue. Thus, it is not unreasonable to presume that any given star in our sample may have a fractional uncertainty in its radius as large as 30%. Trigonometric parallaxes for the fainter members of Upper Sco will become available with the final *Gaia* data release, helping to reduce the radius uncertainties due to distance spreads.

Out of necessity, two other model-dependent parameters are calculated for each of the stars in our sample: temperature and mass. Temperatures are used to calculate realistic limb-darkening coefficients for injected transit signals, and the results of our study are relatively insensitive to this step of the procedure. Stellar masses are used to calculate the semi-major axis for an injected transit of a given period, which is then translated into the transit duration as parameterized by the unitless quantity a/R_* . The SNR of a recovered transit injection depends primarily on the transit depth, secondarily on its duration, and very little on the specific limb darkening parameters. Overall, the uncertainties in a/R_* are relatively unimportant with respect to our ultimate goal of determining the prevalence of planets of a given size and orbital period. For this work, stellar radii remain the largest source of uncertainty.

Stars in the vicinity of Upper Sco are extinguished to varying degrees due to the surrounding nebula. Variable extinction poses a problem in determining accurate radii when converting from colors to physical parameters. In Figure 9.5 we show the visual extinction in magnitudes as measured by three large surveys of GKM members of Upper Sco. The median value reported by these surveys combined is $A_V = 0.7$ mag. Notably, a more careful analysis might calculate the extinction

of each target individually from photometry, but we leave this task to future work. Here, reddening is implicitly accounted for at the stellar characterization stage by approximating the intrinsic $(G - K)$ color for each star based on its G magnitude and using an empirical fit to the $(G - K)$ vs. G cluster sequence (Figure 9.6). Because a sizable number of stars in Upper Sco suffer from very little extinction, this methodology can produce reliable results. However, in assuming a one-to-one relationship between color and temperature/mass/radius one does not account for the large spread in G magnitudes at a given color or spectral type (see Figure 9.4). We note that some, but not all of this luminosity spread is due to distance, which would be implicitly accounted for when converting the $(G - K)$ colors to an intrinsic color scale. However, some of the luminosity spread is likely genuine, and implies a spread in radii at a given mass due to e.g. rotation, accretion history, or a range of stellar ages.

We determined model-dependent stellar radii, masses, and temperature from interpolation of $(G - K)$ color relations predicted by a solar-metallicity 10 Myr PARSECv1.2S isochrone (Bressan et al., 2012; Chen et al., 2014) with no extinction. The $(G - K)$ color provides good dynamic range across the mass range of interest to us and relations between this color and mass, radius, and temperature are all monotonic and single-valued. In a future version of this work, we will investigate the effects of using different model sets and assuming different values for the age of Upper Sco. Along with the model-dependent stellar parameters, we have also determined rotation periods directly from the *K2* light curves for each star in our sample (Rebull et al., *in prep.*). The distribution of rotation periods among stars in our sample is shown in Figure 9.7. We use these rotation periods in § 9.3.5 to investigate the sensitivity of our transit search pipeline as a function of stellar variability timescale.

9.3 Survey design

9.3.1 Aperture photometry and instrumental systematics corrections

For each source in our survey, *Kepler* target pixel files were downloaded from the the Mikulski Archive for Space Telescopes (MAST) and aperture photometry was extracted from the pixel-level data using the publicly available `k2PHOT` code⁴, described in Crossfield et al. (2015) and Crossfield et al. (2016) and Petigura et al. (2015) and Petigura et al. (2016).

⁴<https://github.com/petigura/k2phot>

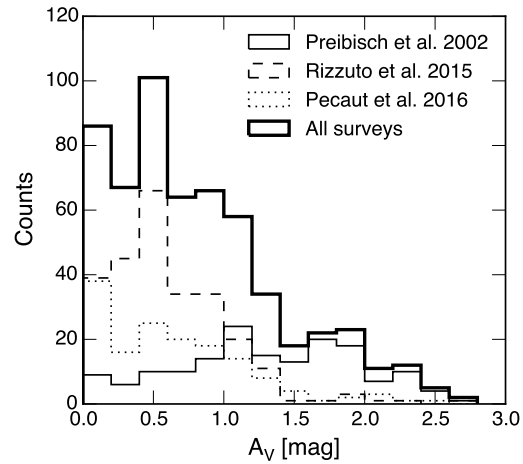


Figure 9.5: Histogram of the visual extinction in magnitudes as reported by three large surveys of GKM type members of Upper Sco.

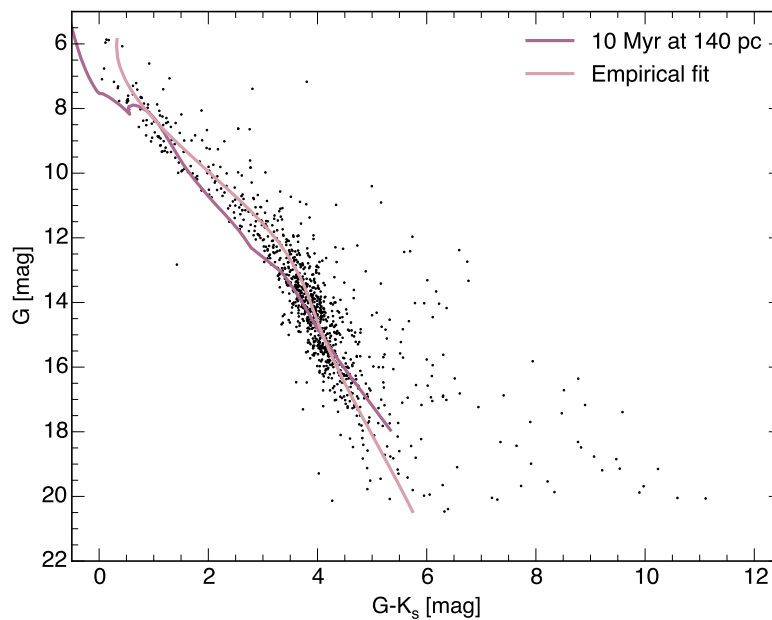


Figure 9.6: $(G - K_s)$ vs. G color-magnitude diagram for our sample, showing our empirical fit to the cluster sequence (pink) and the PARSECv1.2S 10 Myr isochrone (purple). We use the empirical fit to approximate the intrinsic $(G - K_s)$ colors of our stars, some of which have disks and all of which are variably reddened. The approximate intrinsic $(G - K_s)$ color is then used to determine radius, mass, and temperature for our stars based on the PARSECv1.2S models.

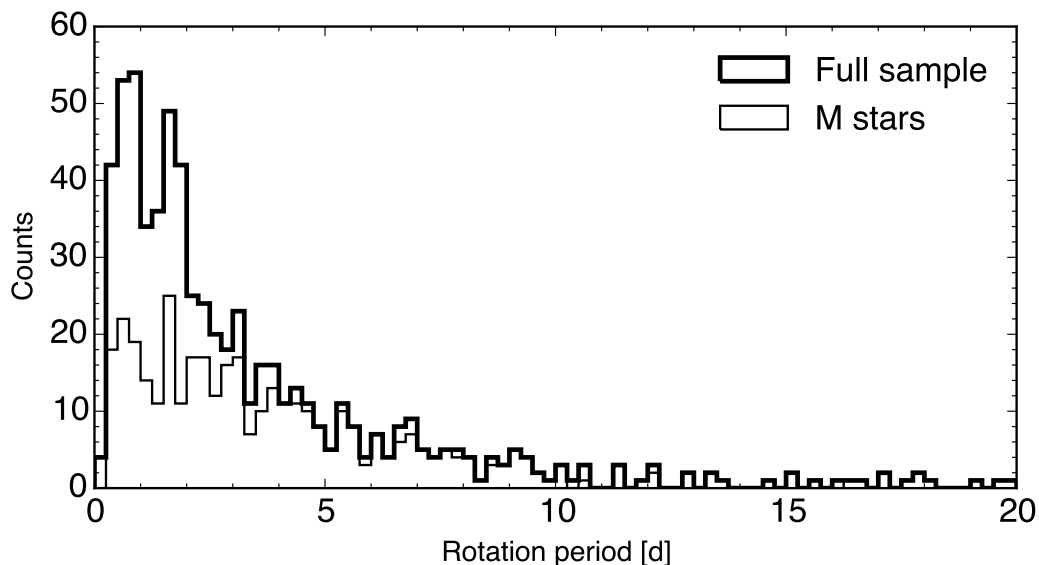


Figure 9.7: Histogram of stellar rotation periods, determined from *K2* photometry (Rebull et al., *in prep.*), for our sample. The median rotation period of the entire sample is 2.1 d, and 3.3 d for the M-type stars (here defined as $11 \leq G \leq 15$ mag).

During a given *K2* campaign, the spacecraft pointing is stabilized in the pitch and yaw dimensions by the remaining functional gyroscopes. Along the boresight, the spacecraft roll is partially balanced by solar radiation pressure when the telescope is pointed towards the ecliptic. The configuration represents an unstable equilibrium and as a result the variable solar radiation pressure imparted on the spacecraft torques the telescope so that measurable roll angle variations occur over short timescales. Consequently, a star observed by *K2* will drift across the detector at a rate of ~ 0.2 pixel hr^{-1} . Thruster firings every ~ 6 hrs will bring a given star back to its nominal detector position, but inter-pixel sensitivity variations are significant and as a result raw aperture photometry from *K2* possesses sawtooth-like, percent-level systematic variations from the roll drift. A star’s apparent brightness variability, as measured with *K2*, is thus composed of three main components: (1) the pointing-related systematics described above, (2) intrinsic astrophysical variability (or the “time-dependent” component), and (3) long-term variability of a systematic nature due to e.g. changing background flux levels. The first two variability components represent the most difficult obstacles to overcome in a search for transiting planets.

Knowledge of the precise spacecraft orientation is required to remove, or “detrend”, the position-correlated systematic artifacts from the photometry. In $\kappa 2_{\text{PHOT}}$, orientation is established by analyzing the positions of ≈ 100 bright but unsaturated

stars ($K_p \approx 12$ mag) on a representative output channel. For each measurement of each reference star, we solve for the affine transformation that maps that frame to an arbitrary reference frame. The sequence of transformations from all of the reference stars is then used to transform a reference pixel coordinate to a reference frame.

Photometry is extracted from stationary apertures containing a specified number of pixels, N_{pix} . The shape of the aperture is determined by an algorithm that encloses the largest amount of flux (while not growing larger than N_{pix} in area) from a composite image constructed from the 90th percentile intensity values of all frames within a campaign. As the spacecraft rolls throughout the campaign, stars near the edge of the FOV will experience the largest shifts in pixel position and be smeared out in the composite image described above. The aperture optimization algorithm attempts to mitigate against aperture losses in these cases. The aperture is constructed by selecting the pixel closest to the expected WCS coordinates of a given target and iteratively adding the brightest adjacent pixels. The total number of pixels in the aperture, N_{pix} , is actually a free parameter which is optimized to minimize noise on three-hour timescales. Systematic noise increases with decreasing aperture size (due to aperture losses), while background noise increases with increasing aperture size. The size optimization thus acts to balance the competing effects. The smallest apertures constructed contain 9 pixels.

After photometric extraction we have a sequence of flux measurements as a function of time and position on the detector. We simultaneously modeled the position-dependent and time-dependent variability of each star using a Gaussian process with a squared-exponential covariance kernel, using the $\kappa 2\text{sc}$ package in PYTHON (Aigrain et al., 2016)⁵. Special care is required in handling periodically variable stars, as most stars in our sample are. The $\kappa 2\text{sc}$ package handles such cases by replacing the time-dependent component of the Gaussian process model with a quasi-periodic covariance function, characterized by the period (determined *a priori* from a Lomb-Scargle periodogram) and parameters describing the amplitude, inverse length scale, and evolutionary timescale of the periodic variations.

9.3.2 Transit search pipeline

Our transit search was performed using the TERRA pipeline, which is described in detail in Petigura et al. (2013). TERRA searches the photometric time series for periodic box-shaped signals by evaluating the signal-to-noise ratio (SNR) over

⁵<https://github.com/OxES/k2sc>

a high-resolution grid in orbital period (P), epoch (t_0), and transit duration (ΔT). For the *K2* photometry considered here, the grid search is performed over an orbital period range of 0.5–35 d. Candidate transit signals that meet an SNR threshold are fit with an analytic Mandel & Agol (2002) transit model, the parameters of which are recorded and logged. To handle cases where multiple transiting planets may be present, TERRA iteratively searches the lightcurves by subtracting the best fit model for the primary signal (i.e. the transit with the highest SNR) and running the software again until no significant signals remain.

9.3.3 Manual vetting

We visually inspected all candidate transit signals found by TERRA with $\text{SNR} > 7.5$ to reach a final assessment on the candidate status of each target. Diagnostic figures were created for each candidate to search for depth variations between odd- and even-numbered transits (i.e. secondary eclipses), which would indicate an eclipsing binary rather than a *bona fide* transiting planet. Additionally, transit-like signals found at the same period as that of the stellar variability are rejected as planet candidates. Such cases are likely associated either with out-of-eclipse modulations (e.g. ellipsoidal modulation) frequently observed in eclipsing binaries or, for young stars like those in our sample, a class of optical variability that may be due to material orbiting at the corotation radius (Stauffer et al., 2017; David et al., 2017). In total, we assessed 872 signals of interest associated with 397 unique stars. Of these, 9 are eclipsing binaries and we find only one convincing and secure transiting planet, the previously published K2-33 b (David et al., 2016c; Mann et al., 2016c).

9.3.4 Transit injection and recovery tests

With a confident accounting of the number of genuine transiting planets in our sample (one, in this case), we turn to carefully measuring the sensitivity of the light curves and our transit search pipeline. The survey completeness in a specified domain of planet size and orbital period is a key parameter in determining the overall occurrence of planets in that region of parameter space. To test the performance and measure the completeness of our planet search pipeline we carried out a suite of transit injection and recovery tests. We used the BATMAN software package (Kreidberg, 2015), based on the Mandel & Agol (2002) analytic transit models, to generate synthetic transit signals which were integrated to the *K2* cadence of 1766 seconds and injected through multiplication with the raw photometry.

Orbital periods, P , between 0.5–35 days were drawn from a log-uniform distribution,

Table 9.2: Parameter distributions of injected transit signals

Parameter	Units	Distribution
Orbital period, P	log(days)	$U(\log 0.5, \log 35)$
Reference transit time, T_0	days	$U(0, P)$
Radius ratio, R_P/R_*	dex	$U(\log 0.005, \log 0.2)$
Impact parameter, b	...	$U(0,1)$

U : uniform distribution

and the reference transit time, T_0 , correspondingly drawn from a uniform distribution between zero and the orbital period. The corresponding scaled semimajor axis, a/R_* , was calculated from Kepler’s third law based on the orbital period and the model-dependent mass derived in § 9.2.7. The radius ratio was drawn from a log-uniform distribution, sampling planets with radii between 0.5–20% the stellar radius. The impact parameter, b , was drawn from a uniform distribution between zero and one to ensure a transiting geometry. All injected planets were assumed to have zero eccentricity, and the inclination could be calculated from the equation $\cos i = b \times R_*/a$. Realistic quadratic limb-darkening coefficients in the *Kepler* bandpass were calculated from the Claret et al. (2012) and Claret et al. (2013) tables, interpolated to the specific effective temperature of each star determined in § 9.2.7 and assuming a surface gravity of $\log g = 4.0$ appropriate for most pre-main-sequence stars. Multiple transiting systems were not injected or considered. In Table 9.2 we summarize the distributions from which our injected transit parameters were drawn.

We performed 200 injections per star in our sample. In a forthcoming analysis, we will present results from these 214,000 total injections. In the present study, we present preliminary results from approximately half of our sample (564 stars) and we will compute an occurrence rate of large planets based on a restricted sample of 278 M-type stars. An injected transit signal was considered to be recovered if the recovered period was within 2% of the injected period, following the scheme of Aigrain et al. (2016).

9.3.5 Survey completeness

As shown in Figure 9.9, our survey completeness is a multivariate function of brightness, variability timescale, variability amplitude, and even detector position (because the most precise light curves are obtained near the center of the FOV, where roll variations are smallest). Some of these parameters are also covariant, such as

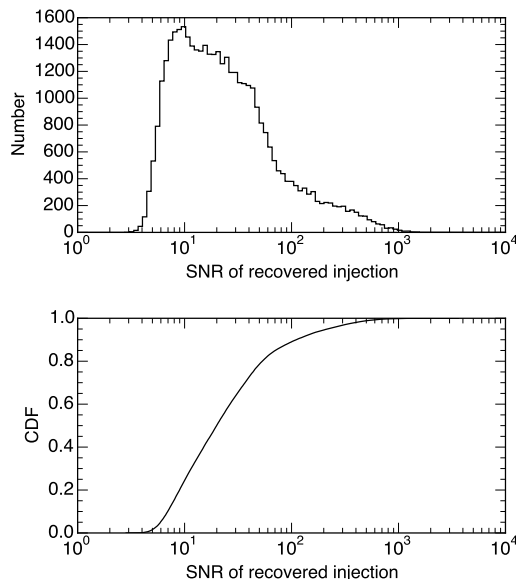


Figure 9.8: Histogram of the signal-to-noise ratios (SNR) of recovered transit injections (top) and the cumulative distribution function (CDF) for SNR.

brightness and the variability amplitude and timescale (i.e. fainter stars in our sample are more likely to show variability due to starspots). We have explored the sensitivity of the injection/recovery tests to brightness, stellar rotation rate, transit depth, and planet orbital period. In Figure 9.9 we show a variety of completeness maps for different subsets of our survey sample. Completeness for stars fainter and brighter than $G = 14$ mag does not vary qualitatively over the $P - R_P$ domain, but quantitatively there is diminished completeness in all cells for fainter stars. The contrast is greatest for small planets. The decline in detection efficiency of small planets towards fainter stars is easily understood as a consequence of photon noise: transits become washed out when the transit depth is comparable to the photometric noise level, which is higher for fainter stars. Overall, sensitivity is low for periods > 20 d due to the fact that these planets can transit at most three times over the ~ 78 d campaign. The two effects above conspire to make sensitivity lowest for small planets on longer-period orbits.

As a function of rotation period, there are clear trends in the completeness of our survey. In a given domain of $P - R_P$, detection efficiency is higher for more slowly rotating stars. It is not surprising that our transit search pipeline struggles to recover transits in rapidly rotating stars ($P_{\text{rot}} < 1$ d). As the ratio of the transit period to the rotation period approaches unity, the GP model is less efficient at identifying outliers and tends to overfit the observations in transit, especially when the transit depth is

shallow. This issue is discussed further in Aigrain et al. (2016). The problem is less of a concern for deeper transits, particularly if they are deep relative to the underlying stellar variability. Rapid rotators constitute a sizable fraction of our sample, as shown in Figure 9.7, so properly understanding the completeness of our pipeline on these variable stars is an important step in determining accurate occurrence rates. In a future version of this work, we will more thoroughly investigate how completeness is a function of a star's variability amplitude and detector position.

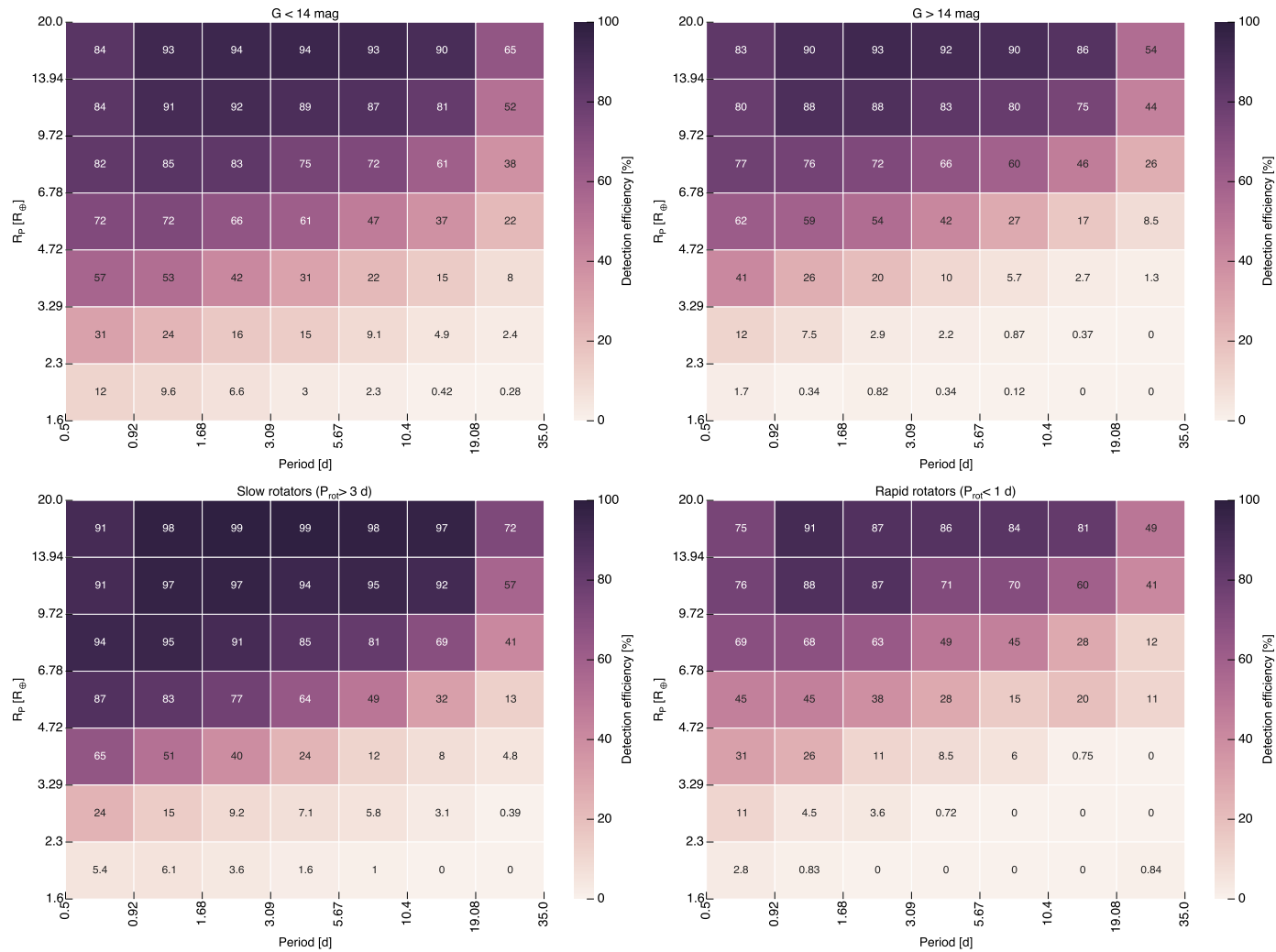


Figure 9.9: Survey completeness in period-planet radius domain for stars brighter and fainter $G = 14$ mag (top left and top right, respectively), as well as slowly rotating (bottom left) and rapidly rotating (bottom right) stars brighter than $G = 15$ mag.

In Figure 9.10, we show our survey completeness for the late-type stars in the $P - (R_P/R_*)$ and $P - R_P$ domains. It is from this subsample that we determine occurrence rates in § 9.4. Converting from transit depth to planet size is a model-dependent step in our work that carries as yet undetermined uncertainties. Nevertheless, what is apparent from these figures is that our survey is insensitive to the populous class of sub-Neptune-sized exoplanets. This is a consequence of the facts that (1) stars have significantly larger radii at younger ages ($\sim 1R_\odot$, as a typical value for late-type stars) and (2) at a distance of 140 pc the late-type stars in Upper Sco are relatively faint in the *Kepler* bandpass.

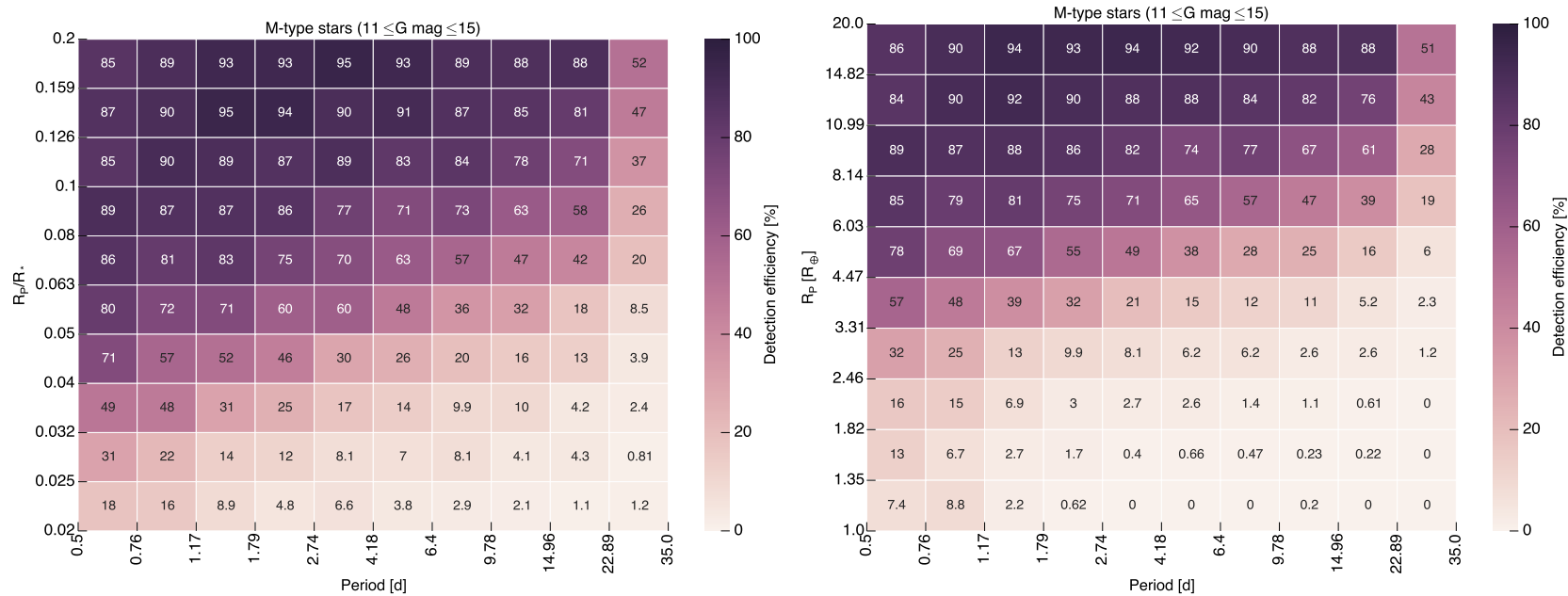


Figure 9.10: Survey completeness in the period-fractional radius domain (left) and the period-planet radius domain (right) for the M-type stars in our sample.

9.4 Determination of planet occurrence rates

Planet occurrence rates are typically cast as the number of planets, in a given domain of planet size and orbital period, per star. Typically, the stars considered in occurrence rate studies are well-defined in the sense that they have a limited range of parameters. This allows investigators to isolate different astrophysical questions of interest, and measure differential occurrence rates as a function of, e.g., stellar mass. In the present study, since the stars are young and active, there are several mass-dependent systematic effects on the completeness of our survey (as discussed in § 9.3.5). Although we surveyed all known and candidate young stars observed during *K2* C2, the only secure transiting planet we detected orbits a low-mass star. Consequently, we focus the remainder of our discussion on the determination of planet occurrence rates among the low-mass stars that are known or likely members of Upper Sco.

This choice is made for the following reasons: (1) low-mass stars (here defined as $M_* \lesssim 0.8 M_\odot$) are the most numerous in a coeval stellar population like Upper Sco, thereby providing a large sample from which meaningful statistical conclusions can be drawn; (2) low-mass stars are known to host compact planetary systems in abundance, and thus a more significant number of planets are expected to be found if field occurrence rates hold at younger ages; and importantly (3) the only planet discovered in our survey, *K2-33 b*, transits a low-mass star. Thus, while limits on the frequency of close-in planets can be placed in other regions of stellar parameter space, an actual rate can be determined for low-mass stars, albeit with large uncertainties.

The planet occurrence rate, f , within a two-dimensional parameter space of planet size, R_P , and orbital period, P , is

$$f(P, R_P) = n_* \sum_{i=1}^{n_P} \frac{(a/R_*)_i}{C_i}, \quad (9.1)$$

where the summation is performed over all detected planets with an SNR > 7.5 , the a/R_* term in the numerator corrects for planets of a similar orbital separation that are missed due to non-transiting geometries, n_* is the number of stars surveyed, and C_i is the completeness in the i -th cell. The completeness here is simply defined as the ratio of the number of transit injections in a specified domain of $P - R_P$ recovered at SNR > 7.5 to the total number of injections in the same domain. Approximately 13% of our injections were recovered with an SNR less than this threshold, and

would thus not count towards the numerator of the completeness calculation. For comparison, we detected K2-33 b with our pipeline at an SNR of 11.43.

Given that our survey detected only one planet, we can determine the occurrence rate of analogous planets over a small cell in $P - R_P$ space and place upper limits on the occurrence rates of other kinds of planets. Alternatively, we can consider a larger cell which encompasses not only our detected planet but also planets encompassing a wider range in $P - R_P$ space. This second approach allows us to make a more meaningful comparison to expectations from field occurrence rates, as a larger number of planets would be expected to be found.

In a large cell spanning orbital periods of 1–10 d and planet sizes of 4–12 R_{\oplus} (Neptune- to Jupiter-sized planets, approximately), we find that our survey is $64.8 \pm 1.1\%$ complete for stars between $11 \leq G \leq 15$ mag, where the completeness error has been calculated from Poisson statistics. The multiplicative factor correcting for non-transiting planets in this cell is given by the average value of a/R_* as calculated from the assigned stellar masses and radii, which we find to be 10.9 ± 0.3 . Given that we found a single planet matching these criteria ($P \approx 5.4$ d, $R_P \approx 5.8 R_{\oplus}$), the overall occurrence rate of large planet in short periods around young stars would be $f \approx 0.0296$ planets per star, where we are $64.6 \pm 1.1\%$ complete in this range. If we invert the problem, we can answer the following question using binomial statistics: assuming our measured occurrence rate is accurate, how probable is it that we would detect a single planet in our survey, after correcting for completeness and non-transiting planets? In our survey of 573 late-type stars, we find only ~ 52 are expected to be aligned such that their planets would transit in the period range considered. Our survey would only be sensitive to ~ 34 of these putative planet hosts, and so the probability we would detect exactly one planet amongst this sample is $\approx 37\%$.

In Table 9.3, we present occurrence rate calculations for a variety of large cells whose boundaries are chosen to match those of Dressing & Charbonneau (2013), hereafter DC13, or Dressing & Charbonneau (2015), hereafter DC15. We note that these are preliminary values, based on injection/recovery simulations for approximately half of our total sample. However, in the denominator of the occurrence rate equation we use the total number of low-mass stars in our sample with brightness $11 \leq G \leq 15$ mag, which is 573. While the number of secure detections will not change, nor the average a/R_* values in a given cell, it is possible there will be some fluctuations in completeness as more simulations are considered. Nevertheless, we do not expect

Table 9.3: Planet occurrence for young low-mass stars

$R_P(R_\oplus)$	0.68–10 days	1.7–5.5 days	1.7–18.2 days
4.0–6.0	$0.0404^{+0.0906}_{-0.0106}$ (46.4±1.6%)	$0.0329^{+0.0729}_{-0.0091}$ (43.8±2.5%)	$0.0864^{+0.1837}_{-0.0210}$ (32.8±1.7%)
4.0–8.0	$0.0332^{+0.0726}_{-0.0095}$ (56.4±1.2%)	$0.0260^{+0.0582}_{-0.0072}$ (55.4±1.9%)	$0.0636^{+0.1400}_{-0.0158}$ (44.6±1.3%)
4.0–11.3	$0.0288^{+0.0649}_{-0.0079}$ (64.9±1.0%)	$0.0226^{+0.0504}_{-0.0064}$ (63.8±1.5%)	$0.0514^{+0.1119}_{-0.0138}$ (55.1±1.1%)
4.0–16.0	$0.0264^{+0.0600}_{-0.0071}$ (71.0±0.9%)	$0.0204^{+0.0466}_{-0.0056}$ (70.4±1.3%)	$0.0448^{+0.0974}_{-0.0124}$ (63.2±0.9%)
4.0–22.6	$0.0253^{+0.0568}_{-0.0070}$ (74.0±0.8%)	$0.0195^{+0.0437}_{-0.0055}$ (73.9±1.2%)	$0.0421^{+0.0943}_{-0.0110}$ (67.4±0.9%)
12–22.6	<0.0011 (91.0±1.4%)	<0.0008 (92.1±2.1%)	<0.0017 (89.8±1.5%)

Note: Occurrence rates expressed in planets per star. Values in parentheses indicate completeness in the corresponding cell.

these values to change drastically.

To determine the error on the occurrence rate in a given cell we calculated the binomial distribution of drawing n_{pl} planets from n_{eff} stars, where in our study n_{pl} is uniformly 1 for cells encompassing K2-33 b. The 1σ errors were then computed from the 15.9 and 84.1 percentile levels in the cumulative binomial distribution, as in (Howard et al., 2012). To calculate upper limits to planet occurrence rates in regions of parameter space where no planets were found we perform the same procedure but replacing n_{pl} with zero and computing the limit as the 95th percentile level of the cumulative binomial distribution, as in (Bowler et al., 2015).

Broadly speaking, what we find is that the occurrence of close-in ($P < 10$ d), large ($R_P > 4\text{--}12R_\oplus$) planets around low-mass stars is significantly higher than the rate expected from studies of field stars (Dressing & Charbonneau, 2013). There are important caveats to this result, however. Notably, we are dealing with a sample size of a few hundred stars compared to samples of a few thousand stars in the field star studies. Perhaps most importantly, it is unclear whether K2-33 b is truly a fully-formed planet larger than Neptune (an intrinsically rare class of planet around low-mass stars) or whether this young planet will undergo significant evolution in its radius through e.g. contraction and/or photoevaporative mass loss. Presently, the planet’s size is approximately $5.8 R_\oplus$, but if it contracts by $\sim 30\text{--}50\%$ over the next several hundred Myr then the planet would be in a region of parameter space that is at least an order of magnitude more populous at field ages. Preliminary simulations using the MESA toolkit suggest that fractional radius changes of this size may not be unreasonable for close-in Neptune-sized planets (Chen & Rogers, *in prep.*). Thus, it is possible that K2-33 b is a sub-Neptune progenitor. One way to test this hypothesis is to measure the rate of atmospheric mass-loss through ultraviolet transit transmission spectroscopy (Benneke et al., *in prep.*).

9.4.1 Expected planet yields

The occurrence rates of transiting planets around low-mass field stars observed during the *Kepler* prime mission were measured in DC13 and DC15. Both studies considered dwarf stars cooler than 4000 K. Broadly speaking, those authors found that close-in planets smaller than $3 R_{\oplus}$ are common, but that occurrence rates drop rather dramatically for larger planets. From Table 4 of DC15 we calculated the number of planets per star in the period range of 0.5–18.2 d for varying planet sizes. We find that in this restricted period range, one expects 0.78–0.96 planets per star in the radius range $0.5 \leq R_P/R_{\oplus} \leq 3$, but only 0.04–0.05 planets per star for $3\text{--}4 R_{\oplus}$ planets. Note that the ranges quoted here reflect the different occurrence rates quoted in DC15 for different stellar radius prescriptions. If we consider larger planets, then the results of DC13 suggest that in the orbital period range of 0.68–10 d, there are approximately 0.014 planets per star in the radius range of $4\text{--}22.6 R_{\oplus}$, where our survey is more complete.

Of course, only a fraction of planets transit and only a fraction of these would be detected by our survey, so in order to calculate the expected yield we must correct for completeness and the geometric transit probabilities. Thus, our expected yield of detectable transiting planets within our data, if the field occurrence rates are assumed to hold at young ages, is given by rearranging Eq. 9.1:

$$n_P = n_* \sum_i^{n_{\text{cells}}} \frac{f(P, R_P)_i C_i}{(a/R_*)_i}, \quad (9.2)$$

where the summation is performed over all $(P - R_P)$ cells of interest. Using the exact occurrence rates and cell divisions from Table 4 of DC15, we calculated the total number of planets expected within each cell given the completeness and (a/R_*) values appropriate for our survey.

From these field occurrence rates, we find that we would expect to find in our survey <1 planet (≈ 0.4 , precisely) in the radius range $0.5 \leq R_P/R_{\oplus} \leq 3$ with orbital periods between 0.5–18.2 d. In the same period range, we again expect <1 planet (≈ 0.2) with a radius $3 \leq R_P/R_{\oplus} \leq 4$ to be found in our survey. For larger planets, we must use the rates published in DC13. In the period range of 0.68–10 d, the number of planets with R_P in the range $4\text{--}22.6 R_{\oplus}$ that we expect in our survey is 0.57. Thus, in each of the various parameter spaces considered we expect <1 planet in our survey. This can be understood as a result of our low completeness for small planets (which

are intrinsically common) and the intrinsic rarity of large close-in planets around low-mass stars (despite our survey's high completeness).

Our detection of a single, secure transiting planet in our survey of young stars is marginally inconsistent with expectations from field occurrence rates and the sensitivity of the *K2* C2 data. One might be tempted to interpret the detection of K2-33 at all as a possible indication of an overabundance of large planets close in to young, low-mass stars. This might be consistent with a picture in which highly irradiated planets with substantial gaseous envelopes undergo sustained atmospheric mass loss at early evolutionary stages. However, given only one detection it is difficult to disentangle genuine evolutionary effects from statistical fluctuations and observational biases that may have allowed us to discover an unusually large planet first.

9.5 Discussion

Several authors have previously studied the roles of stellar age and environment on the measured occurrence rates of exoplanets, through both the transit and radial velocity (RV) detection methods. Gilliland et al. (2000) carried out the first dedicated search for transiting planets within a cluster, using *Hubble Space Telescope* photometry of tens of thousands of stars in the globular cluster 47 Tucanae. With no detections (compared to an expected ~ 17), those authors suggested the occurrence of close-in giant planets in that cluster may be fundamentally lower than the rate measured for field stars. However, that result was reassessed by Masuda & Winn (2017), who argued that the null result is consistent with expectations from field occurrence rates after accounting for stellar mass-dependent effects and the low observed rate of transiting giant planets from *Kepler*. From *Kepler* observations of the Gyr-old solar-metallicity open cluster NGC6811, Meibom et al. (2013) determined the occurrence rate of transiting planets smaller than Neptune to be equivalent for open clusters and field stars. Studies of the solar-age cluster M67 have concluded that giant planet occurrence, as measured by RVs, in the open cluster is in agreement with field statistics but that hot Jupiters seem to be more common in that cluster than in the field (Brucalassi et al., 2016; Brucalassi et al., 2017).

With the advent of *K2*, we are now able to measure the occurrence rates of transiting planets around stars much younger than previously studied. The unprecedented nature of these data sets can not be overstated, in terms of the number of members surveyed, the photometric precision achieved, and the cadence and time baseline

observed. There is already preliminary evidence from *K2* data that by the age of the Hyades/Praesepe ($\sim 700\text{--}900$ Myr) the occurrence rates of small planets are consistent with those measured for field stars (Mann et al., 2017). At the much younger age of Upper Sco ($5\text{--}10$ Myr), we find a rate that is higher than expectations from the field, though with uncertainties that are not yet fully quantified. It is also critical to note that at such young ages, planet radii may not have yet equilibrated. Thus, direct comparisons with field occurrence rates may only be appropriate to the degree that the radii of close-in planets remain constant between ~ 5 Myr and ~ 5 Gyr.

ACKNOWLEDGMENTS

T.J.D. would like to thank Adric Riedel for contributing the section on the proper motion selection of cluster candidates.

BIBLIOGRAPHY

- Abt, H. A., 1958, *ApJ*, 128, 139
- , 1985, *ApJ*, 294, L103
- Abt, H. A., & Levato, H., 1978, *PASP*, 90, 201
- Abt, H. A., Levato, H., & Grosso, M., 2002, *ApJ*, 573, 359
- Aigrain, S., Pont, F., & Zucker, S., 2012, *MNRAS*, 419, 3147
- Aigrain, S., Hodgkin, S. T., Irwin, M. J., Lewis, J. R., & Roberts, S. J., 2015, *MNRAS*, 447, 2880
- Aigrain, S., Parviainen, H., & Pope, B. J. S., 2016, *MNRAS*, 459, 2408
- Allen, P. R., Trilling, D. E., Koerner, D. W., & Reid, I. N., 2003, *ApJ*, 595, 1222
- Allende Prieto, C., & Lambert, D. L., 1999, *A&A*, 352, 555
- ALMA Partnership, Brogan, C. L., Pérez, L. M., et al., 2015, *ApJ*, 808, L3, L3
- Alonso, R., Deeg, H. J., Hoyer, S., et al., 2015, *A&A*, 584, L8, L8
- Ambikasaran, S., Foreman-Mackey, D., Greengard, L., Hogg, D. W., & O’Neil, M., 2014, *ArXiv e-prints*
- Ammons, S. M., Robinson, S. E., Strader, J., et al., 2006, *ApJ*, 638, 1004
- Andersen, J., 1991, *A&A Rev.*, 3, 91
- Andersen, J., Clausen, J. V., & Nordstrom, B., 1980, in *IAU Symposium, Close Binary Stars: Observations and Interpretation*, ed. M. J. Plavec, D. M. Popper, & R. K. Ulrich, Vol. 88, 81
- Andersen, J., & Nordstrom, B., 1983, *A&AS*, 52, 471
- Andersen, J. M., & Korhonen, H., 2015, *MNRAS*, 448, 3053
- Anderson, E., & Francis, C., 2011, *VizieR Online Data Catalog*, 5137
- , 2012, *Astronomy Letters*, 38, 331
- Andrews, S. M., Wilner, D. J., Zhu, Z., et al., 2016, *ApJ*, 820, L40, L40
- Ansdell, M., Gaidos, E., Rappaport, S. A., et al., 2016, *ApJ*, 816, 69, 69
- Ardila, D., Martín, E., & Basri, G., 2000, *AJ*, 120, 479
- Armitage, P. J., 2011, *ARA&A*, 49, 195
- Armstrong, D. J., Kirk, J., Lam, K. W. F., et al., 2015, *A&A*, 579, A19, A19
- Artigau, É., Kouach, D., Donati, J.-F., et al., 2014, in *Proc. SPIE, Ground-based and Airborne Instrumentation for Astronomy V*, Vol. 9147, 914715

- Artiukhina, N. M., & Kalinina, E. P., 1970, *Trudy Gosudarstvennogo Astronomicheskogo Instituta*, 39, 111
- Asiain, R., Torra, J., & Figueras, F., 1997, *A&A*, 322, 147
- Baines, E. K., McAlister, H. A., ten Brummelaar, T. A., et al., 2008, *ApJ*, 680, 728-733, 728
- Baines, E. K., White, R. J., Huber, D., et al., 2012, *ApJ*, 761, 57, 57
- Baldwin, J. E., Haniff, C. A., Mackay, C. D., & Warner, P. J., 1986, *Nature*, 320, 595
- Balona, L. A., 1984, *MNRAS*, 211, 973
- , 1994, *MNRAS*, 268, 119
- Baraffe, I., Chabrier, G., Allard, F., & Hauschildt, P. H., 1998, *A&A*, 337, 403
- Baraffe, I., Chabrier, G., Barman, T. S., Allard, F., & Hauschildt, P. H., 2003, *A&A*, 402, 701
- Baraffe, I., Chabrier, G., & Gallardo, J., 2009, *ApJ*, 702, L27
- Baraffe, I., & Chabrier, G., 2010, *A&A*, 521, A44, A44
- Baraffe, I., Homeier, D., Allard, F., & Chabrier, G., 2015, *A&A*, 577, A42, A42
- Baranec, C., Riddle, R., Law, N. M., et al., 2014, *ApJ*, 790, L8, L8
- Barenfeld, S. A., Carpenter, J. M., Ricci, L., & Isella, A., 2016, *ApJ*, 827, 142, 142
- Barnes, J. R., Collier Cameron, A., Donati, J.-F., et al., 2005, *MNRAS*, 357, L1
- Barnes, J. W., van Eyken, J. C., Jackson, B. K., Ciardi, D. R., & Fortney, J. J., 2013, *ApJ*, 774, 53, 53
- Barrado y Navascues, D., & Stauffer, J. R., 1996, *A&A*, 310, 879
- Barrado y Navascués, D., Stauffer, J. R., Hartmann, L., & Balachandran, S. C., 1997, *ApJ*, 475, 313
- Barrado y Navascués, D., Stauffer, J. R., Song, I., & Caillault, J.-P., 1999, *ApJ*, 520, L123
- Basri, G., & Batalha, C., 1990, *ApJ*, 363, 654
- Bastian, N., Covey, K. R., & Meyer, M. R., 2010, *ARA&A*, 48, 339
- Batygin, K., Bodenheimer, P. H., & Laughlin, G. P., 2016, *ApJ*, 829, 114, 114
- Beeckmans, F., 1977, *A&A*, 60, 1
- Bell, C. P. M., Naylor, T., Mayne, N. J., Jeffries, R. D., & Littlefair, S. P., 2013, *MNRAS*, 434, 806
- Berta, Z. K., Irwin, J., & Charbonneau, D., 2013, *ApJ*, 775, 91, 91
- Bertiau, F. C., 1958, *ApJ*, 128, 533

- Bertone, E., Buzzoni, A., Chávez, M., & Rodríguez-Merino, L. H., 2004, *AJ*, 128, 829
- Bessell, M. S., 2011, *PASP*, 123, 1442
- Bigot, L., Mourard, D., Berio, P., et al., 2011, *A&A*, 534, L3, L3
- Blaauw, A., 1946, *Publications of the Kapteyn Astronomical Laboratory Groningen*, 52, 1
- , 1991, in *NATO Advanced Science Institutes (ASI) Series C, NATO Advanced Science Institutes (ASI) Series C*, ed. C. J. Lada, & N. D. Kylafis, Vol. 342, 125
- Bodman, E. H. L., Quillen, A. C., Ansdell, M., et al., 2016, *ArXiv e-prints*
- Boley, A. C., Granados Contreras, A. P., & Gladman, B., 2016, *ApJ*, 817, L17, L17
- Bonfils, X., Delfosse, X., Udry, S., et al., 2013, *A&A*, 549, A109, A109
- Bouvier, J. 1998, private communication
- Bouvier, J., Forestini, M., & Allain, S., 1997, *A&A*, 326, 1023
- Bouvier, J., Stauffer, J. R., Martin, E. L., et al., 1998, *A&A*, 336, 490
- Bouvier, J., Grankin, K. N., Alencar, S. H. P., et al., 2003, *A&A*, 409, 169
- Bouy, H., & Martín, E. L., 2009, *A&A*, 504, 981
- Bouy, H., Bertin, E., Sarro, L. M., et al., 2015, *A&A*, 577, A148, A148
- Bowler, B. P., 2016, *PASP*, 128.10, 102001
- Bowler, B. P., Liu, M. C., Shkolnik, E. L., & Tamura, M., 2015, *ApJS*, 216, 7, 7
- Boyajian, T. S., McAlister, H. A., van Belle, G., et al., 2012, *ApJ*, 746, 101, 101
- Boyajian, T. S., von Braun, K., van Belle, G., et al., 2013, *ApJ*, 771, 40, 40
- Boyajian, T. S., LaCourse, D. M., Rappaport, S. A., et al., 2016, *MNRAS*, 457, 3988
- Bradshaw, S. J., & Hartigan, P., 2014, *ApJ*, 795, 79, 79
- Bramich, D. M., Horne, K., Bond, I. A., et al., 2005, *MNRAS*, 359, 1096
- Bramich, D. M., & Horne, K., 2006, *MNRAS*, 367, 1677
- Brandt, T. D., & Huang, C. X., 2015a, *ApJ*, 807, 58, 58
- , 2015b, *ApJ*, 807, 24, 24
- Bressan, A., Marigo, P., Girardi, L., et al., 2012, *MNRAS*, 427, 127
- Briceño, C., Hartmann, L., Stauffer, J., & Martín, E., 1998, *AJ*, 115, 2074
- Brown, A. G. A., & Verschueren, W., 1997, *A&A*, 319, 811
- Brown, T. M., Baliber, N., Bianco, F. B., et al., 2013, *PASP*, 125, 1031

- Brucalassi, A., Pasquini, L., Saglia, R., et al., 2016, *A&A*, 592, L1, L1
- Brucalassi, A., Koppenhoefer, J., Saglia, R., et al., 2017, *ArXiv e-prints*
- Bruntt, H., Grundahl, F., Tingley, B., et al., 2003, *A&A*, 410, 323
- Burke, C. J., Gaudi, B. S., DePoy, D. L., & Pogge, R. W., 2006, *AJ*, 132, 210
- Burningham, B., Naylor, T., Littlefair, S. P., & Jeffries, R. D., 2005, *MNRAS*, 363, 1389
- Burns, J. A., Lamy, P. L., & Soter, S., 1979, *Icarus*, 40, 1
- Burrows, A., Sudarsky, D., & Hubeny, I., 2004, *ApJ*, 609, 407
- Caffau, E., Ludwig, H.-G., Steffen, M., Freytag, B., & Bonifacio, P., 2011, *Sol. Phys.*, 268, 255
- Cargile, P. A., Stassun, K. G., & Mathieu, R. D., 2008, *ApJ*, 674, 329-335, 329
- Carpenter, J. M., Mamajek, E. E., Hillenbrand, L. A., & Meyer, M. R., 2006, *ApJ*, 651, L49
- , 2009, *ApJ*, 705, 1646
- Carson, J., Thalmann, C., Janson, M., et al., 2013, *ApJ*, 763, L32, L32
- Casagrande, L., Schönrich, R., Asplund, M., et al., 2011, *A&A*, 530, A138, A138
- Casey, B. W., Mathieu, R. D., Vaz, L. P. R., Andersen, J., & Suntzeff, N. B., 1998, *AJ*, 115, 1617
- Castelli, F., & Kurucz, R. L., 2004, *ArXiv Astrophysics e-prints*
- , 2006, *A&A*, 454, 333
- Chabrier, G., Gallardo, J., & Baraffe, I., 2007, *A&A*, 472, L17
- Chatterjee, S., & Tan, J. C., 2014, *ApJ*, 780, 53, 53
- Chauvin, G., Lagrange, A.-M., Dumas, C., et al., 2004, *A&A*, 425, L29
- Chen, C. H., Mamajek, E. E., Bitner, M. A., et al., 2011, *ApJ*, 738, 122, 122
- Chen, Y., Girardi, L., Bressan, A., et al., 2014, *MNRAS*, 444, 2525
- Chen, Y., Bressan, A., Girardi, L., et al., 2015, *MNRAS*, 452, 1068
- Chiang, E., & Laughlin, G., 2013, *MNRAS*, 431, 3444
- Chiavassa, A., Bigot, L., Kervella, P., et al., 2012, *A&A*, 540, A5, A5
- Choi, J., Dotter, A., Conroy, C., et al., 2016, *ApJ*, 823, 102, 102
- Christiansen, J. L., Jenkins, J. M., Caldwell, D. A., et al., 2012, *PASP*, 124, 1279
- Chubak, C., Marcy, G., Fischer, D. A., et al., 2012, *ArXiv e-prints*
- Ciardi, D. R., van Eyken, J. C., Barnes, J. W., et al., 2015, *ApJ*, 809, 42, 42

- Cignoni, M., Degl'Innocenti, S., Prada Moroni, P. G., & Shore, S. N., 2006, *A&A*, 459, 783
- Claret, A., & Cunha, N. C. S., 1997, *A&A*, 318, 187
- Claret, A., & Bloemen, S., 2011, *A&A*, 529, A75, A75
- Claret, A., Hauschildt, P. H., & Witte, S., 2012, *A&A*, 546, A14, A14
- , 2013, *A&A*, 552, A16, A16
- Clem, J. L., VandenBerg, D. A., Grundahl, F., & Bell, R. A., 2004, *AJ*, 127, 1227
- Code, A. D., Bless, R. C., Davis, J., & Brown, R. H., 1976, *ApJ*, 203, 417
- Cody, A. M., Stauffer, J., Baglin, A., et al., 2014, *AJ*, 147, 82, 82
- Cody, A. M., Hillenbrand, L. A., David, T. J., et al., 2017, *ApJ*, 836, 41, 41
- Collier Cameron, A., & Robinson, R. D., 1989a, *MNRAS*, 236, 57
- , 1989b, *MNRAS*, 238, 657
- Collier Cameron, A., Duncan, D. K., Ehrenfreund, P., et al., 1990, *MNRAS*, 247, 415
- Collier Cameron, A., & Campbell, C. G., 1993, *A&A*, 274, 309
- Collins II, G. W., & Smith, R. C., 1985, *MNRAS*, 213, 519
- Collins, K. A., Kielkopf, J. F., Stassun, K. G., & Hessman, F. V., 2017, *AJ*, 153, 77, 77
- Connelly, J. N., Bizzarro, M., Krot, A. N., et al., 2012, *Science*, 338, 651
- Conroy, K. E., Prša, A., Stassun, K. G., et al., 2014, *PASP*, 126, 914
- Covino, E., Catalano, S., Frasca, A., et al., 2000, *A&A*, 361, L49
- Covino, E., Melo, C., Alcalá, J. M., et al., 2001, *A&A*, 375, 130
- Covino, E., Frasca, A., Alcalá, J. M., Paladino, R., & Sterzik, M. F., 2004, *A&A*, 427, 637
- Crawford, D. L., 1958, *ApJ*, 128, 185
- , 1966, in *IAU Symposium, Spectral Classification and Multicolour Photometry*, ed. K. Loden, L. O. Loden, & U. Sinnerstad, Vol. 24, 170
- , 1979, *AJ*, 84, 1858
- Crawford, D. L., & Mandwewala, N., 1976, *PASP*, 88, 917
- Croll, B., Rappaport, S., & Levine, A. M., 2015, *MNRAS*, 449, 1408
- Crossfield, I. J. M., Petigura, E., Schlieder, J. E., et al., 2015, *ApJ*, 804, 10, 10
- Crossfield, I. J. M., Ciardi, D. R., Petigura, E. A., et al., 2016, *ApJS*, 226, 7, 7

- Cutri, R. M., Skrutskie, M. F., van Dyk, S., et al., 2003, *VizieR Online Data Catalog*, 2246
- Cutri, R. M., & et al., 2012, *VizieR Online Data Catalog*, 2311
- , 2013, *VizieR Online Data Catalog*, 2328
- , 2014, *VizieR Online Data Catalog*, 2328
- Da Rio, N., Robberto, M., Soderblom, D. R., et al., 2010, *ApJ*, 722, 1092
- Dahm, S. E., 2015, *ApJ*, 813, 108, 108
- Dalle Mese, G., López-Cruz, O., Schuster, W. J., Chavarría, C., & García, J. G., 2012, *ArXiv e-prints*
- D'Antona, F., Ventura, P., & Mazzitelli, I., 2000, *ApJ*, 543, L77
- Darwin, G. H., 1879, *Proceedings of the Royal Society of London Series I*, 29, 168
- David, T. J., Stauffer, J., Hillenbrand, L. A., et al., 2015, *ApJ*, 814, 62
- David, T. J., & Hillenbrand, L. A., 2015, *ApJ*, 804, 146
- David, T. J., Conroy, K. E., Hillenbrand, L. A., et al., 2016a, *AJ*, 151, 112
- David, T. J., Hillenbrand, L. A., Cody, A. M., Carpenter, J. M., & Howard, A. W., 2016b, *ApJ*, 816, 21
- David, T. J., Hillenbrand, L. A., Petigura, E. A., et al., 2016c, *Nature*, 534, 658
- David, T. J., Petigura, E. A., Hillenbrand, L. A., et al., 2017, *ApJ*, 835, 168
- Davis, J., & Tango, W. J., 1986, *Nature*, 323, 234
- Davis, J., Ireland, M. J., North, J. R., et al., 2011, *PASA*, 28, 58
- de Bruijne, J. H. J., 1999, *MNRAS*, 310, 585
- de Bruijne, J. H. J., Hoogerwerf, R., & de Zeeuw, P. T., 2001, *A&A*, 367, 111
- de Geus, E. J., de Zeeuw, P. T., & Lub, J., 1989, *A&A*, 216, 44
- De Rosa, R. J., Patience, J., Wilson, P. A., et al., 2014, *MNRAS*, 437, 1216
- de Zeeuw, T., & Brand, J., 1985, in *Astrophysics and Space Science Library, Birth and Evolution of Massive Stars and Stellar Groups*, ed. W. Boland, & H. van Woerden, Vol. 120, 95
- de Zeeuw, P. T., Hoogerwerf, R., de Bruijne, J. H. J., Brown, A. G. A., & Blaauw, A., 1999, *AJ*, 117, 354
- Deacon, N. R., & Hambly, N. C., 2004, *A&A*, 416, 125
- Debernardi, Y., Mermilliod, J.-C., Carquillat, J.-M., & Ginestet, N., 2000, *A&A*, 354, 881
- Delfosse, X., Forveille, T., Ségransan, D., et al., 2000, *A&A*, 364, 217

- Deming, D., Knutson, H., Kammer, J., et al., 2015, *ApJ*, 805, 132, 132
- Desort, M., Lagrange, A.-M., Galland, F., Udry, S., & Mayor, M., 2007, *A&A*, 473, 983
- Di Folco, E., Thévenin, F., Kervella, P., et al., 2004, *A&A*, 426, 601
- Dieterich, S. B., Henry, T. J., Golimowski, D. A., Krist, J. E., & Tanner, A. M., 2012, *AJ*, 144, 64, 64
- Dobbie, P. D., Lodieu, N., & Sharp, R. G., 2010, *MNRAS*, 409, 1002
- Donati, J.-F., & Landstreet, J. D., 2009, *ARA&A*, 47, 333
- Donati, J. F., Moutou, C., Malo, L., et al., 2016, *Nature*, 534, 662
- Dotter, A., 2016, *ApJS*, 222, 8, 8
- Dressing, C. D., & Charbonneau, D., 2013, *ApJ*, 767, 95, 95
- , 2015, *ApJ*, 807, 45, 45
- Duchêne, G., & Kraus, A., 2013, *ARA&A*, 51, 269
- Eggen, O. J., 1995, *AJ*, 110, 823
- Eggleton, P. P., 1983, *ApJ*, 268, 368
- Ekström, S., Georgy, C., Eggenberger, P., et al., 2012, *A&A*, 537, A146, A146
- Elmegreen, B. G., 2000, *ApJ*, 530, 277
- Elmegreen, B. G., & Lada, C. J., 1977, *ApJ*, 214, 725
- Enebo, S., 1907, *Astronomische Nachrichten*, 175, 205
- Etzel, P. B. 1975, MA thesis (Masters Thesis. San Diego State University (1975))
- , 1981, in *Photometric and Spectroscopic Binary Systems*, ed. E. B. Carling, & Z. Kopal, 111
- Evans, P. A., Hellier, C., & Ramsay, G., 2006, *MNRAS*, 369, 1229
- Feiden, G. A., 2015, in *Astronomical Society of the Pacific Conference Series, Living Together: Planets, Host Stars and Binaries*, ed. S. M. Rucinski, G. Torres, & M. Zejda, Vol. 496, 137
- , 2016a, *A&A*, 593, A99, A99
- , 2016b, in *IAU Symposium, Young Stars & Planets Near the Sun*, ed. J. H. Kastner, B. Stelzer, & S. A. Metchev, Vol. 314, 79
- Feiden, G. A., & Chaboyer, B., 2012a, *ApJ*, 757, 42, 42
- , 2012b, *ApJ*, 761, 30, 30
- , 2013, *ApJ*, 779, 183, 183

- Feiden, G. A., & Chaboyer, B., 2014, *ApJ*, 789, 53, 53
- Figueras, F., Torra, J., & Jordi, C., 1991, *A&AS*, 87, 319
- Figueras, F., & Blasi, F., 1998, *A&A*, 329, 957
- Fischer, D. A., & Valenti, J., 2005, *ApJ*, 622, 1102
- Fitzpatrick, E. L., & Massa, D., 2005, *AJ*, 129, 1642
- Foreman-Mackey, D., Hogg, D. W., Lang, D., & Goodman, J., 2013, *PASP*, 125, 306
- Foreman-Mackey, D., Montet, B. T., Hogg, D. W., et al., 2015, *ApJ*, 806, 215, 215
- Fortney, J. J., Marley, M. S., Saumon, D., & Lodders, K., 2008, *ApJ*, 683, 1104-1116, 1104
- Frink, S. 1999, “Kinematics of T Tauri Stars in nearby Star Forming Regions”, PhD thesis (Astronomisches Rechen-Institut Heidelberg)
- Fulton, B. J., Petigura, E. A., Howard, A. W., et al., 2017, ArXiv e-prints
- Gagné, J., Lafrenière, D., Doyon, R., Malo, L., & Artigau, É., 2015, *ApJ*, 798, 73, 73
- Gaia Collaboration, 2016, *VizieR Online Data Catalog*, 1337
- Gaia Collaboration, Brown, A. G. A., Vallenari, A., et al., 2016, *A&A*, 595, A2, A2
- Gaia Collaboration, van Leeuwen, F., Vallenari, A., et al., 2017, *A&A*, 601, A19, A19
- Gaidos, E., & Mann, A. W., 2013, *ApJ*, 762, 41, 41
- Gaidos, E., Fischer, D. A., Mann, A. W., & Howard, A. W., 2013, *ApJ*, 771, 18, 18
- Gaidos, E., Mann, A. W., Rizzuto, A., et al., 2017, *MNRAS*, 464, 850
- Gillen, E., Aigrain, S., McQuillan, A., et al., 2014, *A&A*, 562, A50, A50
- Gillen, E., Hillenbrand, L. A., David, T. J., et al., 2017, ArXiv e-prints
- Gilliland, R. L., Brown, T. M., Guhathakurta, P., et al., 2000, *ApJ*, 545, L47
- Girardi, L., Groenewegen, M. A. T., Hatziminaoglou, E., & da Costa, L., 2005, *A&A*, 436, 895
- Girardi, L., Barbieri, M., Groenewegen, M. A. T., et al., 2012, *Astrophysics and Space Science Proceedings*, 26, 165
- Gizis, J. E., Reid, I. N., & Hawley, S. L., 2002, *AJ*, 123, 3356
- Glebocki, R., & Gnacinski, P., 2005, *VizieR Online Data Catalog*, 3244
- Goldman, B., Röser, S., Schilbach, E., et al., 2013, *A&A*, 559, A43, A43
- Grankin, K. N., Bouvier, J., Herbst, W., & Melnikov, S. Y., 2008, *A&A*, 479, 827

- Granzer, T., Schüssler, M., Caligari, P., & Strassmeier, K. G., 2000, *A&A*, 355, 1087
- Gray, D. F. 2005, *The Observation and Analysis of Stellar Photospheres*
- Gray, R. O., & Kaye, A. B., 1999, *AJ*, 118, 2993
- Gray, R. O., Corbally, C. J., Garrison, R. F., et al., 2006, *AJ*, 132, 161
- Groenewegen, M. A. T., Decin, L., Salaris, M., & De Cat, P., 2007, *A&A*, 463, 579
- Groote, D., & Hunger, K., 1982, *A&A*, 116, 64
- Guinan, E. F., & Ribas, I., 2001, *ApJ*, 546, L43
- Gully-Santiago, M. A., Herczeg, G. J., Czekala, I., et al., 2017, *ApJ*, 836, 200, 200
- Haberreiter, M., Schmutz, W., & Kosovichev, A. G., 2008, *ApJ*, 675, L53, L53
- Habets, G. M. H. J., & Heintze, J. R. W., 1981, *A&AS*, 46, 193
- Haisch Jr., K. E., Lada, E. A., & Lada, C. J., 2001, *ApJ*, 553, L153
- Hambly, N. C., Hawkins, M. R. S., & Jameson, R. F., 1993, *A&AS*, 100, 607
- Hanbury Brown, R., Davis, J., & Allen, L. R., 1974, *MNRAS*, 167, 121
- Hansen, B. M. S., & Murray, N., 2012, *ApJ*, 751, 158, 158
- Hanson, R. B., 1975, *AJ*, 80, 379
- Haro, G., Chavira, E., & Gonzalez, G., 1982, *Boletin del Instituto de Tonantzintla*, 3, 3
- Hartman, J. D., Gaudi, B. S., Holman, M. J., et al., 2009, *ApJ*, 695, 336
- Hartman, J. D., Bakos, G. Á., Kovács, G., & Noyes, R. W., 2010, *MNRAS*, 408, 475
- Hartmann, L., 2001, *AJ*, 121, 1030
- Hartmann, L., Cassen, P., & Kenyon, S. J., 1997, *ApJ*, 475, 770
- Hatzes, A. P., 1995, *ApJ*, 451, 784
- Hauck, B., & Mermilliod, M., 1980, *A&AS*, 40, 1
- , 1998, *A&AS*, 129, 431
- Hauschildt, P. H., Allard, F., Ferguson, J., Baron, E., & Alexander, D. R., 1999a, *ApJ*, 525, 871
- Hauschildt, P. H., Allard, F., & Baron, E., 1999b, *ApJ*, 512, 377
- Hayashi, C., 1961, *PASJ*, 13
- Hebb, L., Wyse, R. F. G., Gilmore, G., & Holtzman, J., 2006, *AJ*, 131, 555
- Hebb, L., Stempels, H. C., Aigrain, S., et al., 2010, *A&A*, 522, A37, A37
- Hebb, L., Cegla, H. M., Stassun, K. G., et al., 2011, *A&A*, 531, A61, A61

- Henden, A. A., Templeton, M., Terrell, D., et al., 2016, *VizieR Online Data Catalog*, 2336
- Henyey, L., Vardya, M. S., & Bodenheimer, P., 1965, *ApJ*, 142, 841
- Herbig, G. H., 1962, *ApJ*, 135, 736
- Herbst, W., Herbst, D. K., Grossman, E. J., & Weinstein, D., 1994, *AJ*, 108, 1906
- Herczeg, G. J., & Hillenbrand, L. A., 2015, *ApJ*, 808, 23, 23
- Hernández, J., Calvet, N., Hartmann, L., et al., 2005, *AJ*, 129, 856
- Hernán-Obispo, M., Gálvez-Ortiz, M. C., Anglada-Escudé, G., et al., 2010, *A&A*, 512, A45, A45
- Hernán-Obispo, M., Tuomi, M., Gálvez-Ortiz, M. C., et al., 2015, *A&A*, 576, A66, A66
- Hertzsprung, E., 1947, *Annalen van de Sterrewacht te Leiden*, 19, A1
- Hidas, M. G., Ashley, M. C. B., Webb, J. K., et al., 2005, *MNRAS*, 360, 703
- Hillenbrand, L. A., 1997, *AJ*, 113, 1733
- , 2005, *ArXiv Astrophysics e-prints*
- Hillenbrand, L. A., & White, R. J., 2004, *ApJ*, 604, 741
- Hillenbrand, L. A., Bauermeister, A., & White, R. J., 2008, in *Astronomical Society of the Pacific Conference Series, 14th Cambridge Workshop on Cool Stars, Stellar Systems, and the Sun*, ed. G. van Belle, Vol. 384, 200
- Hinkley, S., Pueyo, L., Faherty, J. K., et al., 2013, *ApJ*, 779, 153, 153
- Hinkley, S., Kraus, A. L., Ireland, M. J., et al., 2015, *ApJ*, 806, L9, L9
- Hirsch, L. A., Ciardi, D. R., Howard, A. W., et al., 2017, *AJ*, 153, 117, 117
- Høg, E., Fabricius, C., Makarov, V. V., et al., 2000, *A&A*, 355, L27
- Hohle, M. M., Neuhäuser, R., & Schutz, B. F., 2010, *Astronomische Nachrichten*, 331, 349
- Holczer, T., Shporer, A., Mazeh, T., et al., 2015, *ApJ*, 807, 170, 170
- Holmberg, J., Nordström, B., & Andersen, J., 2007, *A&A*, 475, 519
- , 2009, *A&A*, 501, 941
- Hood, B., Collier Cameron, A., Kane, S. R., et al., 2005, *MNRAS*, 360, 791
- Horch, E. P., Casetti-Dinescu, D. I., Camarata, M. A., et al., 2017, *AJ*, 153, 212, 212
- Howard, A. W., Marcy, G. W., Bryson, S. T., et al., 2012, *ApJS*, 201, 15, 15
- Howarth, I. D., 2016, *MNRAS*, 457, 3769

- Howell, S. B., VanOutryve, C., Tonry, J. L., Everett, M. E., & Schneider, R., 2005, *PASP*, 117, 1187
- Howell, S. B., Everett, M. E., Sherry, W., Horch, E., & Ciardi, D. R., 2011, *AJ*, 142, 19, 19
- Howell, S. B., Rowe, J. F., Bryson, S. T., et al., 2012, *ApJ*, 746, 123, 123
- Howell, S. B., Sobeck, C., Haas, M., et al., 2014, *PASP*, 126, 398
- Huang, C. X., Penev, K., Hartman, J. D., et al., 2015, *MNRAS*, 454, 4159
- Huber, D., Ireland, M. J., Bedding, T. R., et al., 2012, *ApJ*, 760, 32, 32
- Huélamo, N., Figueira, P., Bonfils, X., et al., 2008, *A&A*, 489, L9
- Huerta, M., Johns-Krull, C. M., Prato, L., Hartigan, P., & Jaffe, D. T., 2008, *ApJ*, 678, 472-482, 472
- Hughes, A. M., Wilner, D. J., Kamp, I., & Hogerheijde, M. R., 2008, *ApJ*, 681, 626-635, 626
- Hut, P., 1981, *A&A*, 99, 126
- Iben Jr., I., 1965, *ApJ*, 141, 993
- Ireland, M. J., Kraus, A., Martinache, F., Law, N., & Hillenbrand, L. A., 2011, *ApJ*, 726, 113, 113
- Irwin, J., Aigrain, S., Hodgkin, S., et al., 2007, *MNRAS*, 380, 541
- Ismailov, N. Z., Abdi, H. A., & Mamedxanova, G. B., 2014, *Astronomicheskij Tsirkulyar*, 1610, 1
- Jackson, R. J., & Jeffries, R. D., 2014, *MNRAS*, 441, 2111
- Janes, K., & Kim, J.-H., 2009, in *IAU Symposium, Transiting Planets*, ed. F. Pont, D. Sasselov, & M. J. Holman, Vol. 253, 548
- Jeffers, S. V., Donati, J.-F., & Collier Cameron, A., 2007, *MNRAS*, 375, 567
- Jilinski, E., Daflon, S., Cunha, K., & de La Reza, R., 2006, *A&A*, 448, 1001
- Johns-Krull, C. M., 2007, *ApJ*, 664, 975
- Johns-Krull, C. M., McLane, J. N., Prato, L., et al., 2016a, *ApJ*, 826, 206, 206
- Johns-Krull, C. M., Prato, L., McLane, J. N., et al., 2016b, *ApJ*, 830, 15, 15
- Johnson, J. A., Aller, K. M., Howard, A. W., & Crepp, J. R., 2010, *PASP*, 122, 905
- Jones, B. F., Fischer, D., & Soderblom, D. R., 1999, *AJ*, 117, 330
- Jones, J., White, R. J., Boyajian, T., et al., 2015, *ApJ*, 813, 58, 58
- Jørgensen, B. R., & Lindegren, L., 2005, *A&A*, 436, 127
- Joy, A. H., 1945, *ApJ*, 102, 168

- Kains, N., Wyatt, M. C., & Greaves, J. S., 2011, *MNRAS*, 414, 2486
- Kalas, P., Graham, J. R., Chiang, E., et al., 2008, *Science*, 322, 1345
- Kallrath, J., & Milone, E. F. 2009, *Eclipsing Binary Stars: Modeling and Analysis*
- Kamai, B. L., Vrba, F. J., Stauffer, J. R., & Stassun, K. G., 2014, *AJ*, 148, 30, 30
- Kawahara, H., Hirano, T., Kurosaki, K., Ito, Y., & Ikoma, M., 2013, *ApJ*, 776, L6, L6
- Kazarovets, E. V., 1993, *Peremennye Zvezdy*, 23
- Kennedy, G. M., Kenyon, S. J., & Bromley, B. C., 2007, *Ap&SS*, 311, 9
- Kennedy, G. M., & Wyatt, M. C., 2011, *MNRAS*, 412, 2137
- Kervella, P., Thévenin, F., Ségransan, D., et al., 2003, *A&A*, 404, 1087
- Kervella, P., Thévenin, F., Morel, P., et al., 2004, *A&A*, 413, 251
- Kiefer, F., Lecavelier des Etangs, A., Boissier, J., et al., 2014, *Nature*, 514, 462
- Kiraga, M., 2012, *Acta Astron.*, 62, 67
- Kirk, B., Conroy, K., Prša, A., et al., 2016, *AJ*, 151, 68, 68
- Kley, W., & Nelson, R. P., 2012, *ARA&A*, 50, 211
- Kobayashi, H., Kimura, H., Watanabe, S.-i., Yamamoto, T., & Müller, S., 2011, *Earth, Planets, and Space*, 63, 1067
- Kobi, D., & North, P., 1990, *A&AS*, 85, 999
- Koenigl, A., 1991, *ApJ*, 370, L39
- Köhler, R., Kunkel, M., Leinert, C., & Zinnecker, H., 2000, *A&A*, 356, 541
- Kolbl, R., Marcy, G. W., Isaacson, H., & Howard, A. W., 2015, *AJ*, 149, 18, 18
- Kopp, G., & Lean, J. L., 2011, *Geophys. Res. Lett.*, 38, L01706, L01706
- Kovács, G., Zucker, S., & Mazeh, T., 2002, *A&A*, 391, 369
- Kraft, R. P., & Wrubel, M. H., 1965, *ApJ*, 142, 703
- Kraus, A. L., & Hillenbrand, L. A., 2007, *ApJ*, 662, 413
- Kraus, A. L., Ireland, M. J., Martinache, F., & Lloyd, J. P., 2008, *ApJ*, 679, 762-782, 762
- Kraus, A. L., & Hillenbrand, L. A., 2009a, *ApJ*, 704, 531
- , 2009b, *ApJ*, 703, 1511
- Kraus, A. L., Ireland, M. J., Martinache, F., & Hillenbrand, L. A., 2011, *ApJ*, 731, 8, 8
- Kraus, A. L., & Ireland, M. J., 2012, *ApJ*, 745, 5, 5

- Kraus, A. L., & Hillenbrand, L. A., 2012, *ApJ*, 757, 141, 141
- Kraus, A. L., Cody, A. M., Covey, K. R., et al., 2015, *ApJ*, 807, 3, 3
- Kraus, A. L., Ireland, M. J., Huber, D., Mann, A. W., & Dupuy, T. J., 2016, *AJ*, 152, 8, 8
- Kraus, A. L., Douglas, S. T., Mann, A. W., et al., 2017, ArXiv e-prints
- Kreidberg, L., 2015, *PASP*, 127, 1161
- Kuiper, G. P., 1951, *Proceedings of the National Academy of Science*, 37, 1
- Kulkarni, S. R., 2016, ArXiv e-prints
- Kunzli, M., North, P., Kurucz, R. L., & Nicolet, B., 1997, *A&AS*, 122
- Kurosawa, R., Harries, T. J., & Littlefair, S. P., 2006, *MNRAS*, 372, 1879
- Kurucz, R. L., 1979, *ApJS*, 40, 1
- Kuzuhara, M., Tamura, M., Kudo, T., et al., 2013, *ApJ*, 774, 11, 11
- LaCourse, D. M., Jek, K. J., Jacobs, T. L., et al., 2015, *MNRAS*, 452, 3561
- Lacy, C. H. S., Fekel, F. C., Pavlovski, K., Torres, G., & Muterspaugh, M. W., 2016, *AJ*, 152, 2, 2
- Lafrenière, D., Jayawardhana, R., & van Kerkwijk, M. H., 2008, *ApJ*, 689, L153, L153
- Lafrenière, D., Jayawardhana, R., van Kerkwijk, M. H., Brandeker, A., & Janson, M., 2014, *ApJ*, 785, 47, 47
- Lagrange, A.-M., Gratadour, D., Chauvin, G., et al., 2009, *A&A*, 493, L21
- Lagrange, A.-M., Bonnefoy, M., Chauvin, G., et al., 2010, *Science*, 329, 57
- Laughlin, G., Bodenheimer, P., & Adams, F. C., 2004, *ApJ*, 612, L73
- Lawrence, A., Warren, S. J., Almaini, O., et al., 2013, *VizieR Online Data Catalog*, 2319
- Lecavelier Des Etangs, A., 1999, *A&AS*, 140, 15
- Lecavelier Des Etangs, A., Vidal-Madjar, A., & Ferlet, R., 1999, *A&A*, 343, 916
- Lee, B. L., von Braun, K., Mallén-Ornelas, G., et al., 2004, in *American Institute of Physics Conference Series, The Search for Other Worlds*, ed. S. S. Holt, & D. Deming, Vol. 713, 177
- Lee, E. J., & Chiang, E., 2017, ArXiv e-prints
- Lehmann-Filhés, R., 1894, *Astronomische Nachrichten*, 136, 17
- Lejeune, T., Lastennet, E., Westera, P., & Buser, R., 1999, in *Astronomical Society of the Pacific Conference Series, Spectrophotometric Dating of Stars and Galaxies*, ed. I. Hubeny, S. Heap, & R. Cornett, Vol. 192, 207

- Lépine, S., & Simon, M., 2009, *AJ*, 137, 3632
- Lester, J. B., Gray, R. O., & Kurucz, R. L., 1986, *ApJS*, 61, 509
- Levato, H., Malaroda, S., Morrell, N., & Solivella, G., 1987, *ApJS*, 64, 487
- Li, Z., & Han, Z., 2008, *MNRAS*, 387, 105
- Libralato, M., Nardiello, D., Bedin, L. R., et al., 2016, *MNRAS*, 463, 1780
- Ligi, R., Mourard, D., Lagrange, A. M., et al., 2012, *A&A*, 545, A5, A5
- Lin, D. N. C., Bodenheimer, P., & Richardson, D. C., 1996, *Nature*, 380, 606
- Littlefair, S. P., Naylor, T., Mayne, N. J., Saunders, E., & Jeffries, R. D., 2011, *MNRAS*, 413, L56
- Lloyd, J. P., 2013, *ApJ*, 774, L2, L2
- Lodieu, N., 2013, *MNRAS*, 431, 3222
- Lodieu, N., Hambly, N. C., Jameson, R. F., & Hodgkin, S. T., 2008, *MNRAS*, 383, 1385
- Lodieu, N., Dobbie, P. D., & Hambly, N. C., 2011a, *A&A*, 527, A24, A24
- , 2011b, *A&A*, 527, A24, A24
- Lodieu, N., Alonso, R., González Hernández, J. I., et al., 2015a, *A&A*, 584, A128, A128
- , 2015b, *A&A*, 584, A128, A128
- Lomb, N. R., 1976, *Ap&SS*, 39, 447
- Long, M., Romanova, M. M., & Lovelace, R. V. E., 2005, *ApJ*, 634, 1214
- López-Morales, M., 2007, *ApJ*, 660, 732
- López-Morales, M., & Ribas, I., 2005, *ApJ*, 631, 1120
- Lovis, C., & Mayor, M., 2007, *A&A*, 472, 657
- Lowrance, P. J., Schneider, G., Kirkpatrick, J. D., et al., 2000, *ApJ*, 541, 390
- Luger, R., Agol, E., Kruse, E., et al., 2016, *AJ*, 152, 100, 100
- Luger, R., Kruse, E., Foreman-Mackey, D., Agol, E., & Saunders, N., 2017, *ArXiv e-prints*
- Luhman, K. L., & Mamajek, E. E., 2012, *ApJ*, 758, 31, 31
- Lund, M. N., Handberg, R., Davies, G. R., Chaplin, W. J., & Jones, C. D., 2015, *ApJ*, 806, 30, 30
- MacDonald, J., & Mullan, D. J., 2017, *ApJ*, 834, 67, 67
- Mace, G. N., Prato, L., Torres, G., et al., 2012, *AJ*, 144, 55, 55

- Maeder, A., & Peytremann, E., 1970, *A&A*, 7, 120
- Mahadevan, S., Ramsey, L., Bender, C., et al., 2012, in *Proc. SPIE, Ground-based and Airborne Instrumentation for Astronomy IV*, Vol. 8446, 84461S
- Mahmud, N. I., Crockett, C. J., Johns-Krull, C. M., et al., 2011, *ApJ*, 736, 123, 123
- Malagnini, M. L., Morossi, C., Rossi, L., & Kurucz, R. L., 1986, *A&A*, 162, 140
- Malavolta, L., Nascimbeni, V., Piotto, G., et al., 2016, *A&A*, 588, A118, A118
- Maldonado, J., Scandariato, G., Stelzer, B., et al., 2017, *A&A*, 598, A27, A27
- Mamajek, E. E., 2009, in *American Institute of Physics Conference Series, American Institute of Physics Conference Series*, ed. T. Usuda, M. Tamura, & M. Ishii, Vol. 1158, 3
- Mamajek, E. E., & Hillenbrand, L. A., 2008, *ApJ*, 687, 1264-1293, 1264
- Mamajek, E. E., Quillen, A. C., Pecaut, M. J., et al., 2012, *AJ*, 143, 72, 72
- Mandel, K., & Agol, E., 2002, *ApJ*, 580, L171
- Mann, A. W., Gaidos, E., Lépine, S., & Hilton, E. J., 2012, *ApJ*, 753, 90, 90
- Mann, A. W., Feiden, G. A., Gaidos, E., Boyajian, T., & von Braun, K., 2015, *ApJ*, 804, 64, 64
- Mann, A. W., Newton, E. R., Rizzuto, A. C., et al., 2016a, *AJ*, 152, 61, 61
- Mann, A. W., Gaidos, E., Mace, G. N., et al., 2016b, *ApJ*, 818, 46, 46
- Mann, A. W., Newton, E. R., Rizzuto, A. C., et al., 2016c, *AJ*, 152, 61, 61
- Mann, A. W., Gaidos, E., Vanderburg, A., et al., 2017, *AJ*, 153, 64, 64
- Marilli, E., Frasca, A., Covino, E., et al., 2007, *A&A*, 463, 1081
- Marín-Franch, A., Aparicio, A., Piotto, G., et al., 2009, *ApJ*, 694, 1498
- Marois, C., Macintosh, B., Barman, T., et al., 2008, *Science*, 322, 1348
- Marois, C., Zuckerman, B., Konopacky, Q. M., Macintosh, B., & Barman, T., 2010, *Nature*, 468, 1080
- Martín, E. L., 1998, *AJ*, 115, 351
- Mason, K. O., 1997, *MNRAS*, 285, 493
- Mason, B. D., Martin, C., Hartkopf, W. I., et al., 1999, *AJ*, 117, 1890
- Masuda, K., & Winn, J. N., 2017, *AJ*, 153, 187, 187
- Mathieu, R. D., & Mazeh, T., 1988, *ApJ*, 326, 256
- Mathieu, R. D., Baraffe, I., Simon, M., Stassun, K. G., & White, R., 2007, *Protostars and Planets V*, 411

- Mawet, D., Pueyo, L., Lawson, P., et al., 2012, in Proc. SPIE, Space Telescopes and Instrumentation 2012: Optical, Infrared, and Millimeter Wave, Vol. 8442, 844204
- Mayne, N. J., & Naylor, T., 2008, MNRAS, 386, 261
- Mayor, M., Udry, S., Naef, D., et al., 2004, A&A, 415, 391
- Mazeh, T., Holczer, T., & Shporer, A., 2015, ApJ, 800, 142, 142
- McClure, R. D., 1980, in BAAS, Bulletin of the American Astronomical Society, Vol. 12, 867
- , 1982, ApJ, 254, 606
- McQuillan, A., Aigrain, S., & Mazeh, T., 2013, MNRAS, 432, 1203
- Meibom, S., & Mathieu, R. D., 2005, ApJ, 620, 970
- Meibom, S., Mathieu, R. D., & Stassun, K. G., 2006, ApJ, 653, 621
- Meibom, S., Torres, G., Fressin, F., et al., 2013, Nature, 499, 55
- Meibom, S., Barnes, S. A., Platais, I., et al., 2015, Nature, 517, 589
- Melis, C., Reid, M. J., Mioduszewski, A. J., Stauffer, J. R., & Bower, G. C., 2014, Science, 345, 1029
- Melo, C. H. F., Covino, E., Alcalá, J. M., & Torres, G., 2001, A&A, 378, 898
- Meng, H. Y. A., Plavchan, P., Rieke, G. H., et al., 2016, ApJ, 823, 58, 58
- Mermilliod, J. C., 1981, A&A, 97, 235
- Mermilliod, J.-C., Rosvick, J. M., Duquennoy, A., & Mayor, M., 1992, A&A, 265, 513
- Mermilliod, J.-C., Bratschi, P., & Mayor, M., 1997, A&A, 320, 74
- Mermilliod, J.-C., Mayor, M., & Udry, S., 2009, A&A, 498, 949
- Metchev, S. A., & Hillenbrand, L. A., 2009, ApJS, 181, 62
- Meynet, G., & Maeder, A., 2000, A&A, 361, 101
- Mighell, K. J., & Plavchan, P., 2013, AJ, 145, 148, 148
- Miller, A. A., Irwin, J., Aigrain, S., Hodgkin, S., & Hebb, L., 2008, MNRAS, 387, 349
- Milone, E. F., & Schiller, S. J., 2013, in IAU Symposium, Advancing the Physics of Cosmic Distances, ed. R. de Grijs, Vol. 289, 227
- Mochejska, B. J., Stanek, K. Z., Sasselov, D. D., et al., 2005, AJ, 129, 2856
- Mochejska, B. J., Stanek, K. Z., Sasselov, D. D., et al., 2006, AJ, 131, 1090
- Mochejska, B. J., Stanek, K. Z., Sasselov, D. D., et al., 2008, Acta Astron., 58, 263

- Mohanty, S., Basri, G., Jayawardhana, R., et al., 2004, *ApJ*, 609, 854
- Monguió, M., Figueras, F., & Grosbøl, P., 2014, *A&A*, 568, A119, A119
- Montalto, M., Piotto, G., Desidera, S., et al., 2007, *A&A*, 470, 1137
- Montalto, M., Piotto, G., Desidera, S., et al., 2009, *A&A*, 505, 1129
- Montalto, M., Villanova, S., Koppenhoefer, J., et al., 2011, *A&A*, 535, A39, A39
- Montet, B. T., Crepp, J. R., Johnson, J. A., Howard, A. W., & Marcy, G. W., 2014, *ApJ*, 781, 28, 28
- Moon, T. T., 1985, *Commun. Univ. London Obs.*, 78
- Moon, T. T., & Dworetzky, M. M., 1985, *MNRAS*, 217, 305
- Moór, A., Ábrahám, P., Derekas, A., et al., 2006, *ApJ*, 644, 525
- Morales, J. C., Ribas, I., & Jordi, C., 2008, *A&A*, 478, 507
- Morales, J. C., Gallardo, J., Ribas, I., et al., 2010, *ApJ*, 718, 502
- Morales-Calderón, M., Stauffer, J. R., Hillenbrand, L. A., et al., 2011, *ApJ*, 733, 50, 50
- Morossi, C., & Malagnini, M. L., 1985, *A&AS*, 60, 365
- Morton, T. D. 2015, VESPA: False positive probabilities calculator, *Astrophysics Source Code Library*
- Mozurkewich, D., Armstrong, J. T., Hindsley, R. B., et al., 2003, *AJ*, 126, 2502
- Mullan, D. J., & MacDonald, J., 2001, *ApJ*, 559, 353
- Munari, U., Dallaporta, S., Siviero, A., et al., 2004, *A&A*, 418, L31
- Munari, U., Sordo, R., Castelli, F., & Zwitter, T., 2005, *A&A*, 442, 1127
- Napiwotzki, R., Schoenberner, D., & Wenske, V., 1993, *A&A*, 268, 653
- Nascimbeni, V., Bedin, L. R., Piotto, G., De Marchi, F., & Rich, R. M., 2012, *A&A*, 541, A144, A144
- Naylor, T., 2009, *MNRAS*, 399, 432
- Nelson, B., & Davis, W. D., 1972, *ApJ*, 174, 617
- Nesvorný, D., Vokrouhlický, D., & Morbidelli, A., 2007, *AJ*, 133, 1962
- Netopil, M., Paunzen, E., Heiter, U., & Soubiran, C., 2016, *A&A*, 585, A150, A150
- Nidever, D. L., Marcy, G. W., Butler, R. P., Fischer, D. A., & Vogt, S. S., 2002, *ApJS*, 141, 503
- Niels Bohr Institute, U. o. C., Institute of Astronomy UK, C., & Real Instituto y Observatorio de La Armada en San Fernando, 2014, *VizieR Online Data Catalog*, 1327

- Nielsen, E. L., Liu, M. C., Wahhaj, Z., et al., 2013, *ApJ*, 776, 4, 4
- Nieva, M.-F., 2013, *A&A*, 550, A26, A26
- Nieva, M.-F., & Simón-Díaz, S., 2011, *A&A*, 532, A2, A2
- Nordgren, T. E., Sudol, J. J., & Mozurkewich, D., 2001, *AJ*, 122, 2707
- Nordström, B., Mayor, M., Andersen, J., et al., 2004, *A&A*, 418, 989
- North, P., & Zahn, J.-P., 2004, *New A Rev.*, 48, 741
- Norton, A. J., Wheatley, P. J., West, R. G., et al., 2007, *A&A*, 467, 785
- Öberg, K. I., Murray-Clay, R., & Bergin, E. A., 2011, *ApJ*, 743, L16, L16
- Obermeier, C., Henning, T., Schlieder, J. E., et al., 2016, *AJ*, 152, 223, 223
- Ogilvie, G. I., 2014, *ARA&A*, 52, 171
- Olsen, E. H., 1983, *A&AS*, 54, 55
- , 1988, *A&A*, 189, 173
- Olsen, E. H., & Perry, C. L., 1984, *A&AS*, 56, 229
- O’Neal, D., Neff, J. E., & Saar, S. H., 1998, *ApJ*, 507, 919
- O’Neal, D., Neff, J. E., Saar, S. H., & Mines, J. K., 2001, *AJ*, 122, 1954
- O’Neal, D., Neff, J. E., Saar, S. H., & Cuntz, M., 2004, *AJ*, 128, 1802
- Önehag, A., Gustafsson, B., Eriksson, K., & Edvardsson, B., 2009, *A&A*, 498, 527
- Onitsuka, M., Fukui, A., Narita, N., et al., 2017, *PASJ*, 69, L2, L2
- Owen, J. E., & Wu, Y., 2013, *ApJ*, 775, 105, 105
- , 2016, *ApJ*, 817, 107, 107
- , 2017, *ArXiv e-prints*
- Papaloizou, J. C. B., 2007, *A&A*, 463, 775
- Paxton, B., Bildsten, L., Dotter, A., et al., 2011, *ApJS*, 192, 3, 3
- Paxton, B., Cantiello, M., Arras, P., et al., 2013, *ApJS*, 208, 4, 4
- Paxton, B., Marchant, P., Schwab, J., et al., 2015, *ApJS*, 220, 15, 15
- Pearce, J. A., 1957, *Publications of the Dominion Astrophysical Observatory Victoria*, 10, 435
- Pecaut, M. J., Mamajek, E. E., & Bubar, E. J., 2012, *ApJ*, 746, 154, 154
- Pecaut, M. J., & Mamajek, E. E., 2013, *ApJS*, 208, 9, 9
- , 2016, *MNRAS*, 461, 794
- Pepper, J., Stanek, K. Z., Pogge, R. W., et al., 2008, *AJ*, 135, 907

- Pepper, J., Gillen, E., Parviainen, H., et al., 2017, *AJ*, 153, 177, 177
- Pérez, L. M., Carpenter, J. M., Andrews, S. M., et al., 2016, *Science*, 353, 1519
- Perryman, M. A. C., Brown, A. G. A., Lebreton, Y., et al., 1998, *A&A*, 331, 81
- Peterson, D. M., Hummel, C. A., Pauls, T. A., et al., 2006, *Nature*, 440, 896
- Petigura, E. A., Howard, A. W., & Marcy, G. W., 2013, *Proceedings of the National Academy of Science*, 110, 19273
- Petigura, E. A., Schlieder, J. E., Crossfield, I. J. M., et al., 2015, *ApJ*, 811, 102, 102
- Petigura, E. A., Howard, A. W., Lopez, E. D., et al., 2016, *ApJ*, 818, 36, 36
- Petigura, E. A., Sinukoff, E., Lopez, E. D., et al., 2017, *AJ*, 153, 142, 142
- Petrov, P. P., Shcherbakov, V. A., Berdyugina, S. V., et al., 1994, *A&AS*, 107
- Pietrzyński, G., Graczyk, D., Gieren, W., et al., 2013, *Nature*, 495, 76
- Pinfield, D. J., Hodgkin, S. T., Jameson, R. F., et al., 2000, *MNRAS*, 313, 347
- Pinsonneault, M. H., Terndrup, D. M., Hanson, R. B., & Stauffer, J. R., 2004, *ApJ*, 600, 946
- Pollacco, D. L., Skillen, I., Collier Cameron, A., et al., 2006, *PASP*, 118, 1407
- Pont, F., & Eyer, L., 2004, *MNRAS*, 351, 487
- Popper, D. M., & Etzel, P. B., 1981, *AJ*, 86, 102
- Prato, L., Huerta, M., Johns-Krull, C. M., et al., 2008, *ApJ*, 687, L103, L103
- Preibisch, T., & Zinnecker, H., 1999, *AJ*, 117, 2381
- Preibisch, T., Guenther, E., & Zinnecker, H., 2001, *AJ*, 121, 1040
- Preibisch, T., Brown, A. G. A., Bridges, T., Guenther, E., & Zinnecker, H., 2002, *AJ*, 124, 404
- Preibisch, T., & Mamajek, E. “The Nearest OB Association: Scorpius-Centaurus (Sco OB2)”, 2008, in *Handbook of Star Forming Regions, Volume II*, ed. B. Reipurth, 235
- Prša, A., & Zwitter, T., 2005, *ApJ*, 628, 426
- Prša, A., Batalha, N., Slawson, R. W., et al., 2011, *AJ*, 141, 83, 83
- Queloz, D., Allain, S., Mermilliod, J.-C., Bouvier, J., & Mayor, M., 1998, *A&A*, 335, 183
- Quillen, A. C., & Holman, M., 2000, *AJ*, 119, 397
- Quinn, S. N., White, R. J., Latham, D. W., et al., 2012, *ApJ*, 756, L33, L33
- Quinn, S. N., White, R. J., Latham, D. W., et al., 2014, *ApJ*, 787, 27, 27

- Quirrenbach, A., Amado, P. J., Caballero, J. A., et al., 2014, in Proc. SPIE, Ground-based and Airborne Instrumentation for Astronomy V, Vol. 9147, 91471F
- Raetz, S., Schmidt, T. O. B., Czesla, S., et al., 2016, MNRAS, 460, 2834
- Rafikov, R. R., 2006, ApJ, 648, 666
- Rappaport, S., Levine, A., Chiang, E., et al., 2012, ApJ, 752, 1, 1
- Rappaport, S., Sanchis-Ojeda, R., Rogers, L. A., Levine, A., & Winn, J. N., 2013, ApJ, 773, L15, L15
- Rappaport, S., Barclay, T., DeVore, J., et al., 2014, ApJ, 784, 40, 40
- Rappaport, S., Gary, B. L., Kaye, T., et al., 2016, MNRAS, 458, 3904
- Readhead, A. C. S., Nakajima, T. S., Pearson, T. J., et al., 1988, AJ, 95, 1278
- Rebull, L. M., 2001, AJ, 121, 1676
- Rebull, L. M., Stauffer, J. R., Bouvier, J., et al., 2016a, AJ, 152, 113, 113
- Rebull, L. M., Stauffer, J. R., Bouvier, J., et al., 2016b, AJ, 152, 114, 114
- Rebull, L. M., Stauffer, J. R., Hillenbrand, L. A., et al., 2017, ApJ, 839, 92, 92
- Reggiani, M., Robberto, M., Da Rio, N., et al., 2011, A&A, 534, A83, A83
- Reid, N., 1993, MNRAS, 265, 785
- Reiners, A., 2012, Living Reviews in Solar Physics, 9, 1, 1
- Reiners, A., Basri, G., & Mohanty, S., 2005, ApJ, 634, 1346
- Rhee, J. H., Song, I., Zuckerman, B., & McElwain, M., 2007, ApJ, 660, 1556
- Ribas, I., 2003, A&A, 398, 239
- , 2006, Ap&SS, 304, 89
- Ricker, G. R., Winn, J. N., Vanderspek, R., et al., 2015, Journal of Astronomical Telescopes, Instruments, and Systems, 1.1, 014003, 014003
- Rieke, G. H., Su, K. Y. L., Stansberry, J. A., et al., 2005, ApJ, 620, 1010
- Rizzuto, A. C., Ireland, M. J., & Robertson, J. G., 2011, MNRAS, 416, 3108
- Rizzuto, A. C., Ireland, M. J., & Kraus, A. L., 2015, MNRAS, 448, 2737
- Roeser, S., Demleitner, M., & Schilbach, E., 2010, AJ, 139, 2440
- Romanova, M. M., Ustyugova, G. V., Koldoba, A. V., & Lovelace, R. V. E., 2002, ApJ, 578, 420
- , 2004, ApJ, 610, 920
- Romanova, M. M., & Lovelace, R. V. E., 2006, ApJ, 645, L73

- Röser, S., Schilbach, E., Piskunov, A. E., Kharchenko, N. V., & Scholz, R.-D., 2011, *A&A*, 531, A92, A92
- Rosvick, J. M., & Robb, R., 2006, *AJ*, 132, 2309
- Rucinski, S. M., Matthews, J. M., Kuschnig, R., et al., 2008, *MNRAS*, 391, 1913
- Salpeter, E. E., 1955, *ApJ*, 121, 161
- Sanchis-Ojeda, R., Rappaport, S., Pallè, E., et al., 2015, *ApJ*, 812, 112, 112
- Sarro, L. M., Bouy, H., Berihuete, A., et al., 2014, *A&A*, 563, A45, A45
- Sato, B., Izumiura, H., Toyota, E., et al., 2007, *ApJ*, 661, 527
- Scargle, J. D., 1982, *ApJ*, 263, 835
- Schaller, G., Schaerer, D., Meynet, G., & Maeder, A., 1992, *A&AS*, 96, 269
- Schiller, S. J., & Milone, E. F., 1987, *AJ*, 93, 1471
- Schlaufman, K. C., & Winn, J. N., 2013, *ApJ*, 772, 143, 143
- Schlegel, D. J., Finkbeiner, D. P., & Davis, M., 1998, *ApJ*, 500, 525
- Schmidt, T. O. B., Neuhäuser, R., Briceño, C., et al., 2016, *A&A*, 593, A75, A75
- Schröder, C., Reiners, A., & Schmitt, J. H. M. M., 2009, *A&A*, 493, 1099
- Schuessler, M., & Solanki, S. K., 1992, *A&A*, 264, L13
- Sciortino, S., Damiani, F., Favata, F., & Micela, G., 1998, *A&A*, 332, 825
- Seager, S., & Mallén-Ornelas, G., 2003, *ApJ*, 585, 1038
- Short, C. I., & Doyle, J. G., 1998, *A&A*, 336, 613
- Shu, F. H., Adams, F. C., & Lizano, S., 1987, *ARA&A*, 25, 23
- Siess, L., Dufour, E., & Forestini, M., 2000, *A&A*, 358, 593
- Sing, D. K., 2010, *A&A*, 510, A21, A21
- Slawson, R. W., Prša, A., Welsh, W. F., et al., 2011, *AJ*, 142, 160, 160
- Slesnick, C. L., Carpenter, J. M., & Hillenbrand, L. A., 2006, *AJ*, 131, 3016
- Slesnick, C. L., Hillenbrand, L. A., & Carpenter, J. M., 2008, *ApJ*, 688, 377-397, 377
- Smalley, B., 1993, *A&A*, 274, 391
- Smalley, B., & Dworetzky, M. M., 1995, *A&A*, 293, 446
- Soderblom, D. R., 2010, *ARA&A*, 48, 581
- Soderblom, D. R., Stauffer, J. R., Hudon, J. D., & Jones, B. F., 1993a, *ApJS*, 85, 315
- Soderblom, D. R., Jones, B. F., Balachandran, S., et al., 1993b, *AJ*, 106, 1059

- Soderblom, D. R., King, J. R., Siess, L., Jones, B. F., & Fischer, D., 1999, *AJ*, 118, 1301
- Soderblom, D. R., Laskar, T., Valenti, J. A., Stauffer, J. R., & Rebull, L. M., 2009, *AJ*, 138, 1292
- Soderblom, D. R., Hillenbrand, L. A., Jeffries, R. D., Mamajek, E. E., & Naylor, T., 2014, *Protostars and Planets VI*, 219
- Somers, G., & Pinsonneault, M. H., 2015, *ApJ*, 807, 174, 174
- Song, I., Caillault, J.-P., Barrado y Navascués, D., Stauffer, J. R., & Randich, S., 2000, *ApJ*, 533, L41
- Song, I., Caillault, J.-P., Barrado y Navascués, D., & Stauffer, J. R., 2001, *ApJ*, 546, 352
- Southworth, J., 2012, *MNRAS*, 426, 1291
- , 2013, *A&A*, 557, A119, A119
- Southworth, J., Maxted, P. F. L., & Smalley, B., 2004a, *MNRAS*, 351, 1277
- , 2004b, *MNRAS*, 349, 547
- , 2005, *A&A*, 429, 645
- Southworth, J., Bruntt, H., & Buzasi, D. L., 2007, *A&A*, 467, 1215
- Spiegel, D. S., & Burrows, A., 2012, *ApJ*, 745, 174, 174
- Stassun, K. G., Mathieu, R. D., Vaz, L. P. R., Stroud, N., & Vrba, F. J., 2004, *ApJS*, 151, 357
- Stassun, K. G., Mathieu, R. D., & Valenti, J. A., 2006, *Nature*, 440, 311
- , 2007, *ApJ*, 664, 1154
- Stassun, K. G., Mathieu, R. D., Cargile, P. A., et al., 2008, *Nature*, 453, 1079
- Stassun, K. G., Kratter, K. M., Scholz, A., & Dupuy, T. J., 2012, *ApJ*, 756, 47, 47
- Stassun, K. G., Feiden, G. A., & Torres, G., 2014, *New A Rev.*, 60, 1
- Stassun, K. G., & Torres, G., 2016a, *AJ*, 152, 180, 180
- , 2016b, *ApJ*, 831, L6, L6
- Stauffer, J., Klemola, A., Prosser, C., & Probst, R., 1991, *AJ*, 101, 980
- Stauffer, J. R., Caillault, J.-P., Gagne, M., Prosser, C. F., & Hartmann, L. W., 1994, *ApJS*, 91, 625
- Stauffer, J. R., Hartmann, L. W., & Barrado y Navascués, D., 1995, *ApJ*, 454, 910
- Stauffer, J. R., Schultz, G., & Kirkpatrick, J. D., 1998, *ApJ*, 499, L199
- Stauffer, J. R., Barrado y Navascués, D., Bouvier, J., et al., 1999, *ApJ*, 527, 219

- Stauffer, J. R., Hartmann, L. W., Fazio, G. G., et al., 2007, *ApJS*, 172, 663
- Stauffer, J., Cody, A. M., McGinnis, P., et al., 2015, *AJ*, 149, 130, 130
- Stauffer, J., Rebull, L., Bouvier, J., et al., 2016, *AJ*, 152, 115, 115
- Stauffer, J., Collier Cameron, A., Jardine, M., et al., 2017, *AJ*, 153, 152, 152
- Stempels, H. C., Hebb, L., Stassun, K. G., et al., 2008, *A&A*, 481, 747
- Strassmeier, K. G., 2009, *A&A Rev.*, 17, 251
- Street, R. A., Horne, K., Lister, T. A., et al., 2003, *MNRAS*, 340, 1287
- Strom, S. E., Wolff, S. C., & Dror, D. H. A., 2005, *AJ*, 129, 809
- Strömgren, B., 1951, *AJ*, 56, 142
- , 1966, *ARA&A*, 4, 433
- Su, K. Y. L., Rieke, G. H., Stansberry, J. A., et al., 2006, *ApJ*, 653, 675
- Sweet, I. P. A., & Roy, A. E., 1953, *MNRAS*, 113, 701
- Takeda, G., Ford, E. B., Sills, A., et al., 2007, *ApJS*, 168, 297
- Tamura, M., Suto, H., Nishikawa, J., et al., 2012, in *Proc. SPIE, Ground-based and Airborne Instrumentation for Astronomy IV*, Vol. 8446, 84461T
- Tetzlaff, N., Neuhauser, R., & Hohle, M. M., 2011, *MNRAS*, 410, 190
- Thalmann, C., Janson, M., Garufi, A., et al., 2016, *ApJ*, 828, L17, L17
- Thébaud, P., & Beust, H., 2001, *A&A*, 376, 621
- Tian, H.-J., Gupta, P., Sesar, B., et al., 2017, *ArXiv e-prints*
- Tognelli, E., Prada Moroni, P. G., & Degl’Innocenti, S., 2011, *A&A*, 533, A109, A109
- Tokovinin, A., Thomas, S., Sterzik, M., & Udry, S., 2006, *A&A*, 450, 681
- Tonry, J., & Davis, M., 1979, *AJ*, 84, 1511
- Torres, G., 2003, *Information Bulletin on Variable Stars*, 5402
- , 2013, *Astronomische Nachrichten*, 334, 4
- Torres, G., & Ribas, I., 2002, *ApJ*, 567, 1140
- Torres, G., Lacy, C. H., Marschall, L. A., Sheets, H. A., & Mader, J. A., 2006, *ApJ*, 640, 1018
- Torres, G., Andersen, J., & Giménez, A., 2010, *A&A Rev.*, 18, 67
- Townsend, R. H. D., Rivinius, T., Rowe, J. F., et al., 2013, *ApJ*, 769, 33, 33
- Trilling, D. E., Bryden, G., Beichman, C. A., et al., 2008, *ApJ*, 674, 1086-1105, 1086

- Trumpler, R. J., 1921, Lick Observatory Bulletin, 10, 110
- Tuthill, P. G., Monnier, J. D., Danchi, W. C., Wishnow, E. H., & Haniff, C. A., 2000, PASP, 112, 555
- Ungren, A. R., & Weis, E. W., 1977, AJ, 82, 978
- Ungren, A. R., Weis, E. W., & Hanson, R. B., 1985, AJ, 90, 2039
- Vaccaro, T. R., Wilson, R. E., Van Hamme, W., & Terrell, D., 2015, ApJ, 810, 157, 157
- Valenti, J. A., & Fischer, D. A., 2005, ApJS, 159, 141
- van Altena, W. F., 1966, AJ, 71, 482
- , 1969, AJ, 74, 2
- van Belle, G. T., & von Braun, K., 2009, ApJ, 694, 1085
- van Bueren, H. G., 1952, Bull. Astron. Inst. Netherlands, 11, 385
- van Eyken, J. C., Ciardi, D. R., von Braun, K., et al., 2012, ApJ, 755, 42, 42
- Van Eylen, V., Winn, J. N., & Albrecht, S., 2016, ApJ, 824, 15, 15
- van Leeuwen, F., 2009, A&A, 497, 209
- van Maanen, A., 1945, ApJ, 102, 26
- van Saders, J. L., & Gaudi, B. S., 2011, ApJ, 729, 63, 63
- Vanderburg, A., 2014, ArXiv e-prints
- Vanderburg, A., & Johnson, J. A., 2014, PASP, 126, 948
- Vanderburg, A., Johnson, J. A., Rappaport, S., et al., 2015, Nature, 526, 546
- Vanderburg, A., Latham, D. W., Buchhave, L. A., et al., 2016, ApJS, 222, 14, 14
- Vican, L., 2012, AJ, 143, 135, 135
- Vigan, A., Patience, J., Marois, C., et al., 2012, A&A, 544, A9, A9
- Vilardell, F., Ribas, I., Jordi, C., Fitzpatrick, E. L., & Guinan, E. F., 2010, A&A, 509, A70, A70
- Vogt, S. S., Allen, S. L., Bigelow, B. C., et al., 1994, in Proc. SPIE, Instrumentation in Astronomy VIII, ed. D. L. Crawford, & E. R. Craine, Vol. 2198, 362
- von Braun, K., Lee, B. L., Mallén-Ornelas, G., et al., 2004, in American Institute of Physics Conference Series, The Search for Other Worlds, ed. S. S. Holt, & D. Deming, Vol. 713, 181
- von Braun, K., Lee, B. L., Seager, S., et al., 2005, PASP, 117, 141
- Wang, J., Fischer, D. A., Xie, J.-W., & Ciardi, D. R., 2014, ApJ, 791, 111, 111

- Washuettl, A., & Strassmeier, K. G., 2001, *A&A*, 370, 218
- Weinberg, M. D., Shapiro, S. L., & Wasserman, I., 1987, *ApJ*, 312, 367
- Weis, E. W., 1983, *PASP*, 95, 29
- Weis, E. W., Deluca, E. E., & Upgren, A. R., 1979, *PASP*, 91, 766
- Weis, E. W., & Hanson, R. B., 1988, *AJ*, 96, 148
- Weldrake, D. T. F., Sackett, P. D., Bridges, T. J., & Freeman, K. C., 2005, *ApJ*, 620, 1043
- Weldrake, D. T. F., Sackett, P. D., & Bridges, T. J., 2008, *ApJ*, 674, 1117-1129, 1117
- Wesselink, A. J., Paranya, K., & DeVorkin, K., 1972, *A&AS*, 7, 257
- Wiling, B. A., Gagné, M., & Allen, L. E. “Star Formation in the ρ Ophiuchi Molecular Cloud”, 2008, in *Handbook of Star Forming Regions, Volume II*, ed. B. Reipurth, 351
- Wilson, R. E., 1994, *PASP*, 106, 921
- Witte, M. G., & Savonije, G. J., 2002, *A&A*, 386, 222
- Wizinowich, P. L., Acton, D. S., Lai, O., et al., 2000, in *Proc. SPIE, Adaptive Optical Systems Technology*, ed. P. L. Wizinowich, Vol. 4007, 2
- Wolff, S. C., Strom, S. E., Dror, D., & Venn, K., 2007, *AJ*, 133, 1092
- Wraight, K. T., White, G. J., Bewsher, D., & Norton, A. J., 2011, *MNRAS*, 416, 2477
- Wright, E. L., Eisenhardt, P. R. M., Mainzer, A. K., et al., 2010, *AJ*, 140, 1868-1881, 1868
- Wright, N. J., Drake, J. J., Mamajek, E. E., & Henry, G. W., 2011, *ApJ*, 743, 48, 48
- Wu, Y., Singh, H. P., Prugniel, P., Gupta, R., & Koleva, M., 2011, *A&A*, 525, A71, A71
- Wyatt, M. C., 2008, *ARA&A*, 46, 339
- Yadav, R. K., Gastine, T., Christensen, U. R., & Reiners, A., 2015, *A&A*, 573, A68, A68
- Yi, S., Demarque, P., Kim, Y.-C., et al., 2001, *ApJS*, 136, 417
- Yu, L., Winn, J. N., Gillon, M., et al., 2015, *ApJ*, 812, 48, 48
- Yu, L., Donati, J.-F., Hébrard, E. M., et al., 2017, *MNRAS*, 467, 1342
- Zacharias, N., Finch, C. T., Girard, T. M., et al., 2013, *AJ*, 145, 44, 44
- Zacharias, N., Finch, C., Subasavage, J., et al., 2015, *AJ*, 150, 101, 101
- Zacharias, N., Finch, C., & Frouard, J., 2017, *AJ*, 153, 166, 166

- Zahn, J.-P., 1975, *A&A*, 41, 329
- , 1977, *A&A*, 57, 383
- , 1989, *A&A*, 220, 112
- , 2008, in *EAS Publications Series*, *EAS Publications Series*, ed. M.-J. Goupil, & J.-P. Zahn, Vol. 29, 67
- Zahn, J.-P., & Bouchet, L., 1989, *A&A*, 223, 112
- Zinner, E., 1913, *Astronomische Nachrichten*, 195, 453
- Zorec, J., & Royer, F., 2012, *A&A*, 537, A120, A120
- Zuckerman, B., 2001, *ARA&A*, 39, 549
- Zuckerman, B., Rhee, J. H., Song, I., & Bessell, M. S., 2011, *ApJ*, 732, 61, 61
- Zuckerman, B., Melis, C., Rhee, J. H., Schneider, A., & Song, I., 2012, *ApJ*, 752, 58, 58